Research Topics

# New trends in vascular biology
## 2024

**Edited by**
Masanori Aikawa, Hong Chen, Delphine Gomez, Yun Fang,
Gabrielle Fredman, Shizuka Uchida, Margreet R. De Vries,
Hiroshi Iwata and Hiromi Yanagisawa

**Coordinated by**
Sarvesh Chelvanambi

**Published in**
Frontiers in Cardiovascular Medicine

ISSN 1664-8714
ISBN 978-2-8325-6685-5
DOI 10.3389/978-2-8325-6685-5

**Generative AI statement**
Any alternative text (Alt text) provided alongside figures in the articles in this ebook has been generated by Frontiers with the support of artificial intelligence and reasonable efforts have been made to ensure accuracy, including review by the authors wherever possible. If you identify any issues, please contact us.

## About Frontiers

Frontiers is more than just an open access publisher of scholarly articles: it is a pioneering approach to the world of academia, radically improving the way scholarly research is managed. The grand vision of Frontiers is a world where all people have an equal opportunity to seek, share and generate knowledge. Frontiers provides immediate and permanent online open access to all its publications, but this alone is not enough to realize our grand goals.

## Frontiers journal series

The Frontiers journal series is a multi-tier and interdisciplinary set of open-access, online journals, promising a paradigm shift from the current review, selection and dissemination processes in academic publishing. All Frontiers journals are driven by researchers for researchers; therefore, they constitute a service to the scholarly community. At the same time, the *Frontiers journal series* operates on a revolutionary invention, the tiered publishing system, initially addressing specific communities of scholars, and gradually climbing up to broader public understanding, thus serving the interests of the lay society, too.

## Dedication to quality

Each Frontiers article is a landmark of the highest quality, thanks to genuinely collaborative interactions between authors and review editors, who include some of the world's best academicians. Research must be certified by peers before entering a stream of knowledge that may eventually reach the public - and shape society; therefore, Frontiers only applies the most rigorous and unbiased reviews. Frontiers revolutionizes research publishing by freely delivering the most outstanding research, evaluated with no bias from both the academic and social point of view. By applying the most advanced information technologies, Frontiers is catapulting scholarly publishing into a new generation.

## What are Frontiers Research Topics?

Frontiers Research Topics are very popular trademarks of the *Frontiers journals series*: they are collections of at least ten articles, all centered on a particular subject. With their unique mix of varied contributions from Original Research to Review Articles, Frontiers Research Topics unify the most influential researchers, the latest key findings and historical advances in a hot research area.

Find out more on how to host your own Frontiers Research Topic or contribute to one as an author by contacting the Frontiers editorial office: frontiersin.org/about/contact

# New trends in vascular biology 2024

**Topic editors**
Masanori Aikawa — Brigham and Women's Hospital, Harvard Medical School, United States
Hong Chen — Boston Children's Hospital, Harvard Medical School, United States
Delphine Gomez — University of Pittsburgh, United States
Yun Fang — The University of Chicago, United States
Gabrielle Fredman — Albany Medical College, United States
Shizuka Uchida — Aalborg University Copenhagen, Denmark
Margreet R. De Vries — Leiden University Medical Center (LUMC), Netherlands
Hiroshi Iwata — Juntendo University, Japan
Hiromi Yanagisawa — University of Tsukuba, Japan

**Topic coordinator**
Sarvesh Chelvanambi — Department of Medicine, Brigham and Women's Hospital, Harvard Medical School, United States

**Citation**
Aikawa, M., Chen, H., Gomez, D., Fang, Y., Fredman, G., Uchida, S., De Vries, M. R., Iwata, H., Yanagisawa, H., Chelvanambi, S., eds. (2025). *New trends in vascular biology 2024*. Lausanne: Frontiers Media SA. doi: 10.3389/978-2-8325-6685-5

# Table of contents

05 **Editorial: New trends in vascular biology 2024**
Sarvesh Chelvanambi, Hong Chen, Margreet R. De Vries, Yun Fang, Gabrielle Fredman, Delphine Gomez, Hiroshi Iwata, Shizuka Uchida, Hiromi Yanagisawa and Masanori Aikawa

08 **Construction and validation of a clinical prediction model for asymptomatic obstructive coronary stenosis in patients with carotid stenosis**
Cuijie Qin, Chuang Li, Yunpeng Luo, Zhen Li and Hui Cao

17 **Obesity accelerates endothelial-to-mesenchymal transition in adipose tissues of mice and humans**
Nicholas W. Chavkin, Tanvi Vippa, Changhee Jung, Stephanie McDonnell, Karen K. Hirschi, Noyan Gokce and Kenneth Walsh

32 **Endothelial SARS-CoV-2 infection is not the underlying cause of COVID-19-associated vascular pathology in mice**
Siqi Gao, Alan T. Tang, Min Wang, David W. Buchholz, Brian Imbiakha, Jisheng Yang, Xiaowen Chen, Peter Hewins, Patricia Mericko-Ishizuka, N. Adrian Leu, Stephanie Sterling, Avery August, Kellie A. Jurado, Edward E. Morrisey, Hector Aguilar-Carreno and Mark L. Kahn

37 **SARS-CoV-2 infection of endothelial cells, dependent on flow-induced ACE2 expression, drives hypercytokinemia in a vascularized microphysiological system**
Christopher J. Hatch, Sebastian D. Piombo, Jennifer S. Fang, Johannes S. Gach, Makena L. Ewald, William K. Van Trigt, Brian G. Coon, Jay M. Tong, Donald N. Forthal and Christopher C. W. Hughes

51 **The disruptive role of LRG1 on the vasculature and perivascular microenvironment**
Athina Dritsoula, Carlotta Camilli, Stephen E. Moss and John Greenwood

71 **Multimodality assessment of the coronary microvasculature with TIMI frame count versus perfusion PET highlights coronary changes characteristic of coronary microvascular disease**
Nicole Wayne, Qufei Wu, Stephen C. Moore, Victor A. Ferrari, Scott D. Metzler and Marie A. Guerraty

82 **Trends in peripheral artery disease and critical limb ischemia hospitalizations among cocaine and methamphetamine users in the United States: a nationwide study**
Shafaqat Ali, Zaki Al-Yafeai, Md. Ismail Hossain, Md. Shenuarin Bhuiyan, Sanchit Duhan, Richa Aishwarya, Nicholas E. Goeders, Md. Mostafizur Rahman Bhuiyan, Steven A. Conrad, John A. Vanchiere, A. Wayne Orr, Christopher G. Kevil and Mohammad Alfrad Nobel Bhuiyan

100 The role of proprotein convertase subtilisin/kexin 9 (PCSK9) in macrophage activation: a focus on its LDL receptor-independent mechanisms
Shunsuke Katsuki, Prabhash Kumar Jha, Elena Aikawa and Masanori Aikawa

107 The causal relationship between human blood metabolites and risk of peripheral artery disease: a Mendelian randomization study
Zhiyong Dong and Qingyun Wang

118 Case Report: The application of novel imaging technologies in lower extremity peripheral artery disease: NIR-II imaging, OCTA, and LSFG
Yijie Ning, Jie Hu, Haifeng Li, Chuanlong Lu, Zeyu Zhang, Sheng Yan, Peilu Shi, Tingting Gao, Heng Wang, Ruijing Zhang and Honglin Dong

126 Inhibition of angiogenesis and regenerative lung growth in *Lep*$^{ob/ob}$ mice through adiponectin-VEGF/VEGFR2 signaling
Tendai Hunyenyiwa, Priscilla Kyi, Mikaela Scheer, Mrudula Joshi, Mario Gasparri, Tadanori Mammoto and Akiko Mammoto

140 Gene expression profiles of precursor cells identify compounds that reduce NRP1 surface expression in macrophages: Implication for drug repositioning for COVID-19
Akira Iwata, Sarvesh Chelvanambi, Takaharu Asano, Mary Whelan, Yuto Nakamura, Elena Aikawa, Yusuke Sasaki and Masanori Aikawa

152 Trends and patterns in pulmonary arterial hypertension-associated hospital admissions among methamphetamine users: a decade-long study
Amanda Husein, Jolie Boullion, Md Ismail Hossain, Diensn Xing, Md Tareq Ferdous Khan, Md. Shenuarin Bhuiyan, Gopi K. Kolluru, Md Mostafizur Rahman Bhuiyan, Nicholas E. Goeders, Steven A. Conrad, John A. Vanchiere, A. Wayne Orr, Christopher G. Kevil and Mohammad Alfrad Nobel Bhuiyan

frontiers | Frontiers in Cardiovascular Medicine

TYPE Editorial
PUBLISHED 24 July 2025
DOI 10.3389/fcvm.2025.1649558

# Editorial: New trends in vascular biology 2024

Sarvesh Chelvanambi[1], Hong Chen[2], Margreet R. De Vries[1,3], Yun Fang[4], Gabrielle Fredman[5], Delphine Gomez[6], Hiroshi Iwata[7], Shizuka Uchida[8], Hiromi Yanagisawa[9] and Masanori Aikawa[1]*

[1]Center for Interdisciplinary Cardiovascular Sciences, Brigham and Women's Hospital and Harvard Medical School, Boston, MA, United States, [2]Vascular Biology Program, Department of Surgery, Boston Children's Hospital and Harvard Medical School, Boston, MA, United States, [3]Einthoven Laboratory for Experimental Vascular Medicine and Regenerative Medicine, Leiden University Medical Center, Leiden, Netherlands, [4]Department of Medicine, Biological Sciences Division, The University of Chicago, Chicago, IL, United States, [5]Department of Molecular and Cellular Physiology, Albany Medical College, Albany, NY, United States, [6]Department of Medicine, Division of Cardiology, University of Pittsburgh, Pittsburgh, PA, United States, [7]Department of Cardiovascular Biology and Medicine, Juntendo University Graduate School of Medicine, Tokyo, Japan, [8]Center for RNA Medicine, Department of Clinical Medicine, Aalborg University, Copenhagen, Denmark, [9]Life Science Center for Survival Dynamics, Tsukuba Advanced Research Alliance, University of Tsukuba, Tsukuba, Japan

Check for updates

OPEN ACCESS

EDITED AND REVIEWED BY
Hendrik Tevaearai Stahel,
University Hospital of Bern, Switzerland

*CORRESPONDENCE
Masanori Aikawa
✉ maikawa@bwh.harvard.edu

RECEIVED 18 June 2025
ACCEPTED 26 June 2025
PUBLISHED 24 July 2025

CITATION
Chelvanambi S, Chen H, De Vries MR, Fang Y, Fredman G, Gomez D, Iwata H, Uchida S, Yanagisawa H and Aikawa M (2025) Editorial: New trends in vascular biology 2024.
Front. Cardiovasc. Med. 12:1649558.
doi: 10.3389/fcvm.2025.1649558

KEYWORDS

**vascular disease, cardiometabolic disease, macrophage, PCSK9, vascular imaging, endothelial-mesenchymal transition, COVID-19, data science**

Editorial on the Research Topic
New trends in vascular biology 2024

Despite the development of potent drugs for modifiable risk factors, such as statins, and advances in mechanistic biomedical research, vascular disease remains the No.1 killer globally and represents a huge cost to public health (1–3). The underlying mechanisms remain incompletely understood and effective new therapies are needed (4). Such major challenges have promoted technological innovations and their implementations in vascular research (5). Unmet clinical needs and exponential technological development have synergistically advanced vascular medicine. Addressing the challenges associated with the complexity in treating cardiovascular disease requires integration of cross-disciplinary approaches and knowledge (6).This Research Topic thus reports new trends in a wide range of vascular medicine research from fundamental basic science to translational medicine to clinical studies.

This collection particularly focuses on four different areas in vascular medicine; (i) new understandings of cardiometabolic vascular dysfunction; (ii) novel imaging approaches; (iii) COVID-19 pandemic; and (iv) data science.

## New understandings of cardiometabolic vascular dysfunction

In the first area, we featured four articles which identified novel contributors of cardiometabolic vascular dysfunction. Hunyenyiwa et al. used the $Lep^{ob/ob}$ mouse model of obesity to investigate angiogenesis following unilateral pneumonectomy, a critical aspect for successful regenerative lung growth. The authors showed that unilateral pneumonectomy inhibited the pro-angiogenic factor VEGF and its receptor VEGFR2 in an adiponectin dependent fashion. The use of adiponectin agonist aided in vascular and alveolar regeneration, suggesting potential applications for lung regeneration in obese individuals. Katsuki et al. discussed the role of PCSK9 in macrophage activation as a contributor towards the protective role of PCSK9 inhibition in the reduction of adverse cardiovascular outcomes in patients. The authors specifically highlighted the potential for PCSK9 to target receptors other than the classical target LDLR as well as how macrophage activation can be protected in both a lipid-dependent and lipid-independent fashion. Dritsoula et al. reviewed the role of secreted LRG1 as a vasculopathic molecule with the ability to disrupt angiogenesis and thereby impede vascular stability. This review described how LRG1 uses both canonical and non-canonical TGFβ signaling to affect the vasculature in a wide range of pathophysiological conditions. Chavkin et al. used a lineage tracing model of endothelial cells in mice fed a high fat/high sucrose diet as well as human adipose endothelial cells to investigate the presence of endothelial-mesenchymal transition (EndoMT) in obesity. The authors found a time-dependent increase in EndoMT in subcutaneous adipose tissue as well as increased expression of EndoMT gene markers when human adipose endothelial cells were cultured in the presence of pro-inflammatory stimulus. Their findings suggest that chronic obesity promotes EndoMT, which could lead to adipose tissue dysfunction.

## Novel imaging approaches

The second theme focuses on emerging trends in imaging which has enhanced the field of vascular biology research. Ning et al. described their own development of novel imaging modalities to look deeper into lower extremity peripheral artery disease. This case report showcases the use of near-infrared imaging (NIR-II 900-1880nm wavelength), optical coherence tomography angiography and laser speckle flowgraphy to show poor tissue perfusion in a patient with peripheral arterial disease suggesting the utility of these imaging modalities for the diagnoses of disease. Wayne et al. analyzed a cohort of 123 individuals with perfusion PET and coronary angiography with no obstructive coronary artery disease. The authors compared the Thrombolysis in Myocardial Infarction frame count (angiography-based method) and myocardial blood flow reserve (PET-based method) and found an inverse relationship between these parameters which in turn could be used to identify patients with coronary microvascular disease.

## COVID-19 pandemic

The third area was reflective of the emerging landscape of COVID-19 related vascular biology research. Iwata et al. used a machine learning based drug repurposing approach to identify FDA approved compounds with the ability to reduce surface expression of SARS-CoV-2 entry receptor, NRP1 specifically in macrophages. The authors validated that the top predicted compounds indeed reduce NRP1 surface expression in both cell lines and primary derived human macrophages. These findings have important implications for using drug repurposing-based approaches to rapidly identify agents to help prevent infection in niche subpopulations. Hatch et al. developed a vascularized micro-organ 3D microphysiological system consisting of endothelial cells and stromal cells to model SARS-CoV-2 infection using a pseudotyped GFP expressing lentivirus. This system was deployed to show infection with the virus could disrupt the vasculature by promoting inflammation and endothelial activation. Gao et al. developed a mouse model expressing human ACE2 to characterize COVID-19 pathogenicity in an *in vivo* setting. They concluded that direct infection of endothelial cells does not occur in this system and does not indeed contribute to vascular abnormalities. These findings suggest that COVID-19 associated vascular dysfunction can be attributed to inflammatory responses triggered by the viral infection.

## Data science

Four manuscripts represent the fourth theme, leveraging big data to find new trends in vascular biology. Husein et al. investigated three databases from 2008 to 2020 to calculate the impact of methamphetamine use in patients with pulmonary arterial hypertension. Similarly, Ali et al. investigated the National Inpatient Sample database from 2008 to 2020 to identify patients hospitalized with peripheral arterial disease. The use of ICD diagnoses facilitates comparison of sufficiently large real-world datasets to draw conclusions about the prevalence of disease and its associated factors. Dong et al. performed a mendelian randomization analysis on 1,400 serum metabolites in patients with peripheral arterial disease. Using this approach, the authors identified serum metabolites that showed a positive and others that showed a negative association with peripheral arterial disease diagnosis. Qin et al. performed a retrospective analysis of patients undergoing carotid stenosis from January 2018 to January 2022 in their department of endovascular surgery. Their investigation of 227 patients showed that several clinical parameters had independent capacity to predict asymptomatic carotid artery stenosis which could be used to help identify patients at risk.

## Summary and future perspectives

This collection highlights the interdisciplinary advances shaping the future of vascular biology. Through the exploration of cardio- and vascular-metabolic dysfunction, advanced imaging modalities, vascular implication of the COVID-19 pandemic and the integration of data science this collection underscores the complexity and evolving nature of vascular health. The insights presented not only deepen our understanding of disease but also point to innovative diagnostic and therapeutic strategies. This research topic shows how multiple different approaches can work together to provide a more comprehensive insight into disease progression. Such an interdisciplinary approach could rapidly advance our understanding of the disease and help speed up development of effective therapies. Continued research in these domains is essential for translating emerging knowledge into meaningful clinical outcomes.

## Author contributions

SC: Writing – review & editing, Writing – original draft, Conceptualization. HC: Writing – review & editing. MD: Writing – review & editing. YF: Writing – review & editing. GF: Writing – review & editing. DG: Writing – review & editing. HI: Writing – review & editing. SU: Writing – review & editing. HY: Writing – review & editing. MA: Conceptualization, Writing – original draft, Writing – review & editing, Supervision.

## Conflict of interest

The authors declare that the research was conducted in the absence of any commercial or financial relationships that could be construed as a potential conflict of interest.

The author(s) declared that they were an editorial board member of Frontiers, at the time of submission. This had no impact on the peer review process and the final decision.

## Generative AI statement

The author(s) declare that no Generative AI was used in the creation of this manuscript.

## Publisher's note

## References

1. Vervoort D, Wang R, Li G, Filbey L, Maduka O, Brewer LC, et al. Addressing the global burden of cardiovascular disease in women: JACC State-of-the-Art Review. *J Am Coll Cardiol*. (2024) 83(25):2690–707. doi: 10.1016/j.jacc.2024.04.028

2. Vogel B, Acevedo M, Appelman Y, Merz B, Chieffo CN, Figtree A, et al. The lancet women and cardiovascular disease commission: reducing the global burden by 2030. *Lancet*. (2021) 397(10292):2385–438. doi: 10.1016/S0140-6736(21)00684-X

3. Luengo-Fernandez R, Walli-Attaei M, Gray A, Torbica A, Maggioni AP, Huculeci R, et al. Economic burden of cardiovascular diseases in the European Union: a population-based cost study. *Eur Heart J*. (2023) 44(45):4752–67. doi: 10.1093/eurheartj/ehad583

4. Joseph P, Leong D, McKee M, Anand SS, Schwalm JD, Teo K, et al. Reducing the global burden of cardiovascular disease, part 1: the epidemiology and risk factors. *Circ Res*. (2017) 121(6):677–94. doi: 10.1161/CIRCRESAHA.117.308903

5. Aikawa M, Sonawane A, Chelvanambi S, Asano T, Halu A, Matamalas JT, et al. Precision cardiovascular medicine: shifting the innovation paradigm. *Front Sci*. (in press).

6. Chelvanambi S, Decano JL, Winkels H, Giannarelli C, Aikawa M. Decoding macrophage heterogeneity to unravel vascular inflammation as a path to precision medicine. *Arterioscler Thromb Vasc Biol*. (2024) 44(11):2253–7. doi: 10.1161/ATVBAHA.124.319571

Frontiers in Cardiovascular Medicine

TYPE Original Research
PUBLISHED 07 September 2023
DOI 10.3389/fcvm.2023.1096020

OPEN ACCESS

EDITED BY
Marcone Lima Sobreira,
Sao Paulo State University, Brazil

REVIEWED BY
Bu-Lang Gao,
Hebei Medical University, China
Rafael De Athayde Soares,
Hospital do Servidor Público Estadual, Brazil

*CORRESPONDENCE
Hui Cao
✉ fcccaoh2@zzu.edu.cn

RECEIVED 11 November 2022
ACCEPTED 17 August 2023
PUBLISHED 07 September 2023

CITATION
Qin C, Li C, Luo Y, Li Z and Cao H (2023) Construction and validation of a clinical prediction model for asymptomatic obstructive coronary stenosis in patients with carotid stenosis.
Front. Cardiovasc. Med. 10:1096020.
doi: 10.3389/fcvm.2023.1096020

# Construction and validation of a clinical prediction model for asymptomatic obstructive coronary stenosis in patients with carotid stenosis

Cuijie Qin, Chuang Li, Yunpeng Luo, Zhen Li and Hui Cao*

Department of Endovascular Surgery, The First Affiliated Hospital of Zhengzhou University, Zhengzhou University, Zhengzhou, China

**Background:** Coronary artery stenosis occurs frequently in patients with carotid artery stenosis. We developed a clinical predictive model to investigate the clinical risk of asymptomatic obstructive coronary artery stenosis in patients with carotid artery stenosis $\geq 50\%$.

**Methods:** From January 2018 to January 2022, carotid stenosis patients hospitalized at the First Affiliated Hospital of Zhengzhou University's Department of Endovascular Surgery were subjected to a retrospective analysis of their clinical information and imaging results. Excluded criteria were patients with lacking data, symptomatic coronary stenosis, prior coronary artery bypass grafting, and coronary stent implantation. Patients were separated into case and control groups according to whether or not they had obstructive coronary stenosis. Independent predictors were screened using univariate and multivariate logistic regression, and their accuracy was confirmed using least absolute shrinkage and selection operator (LASSO) regression. A Nomogram prediction model was developed using the aforementioned filtered factors. The model's discrimination and specificity were evaluated using the receiver operating characteristic curve (ROC) and Hosmer-Lemeshow goodness-of-fit test. Internal validation employed the Bootstrap procedure. The clinical decision curve analysis (DCA) of the prediction model was developed to assess the clinical applicability of the model.

**Results:** The investigation included a total of 227 patients, of whom 132 (58.1%) had coronary artery stenosis. Hypertension, Grade I plaque, HbA1c $\geq 7.0\%$, MPV $\geq 9.2$fl, and Fib $\geq 3.0$ g/L were independent predictors, with OR values of (2.506, 0.219, 0.457, 1.876, 2.005), according to multivariate logistic regression. Risk factor screening and validation using lasso regression. The predictors chosen based on the optimal $\lambda$ value are consistent with the predictors identified by multiple regression. The area under the ROC curve (AUC) of the model based on the above predictors was 0.701 (0.633–0.770), indicating that the model discriminated well. The calibration curve of the model closely matched the actual curve, and $P > 0.05$ in the Hosmer-Lemeshow goodness-of-fit test indicated the model's accuracy. The results of the DCA curve demonstrate the clinical applicability of the prediction model.

**Conclusion:** Hypertension, grade I plaque, HbA1c $\geq 7.0\%$, MPV $\geq 9.2$ fl, and Fib $\geq$ 3.0 g/L are predictors of asymptomatic coronary stenosis in patients with carotid stenosis $\geq 50\%$. The diagnostic model is clinically applicable and useful for identifying patients at high risk.

KEYWORDS

carotid stenosis, coronary stenosis, prediction model, nomogram, LASSO regression analysis

# Introduction

Stroke has an elevated level of morbidity and mortality and has become a serious hazard to the health of the elderly. According to accounts, carotid stenosis causes 25% to 30% of ischemic strokes (1). Atherosclerosis is the principal cause of carotid stenosis. Stenosis occurs most frequently at the bifurcation of the common carotid, the origin of the internal carotid, and the siphon (2). Effective early treatment of carotid stenosis can reduce the incidence of ischemic stroke. Central interventions included endarterectomy of the carotid artery, stenting of the carotid artery, and drug therapy (3). Atherosclerosis has a variety of effects and can accumulate in both large and medium arteries. Patients with carotid artery stenosis and coronary artery stenosis are not uncommon. Research have demonstrated that patients with both carotid artery stenosis and coronary artery stenosis have a substantially increased risk of acute cardiovascular disease during surgery (4). Compared to symptomatic coronary stenosis, asymptomatic coronary stenosis has an elevated likelihood of misdiagnosis due to the absence of typical symptoms. A number of studies have investigated accurate predictors of asymptomatic coronary artery stenosis in patients. A retrospective study revealed that the thickness, extent, and complexity of aortic arch lesions were independent risk factors for asymptomatic coronary stenosis greater than 50% (5). In addition, patients with insulin resistance are more likely to have asymptomatic coronary artery stenosis ≥ 50% and have a positive correlation with the number and severity of coronary artery stenosis (6). The purpose of this study was to retrospectively analyze the clinical data of patients with carotid artery stenosis ≥ 50% in our center, to investigate the related predictive factors of asymptomatic obstructive coronary stenosis, and to establish a nomogram prediction model in order to provide support for early detection of occult coronary disease in patients with carotid stenosis.

# Materials and methods

## Patients and data collection

This survey included carotid artery stenosis patients admitted to the Department of Endovascular Surgery at the First Affiliated Hospital of Zhengzhou University between January 2018 and January 2022. By carotid ultrasound and carotid computed tomography angiography, a total of 513 patients with unilateral or bilateral carotid stenosis ≥ 50% were identified. Exclusion criteria included 45 patients with symptomatic coronary artery stenosis, 26 patients with a history of coronary stent implantation or coronary artery bypass grafting, 114 patients without carotid contrast-enhanced ultrasonography (CEUS), and 101 patients without coronary angiography. Finally, 227 patients in total met the inclusion criteria. They were split into a case group and a control group based on whether the degree of coronary artery stenosis exceeded 50%. **Figure 1** shows the study's flowchart. The study was approved by the local ethics committee and was conducted in accordance with the 1964 Declaration of Helsinki.

The electronic medical record system was queried to obtain baseline clinical data, laboratory tests, and imaging investigations. Patient characteristics including age, gender, BMI, diabetes mellitus (DM), essential hypertension, and smoking and alcohol history. Laboratory examination indexes including hemoglobin A1c (HbA1c), hematocrit (HCT), lymphocyte percentage (LY%), monocyte percentage (MONO%), platelet count (PLT), mean platelet volume (MPV), albumin (Alb), fibrinogen (Fib), β2-MG, total cholesterol (TC), triglycerides (TG), high density lipoprotein (HDL), low density lipoprotein (LDL), lipoprotein(a) [Lp(a)], glomerular filtration rate (GFR), creatinine (Cr), homocysteine (Hcy). Imaging results including sum (PS) and maximum (P-max) of the plaque thickness, the degree of carotid artery and coronary artery stenosis and the carotid plaque level.

Hypertension was defined as blood pressure > 140/90 mmHg or treatments with antihypertensive medication. The diagnosis of diabetes mellitus was based on the 2017 Standards of Medical Care in Diabetes (7). In coronary computed tomography angiography (CCTA), the degree of coronary stenosis was classified as obstructive (luminal stenosis ≥ 50% of the coronary diameter) or non-obstructive (luminal stenosis < 50%) (8). Multi-site stenosis of a single vessel is determined by the most severe stenosis, and multi-vessel stenosis is defined as stenosis of two or more vessels (9). Guidelines for the diagnosis and treatment of carotid stenosis were used to classify symptomatic carotid stenosis (SCS) and asymptomatic carotid stenosis (3). A current smoker is defined as someone who has smoked cigarettes on a regular basis within the past six months, whereas an alcoholic is defined as someone who has consumed alcohol on a regular basis for over a year. The BMI was computed by dividing the weight (kg) by the square of the height (m). P-max was measured as the vertical distance between the tip of the plaque and adventitia interface of the lumen. PS was the sum of bilateral maximal carotid plaque thickness. The PS and P-max were determined by carotid artery ultrasound (10). Using the CEUS plaque blood flow grading standard, the grade of carotid plaque was classified as grades I to IV. Grade I was defined as the absence of plaque enhancement, grade II as the presence of one to three punctate plaque enhancements, and grade III as the presence of more than three punctate plaque enhancements or one to two short-line plaque enhancements. Grade IV is characterised by the presence of two or more linear enhancements in the plaque that are penetrating or predominantly penetrating the plaque, or by a sense of flow (11).

## Statistical analysis

Data analysis was performed using SPSS 23.0 and R version 4.2.1. Except for age, BMI, and HbA1c, the mean and median were chosen as the boundary values for the continuous variables of normal distribution and non-normal distribution, and the data were converted to binary variables for subsequent analysis. Multiple logistic regression included the binary logistic regression

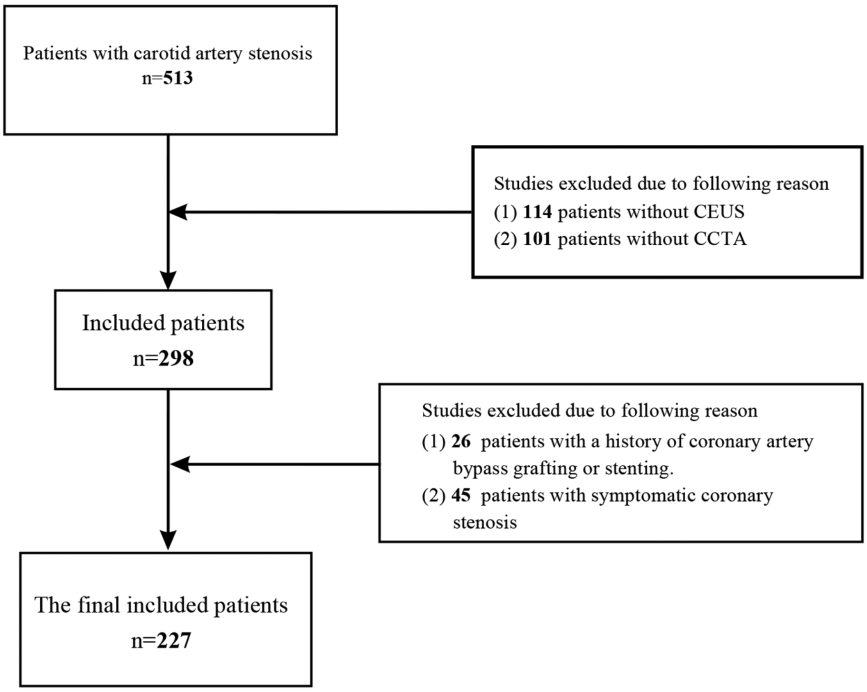

FIGURE 1
The flow chart of this study.

analysis factors with $P < 0.05$. Using backward stepwise multiple logistic analysis, independent predictors were identified. Selected predictors were cross-validated further utilising LASSO regression. The L1-penalized LASSO regression was applied to reduce the data dimensionality to avoid potential collinearity and overfitting among variables. The best lambda value was selected in LASSO regression using tenfold cross-validation. Under the lambda compression (lambda.1se), the variables with small regression coefficients were directly compressed to 0 to eliminate the corresponding variables. Using the "rms" programme, statistically significant factors were used to construct the nomogram and generate a prediction model. To evaluate the accuracy of the prediction model, we calculated the consistency index (C-index) using the "rms" programme. By constructing a calibration curve, the level of calibration was determined. The greater the consistency of the prediction model, the closer the calibration curve of the model to the standard curve. Using DCA, the clinical utility of the nomogram was determined by quantifying the net benefits of the probability of various threshold values in the array. Finally, an internal validation approach was utilised to evaluate the prediction model's stability.

# Results

## Patient characteristics

This study included 227 patients, involving 181 males (79.7%) and 46 females (20.3%). Subjects were divided into case and control groups according to whether they had obstructive coronary stenosis simultaneously. There were 132 cases in the case group (58.1%) and 95 cases in the control group (41.9%). There were 62 cases (47.0%) of single-vessel disease and 70 cases (53.0%) of multi-vessel disease in the case group. All patients exhibited no coronary stenosis-related symptoms.

## Analysis of predictive factors

Thirty laboratory parameters and imaging variables were included as independent variables in the binary logistic regression (**Table 1**). Hypertension, Grade I plaque, HbA1c, MPV, and Fib were statistically significant predictors ($P < 0.05$) based on the results of binary logistic regression. Binary logistic regression showed that Hypertension, Grade I plaque, HbA1c, MPV, and Fib were statistically significant predictors ($P < 0.05$). Multivariate logistic regression included the factors with $P < 0.05$ in binary logistic regression. According to the results, Hypertension, Grade I plaque, HbA1c, MPV, and Fib were independent predictors (**Table 2**). On the included variables, LASSO regressions were conducted to evaluate the selected predictors' reliability further. Five predictors were selected based on the optimal value ($\lambda = 0.0629$). Variables included hypertension, Grade I plaque, HbA1c, MPV, and Fib. Consistent with the independent predictors identified by multiple regression, the regression coefficients were 0.203, −0.242, 0.135, −0.167, and 0.106 (**Figure 2**).

TABLE 1 Results of binary logistic regression analysis of the clinical characteristics of patients in the case and control groups.

| Variables | All patients ($n = 227$) | Case group ($n = 132$) | Control group ($n = 95$) | Odds ratio [95% CI] | *P*-value |
|---|---|---|---|---|---|
| Male | 181 | 107 | 74 | 0.823 [0.429–1.579] | 0.559 |
| Hypertension | 174 | 109 | 65 | 2.187 [1.172–4.082] | 0.014* |
| Smoking | 78 | 45 | 33 | 0.919 [0.558–1.693] | 0.919 |
| Drinking | 47 | 26 | 21 | 0.864 [0.452–1.561] | 0.659 |
| DM | 92 | 57 | 35 | 1.303 [0.759–2.237] | 0.338 |
| SCS | 88 | 50 | 38 | 0.915 [0.533–1.570] | 0.746 |
| Grade I plaque | 13 | 10 | 3 | 0.198 [0.053–0.739] | 0.016* |
| Grade IV plaque | 55 | 36 | 19 | 1.500 [0.797–2.822] | 0.209 |
| P-max ≥ 4 mm | 87 | 53 | 34 | 1.204 [0.698–2.076] | 0.505 |
| PS ≥ 5.6 mm | 114 | 72 | 42 | 1.514 [0.891–2.574] | 0.125 |
| HCT ≥ 0.4 | 112 | 63 | 49 | 0.857 [0.506–1.453] | 0.567 |
| NEUT%≥60% | 117 | 71 | 46 | 1.240 [0.731–2.103] | 0.425 |
| LY%≥28.4% | 116 | 67 | 49 | 0.968 [0.571–1.640] | 0.903 |
| MONO%≥7.4% | 105 | 67 | 38 | 1.546 [0.907–2.637] | 0.110 |
| PLT ≥ 203*$10^9$/L | 112 | 61 | 51 | 0.741 [0.437–1.258] | 0.267 |
| MPV ≥ 9.2 fl | 111 | 55 | 56 | 0.497 [0.291–0.850] | 0.011* |
| Alb ≥ 41 g/L | 107 | 59 | 48 | 0.791 [0.466–1.343] | 0.386 |
| Fib ≥ 3.0 g/L | 106 | 70 | 36 | 1.850 [1.081–3.167] | 0.025* |
| $\beta_2$-MG ≥ 1.8 mg/L | 113 | 69 | 44 | 1.269 [0.748–2.153] | 0.376 |
| TC ≥ 3.5 mmol/L | 112 | 64 | 48 | 0.922 [0.544–1.562] | 0.762 |
| TG ≥ 1.16 mmol/L | 113 | 68 | 45 | 1.181 [0.538–2.002] | 0.538 |
| HDL ≥ 1.0 mmol/L | 95 | 52 | 43 | 0.786 [0.461–1.341] | 0.377 |
| LDL ≥ 1.97 mmol/L | 113 | 61 | 52 | 0.710 [0.418–1.206] | 0.206 |
| Lp(a) ≥ 0.19 mg/dl | 113 | 59 | 54 | 0.614 [0.361–1.044] | 0.072 |
| GFR ≥ 91 ml/min | 110 | 63 | 95 | 0.932 [0.550–1.580] | 0.795 |
| Cr ≥ 71 µmol/L | 113 | 68 | 45 | 1.181 [0.696–2.002] | 0.538 |
| Hcy ≥ 14 µmol/L | 108 | 59 | 49 | 0.759 [0.447–1.288] | 0.306 |
| Age ≥ 70 years | 57 | 34 | 23 | 1.086 [0.590–2.000] | 0.791 |
| BMI ≥ 24 kg/m2 | 146 | 82 | 64 | 0.794 [0.456–1.383] | 0.416 |
| HbA1c ≥ 7.0% | 76 | 53 | 23 | 2.100 [1.171–3.767] | 0.013* |

SCS, symptomatic carotid stenosis; DM, diabetes mellitus; HbA1c, hemoglobin A1c; HCT, hematocrit; LY%, lymphocyte percentage; MONO%, monocyte percentage; PLT, platelet count; MPV, mean platelet volume; Alb, albumin; Fib, fibrinogen; TC, total cholesterol; TG, triglycerides; HDL, high density lipoprotein; LDL, low density lipoprotein; Lp(a), lipoprotein(a); GFR, glomerular filtration rate; Cr, creatinine; Hcy, homocysteine; PS, sum of the plaque thickness; P-max, maximum of the plaque thickness.
*Indicates statistically significant variables.

TABLE 2 Multiple logistic regression analysis results.

| Variables | β | Odds ratio | 95%CI | *P*-value |
|---|---|---|---|---|
| Hypertension | 0.919 | 2.506 | 1.269–4.948 | 0.008* |
| Grade I plaque | −1.518 | 0.219 | 0.055–0.877 | 0.032* |
| MPV ≥ 9.2 fl | −0.783 | 0.457 | 0.258–0.811 | 0.007* |
| Fib ≥ 3.0 g/L | 0.629 | 1.876 | 1.053–3.342 | 0.033* |
| HbA1c ≥ 7.0% | 0.696 | 2.005 | 1.080–3.723 | 0.028* |

MPV, mean platelet volume; Fib, fibrinogen; HbA1c, hemoglobin A1c.
*Indicates statistically significant variables.

## Nomogram's building and apparent performance

On the basis of the outcomes of logistic regression and LASSO regression, five predictors were eliminated and a nomogram risk prediction model was developed (**Figure 3**). Each variable was assigned a score, and the higher the score, the greater the risk of obstructive coronary stenosis in carotid stenosis patients.

## Assessment of the degree of calibration for the risk prediction model

To facilitate the evaluation of the risk prediction model's degree of rectification in this investigation, we developed a correction curve. As shown in **Figure 4**, the x-axis represents the predicted risk for asymptomatic obstructive coronary stenosis, and the y -axis represents the realization of asymptomatic obstructive coronary stenosis. The solid diagonal line represents the prediction of the ideal model, and the dashed line represents the actual predictive ability. The closer the dashed line is to the diagonal, the greater the predictive ability. Hosmer-Lemeshow test showed that the model had good calibration ($\chi^2 = 2.24$, $P = 0.987$).

## Assessment of the accuracy

To evaluate the model's accuracy, we first calculated the C-index. When plotting a ROC curve, we can use AUC to

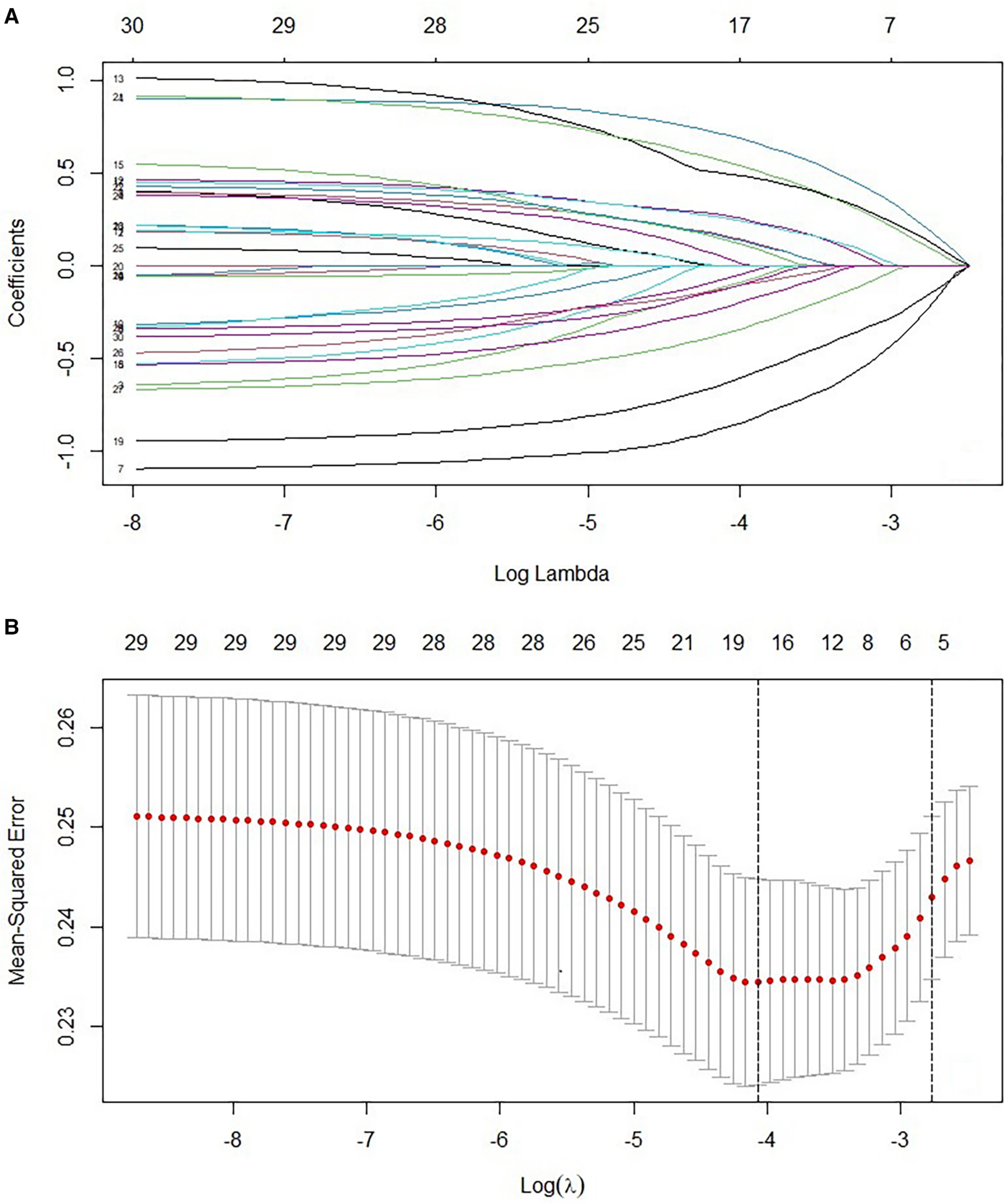

FIGURE 2
(A) LASSO coefficient profiles of 227 patients with obstructive coronary stenosis. A coefficient profile plot was produced against the log (λ) sequence. (B) Texture feature selection by using the least absolute shrinkage and selection operator (LASSO) binary logistic regression model. Tuning parameter (λ) selection in the LASSO model used 10-fold cross-validation via maximum AUC. A λ value of 0.0629 was chosen (1-SE criteria) according to 10-fold cross-validation.

quantify the predictor's efficacy. We then determined the model's AUC and constructed a ROC curve. The calculated AUC values of 0.701 (95% CI: 0.633–0.770) indicate that the model is accurate (Figure 5). The ROC curve was internally validated using the Bootstrap 1,000 times self-sampling method, and the AUC was found to be 0.668.

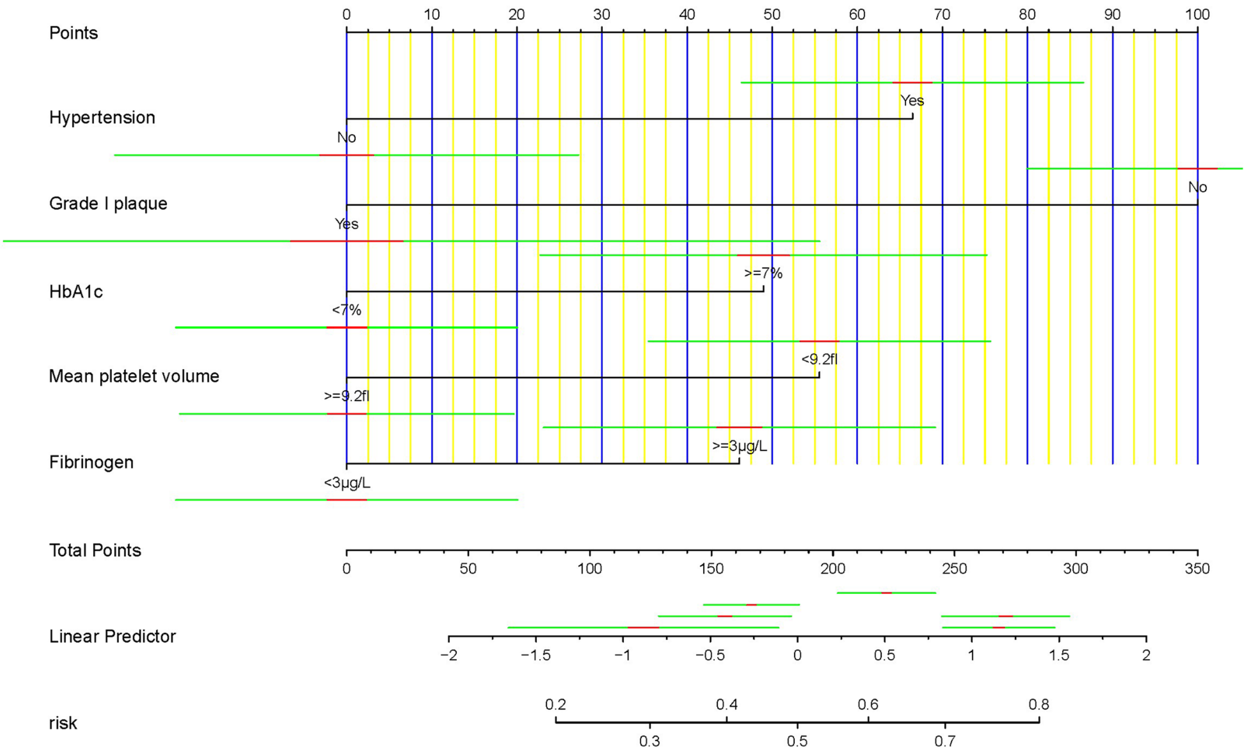

FIGURE 3
Nomogram for predicting the incidence of asymptomatic obstructive coronary stenosis. The construction of the nomogram included Hypertension, Grade I plaque, HbA1c, MPV, and Fib.

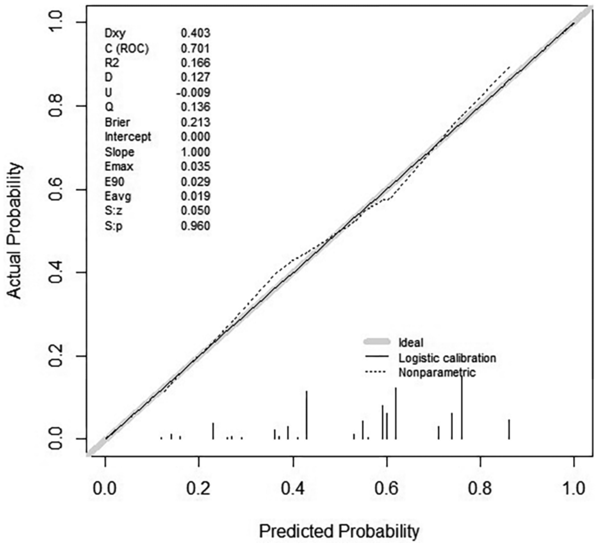

FIGURE 4
Curve of calibration for the risk prediction model of asymptomatic obstructive coronary stenosis.

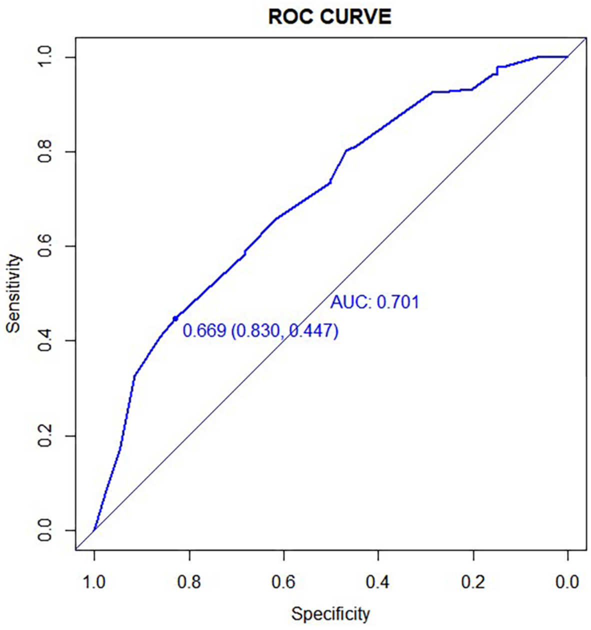

FIGURE 5
The ROC curve corresponding to the asymptomatic obstructive stenosis risk prediction model. The AUC value was 0.701%.

## Clinical net benefit

DCA was utilized to determine if the prediction model could enhance clinical decision-making (**Figure 6**). The y-axis indicates the net benefit, and the x-axis represents the probability of the threshold value. The black solid line represents no intervention, at which the net benefit is zero. The Grey solid line represents

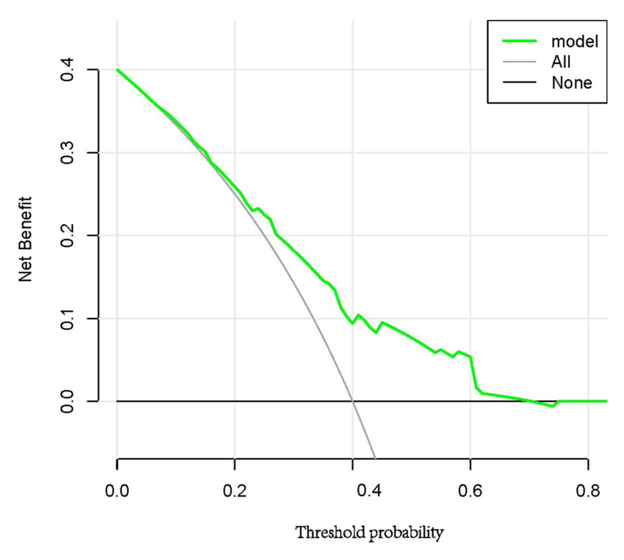

FIGURE 6
DCA for the asymptomatic obstructive coronary stenosis risk prediction model.

the intervention, and the net benefit is an oblique line with a negative slope. The green solid line represents the realized profits of the asymptomatic obstructive coronary stenosis risk prediction model. The DCA curve shows that the threshold of 0.08–0.70 has the largest clinical net income.

## Discussion

This study examined the statistical characteristics, imaging examination, and laboratory examination results of asymptomatic coronary artery stenosis in patients with carotid artery stenosis ≥ 50%. Univariate and multivariate logistic regression were utilized to identify independent risk factors, including hypertension, grade I plaque, HbA1c, MPV, and Fib. Using LASSO regression, the accuracy of the selected predictive factors was further confirmed, and a clinical predictive model was developed. According to the ROC curve, the AUC of the prediction model is 0.701, indicating that the model has a high degree of discrimination. Fit tests and clinical decision curves demonstrated that the predictive model was well calibrated and applicable in the clinical setting. Due to the limited sample size of this study, all data were only modeled as a training set, and the model was Bootstrapped 1,000 times for internal validation. The results demonstrate that the model of prediction is stable.

The most common cause of carotid stenosis is atherosclerosis, a multifactorial, progressive systemic disease (12). Plaque rupture, arterial embolism caused by thrombosis, and hemodynamic disturbance caused by stenosis comprise the majority of the carotid stenosis-induced ischemic stroke mechanism (13). Coronary artery disease is more common in carotid stenosis patients. According to studies, the prevalence of coronary artery disease in patients with carotid stenosis ranges from 13% to 86%, with the prevalence increasing with the severity of carotid stenosis (4). Asymptomatic coronary stenosis is easier to neglect than symptomatic coronary stenosis due to the absence of typical symptoms. Consistent with previous research, 58.1% of the 132 patients in this study experienced moderate or severe coronary stenosis complications. Due to the substantial increase in cardiovascular risk among patients with carotid artery stenosis and coronary artery stenosis coexisting, it is crucial to investigate the coexistence of carotid artery and coronary artery stenosis.

Hypertension was an independent risk factor for carotid stenosis with asymptomatic obstructive coronary stenosis in this study. High blood pressure damages the arterial wall and increases collagen deposition in the stroma, which causes the tunica media to thicken and the artery to become constricted. Hypertension is frequently viewed as a disease that damages large and small arteries, and lesions of corresponding arteries contribute to the occurrence and progression of hypertension. Prior research has demonstrated that hypertension is a risk factor for stroke. Patients with hypertension are substantially more susceptible to suffering a stroke than those with normal blood pressure (14). In a study of the lifetime risk of coronary heart disease, the lifetime risk of coronary heart disease in male hypertensive patients was 26.95% and the lifetime risk of coronary heart disease in female hypertensive patients was 14.85%, both of which were higher than the average level (15). High blood pressure is more likely to cause injury to the carotid and coronary arteries, resulting in their constriction.

HbA1c is produced by a sluggish, continuous, and irreversible glycation reaction and may reflect changes in patients' blood glucose levels over the previous 8 to 12 weeks. In clinical practice, it is considered an essential indicator of blood sugar control in diabetic patients. Studies have shown that HbA1c levels are strongly associated with the risk of diabetes-related complications and cardiovascular disease (16). In general, a glycated hemoglobin level below 7.0% is advised for glycemic control (17). In a study of healthy controls and subjects with T2DM, glycemic fluctuations rather than persistent glycemic elevation caused endothelial cell injury, and intensive glycemic control reduced the incidence of microvascular and macrovascular complications by 25% (18, 19). In this study, patients with HbA1c levels greater than 7.0% were more likely to have asymptomatic coronary stenosis (OR = 2.005). It is advantageous to reduce this risk by enhancing blood glucose regulation and decreasing blood glucose fluctuations.

The investigation included imaging measures to assess the morphology of the plaque. CEUS is a common noninvasive technique for detecting plaque neovascularization. New blood vessels in the plaque are immature and readily rupture, resulting in inflammation of the vessel wall and vessel wall injury (20). High-grade carotid plaques as measured by CEUS are associated with more severe and unstable coronary artery disease, and the carotid plaque enhancement intensity is an independent predictor of secondary cardiovascular events in patients with coronary heart disease (21). This study evaluated the coronary status of patients with grade I or IV plaque and discovered that patients with grade I plaque were substantially less likely to develop asymptomatic obstructive coronary stenosis than controls (OR = 0.219). Using carotid plaque grade as a predictive parameter may increase the probability of identifying coronary stenosis.

Fib is a coagulation factor that promotes platelet aggregation, the growth, proliferation, and contraction of smooth muscle and endothelial cells, as well as increases blood viscosity and damages endothelial cells. Consequently, it is crucial to the pathogenesis of cardiovascular disease. Studies have shown that high levels of Fib are associated with an increased risk of stroke and poor patient outcomes (22). In terms of coronary stenosis, elevated Fib levels are generally regarded as an independent predictor of the presence and severity of coronary artery disease. This may be because fibrinogen stimulates the migration and proliferation of smooth muscle cells, and its degradation products are chemotactic for leukocytes and macrophages (23, 24).

MPV ≥ 9.2fl was a predictor of coronary stenosis events (OR = 0.457) and was protective in this study. MPV reflects the average platelet size, and aberrant MPV is associated with a variety of diseases, including diabetes, cardiovascular disease, and chronic obstructive pulmonary disease (25). High MPV levels have been associated with ST-segment elevation myocardial infarction in patients with coronary heart disease, and it is also regarded as an independent risk factor for inadequate coronary collateral compensation and a poor prognosis (26, 27). The above conclusion differs somewhat from the findings of this study, likely because the majority of the previous studies focused on the effects of acute coronary artery disease. In a study examining the effect of MPV on long-term outcomes following coronary intervention in patients with stable coronary artery disease, decreased MPV levels were associated with inferior outcomes (28). In addition, studies have demonstrated a correlation between systemic inflammation and platelet size. The MPV decreases as the degree of inflammation increases, whereas the MPV increases as the degree of inflammation decreases (29). The aforementioned findings suggest that elevated MPV does not increase the risk of stable coronary artery disease in patients with carotid artery stenosis; however, additional research is required to determine its cardiovascular effects.

This study analyzed the risk factors for asymptomatic obstructive coronary artery stenosis in patients with carotid artery stenosis ≥ 50% and constructed a clinical model with strong predictive ability. Nevertheless, given that this is a retrospective investigation, there are some limitations. First, it is necessary to exclude cases with insufficient data, which could introduce selection bias, and additional prospective studies are required for validation. Secondly, the sample size of this study is insufficient, and the proportion of male patients is high; therefore, it is necessary to increase the sample size in order to further assess the results' reliability.

# Conclusion

This study concluded that there is a significant correlation between carotid artery stenosis and coronary artery stenosis, and that asymptomatic and occult coronary artery stenosis warrants special attention. In patients with carotid stenosis, hypertension, grade I plaque, mean platelet volume ≥ 9.2 fl, fibrinogen ≥ 3.0 g/L, and glycosylated hemoglobin ≥ 7.0% were independent predictors of asymptomatic obstructive coronary stenosis. The clinical diagnostic model based on the aforementioned variables is capable of predicting the risk of coronary artery stenosis to a certain degree.

# Data availability statement

The raw data supporting the conclusions of this article will be made available by the authors, without undue reservation.

# Author contributions

ZL and HC: designed the study. CQ, CL: collected the data. YL: helped with the statistical analysis. CQ: wrote the manuscript. CL, YL, ZL and HC: revised the manuscript. All authors contributed to the article and approved the submitted version.

# Conflict of interest

The authors declare that the research was conducted in the absence of any commercial or financial relationships that could be construed as a potential conflict of interest.

# Publisher's note

# References

1. Kleindorfer DO, Khoury J, Moomaw CJ, Alwell K, Woo D, Flaherty ML, et al. Stroke incidence is decreasing in whites but not in blacks: a population-based estimate of temporal trends in stroke incidence from the greater Cincinnati/northern Kentucky stroke study. *Stroke.* (2010) 41(7):1326–31. doi: 10.1161/strokeaha.109.575043

2. Song P, Fang Z, Wang H, Cai Y, Rahimi K, Zhu Y, et al. Global and regional prevalence, burden, and risk factors for carotid atherosclerosis: a systematic review, meta-analysis, and modelling study. *Lancet Glob Health.* (2020) 8(5):e721–9. doi: 10.1016/s2214-109x (20) 30117-0

3. AbuRahma AF, Avgerinos ED, Chang RW, Darling RC, Duncan AA, Forbes TL, et al. Society for vascular surgery practice guidelines for management of extracranial clinical cerebrovascular disease. *J Vasc Surg*. (2022) 75(1s):4s–22s. doi: 10.1016/j.jvs.2021.04.073

4. Liu ZJ, Fu WG, Guo ZY, Shen LG, Shi ZY, Li JH. Updated systematic review and meta-analysis of randomized clinical trials comparing carotid artery stenting and carotid endarterectomy in the treatment of carotid stenosis. *Ann Vasc Surg*. (2012) 26(4):576–90. doi: 10.1016/j.avsg. 2011.09.009

5. Ma X, Kong Q, Wang C, Rajah G, Ding YC, Zhang YR, et al. Predicting asymptomatic coronary artery stenosis by aortic arch plaque in acute ischemic cerebrovascular disease: beyond the cervicocephalic atherosclerosis? *Chin Med J*. (2019) 132(8):905–13. doi: 10.1097/CM9.0000000000000174

6. Thai PV, Tien HA, Van Minh H, Valensi P. Triglyceride glucose index for the detection of asymptomatic coronary artery stenosis in patients with type 2 diabetes. *Cardiovasc Diabetol*. (2020) 19(1):137. doi: 10.1186/s12933-020-01108-2

7. Shen JI, Nicholas SB, Williams S, Norris KC. Evidence for and against ACC/AHA 2017 guideline for target systolic blood pressure of <130 mmHg in persons with type 2 diabetes. *Curr Cardiol Rep*. (2019) 21(11):149. doi: 10.1007/s11886-019-1251-4

8. Park HB, Heo R, Hartaigh BÓ, Cho I, Gransar H, Nakazato R, et al. Atherosclerotic plaque characteristics by CT angiography to identify coronary lesions that cause ischemia: a direct comparison to fractional flow reserve. *JACC Cardiovasc Imaging*. (2015) 8(1):1–10. doi: 10.1016/j.jcmg. 2014. 11.002

9. Raff GL, Abidov A, Achenbach S, Berman DS, Boxt LM, Budoff MJ, et al. SCCT Guidelines for the interpretation and reporting of coronary computed tomographic angiography. *J Cardiovasc Comput Tomogr*. (2009) 3(2):122–36. doi: 10.1016/j. jcct. 2009.01.001

10. Xia S, Qiu W, Cai A, Kong B, Xu L, Wu Z, et al. The association of lipoprotein (a) and intraplaque neovascularization in patients with carotid stenosis: a retrospective study. *BMC Cardiovasc Disord*. (2021) 21(1):285. doi: 10.1186/s12872-021-02038-x

11. Huang Y, Liu Q, Xu J, Zhu W, Jiang J, Tang L, et al. Contrast-enhanced ultrasound perfusion patterns and serum lipid signatures of vulnerable carotid artery plaque in predicting stroke: a cohort study of carotid stenosis in Chinese patients. *Clin Hemorheol Microcirc*. (2020) 75(3):349–59. doi: 10.3233/ch-190804

12. Kwak BR, Bäck M, Bochaton-Piallat ML, Caligiuri G, Daemen MJ, Davies PF. Biomechanical factors in atherosclerosis: mechanisms and clinical implications. *Eur Heart J*. (2014) 35(43):3013–20, 3020a–3020d. doi: 10.1093/eurheartj/ehu353

13. Heck D, Jost A. Carotid stenosis, stroke, and carotid artery revascularization. *Prog Cardiovasc Dis*. (2021) 65:49–54. doi: 10.1016/j.pcad.2021.03.005

14. Li AL, Ji Y, Zhu S, Hu ZH, Xu XJ, Wang YW, et al. Risk probability and influencing factors of stroke in followed-up hypertension patients. *BMC Cardiovasc Disord*. (2022) 22(1):328. doi: 10.1186/s12872-022-02780-w

15. Turin TC, Okamura T, Afzal AR, Rumana N, Watanabe M, Higashiyama A, et al. Impact of hypertension on the lifetime risk of coronary heart disease. *Hypertens Res*. (2016) 39(7):548–51. doi: 10.1038/hr.2016.23

16. Tong H, Wang D, Fang M. Correlation between the variability of glycosylated hemoglobin and cardiovascular risk in new-onset T2DM patients. *Contrast Media Mol Imaging*. (2022) 2022:5370301. doi: 10.1155/2022/5370301

17. Kim KJ, Choi J, Bae JH, Kim KJ, Yoo HJ, Seo JA, et al. Time to reach target glycosylated hemoglobin is associated with long-term durable glycemic control and risk of diabetic complications in patients with newly diagnosed type 2 diabetes Mellitus: a 6-year observational study. *Diabetes Metab J*. (2021) 45(3):368–78. doi: 10.4093/dmj.2020.0046

18. Ceriello A, Esposito K, Piconi L, Ihnat MA, Thorpe JE, Testa R, et al. Oscillating glucose is more deleterious to endothelial function and oxidative stress than mean glucose in normal and type 2 diabetic patients. *Diabetes*. (2008) 57(5):1349–54. doi: 10.2337/db08-0063

19. Stratton IM, Adler AI, Neil HA, Matthews DR, Manley SE, Cull CA, et al. Association of glycaemia with macrovascular and microvascular complications of type 2 diabetes (UKPDS 35): prospective observational study. *Br Med J*. (2000) 321 (7258):405–12. doi: 10.1136/bmj.321.7258.405

20. Shah F, Balan P, Weinberg M, Reddy V, Neems R, Feinstein M, et al. Contrast-enhanced ultrasound imaging of atherosclerotic carotid plaque neovascularization: a new surrogate marker of atherosclerosis? *Vasc Med*. (2007) 12(4):291–7. doi: 10. 1177/1358863(07083363

21. Deyama J, Nakamura T, Takishima I, Fujioka D, Kawabata K, Obata JE, et al. Contrast-enhanced ultrasound imaging of carotid plaque neovascularization is useful for identifying high-risk patients with coronary artery disease. *Circ J*. (2013) 77(6):1499–507. doi: 10.1253/circj.cj-12-1529

22. Pikija S, Trkulja V, Mutzenbach JS, McCoy MR, Ganger P, Sellner J. Fibrinogen consumption is related to intracranial clot burden in acute ischemic stroke: a retrospective hyperdense artery study. *J Transl Med*. (2016) 14(1):250. doi: 10.1186/ s12967-016-1006-6

23. Deveci B, Gazi E. Relation between globulin, fibrinogen, and albumin with the presence and severity of coronary artery disease. *Angiology*. (2021) 72(2):174–80. doi: 10.1177/0003319720959985

24. Smith EB. Fibrinogen, fibrin and fibrin degradation products in relation to atherosclerosis. *Clin Haematol*. (1986) 15(2):355–70. doi: 10.1016/S0308-2261(18)30021-3

25. Pafili K, Penlioglou T, Mikhailidis DP, Papanas N. Mean platelet volume and coronary artery disease. *Curr Opin Cardiol*. (2019) 34(4):390–8. doi: 10.1097/hco. 0000000000000624

26. Sincer I, Gunes Y, Mansiroglu AK, Cosgun M, Aktas G. Association of mean platelet volume and red blood cell distribution width with coronary collateral development in stable coronary artery disease. *Postepy Kardiol Interwencyjnej*. (2018) 14(3):263–9. doi: 10.5114/aic.2018.78329

27. Choi DH, Kang SH, Song H. Mean platelet volume: a potential biomarker of the risk and prognosis of heart disease. *Korean J Intern Med*. (2016) 31(6):1009–17. doi: 10.3904/kjim.2016.078

28. Wada H, Dohi T, Miyauchi K, Shitara J, Endo H, Doi S, et al. Mean platelet volume and long-term cardiovascular outcomes in patients with stable coronary artery disease. *Atherosclerosis*. (2018) 277:108–12. doi: 10.1016/j.atherosclerosis.2018. 08.08.048

29. Gasparyan AY, Ayvazyan L, Mikhailidis DP, Kitas GD. Mean platelet volume: a link between thrombosis and inflammation? *Curr Pharm Des*. (2011) 17(1):47–58. doi: 10.2174/138161211795049804

Frontiers in Cardiovascular Medicine

TYPE Original Research
PUBLISHED 19 September 2023
DOI 10.3389/fcvm.2023.1264479

EDITED BY
Hong Chen,
Boston Children's Hospital, Harvard Medical School, United States

REVIEWED BY
Jian Xu,
University of Oklahoma Health Sciences Center, United States
Sudarshan Bhattacharjee,
Harvard Medical School, United States

*CORRESPONDENCE
Nicholas W. Chavkin
✉ nwc6qu@virginia.edu
Kenneth Walsh
✉ kw9ar@virginia.edu

RECEIVED 20 July 2023
ACCEPTED 07 September 2023
PUBLISHED 19 September 2023

CITATION
Chavkin NW, Vippa T, Jung C, McDonnell S, Hirschi KK, Gokce N and Walsh K (2023) Obesity accelerates endothelial-to-mesenchymal transition in adipose tissues of mice and humans.
Front. Cardiovasc. Med. 10:1264479.
doi: 10.3389/fcvm.2023.1264479

# Obesity accelerates endothelial-to-mesenchymal transition in adipose tissues of mice and humans

Nicholas W. Chavkin[1,2]*, Tanvi Vippa[1], Changhee Jung[1], Stephanie McDonnell[2], Karen K. Hirschi[1,2,3], Noyan Gokce[4] and Kenneth Walsh[1,5]*

[1]Robert M. Berne Cardiovascular Research Center, University of Virginia School of Medicine, Charlottesville, VA, United States, [2]Department of Cell Biology, University of Virginia School of Medicine, Charlottesville, VA, United States, [3]Department of Medicine, Yale Cardiovascular Research Center, Yale University School of Medicine, New Haven, CT, United States, [4]Department of Medicine and Whitaker Cardiovascular Institute, Boston University School of Medicine, Boston, MA, United States, [5]Hematovascular Biology Center, University of Virginia School of Medicine, Charlottesville, VA, United States

**Introduction:** Vascular dysfunction and chronic inflammation are characteristics of obesity-induced adipose tissue dysfunction. Proinflammatory cytokines can drive an endothelial-to-mesenchymal transition (EndoMT), where endothelial cells undergo a phenotypic switch to mesenchymal-like cells that are pro-inflammatory and pro-fibrotic. In this study, we sought to determine whether obesity can promote EndoMT in adipose tissue.
**Methods:** Mice in which endothelial cells are lineage-traced with eYFP were fed a high-fat/high-sucrose (HF/HS) or Control diet for 13, 26, and 52 weeks, and EndoMT was assessed in adipose tissue depots as percentage of $CD45^{-}CD31^{-}Acta2^{+}$ mesenchymal-like cells that were $eYFP^{+}$. EndoMT was also assessed in human adipose endothelial cells through cell culture assays and by the analysis of single cell RNA sequencing datasets obtained from the visceral adipose tissues of obese individuals.
**Results:** Quantification by flow cytometry showed that mice fed a HF/HS diet display a time-dependent increase in EndoMT over Control diet in subcutaneous adipose tissue (+3.0%, +2.6-fold at 13 weeks; +10.6%, +3.2-fold at 26 weeks; +11.8%, +2.9-fold at 52 weeks) and visceral adipose tissue (+5.5%, +2.3-fold at 13 weeks; +20.7%, +4.3-fold at 26 weeks; +25.7%, +4.8-fold at 52 weeks). Transcriptomic analysis revealed that EndoMT cells in visceral adipose tissue have enriched expression of genes associated with inflammatory and TGFβ signaling pathways. Human adipose-derived microvascular endothelial cells cultured with TGF-β1, IFN-γ, and TNF-α exhibited a similar upregulation of EndoMT markers and induction of inflammatory response pathways. Analysis of single cell RNA sequencing datasets from visceral adipose tissue of obese patients revealed a nascent EndoMT sub-cluster of endothelial cells with reduced *PECAM1* and increased *ACTA2* expression, which was also enriched for inflammatory signaling genes and other genes associated with EndoMT.
**Discussion:** These experimental and clinical findings show that chronic obesity can accelerate EndoMT in adipose tissue. We speculate that EndoMT is a feature of adipose tissue dysfunction that contributes to local inflammation and the systemic metabolic effects of obesity..

KEYWORDS

endothelial-to-mesenchymal transition, obesity, adipose, endothelium, aging, vascular biology

# Introduction

An estimated 39%–49% of the world population is overweight or obese (1, 2), and this condition significantly contributes to cardiovascular morbidity and mortality through the systemic dysregulation of inflammatory cytokines (3). Chronic obesity promotes dysfunctional adipose tissue remodeling, resulting in decreased circulation of anti-inflammatory adipokines and increased pro-inflammatory adipokines (3, 4). In obesity, dysfunctional adipose tissue is characterized by macrophage infiltration (5, 6) and polarization towards a pro-inflammatory phenotype (7), necrotic adipocytes surrounded by macrophages that can be visualized as "crown-like" structures (8), tissue fibrosis (9), and vascular rarefaction (10). In this condition, the local pro-inflammatory milieu of the adipose tissue affects adipocytes, fibroblasts, immune cells, and endothelial cells, contributing to adipose tissue dysfunction (3, 11–13). Additionally, adipose tissue hypoxia caused by vascular rarefaction and impaired endothelial cell function will lead to greater cellular stress and inflammation (14–16). These features contribute to a feedforward loop that increasingly favors systemic metabolic dysfunction under conditions of chronic obesity. Thus, a more detailed understanding the multicellular responses that promote dysregulated remodeling in adipose tissue is critical to determining underlying mechanisms of obesity-induced pathologies.

A known consequence of pro-inflammatory cytokines on endothelial cells is a transition from an endothelial to a mesenchymal phenotype (17). This process, termed Endothelial-to-Mesenchymal Transition (EndoMT), has been identified in numerous cardiovascular disease states, including atherosclerosis (18), myocardial infarction (19), pulmonary hypertension (20), and other conditions (21, 22). EndoMT occurring in obese adipose tissue could contribute to the pro-inflammatory, pro-fibrotic, and hypoxic environment that drives dysfunctional adipose tissue remodeling. Notably, a prior clinical study identified transitioning endothelial cells in visceral adipose tissue of obese patients through colocalized immunofluorescence imaging of Smooth Muscle alpha-Actin (mesenchymal marker) and CD31 (endothelial marker) in vessels (23). However, quantitative analysis of the extent of EndoMT enabled by mouse lineage tracing models, and elucidation of the conditions that promote EndoMT in adipose tissue, have not been investigated previously. As EndoMT involves the transition of endothelial cells to a new phenotypic state, studies describing EndoMT can be facilitated by murine transgenic methodologies and by mechanistic and single cell transcriptome analyses of EndoMT in human cells and tissues, respectively.

Herein, we examine EndoMT and underlying mechanisms in adipose tissue with experimental models and clinical datasets. First, employing methods that trace the endothelial cell lineage in mice, it was found that diet-induced obesity accelerates the rate of EndoMT in adipose tissue, particularly in visceral compared to subcutaneous adipose tissue. Transcriptomic analysis of the EndoMT cells from obese mice revealed the upregulation of EndoMT-related genes, including the enrichment of inflammatory response genes. A similar transcriptional profile was also observed in human primary adipose-derived endothelial cells treated with a pro-inflammatory cytokine cocktail to induce EndoMT. Finally, the analysis of single cell RNA sequencing (scRNAseq) datasets of stromal cells from the visceral adipose tissue of individuals with obesity revealed a subset of endothelial cells expressing transcripts associated with EndoMT. The combined analysis of these human single cell datasets identified transcription profiles that were also found in the experimental models of EndoMT. Collectively, these data support the conclusion that obesity accelerates EndoMT in adipose tissue and that this is associated with an inflammatory transcriptional response within the EndoMT cells.

# Materials and methods

## Animal work

All experiments and handling of mice was approved by the University of Virginia Animal Care and Use Committee (ACUC). Mice used in these experiments were generated from two transgenic alleles: Cdh5-CreERT2 (24) and ROSA26-eYFP (25). Tamoxifen was administered to mice at 6 weeks of age by 10 injections of 100 µl of 10 mg/ml Tamoxifen (Sigma, Cat #T5648) dissolved in peanut oil. Injections were performed once per day for 5 days, followed by 2 days of recovery, then once per day for 5 days. Mice were then given a recovery period of 14 days before further assays were performed. Euthanasia of mice was performed by overdose of inhaled isoflurane followed by surgical pneumothorax induction. Both male and female mice were used in these experiments.

## High fat and high sucrose (HF/HS) diet-induced obesity model

Mice were fed *ad libitum* with either a normal chow (NC) diet or high fat and high sucrose (HF/HS) diet (F1850, Bio-Serv) for 13, 26, or 52 weeks starting at 10 weeks after the tamoxifen injection protocol. Several mice were maintained on NC diet for 104 weeks. Total number of mice analyzed at 13 weeks was 8 NC diet (3 female, 5 male) and 15 HF/HS diet (8 female, 7 male), at 26 weeks was 9 NC diet (4 female, 5 male) and 17 HF/HS diet (9 female, 8 male), at 52 weeks was 9 NC diet (4 female, 5 male) and 13 HF/HS diet (8 female, 5 male), and at 104 weeks was 11 NC diet (4 female, 7 male). The composition of the HF/HS diet is 35.8% fat, 36.8% carbohydrate, and 20.3% protein. Mice were weighed at initiation of diet and at euthanasia. Metabolic function in some mice was assessed by glucose tolerance test (GTT) and insulin tolerance test (ITT) before euthanasia. GTT was performed by fasting mice overnight, administering an intraperitoneal injection of 1 mg glucose (50% dextrose injection, Hospira, Cat# 0409-6648-02) per 1 g body weight, then measuring blood glucose by glucose test strips (Accuchek, Roche) at 0, 15, 30, 60, 90, and 120 min after injection. ITT was performed by fasting mice for 4–6 h, administering an intraperitoneal injection of 0.75 U insulin (Humulin, Eli Lilly, Cat# 0002-8215-17) per 1 kg body weight, then measuring blood glucose at 0, 15, 30, 60, 90, and 120 min after injection.

## Tissue collection and analysis

Mice were euthanized according to protocols approved by the University of Virginia ACUC at 13, 26, and 52 weeks after diet, along with several mice at 104 weeks after normal control diet. Subcutaneous adipose tissue was collected from the inguinal fat pad. Visceral adipose tissue was collected from the epididymal fat pad. Lung, kidney, and liver were isolated. Small tissue samples were collected and fixed with 4% paraformaldehyde for immunofluorescent staining and imaging analysis. Cells were isolated from fresh tissues by physical mincing with dissection scissors and then incubation in digestion solution of 5 mg/ml Liberase$^{TM}$ (Sigma, Cat #LIBTM-RO) and 5 µl/ml elastase (Sigma, Cat #E1250) in HBSS (Gibco, Cat #14025092) at 37°C for 60 min. Digested tissue was then centrifuged at 1000 × g for 5 min, and the supernatant containing adipocytes was removed. The cell pellet was resuspended and passed through a 70 µm filter. If used for flow cytometry, cells were fixed with 4% paraformaldehyde for 10 min on ice. Cells were then washed and incubated in immunofluorescent antibodies for flow cytometry analysis and FACS in staining buffer containing 1% BSA (Sigma, Cat #A6003) in PBS (Gibco, Cat #10010023). If used for FACS, a viability stain was included to eliminate cells with ruptured membranes. Immunofluorescent antibodies were used for flow cytometry and FACS: BV421-conjugated anti-mouse CD31 (MEC 13.3, BD Biosciences, Cat #562939), PerCP-conjugated anti-mouse CD45 (30-F11, BD Biosciences, Cat #557235), AlexaFluor594-conjugated anti-Acta2 (D4K9N, Cell Signaling Technologies, Cat #36110). Flow cytometry and FACS were performed using a FACSMelody (BD Biosciences). Flow cytometry was analyzed using FlowJo v10.6.1. Linear and multivariate regression analysis was performed using the Fitting Linear Models function in R with the “lm()” function.

## Fluorescence immunostaining

Adipose tissue was isolated and fixed as described above. Tissues were dehydrated by sequential incubation in ethanol and xylene, embedded in paraffin wax, sectioned to 10 µm thick, incubated on slides to attach, and rehydrated by reverse incubation in xylene and ethanol into PBS. Tissue sections were prepared for immunostaining by performing antigen retrieval using antigen unmasking solution (Vector Labs, Cat #H-3300), permeabilized by incubating with 1% Tween20 in PBS for 30 min at room temperature, then blocked using 3% donkey serum and 0.1% Tween20 in PBS for 1 h at room temperature. Tissue sections were immunostained by incubation in primary antibodies (goat anti-CD31, Q08481, R&D Systems, Cat #AF3628; AlexaFluor594-conjugated rabbit anti-Acta2, D4K9N, Cell Signaling Technologies, Cat #36110; chicken anti-GFP, AbCam, Cat #ab13970) for 1 h at room temperature. After washing, fluorescence-conjugated secondary antibodies were incubated for 1 h at room temperature. DAPI (Thermo Scientific, Cat #62248) was incubated on tissue sections for 5 min at room temperature. Immunostained sections were imaged using a Leica Thunder DMi8 Fluorescence Microscope.

## Bulk RNA sequencing

Bulk RNA sequencing was performed on cells isolated from visceral adipose tissue after FACS or cultured human primary adipose-derived microvascular endothelial cells (described below). RNA from visceral adipose tissue was isolated from mice on NC diet ($n = 3$ male) or HF/HS diet ($n = 3$ male) for 52 weeks. RNA from cultured cells was isolated from Control treatment ($n = 3$) or EndoMT treatment ($n = 3$) as described below. RNA was purified using the RNeasy MinElute kit (Qiagen, Cat #74204). Purified RNA was submitted to the Yale Center for genome analysis for quality control analysis, low-input RNA sequencing amplification, PolyA RNA library preparation, and paired-end 100 bp sequencing (NovaSeq v2, Illumina). Samples were multiplexed in sequencing runs to average 20M reads per sample. Raw sequencing reads were demultiplexed into sample specific Fastq files, which were analyzed by aligning to reference genomes (mouse mm10 or human hg38) by Kallisto v0.46.2 (26). Differential gene expression analysis was performed with Sleuth v0.30.0 (27). Gene set enrichment analysis was performed with GSEA v4.1 software (Broad Institute).

## Cell culture EndoMT model

The EndoMT cell culture model was performed as previously described (23). Briefly, primary human adipose-derived microvascular endothelial cells (HAMVEC, ScienCell, Cat #7200) were obtained and passaged in EGM-2 (Lonza, Cat #CC-3162). For bulk RNA sequencing, HAMVEC were seeded into 6-well plates at $2.5 \times 10^5$ cells per well and grown overnight, then induced with either control media (EGM-2) or EndoMT induction media (EGM-2 with 5 ng/ml TNF-$\alpha$, 5 ng/ml IFN$\gamma$, and 5 ng/ml TGFβ1) for 4 days with an induction media change at 2 days, and RNA was collected and purified using the RNeasy MinElute kit (Qiagen, Cat #74204). Purified RNA was submitted for bulk RNA sequencing and analyzed, as described above. For immunofluorescence staining, HAMVEC were seeded onto 4-well chamber slides (ThermoFisher, Cat #154526) at $2.5 \times 10^4$ cells per chamber and subjected to the same EndoMT induction assay as above, then fixed with 4% paraformaldehyde and immunostained in staining buffer containing PBS with 3% donkey serum and 0.1% Tween20 with primary antibodies (Armenian hamster anti-CD31, 2H8, ThermoFisher, Cat #MA3105; AlexaFluor594-conjugated rabbit anti-Acta2, D4K9N, Cell Signaling Technology, Cat #36110), followed by staining with secondary fluorescent-labeled antibodies. DAPI was used as a nuclei counterstain. Immunostained fluorescent cells were imaged using a Leica SP8 Confocal Microscope.

## Analysis of single cell RNA sequencing datasets

Clinical single cell RNA sequencing datasets were obtained from previously published studies (28–30). De-multiplexed, aligned, and normalized data tables were downloaded from online repositories. Seurat v4 (31) was used to analyze each dataset individually. Data was selected for samples from visceral adipose tissue of obese patients, yielding 12,899 cells with 18,306 genes in the Vijay et al. dataset (28), 18,261 cells with 33,538 genes in the Hildreth et al. dataset (29), and 46,539 cells with 31,533 genes in the Emont et al. dataset (30). Cells were scaled and clustered using standard Seurat functions and variables, and UMAP dimensionality reduction was performed with 20 principal components. Endothelial cell clusters yielded 472 endothelial cells with 18,306 genes in the Vijay et al. dataset (28), 1,274 endothelial cells with 33,538 genes in the Hildreth et al. dataset (29), and 1,269 endothelial cells with 33,538 genes in the Emont et al. dataset (30), and they were further analyzed by scaling, clustering, and performing UMAP dimensionality reduction. Endothelial cell clusters were combined by SCT Integration following the Seurat analysis pipeline. Cell scoring was performed by the AddModuleScore function in the Seurat package using described gene sets. Imputation of gene expression was performed using the MAGIC algorithm (32) and visualized over UMAP reduction plots.

## Statistical analysis

Statistical tests were performed as stated in the figure legends. Tests were performed using either GraphPad Prism v9.4.1 or statistical testing from software used in R on either linear regression analysis, multivariate regression analysis, gene set enrichment analysis, or differential gene expression in Sleuth for bulk RNA sequencing analysis.

# Results

## Diet-induced obesity promotes EndoMT in murine adipose tissue

Endothelial cells lose the expression of endothelial-specific genes as they transition into a mesenchymal phenotype. Therefore, rigorous quantification of EndoMT can be facilitated by the pre-labeling of endothelial cells with a lineage tracing mouse model (Cdh5-CreER$^{T2}$; ROSA26-eYFP). In this system, endothelial cells are pre-labelled with eYFP by tamoxifen-induced Cre recombination, which removes a flox-stop-flox DNA cassette before the eYFP transgene and allows for permanent eYFP expression in any Cdh5 + endothelial cell prior to the initiation of the experimental diets and continues after tamoxifen administration is withdrawn and Cre is inactive. Through this method, endothelial cells that transition away from an endothelial cell phenotype over time and with diet, and therefore lose endothelial cell gene expression, can still be identified by eYFP expression. Mice are then fed either a normal control diet (NC diet) or an obesogenic high fat high sucrose diet (HF/HS diet) for 13, 26, or 52 weeks (**Figure 1A**). As expected, HF/HS diet significantly increased mouse body mass at all time points, and these mice increasingly exhibited impairments in their metabolic responses to the administration of glucose or insulin, indicative of systemic metabolic dysfunction (**Supplementary Figure S1**). EndoMT was then quantified in subcutaneous and visceral adipose tissue depots by isolating the stromal vascular fraction and performing flow cytometry to determine the percentage of eYFP$^{+}$ endothelial-derived cells within the CD45$^{-}$CD31$^{-}$Acta2$^{+}$ mesenchymal population (**Figure 1B**). Quantification showed that HF/HS diet induces a time-dependent increase in EndoMT cells that was greater in the visceral adipose tissue (9.6 ± 1.5% eYFP$^{+}$ of the CD45$^{-}$CD31$^{-}$Acta2$^{+}$ cells at 13 weeks, 27.0 ± 2.4% at 26 weeks, 32.4 ± 3.8% at 52 weeks, mean ± S.E.M) compared to subcutaneous adipose tissue (4.9 ± 0.4% at 13 weeks, 15.4 ± 2.2% at 26 weeks, 18.0 ± 2.7% at 52 weeks, mean ± S.E.M) at all time points analyzed (**Figure 1C**). In mice on NC diet, a time-dependent increase in EndoMT was also observed in the visceral adipose tissue (4.2 ± 0.4% at 13 weeks, 6.3 ± 1.2% at 26 weeks, 6.7 ± 1.1% at 52 weeks, mean ± S.E.M) and subcutaneous adipose tissues (1.9 ± 0.5% at 13 weeks, 4.8 ± 1.1% at 26 weeks, 6.2 ± 1.0% at 52 weeks, mean ± S.E.M) (**Figure 1C**). The rate of EndoMT in HF/HS diet compared to NC diet increased over time on diet in visceral adipose tissue (+5.5% eYFP$^{+}$ of the CD45$^{-}$CD31$^{-}$Acta2$^{+}$ cells, +2.3-fold at 13 weeks; + 20.7%, +4.3-fold at 26 weeks; +25.7%, +4.8-fold at 52 weeks) and subcutaneous adipose tissue (+3.0%, +2.6-fold at 13 weeks; +10.6%, +3.2-fold at 26 weeks; +11.8%, +2.9-fold at 52 weeks). Further, the percentage of EndoMT in subcutaneous and visceral adipose tissue are also linearly correlated with time on diet, with a greater correlation slope in mice on HF/HS diet in both adipose depots (0.235% per week in subcutaneous, 0.420% per week in visceral) compared to NC diet (0.115% per week in subcutaneous, 0.036% per week in visceral) and a greater slope of linear regression in HF/HS visceral adipose tissue compared to HF/HS subcutaneous adipose tissue (**Figure 1D**). Of note, EndoMT percentage was significantly correlated with age of mice on NC diet. This was investigated by maintaining mice on NC diet for 104 weeks and quantifying EndoMT percentage in visceral adipose tissue, revealing a continuation of the linear correlation between EndoMT percentage and age.

As many variables could be contributing to the extent of EndoMT in adipose tissue, the association of EndoMT with time on diet, body weight, and sex were investigated by multivariate regression analyses. These analyses showed that time on diet has a greater contribution to rate of EndoMT

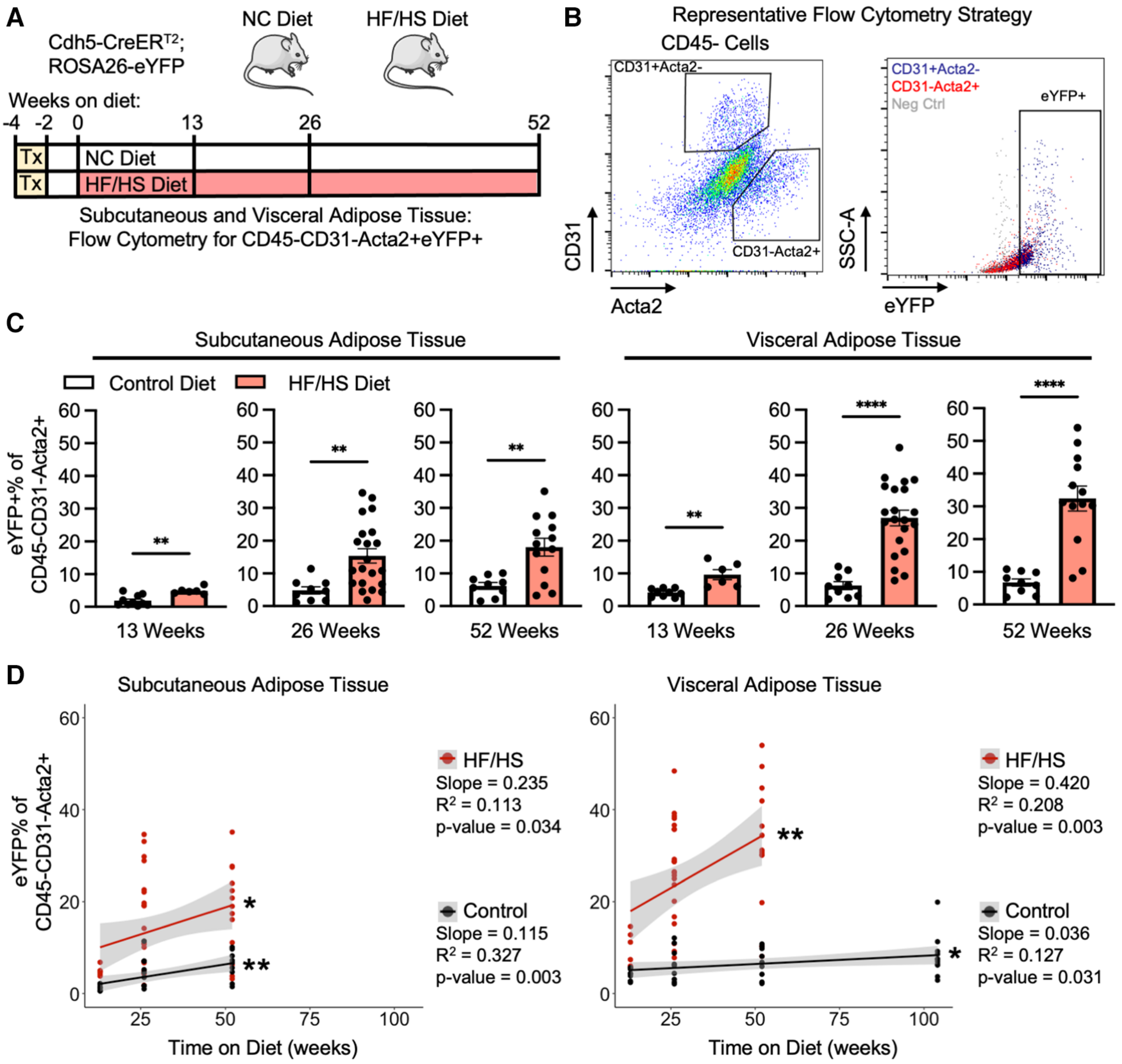

FIGURE 1
Adipose tissue endoMT in obesity-induced endothelial cell lineage tracing mice. (A) Overview schematic of the experimental strategy. (B) Representative flow cytometry gating strategy describes the identification of CD31-Acta2 + cells, then quantification of eYFP% of this population. (C) EndoMT rate defined as eYFP% of CD45-CD31-Acta2 + cells in subcutaneous and visceral adipose tissue from mice on Control or HF/HS diet for 13, 26, or 52 weeks (student's *t*-test, *p*-values: * <0.05, ** <0.01, *** <0.001, **** <0.0001). (D) Linear regression between rate of EndoMT and age in individual mice in subcutaneous or visceral adipose tissue between Control diet and HF/HS diet (linear correlation analysis, *p*-values: * <0.05, ** <0.01).

accumulation compared to overall mouse body weight in either subcutaneous or visceral adipose tissue (Figures 2A,B). This relationship was found regardless of whether mice are on HF/HS diet or NC diet. As expected, the relative rates of EndoMT accumulation are greater in visceral adipose compared to subcutaneous tissue depots, and this was also evident through paired longitudinal analyses of EndoMT in subcutaneous and visceral adipose tissues of individual mice at 13, 26, and 52 weeks on diet (Figure 2C). Sex as a biological variable for EndoMT was also investigated. Although overall weight gain is higher in male mice on HF/HS diet, the rate of EndoMT accumulation did not significantly differ between male and female mice in subcutaneous or visceral adipose tissue at 13, 26, or 52 weeks on either NC diet or HF/HS diet (Supplementary Figure S2). Finally, the extent of EndoMT was also investigated in other tissues. At 13 weeks on HF/HS diet, little or no EndoMT could be detected in lung, kidney, or liver, as determined by comparison with Cre-negative control mice, whereas EndoMT was readily observed in the subcutaneous and visceral adipose tissue (Figure 2D). Together, these analyses show that time on diet and visceral location provide the greatest contributions to the development of EndoMT in adipose tissue.

## Adipose EndoMT cells display increased inflammatory and TGFβ transcriptional responses

The localization of EndoMT cells was performed in the endothelial lineage tracing model through immunofluorescent imaging. In this analysis, a cell that is positive for eYFP and Acta2 but negative for

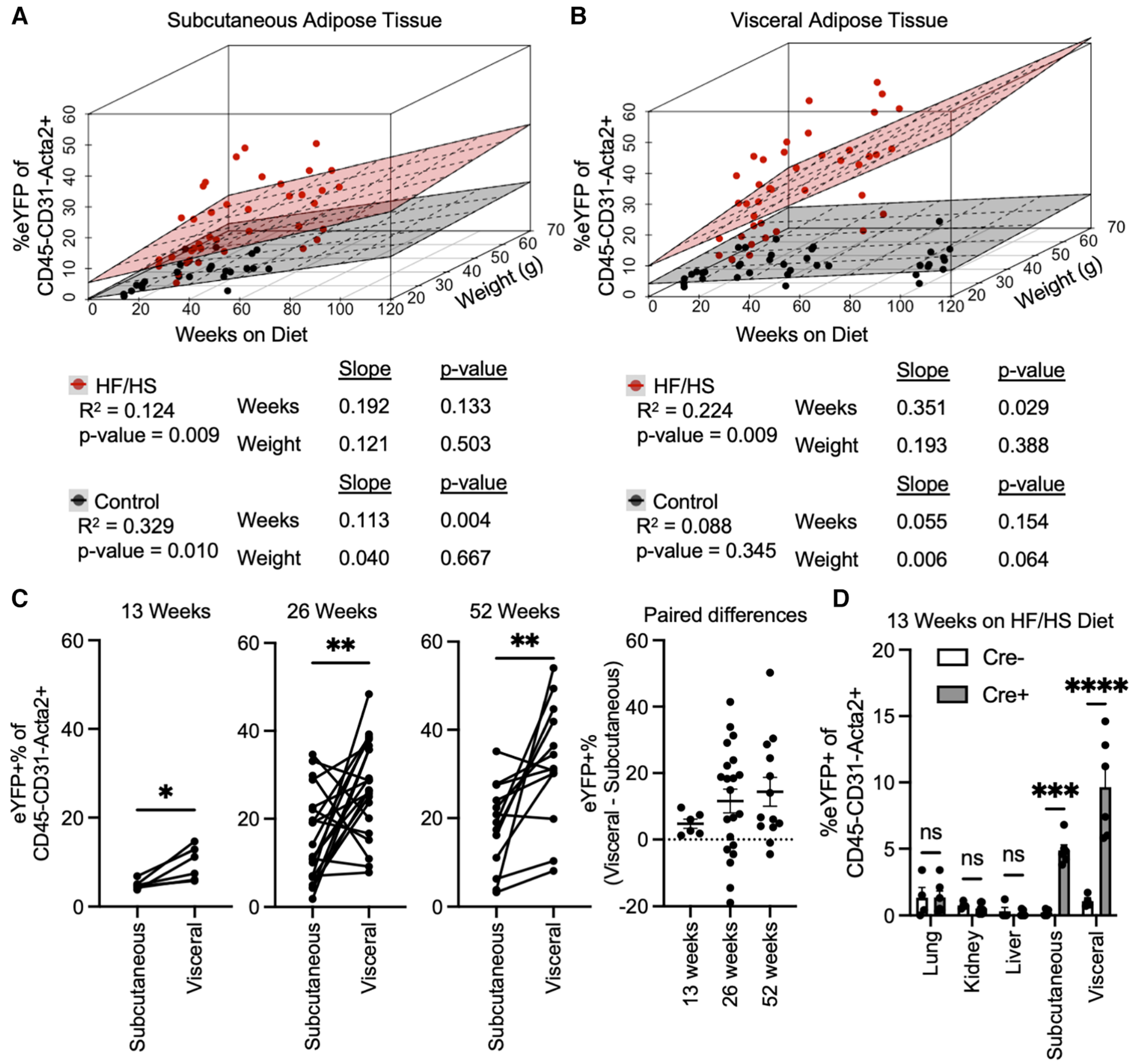

FIGURE 2
Associations of EndoMT to time on diet, body weight, and adipose tissue location. Multivariate regression analysis quantified relative association of EndoMT to weeks on diet or weight of mice in (A) subcutaneous or (B) visceral adipose tissue (slope and *p*-value presented from multivariate regression analysis). (C) Pairwise analysis of EndoMT in subcutaneous and visceral adipose tissues from the same mice are connected by lines in 13, 26, and 15 weeks on HF/HS diet, with paired differences quantified and presented as EndoMT in visceral minus EndoMT in subcutaneous adipose tissue (paired student's *t*-test, *p*-values: * <0.05, ** <0.01). (D) Rate of EndoMT was quantified in lung, kidney, liver, subcutaneous adipose tissue, and visceral adipose tissue in negative control mice (Cre- with no lineage tracing) and in reporter mice (Cre + with lineage tracing) at 13 weeks on HF/HS diet (one-way ANOVA with post-hoc Tukey, *p*-values: * <0.05, ** <0.01, *** <0.001, **** <0.0001).

CD31 is scored as an EndoMT-positive cell. Samples of visceral adipose tissue from mice fed HF/HS diet were isolated at 26 weeks on diet, and the tissues were fixed, sectioned, and immunostained for CD31, Acta2, and eYFP. Imaging of these sections revealed that EndoMT cells are found on the exterior to arterial vessels with protrusions that are oriented away from the vessel lumen (Figure 3A). A similar localization pattern has been observed in clinical specimens where the putative transitioning endothelial cells are identified within arterial vessels via the simultaneous expression of CD31 and ACTA2 (18, 20, 22, 23). In addition to the perivascular location, EndoMT cells were also identified in the regions of the visceral adipose tissue stroma (Figure 3B).

The transition from endothelial-to-mesenchymal phenotype corresponds to transcriptional changes that can have functional consequences (33). To investigate these transcriptional changes in the current context, stromal vascular fraction cells were isolated from the visceral adipose tissue of endothelial lineage-traced mice that were fed HF/HS diet for 52 weeks, and cells were separated by FACS into $CD31^+eYFP^+$ endothelial cells and $CD31^-eYFP^+$ EndoMT cells. RNA was isolated and bulk RNA sequencing was performed after low-input cDNA amplification on three paired replicate samples. The transcriptional profile of 885 genes was significantly different between endothelial cells and EndoMT cells, with 218 transcripts enriched in endothelial cells and 667

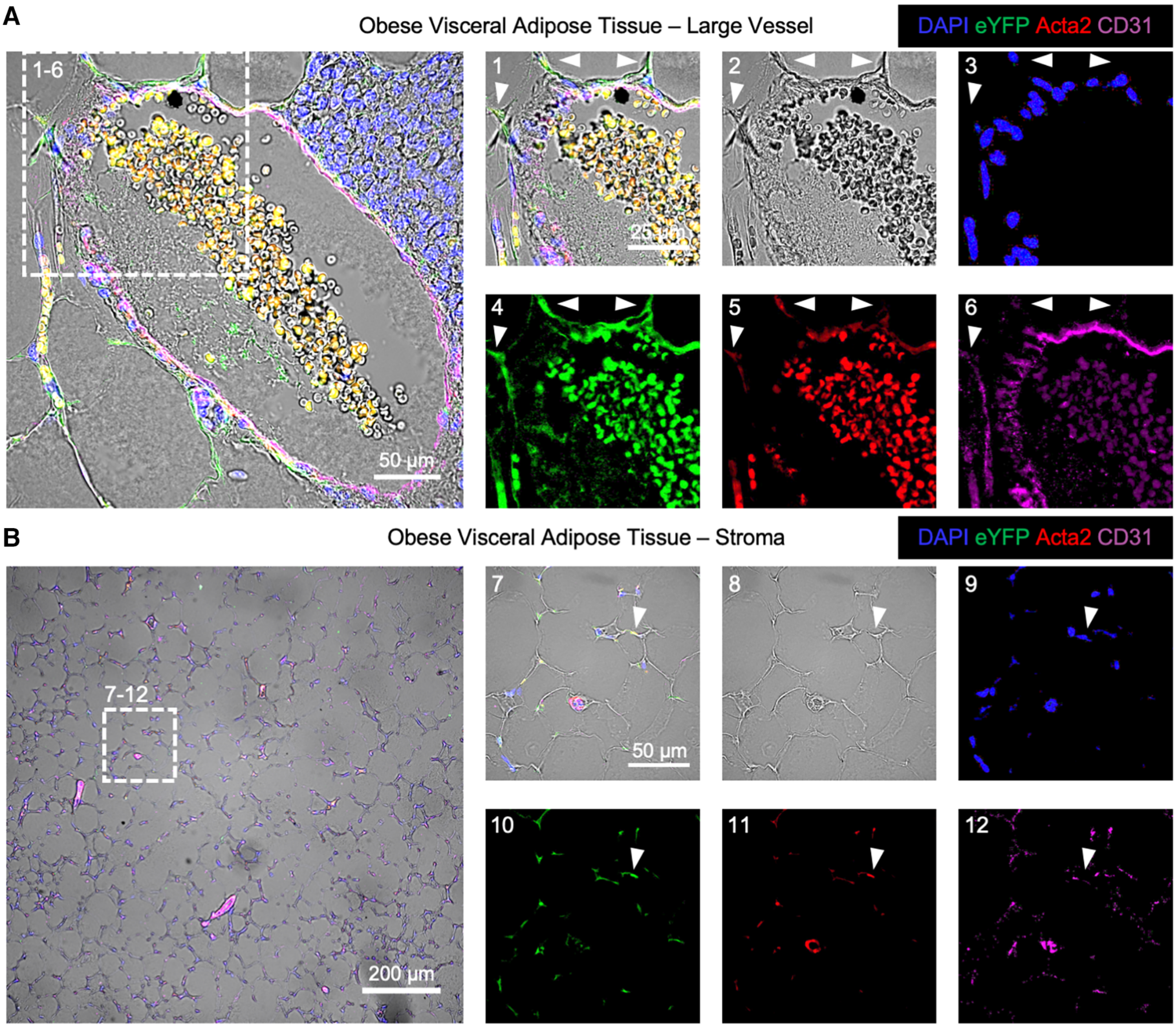

FIGURE 3
Immunofluorescence imaging of endoMT cells in obese visceral adipose tissue of mice. Visceral adipose tissue from Cdh5CreER$^{T2}$; Rosa26eYFP lineage tracing mice on HF/HS diet was immunofluorescently labeled for cell nuclei by DAPI, the eYFP reporter, Acta2, and CD31 overlaid with brightfield imaging to visualize EndoMT cells as DAPI + eYFP + Acta2 + CD31-. (A) A representative large vessel is shown, with a magnified section to highlight EndoMT cells by white arrows in (1) all channels, (2) brightfield, (3) DAPI, (4) eYFP, (5) Acta2, and (6) CD31. (B) A representative image of the stroma with small vessels is shown, with a magnified section to highlight an EndoMT cell by a white arrow in (1) all channels, (2) brightfield, (3) DAPI, (4) eYFP, (5) Acta2, and (6) CD31.

transcripts enriched in EndoMT cells (Figure 4A). Several genes enriched in endothelial cells are involved in reactive oxygen species signaling (e.g., *Sod1*, *Prdx1*), fatty acid metabolism (e.g., *Prdx6*, *Prdx1*, *Mgll*, *Pts*, *Dld*, *Rdh16*), and peroxisome signaling (e.g., *Pex11b*, *Gnpat*). Several genes enriched in EndoMT cells are involved in TGFβ signaling (e.g., *Tgfbr2*, *Tgfb2*), inflammation (e.g., *Il6*, *Il6ra*, *Il10rb*, *Fosb*, *Jun*, *Fosl2*, *Klf4*, *Cxcl1*, *Ripk1*), epithelial-to-mesenchymal transition (e.g., *Fbn1*, *Itgb3*, *Ccn1*), and extracellular matrix components (e.g., *Fn1*, *Col1a2*, *Col12a1*) (Figure 4A). Gene set enrichment analysis (GSEA) revealed that pathways characteristic of EndoMT cells, including epithelial-to-mesenchymal transition, inflammatory response, and TGFβ signaling, were significantly enriched or trending towards enrichment in CD31$^{-}$eYFP$^{+}$ EndoMT fraction (Figures 4B,C). In contrast, GSEA of the CD31$^{+}$eYFP$^{+}$ endothelial cells revealed a significant enrichment in reactive oxygen species signaling and peroxisome biology, and trending towards enrichment in fatty acid metabolism, which are hallmark pathways of vascular endothelial cells (Figures 4B,C). The cumulative transcriptional pattern of EndoMT cells compared to endothelial cells, including upregulation of genes known to promote inflammation and enrichment of downstream inflammatory pathways, suggests an activation of inflammatory processes during obesity associated EndoMT in adipose tissue.

## Human adipose endothelial cells can be induced to undergo EndoMT in cell culture

The potential for human adipose endothelial cells to undergo EndoMT was also assessed in a cell culture system. Primary human adipose-derived microvascular endothelial cells (HAMEC) were

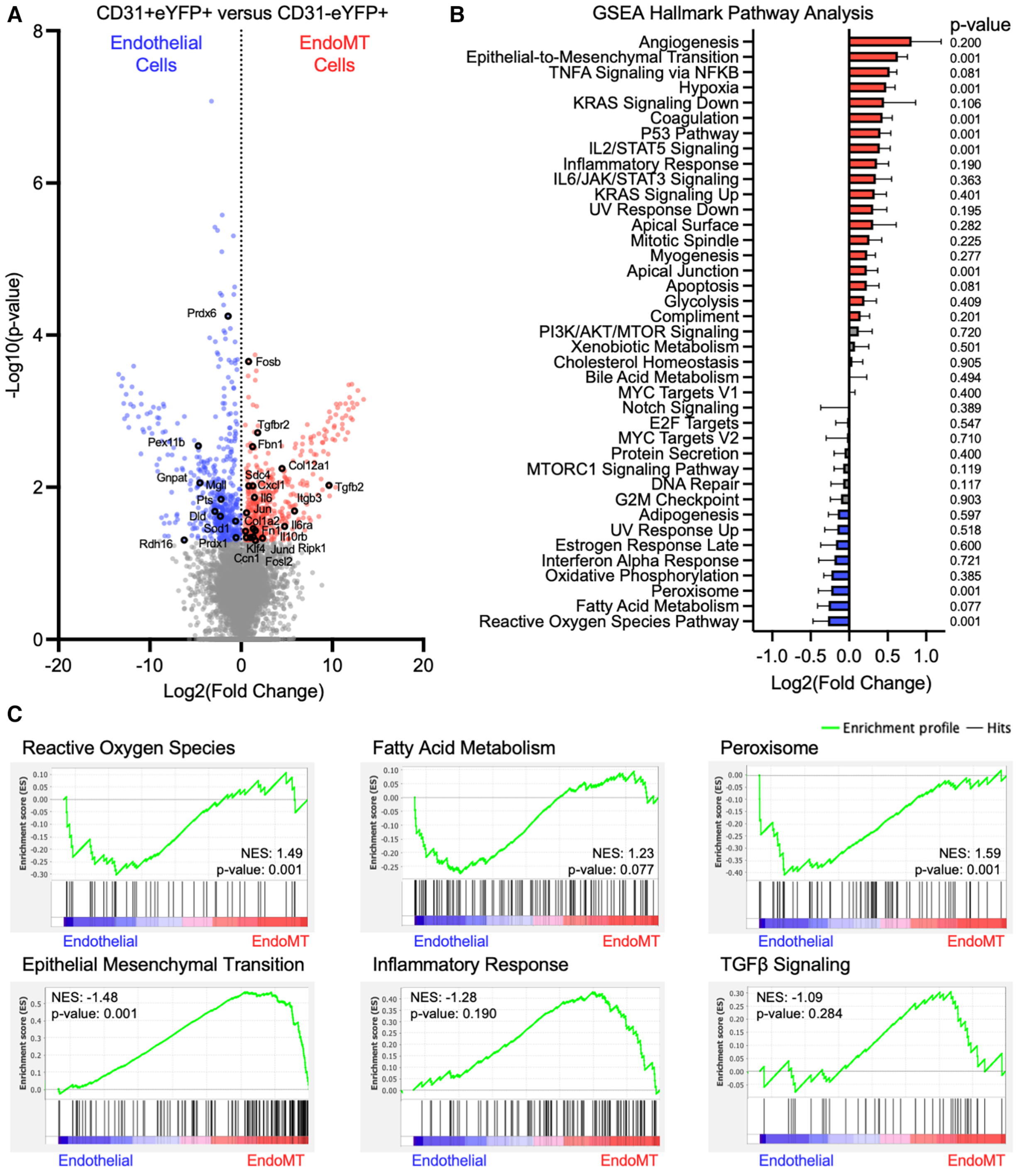

FIGURE 4
Transcriptomic analysis of murine endoMT cells in visceral adipose tissue of obese mice. (A) Differential expression of all genes identified through bulk RNA sequencing of CD31 + eYFP + endothelial cells vs. CD31-eYFP + EndoMT cells ($n = 3$ in each condition) was visualized by volcano plot showing the log2 (fold change) vs. the -log10 ($p$-value) of the change in gene expression, with genes significantly upregulated in endothelial cells in blue, EndoMT cells in red, and specific genes involved in endothelial cell function or EndoMT labeled. (B) Enrichment of GSEA Hallmark Pathways in all differentially expressed genes were visualized by log2 (fold change) and $p$-values listed, with pathways upregulated by 10% in red and downregulated by 10% in blue. (C) Enrichment profiles presented for terms enriched in endothelial cells (reactive oxygen species, fatty acid metabolism, peroxisome) and in EndoMT cells (epithelial mesenchymal transition, inflammatory response, TGFβ signaling).

treated with a pro-transition cocktail of TGF-β1, IFN-$\gamma$, and TNF-$\alpha$ to induce EndoMT, as previously described (23) (**Figure 5A**). The response of HAMEC to the treatment was visualized by fluorescence immunostaining of CD31 and ACTA2, revealing that cells transition from rounded CD31$^+$ endothelial cells to spindle-shaped ACTA2$^+$ mesenchymal-like cells (**Figure 5B**). RNA sequence analysis, performed on control and EndoMT cocktail-treated HAMEC, revealed genes that were significantly upregulated

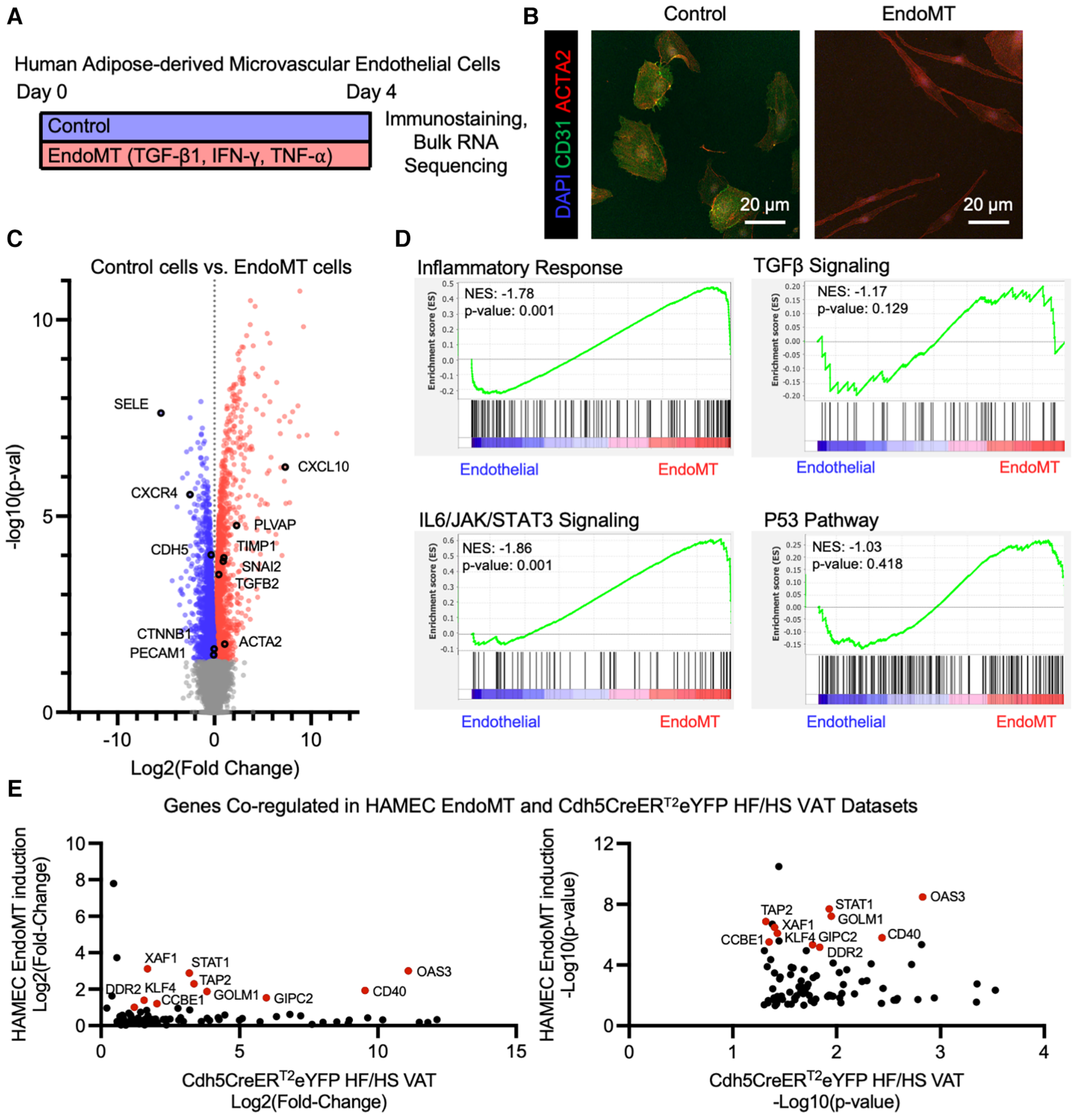

FIGURE 5
Endomt in cultured human adipose-derived microvascular endothelial cells. (A) Overview schematic of experimental strategy. (B) Representative immunofluorescence image of HAMEC induced with pro-inflammatory cytokines, visualizing DAPI, CD31, and ACTA2. (C) Differential expression of all genes identified through bulk RNA sequencing of Control vs. EndoMT cells ($n = 3$ in each condition) was visualized by volcano plot showing the log2 (fold change) vs. the -log10 ($p$-value) of the change in gene expression, with genes significantly upregulated in Control cells in blue, EndoMT cells in red, and specific genes involved in endothelial cell function or EndoMT labeled. (D) Enrichment plots of GSEA Hallmark Pathway analysis of inflammatory response, TGFβ signaling, IL6/JAK/STAT3 signaling, and P53 pathway. (E) Genes that are significantly upregulated in both EndoMT conditions (HAMEC and Cdh5CreER$^{T2}$; Rosa26eYFP HF/HS datasets), presented as relative log2 (fold change) and -log10 ($p$-value) quantifications, and genes with a 2-fold increase in both conditions labeled and highlighted in red.

and downregulated (**Figure 5C**). GSEA revealed significant enrichment of genes involved in inflammatory response and IL6/JAK/STAT3 signaling, and trending enrichment of P53 pathway and TGFβ signaling, in the transitioned cells (**Figure 5D**). Additionally, a comparison of transcriptomes from the obesogenic mouse (**Figure 4**) and human cell culture EndoMT models identified 86 genes that are significantly upregulated in both RNA sequencing datasets, with 10 genes significantly upregulated greater than 2-fold in both datasets (**Figure 5E**). These 10 genes are directly involved in the response to inflammatory stimuli (*STAT1, TAP2, CD40, OAS3, XAF1*), extracellular matrix remodeling (*CCBE1, DDR2*), or epithelial-to-mesenchymal transition (*KLF4, FOLM1, GIPC2*). Collectively, these analyses indicate that human adipose endothelial cells have the potential to undergo EndoMT, yielding a transcriptional profile that is similar to the transcriptional profile identified in the murine obesity-induced EndoMT model.

### Individual transitioning EndoMT cells are present in adipose tissues of individuals with obesity

To detect evidence of an EndoMT transcriptional profile in human adipose tissue, we analyzed publicly available scRNAseq datasets from the visceral adipose stromal vascular fraction of patients with obesity (28, 29, 30). Raw single cell RNA expression data from each of these three datasets was visualized by UMAP dimensionality reduction analysis and clustered into similar cell types, with endothelial cell clusters identified by expression of *PECAM1* (**Supplementary Figures S4A,B**). Within the endothelial cell clusters within each dataset, we could detect a sub-cluster of cells that expresses a relatively low level of *PECAM1* and relatively high level of *ACTA2* (**Supplementary Figures S4C,E**), suggesting these cells are undergoing EndoMT. Combining and integrating data from the endothelial cell clusters of all three datasets revealed a similar cluster of cells that are $PECAM1^{low}$ and $ACTA2^{high}$ in the pooled data (**Figure 6A**). This $PECAM1^{low}ACTA2^{high}$ cluster displayed an enrichment of genes that was similar to the EndoMT gene set enrichment observed in the obese lineage-traced mice and the HAMEC treated with EndoMT transitioning cocktail (**Figure 5E** and **Supplementary Figure S5A**). Inflammatory response genes associated with EndoMT processes in the murine and cell culture models were also observed in the human $PECAM1^{low}ACTA2^{high}$ cluster (**Supplementary Figure S5B**). Furthermore, there was a correlation between EndoMT transcript expression and inflammatory response gene expression within this cluster of human cells (**Supplementary Figure S5C**).

Differential gene expression analysis of the pooled EndoMT cluster from human visceral adipose tissue identified the enrichment of 23 genes (**Figure 6B**). Several of these genes have been associated with EndoMT in vascular-related diseases (*KLF4* (22, 34–36), *TIMP2* (18, 37), *JUN* (38)), and others have been associated with the similar process of Epithelial-to-Mesenchymal transition (*ANXA1* (39), *ERRFI1* (40), *IFITM3* (41), *IGFBP7* (42)). Notably, the upregulation of *KLF4* (Kruppel-Like Factor 4) (**Figure 6C**) was also observed in the bulk RNA sequencing analyses of the murine adipose tissue and human cell culture models (**Figure 5E**). KLF4 is a key transcription factor previously shown to promote EndoMT in cell culture models (22, 34, 43, 44). Thus, *KLF4* expression in the individual cells of the pooled EndoMT cluster from human visceral adipose tissue was compared to expression patterns of the gene sets enriched in the bulk RNA sequencing analyses of EndoMT in the model systems from **Figures 4**, **5**. This analysis revealed that increasing *KLF4* expression in human visceral adipose tissue correlates with increasing expression of the EndoMT gene set components identified in the model system. Similarly, a strong correlation was found between *KLF4* expression, and the expression of genes annotated in the Inflammatory Response GSEA pathway (**Figure 6D**). Collectively, these analyses reveal a consistency of data among the human adipose tissue, human cell culture, and murine lineage-tracing model, supporting the hypothesis that EndoMT occurs in visceral adipose tissue under conditions of obesity.

## Discussion

In this study, we investigated the effects of obesity on the transition of vascular endothelial cells to cells that display a mesenchymal phenotype within adipose tissue. EndoMT in adipose tissue was visualized, quantified and transcriptionally defined using endothelial cell lineage-traced mice fed an obesogenic diet, a cell culture model of HAMEC treated with an EndoMT pro-transition cocktail, and scRNAseq datasets from visceral adipose tissue biopsies of obese patients. In the mouse model, it was found that an obesogenic diet induces EndoMT in adipose tissue in a time-dependent manner. The increase in rate of EndoMT was greater in the visceral compared to subcutaneous adipose tissue depot, and a greater rate of EndoMT was more closely correlated to time-on-diet rather than overall mouse weight. RNA sequence analysis comparing vascular endothelial cells ($eYFP^{+}CD31^{high}ACT2A^{low}$) and EndoMT cells ($eYFP^{+}CD31^{low}ACT2A^{high}$) within the mouse visceral adipose documented the expression of EndoMT pathways that had been identified previously in other tissues, and also identified a robust increase in transcripts that encode for pro-inflammatory proteins. In the human cell culture model, RNA sequence analysis of HAMEC treated with the pro-transition cocktail of TGF-β1, TNF-alpha, and IFN-gamma also displayed transcriptional profiles consistent with a transition to a mesenchymal phenotype and the upregulation of multiple pro-inflammatory pathways. Finally, the interrogation of scRNAseq data sets from the visceral adipose tissues of obese individuals revealed subsets of cells with transcriptional profiles that are consistent with cells that are undergoing EndoMT. These three independent lines of evidence provide consistent evidence for EndoMT in the vasculature of adipose tissue in response to obesogenic stimuli.

These results suggest several mechanisms by which EndoMT could contribute to adipose tissue dysfunction. The transcriptional analyses of samples from murine models and human cell culture, as well as of scRNAseq data from clinical samples, all identified a widespread increase in pro-inflammatory signaling in the EndoMT cells. These data are consistent with a prior clinical study that identified histological markers of EndoMT in adipose tissue of obese patients and provided evidence that EndoMT cells promote tissue dysfunction through the release of pro-inflammatory extracellular vesicles (23). In the current study, we found an induction of IL-6 signaling in EndoMT cells. In other tissues, IL-6 has been shown to be produced by EndoMT cells (45), and that it is associated with EndoMT processes in pulmonary arterial hypertension (46), cardiac valves (47), and fibrosis in hearts and kidneys (48). In addition to inflammation, our transcriptomic analyses of EndoMT also identified enrichment of several pro-fibrotic genes, which has been associated with EndoMT cells in cardiovascular diseases (17). Fibrosis is a hallmark of dysfunctional adipose

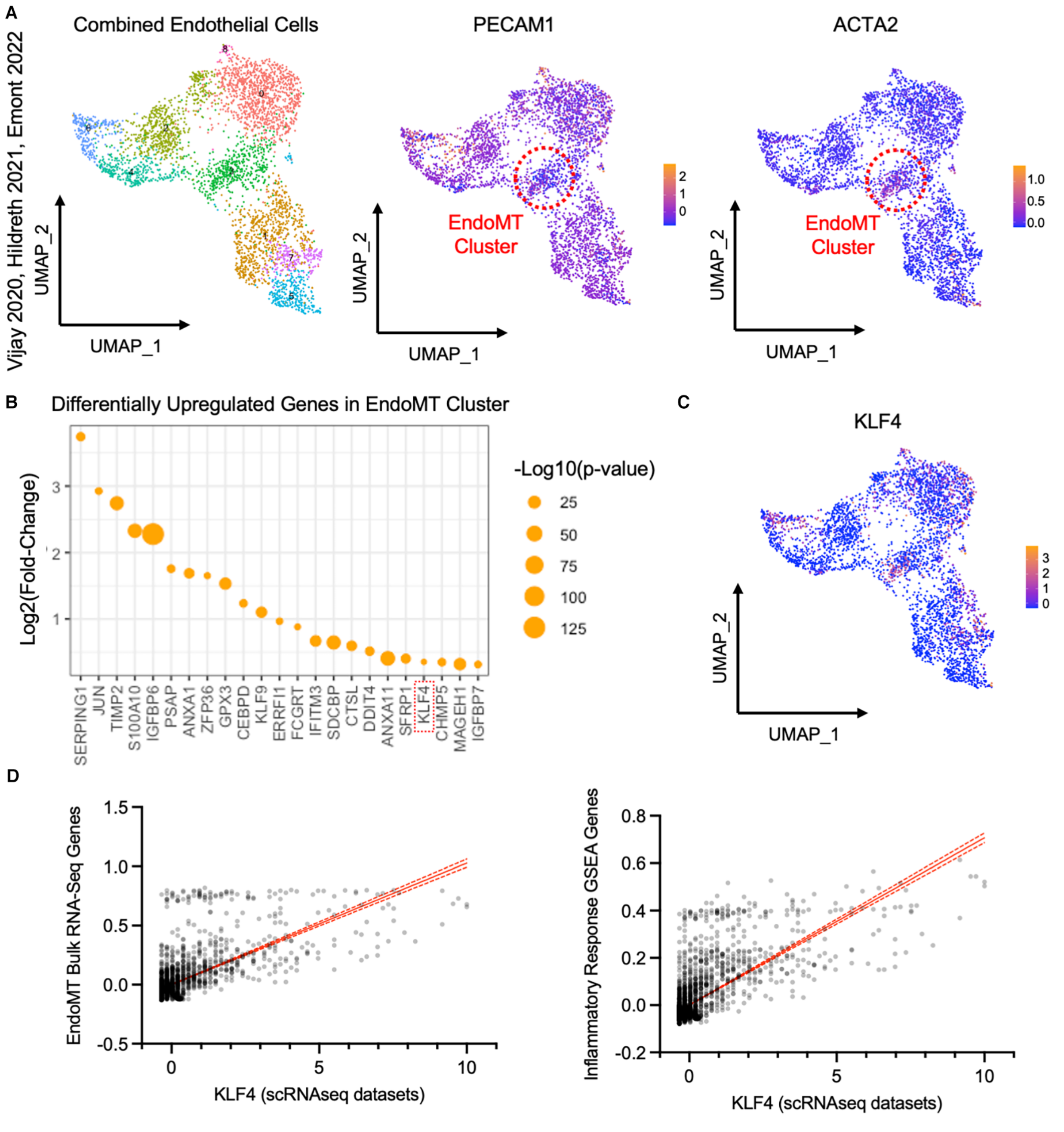

FIGURE 6
Analysis of endothelial cells from single cell RNA sequencing datasets of visceral adipose tissue from obese patients. (A) UMAP of endothelial cells from datasets published in Vijay 2020, Hildreth 2021, and Emont 2022, with an EndoMT cell cluster highlighted by a red circle, identified by reduced relative *PECAM1* expression and increased relative *ACTA2* expression plotted by UMAP. (B) Log2 (fold change) and -log10 (*p*-value) of genes upregulated in the EndoMT cell cluster compared to other endothelial cells. (C) Relative *KLF4* expression in endothelial cells plotted by UMAP. (D) Linear correlation between expression of *KLF4* and combined expression of genes that are co-regulated in bulk RNA sequencing datasets from HAMEC and Cdh5CreER$^{T2}$; Rosa26eYFP ($r^2$ = 0.456, *p*-value <0.0001, left) and genes in the inflammatory response GSEA ($r^2$ = 0.527, *p*-value <0.0001, right).

tissue that inhibits adipocyte lipid accumulation and adipocyte expansion, leading to pro-inflammatory cytokine secretion by adipocytes and impaired adipocyte function that increases systemic insulin resistance and glucose intolerance (49). Endothelial cell dysfunction in adipose tissue can promote fibrosis through impaired angiogenesis and increased inflammatory processes that activate adipose fibroblasts (11, 14) many of which we identified to be enriched in EndoMT cells. Furthermore, EndoMT affects vascular integrity and promotes vascular rarefaction (50, 51), which could further promote adipose tissue dysfunction. Vascular rarefaction promotes hypoxia, and we identified hypoxia as an enriched pathway in EndoMT cells in obese murine adipose tissues. Additionally, vascular rarefaction is induced in adipose tissue by an obesogenic diet (16) and is known to promote tissue fibrosis and dysfunction (52). Consistent with these possible connections to tissue pathology, we found that the rate of EndoMT was greater in visceral adipose tissue compared to subcutaneous adipose tissue. These pathologic responses in the adipose microenvironment (inflammation, fibrosis, vascular rarefaction) have been shown to be greater in visceral adipose tissue compared to subcutaneous adipose tissue, contributing to greater obesity-induced adipose tissue dysfunction in visceral depots (3). Future studies into differences between progression of EndoMT in subcutaneous vs. visceral adipose tissue depots may further elucidate the connection between obesity associated pathology and adipose EndoMT. Through these pathways involving hypoxia, inflammation, and fibrosis, EndoMT may constitute an aspect of endothelial cell dysfunction that contributes to many of the features that are recognized to be components of the pathophysiology of adipose tissue dysfunction.

Our results suggest that aging, in addition to obesity, may be contributing to the EndoMT in adipose tissue. We found that mice on a control diet also displayed detectable EndoMT in adipose tissue that increases with time, albeit at a slower rate. Supporting this notion, we also found that the amount of time mice spent on a HF/HS diet has a greater association with degree of EndoMT than does the weight of the mice. Several studies have suggested that age may induce EndoMT through activation of pathways that are shared between aging and EndoMT processes (33), including oxidative stress and inflammation (53), Nrf2 inhibition (54), and mTOR inhibition (55). Additionally, it has been reported that human endothelial cells undergo EndoMT after replicative aging in culture (56, 57), suggesting that this effect of aging is intrinsic to endothelial cells. It can be speculated that the extrinsic effects of obesogenic diet can accelerate these processes. In this regard, EndoMT is known to be induced by high concentrations of glucose (58, 59) and oxidized low-density lipoprotein (60), and inhibited by high-density lipoproteins (61), indicating that changes in serum metabolites and lipoprotein particles could be features of the obesogenic diet that promotes EndoMT in adipose tissues. Our results showed that an obesogenic diet did not promote EndoMT in lung, liver, or kidney tissues, but was instead restricted to adipose tissue. These findings may suggest that other aspects of early adipose tissue dysfunction induced by an obesogenic diet may initiate or promote adipose EndoMT. It is also possible that obesity could exacerbate EndoMT in other tissues, but this may also require direct injury to these tissues. Further investigations are necessary to test this hypothesis.

Our analysis of the human scRNAseq datasets revealed changes in several transcripts that were unique to the identified EndoMT cluster of visceral adipose tissue. Of these genes, the transcription factor KLF4 was identified in transcript analysis of the cultured human adipose tissue endothelial cell model, and its expression level correlated with the expression of genes associated with inflammation and EndoMT. KLF4 is of particular interest because of its reported role in promoting EndoMT in several vascular diseases, including cerebral cavernous malformations (22, 34), coronary arterial wall damage in Kawasaki disease (35), and tumor vascular dysfunction (36). It has also been shown that the downregulation of *KLF4* in cultured endothelial cells inhibits the process of EndoMT (43, 44). In addition to *KLF4*, several other genes identified in the EndoMT cluster have been associated with EndoMT, including *TIMP2* (18, 37) and *JUN* (38), while other genes have been associated with the similar process of Epithelial-to-Mesenchymal Transition including *ANXA1* (39), *ERRFI1* (40), *IFITM3* (41), *IGFBP7* (42). These gene expression patterns provide further support for the notion that EndoMT in adipose tissue is a feature of obesity in humans and mice. Furthermore, these gene expression patterns also resemble inflammation-induced EndoMT (62), which leads to the development of tissue fibrosis, another feature of adipose tissue dysfunction (49), as well as atherosclerosis and neointimal thickening (63, 64).

Recent studies, in various contexts, have highlighted the limitations of drawing conclusions about EndoMT from individual lines of evidence, as discussed in several recent reviews (33, 65, 66). Thus, we have endeavored to provide multiple lines of corroborating experimental evidence from mouse and human systems to document the presence of EndoMT in adipose tissue. However, we acknowledge that this study has limitations. For example, the murine lineage tracing strategy employed here does not provide evidence for a permanent transition to a cell with a mesenchymal identity. A partial EndoMT or reversible EndoMT process has been described in myocardial infarction (19), and the lineage tracing model does not distinguish between permanent and partial EndoMT. Our methods for identifying endothelial cells may also have limitations, since some tissue-specific endothelial cells may have reduced or no expression of traditional endothelial cell markers that might not be labeled by the Cdh5-Cre$^{ERT2}$; Rosa26-eYFP model or the CD31-mediated flow cytometry strategy [e.g., liver sinusoidal endothelial cells (67)]. Although this may limit our interpretation of results on EndoMT in other tissues, this has not been reported for adipose endothelial cells. Additionally, age-dependent declines in the efficiency of the Cdh5-Cre$^{ERT2}$ construct or stability of Rosa26-eYFP reporter may impact the measured rates of EndoMT. However, these murine reporter-based limitations would decrease, and not increase, the calculated rates of EndoMT. Furthermore, the murine HF/HS diet induces both adiposity and overall metabolic dysfunction. Thus, our model cannot distinguish between fat mass expansion *per se* or the subsequent metabolic dysfunction as the mechanistic cause of the EndoMT in adipose tissue. The HF/HS model is designed to recapitulate clinical consequences of obesity, and our analysis of clinical samples also revealed an EndoMT signature in visceral adipose tissue of obese patients. Thus, we believe these findings have clinical significance for the understanding of obesity-induced adipose tissue dysfunction. Finally, interpretations of cell transitions in scRNAseq data analyses can be influenced by technical limitations associated with cell or nuclei isolations from patient tissue samples or the lack of sensitivity of next-generation sequencing. However, we believe that the identification of multiple unique gene transcripts associated with EndoMT in human adipose tissue strongly supports the interpretation that EndoMT is present in these clinical samples.

In summary, the combination of results from an obesogenic murine lineage tracing model, cell culture induction model, and the scRNAseq datasets from human adipose tissue support the conclusion that obesity promotes EndoMT in adipose tissue.

## Data availability statement

The datasets presented in this study can be found in online repositories. The names of the repository/repositories and accession number(s) can be found below: https://www.ncbi.nlm.nih.gov/geo/, GSE241015.

## Ethics statement

The animal study was approved by University of Virginia Animal Care and Use Committee (ACUC). The study was conducted in accordance with the local legislation and institutional requirements.

## Author contributions

NC: Conceptualization, Funding acquisition, Investigation, Writing – original draft. TV: Investigation, Writing – review & editing. CJ: Investigation, Writing – review & editing. SM: Investigation, Writing – review & editing. KH: Funding acquisition, Project administration, Supervision, Writing – review & editing. NG: Funding acquisition, Writing – review & editing. KW: Conceptualization, Funding acquisition, Project administration, Supervision, Writing – review & editing.

## Funding

The author(s) declare financial support was received for the research, authorship, and/or publication of this article.

Grant awards from the National Institutes of Health have funded the presented experiments. The following grant funding was awarded to the listed individuals: NWC. (AHA 23CDA1054358, T32 HL007224, T32 HL007284), KKH. (R01 HL146056, R01 DK118728, UH3 EB025765), NG. and KW. (Co-PI R01 HL142650), NG. (R01 HL140836), KW. (R01 AG073249, R21 AG072095, R01 HL139819, R01 HL141256, R01 HL152174).

## Acknowledgments

We thank the Yale Center for Genomic Analysis for advice on RNA library preparation and performing bulk RNA sequencing.

## Conflict of interest

The authors declare that the research was conducted in the absence of any commercial or financial relationships that could be construed as a potential conflict of interest.

## Publisher's note

## Supplementary material

The Supplementary Material for this article can be found online at: https://www.frontiersin.org/articles/10.3389/fcvm.2023.1264479/full#supplementary-material

## References

1. Maffetone PB, Rivera-Dominguez I, Laursen PB. Overfat and underfat: new terms and definitions long overdue. *Front Public Health*. (2016) 4:279. doi: 10.3389/fpubh.2016.00279

2. Powell-Wiley TM, Poirier P, Burke LE, Després JP, Gordon-Larsen P, Lavie CJ, et al. Obesity and cardiovascular disease: a scientific statement from the American heart association. *Circulation*. (2021) 143(21):e984–e1010. doi: 10.1161/CIR.0000000000000973

3. Fuster JJ, Ouchi N, Gokce N, Walsh K. Obesity-induced changes in adipose tissue microenvironment and their impact on cardiovascular disease. *Circ Res*. (2016) 118(11):1786–807. doi: 10.1161/CIRCRESAHA.115.306885

4. Ouchi N, Parker JL, Lugus JJ, Walsh K. Adipokines in inflammation and metabolic disease. *Nat Rev Immunol*. (2011) 11(2):85–97. doi: 10.1038/nri2921

5. Weisberg SP, McCann D, Desai M, Rosenbaum M, Leibel RL, Ferrante AW. Obesity is associated with macrophage accumulation in adipose tissue. *J Clin Invest*. (2003) 112(12):1796–808. doi: 10.1172/JCI19246

6. Amano SU, Cohen JL, Vangala P, Tencerova M, Nicoloro SM, Yawe JC, et al. Local proliferation of macrophages contributes to obesity-associated adipose tissue inflammation. *Cell Metab*. (2014) 19(1):162–71. doi: 10.1016/j.cmet.2013.11.017

7. Kratz M, Coats BR, Hisert KB, Hagman D, Mutskov V, Peris E, et al. Metabolic dysfunction drives a mechanistically distinct proinflammatory phenotype in adipose tissue macrophages. *Cell Metab*. (2014) 20(4):614–25. doi: 10.1016/j.cmet.2014.08.010

8. Cinti S, Mitchell G, Barbatelli G, Murano I, Ceresi E, Faloia E, et al. Adipocyte death defines macrophage localization and function in adipose tissue of obese mice and humans. *J Lipid Res*. (2005) 46(11):2347–55. doi: 10.1194/jlr.M500294-JLR200

9. Divoux A, Tordjman J, Lacasa D, Veyrie N, Hugol D, Aissat A, et al. Fibrosis in human adipose tissue: composition, distribution, and link with lipid metabolism and fat mass loss. *Diabetes*. (2010) 59(11):2817–25. doi: 10.2337/db10-0585

10. Pasarica M, Sereda OR, Redman LM, Albarado DC, Hymel DT, Roan LE, et al. Reduced adipose tissue oxygenation in human obesity: evidence for rarefaction, macrophage chemotaxis, and inflammation without an angiogenic response. *Diabetes*. (2009) 58(3):718–25. doi: 10.2337/db08-1098

11. Crewe C, An YA, Scherer PE. The ominous triad of adipose tissue dysfunction: inflammation, fibrosis, and impaired angiogenesis. *J Clin Invest*. (2017) 127(1):74–82. doi: 10.1172/JCI88883

12. Guzik TJ, Skiba DS, Touyz RM, Harrison DG. The role of infiltrating immune cells in dysfunctional adipose tissue. *Cardiovasc Res*. (2017) 113(9):1009–23. doi: 10.1093/cvr/cvx108

13. Marcelin G, Silveira ALM, Martins LB, Ferreira AV, Clement K. Deciphering the cellular interplays underlying obesity-induced adipose tissue fibrosis. *J Clin Invest*. (2019) 129(10):4032–40. doi: 10.1172/JCI129192

14. Herold J, Kalucka J. Angiogenesis in adipose tissue: the interplay between adipose and endothelial cells. *Front Physiol*. (2020) 11:624903. doi: 10.3389/fphys.2020.624903

15. Trayhurn P. Hypoxia and adipose tissue function and dysfunction in obesity. *Physiol Rev*. (2013) 93(1):1–21. doi: 10.1152/physrev.00017.2012

16. Shimizu I, Aprahamian T, Kikuchi R, Shimizu A, Papanicolaou KN, MacLauchlan S, et al. Vascular rarefaction mediates whitening of brown fat in obesity. *J Clin Invest*. (2014) 124(5):2099–112. doi: 10.1172/JCI71643

17. Kovacic JC, Dimmeler S, Harvey RP, Finkel T, Aikawa E, Krenning G, et al. Endothelial to mesenchymal transition in cardiovascular disease: jacc state-of-the-art review. *J Am Coll Cardiol*. (2019) 73(2):190–209. doi: 10.1016/j.jacc.2018.09.089

18. Evrard SM, Lecce L, Michelis KC, Nomura-Kitabayashi A, Pandey G, Purushothaman KR, et al. Endothelial to mesenchymal transition is common in atherosclerotic lesions and is associated with plaque instability. *Nat Commun*. (2016) 7:11853. doi: 10.1038/ncomms11853

19. Tombor LS, John D, Glaser SF, Luxan G, Forte E, Furtado M, et al. Single cell sequencing reveals endothelial plasticity with transient mesenchymal activation after myocardial infarction. *Nat Commun*. (2021) 12(1):681. doi: 10.1038/s41467-021-20905-1

20. Ranchoux B, Antigny F, Rucker-Martin C, Hautefort A, Pechoux C, Bogaard HJ, et al. Endothelial-to-mesenchymal transition in pulmonary hypertension. *Circulation*. (2015) 131(11):1006–18. doi: 10.1161/CIRCULATIONAHA.114.008750

21. Wirrig EE, Yutzey KE. Conserved transcriptional regulatory mechanisms in aortic valve development and disease. *Arterioscler Thromb Vasc Biol*. (2014) 34(4):737–41. doi: 10.1161/ATVBAHA.113.302071

22. Bravi L, Malinverno M, Pisati F, Rudini N, Cuttano R, Pallini R, et al. Endothelial cells lining sporadic cerebral cavernous malformation cavernomas undergo endothelial-to-mesenchymal transition. *Stroke*. (2016) 47(3):886–90. doi: 10.1161/STROKEAHA.115.011867

23. Haynes BA, Yang LF, Huyck RW, Lehrer EJ, Turner JM, Barabutis N, et al. Endothelial-to-mesenchymal transition in human adipose tissue vasculature alters the particulate secretome and induces endothelial dysfunction. *Arterioscler Thromb Vasc Biol*. (2019) 39(10):2168–91. doi: 10.1161/ATVBAHA.119.312826

24. Sorensen I, Adams RH, Gossler A. Dll1-Mediated notch activation regulates endothelial identity in mouse fetal arteries. *Blood*. (2009) 113(22):5680–8. doi: 10.1182/blood-2008-08-174508

25. Srinivas S, Watanabe T, Lin CS, William CM, Tanabe Y, Jessell TM, et al. Cre reporter strains produced by targeted insertion of Eyfp and Ecfp into the Rosa26 locus. *BMC Dev Biol*. (2001) 1:4. doi: 10.1186/1471-213x-1-4

26. Bray NL, Pimentel H, Melsted P, Pachter L. Near-Optimal probabilistic RNA-Seq quantification. *Nat Biotechnol*. (2016) 34(5):525–7. doi: 10.1038/nbt.3519

27. Pimentel H, Bray NL, Puente S, Melsted P, Pachter L. Differential analysis of RNA-Seq incorporating quantification uncertainty. *Nat Methods*. (2017) 14(7):687–90. doi: 10.1038/nmeth.4324

28. Vijay J, Gauthier MF, Biswell RL, Louiselle DA, Johnston JJ, Cheung WA, et al. Single-cell analysis of human adipose tissue identifies depot and disease specific cell types. *Nat Metab*. (2020) 2(1):97–109. doi: 10.1038/s42255-019-0152-6

29. Hildreth AD, Ma F, Wong YY, Sun R, Pellegrini M, O'Sullivan TE. Single-cell sequencing of human white adipose tissue identifies new cell states in health and obesity. *Nat Immunol*. (2021) 22(5):639–53. doi: 10.1038/s41590-021-00922-4

30. Emont MP, Jacobs C, Essene AL, Pant D, Tenen D, Colleluori G, et al. A single-cell atlas of human and mouse white adipose tissue. *Nature*. (2022) 603(7903):926–33. doi: 10.1038/s41586-022-04518-2

31. Hao Y, Hao S, Andersen-Nissen E, Mauck WM, Zheng S, Butler A, et al. Integrated analysis of multimodal single-cell data. *Cell*. (2021) 184(13):3573–87. doi: 10.1016/j.cell.2021.04.048

32. van Dijk D, Sharma R, Nainys J, Yim K, Kathail P, Carr AJ, et al. Recovering gene interactions from single-cell data using data diffusion. *Cell*. (2018) 174(3):716–29. doi: 10.1016/j.cell.2018.05.061

33. Xu Y, Kovacic JC. Endothelial to mesenchymal transition in health and disease. *Annu Rev Physiol*. (2023) 85:245–67. doi: 10.1146/annurev-physiol-032222-080806

34. Cuttano R, Rudini N, Bravi L, Corada M, Giampietro C, Papa E, et al. Klf4 is a key determinant in the development and progression of cerebral cavernous malformations. *EMBO Mol Med*. (2016) 8(1):6–24. doi: 10.15252/emmm.201505433

35. He M, Chen Z, Martin M, Zhang J, Sangwung P, Woo B, et al. Mir-483 targeting of ctgf suppresses endothelial-to-mesenchymal transition: therapeutic implications in Kawasaki disease. *Circ Res*. (2017) 120(2):354–65. doi: 10.1161/CIRCRESAHA.116.310233

36. Chen HF, Wu KJ. Endothelial transdifferentiation of tumor cells triggered by the Twist1-Jagged1-Klf4 axis: relationship between cancer stemness and angiogenesis. *Stem Cells Int*. (2016) 2016:6439864. doi: 10.1155/2016/6439864

37. Qin W, Zhang L, Li Z, Xiao D, Zhang Y, Zhang H, et al. Endothelial to mesenchymal transition contributes to nicotine-induced atherosclerosis. *Theranostics*. (2020) 10(12):5276–89. doi: 10.7150/thno.42470

38. Rieder F, Kessler SP, West GA, Bhilocha S, de la Motte C, Sadler TM, et al. Inflammation-induced endothelial-to-mesenchymal transition: a novel mechanism of intestinal fibrosis. *Am J Pathol*. (2011) 179(5):2660–73. doi: 10.1016/j.ajpath.2011.07.042

39. Oshi M, Tokumaru Y, Mukhopadhyay S, Yan L, Matsuyama R, Endo I, et al. Annexin A1 expression is associated with epithelial-mesenchymal transition (Emt), cell proliferation, prognosis, and drug response in pancreatic cancer. *Cells*. (2021) 10(3):653. doi: 10.3390/cells10030653

40. Xu D, Li C. Gene 33/Mig6/Errfi1, an adapter protein with complex functions in cell biology and human diseases. *Cells*. (2021) 10(7):1574. doi: 10.3390/cells10071574

41. Liu X, Chen L, Fan Y, Hong Y, Yang X, Li Y, et al. Ifitm3 promotes bone metastasis of prostate cancer cells by mediating activation of the Tgf-B signaling pathway. *Cell Death Dis*. (2019) 10(7):517. doi: 10.1038/s41419-019-1750-7

42. Watanabe J, Takiyama Y, Honjyo J, Makino Y, Fujita Y, Tateno M, et al. Role of Igfbp7 in diabetic nephropathy: Tgf-B1 induces Igfbp7 via Smad2/4 in human renal proximal tubular epithelial cells. *PLoS One*. (2016) 11(3):e0150897. doi: 10.1371/journal.pone.0150897

43. Huang Y, Han X, Tang J, Long X, Wang X. Salidroside inhibits endothelial-mesenchymal transition via the Klf4/enos signaling pathway. *Mol Med Rep*. (2021) 24(4):692. doi: 10.3892/mmr.2021.12324

44. Zhang Y, Li C, Huang Y, Zhao S, Xu Y, Chen Y, et al. Eofaz inhibits endothelial-to-mesenchymal transition through downregulation of Klf4. *Int J Mol Med*. (2020) 46(1):300–10. doi: 10.3892/ijmm.2020.4572

45. Isobe S, Kataoka M, Endo J, Moriyama H, Okazaki S, Tsuchihashi K, et al. Endothelial-mesenchymal transition drives expression of Cd44 variant and Xct in pulmonary hypertension. *Am J Respir Cell Mol Biol*. (2019) 61(3):367–79. doi: 10.1165/rcmb.2018-0231OC

46. Szulcek R, Sanchez-Duffhues G, Rol N, Pan X, Tsonaka R, Dickhoff C, et al. Exacerbated inflammatory signaling underlies aberrant response to Bmp9 in pulmonary arterial hypertension lung endothelial cells. *Angiogenesis*. (2020) 23(4):699–714. doi: 10.1007/s10456-020-09741-x

47. Mahler GJ, Farrar EJ, Butcher JT. Inflammatory cytokines promote mesenchymal transformation in embryonic and adult valve endothelial cells. *Arterioscler Thromb Vasc Biol*. (2013) 33(1):121–30. doi: 10.1161/ATVBAHA.112.300504

48. Takagaki Y, Lee SM, Dongqing Z, Kitada M, Kanasaki K, Koya D. Endothelial autophagy deficiency induces Il6—dependent endothelial mesenchymal transition and organ fibrosis. *Autophagy*. (2020) 16(10):1905–14. doi: 10.1080/15548627.2020.1713641

49. Marcelin G, Gautier EL, Clement K. Adipose tissue fibrosis in obesity: etiology and challenges. *Annu Rev Physiol*. (2022) 84:135–55. doi: 10.1146/annurev-physiol-060721-092930

50. Lovisa S, Fletcher-Sananikone E, Sugimoto H, Hensel J, Lahiri S, Hertig A, et al. Endothelial-to-mesenchymal transition compromises vascular integrity to induce myc-mediated metabolic reprogramming in kidney fibrosis. *Sci Signal*. (2020) 13(635):1–17. doi: 10.1126/scisignal.aaz2597

51. Charytan DM, Padera R, Helfand AM, Zeisberg M, Xu X, Liu X, et al. Increased concentration of circulating angiogenesis and nitric oxide inhibitors induces endothelial to mesenchymal transition and myocardial fibrosis in patients with chronic kidney disease. *Int J Cardiol*. (2014) 176(1):99–109. doi: 10.1016/j.ijcard.2014.06.062

52. Goligorsky MS. Microvascular rarefaction: the decline and fall of blood vessels. *Organogenesis*. (2010) 6(1):1–10. doi: 10.4161/org.6.1.10427

53. Ungvari Z, Tarantini S, Donato AJ, Galvan V, Csiszar A. Mechanisms of vascular aging. *Circ Res*. (2018) 123(7):849–67. doi: 10.1161/CIRCRESAHA.118.311378

54. Chen Y, Yuan T, Zhang H, Yan Y, Wang D, Fang L, et al. Activation of Nrf2 attenuates pulmonary vascular remodeling via inhibiting endothelial-to-mesenchymal transition: an insight from a plant polyphenol. *Int J Biol Sci*. (2017) 13(8):1067–81. doi: 10.7150/ijbs.20316

55. Weichhart T. Mtor as regulator of lifespan, aging, and cellular senescence: a Mini-review. *Gerontology*. (2018) 64(2):127–34. doi: 10.1159/000484629

56. Fleenor BS, Marshall KD, Rippe C, Seals DR. Replicative aging induces endothelial to mesenchymal transition in human aortic endothelial cells: potential role of inflammation. *J Vasc Res*. (2012) 49(1):59–64. doi: 10.1159/000329681

57. Kuosmanen SM, Kansanen E, Sihvola V, Levonen AL. Microrna profiling reveals distinct profiles for tissue-derived and cultured endothelial cells. *Sci Rep*. (2017) 7(1):10943. doi: 10.1038/s41598-017-11487-4

58. Yu CH, Gong M, Liu WJ, Cui NX, Wang Y, et al. High glucose induced endothelial to mesenchymal transition in human umbilical vein endothelial cell. *Exp Mol Pathol*. (2017) 102(3):377–83. doi: 10.1016/j.yexmp.2017.03.007

59. Liu X, Mujahid H, Rong B, Lu QH, Zhang W, Li P, et al. Irisin inhibits high glucose-induced endothelial-to-mesenchymal transition and exerts a dose-dependent bidirectional effect on diabetic cardiomyopathy. *J Cell Mol Med*. (2018) 22(2):808–22. doi: 10.1111/jcmm.13360

60. Kim M, Choi SH, Jin YB, Lee HJ, Ji YH, Kim J, et al. The effect of oxidized low-density lipoprotein (ox-ldl) on radiation-induced endothelial-to-mesenchymal transition. *Int J Radiat Biol.* (2013) 89(5):356–63. doi: 10.3109/09553002.2013.763193

61. Spillmann F, Miteva K, Pieske B, Tschope C, Van Linthout S. High-Density lipoproteins reduce endothelial-to-mesenchymal transition. *Arterioscler Thromb Vasc Biol.* (2015) 35(8):1774–7. doi: 10.1161/ATVBAHA.115.305887

62. Yoshimatsu Y, Watabe T. Emerging roles of inflammation-mediated endothelial-mesenchymal transition in health and disease. *Inflamm Regen.* (2022) 42(1):9. doi: 10.1186/s41232-021-00186-3

63. Lai B, Li Z, He M, Wang Y, Chen L, Zhang J, et al. Atheroprone flow enhances the endothelial-to-mesenchymal transition. *Am J Physiol Heart Circ Physiol.* (2018) 315(5):H1293–H303. doi: 10.1152/ajpheart.00213.2018

64. Chen PY, Qin L, Baeyens N, Li G, Afolabi T, Budatha M, et al. Endothelial-to-mesenchymal transition drives atherosclerosis progression. *J Clin Invest.* (2015) 125 (12):4514–28. doi: 10.1172/JCI82719

65. Peng Q, Shan D, Cui K, Li K, Zhu B, Wu H, et al. The role of endothelial-to-mesenchymal transition in cardiovascular disease. *Cells.* (2022) 11(11):1834. doi: 10.3390/cells11111834

66. Sun X, Nkennor B, Mastikhina O, Soon K, Nunes SS. Endothelium-mediated contributions to fibrosis. *Semin Cell Dev Biol.* (2020) 101:78–86. doi: 10.1016/j.semcdb.2019.10.015

67. DeLeve LD, Maretti-Mira AC. Liver sinusoidal endothelial cell: an update. *Semin Liver Dis.* (2017) 37(4):377–87. doi: 10.1055/s-0037-1617455

frontiers | Frontiers in Cardiovascular Medicine

TYPE Original Research
PUBLISHED 26 September 2023
DOI 10.3389/fcvm.2023.1266276

OPEN ACCESS

EDITED BY
Masanori Aikawa,
Harvard Medical School, United States

REVIEWED BY
Antonin Trimaille,
Hôpitaux Universitaires de Strasbourg, France
Nicolas Gendron,
Hôpital Européen Georges Pompidou, France

*CORRESPONDENCE
Mark L. Kahn
✉ markkahn@pennmedicine.upenn.edu

†These authors share first authorship

RECEIVED 24 July 2023
ACCEPTED 05 September 2023
PUBLISHED 26 September 2023

CITATION
Gao S, Tang AT, Wang M, Buchholz DW, Imbiakha B, Yang J, Chen X, Hewins P, Mericko-Ishizuka P, Leu N.A, Sterling S, August A, Jurado KA, Morrisey EE, Aguilar-Carreno H and Kahn ML (2023) Endothelial SARS-CoV-2 infection is not the underlying cause of COVID-19-associated vascular pathology in mice. Front. Cardiovasc. Med. 10:1266276. doi: 10.3389/fcvm.2023.1266276

# Endothelial SARS-CoV-2 infection is not the underlying cause of COVID-19-associated vascular pathology in mice

Siqi Gao[1†], Alan T. Tang[1†], Min Wang[1], David W. Buchholz[2], Brian Imbiakha[2], Jisheng Yang[1], Xiaowen Chen[1], Peter Hewins[3], Patricia Mericko-Ishizuka[1], N. Adrian Leu[4], Stephanie Sterling[4], Avery August[2], Kellie A. Jurado[3], Edward E. Morrisey[1,5], Hector Aguilar-Carreno[2] and Mark L. Kahn[1*]

[1]Department of Medicine and Cardiovascular Institute, University of Pennsylvania, Philadelphia, PA, United States, [2]Department of Microbiology and Immunology, College of Veterinary Medicine, Cornell University, Ithaca, NY, United States, [3]Department of Microbiology, University of Pennsylvania Perelman School of Medicine, Philadelphia, PA, United States, [4]Department of Biomedical Sciences, School of Veterinary Medicine, University of Pennsylvania, Philadelphia, PA, United States, [5]Penn-CHOP Lung Biology Institute, Perelman School of Medicine, University of Pennsylvania, Philadelphia, PA, United States

Endothelial damage and vascular pathology have been recognized as major features of COVID-19 since the beginning of the pandemic. Two main theories regarding how severe acute respiratory syndrome coronavirus 2 (SARS-CoV-2) damages endothelial cells and causes vascular pathology have been proposed: direct viral infection of endothelial cells or indirect damage mediated by circulating inflammatory molecules and immune mechanisms. However, these proposed mechanisms remain largely untested *in vivo*. In the present study, we utilized a set of new mouse genetic tools developed in our lab to test both the necessity and sufficiency of endothelial human angiotensin-converting enzyme 2 (hACE2) in COVID-19 pathogenesis. Our results demonstrate that endothelial ACE2 and direct infection of vascular endothelial cells do not contribute significantly to the diverse vascular pathology associated with COVID-19.

KEYWORDS

SARS-CoV-2, endothelial cell, COVID-19, vascular, hACE2

## Introduction

The most common clinical feature reported in patients with COVID-19 is respiratory symptoms (1, 2). In addition to primarily causing pulmonary symptoms, COVID-19 disease is accompanied by vascular pathology, endothelial damage, and vascular coagulopathy (3–5). Reports emerged around the world confirming a disproportionate prevalence of abnormal thrombotic events and vascular pathology in patients with COVID-19, even in those not in intensive care units (6–14). Theories regarding the mechanism of vascular disease observed in patients with COVID-19 have been proposed, including direct infection of endothelial cells and systemic inflammatory responses (15–22). However, these hypotheses remain largely untested, and the cellular basis of vascular pathology remains controversial. In this study, we used a set of new mouse genetic tools (23) to rigorously test endothelial contribution to COVID-19-associated vascular pathology.

# Materials and methods

## Mice

*hACE2$^{fl/y}$* mice and LSL-hACE2$^{+/0}$ mice have been generated through CRISPR/Cas9-assisted mouse embryonic stem cell targeting and have been described (23). Briefly, for loss of function mouse line, the human ACE2 cDNA sequence was inserted after the ATG-start codon of mouse *Ace2* in exon2, flanking the polyA cassette with loxP sites, to achieve Cre-mediated cell type-specific deletion of ACE2. For gain of function mouse line, the human ACE2 cDNA sequence was targeted to Rosa26 locus with Lox-STOP-Lox cassette to permit tissue-specific gain of expression of ACE2. Tie2-Cre transgenic mice have been used for tissue-specific drivers as previously described (24). All mice were maintained on a mixed genetic background, including C57BL/8 and other strains, at the University of Pennsylvania animal facility. Mice were genotyped by PCR as described (23). The number of male mice used in each experiment ranged from three to nine.

## Viral inoculation and tissue harvest

Viral inoculations were performed as described previously (23). Briefly, mice were anesthetized with isoflurane and then intranasally infected with SARS-CoV-2 (Isolate USA-WA1/2020; BEI resources: NR-52281) that was obtained from BEI Resource. Mice were monitored and weighed daily, then euthanized at a humane endpoint when they lost 20% of their starting weights. Mice studies were combined results from Penn ABSL3 laboratory and Cornell ABSL3 laboratory in accordance with protocols approved by the IACUC at the University of Pennsylvania and Cornell University. For tissue harvest, mice were euthanized with ketamine/xylazine. Lungs were gently inflated with PBS infusion via trachea cannulation. Then lungs were fixed in 4% paraformaldehyde with a minimum of 72 h to ensure viral inactivation. Tissues were removed from the animal BSL3 facility, followed by ethanol dehydration and embedding in paraffin blocks for histology. Hematoxylin and eosin staining was performed on paraffin sections.

## Immunofluorescence staining and analysis

Immunohistochemistry staining was performed as previously described (23) with control and experimental samples on the same slide and under identical staining conditions. Primary antibodies were as follows: pan-ACE2 (goat, 1:1,000, R&D AF933), hACE2 (rabbit, 1:200, Abcam ab108209), SARS-CoV-2 nucleocapsid (rabbit, 1:500, Rockland 200-401-A50), ICAM-1 (rabbit, 1:500, Abcam ab179707), vWF (rabbit 1:1,000, Novus Biologicals NB600-586), and PECAM (goat 1:500, R&D AF3628). Fluorescence-conjugated Alexa Fluor secondary antibodies were used (1:500, Invitrogen) according to the primary antibody species and counterstained with DAPI (1:1,000). ICAM1 and vWF fluorescence intensity were calculated by integrated fluorescence intensity. All images were analyzed using ImageJ/FIJI software.

## Statistics

Mice were inoculated with SARS-CoV-2 in a blinded fashion without knowledge of genotypes, and infections were performed in two different ABSL-3 facilities with independent experimenters. Statistical tests used to determine significance are described in the figure legends. GraphPad Prism 9.5.1 was used to generate graphs and statistical analyses. Survival curve statistics were performed with log-rank Mantel-Cox tests. All *t*-tests performed were two-tailed.

# Results and discussion

Cellular expression of ACE2 is indispensable for SARS-CoV-2 infection in pneumocytes (25, 26), but SARS-CoV-2 is unable to bind mouse ACE2. To determine if endothelial cells directly contribute to lethal infection, we generated animals that express human ACE2 (hACE2) from the mouse Ace2 locus in a manner that enables cell-specific loss of hACE2 using Cre recombinase (*hACE2$^{fl/y}$* mice) (23). We crossed *hACE2$^{fl/y}$* mice onto a *Tie2-Cre* transgenic mouse line that drives Cre expression in endothelial cells (ECs) to generate mice that express hACE2 in all cells except vascular ECs. *hACE2$^{fl/y}$*; *Tie2-Cre$^{+}$* mice and control littermates were exposed to $10^5$ PFU of SARS-CoV-2 virus via nasal inhalation. *hACE2$^{fl/y}$*; *Tie2-Cre$^{+}$* mice showed no significant difference in survival after exposure to SARS-CoV-2 compared with the littermate controls (**Figure 1A**). Histological analysis revealed the presence of alveolar infiltrates and pulmonary vascular thrombi in the lungs of infected *hACE2$^{fl/y}$*; *Tie2-Cre$^{+}$* mice that were indistinguishable from findings observed in control *hACE2$^{fl/y}$* mice (**Figure 1B**). Histological analysis using hematoxylin-eosin staining of tissue sections from the small intestine, kidney, liver, and heart also failed to identify any vascular pathology (**Supplementary Figure S1**). Next, we evaluated the expression of inflammation-induced protein intracellular adhesion marker 1 (ICAM1) and the pro-coagulant, inflammation-induced protein Von Willebrand factor (vWF) in the mice following the SARS-CoV-2 infection, given both ICAM1 and vWF have been closely associated with COVID-19 induced vascular damage (27, 28). Expression of ICAM1 and vWF were also similar in the lung capillary endothelial cells of SARS-CoV-2-infected *hACE2$^{fl/y}$* and *hACE2$^{fl/y}$*; *Tie2-Cre$^{+}$* mice (**Figures 1C,D**).

The studies described above suggested that endothelial cell infection is not required for vascular COVID-19 pathology when hACE2 is expressed at endogenous levels. In fact, immunostaining of lung sections using anti-ACE2 antibodies was able to detect ACE2 expression in epithelial but not endothelial cells (23) (**Figure 1E**). To more rigorously test the role of endothelial hACE2, we next crossed *Tie2-Cre* onto a recently described Cre-activated gain of function hACE2 allele (loxP-stop-loxP-hACE2 or LSL-hACE2$^{+/0}$) (23) to over-express hACE2 in vascular endothelial cells. *Tie2-Cre*;LSL-hACE2$^{+/0}$ animals exhibited very high endothelial-specific expression of hACE2, assessed by immunostaining of tissue sections compared with

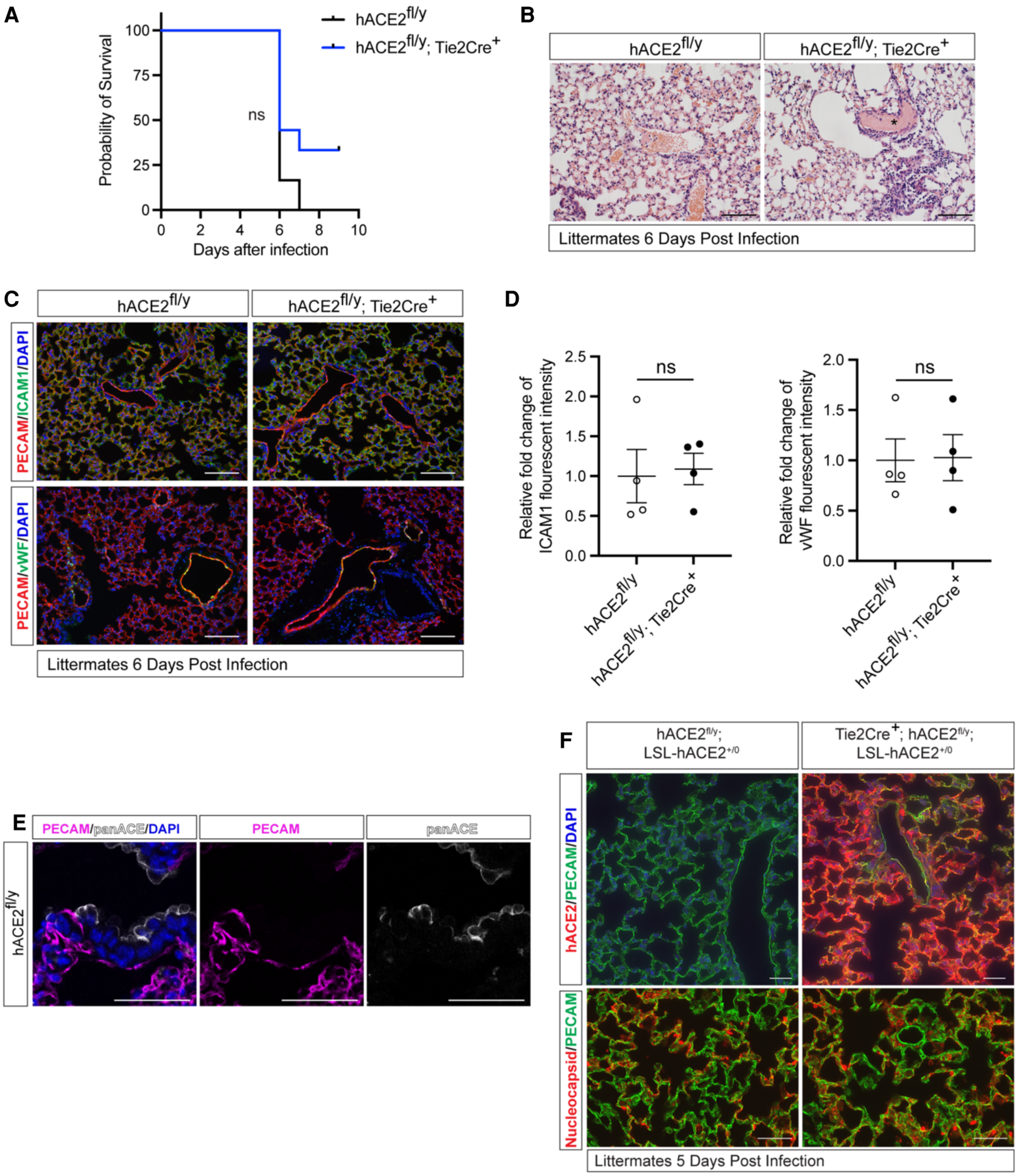

FIGURE 1
Loss or gain of endothelial hACE2 does not alter SARS-CoV2 infection. (A) Survival of *hACE2*$^{fl/y}$ and *hACE2*$^{fl/y}$*; Tie2-Cre*$^{+}$ male mice (12 to 16-week-old males) after infection with $10^5$ PFU of SARS-CoV-2 via intranasal administration. This viral inoculation method was used in all experiments. $n = 6$ (*hACE2*$^{fl/y}$) and 9 (*hACE2*$^{fl/y}$*; Tie2-Cre*$^{+}$); ns, non-significant; data are from two independent experiments. (B) H&E staining of *hACE2*$^{fl/y}$ and *hACE2*$^{fl/y}$*; Tie2-Cre*$^{+}$ lung tissue 6 days after infection. The asterisk indicates intravascular thrombosis. Scale bars: 100 µm. (C) Immunofluorescent staining of the lung from *hACE2*$^{fl/y}$ and *hACE2*$^{fl/y}$*; Tie2-Cre*$^{+}$ mice with antibodies against ICAM1 or vWF (green), and PECAM (red). Images are representative of four animals per genotype. Scale bars: 100 µm. (D) Quantification of ICAM1 and vWF fluorescent intensity. The error bars represent mean ± s.d; statistical analyses were performed using an unpaired two-tailed *t*-test; ns, non-significant. (E) Immunofluorescent staining of *hACE2*$^{fl/y}$ lung tissue using pan-ACE2 antibodies (grey) that recognize both hACE2 and mACE2 proteins and co-stained with PECAM (magenta). Images are representative of three animals. Scale bars 50 µm. (F) Immunofluorescent staining of the lung from *hACE2*$^{fl/y}$*;* LSL-hACE2$^{+/0}$ and Tie2Cre$^{+}$; *hACE2*$^{fl/y}$*;* LSL-hACE2$^{+/0}$ mice is performed using anti-hACE2 antibody or anti-SARS-CoV-2 nucleocapsid (red) and costained with PECAM (green) 5 days after infection with SARS-CoV-2. The *hACE2*$^{fl/y}$ allele enables these mice to be productively infected intranasally. Representative of three animals per genotype. Scale bars 100 µm.

*hACE2*$^{fl/y}$ mice (**Figure 1F**). To ensure that *Tie2-Cre*;LSL-hACE2$^{+/0}$ animals would be productively infected following SARS-CoV-2 exposure, we generated *Tie2-Cre*;LSL-hACE2$^{+/0}$;*hACE2*$^{fl/y}$ animals that support robust infection of the nasal and respiratory epithelium (23) (**Figure 1F**). Despite high levels of endothelial hACE2 expression, we failed to detect nucleocapsid protein that colocalized with PECAM$^{+}$ endothelial cells following nasal SARS-CoV-2 infection (**Figure 1F**). In contrast, we have previously shown that this gain of function allele is sufficient to drive hACE2 expression and support SARS-CoV-2 infection in both neuronal cells and lung epithelial cells (23). These studies support the conclusion that SARS-CoV-2 does not confer endothelial cell damage and vascular thrombosis through direct viral infection of those cells. They further demonstrate that the levels of circulating virus are too low to infect even endothelial cells that express very high levels of hACE2, and therefore that most COVID-19 pathology arises due to aerosol infection of the nasal and pulmonary epithelium.

It has been debated whether direct viral infection of endothelial cells or indirect damage from systematic inflammation underlie COVID-19-associated vascular pathology (3). Our murine vascular endothelial loss and gain of function studies reported here provide strong *in vivo* evidence that endothelial ACE2 and direct infection of vascular endothelial cells do not contribute significantly to the diverse vascular pathology associated with COVID-19. These findings are consistent with previously reported *in vitro* studies that showed human endothelial cells are not readily infected by SARS-CoV-2 (21). Together with our recently reported studies, these findings strongly support a mechanism in which SARS-CoV-2 infection of nasal epithelial and neuronal cells stimulates a powerful inflammatory response that is the cause of COVID-19 vascular pathology.

# Limitations of the study

In the present study, we utilized both loss of function and gain of function hACE2 mouse lines and demonstrated that direct endothelial viral infection does not contribute to COVID-19-associated vascular pathology. Future studies are needed to define the cytokines that likely drive secondary vascular inflammation and thrombosis and to understand the molecular mechanism by which systemic inflammation damages endothelium following SARS-CoV-2 infection. We used the original isolate SARS-CoV-2 USA-WA1/2020 strain in our study because that isolate is the best characterized regarding vascular complication. Omicron BA.1 variant failed to confer lethal disease and associated vascular phenotypes in our mouse models (23). Future studies testing the impact of other variants on the vascular system will be needed. We performed our studies on male mice due to the *Ace2* allele being located on the X chromosome, enabling a straightforward comparison. Mouse models are not humans, and our mouse model *hACE2*$^{fl/y}$ expresses a higher level of hACE2 as previously reported (23). Thus there are likely to be differences in pathogenic mechanisms identified using our model compared to human studies. However, this difference should bias toward rather than against a direct endothelial infection mechanism and it does not weaken our negative conclusions. Future studies looking at longer-term vascular events in mice with lower levels of hACE2 expression will be needed to address non-acute mechanisms of COVID-19-related cardiovascular disease.

# Data availability statement

The original contributions presented in the study are included in the article/**Supplementary Material**, further inquiries can be directed to the corresponding author.

# Ethics statement

The animal study was approved by University of Pennsylvania IACUC. The study was conducted in accordance with the local legislation and institutional requirements.

# Author contributions

MK: Conceptualization, Formal analysis, Funding acquisition, Project administration, Writing – original draft. SG: Conceptualization, Data curation, Formal analysis, Funding acquisition, Investigation, Methodology, Writing – original draft. AT: Conceptualization, Formal analysis, Writing – original draft. MW: Conceptualization, Data curation, Formal analysis, Methodology, Writing – original draft. DB: Conceptualization, Data curation, Writing – original draft. BI: Data curation, Formal analysis, Conceptualization, Writing – original draft. JY: Data curation, Formal analysis, Writing – original draft. XC: Conceptualization, Data curation, Formal analysis, Writing – original draft. PM: Methodology, Project administration, Writing – original draft. NL: Data curation, Formal analysis, Methodology, Writing – original draft. SS: Methodology, Project administration, Writing – original draft. AA: Project administration, Data curation, Methodology, Writing – original draft. KJ: Data curation, Methodology, Project administration, Investigation, Writing – original draft. EM: Data curation, Formal analysis, Funding acquisition, Investigation, Methodology, Project administration, Writing – original draft, Conceptualization. HA: Conceptualization, Data curation, Formal analysis, Funding acquisition, Project administration, Writing – original draft. PH: Formal analysis, Writing – original draft.

# Funding

The author(s) declare that no financial support was received for the research, authorship, and/or publication of this article.

This work was supported by National Institute of Health grants R01HL39552-04S1 (MLK), R01HL164929 (MLK and EEM), AHA

963048 (MLK), R01AI109022 and R21AI156731 (HAC), and T32EB023860 (DWB), an AHA Postdoctoral Fellowship 906488 (SG), and a Penn CVI Dream Team grant (MK).

## Acknowledgments

We thank Kahn lab members for their helpful discussions.

## Conflict of interest

The authors declare that the research was conducted in the absence of any commercial or financial relationships that could be construed as a potential conflict of interest.

## Publisher's note

## Supplementary material

The Supplementary Material for this article can be found online at: https://www.frontiersin.org/articles/10.3389/fcvm.2023.1266276/full#supplementary-material

## References

1. Zhou P, Yang XL, Wang XG, Hu B, Zhang L, Zhang W, et al. A pneumonia outbreak associated with a new coronavirus of probable bat origin. *Nature*. (2020) 579:270–3. doi: 10.1038/s41586-020-2012-7

2. Huang C, Wang Y, Li X, Ren L, Zhao J, Hu Y, et al. Clinical features of patients infected with 2019 novel coronavirus in Wuhan, China. *Lancet*. (2020) 395:497–506. doi: 10.1016/S0140-6736(20)30183-5

3. Teuwen LA, Geldhof V, Pasut A, Carmeliet P. COVID-19: the vasculature unleashed. *Nat Rev Immunol*. (2020) 20:389–91. doi: 10.1038/s41577-020-0343-0

4. Smadja DM, Mentzer SJ, Fontenay M, Laffan MA, Ackermann M, Helms J, et al. COVID-19 is a systemic vascular hemopathy: insight for mechanistic and clinical aspects. *Angiogenesis*. (2021) 24:755–88. doi: 10.1007/s10456-021-09805-6

5. Connors JM, Levy JH. COVID-19 and its implications for thrombosis and anticoagulation. *Blood*. (2020) 135:2033–40. doi: 10.1182/blood.2020006000

6. Zhou F, Yu T, Du R, Fan G, Liu Y, Liu Z, et al. Clinical course and risk factors for mortality of adult inpatients with COVID-19 in Wuhan, China: a retrospective cohort study. *Lancet*. (2020) 395:1054–62. doi: 10.1016/S0140-6736(20)30566-3

7. Tang N, Li D, Wang X, Sun Z. Abnormal coagulation parameters are associated with poor prognosis in patients with novel coronavirus pneumonia. *J Thromb Haemost*. (2020) 18:844–7. doi: 10.1111/jth.14768

8. Oxley TJ, Mocco J, Majidi S, Kellner CP, Shoirah H, Singh IP, et al. Large-vessel stroke as a presenting feature of COVID-19 in the young. *N Engl J Med*. (2020) 382: e60. doi: 10.1056/NEJMc2009787

9. Klok FA, Kruip M, van der Meer NJM, Arbous MS, Gommers D, Kant KM, et al. Confirmation of the high cumulative incidence of thrombotic complications in critically ill ICU patients with COVID-19: an updated analysis. *Thromb Res*. (2020) 191:148–50. doi: 10.1016/j.thromres.2020.04.041

10. Song WC, FitzGerald GA. COVID-19, microangiopathy, hemostatic activation, and complement. *J Clin Invest*. (2020) 130:3950–3. doi: 10.1172/JCI140183

11. Goshua G, Pine AB, Meizlish ML, Chang CH, Zhang H, Bahel P, et al. Endotheliopathy in COVID-19-associated coagulopathy: evidence from a single-centre, cross-sectional study. *Lancet Haematol*. (2020) 7:e575–82. doi: 10.1016/S2352-3026(20)30216-7

12. Al-Samkari H, Karp Leaf RS, Dzik WH, Carlson JCT, Fogerty AE, Waheed A, et al. COVID-19 and coagulation: bleeding and thrombotic manifestations of SARS-CoV-2 infection. *Blood*. (2020) 136:489–500. doi: 10.1182/blood.2020006520

13. Ackermann M, Verleden SE, Kuehnel M, Haverich A, Welte T, Laenger F, et al. Pulmonary vascular endothelialitis, thrombosis, and angiogenesis in COVID-19. *N Engl J Med*. (2020) 383:120–8. doi: 10.1056/NEJMoa2015432

14. Jimenez D, Garcia-Sanchez A, Rali P, Muriel A, Bikdeli B, Ruiz-Artacho P, et al. Incidence of VTE and bleeding among hospitalized patients with coronavirus disease 2019: a systematic review and meta-analysis. *Chest*. (2021) 159:1182–96. doi: 10.1016/j.chest.2020.11.005

15. Merrill JT, Erkan D, Winakur J, James JA. Emerging evidence of a COVID-19 thrombotic syndrome has treatment implications. *Nat Rev Rheumatol*. (2020) 16:581–9. doi: 10.1038/s41584-020-0474-5

16. He L, Mäe MA, Muhl L, Sun Y, Pietilä R, Nahar K, et al. Pericyte-specific vascular expression of SARS-CoV-2 receptor ACE2—implications for microvascular inflammation and hypercoagulopathy in COVID-19. *bioRxiv*. 2020:2020.2005.2011.088500. doi: 10.1101/2020.05.11.088500

17. Henry BM, Vikse J, Benoit S, Favaloro EJ, Lippi G. Hyperinflammation and derangement of renin-angiotensin-aldosterone system in COVID-19: a novel hypothesis for clinically suspected hypercoagulopathy and microvascular immunothrombosis. *Clin Chim Acta*. (2020) 507:167–73. doi: 10.1016/j.cca.2020.04.027

18. Gu SX, Tyagi T, Jain K, Gu VW, Lee SH, Hwa JM, et al. Thrombocytopathy and endotheliopathy: crucial contributors to COVID-19 thromboinflammation. *Nat Rev Cardiol*. (2020) 18(3):194–209. doi: 10.1038/s41569-020-00469-1

19. Perico L, Benigni A, Casiraghi F, Ng LFP, Renia L, Remuzzi G. Immunity, endothelial injury and complement-induced coagulopathy in COVID-19. *Nat Rev Nephrol*. (2021) 17:46–64. doi: 10.1038/s41581-020-00357-4

20. Schimmel L, Chew KY, Stocks CJ, Yordanov TE, Essebier P, Kulasinghe A, et al. Endothelial cells are not productively infected by SARS-CoV-2. *Clin Transl Immunology*. (2021) 10:e1350. doi: 10.1002/cti2.1350

21. McCracken IR, Saginc G, He L, Huseynov A, Daniels A, Fletcher S, et al. Lack of evidence of angiotensin-converting enzyme 2 expression and replicative infection by SARS-CoV-2 in human endothelial cells. *Circulation*. (2021) 143:865–8. doi: 10.1161/CIRCULATIONAHA.120.052824

22. Nicosia RF, Ligresti G, Caporarello N, Akilesh S, Ribatti D. COVID-19 vasculopathy: mounting evidence for an indirect mechanism of endothelial injury. *Am J Pathol*. (2021) 191:1374–84. doi: 10.1016/j.ajpath.2021.05.007

23. Tang AT, Buchholz DW, Szigety KM, Imbiakha B, Gao S, Frankfurter M, et al. Cell-autonomous requirement for ACE2 across organs in lethal mouse SARS-CoV-2 infection. *PLoS Biol*. (2023) 21:e3001989. doi: 10.1371/journal.pbio.3001989

24. Kisanuki YY, Hammer RE, Miyazaki J, Williams SC, Richardson JA, Yanagisawa M. Tie2-Cre transgenic mice: a new model for endothelial cell-lineage analysis in vivo. *Dev Biol*. (2001) 230:230–42. doi: 10.1006/dbio.2000.0106

25. Oudit GY, Wang K, Viveiros A, Kellner MJ, Penninger JM. Angiotensin-converting enzyme 2-at the heart of the COVID-19 pandemic. *Cell*. (2023) 186:906–22. doi: 10.1016/j.cell.2023.01.039

26. Delorey TM, Ziegler CGK, Heimberg G, Normand R, Yang Y, Segerstolpe A, et al. COVID-19 tissue atlases reveal SARS-CoV-2 pathology and cellular targets. *Nature*. (2021) 595:107–13. doi: 10.1038/s41586-021-03570-8

27. Nagashima S, Mendes MC, Camargo Martins AP, Borges NH, Godoy TM, Miggiolaro A, et al. Endothelial dysfunction and thrombosis in patients with COVID-19-brief report. *Arterioscler Thromb Vasc Biol*. (2020) 40:2404–7. doi: 10.1161/ATVBAHA.120.314860

28. Philippe A, Chocron R, Gendron N, Bory O, Beauvais A, Peron N, et al. Circulating Von willebrand factor and high molecular weight multimers as markers of endothelial injury predict COVID-19 in-hospital mortality. *Angiogenesis*. (2021) 24:505–17. doi: 10.1007/s10456-020-09762-6

Frontiers in Cardiovascular Medicine

TYPE Original Research
PUBLISHED 21 March 2024
DOI 10.3389/fcvm.2024.1360364

OPEN ACCESS

EDITED BY
Masanori Aikawa,
Harvard Medical School, United States

REVIEWED BY
Martina B. Lorey,
Wihuri Research Institute, Finland
Delphine Gomez,
University of Pittsburgh, United States

*CORRESPONDENCE
Christopher C. W. Hughes
✉ cchughes@uci.edu

[†]These authors have contributed equally to this work and share first authorship

RECEIVED 22 December 2023
ACCEPTED 11 March 2024
PUBLISHED 21 March 2024

CITATION
Hatch CJ, Piombo SD, Fang JS, Gach JS, Ewald ML, Van Trigt WK, Coon BG, Tong JM, Forthal DN and Hughes CCW (2024) SARS-CoV-2 infection of endothelial cells, dependent on flow-induced ACE2 expression, drives hypercytokinemia in a vascularized microphysiological system.
Front. Cardiovasc. Med. 11:1360364.
doi: 10.3389/fcvm.2024.1360364

# SARS-CoV-2 infection of endothelial cells, dependent on flow-induced ACE2 expression, drives hypercytokinemia in a vascularized microphysiological system

Christopher J. Hatch[1†], Sebastian D. Piombo[2†], Jennifer S. Fang[3], Johannes S. Gach[4], Makena L. Ewald[3], William K. Van Trigt[3], Brian G. Coon[5,6], Jay M. Tong[1], Donald N. Forthal[3,4] and Christopher C. W. Hughes[1,3*]

[1]Department of Biomedical Engineering, University of California, Irvine, CA, United States, [2]Department of Pediatrics, School of Medicine, Institute for Clinical and Translational Science, University of California, Irvine, CA, United States, [3]Department of Molecular Biology and Biochemistry, University of California, Irvine, CA, United States, [4]Division of Infectious Diseases, School of Medicine, University of California, Irvine, CA, United States, [5]Cardiovascular Biology Research Program, Oklahoma Medical Research Foundation, Oklahoma City, OK, United States, [6]Department of Cell Biology, University of Oklahoma Health Sciences Center, Oklahoma City, OK, United States

**Background:** Severe acute respiratory syndrome coronavirus 2 (SARS-CoV-2), responsible for COVID-19, has caused nearly 7 million deaths worldwide. Severe cases are marked by an aggressive inflammatory response known as hypercytokinemia, contributing to endothelial damage. Although vaccination has reduced hospitalizations, hypercytokinemia persists in breakthrough infections, emphasizing the need for disease models mimicking this response. Using a 3D microphysiological system (MPS), we explored the vascular role in SARS-CoV-2-induced hypercytokinemia.

**Methods:** The vascularized micro-organ (VMO) MPS, consisting of human-derived primary endothelial cells (ECs) and stromal cells within an extracellular matrix, was used to model SARS-CoV-2 infection. A non-replicative pseudotyped virus fused to GFP was employed, allowing visualization of viral entry into human ECs under physiologic flow conditions. Expression of ACE2, TMPRSS2, and AGTR1 was analyzed, and the impact of viral infection on ACE2 expression, vascular inflammation, and vascular morphology was assessed.

**Results:** The VMO platform facilitated the study of COVID-19 vasculature infection, revealing that ACE2 expression increased significantly in direct response to shear stress, thereby enhancing susceptibility to infection by pseudotyped SARS-CoV-2. Infected ECs secreted pro-inflammatory cytokines, including IL-6 along with coagulation factors. Cytokines released by infected cells were able to activate downstream, non-infected EC, providing an amplification mechanism for inflammation and coagulopathy.

**Discussion:** Our findings highlight the crucial role of vasculature in COVID-19 pathogenesis, emphasizing the significance of flow-induced ACE2 expression and subsequent inflammatory responses. The VMO provides a valuable tool for studying SARS-CoV-2 infection dynamics and evaluating potential therapeutics.

KEYWORDS

COVID-19, endothelial dysfunction, hypercytokinemia, microphysiological systems, shear stress

# 1 Introduction

The SARS-CoV-2, or COVID-19, pandemic has required major adaptations in how the medical and scientific community approaches infectious disease prevention and study (1, 2). One primary need has been the rapid development of new tools to analyze viral infection and the subsequent development of vaccines to combat the global dissemination of this deadly pathogen (3). To address the dearth of apt translational models for studying the pathogenesis of COVID-19, we have utilized a 3D microphysiological system platform—the vascularized micro-organ (VMO) model (4)—to interrogate the role of the vasculature in driving hypercytokinemia, which is a crucial pathological indicator associated with SARS-CoV-2 infection (5).

While COVID-19 was initially characterized as an infection that predominately manifests in the respiratory system, it is now also recognized to be a vascular disease (6), with potential long-term sequelae likely arising due to micro-clots associated with dysregulation of thrombosis in many patients (7). While the long-term effects of COVID-19 infection appear to be mediated by these thrombotic events, the most severe acute impact of the disease is driven by profound hypercytokinemia, a process associated with uncontrolled upregulation of key inflammatory mediators such as IL-1 and IL-6, and endothelial cell (EC) leukocyte adhesion molecules such as ICAM-1 and VCAM-1 (8, 9). Of note, however, is that IL-6 also drives the expression of pro-coagulation factors (10), potentially linking acute cytokine release with downstream coagulation.

This cascading inflammatory response frequently results in pneumonia and, in severe cases, acute respiratory distress syndrome, accounting for the high mortality prior to the introduction of the COVID-19 vaccine (11). Therapies such as glucocorticoids and antivirals such as remdesivir have been developed to combat these cases; however, the biological mechanisms that produce hypercytokinemia in COVID-19 patients remain elusive, although the use of tociluzumab, targeted to the IL-6 receptor, has proven useful in many patients (12). To further our understanding of the pathology of COVID-19 and the role of the vasculature, we have challenged the VMO platform with a non-replicative pseudotyped SARS-CoV-2 virus, allowing us to model and visualize viral entry into human EC in a system that closely recapitulates human vasculature. The VMO consists of human-derived primary EC and stromal cells suspended in a hydrogel matrix housed within a polydimethylsiloxane microfluidic system (13). Over the course of a few days, a complex vascular network forms that is then perfused by a blood substitute, which nourishes the surrounding tissue. These microvascular networks demonstrate key characteristics of human vasculature, such as tight junctions, expression of vascular markers, and response to inflammatory stimuli, and can support a variety of tissues, including heart, liver, pancreas, brain, and various tumors (4, 14, 15).

The key mediator of SARS-CoV-2 viral entry into host cells is angiotensin-converting enzyme 2 (ACE2), which acts as a receptor for the viral spike protein (16). While other renin-angiotensin system mediators, such as AGTR1, play a role in the resultant hypercytokinemia (17), ACE2 expression on the surface of EC is critical to the initial infection, and without adequate expression, viral infection fails to occur (18). The primary challenge of studying SARS-CoV-2 infection in commonly utilized models of the vasculature is the dependence of ACE2 expression on the shear force EC are exposed to *in vivo* (19, 20). As the VMO provides flow and shear force equivalent to that found in human capillary networks, the platform provides a unique model in which to study not only how ACE2 mediates viral infection and how viral entry clears ACE2 from the surface of the EC but also how these events trigger cytokine release from the EC lining the vascular network.

# 2 Materials and methods

## 2.1 Microfluidic device design

The design of the platform is a modified version of our previously published VMO microphysiological system (13, 14). The platform is designed to fit a standard bottomless 96-well plate (FLUOTRAC$^{TM}$, Greiner Bio-One). The design is shown in Figure 1A and comprises two polydimethylsiloxane (PDMS) layers adhered to a commercial 96-well plate with the wells aligned with the microfluidic features. The middle layer contains 16 microfluidic device units within the PDMS device layer, and the bottom layer is a thin transparent polymer membrane (Rogers Corp, HT-6240).

A single microfluidic device unit covers six horizontal wells of the 96-well plate, with the tissue chamber containing three diamond-shaped units (T1–T3) covering one well. A gel loading inlet (GLI) and outlet (GLO) are connected to either side of the tissue chamber, and each is aligned with an additional well. Each diamond-shaped unit is 2 mm in length and 1 mm in width, connected to 200 µm wide microfluidic channels through anastomosis points. The entire design is 200 µm thick. A

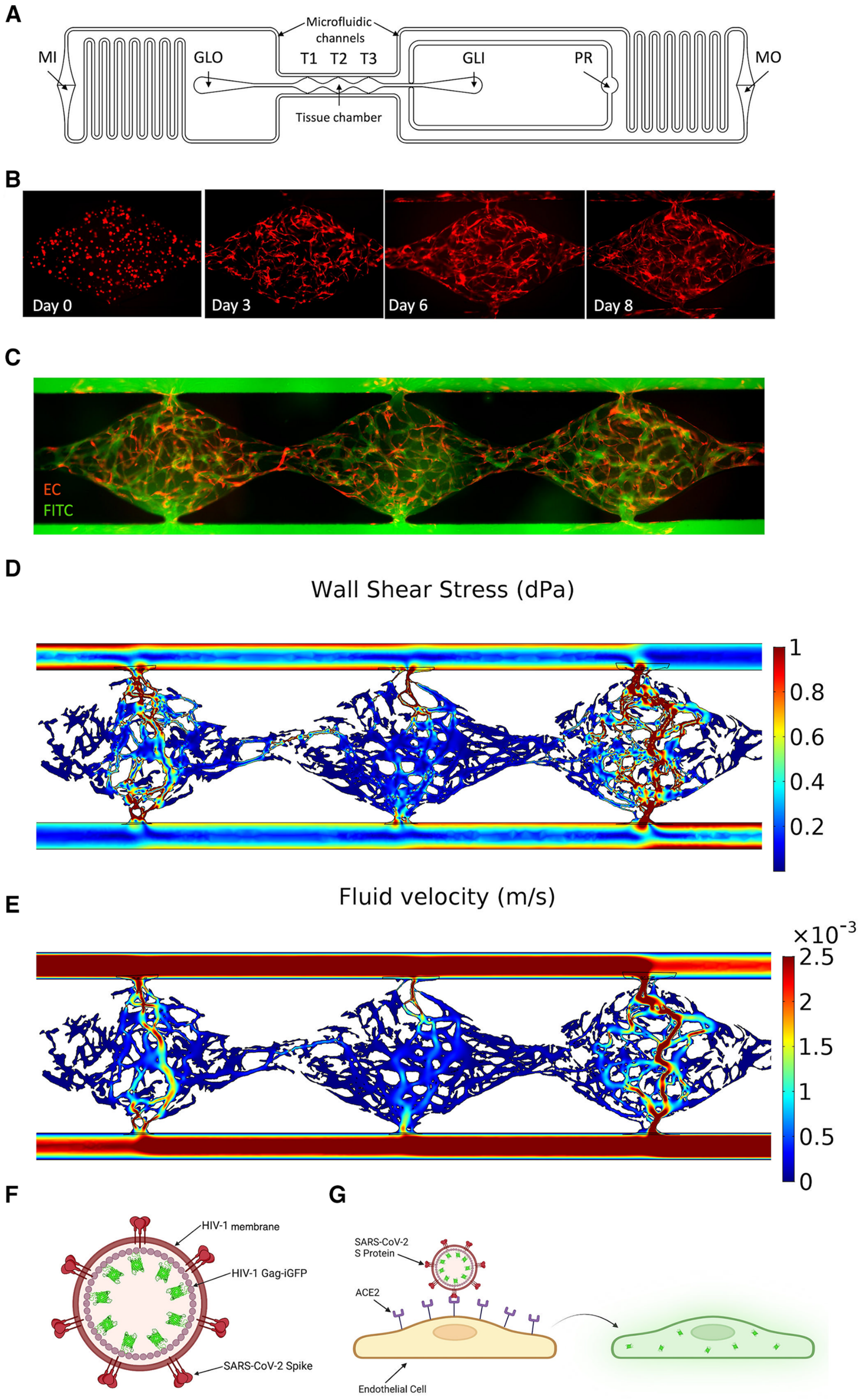

FIGURE 1

Development of a vascularized micro-organ microphysiological system and SARS-CoV-2 pseudotyped virus. (A) Schematic of an individual microfluidic device unit. Hydrostatic pressure drives medium from the inlet (MI) through the microfluidic channels and tissue chamber (T1–T3) to the medium outlet (MO). Hydrogel is loaded via the gel loading inlet (GLI) and outlet (GLO) with the pressure regulator (PR) to prevent leak into the microfluidic channel in the case of over-pressure during injection. (B) Development of the vasculature over time. EC labeled red; fibroblasts unlabeled. (C) Perfusion of 70 kDa FITC-Dextran through the vasculature (EC eRFP) at day 8. (D) COMSOL modeling of the shear stress (dynes/cm$^2$) through each tissue chamber. (E) Quantification of fluid flow through each chamber (m/s). (F) Schematic of SARS-CoV-2 pseudotyped virus. SARS-CoV-2 spike protein is inserted into the membrane of an HIV-1 envelope with a Gag-iGFP construct. (G) Schematic showing infectivity of the pseudotyped virus into EC using ACE2, leading to GFP expression.

redundant gel outlet is integrated into the GLI to act as a pressure regulator (PR) and prevent hydrogel from entering the microfluidic channel when the loading pressure exceeds the anastomosis point burst valve pressure. The microfluidic channels contain resistors in an asymmetric design to generate a hydrostatic pressure drop across the tissue chamber. This drives interstitial flow as the medium moves from the medium inlet (MI) to the medium outlet (MO).

## 2.2 Microfluidic device fabrication

The fabrication of the VMO has been previously described (4, 14). Briefly, a customized polyurethane (PU) master mold is fabricated from a two-part PU liquid plastic (Smooth-Cast 310, Smooth-On Inc.). A PDMS replica is made from the master mold, and holes are punched on the replica for the inlets and outlets (MI, MO, GLI, GLO, PR). The replica is secured to the bottom of a 96-well plate by chemical glue and oxygen plasma treatment. The bottom thin transparent membrane is bonded to the PDMS layer with oxygen plasma treatment. The complete platform is placed in a 60°C oven overnight. Before the platform is loaded with cells, a standard 96 well-plate polystyrene lid with condensation rings (Greiner Bio-One) is placed on top, and both parts are sterilized using a UV light for 30 min.

## 2.3 Cell culture

Human endothelial colony-forming cell-derived endothelial cells (ECFC-EC) were isolated from cord blood (21), expanded on 0.1% gelatin-coated flasks, and cultured in EGM-2 (Lonza). ECFC-EC were transduced with lentiviruses encoding azurite fluorescent protein (Azurite/Addgene) and used between passages 7–9. Note that images are false-colored so that ECs appear red. Normal human lung fibroblasts (NHLF) (Lonza) were cultured in DMEM (Corning) containing 10% FBS (VWR) and used between passages 7–10. All cells were cultured at 37°C/20% $O_2$/ 5% $CO_2$ and checked for mycoplasma contamination using MycoAlert (Lonza) before use.

## 2.4 Microfluidic device loading

The tissue chamber was loaded with ECFC-EC and NHLF. The cells were trypsinized, lifted, and resuspended at a 1.4:1 ratio at a density of $1.4 \times 10^7$ cells/ml in an 8 mg/ml fibrinogen solution (Sigma-Aldrich). Next, the cell-matrix solution was mixed with 3 U/ml thrombin (Sigma-Aldrich) and loaded in the tissue chambers. The VMO was placed into a 37°C incubator for 15 min to enable polymerization of the cell-matrix mix. Next, laminin (1 mg/ml, Life Technologies) was pushed through the microfluidic channels and incubated for 15 min at room temperature. Finally, EGM-2 culture medium was pushed through the microfluidic channels and dispensed in the inlet and outlet wells to generate hydrostatic pressure heads that drive perfusion. The medium was changed every day to maintain the pressure heads.

## 2.5 Fluorescence imaging and analyses

Fluorescence images were captured on an Olympus IX70 inverted microscope using SPOT software (SPOT Imaging), a Nikon Ti-E Eclipse epifluorescent microscope with a 4xPlan Apochromat Lambda objective, and an Agilent BioTek Lionheart FX microscope. In addition, confocal images were captured on a Leica TCS SP8 confocal microscope using a standard 10× air or 20× multi-immersion objective (Leica Microsystems).

FIJI (22) was used to determine each microfluidic unit's mean fluorescent intensity (MFI). Before measuring the average pixel intensity, all images underwent thresholding and default background subtraction with the same setting using a custom macro. Then, all values were normalized to the mean control fluorescent intensity for analysis.

## 2.6 Perfusion testing

To test the vascular leak of device networks, 70 kDa FITC-dextran (Sigma-Aldrich) was diluted in EGM-2 to 50 µg/ml and added to well MI for perfusion through the device. Images were taken after 15 min, and the vessel patency was assessed by demonstrating dextran flow through the entirety of the vascular chamber with no leakage at any of the anastomosis points.

## 2.7 Generation of pseudotyped SARS-CoV-2 virus and infection of the microfluidic device

Pseudotyped SARS-CoV-2 virions were generated by co-transfecting $1.5 \times 10^7$ 293-*T* cells with a single round infectious HIV-1 NL4-3 Gag-iGFP *Δ*Env plasmid as well as a SARS-CoV-2 spike protein expressing plasmid [pcDNA 3.1 SARS CoV-2 S or pcDNA3.3_SARS2_omicron BA.2 (23)]. Plasmids (1 µg plasmid per $1 \times 10^6$ cells) were mixed with polyethyleneimine (PEI) at a DNA/PEI ratio of 1:3 and added to the cells. After 3–4 days, cell supernatants were harvested and cleared from cells. Virus aliquots were stored at −80°C. To concentrate the virus, frozen supernatants were thawed and spun (14,000 rpm) in a microcentrifuge for 75 min at 4°C, and viral pellets were resuspended in the respective medium. Virus infectivity was determined by infecting $1 \times 10^4$ human ACE2 receptor expressing HEK 293 T target cells (BEI Resources) per well with a serial dilution of the CoV-2/HIV-1 pseudotyped virus particles. After 2–3 days, cells were detached, washed, and fixed with 4% PFA. Target cells were subsequently analyzed by flow cytometry (NovoCyte flow cytometer; ACEA) for green fluorescence protein expression. After performing perfusion tests to confirm the robustness of the vascular networks, the pseudotyped virus was added to the device inlet. Unless specified,

$7 \times 10^5$ IFU/ml of pseudotyped virus were used. Recombinant angiotensin II (rAngII, Sigma-Aldrich, 4474-91-3) was added to the inlet at a 300 pM concentration to activate the renin-angiotensin system. After 24 h, medium heights were reestablished by taking the media from the outlet well and placing it back in the inlet. After 48 h, the effluent was collected.

## 2.8 Immunostaining

VMO devices were fixed overnight at 4°C by replacing the circulating media in the inlet and outlet reservoirs with 4% paraformaldehyde diluted in phosphate-buffered saline (PBS). Following fixation, the transparent polymer seal was removed, exposing VMO networks embedded within the microfluidic feature layer, which was then placed face-up in each well of either a 4-well chamber slide (Nunc) or a 24-well plate. Fixed devices were then post-fixed for an additional 20 min in 4% paraformaldehyde at room temperature and then incubated in blocking solution [PBS containing 3% bovine serum albumin (BSA) and 0.1% Triton X, supplemented with 1% donkey serum] for 1 h at room temperature. Devices were then incubated in primary antibody diluted in staining solution [PBS containing 1% bovine serum albumin (BSA) 0.1% Triton X] overnight at 4° C. Following the wash, devices were incubated in fluorescently conjugated secondary antibodies diluted in staining solution for 2 h at room temperature. This was followed by incubation in 10 ug/ml Hoechst 33,342 (Sigma 14,533) for 15 min at room temperature. Devices were then washed in PBS and mounted in 4-well glass chamber slides (Nunc Lab-Tek, Thermo 177,399) in Vectashield (Vector Labs H1300) anti-fade mounting media. High-magnification multi-channel images of stained VMO devices were acquired using a Leica SP8 confocal microscope. Primary antibodies used: anti-ACE2 (Novus NBP2-67692, 1:300), anti-TMPRSS2 (Abcam ab242384, 1:300), anti-CD31 (Abcam ab28364, 1:300). Fluorescently conjugated secondary antibodies used: anti-Rabbit-Alexa 488 (1:500), anti-mouse-Alexa 568 (1:500), anti-goat-Alexa 647 (1:500).

## 2.9 ELISAs

Effluent from devices was collected after 48 h of exposure to experimental treatments. If not used immediately, the effluent was stored in the vapor phase of liquid nitrogen. Before use, the effluent was allowed to reach room temperature and was centrifuged at 2000g for 10 min. ELISAs for IL-6 (Abcam, ab178013), sICAM-1 (Abcam, ab229383), sVCAM-1 (Abcam, ab223591), Factor VIII (Abcam, ab272771), and IL-1β (Thermo Fischer Sci, BMS224-2) were run. A 100 K molecular weight cutoff protein concentrator (Thermo Scientific, 88523) was used to pool two samples and concentrate them for the Factor VIII ELISA. The drc package (24) in RStudio (25) fit the standard data to point curves as the manufacturers' protocols recommended. Values that fell outside the range of the standards were excluded from the analysis.

## 2.10 RNA isolation and qRT-PCR analysis

For RNA isolation, the protective plastic cover underneath the platform was removed. A razor blade was used to extract the tissue chamber and surrounding chamber inlets and outlets. Carefully, tweezers were used to separate the bottom polymer layer from the PDMS layer. Approximately 20 µl of RNA lysis buffer from the Quick RNA micro prep kit (Zymo Research, R1051) was added dropwise to the tissue chamber and bottom polymer layer and allowed to sit for 3–5 min. RNA lysis buffer was collected and diluted in a 1:1 ratio with pure ethanol before transfer to a Zymo-Spin IC Column. The RNA was then isolated following the manufacturer's protocol. The RNA was checked for quantity and quality using a NanoDrop before storage at −80°C or immediate conversion into cDNA.

Total purified RNA was synthesized into cDNA with the iScript cDNA Synthesis Kit (BioRad, 1708891) before use in quantitative real-time polymerized chain reaction (qRT-PCR) (BioRad). The average cycle threshold values were normalized using 18S expression levels and compared to their appropriate controls. Any cycle threshold values greater than 40 had a fold change set to one. All samples were measured in triplicate. Primers were designed with PrimerQuest Tool and synthesized by Integrated DNA Technologies.

## 2.11 Ibidi chip

ECFC-EC were plated into the 0.4 mm $\mu$-Slide I Luer (Ibidi, 80176) at $1 \times 10^6$ cell/ml and 100 µl and allowed to adhere overnight following the manufacturer's protocol. Next, the cells were exposed to 4 h of shear stress at 0.5, 1.0, or 2.0 dynes/cm$^2$ using a syringe pump (Pump Systems Inc) with the flow rate set via ibidi's recommended values. After 4 h, the chips were washed with DPBS 3X, and RNA lysis buffer using the Quick RNA micro prep kit (Zymo Research, R1051) was pushed through the chamber following the manufacturer's protocol. As previously described, steps were followed to isolate the RNA and run qPCR.

## 2.12 Vessel morphometry

Vascular network images were analyzed with AngioTool software (National Cancer Institute) (26) to quantify vessel area, length, lacunarity, and the number of vascular junctions and endpoints. The mean vessel diameters were computed using a modified version of the REAVER package (27) to output all vessel diameters instead of the mean for the entire network. The forked repository is available on GitHub (https://github.com/cjhatch/public_REAVER_diams). For vessel morphometry, replicates from two loadings were used. In loading 1, the control condition had biological replicates from 7 tissue chambers, with 21 diamond-shaped units quantified, while the pseudovirus and rAngII condition had 7 tissue chambers, with 16 diamond-shaped units quantified. For loading 2, the control condition had 4 tissue chambers, with 9 diamond-shaped units quantified, while the pseudovirus and rAngII condition had 7 tissue chambers, with 21 diamond-shaped units quantified.

## 2.13 NFκB reporter and monolayer response

ECFC-EC were transduced with an NFκB reporter and plated into 12-well plates. In brief, a Generation II lentiviral construct consisting of three tandem NFκB response elements upstream of the mCherry coding sequence, followed by a PGK reporter upstream of a SNAP-tag constitutive reporter were packaged into lentivirus and used to infect ECFC-EC. Thus, mCherry expression was driven by NFκB expression, which allowed for indirect quantification of inflammatory status via real-time fluoroscopy. Following validation of the reporter construct, 1.5 ml of effluent was collected from the VMOs and then layered onto NFκB reporter-transduced EC. Each well was imaged at 0, 24, and 48 h. MFI was calculated from each well to quantify the inflammatory response to downstream mediators.

## 2.14 Drug treatments

After performing perfusion tests to confirm the robustness of the vascular networks, pharmacological agents were added at the same time as the pseudotyped virus to test their ability to limit infectivity. Recombinant ACE2 (25 µg/ml, Sigma-Aldrich, SAE0065-50UG) or camostat mesylate (100 µM, Sigma-Aldrich, SML0057-10MG) was premixed with medium ± pseudotyped virus ± rAngII for 30 min before perfusing through devices. The pressure heads were readjusted by recycling media from the outlet well back into the inlet after 24 h, and effluent was collected after 48 h. Images were taken at 0, 24, and 48 h.

## 2.15 Computational fluid dynamics

Image masks were converted into .tiff RGB files using FIJI. The image files were then binarized, skeletonized, and traced using a custom MATLAB script. The traced images were converted to .DXF files using the DXFLib package (28) and imported into AutoCAD to overlay the schematics for the microfluidic devices. The traced vessels and microfluidic devices were imported into COMSOL 5.2.1. The velocity and shear stress were calculated using the laminar flow steady-state model, with water as the fluid material. Using the Bernoulli equation, all pressure heads were calculated based on medium height in the inlet/outlet wells to provide input to the COMSOL model.

## 2.16 Plotting and statistical analysis

All plots were generated in RStudio (25) using R version 4.0.3 with the ggplot2 package (29), ggpubr package (30), and gridExtra package (31).

For ELISAs and qPCR data, one-way ANOVAs with posthoc Tukey's HSD tests were run using the rstatix package (32) for parametric data. For nonparametric data, a Kruskal–Wallis H test was run with a Conover-Iman *post hoc* test using the conover.test package (33). For the time course for MFI infectivity at various doses (Figure 2F), an unbalanced two-way ANOVA on rank-transformed data was run using the car package (34), and the type III sum of squares was used to determine the significance of the main effects and interactions. Tukey's HSD was run to determine the significance between treatments.

# 3 Results

## 3.1 A microphysiological model for vascular SARS-CoV-2 infection

The VMO is a 3D vascularized microtissue platform comprising ECs and stromal cells (fibroblasts, pericytes, etc.) suspended in an extracellular matrix (ECM) that we have used as a base platform for the development of multiple tissue-specific models including heart, pancreas, liver, brain, and tumors. Here, we have used a modified version of this device to study infection of the vasculature by the COVID-19-causative agent, SARS-CoV-2 (Figure 1). We array 16 individual tissues in a 96-well plate format, where each unit consists of three interconnected tissue chambers that rely on hydrostatic pressure to drive interstitial flow through the vessels (Figure 1A). Once seeded as a dispersed cell suspension in gel the ECs and fibroblasts undergo vasculogenesis and angiogenesis over the course of 5–6 days to form a perfusable vascular network (Figures 1B,C) (13). ECs also migrate into the microfluidic channels that represent the artery and vein, and these anastomose with the vascular network to allow pressure-driven fluid flow from the artery, through the network, and out of the vein. The perfused vasculature thereby experienced physiologically-relevant fluid flow and shear stress (35) (Figures 1D,E).

## 3.2 Vasculature in the VMO is a target for SARS-CoV-2 infection

A non-replicative pseudotyped virus was generated, consisting of HIV-1 Gag fused to GFP and enveloped with either the original SARS-CoV-2 spike protein strain or the omicron strain (Figures 1F,G). The spike protein of COVID-19 recognizes the cell surface receptor ACE2 and is reliant on binding to it to enable membrane fusion (36), with TMPRSS2 acting to prime the spike protein (37). In healthy vasculature, angiotensin II, generated by ACE, is usually rapidly degraded by ACE2, limiting its effective range and duration of action. Downstream of ACE and ACE2 is AGTR1/AT1R, which responds to angiotensin II to activate the classical, pro-inflammatory arm of the renin-angiotensin system (38). We first compared the RNA expression levels of

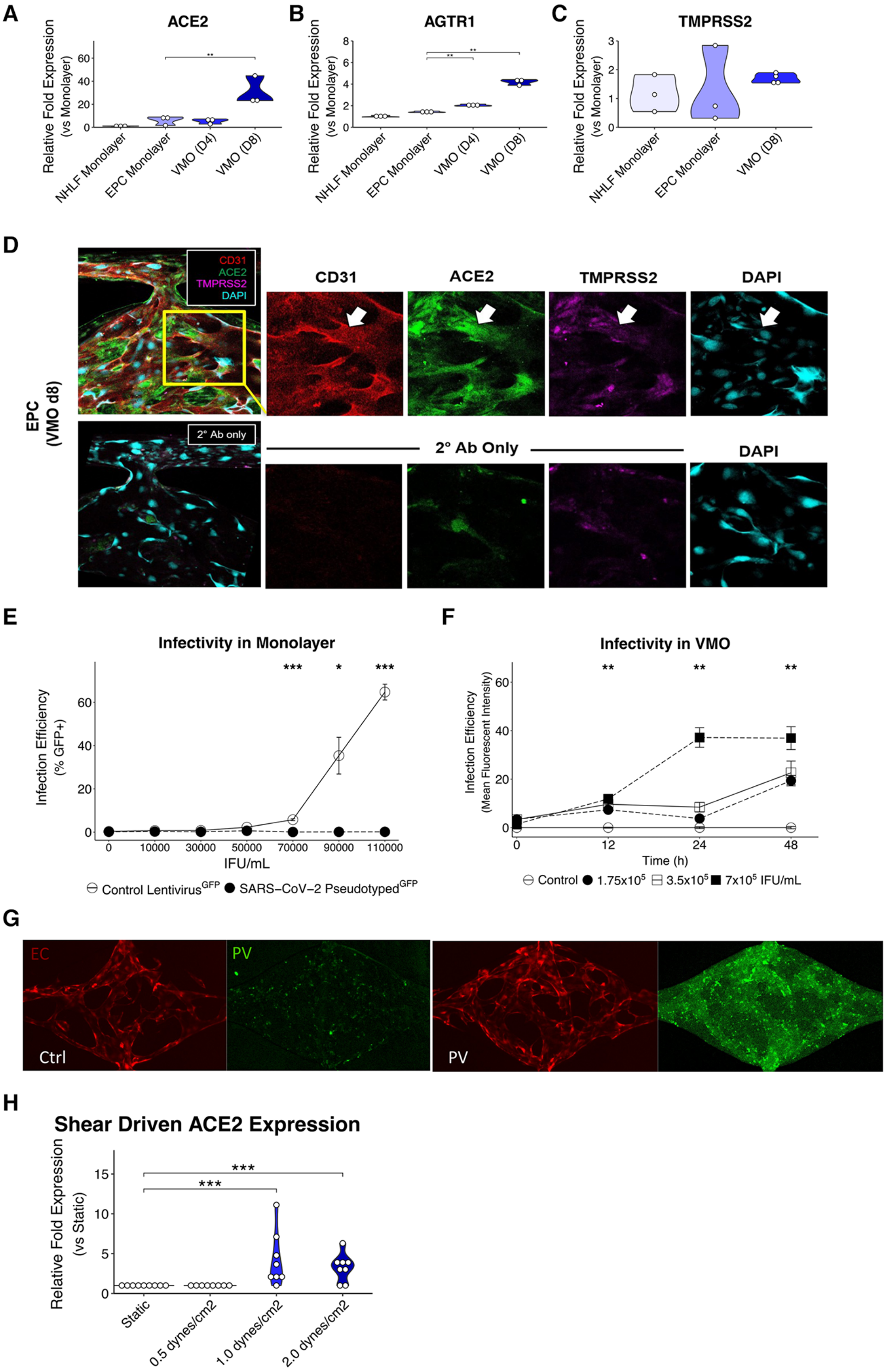

FIGURE 2

Upregulated ACE2 expression in the vascularized micro-organ supports SARS-CoV-2 pseudotyped infectivity. qPCR analysis of (A) ACE2, (B) AGTR1, and (C) TMPRSS2, which are necessary for SARS-CoV-2 infectivity, comparing monolayer normal human lung fibroblasts (NHLF), monolayer EC, the vascularized micro-organ (VMO) before (D4) and after (D8) the formation of perfusable vasculature. (D) Immunofluorescence staining of a D8 VMO showing CD31/PECAM1 (red), DAPI (blue), and localization of ACE2 (green) and TMPRSS2 (purple) to the endothelium. Showing nonspecificity of secondary antibodies alone. (E) Infectivity efficiency (mean fluorescent intensity) of SARS-CoV-2 pseudotyped virus compared to a lentivirus expressing green fluorescent protein (GFP). (F) Titering of GFP SARS-CoV-2 pseudotyped virus in a perfused VMO. Infectivity is measured as an increase in the mean fluorescent intensity of the GFP channel. (G) Subset of a D8 VMO EC (mCherry) and background fluorescence or fluorescence induced by infection with SARS-CoV-2 pseudotyped virus (GFP). Ctrl, control; PV, pseudotyped virus. (H) qPCR analysis of ACE2 expression induced by shear stress in an ibidi microfluidic chip. *<0.05, **<0.01, ***<0.001.

ACE2, TMPRSS2, and AGTR1 in endothelial monolayers and in the VMO on days 4 and 8 (Figures 2A–C). We observed a significant increase in ACE2 and AGTR1 expression in the VMO vasculature compared to cells in the monolayer, and expression was higher still once flow was fully established (day 8) compared to the early stages of lumen formation (day 4). There was no apparent change in TMPRSS2 mRNA expression in the VMO. We performed immunofluorescence staining and confirmed ACE2 and TMPRSS2 in the VMO (Figure 2D). Consistent with our expression data showing an extremely low level of ACE2 expression by monolayer EC; these cells were not infectable with pseudotyped virus; however, they were infectable with a control, VSV coat protein, GFP-expressing virus (Figure 2E). In contrast, the SARS-CoV2-pseudotyped virus readily infected the endothelium when perfused through the VMO for 48 h (Figures 2F,G), again consistent with our expression data showing induction of ACE2 under flow conditions. We hypothesized that the increase in ACE2 in the VMO is likely caused by exposure to shear stress, as demonstrated by others (19). To test this directly, we exposed monolayer ECs to a range of shear stresses comparable to those found at various points throughout the vascular network in the VMO. Analysis of mRNA expression revealed that ACE2 is indeed induced dose-dependently by flow (Figure 2H).

## 3.3 SARS-CoV-2-pseudotyped virus infection in the VMO generates local EC inflammation

Having demonstrated that ECs in the VMO are infectable by a SARS-CoV-2-pseudotyped virus, we next wished to determine the impact of infectivity on ACE2 mRNA expression levels and downstream inflammation, as others have shown decreasing mRNA ACE2 expression during the course of infection in patients and the impact it has on inflammation (39). As noted above, in the body, the effects of angiotensin (AngII), mediated by AGTR1, are transient due to the rapid degradation of AngII by ACE2. Peptide degradation products of this reaction (specifically Ang$_{1-7}$) bind to the Mas receptor (MasR), which mediates an anti-inflammatory signal. Loss of ACE2 leads to prolonged activation of AGTR1 and loss of MasR signaling, the combination of which has been shown to be pro-inflammatory (40). We therefore tested whether recombinant AngII (rAngII) in the presence or absence of pseudotyped virus would lead to a pro-inflammatory EC phenotype in the VMO and potentially influence ACE2 expression. Consistent with our hypothesis, both rAngII and the pseudotyped virus reduced ACE2 mRNA expression levels in EC in the VMO (Supplementary Figures S1A,B). AGTR1 expression levels were also reduced.

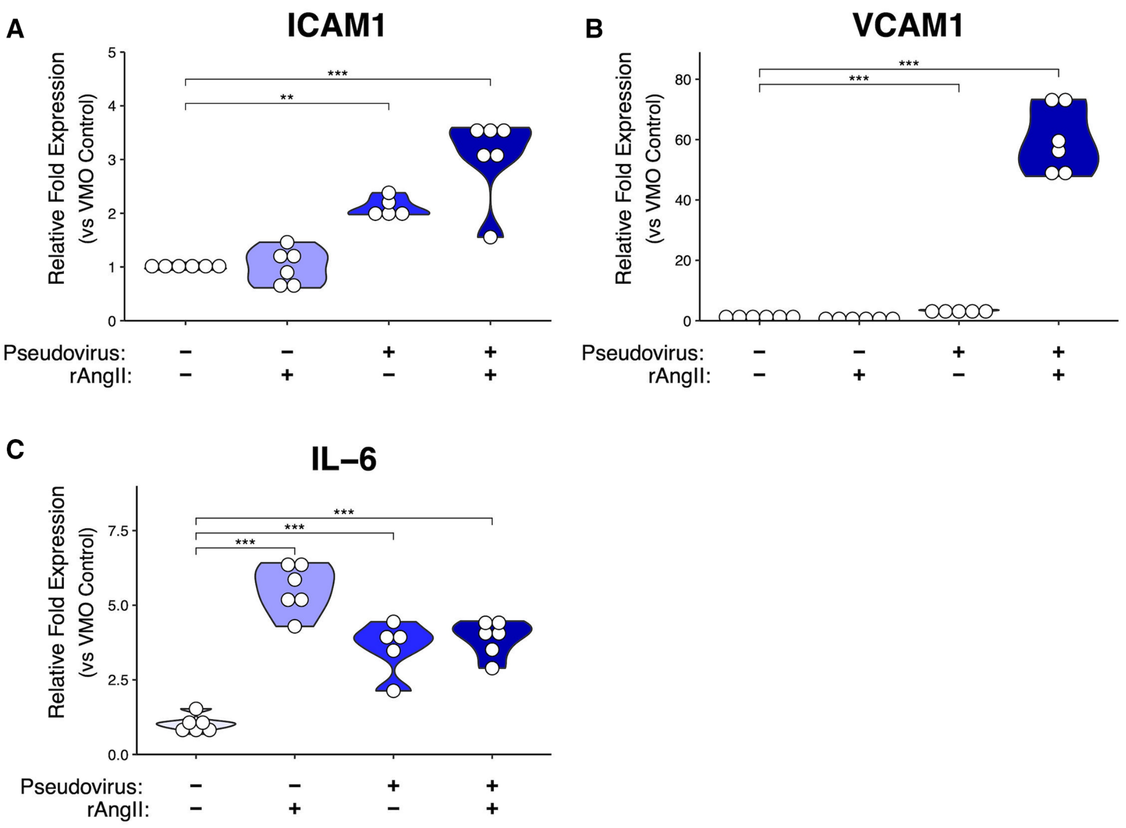

FIGURE 3
Modeled SARS-CoV-2 infection alters VMO transcriptomic profiles. In the VMO, qPCR analysis of pro-inflammatory markers (A) ICAM-1, (B) VCAM-1, and (C) IL-6 for perfused vascularized micro-organ (VMO) that have been treated with SARS-CoV-2 pseudotyped virus (pseudovirus), recombinant angiotensin II (rAngII) or both for 48 h. *<0.05, **<0.01, ***<0.001.

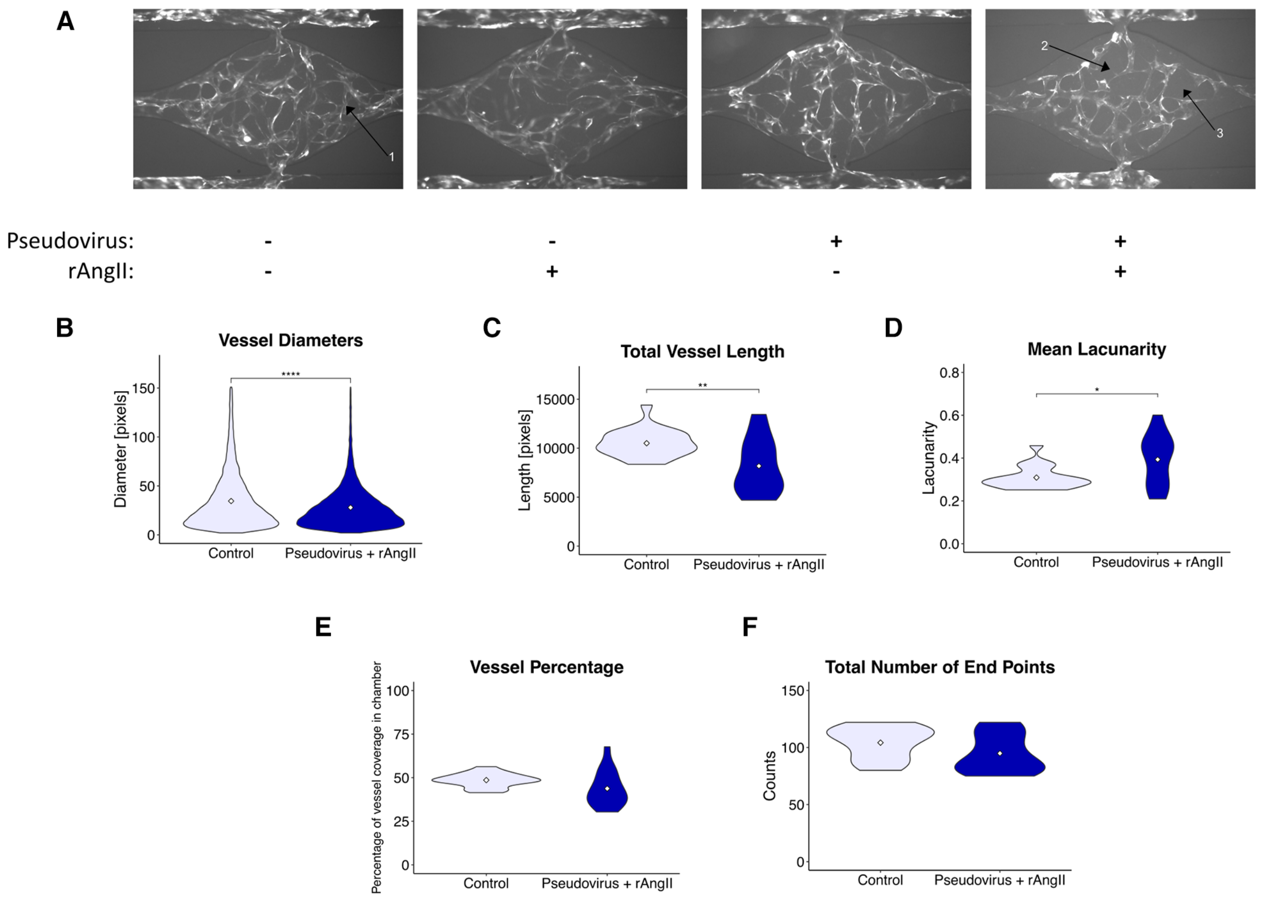

FIGURE 4
Modeled SARS-CoV-2 infection alters vessel morphometry. (A) Representative images of perfused VMOs treated with SARS-CoV-2 pseudotyped virus (pseudovirus) and/or recombinant angiotensin II (rAngII) for 48 h. Arrow 1: Under control conditions, vasculature is continuous and extends to the edges of the tissue chamber. Arrow 2: Discontinuous vessels, likely undergoing pruning and retraction. Arrow 3: Larger regions of perivascular space emerge due to vessel pruning. (B–G) Quantification of morphometry of devices showing changes in (B) vessel diameter, (C) total vessel length, (D) mean lacunarity, (E) vessel coverage percentage, and (F) total number of end points. *<0.05, **<0.01, ***<0.001, ****<0.0001. Control *n* = 11, Pseudovirus + rAngII *n* = 14 (See methods for more detail about replicates).

We then evaluated the expression of two key leukocyte adhesion molecules expressed by EC—ICAM-1 and VCAM-1—which are typically upregulated on EC in response to inflammatory stimuli such as IL-1 and TNF (41, 42), but also by the pleiotropic pro-inflammatory cytokine IL-6, the elevated expression of which is often associated with cytokine storms (43). We found both ICAM-1 and VCAM-1 genes were strongly upregulated by a combination of pseudotyped virus and rAngII (Figures 3A,B). Interestingly, ICAM-1 was also upregulated quite substantially by pseudotyped virus alone, whereas VCAM-1 was only marginally induced by this treatment, suggesting perhaps a higher required threshold for induction. IL-6 was induced by rAngII or virus alone, and there was no further induction in our system in combination (Figure 3C). Thus, our data suggest that downregulation of ACE2 mRNA expression levels as a consequence of viral infection in COVID-19 can lead to the expression of pro-inflammatory genes by the vasculature.

To better understand how this pro-inflammatory signature might disrupt the local vascular niche, we quantified morphological changes in the vasculature induced by the modeled COVID-19 infection (Figure 4A). After infection, we noted a modest reduction in vessel diameter (Figure 4B), total vessel length (Figure 4C), and an increase in lacunarity (Figure 4D), which characterizes vessel non-uniformity and is often increased in pathological vasculature (26). In addition, although not significant, there was a trend towards a reduction in vessel percentage coverage (Figure 4E); however, there was no change in the total number of endpoints (Figure 4F), suggesting that angiogenic sprouting was not induced.

## 3.4 SARS-CoV-2-pseudotyped virus infection in the VMO stimulates release of soluble inflammatory mediators

To characterize the extent to which a localized COVID-19 infection could generate the pro-inflammatory and pro-thrombotic environment produced by infected ECs (44), we investigated inflammatory protein secretion via ELISA (Figure 5). Coagulation Factor VIII is secreted by EC Weibel-Palade bodies and is a

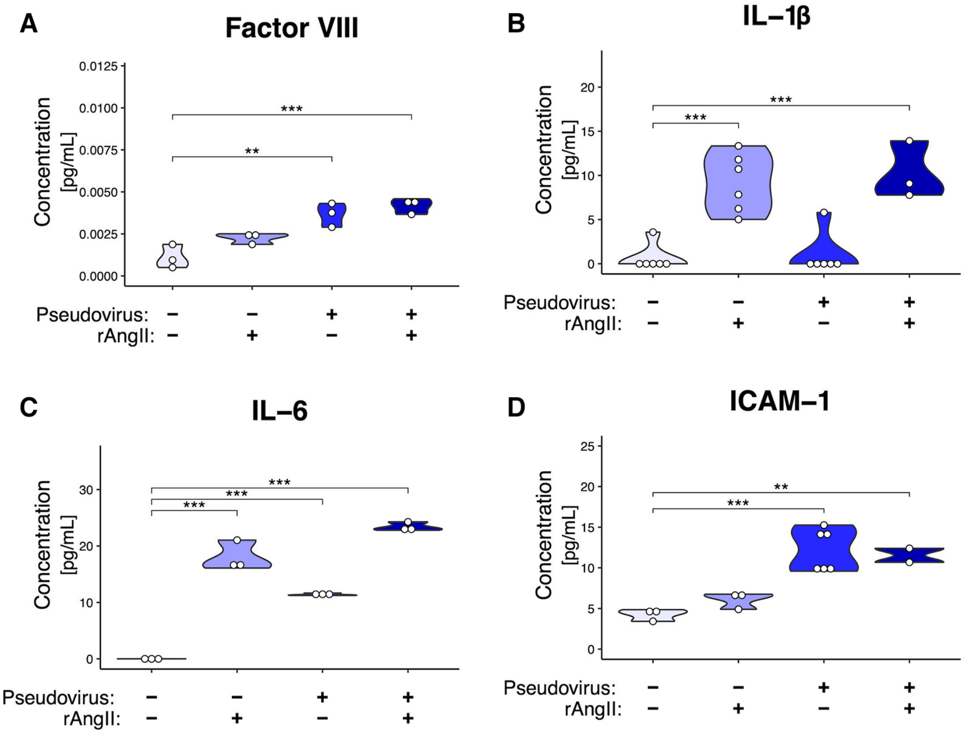

FIGURE 5
Modeled SARS-CoV-2 infection induces cytokine production. ELISAs from effluent collected from VMOs treated with SARS-CoV-2 pseudotyped virus (pseudovirus) and/or recombinant angiotensin II (rAngII) for 48 h. (A) Factor VIII, (B) IL-1β, (C) IL-6, (D) sICAM-1 protein content (pg/mL). *<0.05, **<0.01, ***<0.001.

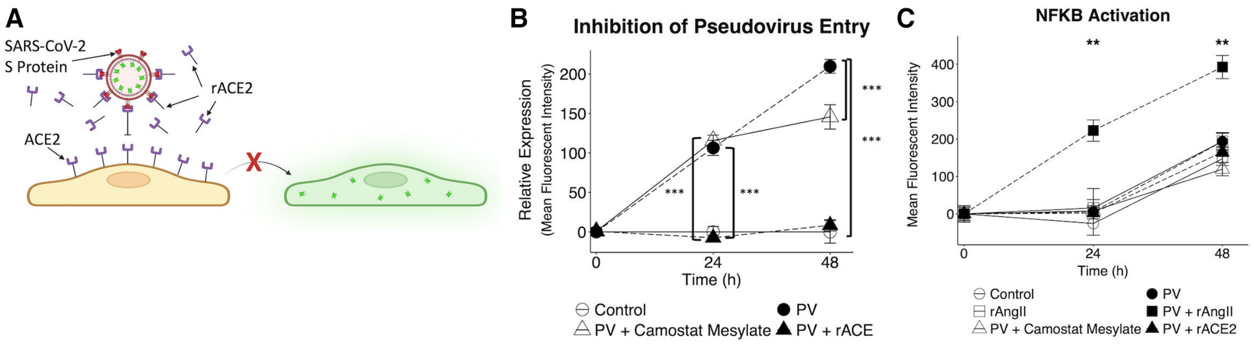

FIGURE 6
Pharmacological intervention inhibits SARS-CoV-2 pseudotyped virus entry and reduces downstream nFκB activation. (A) Recombinant ACE2 (rACE2) prevented pseudotyped infectivity through competitive binding of the SARS-CoV-2 spike protein. (B) VMOs were treated with SARS-CoV-2 pseudotyped virus and rACE2 or camostat mesylate (camostat). The mean fluorescent intensity of the GFP pseudotyped virus was measured. Camostat mesylate had minimal protective ability, and rACE2 prevented infection. (C) Effluent from non-treated and treated devices was placed on EC transduced with an NFκB induced mCherry reporter. The mean fluorescent intensity of mCherry was measured. *<0.05, **<0.01, ***<0.001.

cofactor for activating factor IX, which induces the intrinsic coagulation cascade (45). In perfused VMOs treated with rAngII, pseudotyped virus, or a combination of the two, there was an increase in coagulation Factor VIII secretion (Figure 5A). Additionally, there was increased secretion of several EC-derived inflammatory molecules previously identified in COVID-19 patients (46), including IL-1β, IL-6, and sICAM-1 (Figures 5B-D).

## 3.5 Pharmacological intervention blocks SARS-CoV-2-pseudotyped virus infection and cytokine release

Since the VMO can also be used to conduct drug studies (47), we tested the efficacy of camostat mesylate—a TMPRSS2 inhibitor (37)—and recombinant ACE2 (Figure 6). As shown in Figure 6B,

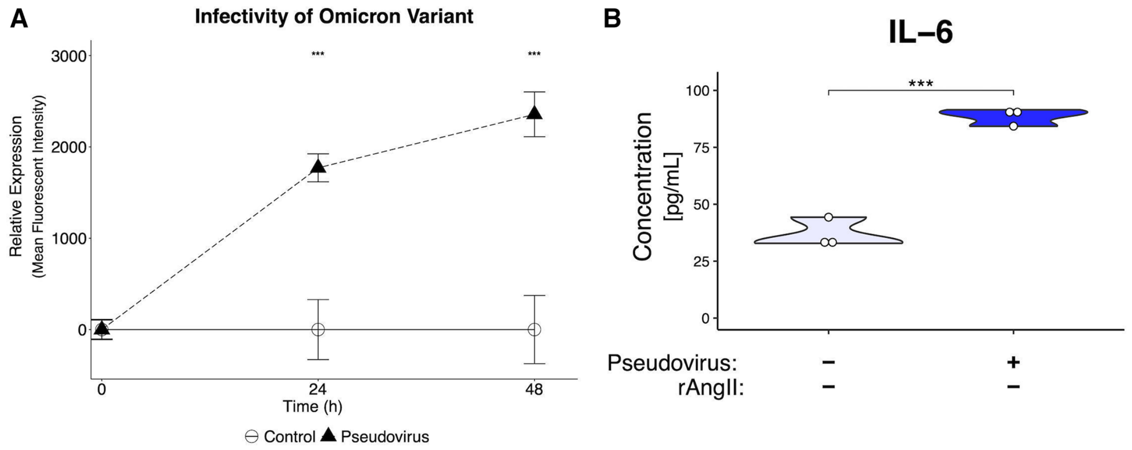

FIGURE 7
Generation of pseudotyped virus with omicron spike protein leads to infectivity and inflammatory response. (A) Mean fluorescent intensity of GFP signal for pseudotyped-virus with omicron variant spike protein. The virus can infect EC in the VMO. (B) ELISA of effluent from omicron-infected VMOs shows a significantly increased production of IL-6. ***<0.001.

rACE2 almost completely blocked infectivity by the pseudotyped virus, whereas TMPRSS2 had only a moderate impact. To determine whether the combination of factors released by infected EC might affect distant vessels—i.e., systemic effects—we collected effluent from the treated tissues and added this to EC transduced with an NFκB promoter-mCherry reporter. NFκB is a key pro-inflammatory transcription factor in EC. As shown in Figure 6C, we found strong induction of mCherry by supernatant from VMOs previously treated with virus and rAngII (and subsequently fed with fresh medium in the absence of virus or recombinant protein) that was apparent by 24 h of treatment. Interestingly, medium from VMOs treated with pseudotyped virus alone had no effect relative to control, indicating that systemic effects have a multi-factorial origin—loss of ACE2 in conjunction with Angiotensin II generation. Consistent with its effect on viral entry, rACE2 completely blocked the effects of pseudotyped virus effluent on NFκB expression (Figure 6C). These data are therefore consistent with a mechanism whereby local infection of EC by SARS-CoV-2 could lead to systemic effects due to released cytokines and pro-coagulatory factors.

### 3.6 Later SARS-CoV-2 spike protein variants are also infectious in the VMO

To determine if the key findings generated using the pseudotyped virus carrying the original spike protein from 2019 could be replicated with the more a recent variant, a pseudotyped virus with the same backbone used for the 2019 variant was generated with the omicron BA.2 variant spike protein (23). The omicron pseudotyped virus was able to infect the VMO (Figure 7A), leading to strongly increased GFP expression. Importantly, effluent from infected VMOs had an increase in IL-6 cytokine levels (Figure 7B), consistent with our earlier results. Taken together, these data demonstrate the utility of the VMO for studying multiple SARS-CoV-2 variants.

## 4 Discussion

Leveraging the unique benefits that the VMO provides, we analyzed COVID-19 infection and the subsequent inflammatory response in a vascularized, fully human, and physiologically relevant system. Real-time fluorescent imaging allowed for direct quantification of the rate of viral entry within the endothelium, demonstrating the pivotal role of ACE2 in viral infection under shear conditions.

While previous work has relied on animal models or static monolayer studies to provide insight into the mechanisms that drive hypercytokinemia and tissue damage (48, 49), we show in this work the importance of flow in inducing the mRNA expression of ACE2, the SARS-CoV2 receptor. The internalization of ACE2 during viral entry removes the enzyme responsible for limiting the spread and duration of Angiotensin II effects. This loss of ACE2 results in prolonged pro-inflammatory signaling through AGTR1 and a loss of the negative, anti-inflammatory signal usually mediated by binding of the Angiotensin II breakdown product $Ang_{1-7}$ to MasR.

Using the VMO allowed us to quantify this inflammatory response with various metrics, including immediate tissue changes in vessel morphometry and cytokine production, and effects of cytokine release from the infected cells on downstream, non-infected cells. The induction of NFκB activity in these non-infected cells is significant as this transcription factor is the key mediator of endothelial inflammatory responses, driving the expression of both cytokines and leukocyte adhesion molecules. Thus, the endothelium can be seen as an initiator and amplifier of the hypercytokinemia that proved so devastating to patients in the early stage of the pandemic. In addition to cytokine release, including upregulation of the pro-thrombotic cytokine IL-6, we show that viral infection also triggered the release of Factor VIII, a component of the intrinsic coagulation pathway. Thus, infected EC could contribute to hyper-coagulation in two ways, by direct release of Factor VIII and by release of IL-6, which can drive expression of other pro-thrombotic factors, including Tissue Factor (50), the initiator of clotting through the extrinsic pathway.

While using primary lung endothelial cells might enhance the findings of this study, we have found that commercially available primary EC from specific tissues mostly perform very poorly in vasculogenesis and angiogenesis assays, likely due to over-expansion prior to shipping. Indeed, we find that cells at passages below ∼5 work best in our VMO platform. That said, previous work from our group has shown that incorporating stromal cells from various sources, such as the lung or heart, leads to transcriptomic changes in the ECFC-EC, and that these model systems show similarity with *in vivo* data (51), suggesting that the stroma can influence EC phenotype. Additionally, unpublished data suggest that developing VMOs with NHLF upregulates lung marker expression on the EC, such as ACE, which a published study showed was only expressed at high and uniform levels in lung EC *in vivo*, with some organ vasculature being completely devoid of expression (52). Therefore, while primary lung endothelial cells may improve the translational impact of these findings, ECFC-EC are better suited for this work due to their vasculogenic and angiogenic potential, as well as plasticity in taking on tissue-specific phenotypes.

While COVID-19 mortality rates have been far lower since the introduction of mRNA vaccines (53), there is still a pressing need to better understand both the acute infection stage and the long-term effects of the disease following recovery. Currently, it is theorized that the profound impact of long-term COVID-19 is due to the dysregulation of thrombotic pathways leading to disseminated intravascular coagulation (54, 55). The VMO, along with other microphysiological systems, provides a unique avenue to study thrombosis and coagulation in a real-time system. Importantly, we have also demonstrated the utility of our platform for studying the impact of potential therapeutics such as rACE2 and camostat mesylate on reducing viral entry. In summary, we have demonstrated through the use of a sophisticated vascularized microphysiological system platform the critical role of flow in the induction of ACE2, and furthermore, have provided clear evidence that the vasculature could play a central role in the initiation and amplification of hypercytokinemia, a major driver of patient death in the early stages of the pandemic.

## Data availability statement

The raw data supporting the conclusions of this article will be made available by the authors, without undue reservation.

## Ethics statement

Ethical approval was not required for the studies involving humans because endothelial cells were derived from discarded umbilical cords with no identifiers. Therefore, the work does not fall under the definition of human subjects work and does not require IRB approval. IBC approval was obtained for using human cells in the lab. The studies were conducted in accordance with the local legislation and institutional requirements. The human samples used in this study were acquired from a by- product of routine care or industry. Written informed consent to participate in this study was not required from the participants or the participants' legal guardians/next of kin in accordance with the national legislation and the institutional requirements.

## Author contributions

CJH: Conceptualization, Investigation, Visualization, Writing – original draft, Writing – review & editing. SP: Conceptualization, Investigation, Writing – original draft, Writing – review & editing. JF: Conceptualization, Investigation, Project administration, Writing – original draft, Writing – review & editing. JG: Methodology, Writing – review & editing. ME: Investigation, Writing – review & editing. WV: Investigation, Writing – review & editing. BC: Methodology, Writing – review & editing. JT: Investigation, Writing – review & editing. DF: Supervision, Writing – review & editing. CCWH: Conceptualization, Supervision, Writing – original draft, Writing – review & editing.

## Funding

The author(s) declare financial support was received for the research, authorship, and/or publication of this article.

This study was supported by the NHLBI award UH3-HL141799. CJH was supported by NIH T32 training grant (T32-HL116270), ME was supported by NIH T32 training grant (T32-CA009054), and WV was supported by NIH T32 training grant (T32-NS082174-08).

## Acknowledgments

We thank the entire Hughes Lab for suggestions and scientific discussion. We would like to thank BioRender.com for helping generate cartoon illustrations.

## Conflict of interest

CCWH is a founder of, and has an equity interest in, Aracari Biosciences, Inc., which is commercializing the vascularized microtissue model. All work is with the full knowledge and approval of the UCI Conflict of Interest Oversight Committee.

The remaining authors declare that the research was conducted in the absence of any commercial or financial relationships that could be construed as a potential conflict of interest.

The author(s) declared that they were an editorial board member of Frontiers, at the time of submission. This had no impact on the peer review process and the final decision.

## Publisher's note

## Supplementary material

The Supplementary Material for this article can be found online at: https://www.frontiersin.org/articles/10.3389/fcvm.2024.1360364/full#supplementary-material

## References

1. Xiao Y, Torok ME. Taking the right measures to control COVID-19. *Lancet Infect Dis*. (2020) 20(5):523–4. doi: 10.1016/S1473-3099(20)30152-3

2. Kluge HHP, Wickramasinghe K, Rippin HL, Mendes R, Peters DH, Kontsevaya A, et al. Prevention and control of non-communicable diseases in the COVID-19 response. *Lancet Lond Engl*. (2020) 395(10238):1678–80. doi: 10.1016/S0140-6736(20)31067-9

3. Le T T, Andreadakis Z, Kumar A, Gómez Román R, Tollefsen S, Saville M, et al. The COVID-19 vaccine development landscape. *Nat Rev Drug Discov*. (2020) 19 (5):305–6. doi: 10.1038/d41573-020-00073-5

4. Sobrino A, Phan DTT, Datta R, Wang X, Hachey SJ, Romero-López M, et al. 3D microtumors in vitro supported by perfused vascular networks. *Sci Rep*. (2016) 6 (1):1–11. doi: 10.1038/srep31589

5. Tang Y, Liu J, Zhang D, Xu Z, Ji J, Wen C. Cytokine storm in COVID-19: the current evidence and treatment strategies. *Front Immunol*. (2020) 11:1708. doi: 10.3389/fimmu.2020.01708

6. Potus F, Mai V, Lebret M, Malenfant S, Breton-Gagnon E, Lajoie AC, et al. Novel insights on the pulmonary vascular consequences of COVID-19. *Am J Physiol Lung Cell Mol Physiol*. (2020) 319(2):L277–88. doi: 10.1152/ajplung.00195.2020

7. Roberts KA, Colley L, Agbaedeng TA, Ellison-Hughes GM, Ross MD. Vascular manifestations of COVID-19—thromboembolism and microvascular dysfunction. *Front Cardiovasc Med*. (2020) 7:598400. doi: 10.3389/fcvm.2020.598400

8. Hu B, Huang S, Yin L. The cytokine storm and COVID-19. *J Med Virol*. (2021) 93 (1):250–6. doi: 10.1002/jmv.26232

9. Copaescu A, Smibert O, Gibson A, Phillips EJ, Trubiano JA. The role of IL-6 and other mediators in the cytokine storm associated with SARS-CoV-2 infection. *J Allergy Clin Immunol*. (2020) 146(3):518–534.1. doi: 10.1016/j.jaci.2020.07.001

10. van der Poll T, Levi M, Hack CE, ten Cate H, van Deventer SJ, Eerenberg AJ, et al. Elimination of interleukin 6 attenuates coagulation activation in experimental endotoxemia in chimpanzees. *J Exp Med*. (1994) 179(4):1253–9. doi: 10.1084/jem.179.4.1253

11. Gibson PG, Qin L, Puah SH. COVID-19 acute respiratory distress syndrome (ARDS): clinical features and differences from typical pre-COVID-19 ARDS. *Med J Aust*. (2020) 213(2):54–56.1. doi: 10.5694/mja2.50674

12. Rosas IO, Bräu N, Waters M, Go RC, Hunter BD, Bhagani S, et al. Tocilizumab in hospitalized patients with severe COVID-19 pneumonia. *N Engl J Med*. (2021) 384 (16):1503–16. doi: 10.1056/NEJMoa2028700

13. Moya ML, Hsu YH, Lee AP, Hughes CCW, George SC. In vitro perfused human capillary networks. *Tissue Eng Part C Methods*. (2013) 19(9):730–7. doi: 10.1089/ten.tec.2012.0430

14. Phan DT, Bender RHF, Andrejecsk JW, Sobrino A, Hachey SJ, George SC, et al. Blood–brain barrier-on-a-chip: microphysiological systems that capture the complexity of the blood–central nervous system interface. *Exp Biol Med*. (2017) 242 (17):1669–78. doi: 10.1177/1535370217694100

15. Hachey SJ, Hughes CCW. Applications of tumor chip technology. *Lab Chip*. (2018) 18(19):2893–912. doi: 10.1039/C8LC00330K

16. Davidson AM, Wysocki J, Batlle D. Interaction of SARS-CoV-2 and other coronavirus with ACE (angiotensin-converting enzyme)-2 as their main receptor: therapeutic implications. *Hypertens Dallas Tex 1979*. (2020) 76(5):1339–49. doi: 10.1161/HYPERTENSIONAHA.120.15256

17. Ramasamy S, Subbian S. Critical determinants of cytokine storm and type I interferon response in COVID-19 pathogenesis. *Clin Microbiol Rev*. (2021) 34(3): e00299–20. doi: 10.1128/CMR.00299-20

18. Hamming I, Timens W, Bulthuis MLC, Lely AT, Navis GJ, van Goor H. Tissue distribution of ACE2 protein, the functional receptor for SARS coronavirus. A first step in understanding SARS pathogenesis. *J Pathol*. (2004) 203(2):631–7. doi: 10.1002/path.1570

19. Song J, Hu B, Qu H, Wang L, Huang X, Li M, et al. Upregulation of angiotensin converting enzyme 2 by shear stress reduced inflammation and proliferation in vascular endothelial cells. *Biochem Biophys Res Commun*. (2020) 525(3):812–8. doi: 10.1016/j.bbrc.2020.02.151

20. Kashima Y, Sakamoto Y, Kaneko K, Seki M, Suzuki Y, Suzuki A. Single-cell sequencing techniques from individual to multiomics analyses. *Exp Mol Med*. (2020) 52(9):1419–27. doi: 10.1038/s12276-020-00499-2

21. Melero-Martin JM, De Obaldia ME, Kang SY, Khan ZA, Yuan L, Oettgen P, et al. Engineering robust and functional vascular networks in vivo with human adult and cord blood-derived progenitor cells. *Circ Res*. (2008) 103(2):194–202. doi: 10.1161/CIRCRESAHA.108.178590

22. Schindelin J, Arganda-Carreras I, Frise E, Kaynig V, Longair M, Pietzsch T, et al. Fiji: an open-source platform for biological-image analysis. *Nat Methods*. (2012) 9 (7):676–82. doi: 10.1038/nmeth.2019

23. Dacon C, Tucker C, Peng L, Lee CCD, Lin TH, Yuan M, et al. Broadly neutralizing antibodies target the coronavirus fusion peptide. *Science*. (2022) 377 (6607):728–35. doi: 10.1126/science.abq3773

24. Ritz C, Baty F, Streibig JC, Gerhard D. Dose-response analysis using R. *PLoS One*. (2015) 10(12):e0146021. doi: 10.1371/journal.pone.0146021

25. RStudio Team. RStudio: Integrated Devlopment for R (2020); Available online at: http://www.rstudio.com/ (accessed March 8, 2022).

26. Zudaire E, Gambardella L, Kurcz C, Vermeren S. A computational tool for quantitative analysis of vascular networks. *PLoS One*. (2011) 6(11):e27385. doi: 10.1371/journal.pone.0027385

27. Corliss BA, Doty RW, Mathews C, Yates PA, Zhang T, Peirce SM. REAVER: a program for improved analysis of high-resolution vascular network images. *Microcirculation*. (2020) 27(5):e12618. doi: 10.1111/micc.12618

28. Kwiatek G. DXFLib (2023). Available online at: https://www.mathworks.com/matlabcentral/fileexchange/33884-dxflib (accessed December 4, 2023).

29. Wickham H. Ggplot2. *WIRES Comput Stat*. (2011) 3(2):180–5. doi: 10.1002/wics.147

30. Kassambara A. ggpubr: "ggplot2" Based Publication Ready Plots (2023). Available online at: https://cran.r-project.org/web/packages/ggpubr/index.html (accessed December 4, 2023).

31. Auguie B, Antonov A. gridExtra: Miscellaneous Functions for "Grid" Graphics (2017). Available online at: https://cran.r-project.org/web/packages/gridExtra/index.html (accessed December 4, 2023).

32. Kassambara A. rstatix: Pipe-friendly Framework for Basic Statistical Tests (2023). Available online at: https://cran.r-project.org/web/packages/rstatix/index.html (accessed December 4, 2023).

33. Dinno A. conover.test: Conover–Iman Test of Multiple Comparisons Using Rank Sums (2017). Available online at: https://cran.r-project.org/web/packages/conover.test/index.html (accessed December 4, 2023).

34. Fox J, Weisberg S, Price B, Adler D, Bates D, Baud-Bovy G, et al. car: Companion to Applied Regression (2023). Available online at: https://cran.r-project.org/web/packages/car/index.html (accessed December 4, 2023).

35. Roux E, Bougaran P, Dufourcq P, Couffinhal T. Fluid shear stress sensing by the endothelial layer. *Front Physiol*. (2020) 11:861. doi: 10.3389/fphys.2020.00861

36. Li W, Moore MJ, Vasilieva N, Sui J, Wong SK, Berne MA, et al. Angiotensin-converting enzyme 2 is a functional receptor for the SARS coronavirus. *Nature*. (2003) 426(6965):450–4. doi: 10.1038/nature02145

37. Hoffmann M, Kleine-Weber H, Schroeder S, Krüger N, Herrler T, Erichsen S, et al. SARS-CoV-2 cell entry depends on ACE2 and TMPRSS2 and is blocked by a clinically proven protease inhibitor. *Cell*. (2020) 181(2):271–280.8. doi: 10.1016/j.cell.2020.02.052

38. Kouhpayeh HR, Tabasi F, Dehvari M, Naderi M, Bahari G, Khalili T, et al. Association between angiotensinogen (AGT), angiotensin-converting enzyme (ACE) and angiotensin-II receptor 1 (AGTR1) polymorphisms and COVID-19 infection in the southeast of Iran: a preliminary case-control study. *Transl Med Commun*. (2021) 6(1):26. doi: 10.1186/s41231-021-00106-0

39. Gutiérrez-Chamorro L, Riveira-Muñoz E, Barrios C, Palau V, Nevot M, Pedreño-López S, et al. SARS-CoV-2 infection modulates ACE2 function and subsequent inflammatory responses in swabs and plasma of COVID-19 patients. *Viruses*. (2021) 13(9):1715. doi: 10.3390/v13091715

40. Mahmudpour M, Roozbeh J, Keshavarz M, Farrokhi S, Nabipour I. COVID-19 cytokine storm: the anger of inflammation. *Cytokine*. (2020) 133:155151. doi: 10.1016/j.cyto.2020.155151

41. Bui TM, Wiesolek HL, Sumagin R. ICAM-1: a master regulator of cellular responses in inflammation, injury resolution, and tumorigenesis. *J Leukoc Biol*. (2020) 108(3):787–99. doi: 10.1002/JLB.2MR0220-549R

42. Kong DH, Kim YK, Kim MR, Jang JH, Lee S. Emerging roles of vascular cell adhesion molecule-1 (VCAM-1) in immunological disorders and cancer. *Int J Mol Sci*. (2018) 19(4):1057. doi: 10.3390/ijms19041057

43. Kang S, Kishimoto T. Interplay between interleukin-6 signaling and the vascular endothelium in cytokine storms. *Exp Mol Med*. (2021) 53(7):1116–23. doi: 10.1038/s12276-021-00649-0

44. Xu J, Lupu F, Esmon CT. Inflammation, innate immunity and blood coagulation. *Hamostaseologie*. (2010) 30(1):5–6. 8–9. doi: 10.1055/s-0037-1617146

45. Turner NA, Moake JL. Factor VIII is synthesized in human endothelial cells, packaged in weibel-palade bodies and secreted bound to ULVWF strings. *PLoS One*. (2015) 10(10):e0140740. doi: 10.1371/journal.pone.0140740

46. Xu SW, Ilyas I, Weng JP. Endothelial dysfunction in COVID-19: an overview of evidence, biomarkers, mechanisms and potential therapies. *Acta Pharmacol Sin*. (2023) 44(4):695–709. doi: 10.1038/s41401-022-00998-0

47. Phan DTT, Wang X, Craver BM, Sobrino A, Zhao D, Chen JC, et al. A vascularized and perfused organ-on-a-chip platform for large-scale drug screening applications. *Lab Chip*. (2017) 17(3):511–20. doi: 10.1039/C6LC01422D

48. Droebner K, Reiling SJ, Planz O. Role of hypercytokinemia in NF-κB p50-deficient mice after H5N1 influenza A virus infection. *J Virol*. (2008) 82 (22):11461–6. doi: 10.1128/JVI.01071-08

49. de Jong MD, Simmons CP, Thanh TT, Hien VM, Smith GJD, Chau TNB, et al. Fatal outcome of human influenza A (H5N1) is associated with high viral load and hypercytokinemia. *Nat Med*. (2006) 12(10):1203–7. doi: 10.1038/nm1477

50. Gao H, Liu L, Zhao Y, Hara H, Chen P, Xu J, et al. Human IL-6, IL-17, IL-1β, and TNF-α differently regulate the expression of pro-inflammatory related genes, tissue factor, and swine leukocyte antigen class I in porcine aortic endothelial cells. *Xenotransplantation*. (2017) 24(2):e12291. doi: 10.1111/xen.12291

51. Curtis MB, Kelly N, Hughes CCW, George SC. Organotypic stromal cells impact endothelial cell transcriptome in 3D microvessel networks. *Sci Rep*. (2022) 12 (1):20434. doi: 10.1038/s41598-022-24013-y

52. Metzger R, Franke FE, Bohle RM, Alhenc-Gelas F, Danilov SM. Heterogeneous distribution of angiotensin I-converting enzyme (CD143) in the human and rat vascular systems: vessel, organ and species specificity. *Microvasc Res*. (2011) 81 (2):206–15. doi: 10.1016/j.mvr.2010.12.003

53. Mohammed I, Nauman A, Paul P, Ganesan S, Chen KH, Jalil SMS, et al. The efficacy and effectiveness of the COVID-19 vaccines in reducing infection, severity, hospitalization, and mortality: a systematic review. *Hum Vaccines Immunother*. (2022) 18(1):2027160. doi: 10.1080/21645515.2022.2027160

54. Asakura H, Ogawa H. COVID-19-associated coagulopathy and disseminated intravascular coagulation. *Int J Hematol*. (2021) 113(1):45–57. doi: 10.1007/s12185-020-03029-y

55. Crook H, Raza S, Nowell J, Young M, Edison P. Long COVID-mechanisms, risk factors, and management. *Br Med J*. (2021) 374:n1648. doi: 10.1136/bmj.n1648

Frontiers in Cardiovascular Medicine

TYPE Review
PUBLISHED 30 April 2024
DOI 10.3389/fcvm.2024.1386177

OPEN ACCESS

EDITED BY
Margreet R. De Vries,
Leiden University Medical Center (LUMC),
Netherlands

REVIEWED BY
Kyung Lee,
Icahn School of Medicine at Mount Sinai,
United States
Roberta Soares,
University of Miami, United States

*CORRESPONDENCE
Athina Dritsoula
✉ athina.dritsoula.09@ucl.ac.uk

RECEIVED 14 February 2024
ACCEPTED 17 April 2024
PUBLISHED 30 April 2024

CITATION
Dritsoula A, Camilli C, Moss SE and Greenwood J (2024) The disruptive role of LRG1 on the vasculature and perivascular microenvironment.
Front. Cardiovasc. Med. 11:1386177.
doi: 10.3389/fcvm.2024.1386177

# The disruptive role of LRG1 on the vasculature and perivascular microenvironment

Athina Dritsoula*, Carlotta Camilli, Stephen E. Moss and John Greenwood

UCL Institute of Ophthalmology, University College London, London, United Kingdom

The establishment of new blood vessels, and their subsequent stabilization, is a critical process that facilitates tissue growth and organ development. Once established, vessels need to diversify to meet the specific needs of the local tissue and to maintain homeostasis. These processes are tightly regulated and fundamental to normal vessel and tissue function. The mechanisms that orchestrate angiogenesis and vessel maturation have been widely studied, with signaling crosstalk between endothelium and perivascular cells being identified as an essential component. In disease, however, new vessels develop abnormally, and existing vessels lose their specialization and function, which invariably contributes to disease progression. Despite considerable research into the vasculopathic mechanisms in disease, our knowledge remains incomplete. Accordingly, the identification of angiocrine and angiopathic molecules secreted by cells within the vascular microenvironment, and their effect on vessel behaviour, remains a major research objective. Over the last decade the secreted glycoprotein leucine-rich α-2 glycoprotein 1 (LRG1), has emerged as a significant vasculopathic molecule, stimulating defective angiogenesis, and destabilizing the existing vasculature mainly, but not uniquely, by altering both canonical and non-canonical TGF-β signaling in a highly cell and context dependent manner. Whilst LRG1 does not possess any overt homeostatic role in vessel development and maintenance, growing evidence provides a compelling case for LRG1 playing a pleiotropic role in disrupting the vasculature in many disease settings. Thus, LRG1 has now been reported to damage vessels in various disorders including cancer, diabetes, chronic kidney disease, ocular disease, and lung disease and the signaling processes that drive this dysfunction are being defined. Moreover, therapeutic targeting of LRG1 has been widely proposed to re-establish a quiescent endothelium and normalized vasculature. In this review, we consider the current status of our understanding of the role of LRG1 in vascular pathology, and its potential as a therapeutic target.

KEYWORDS

LRG1, TGF-β, vascular dysfunction, inflammation, fibrosis, angiogenesis, vessel normalization, vascular

## Introduction

The formation of a vascular network is a fundamental prerequisite in serving the needs of the surrounding tissue and enabling normal tissue function. The process of angiogenesis, whether during development or postnatally as during reproduction and wound healing, has been studied extensively and many of the controlling elements have been defined (1, 2). Vascular endothelial growth factor (VEGF) has emerged as the master regulator, but other factors also contribute to vessel growth and the subsequent stabilization and maturation processes, which are necessary for the establishment of functional vessels (3). The vasculature, however, is highly heterogeneous with vessel structure and function depending on position in the vascular hierarchy and on the physiological requirements of the surrounding tissue. To achieve such diverse functionality, different local signaling factors are required during development and throughout life to maintain this site-specific specialization. Nevertheless, some ubiquitous signaling interactions are deemed essential for vessel maturation, most notably the crosstalk between the endothelium and perivascular mural cells, which are critical to vascular homeostasis. Indeed, disruption of this cellular interplay is recognised as a major factor in the destabilization of existing vessels in several diseases.

Aside from the disruption of existing vessels, the formation of new vessels in disease has attracted enormous attention as they are usually abnormal, often forming a chaotic and immature network that may be poorly perfused, leaky, and fragile (2). Whilst many of the factors driving new vessel growth in disease are also those responsible for developmental and physiological angiogenesis, it is clear that differences must exist. Thus, it has been proposed that the balance of expression between pro- and anti-angiogenic factors may be disturbed, while additional disease-specific players may corrupt the normal angiogenic and maturation processes. Although our understanding of these factors, and the associated signaling pathways that disrupt both new and existing vascular structure and function is considerable, there remain significant gaps in our knowledge as highlighted by the large number of patients who fail to respond favourably to standard of care therapies aimed at alleviating vascular dysfunction (2, 4).

The interaction between the endothelium and perivascular mural cells is an imperative and extremely complex process that is central to normal blood vessel development and long-term homeostasis. Abnormalities in this relationship are implicated in numerous vascular diseases, such as diabetic retinopathy, pulmonary hypertension, kidney disease and cancer, where decreased mural cell coverage or abnormal recruitment results in destabilized leaky microvessels and vascular rarefication (5–9). In addition, activation or de-differentiation of vascular smooth muscle cells and pericytes can lead to vascular remodeling and medial thickening in larger vessels (5). Also emerging is the disruptive role played by endothelial to mesenchymal transition (EndMT) (10), a process similar to epithelial to mesenchymal transition (EMT), in which TGF-β plays a predominant role. Irrespective of cause, when vessels become dysfunctional, they not only fail to provide their selective barrier and delivery functions but can also negatively influence the behaviour of surrounding tissue. Designing therapeutic strategies, therefore, that aim to normalize the vasculature has received increasing attention, especially in cancer (11), but further insight into our understanding of interactions that drive vascular dysfunction in disease is needed. Through such improved insight, new therapeutic targets will be identified for which activation or inhibition will enable repair of dysfunctional vessels and the facilitation of physiological revascularization during disease. One recently identified candidate, the angiocrine factor leucine-rich α-2 glycoprotein 1 (LRG1), is emerging as a ubiquitous and potentially critical player in driving vascular pathology, and therefore offers substantial potential as a new therapeutic target in many different diseases. This review aims to present the diverse and emerging vasculopathic roles that LRG1 has on the vasculature and its influence on the local microenvironment.

## LRG1 in homeostasis and disease

LRG1 is a member of the conserved family of leucine-rich repeat glycoproteins that are involved in numerous physiological functions, including protein-protein interactions and innate immune responses (12, 13). Under normal conditions LRG1 is expressed almost exclusively by liver hepatocytes, from where it is secreted into the circulation and maintained at an approximate concentration of 20–50 µg/ml in the plasma (14) (Figure 1). Neutrophils, which are powerful mediators of innate immunity, are also known to express LRG1 constitutively and are likely to contribute to LRG1-mediated pathogenic effects in inflamed tissues and diseased vasculature (Figure 1). In these cells, LRG1 is stored within granules, and its expression has been associated with accelerated neutrophilic granulopoiesis, suggesting a potential role for LRG1 in myeloid cell differentiation (15, 16). Moreover, LRG1 has been shown to be involved in the formation of neutrophil extracellular traps (NETs), a process known as NETosis, via a signaling pathway involving ALK5 and AKT (17). NETosis is an innate immune response initiated against pathogens but is also frequently associated with vascular dysfunction (18). These findings, together with increased LRG1 levels in serum in response to microbial or viral infections and other inflammatory stimuli, as well as the high binding affinity of LRG1 for cytochrome c (Cyt c) following its release upon apoptotic signals, have led to the proposal that LRG1 functions as an acute phase protein involved in the innate immune response (19, 20). Aside from these major sources of LRG1, low levels of expression have been reported under normal conditions in other tissues including lung, kidney, heart, brain, testis, and the vasculature, where LRG1 is predominantly expressed in endothelial cells (21) (Figure 1). Many of these studies, however, use immunohistochemical detection, which might reflect the presence of extracellular, and matrix/endothelial cell sequestered LRG1 derived from the circulation. Nevertheless, a recent transcriptomics study dissecting the molecular heterogeneity of blood vascular endothelial cells from skin has shown that *LRG1* transcript is exclusively found in the blood vessels and more specifically in healthy skin enriched in the postcapillary venules (22).

Although current evidence suggests that LRG1 expression may be important to the functions of different organs and processes, its primary physiological role remains poorly defined, with *Lrg1*-deficient mice presenting with normal development and fertility, and no obvious phenotype indicating a non-essential role. In recent years, however, accumulating evidence points to the involvement of LRG1 in a wide range of diseases (23, 24). Since 2013, when LRG1 was initially identified as a key vasculopathic molecule in abnormal angiogenesis (25), more causative roles have been attributed. Among others, LRG1 has been found to drive IL-6-dependent pathological angiogenesis through the

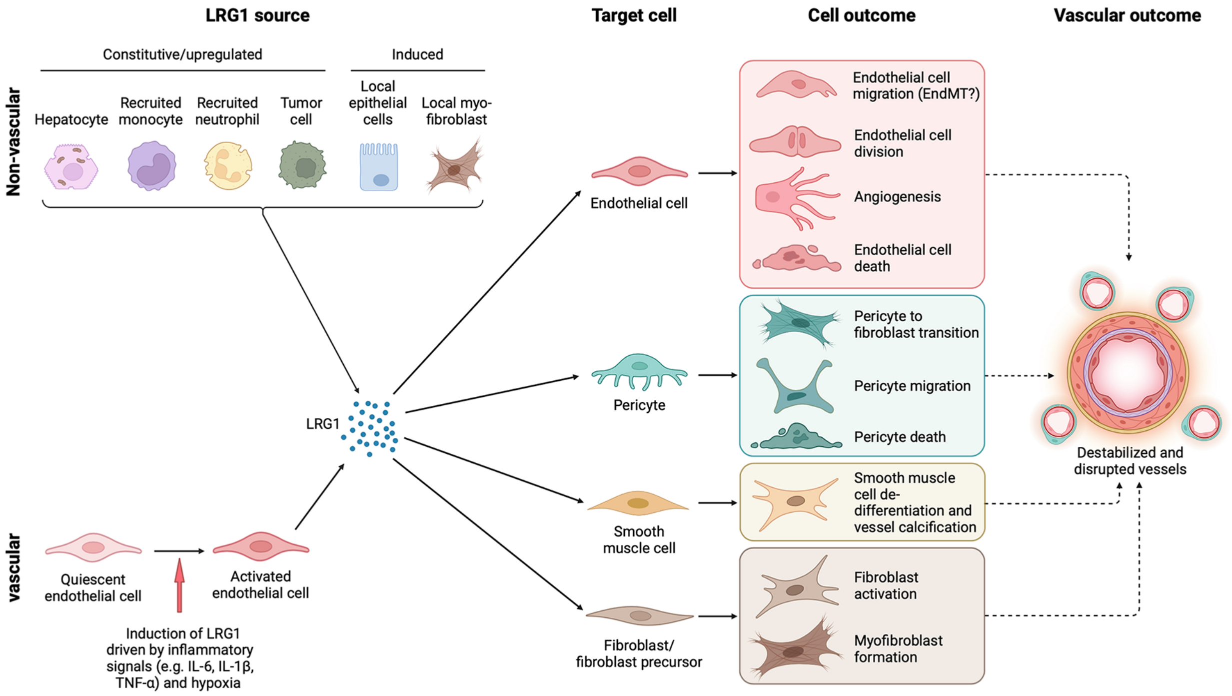

FIGURE 1
Cell source, target cells and outcome of LRG1 in the vasculature. LRG1 is expressed constitutively by only a few cell types, including hepatocytes and neutrophils, but during disease can be induced in various other cells. In the vasculature, endothelial cells are the only source of LRG1, but other local cells may also be induced to express LRG1 such as fibroblasts and tumor cells. Irrespective of the source, LRG1 affects the function of all cellular components of blood vessels resulting in vascular damage. Vascular dysfunction is closely associated with fibrosis, and both may influence each other through LRG1 signaling. EndMT, endothelial to mesenchymal transition. Created with BioRender.com.

STAT3 signaling pathway (26, 27), destabilize tumor vasculature and promote tumor growth and metastasis (28–32), drive chronic kidney and lung disease (33–40), stimulate fibrosis (33, 34, 41–48), contribute to diabetes-related pathology (17, 49–57), and regulate pathological placental angiogenesis (58). High circulating LRG1 levels have been reported in many cancers, where LRG1 has been proposed, or used, as a prognostic and diagnostic marker. Indeed, high LRG1 levels in cancer patients' plasma correlate with poor prognosis and survival (59–61), and resistance to standard of care therapy (62). The involvement and roles of LRG1 in key vascular processes are the scope of this review and will be discussed in detail.

## Regulation of LRG1 expression

Several transcriptomic and post-transcriptional regulatory studies have shown that the IL-6/STAT3 signaling pathway is a major activator of LRG1 expression (26, 29, 31, 63). Indeed, it was recently reported that LRG1 transcriptional activation is abolished upon deletion of the STAT3 binding site on the *LRG1* promoter (26). Inflammation seems to be an important driver of LRG1 expression, with many different cytokines activating LRG1 in a range of cells and disease settings (Figure 2). These include IL-6, IL-1β, TNF-α, IL-17, IL-4, IL-10 and IL-33 and they may act either alone or synergistically (36, 64–68). In addition, PPARβ/δ is able to bind the *LRG1* promoter to activate transcription as reported in a chromatin immunoprecipitation assay (47), and similarly, both ELK1 and ELK4 transcription factors have been shown to initiate *LRG1* transcription upon mechanical strain (41) and through cooperation with Sp1/Sp3 complex (69), respectively. FOS-like 1 was also identified as a novel activator of *LRG1* in a transcriptomics study (39). There is also evidence that hypoxia can induce LRG1 expression (70), consistent with the presence of potentially active HIF-1α binding elements in the *LRG1* promoter. At the post-transcriptional and post-translational levels, microRNAs, long non-coding RNAs, and histone modifications have also been reported to regulate LRG1 expression (23) (Figure 2). Furthermore, different glycosylation patterns have been identified and these might influence LRG1 function (23). Overall, while experimental evidence that unravels the pleiotropic functions of LRG1 continues to accumulate, further work is required to establish the key regulatory mechanisms that control LRG1 expression and function, some of which will be discussed in detail later.

## LRG1 and angiogenesis

In the early stages of development, blood vessels are formed through a tightly orchestrated process called vasculogenesis, where mesoderm-derived angioblasts, the precursor of endothelial cells, establish angioblastic cords that advance into a

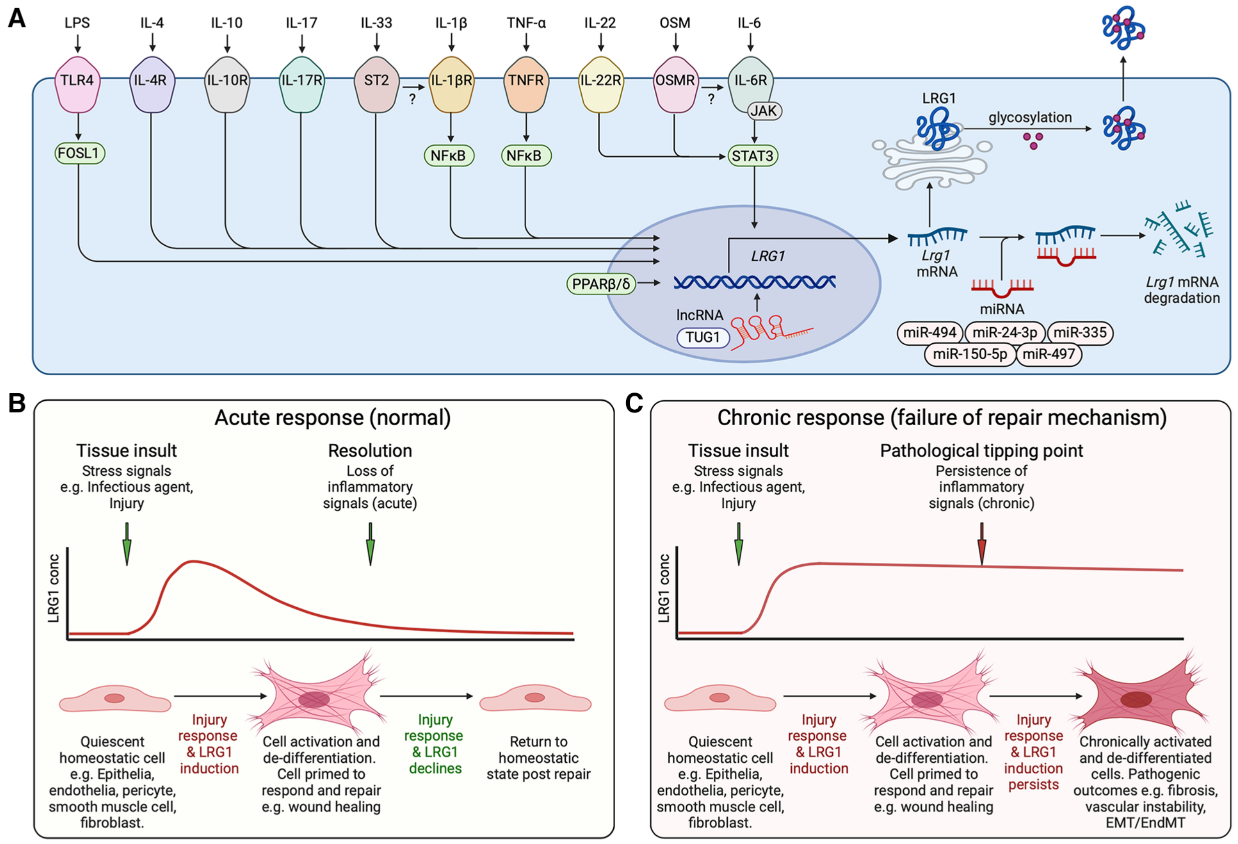

FIGURE 2
Induction of LRG1. (A) Schematic representation of inflammatory factors reported to activate LRG1 gene expression and known transcriptional and post-transcriptional regulatory mechanisms. Cytokines and lipopolysaccharide (LPS) acting through their cognate receptors and downstream transcription factors drive *LRG1* gene induction. lncRNA TUG1 facilitates *LRG1* transcription while miR-335, miR-494, miR-497, miR-150-5p and miR-24-3p promote the degradation of *LRG1* mRNA. LRG1 protein is differentially glycosylated in a cell- and function-specific manner that may affect its activity. The secreted protein may combine to form dimers and trimers. OSM, oncostatin M; IL, interleukin; TLR4, toll-like receptor 4; lncRNA, long non-coding RNA; miRNA, microRNA. (B) LRG1 is induced during cell damage and infection as part of the repair mechanism. In the presence of LRG1 and TGF-β, we propose that cells are activated and de-differentiated into a less mature state to enable wound healing. As inflammatory signals subside, LRG1 expression diminishes allowing resolution of tissue damage and cells to return to a quiescent state. (C) Under chronic conditions, inflammatory signals maintain LRG1 expression perpetuating the unstable cell state and preventing completion of the healing process. EMT, epithelial to mesenchymal transition; EndMT, endothelial to mesenchymal transition. Created with BioRender.com.

primitive vascular plexus and subsequently into blood vessels. At later stages of development, and postnatally in the reproductive system and during physiological tissue repair, angiogenesis occurs in response to tissue growth and hypoxia. The angiogenic mechanism is tightly regulated and influenced by pro-angiogenic factors, with VEGF being a key master regulator, essential for the development and maintenance of the vascular system (3). Other growth factors with established pro-angiogenic activities include the FGFs, PDGF, angiopoietins, HGF and the TGF-β superfamily. In particular, PDGF and the angiopoietins exert their functions on the endothelium in a paracrine manner through their binding to, or their expression by, perivascular mural cells. In addition, angiopoietins regulate vascular homeostasis and promote vessel stability through the recruitment of mural cells and mediate their interactions with the endothelium (71). Among other potent angiogenic molecules are angiopoietin-like 4 (72), apelin (73), Frizzled A (74, 75), thrombomodulin (76), AGGF1 (77), Slit3 (78), as well as a plethora of pro-angiogenic peptides, the therapeutic potential of which is reviewed elsewhere (79). Aside from the established regulators of angiogenesis, there are many ancillary factors that influence vessel growth and maturation and which, under certain circumstances, may even circumvent the angiogenic dependency on VEGF. As will be seen in this review, LRG1 is now considered to be one of these adjunct pro-angiogenic factors and hence can be added to this extensive list. However, contrary to many of the factors mentioned above, LRG1 does not play a role in developmental or physiological angiogenesis as knock-out mice exhibit no overt phenotype, breed successfully and live a normal life span (21). In the context of disease, however, LRG1 is now recognised as a potent pro-neoangiogenic factor as it has been shown to promote pathological angiogenesis in numerous diseases and *de novo* growth in *in vitro* experimental settings (Table 1). It is worth noting, however, that angiogenesis under *in vitro*/*ex vivo* conditions is unlikely to represent normal angiogenesis, as the environment is more aligned to a pathogenic than homeostatic state. As outlined in more detail in the sections

TABLE 1 Evidence for the functional role of LRG1 in disease pathogenesis and vascular processes.

| Disease/Condition | Process | Functional evidence | Publication |
|---|---|---|---|
| Cancer | Tumor progression, Angiogenesis (Bladder cancer) | Increased tumor cell proliferation, migration, invasion, EC angiogenesis (tube formation) (*in vitro*). | (80) |
| | Tumor progression, Angiogenesis (Pancreatic cancer) | Improved tumor cell viability, migration, invasion, EC angiogenesis (tube formation) through VEGFR activation (*in vitro*). | (81) |
| | Tumor progression, Angiogenesis (Gastric cancer) | Increased EC proliferation, migration, and angiogenesis (tube formation). Tumor cell angiogenesis and tumor progression (*in vitro*). | (27) |
| | Vessel normalization | Improved vessel structure and vascular function (Antibody blockade or gene deletion in tumor models *in vivo*). | (32) |
| | Metastasis | Promoted metastasis in lung cancer via NG2$^+$ perivascular cells and STAT3 signaling (*in vivo*). | (29) |
| | Metastasis (Melanoma) | Reduced tumor cell metastasis, growth, proliferation, and angiogenesis in the absence of LRG1 (*in vivo*, *in vitro*). | (28) |
| | Angiogenesis (Non-small-cell lung cancer) | Promoted tumor cell proliferation, migration, invasion, EC angiogenesis (tube formation) through TGF-β (*in vitro*). | (82) |
| | Angiogenesis (Ovarian cancer) | Induced EC angiogenesis (tube formation) by upregulating VEGF, Ang1, TGF-β (*in vitro*). | (83) |
| | Angiogenesis (Colorectal cancer) | Promoted tumor cell invasion, EMT, EC migration, angiogenesis and sprouting (*ex vivo*, *in vitro*) through HIF-1α. | (84) |
| Diabetes | Angiogenesis | Induced angiogenic and neurotrophic function, EC angiogenesis (tube formation), proliferation, migration (*in vivo*, *ex vivo*, *in vitro*). | (85) |
| | Wound healing | Promoted EC viability, proliferation, migration, angiogenesis (*in vitro*), and wound healing (*in vivo*). | (86) |
| | Wound healing | Controlled immune cell infiltration, re-epithelialization, and EC angiogenesis/proliferation (tube formation) through phosphorylation of SMAD1/5. | (17) |
| | Wound healing | Corneal epithelial wound healing and nerve regeneration via regulation of matrix metalloproteinases (*in vivo*, *in vitro*). | (54) |
| | Angiogenesis | Induced angiogenesis (*in vivo*) through ALK1-SMAD1/5/8 in glomerular EC. | (53) |
| | Pathogenesis | Elevated expression in glomerular EC (*in vitro*). | (52) |
| | Angiogenesis | Elevated expression in glomerular EC and angiogenesis (tube formation) (*in vitro*). | (87) |
| Fibrosis | Skin | Induced EC proliferation, migration, and angiogenesis (*in vitro*) and promoted skin fibrosis through ELK1 and ERK signaling. | (41) |
| | Lung | Promoted lung fibrosis through TGF-β-induced Smad2 (*in vivo*, *in vitro*). | (42) |
| | Kidney, DKD | Induced expression in glomerular EC and promoted fibrosis through p38 signaling (*in vitro*). | (88) |
| | Kidney, CKD | Promoted EC angiogenesis (tube formation) and proliferation (protective role). | (34) |
| | Heart fibrosis, myocardial infarction | Gene ablation aggravated myocardial fibrosis and cardiac remodeling by suppressing SMAD1/5/8 (*in vivo*) (protective role). | (89) |
| Acute respiratory distress syndrome | Vascular repair, tissue healing | Exhibited angiogenic properties and tissue repair through TGF-βR2 and SMAD1/5/8. | (90) |
| Osteoarthritis | Angiogenesis | Induced EC angiogenesis and mesenchymal stem cell migration (*in vitro*). | (64) |
| Corneal neovascularization | Angiogenesis | Induced angiogenesis and lymphangiogenesis via activating VEGF signaling (*in vivo*). | (91) |
| Ischemia | Angiogenesis | Promoted blood vessel formation through upregulating the TGF-β1 signaling (*in vivo*). | (92) |
| Atherosclerosis | Calcification | Endothelial LRG1 induced VSMC de-differentiation and calcification through SMAD1/5 signaling (*in vivo*). | (93) |
| De novo angiogenesis | Vessel formation (placenta) | Exhibited pro-angiogenic functions and hypervascularization in gestational diabetic placenta (*ex vivo*, *in vitro*). | (58) |
| | Vessel formation | Induced *de novo* angiogenesis upon activation by IL-6/STAT3 (*ex vivo*, *in vitro*). | (26) |
| | Vessel formation (ocular) | Induced *de novo* angiogenesis through SMAD1/5/8 (*ex vivo*, *in vitro*). | (25) |

EC, endothelial cell; EMT, epithelial to mesenchymal transition; CKD, chronic kidney disease; DKD, diabetic kidney disease; VSMC, vascular smooth muscle cells.

below, and with the caveat above, several studies have investigated the pro-angiogenic properties of LRG1 and have shown that it can act directly on endothelial cells, inducing cell proliferation and tube formation *in vitro* as well as on other cells impacting proliferation, migration and viability (17, 27, 34, 41, 80–84, 86). In addition, LRG1 promotes vessel growth and sprouting in *ex vivo* mouse metatarsal bone and aortic ring angiogenesis assays (25, 26). This is attenuated in explant tissues derived from *Lrg1*$^{-/-}$ mice or when a function-blocking anti-LRG1 antibody is used (25, 26, 84, 94). Similarly, knocking down LRG1 through siRNA silencing decreased the tube formation capacity of HUVEC co-cultured with pancreatic cancer cells (81). Vessels that develop in response to LRG1 stimulation, in the absence of other exogenous drivers, exhibit a pathological phenotype. In particular, LRG1 treatment of metatarsal bones and aortic rings resulted in vessels with reduced coverage of αSMA$^+$ and NG2$^+$ mural cells (26). Although the mechanisms behind this remain unknown, it seems likely that both autocrine and paracrine mechanisms affect the recruitment, proliferation, migration and differentiation state of mural cells in a LRG1-dependent manner. These studies raise the question whether LRG1 is a true angiogenic factor or whether it affects the stability of existing vessels permitting them to be more permissive to other angiogenic stimuli. Indeed, similar to VEGF, LRG1 can destabilize existing vessels and this may promote the angiogenic process. In addition, as LRG1 is ubiquitously present in the circulation it remains unclear what the relative contribution of systemic LRG1 vs. locally produced LRG1 is to vascular pathology. As with TGF-β, the effect of LRG1 on cell function is dependent on multiple factors one of which appears to be its local concentration, indicating a possible threshold effect achieved through local production. Moreover, the differential effect of luminal vs. abluminal exposure has yet to be determined as this may also dictate outcome.

The data above support the idea that in contrast to many angiogenic factors with homeostatic roles in the maintenance of a healthy vasculature, LRG1 expression is induced locally in response to pathogenic cues to drive the formation of a destabilized vasculature (Figure 3). These cues include inflammatory signals, hypoxia and vessel destabilizing factors that not only induce LRG1 expression but may also act on the vasculature independently creating an overall disruptive milieu. Acute inflammation, for example, causes dysfunction to existing vessels and often precedes neovascularization. Indeed, when inflammation becomes chronic and unresolved, it can promote the sustained activation of downstream mechanisms that trigger endothelial dysfunction, vascular remodeling, and abnormal neovascularization all of which serve as major risk factors for the

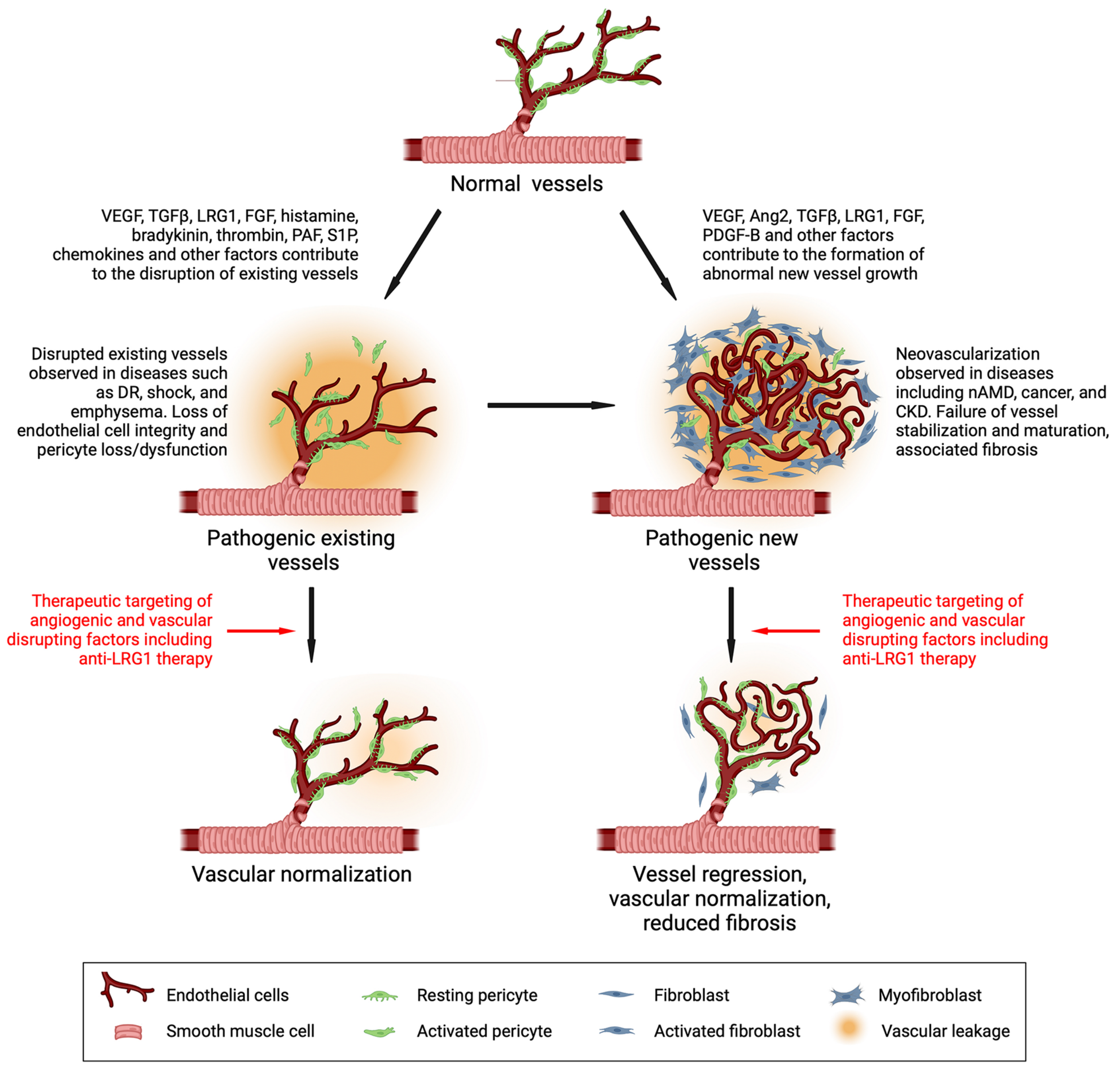

FIGURE 3
Drivers of vascular dysfunction and its therapeutic reversal. Vessels under normal conditions are stabilized and maintained in a mature functional state through cross-talk between the endothelial cell and mural cells (pericytes and smooth muscle cells). During disease, vasoactive factors are released that destabilize existing vessels and stimulate new dysfunctional vessel growth, both of which contribute to disease progression. Targeting factors that alter vascular function in disease is a common therapeutic objective. Inhibiting LRG1 activity has been shown to normalize vessels and may therefore be a promising therapeutic approach. DR, diabetic retinopathy; nAMD, neovascular age-related macular degeneration; CKD, chronic kidney disease. Created with BioRender.com.

development of cardiovascular disease (95). Our studies, and other recent evidence, demonstrate that endothelial cells themselves represent a key source of LRG1 in the diseased milieu (Figure 1). For instance, single cell RNA sequencing revealed *Lrg1* as one of the most upregulated genes in disease-associated endothelial cells in murine models of liver cancer (96) and atherosclerosis (97), while a seminal study demonstrated that LRG1 originating from endothelial cells contributes primarily, in an autocrine fashion, to vessel malfunction and disease severity in a model of emphysema (37). Interestingly, transcriptomics studies also showed higher *Lrg1* expression in endothelial cells isolated from LPS-treated lungs, pointing to inflammation-induced LRG1 being responsible for aberrant vasculogenesis (39). Similarly, *Lrg1* was found upregulated in diseased endothelium from inflamed retinal vessels in a mouse model of experimental autoimmune uveitis, suggesting a role for LRG1 in retinal inflammation and angiogenesis (98).

Abnormal angiogenesis is associated with numerous conditions, and the role of LRG1 in this pathology has become evident. Thus, as discussed in more detail below, it has been reported to be involved in neovascular dysfunction in ocular disease, diabetes, kidney disease, lung disease, impaired wound healing, inflammatory conditions, gestational diabetes and cancer. In addition, LRG1 may also contribute to destabilization of existing vessels by impacting on endothelial cell adhesion and permeability (Figure 3). Such emerging evidence highlights the potential of targeting LRG1 with novel therapeutic strategies to attenuate vascular disruption in disease. In support of this, and as highlighted elsewhere in this review, deletion of the *Lrg1* gene or blocking LRG1 function has been shown to partially reverse the vascular pathology in many conditions. Thus, therapeutic blockade of the angiopathic properties of LRG1 will therefore not only permit vessels to revascularize tissue in a more physiological manner but has the potential to re-establish a quiescent endothelial state in existing disrupted vessels.

In order to devise therapeutic strategies targeting LRG1, it is important to understand the mode of action through which LRG1 promotes defective angiogenesis or impairs the established vasculature. To date, it is evident that TGF-β signaling is a key downstream mediator of LRG1 activity. In endothelial cells, TGF-β signals through binding to the TGF-βRII receptor followed by initiation of signaling either via the ALK1 or ALK5 kinase. In homeostasis, TGF-β signaling maintains endothelial cell quiescence by regulating ALK5 and the downstream SMAD2/3 transcription factors (99). However, high levels of LRG1 can shift the balance of endothelial TGF-β signaling towards the ALK1 kinase, which associates with Endoglin (ENG) to activate the pro-angiogenic SMAD1/5/8 arm of transcription factors leading to endothelial cell proliferation, migration and pathological angiogenesis (25, 26, 53, 99) (Figure 4). Indeed,

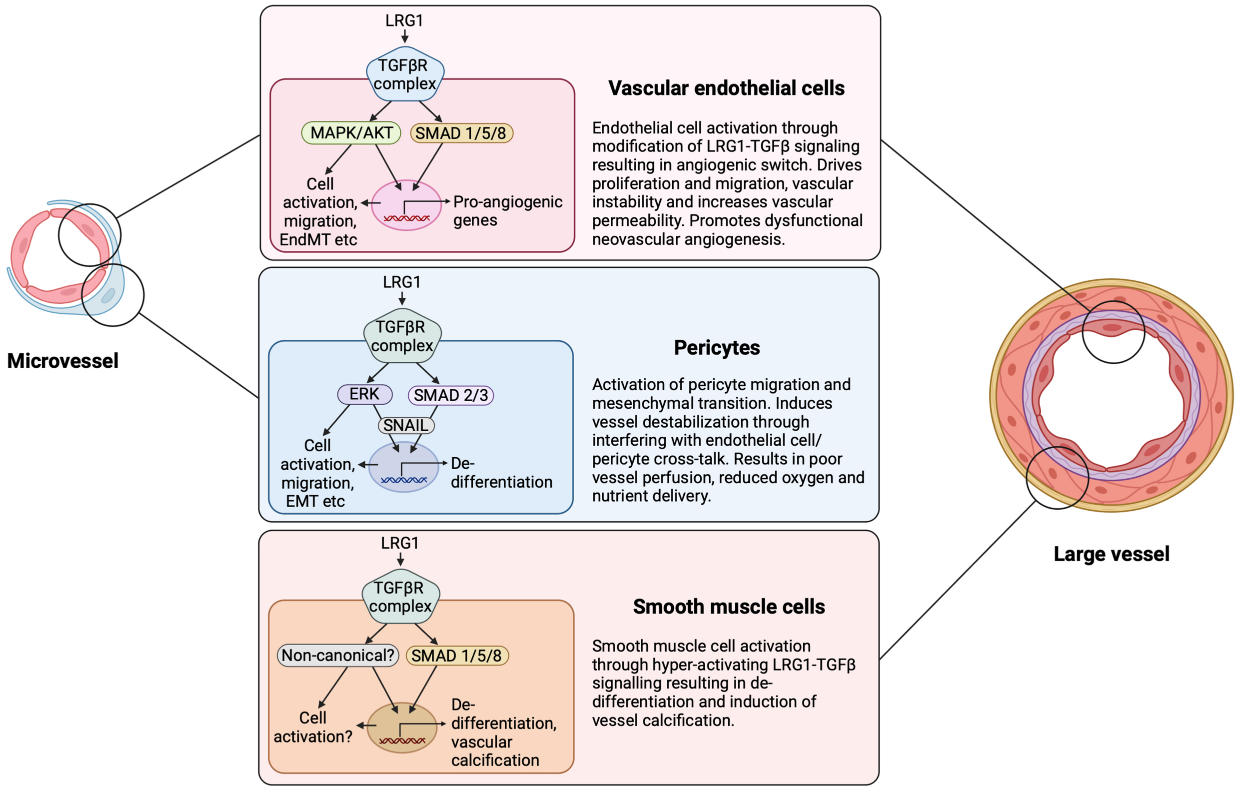

FIGURE 4
LRG1 cell-dependent signaling and outcome. LRG1 can induce signaling in all cellular constituents of the vasculature. Depending on the configuration of signaling receptors and downstream influences, LRG1 can cause the TGF-β angiogenic switch through acting on the endothelial cell, pericyte and smooth muscle cell. LRG1 has been shown to alter the canonical and non-canonical TGF-β signaling pathways in a cell-dependent manner. EndMT, endothelial to mesenchymal transition; EMT, epithelial to mesenchymal transition. Created with BioRender.com.

ENG has been proposed as being essential to allow the interactions between LRG1, TGF-β and ALK1 (25, 100) but evidence from other cell types demonstrates that it can still elicit TGF-βRII signaling in the absence of ENG. Nevertheless, this so called TGFβ angiogenic switch is not a binary response as outcome is more likely due to the relative balance between these two canonical signaling arms that dictates the context-dependent nuanced response. Moreover, LRG1 also activates the non-canonical TGF-β pathway in various cells and settings (23), which may influence vascular structure and function (Figure 4). Merely promoting the pro-angiogenic TGF-β switch, therefore, is unlikely to fully explain the complex angiopathic effects of LRG1. There also exists the distinct possibility that LRG1 can modify BMP signaling although this remains to be determined. Outside the TGF-β axis, an alternative mechanism has been noted, whereby LRG1 binds to the Latrophilin-2 receptor to promote LRG1-dependent angioneurin effects in diabetes, where angiogenic and neurotrophic processes are in place (85). Additionally, recent studies have provided evidence that LRG1 disrupts vascular homeostasis by altering the fine balance between endothelial cells and pericytes causing leaky and destabilized vessels (26, 32). How this imbalance is achieved needs to be further explored, but autocrine and paracrine signaling mechanisms between the endothelium and pericytes appear to be critical. Those mechanisms may involve the release of angiocrine factors including Ang1 and Ang2, or LRG1-driven signaling in pericytes.

## LRG1, tissue repair and wound healing

Postnatally, angiogenesis is an important part of the repair and wound healing process. This involves a tightly regulated sequence of events including the recruitment of many different cell types driven in part by overlapping phases of inflammation and tissue remodeling (101). Failure of wound healing can lead to chronic wounds, which can be observed in many conditions such as eye disease, lung and heart disease, and diabetes (102). Upregulation of LRG1 in various cell types during the normal wound healing process clearly suggests its involvement, possibly through the promotion of new vessels and cell de-differentiation and migration (Figure 1). Whilst the role of LRG1 in normal blood vessel formation during wound healing is still unknown, reduced blood vessel density has been observed in the wound bed of *Lrg1*$^{-/-}$ mice (17), suggesting its involvement in post-developmental vessel formation. In a murine skin wound healing model, LRG1 drives keratinocyte migration and re-epithelization by improving HIF-1α stability through ELK3 (103), whereas in a similar setting, LRG1 promoted endothelial cell proliferation, angiogenesis and EMT (17). In the latter study, LRG1 expression within the wound was also observed in bone-marrow-derived cells such as neutrophils, monocytes, macrophages and dendritic cells. The presence of LRG1 was shown to be essential for timely wound repair as *Lrg1*$^{-/-}$ mice exhibited a significant delay in wound closure, which was reversed when bone marrow-derived LRG1-expressing stem cells were transfused into the knock-out animals (17). However, in wounds from diabetic mice, as well as from patients with diabetes, LRG1 expression was markedly enhanced and in mice was shown to result in delayed wound closure. LRG1 was also associated with the adverse inflammatory response by stimulating excessive neutrophil attraction and promoting NETosis in a TGF-β/ALK5/AKT-dependent manner (17). The delay in wound healing in diabetic mice was reversed in *Lrg1*$^{-/-}$ mice, demonstrating its context dependent activity. In diabetic wounds in the rat, LRG1 has also been shown to increase blood vessel density through activating the WNT/β-catenin pathway, which, counterintuitively, may exacerbate the wound healing process (86).

Whilst not entirely consistent, these studies suggest that under normal conditions LRG1 promotes physiological tissue repair by promoting angiogenesis and cell migration, but in a chronic inflammatory setting, as seen in diabetes, LRG1 remains induced prolonging the initiating stage of wound healing (Figure 2). Our current understanding, therefore, is that LRG1 is induced as part of the acute innate immune response mechanism that sequesters Cyt c, and through modification of TGF-β signaling activates endothelial cells and pericytes resulting in destabilized vessels and stimulation of sprouting angiogenesis. We propose that through other switches in the TGF-β signaling, LRG1 also drives EMT that permits loss of epithelial junctional integrity, cell division and migration required for wound closure. As the inflammatory response resolves under normal conditions LRG1 expression is attenuated allowing for cellular re-differentiation, wound stabilization, and maturation. However, in the presence of a continuing chronic inflammatory stimulus LRG1 expression is sustained, and even increased, which maintains cells in a de-differentiated less mature state and thus prevents wound resolution and tissue homeostasis (Figure 2).

## LRG1, ischemia and stroke

A role for LRG1 has been reported to be part of the repair mechanism in cerebral damage due to ischaemic injury. Interestingly, high circulating LRG1 levels have been found positively associated with stroke severity and poor functional outcomes (104–106), as well as with poor cognitive impairment and neurological function (107). In the brain, following ischemic stroke injury a single cell transcriptomics study revealed the emergence of a LRG1-positive endothelial cell subpopulation in the brain infarct area, the expression profile of which suggests its involvement in the complex regulation of angiogenesis, with both pro- and anti-angiogenic factors expressed (108). In fact, in a mouse cerebral artery occlusion model, LRG1 increased apoptosis and autophagy through TGF-β and SMAD1/5 exacerbating the ischemic injury (109). Similarly, increased LRG1 was found in brain endothelial cells in a rat brain ischemia model with expression correlating positively with VEGF, Ang2 and TGF-β (92), indicating a protective role for LRG1 by promoting *de novo* formation of blood vessels, possibly through TGF-β (92). De novo vessel formation was confirmed, with CD34 staining showing significantly increased microvessel density after stroke, which again correlated with LRG1 expression (92). However, whilst new vessels were observed which may confer survival benefit, the likelihood is that these penumbral vessels are dysfunctional compromising their beneficial effect (110). A more recent study employing a cerebral ischemia-reperfusion injury model in the mouse demonstrated that in the *Lrg1*$^{-/-}$ mouse there was reduced cerebral oedema and infarct size, which was accompanied by improvement in neurological function (111). Crucially, this study showed that following cerebral ischaemia, cells of the blood-brain barrier were able to retain the expression of barrier function related genes, such as claudin 11, integrin β5, protocadherin 9, and annexin A2, more effectively in the absence of LRG1 (111). This demonstrates that LRG1 has a detrimental effect on the blood-brain barrier and thus contributes to vasogenic cerebral oedema. In its wider role, *Lrg1* knockout also permitted a more anti-inflammatory and tissue-repairing environment and reduced neuronal cell death. In a different ischaemic setting, tissue remodeling after myocardial infarction involved the infiltration of LRG1 expressing myeloid cells that were reported to exert a cardioprotective role by promoting signaling through the pro-angiogenic TGF-β/SMAD1/5/8 axis and contributing to post-infarct vessel formation (89).

# LRG1 and vascular pathology of the eye

## Retinal neovascularization

Vascular problems of the eye, such as in diabetic retinopathy or neovascular (exudative or wet) age-related macular degeneration (nAMD), are characterized by vessel remodeling and angiogenesis and can occur intraretinally, subretinally or at the vitreal interface. Irrespective of the ocular disease, vascular dysfunction is often a major contributing factor to loss of vision in the developed world (112). The first evidence that LRG1 is actively implicated in pathogenic neovascularization emerged from its identification as the most up-regulated gene in a transcriptomics analysis of retinal microvessels isolated from three different animal models (retinal dystrophy 1, VLDLR knock out, *Grhl13*$^{ct}$*/J* curly tail), each of which showed marked retinal vascular remodeling and pathology (25). This study went on to show that the *Lrg1* transcript is almost undetectable in the healthy mouse retina but in experimental retinal vascular diseases such as experimental choroidal neovascularization (CNV) (113) and oxygen-induced retinopathy (OIR) (114) that model choroidal and retinal neovascularization respectively, expression of LRG1 is induced in endothelial cells (25). In OIR, the abnormal retinal neovascularization that occurs at the vitreous interface is believed to be driven largely by hypoxia, whereas in CNV the laser burn to the retinal pigment epithelium (RPE) results in vessels sprouting from the choriocapillaris through the breached RPE into the subretinal space as a result of injury-induced hypoxic and inflammatory cues. Irrespective of the model system employed, genetic deletion of *Lrg1* led to a diminished pathogenic neovascular response coupled with a reduction in vascular leakage as assessed by fundus fluorescein angiography. Of note, however, revascularization of the hyperoxia-induced vessel ablated region in OIR proceeds in a more physiological patterned manner and is not affected by *Lrg1* deletion (25, 94), further demonstrating that LRG1 contributes to pathogenic, but not physiological, neovascularization. Similar findings were seen when LRG1 activity was blocked by intravitreal delivery of a specific function-blocking antibody, the application of which significantly reduced OIR and CNV lesion size (25, 94) and lends credence to its potential as a therapeutic target.

In addition to the disease-associated induction of endothelial LRG1 expression, myeloid cells have also been found to express LRG1 in choroidal neovascularization. A recent study exploring the transcriptional profiling of immunosenescence in myeloid cells during the development of CNV showed that aged senescent myeloid cells of CNV-induced animals exhibited an upregulated angiogenic transcriptional profile with significantly elevated *Lrg1* and *Arg1* expression compared to young cells (115). This is the first study to provide evidence of upregulated *Lrg1* expression in cells other than the endothelium contributing to choroidal neovascularization. Although it is not clear yet whether this is an epiphenomenon or there is a direct causal role for LRG1 in CNV-related immunosenescence, the data suggest a potential role for LRG1 and myeloid cells in the immunoregulation of CNV that merits further investigation.

Corroborating the mouse studies above, elevated expression of LRG1 has also been found in the aqueous and vitreous humour and in retinal choroidal neovascular membranes of nAMD patients (116–119), as well as in dry (atrophic) AMD (120). Mundo et al., showed that in ocular sections of nAMD membranes LRG1 is co-localized not only with endothelial cells but also with myofibroblasts, suggesting an alternative cell source through which LRG1 may exert its pathological effects (118). Thus, myofibroblast-derived LRG1 may contribute to endothelial dysfunction in the retina in a paracrine manner, but it may also be involved in promoting retinal fibrosis through autocrine mechanisms (118). This suggests that, two-way LRG1 cross talk between endothelial cells and fibroblasts may drive both vascular dysfunction and fibrosis. This is in accordance with other findings showing that LRG1 promotes fibrosis in various tissues and conditions including the skin (41), idiopathic pulmonary fibrosis (42), renal fibrosis (34) as well as diabetic nephropathy (33, 121), by directly affecting the physiology and activity of fibroblast-like tissue resident cells (Figure 1). Interestingly, a recent study showed that exogenous LRG1 promotes the EMT of RPE cells as evidenced through high levels of αSMA and fibronectin and low levels of ZO-1 (122). The concept that vascular dysfunction can contribute to fibrosis is not new (123) and it raises the interesting possibility that endothelial derived LRG1 may also trigger the fibrotic response in the eye. Similarly, endothelial cells have been shown to contribute to matrix deposition when they undergo phenotypic differentiation via EndMT, a process predominantly regulated by TGF-β. EndMT is a hallmark of cardiovascular disease and has been studied in a variety of experimental models (124). Although there is no known link between EndMT and LRG1, unpublished evidence from our laboratory suggests that LRG1 is overexpressed in a cytokine induced EndMT model system and may therefore play a role in the eye.

## Diabetic retinopathy

In diabetic retinopathy, where retinal vascular dysfunction, dropout and neovascularization are prominent, LRG1 has been reported to be upregulated not only in the vitreous humour and in ocular tissues (25, 50, 125, 126), but also systemically in the plasma of patients with proliferative diabetic retinopathy (PDR) (50, 127). Diabetic retinopathy is the most common complication of diabetes, leading to impaired vision and ultimately to vision loss (128). The first stage of the disease is non-proliferative and is characterized by microvascular abnormalities leading to macular oedema, microaneurysms, micro-haemorrhages, and poorly perfused, occluded, and de-endothelialized capillaries. In PDR, the later stage of the disease, loss of vessels and subsequent hypoxia results in the growth of abnormal neovessels leading to vitreous haemorrhage, tractional detachment and eventually blindness. Since LRG1 is almost undetectable in a healthy human eye, its elevated expression in the vitreous in diabetes is most likely to be due to activated local production in response to disease, but it may also derive from the plasma as a consequence of vascular leakage. Whether the upregulated expression drives the vascular complications in the eye or contributes to other diabetes-associated pathology remains to be elucidated. Indeed, accumulating evidence indicates that LRG1 is upregulated in the plasma (56, 129) and urine (130) of people with diabetes, hence it can serve as a biomarker for PDR (131). However, LRG1 did not offer a significant improvement when used in a risk prediction model for PDR (57). Nevertheless, the greater evidence so far implicates LRG1 in retinal neovascularization, with its genetic deletion or inhibition of function through antibody blockade ameliorating vascular pathology, lesion size and leakage in animal models (25, 94). In addition, unpublished data from our lab shows that LRG1 can promote the phenotypic and functional differentiation of pericytes towards a fibrotic state and that this contributes to vascular dysfunction in diabetic retinopathy through both canonical and non-canonical TGF-β signaling (20) (Figures 1, 4). This evidence highlights the possibility that endothelial derived LRG1 may also impact retinal function in a paracrine manner. Although our understanding of diabetic retinopathy has increased substantially, and anti-VEGF therapeutics have revolutionized diabetic macular oedema and PDR treatment, a substantial number of patients remain or become refractive which clearly implicates the involvement of other players and highlights the need for further research. The evidence to date suggests that LRG1 may be a contributing factor to resistance to anti-VEGF strategies and thus LRG1 blockade could improve outcome.

## Corneal neovascularization

The angiogenic properties of LRG1 have also been described in the context of corneal neovascularization in a corneal alkali burn mouse model, where LRG1 promoted a significant outgrowth not only of blood vessels, but also of lymphatic vessels (91). The normal cornea is avascular in order to maintain transparency but under pathological conditions, such as inflammation or trauma, new vessels invade the avascular tissue causing visual impairment. In *Lrg1* knock down studies using siRNA, a limited angiogenic and lymphangiogenic response was observed compared to control mice (91). In this study, different members of the VEGF family were implicated in LRG1-driven corneal angiogenesis and lymphangiogenesis, with VEGF-A/B and their receptors VEGFR-1/2 regulating the former and VEGF-C/D together with VEGFR-2/3 regulating the latter (91). How LRG1 impacts on this remains unclear but it raises the possibility of cross regulation between these pathways. Apart from neovascularization, LRG1 was also found to promote corneal fibrosis by increased deposition of αSMA, collagen type I and CTGF in the corneal epithelium (48). This LRG1-driven effect was mediated by neutrophil infiltration at the site of corneal injury through the phosphorylation of STAT3 and the upregulation of IL-6/STAT3 signaling (48). These data point to LRG1 as a potential therapeutic target to ameliorate pathogenesis in corneal disease.

## LRG1 and chronic kidney disease

The role of LRG1 in kidney disease, in particular diabetic nephropathy, is gaining interest (132) with growing evidence that LRG1 contributes to vascular rarefaction and abnormal neovascularization. In normal kidney, LRG1 expression is found in glomerular endothelial cells co-localized with that of CD31, as well as in the tubulointerstitium (53). The kidney is a highly vascularized organ, where maintenance of normal blood flow is crucial for renal function which, following pathological complications such as vessel loss and fibrosis, may become seriously compromised. Endothelial dysfunction coupled with abnormal angiogenesis have long been known to contribute to the pathogenesis of diabetic nephropathy and other chronic kidney conditions, although the underlying molecular mechanisms are poorly understood (33, 53, 133). Several studies show that in a variety of chronic kidney disease (CKD) models LRG1 gene and protein expression is significantly increased. Indeed, a transcriptomics study has shown that in a model of diabetic nephropathy, *Lrg1* was upregulated in glomerular endothelial cells, where it mediated high glucose-induced pathological angiogenesis (87). Similarly, other studies have also shown that in experimental diabetic kidney disease (DKD) *Lrg1* gene expression induced in glomerular endothelial cells is involved in vascular rarefication and subsequent neovascularization and fibrosis, partly via activation of the p38 and TGF-β-SMAD1/5/8 pathway (52, 53, 87, 88). Consistent with these reports, LRG1 overexpression has also been shown to result in exacerbation of disease (33, 53). What is interesting, but needs further corroboration, is the suggestion that the initiating mechanism driving vascular dysfunction is mediated by LRG1 and is independent of VEGF. This is based on the finding that LRG1 expression precedes the expression of VEGF and its receptor VEGFR-2 in diabetic nephropathy (52) and that VEGF is expressed mainly in the injured podocytes following endothelial injury (134, 135). These data prompted the authors to suggest that glomerular endothelial LRG1 may be an initiating factor in vascular pathology in the diabetic kidney.

In various other *in vivo* models of CKD, including the albumin overload model (136), unilateral ureteral obstruction (UUO) model (34), and the aristolochic acid-induced nephrotoxicity (AAN) model (33), LRG1 protein levels have also been shown to be higher, often correlating with increased pro-inflammatory and pro-fibrotic cytokines. Such findings support the contention that LRG1 is not only induced by inflammatory cues but that it also promotes the renal inflammatory response including the activation of macrophages in a TGF-βR1-dependent manner (137).

In the kidney, endothelial cells are not the only source of LRG1, as it has also been shown that renal tubular epithelial cells (33) and HK-2 human proximal tubular epithelial cells (34) can be induced *in vitro* to express LRG1. Tubular epithelial cell derived LRG1 has been shown to activate the TGF-β-SMAD3 pathway in fibroblasts resulting in increased renal fibrosis (33). This additional cellular source of LRG1 may not only trigger fibrosis but also contribute further to endothelial cell dysfunction. Indeed, it has also been proposed that LRG1 mediated microvascular dysfunction in the kidney may facilitate the onset and progression of fibrosis (34), supporting the notion that these two phenomena are interrelated (123). What is clear from these studies is that in the kidney LRG1 not only stimulates vessel loss and the formation of abnormal neovessels, it also drives the fibrotic response, all of which combine to reduce glomerular filtration rates (121, 138). In accordance with the studies above, increased renal LRG1 expression is reflected in the urine, where significantly elevated levels correlate closely with the degree of renal tubular dysfunction (136). Consistent with these findings, *Lrg1* knockout reduces the deterioration of kidney function (33, 53). Similarly, suppression of LRG1 and ALK1-dependent angiogenesis by metformin showed significant renoprotective effects in a diabetic rat model (139).

Clinical evidence also points to LRG1 playing a role in the pathogenesis of CKD. Thus, it has been shown that in people with type 2 diabetes and DKD, plasma LRG1 levels predict both albuminuria and CKD progression beyond traditional risk factors (56, 140). Similarly, in children with type 1 diabetes a clear relationship between plasma LRG1 and estimated glomerular filtration rate (eGFR) decline suggests that LRG1 may be an early marker of DKD progression (49). In separate studies, using human DKD tissue, *LRG1* gene expression has been found to be increased in glomerular endothelial cells (53). Moreover, in other forms of CKD, including lupus nephritis (36), IgA nephropathy (34), and end-stage kidney disease dialysis patients (35), increased LRG1 plasma and biopsy tissue levels correlate with worse outcome, increased inflammatory markers, and greater fibrosis. Of note, LRG1 levels correlated positively with IL-6, a known activator of LRG1 gene expression, as well as with a more advanced state of T cell differentiation and the presence of cardiovascular disease and peripheral arterial occlusive disease (35) demonstrating its potential systemic involvement.

In addition to plasma, increased urine LRG1 levels in diabetes is also associated with an increased risk of progression to end stage kidney disease independent of traditional cardiorenal risk factors (55), and in kidney transplant recipients LRG1 has been considered a potential kidney injury marker that correlates with other tubular injury markers and functional deterioration (141). These human data support the evidence from experimental studies that LRG1 is an important factor in driving CKD through initial effects on the kidney vasculature and the subsequent fibrotic response. One of the most compelling pieces of clinical evidence that LRG1 contributes to DKD, however, was a recently reported GWAS study in people with type 2 diabetes and CKD, where a 5’UTR variant (rs4806985) in the promoter region of *LRG1* was found to influence its gene expression resulting in elevated plasma LRG1 and a robust association with increased risk of rapid decline in kidney function (51). This is the first study describing a polymorphism risk to LRG1 circulating levels, suggesting a potential use for LRG1 in stratifying patients with diabetes into subsets based on their genetic predisposition. Additionally, genetically influenced plasma LRG1 levels were also associated with lower cognitive function, further supporting a role for LRG1 as a novel biomarker for cognitive decline in type 2 diabetes mellitus (142). The conclusion drawn in many of these studies is that LRG1 is a potentially important therapeutic target as it is seen as a master upstream orchestrator of pathogenic TGF-β signaling. It is well established that the TGF-β pathway has a critical role in neovascular and fibrotic processes and that targeting constituents of this pathway continues to be considered an attractive therapeutic strategy. However, the need to retain homeostatic TGF-β signaling remains a challenge but one which may be overcome by targeting LRG1 as this is a key upstream factor in causing the switch from quiescent housekeeping to pathogenic disruptive signaling.

## LRG1 and lung disease

Inflammation, tissue repair, endothelial dysfunction and increased interstitial pressure are common phenomena in pulmonary disease leading to prominent vascular-related complications such as pulmonary embolism, abnormal microthrombi, and microvascular damage (143). Alveolar epithelial and endothelial permeability are also compromised with impaired gas exchange and vascular leakage due to loss or destabilization of cell junctions. In addition, the damaged endothelium may disrupt vascular tone and cause dysregulation of anti-inflammatory and anti-thrombogenic endothelial properties, and together with damaged epithelium can trigger the tissue repair process (144). To date, evidence shows that LRG1 is involved in pulmonary vascular dysfunction with increased expression seen in lung disease, including chronic obstructive pulmonary disease (COPD), interstitial pneumonia, airway inflammation in asthma, and active tuberculosis, with LRG1 levels serving as a biomarker for early diagnosis, progression, and prognosis (38, 66, 145–148).

Several reports show that LRG1 is upregulated in lung epithelial and endothelial cells, mainly but not exclusively in inflammation-induced pathology (37, 39, 66, 90). In particular, in human COPD tissue, upregulated LRG1 was localized specifically to the endothelium and correlated positively with marked airflow obstruction, decline in lung function and severity of emphysema (37). COPD is a heterogeneous long term lung disease characterized by persistent airway inflammation, microvascular dysfunction, dysregulated angiogenesis, and endothelial apoptosis (149). Specific endothelial deletion of LRG1 in a murine elastase model of COPD protected against severe parenchymal destruction, highlighting a critical role for LRG1 in promoting the development of maladaptive lung vasculature (37).

Although the exact mechanism that mediates this process has not yet been defined, it is possible that LRG1 impacts angiogenic responses following endothelial injury either by promoting defective angiogenesis or through the development of fibrosis. Indeed, LRG1 has been shown to trigger a pro-fibrotic response in the lung by activating lung fibroblasts and the subsequent production and deposition of extracellular matrix via TGF-β signaling and the phosphorylation of SMAD2 and SMAD3 in mouse bleomycin models (42, 44). Strikingly, in a recent single cell transcriptomics study, *LRG1* was described as an extracellular matrix coding gene and its expression was found increased and maintained at high levels in aging lung, which associated LRG1 with age-related inflammation and tissue stiffness (150). However, LRG1-mediated fibroblast activation and proliferation was not regulated by SMAD2 or 3, the levels of which were either unchanged or repressed, respectively, implying that other signaling mechanisms, such as activation of alternative canonical or non-canonical pathways, are in place (150). Indeed, consistent with previously published data (25, 26, 53), in viral-induced lung injury, LRG1 upregulation drives endothelial cell proliferation and the angiogenic responses required for tissue repair by activating SMAD1/5 signaling (90).

Elevated levels of circulating LRG1 have also been reported in severe COVID-19 patients in blood, plasma, and tissue proteomic studies (151–156). Although most of these studies associate elevated LRG1 expression with an early immune and inflammatory response, it is possible that LRG1 exerts an angiopathic role in the pulmonary microvasculature related to COVID-19. In fact, a dysregulated cytokine immune response, known as a "cytokine storm", has been established and studied extensively in patients with COVID-19 (157). This includes highly elevated expression of pro-inflammatory cytokines that correlates with COVID-19 disease severity and requires immediate attention, as excessive activation of immune cells can lead to complicated and potentially lethal medical syndromes (158). Among others, IL-6 is a key player in this cytokine response with significantly elevated circulating levels in the plasma of patients with COVID-19, and consequently it has been reported to contribute to the related vascular pathology (159, 160). Blocking IL-6 signaling as a therapeutic intervention has been extensively studied in many diseases (161, 162), and COVID-19 randomized controlled clinical trials with biologics targeting the IL-6 receptor, including the Tocilizumab antibody, have shown evidence of clinical benefit (163–166). Elevation of both IL-6 and LRG1 in patients with COVID-19 suggests that circulating pro-inflammatory IL-6 may induce systemic and local upregulation of angiopathic LRG1 in the pulmonary microvasculature. Indeed, IL-6 upregulates LRG1 expression in human pulmonary microvascular endothelial cells, and this effect is reversed when IL-6 signaling is blocked by the tocilizumab antibody (26). Upregulated LRG1 in turn may contribute to the development of a destabilized vasculature with prominent endothelial dysfunction and vascular leakage during impaired lung tissue wound healing (Figures 1, 4). This LRG1-dependent microangiopathy may be mediated by the pro-angiogenic TGF-β-SMAD1/5 signaling arm, as evidenced in other endothelial-related disease settings (25, 26, 90). As reported in experimental CKD, and described above, dysregulated microvascular endothelial cells in the lung in COVID may also be a driver of fibrosis (37), linking LRG1 to these two key pathogenic processes.

## LRG1 and inflammation-associated disease

Over the past decade several studies have provided evidence that LRG1 is involved in various inflammatory and autoimmune diseases, and may act as a useful clinical and diagnostic biomarker (23, 167–174). In such conditions, levels of LRG1 are upregulated at the site of inflammation, with expression induced by pro-inflammatory cytokines secreted by various cell types, followed by the initiation of a series of downstream vascular events. During inflammation, one of the key vascular responses is an increase in vessel permeability that, alongside other inflammatory changes, facilitates the extravasation of immune molecules and cells to the site of injury (175). In addition to tissue resident cells, recruited immune cells provide an additional source of angiogenic factors that play a part in the inflammatory and reparative response. Over time this response resolves but under certain chronic conditions unresolved inflammation, including the persistence of LRG1 expression, continues through an imbalance of stimulatory, inhibitory and disruptive factors, and can give rise to long-term vasculopathic outcomes (176) (Figure 2).

Osteoarthritis (OA) is the most common inflammatory joint disorder, with aberrant endothelial cell proliferation, vascular penetration, and synovial fibrosis being the main disease leading mechanisms that contribute to structural damage and pain (177). *Lrg1* transcript has been found to be upregulated in chondrocytes upon IL-6 stimulation (178). In OA the pro-inflammatory cytokine TNF-α, a key player in the pathophysiology of the disease and major activator of pro-angiogenic factors (179, 180), was also shown to induce LRG1 expression in the subchondral bone and articular cartilage (64). In this setting it promoted angiogenesis, mesenchymal stem cell migration and aberrant bone formation via MAPK-dependent p38/p65 signaling. This highlights a new potential mechanism through which LRG1 promotes abnormal neovascularization coupled with *de novo* bone formation. Supplementary to its role in angiogenesis in OA, LRG1 has also been shown to contribute to synovial fibrosis and joint stiffness by promoting secretion of extracellular matrix in synovial cells, cell migration and wound healing (46), further suggesting that LRG1 not only affects endothelial cells but also other cells in the cartilage exerting multiple parallel pathogenic responses.

Although LRG1 has attracted substantial interest with regards to its use as a clinical biomarker in a plethora of inflammatory conditions, little is known about its mechanistic involvement in the development and progression of vascular defects in these conditions. Nevertheless, LRG1 has been implicated in Kawasaki disease, an acute systemic vasculitis causing inflammation of small to medium sized blood vessels resulting in cardiovascular complications (181, 182). The main cytokines responsible for inducing LRG1, TFN-α and IL-6, are elevated in the plasma of patients with Kawasaki disease, and a proteomic analysis of serum exosomes of patients with coronary artery aneurysms caused by Kawasaki disease showed upregulated LRG1 levels, although no causal link with pathology was shown (183). Similarly, another study on Kawasaki disease in children identified LRG1 as a potential trigger of endothelial cell activation and cardiac remodeling that closely associated with IL-1β signaling (184). The cell source contributing to increased circulating LRG1 levels in these conditions has not yet been identified but evidence from other conditions suggests that upon inflammatory stimulation LRG1 is most likely produced by endothelial cells, where it exerts its vasculopathic effects via autocrine and paracrine pathways on the endothelium and the adjacent mural cells, respectively. Although the exact vascular pathogenesis in Kawasaki disease is not well understood, vascular complications include necrotizing arteritis associated with neutrophilic and immune cell infiltration, the release of pro-inflammatory cytokines, luminal myofibroblast proliferation and progressive obstruction of the coronary lumen have all been linked with LRG1 in other conditions and so it is likely that it plays a role in this and other vasculitides. In support of this, LRG1 has also been found to be a promising serum biomarker for large vessel vasculitis (LVV) (185), and antineutrophil cytoplasmic antibody (ANCA)-associated vasculitis (AAV) (186, 187).

Inflammation is a hallmark of cardiovascular disease and destabilized vasculature, and frequently serves as a trigger during the early stages of disease, while increased expression of inflammatory cytokines is associated with a higher risk of cardiovascular diseases (188). Thus, LRG1 may be anticipated to initiate or mediate inflammatory responses to some extent in conditions with cardiovascular risk. In fact, LRG1 has been shown to promote cardiovascular disease by regulating endothelial dysfunction and inflammation through TGF-β and SMAD1/5/8 signaling in endothelial cells, interrupting normal endothelium-dependent vasodilation and availability of nitric oxide (129). Furthermore, in a recent study employing the Western diet apolipoprotein E knockout ($ApoE^{-/-}$) mouse model of atherosclerosis, LRG1 was detected within the atherosclerotic plaque, particularly in calcified regions (93). The cell source of LRG1 was found to be endothelial cells that had been activated by inflammatory mediators. Furthermore, this study demonstrated that LRG1 was responsible for inducing vascular smooth muscle cell activation and vessel calcification via a SMAD1/5 signaling pathway (Figure 4). The authors conclude that LRG1 is a significant contributor to the development of plaque complications and therefore a potential therapeutic target. On the other hand, and in contrast to most other studies, in arterial stenosis it was suggested that endothelial LRG1 could serve as a negative regulator of inflammation in response to TNF-α by inhibiting expression of ICAM1 and VCAM1 and thus blocking monocyte recruitment, offering a significant atheroprotective effect (189). Interestingly, this is consistent with what has been observed in cancer (see below) where endothelial anergy, as indicated by ICAM1 and VCAM1 expression, is reversed upon LRG1 inhibition.

Exactly how LRG1 mediates vascular inflammation is not clear although there is growing evidence for LRG1 regulating a pro-inflammatory accumulation of immune cells. In particular, LRG1 is involved in neutrophil function modulating NETosis, which is closely associated with inflammatory processes (17). NETosis has been described as a form of necrosis and is associated with many diseases including COVID, thrombosis and CKD, as well as wound healing and other vascular processes (190–192). As mentioned above, a recent study suggested that LRG1 mediates NETosis and contributes to poor wound healing in diabetic mice (17). Although future work is required to unravel the role of LRG1 in regulating neutrophil function, we speculate that NETosis might be an important additional mechanism through which LRG1 may impact on vascular structure and function.

## LRG1 and cancer

LRG1 expression has been studied in a range of malignancies where it has been shown to be elevated and to associate with poor prognosis and survival (23, 61, 62, 193, 194). In addition, raised blood LRG1 levels have been established as a tumor biomarker with potential clinical value and also as a predictive marker for cancer onset (30, 59, 60, 62, 193, 195–200). A growing number of studies support an integral role for LRG1 in cancer, where it has been shown to control cell viability and apoptosis, and promote epithelial cells to undergo EMT, a crucial step in tumor progression and metastasis (27, 28, 30, 31, 80–84, 201–203). In particular, LRG1 acts directly on tumor cell proliferation, migration, and invasion contributing to tumor growth and survival (Table 1), and these functions have been described in detail elsewhere (23, 29, 193). Consistent with LRG1 playing a role in tumor progression, LRG1 blockade in different tumor models inhibits growth and improves survival and thus has been proposed as a potentially beneficial therapeutic target (29, 32). There is also accumulating evidence that LRG1 has important angiocrine and angiopathic functions in cancer, not only by promoting the development of destabilized and immature neo-vessels, but also by impairing already established co-opted vasculature (Figure 3). As widely acknowledged, growing tumors require a constant supply of oxygen and nutrients, and serving these needs often relies on a concomitant developing vascular network. The tumor vasculature, however, is typically abnormal exhibiting impaired structure and function. In particular, tumor blood vessels are immature, tortuous and chaotic in organisation, with an abnormal vessel wall characterized by a discontinuous endothelium, incomplete coverage of mural cells, and atypical basement membrane structures leading to poor perfusion and leakiness (204). These characteristics also create a hypoxic and acidic environment within the tumor tissue that favours malignancy and metastasis and combine to reduce immune cell infiltration and effective immune responses, and restrict the delivery of therapeutics and effectiveness of radiotherapy.

The angiogenic potential of LRG1 has been assessed and described in various types of tumors, including colorectal, gastric, pancreatic, ovarian, and non-small-cell lung cancer (193). Specifically, LRG1 has been proposed to enhance the angiogenic process through acting directly on endothelial cells to induce proliferation and migration, but also indirectly through stimulating proangiogenic factors such as VEGFA (84). Moreover, LRG1 has been associated with increased microvessel density, suggesting that it impacts tumor vascular growth (26). As in other diseases, the direct effect of LRG1 on vessel function is believed to be mediated primarily through modification of canonical TGF-β and SMAD signaling, but in all likelihood also through hyperactivation of non-canonical TGF-β pathways. Alternative mechanisms for LRG1-driven angiogenesis have been proposed including regulation through HIF-1α, which is associated with resistance to cancer chemotherapy and increased patient mortality (205). HIF-1α knockdown was shown to block LRG1-mediated angiogenesis, EMT, and tumor invasiveness, and is consistent with LRG1 being induced in response to hypoxia (84). In another study, ERK mediated phosphorylation of ELK4 in a human colorectal cell line resulted in complex formation with SP1/3 and the induction of *LRG1* gene expression (69). This, it was argued, results in enhanced tumor angiogenesis through activation of the TGF-β-SMAD1/5 pathway in endothelial cells. Whatever the mechanism, the evidence is clear that LRG1 plays a central role in driving abnormal vessel formation in solid tumors.

In line with LRG1 driving vessel abnormalization, strong evidence indicates that vessel structure and function in tumors can be improved by knocking out *Lrg1* or by its inhibition. Indeed, restoring vessel function, a process referred to as vascular normalization, represents a promising strategy to facilitate drug delivery, enhance cytotoxic T cell function, and increase the tumor response to standards of care and immunotherapies (206, 207). In this context, *Lrg1* gene deletion, or functional blockade of the protein, has been shown to improve tumor vascular function as manifested by better perfusion, reduced tumor hypoxia and reduced vascular leakage (32). In particular, vessel size, basement membrane and perivascular mural cell coverage of the endothelium were all significantly increased in the absence of LRG1 (32). As a likely consequence of vascular normalization, LRG1 inhibition not only led to significant improvements in the delivery and efficacy of anti-tumor therapies, but also improved immune-cell infiltration (32). This may partly be explained by re-activation of anergic endothelial cells to allow leukocyte infiltration, seen for example by increased ICAM-1 and VCAM-1 expression. Collectively, these data show that the angiopathic functions of LRG1 not only promote a pro-oncogenic vascular microenvironment in primary and metastatic tumors, but also contribute to immune modulation. Unpublished data from our lab show that in addition to the vascular normalization effects, inhibition of LRG1 also promotes tumor infiltration of T-cells by modulating the immunosuppressive tumor microenvironment, thereby supporting a switch from being immunologically “cold” to “hot”.

Angiogenesis is not the only means through which tumors obtain a vascular supply. Vessel co-option is a surrogate mechanism whereby tumor cells employ the established vasculature to support growth, survival, and metastasis. In a recent study where, in the presence of sunitinib, tumor growth escapes from VEGF-dependent angiogenesis through vessel co-option, single cell transcriptomics revealed a surprisingly similar signature between tumor co-opted endothelial cells and pericytes and their healthy non-tumor bearing counterparts (208). This finding was further confirmed in other vessel co-opted tumor metastatic models. The similarity in the cell transcriptome was predominantly due to the lack of genes associated with angiogenesis and pericyte activation that are observed in angiogenic tumors. Intriguingly, however, *Lrg1* was found to be one of the top 10 genes that were differentially expressed in co-opted postcapillary vein endothelial cells compared to normal endothelium (208). This suggests that *Lrg1* is one of the few genes to be expressed in both tumor angiogenic and co-opted endothelial cells. Further studies, however, will be required to determine whether *Lrg1* induction in co-opted vessels exerts similar vasculopathic effects as observed in angiogenic tumor vessels and in vessels of other diseases.

Aside from endothelial cells, a major cell source of LRG1 in cancer is frequently the tumor cells (Figure 1) but this is not always the case. As in other diseases, there is evidence that LRG1 is also expressed by other cell types including fibroblasts, and immune cells. In all experimental studies conducted thus far, however, LRG1 expression has been shown to co-localize with vessel markers, such as CD31 and CD34 (60, 209) illustrating its ubiquitous presence in tumor endothelial cells. Recent work on the role of LRG1 in cancer showed that in some cancer models *Lrg1* expression was mostly restricted to the vascular endothelium, with no expression detected in the perivascular mural cell population or the cancer cells themselves (29, 32). Nevertheless, this was sufficient to impact on tumor growth as *Lrg1* knock-out or antibody blockade were still effective in reducing tumor growth. Interestingly, using similar tumor models it has been shown that the primary tumor induces systemic vascular LRG1 expression and that this primes the vascular metastatic niche and promotes tumor metastasis (29). This priming was also associated with an expansion of $NG2^+$ perivascular mural cells, which have been described as effective mediators of metastasis (210). LRG1 induction in the tumor mass and systemically in cancer is most probably through IL-6 and STAT3, with contributions from other signaling pathways. Indeed, in metastasis models the STAT3 signaling pathway has been shown to mediate LRG1-driven tumor metastasis, and that this can be significantly reduced in *Lrg1* deficient mice or following LRG1 antibody blockade (28, 29, 31). Through a different mechanism, liver endothelium-derived LRG1 has been shown to promote tumor growth and metastasis of colorectal cancer in a paracrine manner through binding to the HER3 receptor, leading to its phosphorylation and activation (202). If evidence from other diseases translates to cancer, other cell sources of LRG1 are likely to impact the tumor microenvironment. In particular, fibroblasts and neutrophils are a key source in other disease settings and their contribution to cancer merits further investigation.

## Conclusion

Over the last 10 years our understanding of how the secreted glycoprotein LRG1 contributes to physiological and pathological processes has grown exponentially and, in the latter case, demonstrates beyond doubt that it plays a significant contributing role in disease. Whilst we are only just beginning to appreciate the extensive biological role of LRG1, it is clear that much of its activity is mediated through its switching effect on the ubiquitous and complex TGF-β signaling network. Not surprisingly, therefore, the biological effect of LRG1 is wide ranging and highly cell and context dependent, reflecting the biological diversity of TGF-β activity. Accordingly, LRG1 exerts pleiotropic effects depending on the cell target and the influence of other environmental cues, affecting not only the vasculature but also other cell types that are under the influence of TGF-β including epithelial cells, cancer cells, immune cells, and fibroblasts, that in turn may also feedback to affect vascular function. Whilst much speculation remains surrounding the normal physiological role of LRG1, the weight of evidence that it exerts pathological effects is now compelling even though its acceptance as a mainstream pathogenic effector molecule is only just gaining traction. Amongst its effects, those it has on the vasculature are likely to be of substantial clinical importance in a wide range of diseases including cancer, chronic kidney disease, diabetic retinopathy, and emphysema. Indeed, its potential role as a major pathogenic mediator of systemic cardiovascular disease is only just beginning to be considered.

LRG1 has been found to be over-expressed in many disease tissues, where its local production, especially under chronic inflammatory conditions, appears to exacerbate pathological cell dysfunction. This is in line with its likely physiological role as a component of the repair mechanism. Thus, LRG1 can induce de-differentiation of epithelial, endothelial and pericyte cells to support the wound healing process, but under chronically stressed cell conditions, LRG1 is not switched off and its persistence has destabilizing effects resulting in aberrant pathological responses (Figure 2). In the context of vascular function, LRG1 can act on endothelial cells and mural cells affecting the fine interactive balance needed for a stable and mature vasculature (Figure 4). In its sustained and heightened presence, existing and new vessels become unstable and reactive resulting in vascular leakage, fragility, and the failure of new vessels to mature (Figure 3). It presents, therefore, an intriguing and potentially valuable therapeutic target. Critically, LRG1 is particularly attractive in the context of therapeutic targeting of TGF-β signaling as this has been fraught with setbacks, predominantly because TGF-β and its receptors all have critical housekeeping roles. To date no essential homeostatic role for LRG1 has been described rendering it a potentially more suitable therapeutic target. Thus, we reason that inhibiting LRG1 will block the pathogenic activity of TGF-β without disturbing these key homeostatic functions. We anticipate, therefore, that over the next decade our understanding of LRG1 biology will be substantially enhanced and that its therapeutic targeting in multiple indications will be well advanced.

## Author contributions

AD: Visualization, Writing – original draft, Writing – review & editing. CC: Writing – review & editing. SEM: Writing – review & editing. JG: Conceptualization, Visualization, Writing – review & editing.

## Funding

The author(s) declare financial support was received for the research, authorship, and/or publication of this article.

Supported by grants awarded to JG and SEM from The British Heart Foundation (PG/16/50/32182), the Wellcome Trust (Investigator Awards 206413/Z/17/Z and 206413/B/17/Z), the UK Research and Innovation/Medical Research Council UK project grants G1000466 and MR/L002973/1; DPFS/DCS award G0902206 and MR/N006410/1; the Confidence in Concept award MC/PC/14118, the Diabetes UK grant 18/0005856, the UCL Proof of Concept fund and the UCL Technology Fund. JG and SEM were also supported by the National Institute for Health Research (NIHR) Biomedical Research Centre based at Moorfields Eye Hospital NHS Foundation Trust and UCL Institute of Ophthalmology. The views expressed are those of the author(s) and not necessarily those of the NHS, the NIHR or the Department of Health.

## Conflict of interest

JG and SEM are founders of a company spun out by UCL Business to commercialize a LRG1 function-blocking therapeutic antibody developed through the UK Medical Research Council DPFS funding scheme. JG and SEM are members of the scientific advisory board and are shareholders of this company and named inventors on three patents related to LRG1 as a therapeutic target.

The remaining authors declare that the research was conducted in the absence of any commercial or financial relationships that could be construed as a potential conflict of interest.

## Publisher's note

# References

1. Eelen G, Treps L, Li X, Carmeliet P. Basic and therapeutic aspects of angiogenesis updated. *Circ Res*. (2020) 127(2):310–29. doi: 10.1161/circresaha.120.316851

2. Dudley AC, Griffioen AW. Pathological angiogenesis: mechanisms and therapeutic strategies. *Angiogenesis*. (2023) 26(3):313–47. doi: 10.1007/s10456-023-09876-7

3. Apte RS, Chen DS, Ferrara N. VEGF in signaling and disease: beyond discovery and development. *Cell*. (2019) 176(6):1248–64. doi: 10.1016/j.cell.2019.01.021

4. Wu JB, Tang YL, Liang XH. Targeting VEGF pathway to normalize the vasculature: an emerging insight in cancer therapy. *Onco Targets Ther*. (2018) 11:6901–9. doi: 10.2147/ott.S172042

5. Zhuge Y, Zhang J, Qian F, Wen Z, Niu C, Xu K, et al. Role of smooth muscle cells in cardiovascular disease. *Int J Biol Sci*. (2020) 16(14):2741–51. doi: 10.7150/ijbs.49871

6. van Splunder H, Villacampa P, Martínez-Romero A, Graupera M. Pericytes in the disease spotlight. *Trends Cell Biol*. (2024) 34(1):58–71. doi: 10.1016/j.tcb.2023.06.001

7. Armulik A, Abramsson A, Betsholtz C. Endothelial/pericyte interactions. *Circ Res*. (2005) 97(6):512–23. doi: 10.1161/01.RES.0000182903.16652.d7

8. Armulik A, Genové G, Betsholtz C. Pericytes: developmental, physiological, and pathological perspectives, problems, and promises. *Dev Cell*. (2011) 21(2):193–215. doi: 10.1016/j.devcel.2011.07.001

9. von Tell D, Armulik A, Betsholtz C. Pericytes and vascular stability. *Exp Cell Res*. (2006) 312(5):623–9. doi: 10.1016/j.yexcr.2005.10.019

10. Xu Y, Kovacic JC. Endothelial to mesenchymal transition in health and disease. *Annu Rev Physiol*. (2023) 85:245–67. doi: 10.1146/annurev-physiol-032222-080806

11. Goel S, Duda DG, Xu L, Munn LL, Boucher Y, Fukumura D, et al. Normalization of the vasculature for treatment of cancer and other diseases. *Physiol Rev*. (2011) 91 (3):1071–121. doi: 10.1152/physrev.00038.2010

12. Kobe B, Kajava AV. The leucine-rich repeat as a protein recognition motif. *Curr Opin Struct Biol*. (2001) 11(6):725–32. doi: 10.1016/S0959-440X(01)00266-4

13. Ng A, Xavier RJ. Leucine-rich repeat (LRR) proteins: integrators of pattern recognition and signaling in immunity. *Autophagy*. (2011) 7(9):1082–4. doi: 10.4161/auto.7.9.16464

14. Weivoda S, Andersen JD, Skogen A, Schlievert PM, Fontana D, Schacker T, et al. Elisa for human serum leucine-rich alpha-2-glycoprotein-1 employing cytochrome C as the capturing ligand. *J Immunol Methods*. (2008) 336(1):22–9. doi: 10.1016/j.jim.2008.03.004

15. O'Donnell LC, Druhan LJ, Avalos BR. Molecular characterization and expression analysis of leucine-rich alpha2-glycoprotein, a novel marker of granulocytic differentiation. *J Leukocyte Biol*. (2002) 72(3):478–85. doi: 10.1189/jlb.72.3.478

16. Ai J, Druhan LJ, Hunter MG, Loveland MJ, Avalos BR. LRG-accelerated differentiation defines unique G-CSFR signaling pathways downstream of PU.1 and C/EBPepsilon that modulate neutrophil activation. *J Leukocyte Biol*. (2008) 83 (5):1277–85. doi: 10.1189/jlb.1107751

17. Liu C, Teo MHY, Pek SLT, Wu X, Leong ML, Tay HM, et al. A multifunctional role of leucine-rich A-2-glycoprotein 1 in cutaneous wound healing under normal and diabetic conditions. *Diabetes*. (2020) 69(11):2467–80. doi: 10.2337/db20-0585

18. Bonaventura A, Liberale L, Carbone F, Vecchié A, Diaz-Cañestro C, Camici GG, et al. The pathophysiological role of neutrophil extracellular traps in inflammatory diseases. *Thromb Haemostasis*. (2018) 118(1):6–27. doi: 10.1160/th17-09-0630

19. Jemmerson R. Paradoxical roles of leucine-rich α(2)-glycoprotein-1 in cell death and survival modulated by transforming growth factor-beta 1 and cytochrome C. *Front Cell Dev Biol*. (2021) 9:744908. doi: 10.3389/fcell.2021.744908

20. Cummings C, Walder J, Treeful A, Jemmerson R. Serum leucine-rich alpha-2-glycoprotein-1 binds cytochrome C and inhibits antibody detection of this apoptotic marker in enzyme-linked immunosorbent assay. *Apoptosis*. (2006) 11 (7):1121–9. doi: 10.1007/s10495-006-8159-3

21. Uhlén M, Fagerberg L, Hallström BM, Lindskog C, Oksvold P, Mardinoglu A, et al. Tissue-based map of the human proteome. *Science*. (2015) 347(6220):1260419. doi: 10.1126/science.1260419

22. He Y, Tacconi C, Dieterich LC, Kim J, Restivo G, Gousopoulos E, et al. Novel blood vascular endothelial subtype-specific markers in human skin unearthed by single-cell transcriptomic profiling. *Cells*. (2022) 11(7):1111. doi: 10.3390/cells11071111

23. Camilli C, Hoeh AE, De Rossi G, Moss SE, Greenwood J. LRG1: an emerging player in disease pathogenesis. *J Biomed Sci*. (2022) 29(1):6. doi: 10.1186/s12929-022-00790-6

24. De Rossi G, Da Vitoria Lobo ME, Greenwood J, Moss SE. LRG1 as a novel therapeutic target in eye disease. *Eye (Lond)*. (2022) 36(2):328–40. doi: 10.1038/s41433-021-01807-4

25. Wang X, Abraham S, McKenzie JAG, Jeffs N, Swire M, Tripathi VB, et al. LRG1 promotes angiogenesis by modulating endothelial TGF-β signalling. *Nature*. (2013) 499(7458):306–11. doi: 10.1038/nature12345

26. Dritsoula A, Dowsett L, Pilotti C, O'Connor MN, Moss SE, Greenwood J. Angiopathic activity of LRG1 is induced by the il-6/STAT3 pathway. *Sci Rep*. (2022) 12(1):4867. doi: 10.1038/s41598-022-08516-2

27. He L, Feng A, Guo H, Huang H, Deng Q, Zhao E, et al. LRG1 mediated by ATF3 promotes growth and angiogenesis of gastric cancer by regulating the SRC/STAT3/VEGFA pathway. *Gastric Cancer*. (2022) 25(3):527–41. doi: 10.1007/s10120-022-01279-9

28. Kwan YP, Teo MHY, Lim JCW, Tan MS, Rosellinny G, Wahli W, et al. LRG1 promotes metastatic dissemination of melanoma through regulating eGFR/STAT3 signalling. *Cancers (Basel)*. (2021) 13(13):3279. doi: 10.3390/cancers13133279

29. Singhal M, Gengenbacher N, Abdul Pari AA, Kamiyama M, Hai L, Kuhn BJ, et al. Temporal multi-omics identifies LRG1 as a vascular niche instructor of metastasis. *Sci Transl Med*. (2021) 13(609):eabe6805. doi: 10.1126/scitranslmed.abe6805

30. Yamamoto M, Takahashi T, Serada S, Sugase T, Tanaka K, Miyazaki Y, et al. Overexpression of leucine-rich α2-glycoprotein-1 is a prognostic marker and enhances tumor migration in gastric cancer. *Cancer Sci*. (2017) 108(10):2052–60. doi: 10.1111/cas.13329

31. Zhong B, Cheng B, Huang X, Xiao Q, Niu Z, Chen YF, et al. Colorectal cancer-associated fibroblasts promote metastasis by up-regulating LRG1 through stromal il-6/STAT3 signaling. *Cell Death Dis*. (2021) 13(1):16. doi: 10.1038/s41419-021-04461-6

32. O'Connor MN, Kallenberg DM, Camilli C, Pilotti C, Dritsoula A, Jackstadt R, et al. LRG1 destabilizes tumor vessels and restricts immunotherapeutic potency. *Med*. (2021) 2(11):1231–52.e10. doi: 10.1016/j.medj.2021.10.002

33. Hong Q, Cai H, Zhang L, Li Z, Zhong F, Ni Z, et al. Modulation of transforming growth factor-β-induced kidney fibrosis by leucine-rich ⍰-2 glycoprotein-1. *Kidney Int*. (2022) 101(2):299–314. doi: 10.1016/j.kint.2021.10.023

34. Liu TT, Luo R, Yang Y, Cheng YC, Chang D, Dai W, et al. LRG1 mitigates renal interstitial fibrosis through alleviating capillary rarefaction and inhibiting inflammatory and pro-fibrotic cytokines. *Am J Nephrol*. (2021) 52(3):228–38. doi: 10.1159/000514167

35. Yang FJ, Hsieh CY, Shu KH, Chen IY, Pan SY, Chuang YF, et al. Plasma leucine-rich α-2-glycoprotein 1 predicts cardiovascular disease risk in End-stage renal disease. *Sci Rep*. (2020) 10(1):5988. doi: 10.1038/s41598-020-62989-7

36. Yang Y, Luo R, Cheng Y, Liu T, Dai W, Li Y, et al. Leucine-rich α2-glycoprotein-1 upregulation in plasma and kidney of patients with lupus nephritis. *BMC Nephrol*. (2020) 21(1):122. doi: 10.1186/s12882-020-01782-0

37. Hisata S, Racanelli AC, Kermani P, Schreiner R, Houghton S, Palikuqi B, et al. Reversal of emphysema by restoration of pulmonary endothelial cells. *J Exp Med*. (2021) 218(8):e20200938. doi: 10.1084/jem.20200938

38. Li R, Zhao X, Liu P, Wang D, Chen C, Wang Y, et al. Differential expression of serum proteins in chronic obstructive pulmonary disease assessed using label-free proteomics and bioinformatics analyses. *Int J Chron Obstruct Pulmon Dis*. (2022) 17:2871–91. doi: 10.2147/copd.S383976

39. Nitkin CR, Xia S, Menden H, Yu W, Xiong M, Heruth DP, et al. Fosl1 is a novel mediator of endotoxin/lipopolysaccharide-induced pulmonary angiogenic signaling. *Sci Rep*. (2020) 10(1):13143. doi: 10.1038/s41598-020-69735-z

40. Chen J, Zhang Z, Feng L, Liu W, Wang X, Chen H, et al. LRG1 silencing attenuates ischemia-reperfusion renal injury by regulating autophagy and apoptosis through the TGFβ1- Smad1/5 signaling pathway. *Arch Biochem Biophys*. (2024) 753:109892. doi: 10.1016/j.abb.2024.109892

41. Gao Y, Zhou J, Xie Z, Wang J, Ho CK, Zhang Y, et al. Mechanical strain promotes skin fibrosis through LRG-1 induction mediated by ELK1 and ERK signalling. *Commun Biol*. (2019) 2:359. doi: 10.1038/s42003-019-0600-6

42. Honda H, Fujimoto M, Serada S, Urushima H, Mishima T, Lee H, et al. Leucine-rich α-2 glycoprotein promotes lung fibrosis by modulating TGF-β signaling in fibroblasts. *Physiol Rep*. (2017) 5(24):e13556. doi: 10.14814/phy2.13556

43. Liu C, Lim ST, Teo MHY, Tan MSY, Kulkarni MD, Qiu B, et al. Collaborative regulation of LRG1 by TGF-β1 and PPAR-β/δ modulates chronic pressure overload-induced cardiac fibrosis. *Circ Heart Fail*. (2019) 12(12):e005962. doi: 10.1161/circheartfailure.119.005962

44. Nakajima H, Nakajima K, Serada S, Fujimoto M, Naka T, Sano S. The involvement of leucine-rich α-2 glycoprotein in the progression of skin and lung fibrosis in bleomycin-induced systemic sclerosis model. *Mod Rheumatol*. (2021) 31 (6):1120–8. doi: 10.1080/14397595.2021.1883841

45. Park HN, Song MJ, Choi YE, Lee DH, Chung JH, Lee ST. LRG1 promotes ECM integrity by activating the TGF-β signaling pathway in fibroblasts. *Int J Mol Sci*. (2023) 24(15):12445. doi: 10.3390/ijms241512445

46. Sarkar A, Chakraborty D, Kumar V, Malhotra R, Biswas S. Upregulation of leucine-rich alpha-2 glycoprotein: a key regulator of inflammation and joint fibrosis in patients with severe knee osteoarthritis. *Front Immunol*. (2022) 13:1028994. doi: 10.3389/fimmu.2022.1028994

47. Sng MK, Chan JSK, Teo Z, Phua T, Tan EHP, Wee JWK, et al. Selective deletion of PPARβ/δ in fibroblasts causes dermal fibrosis by attenuated LRG1 expression. *Cell Discov*. (2018) 4:15. doi: 10.1038/s41421-018-0014-5

48. Yu B, Yang L, Song S, Li W, Wang H, Cheng J. LRG1 facilitates corneal fibrotic response by inducing neutrophil chemotaxis via STAT3 signaling in alkali-burned mouse corneas. *Am J Physiol Cell Physiol*. (2021) 321(3):C415–28. doi: 10.1152/ajpcell.00517.2020

49. Altıncık SA, Yıldırımçakar D, Avcı E, Özhan B, Girişgen İ, Yüksel S. Plasma leucine-rich α-2-glycoprotein 1—a novel marker of diabetic kidney disease in children and adolescents with type 1 diabetes Mellitus? *Pediatr Nephrol*. (2023) 38 (12):4043–9. doi: 10.1007/s00467-023-06019-4

50. Chen C, Chen X, Huang H, Han C, Qu Y, Jin H, et al. Elevated plasma and vitreous levels of leucine-rich-α2-glycoprotein are associated with diabetic retinopathy progression. *Acta Ophthalmol (Copenh)*. (2019) 97(3):260–4. doi: 10.1111/aos.13633

51. Gurung RL, Dorajoo R, Yiamunaa M, Liu JJ, Pek SLT, Wang J, et al. Association of genetic variants for plasma LRG1 with rapid decline in kidney function in patients with type 2 diabetes. *J Clin Endocrinol Metab*. (2021) 106(8):2384–94. doi: 10.1210/clinem/dgab268

52. Haku S, Wakui H, Azushima K, Haruhara K, Kinguchi S, Ohki K, et al. Early enhanced leucine-rich α-2-glycoprotein-1 expression in glomerular endothelial cells of type 2 diabetic nephropathy model mice. *BioMed Res Int*. (2018) 2018:2817045. doi: 10.1155/2018/2817045

53. Hong Q, Zhang L, Fu J, Verghese DA, Chauhan K, Nadkarni GN, et al. LRG1 promotes diabetic kidney disease progression by enhancing TGF-β-induced angiogenesis. *J Am Soc Nephrol*. (2019) 30(4):546–62. doi: 10.1681/asn.2018060599

54. Li W, Wang X, Cheng J, Li J, Wang Q, Zhou Q, et al. Leucine-rich α-2-glycoprotein-1 promotes diabetic corneal epithelial wound healing and nerve regeneration via regulation of matrix metalloproteinases. *Exp Eye Res*. (2020) 196:108060. doi: 10.1016/j.exer.2020.108060

55. Liu JJ, Liu S, Wang J, Pek SLT, Lee J, Gurung RL, et al. Urine leucine-rich α-2 glycoprotein 1 (LRG1) predicts the risk of progression to end-stage kidney disease in patients with type 2 diabetes. *Diabetes Care*. (2023) 46(2):408–15. doi: 10.2337/dc22-1611

56. Liu JJ, Pek SLT, Ang K, Tavintharan S, Lim SC. Plasma leucine-rich α-2-glycoprotein 1 predicts rapid eGFR decline and albuminuria progression in type 2 diabetes mellitus. *J Clin Endocrinol Metab*. (2017) 102(10):3683–91. doi: 10.1210/jc.2017-00930

57. Zhang X, Pek SLT, Tavintharan S, Sum CF, Lim SC, Ang K, et al. Leucine-rich α-2-glycoprotein predicts proliferative diabetic retinopathy in type 2 diabetes. *J Diabetes Complicat*. (2019) 33(9):651–6. doi: 10.1016/j.jdiacomp.2019.05.021

58. Yao J, Chang X, He Q, Li H, Duan T, Wang K. Exosome enriched leucine-rich alpha-2-glycoprotein-1 and extracellular matrix protein 1 proteins induce abnormal placental angiogenesis in pregnant mice. *Placenta*. (2023) 143:45–53. doi: 10.1016/j.placenta.2023.09.008

59. Wang CH, Li M, Liu LL, Zhou RY, Fu J, Zhang CZ, et al. LRG1 expression indicates unfavorable clinical outcome in hepatocellular carcinoma. *Oncotarget*. (2015) 6(39):42118–29. doi: 10.18632/oncotarget.5967

60. Sun DC, Shi Y, Wang LX, Lv Y, Han QL, Wang ZK, et al. Leucine-rich alpha-2-glycoprotein-1, relevant with microvessel density, is an independent survival prognostic factor for stage iii colorectal cancer patients: a retrospective analysis. *Oncotarget*. (2017) 8(39):66550–8. doi: 10.18632/oncotarget.16289

61. Guldvik IJ, Zuber V, Braadland PR, Grytli HH, Ramberg H, Lilleby W, et al. Identification and validation of leucine-rich α-2-glycoprotein 1 as a noninvasive biomarker for improved precision in prostate cancer risk stratification. *Eur Urol Open Sci*. (2020) 21:51–60. doi: 10.1016/j.euros.2020.08.007

62. Hoefsmit EP, Völlmy F, Rozeman EA, Reijers ILM, Versluis JM, Hoekman L, et al. Systemic LRG1 expression in melanoma is associated with disease progression and recurrence. *Cancer Res Commun*. (2023) 3(4):672–83. doi: 10.1158/2767-9764.Crc-23-0015

63. Hughes K, Wickenden JA, Allen JE, Watson CJ. Conditional deletion of STAT3 in mammary epithelium impairs the acute phase response and modulates immune cell numbers during post-lactational regression. *J Pathol*. (2012) 227(1):106–17. doi: 10.1002/path.3961

64. Wang Y, Xu J, Zhang X, Wang C, Huang Y, Dai K, et al. Tnf-α-induced LRG1 promotes angiogenesis and mesenchymal stem cell migration in the subchondral bone during osteoarthritis. *Cell Death Dis*. (2017) 8(3):e2715. doi: 10.1038/cddis.2017.129

65. Naka T, Fujimoto M. LRG is a novel inflammatory marker clinically useful for the evaluation of disease activity in rheumatoid arthritis and inflammatory bowel disease. *Immunol Med*. (2018) 41(2):62–7. doi: 10.1080/13497413.2018.1481582

66. Honda H, Fujimoto M, Miyamoto S, Ishikawa N, Serada S, Hattori N, et al. Sputum leucine-rich alpha-2 glycoprotein as a marker of airway inflammation in asthma. *PLoS One*. (2016) 11(9):e0162672. doi: 10.1371/journal.pone.0162672

67. Shirai R, Hirano F, Ohkura N, Ikeda K, Inoue S. Up-regulation of the expression of leucine-rich alpha(2)-glycoprotein in hepatocytes by the mediators of acute-phase response. *Biochem Biophys Res Commun*. (2009) 382(4):776–9. doi: 10.1016/j.bbrc.2009.03.104

68. Makita N, Hizukuri Y, Yamashiro K, Murakawa M, Hayashi Y. Il-10 enhances the phenotype of M2 macrophages induced by IL-4 and confers the ability to increase eosinophil migration. *Int Immunol*. (2015) 27(3):131–41. doi: 10.1093/intimm/dxu090

69. Zhu Z, Guo Y, Liu Y, Ding R, Huang Z, Yu W, et al. ELK4 promotes colorectal cancer progression by activating the neoangiogenic factor LRG1 in a noncanonical SP1/3-dependent manner. *Adv Sci (Weinh)*. (2023) 10(32):e2303378. doi: 10.1002/advs.202303378

70. Feng J, Zhan J, Ma S. LRG1 promotes hypoxia-induced cardiomyocyte apoptosis and autophagy by regulating hypoxia-inducible factor-1α. *Bioengineered*. (2021) 12 (1):8897–907. doi: 10.1080/21655979.2021.1988368

71. Thorin E, Labbé P, Lambert M, Mury P, Dagher O, Miquel G, et al. Angiopoietin-like proteins: cardiovascular biology and therapeutic targeting for the prevention of cardiovascular diseases. *Can J Cardiol*. (2023) 39(12):1736–56. doi: 10.1016/j.cjca.2023.06.002

72. Fernández-Hernando C, Suárez Y. ANGPTL4: a multifunctional protein involved in metabolism and vascular homeostasis. *Curr Opin Hematol*. (2020) 27 (3):206–13. doi: 10.1097/moh.0000000000000580

73. Wu L, Chen L, Li L. Apelin/APJ system: a novel promising therapy target for pathological angiogenesis. *Clin Chim Acta*. (2017) 466:78–84. doi: 10.1016/j.cca.2016.12.023

74. Barandon L, Couffinhal T, Dufourcq P, Ezan J, Costet P, Daret D, et al. Frizzled a, a novel angiogenic factor: promises for cardiac repair. *Eur J Cardiothorac Surg*. (2004) 25(1):76–83. doi: 10.1016/s1010-7940(03)00506-2

75. Huang A, Huang Y. Role of SFRPS in cardiovascular disease. *Ther Adv Chronic Dis*. (2020) 11:2040622320901990. doi: 10.1177/2040622320901990

76. Shi CS, Shi GY, Chang YS, Han HS, Kuo CH, Liu C, et al. Evidence of human thrombomodulin domain as a novel angiogenic factor. *Circulation*. (2005) 111 (13):1627–36. doi: 10.1161/01.Cir.0000160364.05405.B5

77. Wang J, Peng H, Timur AA, Pasupuleti V, Yao Y, Zhang T, et al. Receptor and molecular mechanism of AGGF1 signaling in endothelial cell functions and angiogenesis. *Arterioscler Thromb Vasc Biol*. (2021) 41(11):2756–69. doi: 10.1161/atvbaha.121.316867

78. Zhang B, Dietrich UM, Geng JG, Bicknell R, Esko JD, Wang L. Repulsive axon guidance molecule SLIT3 is a novel angiogenic factor. *Blood*. (2009) 114(19):4300–9. doi: 10.1182/blood-2008-12-193326

79. Selvaprithviraj V, Sankar D, Sivashanmugam A, Srinivasan S, Jayakumar R. Pro-angiogenic molecules for therapeutic angiogenesis. *Curr Med Chem*. (2017) 24 (31):3413–32. doi: 10.2174/0929867324666170724142641

80. Zhao X, Chen J, Zhang C, Xie G, Othmane B, Kuang X, et al. LncRNA AGAP2-AS1 interacts with IGF2BP2 to promote bladder cancer progression via regulating LRG1 mRNA stability. *Cell Signal*. (2023) 111:110839. doi: 10.1016/j.cellsig.2023.110839

81. Cai D, Chen C, Su Y, Tan Y, Lin X, Xing R. LRG1 in pancreatic cancer cells promotes inflammatory factor synthesis and the angiogenesis of Huvecs by activating VEGFR signaling. *J Gastrointest Oncol*. (2022) 13(1):400–12. doi: 10.21037/jgo-21-910

82. Li Z, Zeng C, Nong Q, Long F, Liu J, Mu Z, et al. Exosomal leucine-rich-Alpha2-glycoprotein 1 derived from non-small-cell lung cancer cells promotes angiogenesis via TGF-β signal pathway. *Mol Ther Oncolytics*. (2019) 14:313–22. doi: 10.1016/j.omto.2019.08.001

83. Fan M, Li C, He P, Fu Y, Li M, Zhao X. Knockdown of long noncoding RNA-taurine-upregulated gene 1 inhibits tumor angiogenesis in ovarian cancer by regulating leucine-rich α-2-glycoprotein-1. *Anticancer Drugs*. (2019) 30(6):562–70. doi: 10.1097/cad.0000000000000734

84. Zhang J, Zhu L, Fang J, Ge Z, Li X. LRG1 modulates epithelial-mesenchymal transition and angiogenesis in colorectal cancer via HIF-1α activation. *J Exp Clin Cancer Res*. (2016) 35:29. doi: 10.1186/s13046-016-0306-2

85. Yin GN, Kim DK, Kang JI, Im Y, Lee DS, Han AR, et al. Latrophilin-2 is a novel receptor of LRG1 that rescues vascular and neurological abnormalities and restores diabetic erectile function. *Exp Mol Med*. (2022) 54(5):626–38. doi: 10.1038/s12276-022-00773-5

86. Yang P, Li S, Zhang H, Ding X, Tan Q. LRG1 accelerates wound healing in diabetic rats by promoting angiogenesis via the Wnt/β-catenin signaling pathway. *Int J Low Extrem Wounds*. (2022):15347346221081610. doi: 10.1177/15347346221081610

87. Fu J, Wei C, Zhang W, Schlondorff D, Wu J, Cai M, et al. Gene expression profiles of glomerular endothelial cells support their role in the glomerulopathy of diabetic mice. *Kidney Int*. (2018) 94(2):326–45. doi: 10.1016/j.kint.2018.02.028

88. Tsuruta H, Yasuda-Yamahara M, Yoshibayashi M, Kuwagata S, Yamahara K, Tanaka-Sasaki Y, et al. Fructose overconsumption accelerates renal dysfunction with aberrant glomerular endothelial-mesangial cell interactions in db/db mice. *Biochim Biophys Acta Mol Basis Dis*. (2024) 1870(4):167074. doi: 10.1016/j.bbadis.2024.167074

89. Kumagai S, Nakayama H, Fujimoto M, Honda H, Serada S, Ishibashi-Ueda H, et al. Myeloid cell-derived LRG attenuates adverse cardiac remodelling after myocardial infarction. *Cardiovasc Res*. (2016) 109(2):272–82. doi: 10.1093/cvr/cvv273

90. Zhao G, Xue L, Weiner AI, Gong N, Adams-Tzivelekidis S, Wong J, et al. TGF-βr2 signaling coordinates pulmonary vascular repair after viral injury in mice and human tissue. *Sci Transl Med*. (2024) 16(732):eadg6229. doi: 10.1126/scitranslmed.adg6229

91. Song S, Cheng J, Yu BJ, Zhou L, Xu HF, Yang LL. LRG1 promotes corneal angiogenesis and lymphangiogenesis in a corneal alkali burn mouse model. *Int J Ophthalmol*. (2020) 13(3):365–73. doi: 10.18240/ijo.2020.03.01

92. Meng H, Song Y, Zhu J, Liu Q, Lu P, Ye N, et al. LRG1 promotes angiogenesis through upregulating the TGF-β1 pathway in ischemic rat brain. *Mol Med Rep*. (2016) 14(6):5535–43. doi: 10.3892/mmr.2016.5925

93. Grzesiak L, Amaya-Garrido A, Feuillet G, Malet N, Swiader A, Sarthou MK, et al. Leucine-rich alpha-2 glycoprotein 1 accumulates in complicated atherosclerosis and promotes calcification. *Int J Mol Sci*. (2023) 24(22):16537. doi: 10.3390/ijms242216537

94. Kallenberg D, Tripathi V, Javaid F, Pilotti C, George J, Davis S, et al. A humanized antibody against LRG1 that inhibits angiogenesis and reduces retinal vascular leakage. *J bioRxiv*. (2021):2020.07.25.218149. doi: 10.1101/2020.07.25.218149

95. Jeong JH, Ojha U, Lee YM. Pathological angiogenesis and inflammation in tissues. *Arch Pharmacal Res*. (2021) 44(1):1–15. doi: 10.1007/s12272-020-01287-2

96. Zhao Q, Molina-Portela MDP, Parveen A, Adler A, Adler C, Hock E, et al. Heterogeneity and chimerism of endothelial cells revealed by single-cell transcriptome in orthotopic liver tumors. *Angiogenesis*. (2020) 23(4):581–97. doi: 10.1007/s10456-020-09727-9

97. Örd T, Lönnberg T, Nurminen V, Ravindran A, Niskanen H, Kiema M, et al. Dissecting the polygenic basis of atherosclerosis via disease-associated cell state signatures. *Am J Hum Genet*. (2023) 110(5):722–40. doi: 10.1016/j.ajhg.2023.03.013

98. Lipski DA, Foucart V, Dewispelaere R, Caspers LE, Defrance M, Bruyns C, et al. Retinal endothelial cell phenotypic modifications during experimental autoimmune uveitis: a transcriptomic approach. *BMC Ophthalmol*. (2020) 20(1):106. doi: 10.1186/s12886-020-1333-5

99. Goumans MJ, Valdimarsdottir G, Itoh S, Rosendahl A, Sideras P, ten Dijke P. Balancing the activation state of the endothelium via two distinct TGF-beta type I receptors. *EMBO J*. (2002) 21(7):1743–53. doi: 10.1093/emboj/21.7.1743

100. Lebrin F, Goumans MJ, Jonker L, Carvalho RL, Valdimarsdottir G, Thorikay M, et al. Endoglin promotes endothelial cell proliferation and TGF-beta/ALK1 signal transduction. *EMBO J*. (2004) 23(20):4018–28. doi: 10.1038/sj.emboj.7600386

101. DiPietro LA. Angiogenesis and wound repair: when enough is enough. *J Leukocyte Biol*. (2016) 100(5):979–84. doi: 10.1189/jlb.4MR0316-102R

102. Jung K, Covington S, Sen CK, Januszyk M, Kirsner RS, Gurtner GC, et al. Rapid identification of slow healing wounds. *Wound Repair Regen*. (2016) 24(1):181–8. doi: 10.1111/wrr.12384

103. Gao Y, Xie Z, Ho C, Wang J, Li Q, Zhang Y, et al. LRG1 promotes keratinocyte migration and wound repair through regulation of HIF-1α stability. *J Invest Dermatol*. (2020) 140(2):455–64.e8. doi: 10.1016/j.jid.2019.06.143

104. Zhang M, Wang Y, Wang J, Li X, Ma A, Pan X. Serum LRG1 as a novel biomarker for cardioembolic stroke. *Clin Chim Acta*. (2021) 519:83–91. doi: 10.1016/j.cca.2021.04.002

105. Gu J, Liu C, Yao Y. Prognostic potency of plasma LRG1 measurement at multiple time points in acute ischemic stroke patients. *Biomark Med*. (2024) 18(5):181–90. doi: 10.2217/bmm-2023-0545

106. Savarraj JPJ, McBride DW, Park E, Hinds S, Paz A, Gusdon A, et al. Leucine-rich alpha-2-glycoprotein 1 is a systemic biomarker of early brain injury and delayed cerebral ischemia after subarachnoid hemorrhage. *Neurocrit Care*. (2023) 38(3):771–80. doi: 10.1007/s12028-022-01652-7

107. Cheng X, Wei H, Liu Y, Sun Y, Ye J, Lu P, et al. Relation between LRG1 and CD4(+) T cells, cognitive impairment and neurological function in patients with acute ischemic stroke. *Biomark Med*. (2024) 18(1):5–14. doi: 10.2217/bmm-2023-0674

108. Jin C, Shi Y, Shi L, Leak RK, Zhang W, Chen K, et al. Leveraging single-cell RNA sequencing to unravel the impact of aging on stroke recovery mechanisms in mice. *Proc Natl Acad Sci U S A*. (2023) 120(25):e2300012120. doi: 10.1073/pnas.2300012120

109. Jin J, Sun H, Liu D, Wang H, Liu Q, Chen H, et al. LRG1 promotes apoptosis and autophagy through the TGFβ-smad1/5 signaling pathway to exacerbate ischemia/reperfusion injury. *Neuroscience*. (2019) 413:123–34. doi: 10.1016/j.neuroscience.2019.06.008

110. Rust R. Insights into the dual role of angiogenesis following stroke. *J Cereb Blood Flow Metab*. (2020) 40(6):1167–71. doi: 10.1177/0271678×20906815

111. Ruan Z, Cao G, Qian Y, Fu L, Hu J, Xu T, et al. Single-cell RNA sequencing unveils LRG1's role in cerebral ischemia‐reperfusion injury by modulating various cells. *J Neuroinflammation*. (2023) 20(1):285. doi: 10.1186/s12974-023-02941-4

112. Campochiaro PA. Ocular neovascularization. *J Mol Med (Berl)*. (2013) 91(3):311–21. doi: 10.1007/s00109-013-0993-5

113. Lambert V, Lecomte J, Hansen S, Blacher S, Gonzalez ML, Struman I, et al. Laser-induced choroidal neovascularization model to study age-related macular degeneration in mice. *Nat Protoc*. (2013) 8(11):2197–211. doi: 10.1038/nprot.2013.135

114. Smith LE, Wesolowski E, McLellan A, Kostyk SK, D'Amato R, Sullivan R, et al. Oxygen-induced retinopathy in the mouse. *Invest Ophthalmol Visual Sci*. (1994) 35(1):101–11. PMID: 7507904.

115. Schlecht A, Thien A, Wolf J, Prinz G, Agostini H, Schlunck G, et al. Immunosenescence in choroidal neovascularization (CNV)-transcriptional profiling of naïve and CNV-associated retinal myeloid cells during aging. *Int J Mol Sci*. (2021) 22(24):13318. doi: 10.3390/ijms222413318

116. Kim TW, Kang JW, Ahn J, Lee EK, Cho KC, Han BN, et al. Proteomic analysis of the aqueous humor in age-related macular degeneration (AMD) patients. *J Proteome Res*. (2012) 11(8):4034–43. doi: 10.1021/pr300080s

117. Koss MJ, Hoffmann J, Nguyen N, Pfister M, Mischak H, Mullen W, et al. Proteomics of vitreous humor of patients with exudative age-related macular degeneration. *PLoS One*. (2014) 9(5):e96895. doi: 10.1371/journal.pone.0096895

118. Mundo L, Tosi GM, Lazzi S, Pertile G, Parolini B, Neri G, et al. LRG1 expression is elevated in the eyes of patients with neovascular age-related macular degeneration. *Int J Mol Sci*. (2021) 22(16):8879. doi: 10.3390/ijms22168879

119. Nobl M, Reich M, Dacheva I, Siwy J, Mullen W, Schanstra JP, et al. Proteomics of vitreous in neovascular age-related macular degeneration. *Exp Eye Res*. (2016) 146:107–17. doi: 10.1016/j.exer.2016.01.001

120. Qu SC, Xu D, Li TT, Zhang JF, Liu F. iTRAQ-based proteomics analysis of aqueous humor in patients with dry age-related macular degeneration. *Int J Ophthalmol*. (2019) 12(11):1758–66. doi: 10.18240/ijo.2019.11.15

121. Zhang A, Fang H, Chen J, He L, Chen Y. Role of VEGF-a and LRG1 in abnormal angiogenesis associated with diabetic nephropathy. *Front Physiol*. (2020) 11:1064. doi: 10.3389/fphys.2020.01064

122. Zhou L, Shi DP, Chu WJ, Yang LL, Xu HF. LRG1 promotes epithelial-mesenchymal transition of retinal pigment epithelium cells by activating Nox4. *Int J Ophthalmol*. (2021) 14(3):349–55. doi: 10.18240/ijo.2021.03.03

123. Huang C, Ogawa R. The vascular involvement in soft tissue fibrosis-lessons learned from pathological scarring. *Int J Mol Sci*. (2021) 22(16):8879. doi: 10.3390/ijms21072542

124. Alvandi Z, Bischoff J. Endothelial-mesenchymal transition in cardiovascular disease. *Arterioscler Thromb Vasc Biol*. (2021) 41(9):2357–69. doi: 10.1161/atvbaha.121.313788

125. Gao BB, Chen X, Timothy N, Aiello LP, Feener EP. Characterization of the vitreous proteome in diabetes without diabetic retinopathy and diabetes with proliferative diabetic retinopathy. *J Proteome Res*. (2008) 7(6):2516–25. doi: 10.1021/pr800112g

126. Kim T, Kim SJ, Kim K, Kang UB, Lee C, Park KS, et al. Profiling of vitreous proteomes from proliferative diabetic retinopathy and nondiabetic patients. *Proteomics*. (2007) 7(22):4203–15. doi: 10.1002/pmic.200700745

127. Hase K, Kanda A, Hirose I, Noda K, Ishida S. Systemic factors related to soluble (pro)renin receptor in plasma of patients with proliferative diabetic retinopathy. *PLoS One*. (2017) 12(12):e0189696. doi: 10.1371/journal.pone.0189696

128. Lee R, Wong TY, Sabanayagam C. Epidemiology of diabetic retinopathy, diabetic macular edema and related vision loss. *Eye Vis (Lond)*. (2015) 2:17. doi: 10.1186/s40662-015-0026-2

129. Pek SL, Tavintharan S, Wang X, Lim SC, Woon K, Yeoh LY, et al. Elevation of a novel angiogenic factor, leucine-rich-α2-glycoprotein (LRG1), is associated with arterial stiffness, endothelial dysfunction, and peripheral arterial disease in patients with type 2 diabetes. *J Clin Endocrinol Metab*. (2015) 100(4):1586–93. doi: 10.1210/jc.2014-3855

130. Singh H, Yu Y, Suh MJ, Torralba MG, Stenzel RD, Tovchigrechko A, et al. Type 1 diabetes: urinary proteomics and protein network analysis support perturbation of lysosomal function. *Theranostics*. (2017) 7(10):2704–17. doi: 10.7150/thno.19679

131. Frudd K, Sivaprasad S, Raman R, Krishnakumar S, Revathy YR, Turowski P. Diagnostic circulating biomarkers to detect vision-threatening diabetic retinopathy: potential screening tool of the future? *Acta Ophthalmol*. (2022) 100(3):e648–68. doi: 10.1111/aos.14954

132. Chen C, Zhang J, Yu T, Feng H, Liao J, Jia Y. LRG1 contributes to the pathogenesis of multiple kidney diseases: a comprehensive review. *Kidney Dis (Basel)*. (2024):1. doi: 10.1159/000538443

133. Baaten C, Vondenhoff S, Noels H. Endothelial cell dysfunction and increased cardiovascular risk in patients with chronic kidney disease. *Circ Res*. (2023) 132(8):970–92. doi: 10.1161/circresaha.123.321752

134. Simon M, Gröne HJ, Jöhren O, Kullmer J, Plate KH, Risau W, et al. Expression of vascular endothelial growth factor and its receptors in human renal ontogenesis and in adult kidney. *Am J Physiol*. (1995) 268(2 Pt 2):F240–50. doi: 10.1152/ajprenal.1995.268.2.F240

135. Tanabe K, Maeshima Y, Sato Y, Wada J. Antiangiogenic therapy for diabetic nephropathy. *BioMed Res Int*. (2017) 2017:5724069. doi: 10.1155/2017/5724069

136. Lee H, Fujimoto M, Ohkawara T, Honda H, Serada S, Terada Y, et al. Leucine rich α-2 glycoprotein is a potential urinary biomarker for renal tubular injury.

*Biochem Biophys Res Commun*. (2018) 498(4):1045–51. doi: 10.1016/j.bbrc.2018.03.111

137. Jiang WJ, Xu CT, Du CL, Dong JH, Xu SB, Hu BF, et al. Tubular epithelial cell-to-macrophage communication forms a negative feedback loop via extracellular vesicle transfer to promote renal inflammation and apoptosis in diabetic nephropathy. *Theranostics*. (2022) 12(1):324–39. doi: 10.7150/thno.63735

138. Fadini GP, Albiero M, Bonora BM, Avogaro A. Angiogenic abnormalities in diabetes mellitus: mechanistic and clinical aspects. *J Clin Endocrinol Metab*. (2019) 104(11):5431–44. doi: 10.1210/jc.2019-00980

139. Mohammad HMF, Galal Gouda S, Eladl MA, Elkazaz AY, Elbayoumi KS, Farag NE, et al. Metformin suppresses LRG1 and TGFβ1/ALK1-induced angiogenesis and protects against ultrastructural changes in rat diabetic nephropathy. *Biomed Pharmacother*. (2023) 158:114128. doi: 10.1016/j.biopha.2022.114128

140. Chung JO, Park SY, Cho DH, Chung DJ, Chung MY. Relationship between plasma leucine-rich α-2-glycoprotein 1 and urinary albumin excretion in patients with type 2 diabetes. *Front Endocrinol (Lausanne)*. (2023) 14:1232021. doi: 10.3389/fendo.2023.1232021

141. Popova A, Vasiļvolfa A, Rācenis K, Erts R, Šlisere B, Saulīte AJ, et al. Leucine-rich alpha-2-glycoprotein (LRG-1) as a potential kidney injury marker in kidney transplant recipients. *Ann Transplant*. (2022) 27:e936751. doi: 10.12659/aot.936751

142. Low S, Moh A, Pandian B, Tan XL, Pek S, Zheng H, et al. Association between plasma LRG1 and lower cognitive function in Asians with type 2 diabetes mellitus. *J Clin Endocrinol Metab*. (2024):dgad768. doi: 10.1210/clinem/dgad768

143. Kropski JA, Richmond BW, Gaskill CF, Foronjy RF, Majka SM. Deregulated angiogenesis in chronic lung diseases: a possible role for lung mesenchymal progenitor cells (2017 Grover conference series). *Pulm Circ*. (2018) 8 (1):2045893217739807. doi: 10.1177/2045893217739807

144. Lucas A, Yasa J, Lucas M. Regeneration and repair in the healing lung. *Clin Transl Immunol*. (2020) 9(7):e1152. doi: 10.1002/cti2.1152

145. Ishida T, Kotani T, Serada S, Fujimoto M, Takeuchi T, Makino S, et al. Correlation of increased serum leucine-rich α2-glycoprotein levels with disease prognosis, progression, and activity of interstitial pneumonia in patients with dermatomyositis: a retrospective study. *PLoS One*. (2020) 15(6):e0234090. doi: 10.1371/journal.pone.0234090

146. Fujimoto M, Matsumoto T, Serada S, Tsujimura Y, Hashimoto S, Yasutomi Y, et al. Leucine-rich alpha 2 glycoprotein is a new marker for active disease of tuberculosis. *Sci Rep*. (2020) 10(1):3384. doi: 10.1038/s41598-020-60450-3

147. Tan DBA, Ito J, Peters K, Livk A, Lipscombe RJ, Casey TM, et al. Protein network analysis identifies changes in the level of proteins involved in platelet degranulation, proteolysis and cholesterol metabolism pathways in AECOPD patients. *COPD*. (2020) 17(1):29–33. doi: 10.1080/15412555.2019.1711035

148. Schiff HF, Walker NF, Ugarte-Gil C, Tebruegge M, Manousopoulou A, Garbis SD, et al. Integrated plasma proteomics identifies tuberculosis-specific diagnostic biomarkers. *JCI Insight*. (2024):e173273. doi: 10.1172/jci.insight.173273

149. Christenson SA, Smith BM, Bafadhel M, Putcha N. Chronic obstructive pulmonary disease. *Lancet*. (2022) 399(10342):2227–42. doi: 10.1016/S0140-6736(22)00470-6

150. He M, Borlak J. A genomic perspective of the aging human and mouse lung with a focus on immune response and cellular senescence. *Immun Ageing*. (2023) 20(1):58. doi: 10.1186/s12979-023-00373-5

151. Messner CB, Demichev V, Wendisch D, Michalick L, White M, Freiwald A, et al. Ultra-high-throughput clinical proteomics reveals classifiers of COVID-19 infection. *Cell Syst*. (2020) 11(1):11–24.e4. doi: 10.1016/j.cels.2020.05.012

152. Demichev V, Tober-Lau P, Nazarenko T, Lemke O, Kaur Aulakh S, Whitwell HJ, et al. A proteomic survival predictor for COVID-19 patients in intensive care. *PLoS Digit Health*. (2022) 1(1):e0000007. doi: 10.1371/journal.pdig.0000007

153. Nie X, Qian L, Sun R, Huang B, Dong X, Xiao Q, et al. Multi-organ proteomic landscape of COVID-19 autopsies. *Cell*. (2021) 184(3):775–91.e14. doi: 10.1016/j.cell.2021.01.004

154. Mohammed Y, Goodlett DR, Cheng MP, Vinh DC, Lee TC, McGeer A, et al. Longitudinal plasma proteomics analysis reveals novel candidate biomarkers in acute COVID-19. *J Proteome Res*. (2022) 21(4):975–92. doi: 10.1021/acs.jproteome.1c00863

155. Park J, Kim H, Kim SY, Kim Y, Lee J-S, Dan K, et al. In-depth blood proteome profiling analysis revealed distinct functional characteristics of plasma proteins between severe and non-severe COVID-19 patients. *Sci Rep*. (2020) 10(1):22418. doi: 10.1038/s41598-020-80120-8

156. Pagani L, Chinello C, Risca G, Capitoli G, Criscuolo L, Lombardi A, et al. Plasma proteomic variables related to COVID-19 severity: an untargeted nLC-MS/MS investigation. *Int J Mol Sci*. (2023) 24(4):3570. doi: 10.3390/ijms24043570

157. Henderson LA, Canna SW, Schulert GS, Volpi S, Lee PY, Kernan KF, et al. On the alert for cytokine storm: immunopathology in COVID-19. *Arthritis Rheumatol*. (2020) 72(7):1059–63. doi: 10.1002/art.41285

158. Mangalmurti N, Hunter CA. Cytokine storms: understanding COVID-19. *Immunity*. (2020) 53(1):19–25. doi: 10.1016/j.immuni.2020.06.017

159. Santa Cruz A, Mendes-Frias A, Oliveira AI, Dias L, Matos AR, Carvalho A, et al. Interleukin-6 is a biomarker for the development of fatal severe acute respiratory syndrome coronavirus 2 pneumonia. *Front Immunol*. (2021) 12:613422. doi: 10.3389/fimmu.2021.613422

160. Han H, Ma Q, Li C, Liu R, Zhao L, Wang W, et al. Profiling serum cytokines in COVID-19 patients reveals IL-6 and IL-10 are disease severity predictors. *Emerg Microbes Infect*. (2020) 9(1):1123–30. doi: 10.1080/22221751.2020.1770129

161. Garbers C, Heink S, Korn T, Rose-John S. Interleukin-6: designing specific therapeutics for a complex cytokine. *Nat Rev Drug Discov*. (2018) 17(6):395–412. doi: 10.1038/nrd.2018.45

162. Rose-John S. Blocking only the bad side of IL-6 in inflammation and cancer. *Cytokine*. (2021) 148:155690. doi: 10.1016/j.cyto.2021.155690

163. Kaye AG, Siegel R. The efficacy of il-6 inhibitor tocilizumab in reducing severe COVID-19 mortality: a systematic review. *PeerJ*. (2020) 8:e10322. doi: 10.7717/peerj.10322

164. Campochiaro C, Dagna L. The conundrum of interleukin-6 blockade in COVID-19. *Lancet Rheumatol*. (2020) 2(10):e579–e80. doi: 10.1016/S2665-9913(20)30287-3

165. Rubin EJ, Longo DL, Baden LR. Interleukin-6 receptor inhibition in COVID-19—cooling the inflammatory soup. *N Engl J Med*. (2021) 384(16):1564–5. doi: 10.1056/NEJMe2103108

166. Murthy S, Lee TC. Il-6 blockade for COVID-19: a global scientific call to arms. *Lancet Respir Med*. (2021) 9(5):438–40. doi: 10.1016/S2213-2600(21)00127-2

167. Serada S, Fujimoto M, Ogata A, Terabe F, Hirano T, Iijima H, et al. iTRAQ-based proteomic identification of leucine-rich alpha-2 glycoprotein as a novel inflammatory biomarker in autoimmune diseases. *Ann Rheum Dis*. (2010) 69 (4):770–4. doi: 10.1136/ard.2009.118919

168. Muruganandam M, Ariza-Hutchinson A, Patel RA, Sibbitt WL Jr. Biomarkers in the pathogenesis, diagnosis, and treatment of systemic sclerosis. *J Inflamm Res*. (2023) 16:4633–60. doi: 10.2147/jir.S379815

169. Bălănescu P, Bălănescu E, Băicuş C, Bălănescu A. Circulatory cytokeratin 17, marginal zone B1 protein and leucine-rich α2-glycoprotein-1 as biomarkers for disease severity and fibrosis in systemic sclerosis patients. *Biochem Med (Zagreb)*. (2022) 32(3):030707. doi: 10.11613/bm.2022.030707

170. Kawanami T, Kawanami-Iwao H, Takata T, Ishigaki Y, Tomosugi N, Takegami T, et al. Comprehensive analysis of protein-expression changes specific to immunoglobulin G4-related disease. *Clin Chim Acta*. (2021) 523:45–57. doi: 10.1016/j.cca.2021.08.025

171. Sun Y, Wang F, Zhou Z, Teng J, Su Y, Chi H, et al. Urinary proteomics identifying novel biomarkers for the diagnosis of adult-onset still's disease. *Front Immunol*. (2020) 11:2112. doi: 10.3389/fimmu.2020.02112

172. Shimizu M, Inoue N, Mizuta M, Nakagishi Y, Yachie A. Serum leucine-rich α2-glycoprotein as a biomarker for monitoring disease activity in patients with systemic juvenile idiopathic arthritis. *J Immunol Res*. (2019) 2019:3140204. doi: 10.1155/2019/3140204

173. Fujimoto M, Serada S, Suzuki K, Nishikawa A, Ogata A, Nanki T, et al. Leucine-rich α2 -glycoprotein as a potential biomarker for joint inflammation during anti-interleukin-6 biologic therapy in rheumatoid arthritis. *Arthritis Rheumatol*. (2015) 67(8):2056–60. doi: 10.1002/art.39164

174. Tintor G, Jukić M, Šupe-Domić D, Jerončić A, Pogorelić Z. Diagnostic utility of serum leucine-rich α-2-glycoprotein 1 for acute appendicitis in children. *J Clin Med*. (2023) 12(7):2455. doi: 10.3390/jcm12072455

175. Aguilar-Cazares D, Chavez-Dominguez R, Carlos-Reyes A, Lopez-Camarillo C, Hernadez de la Cruz ON, Lopez-Gonzalez JS. Contribution of angiogenesis to inflammation and cancer. *Front Oncol*. (2019) 9:1399. doi: 10.3389/fonc.2019.01399

176. Alfaro S, Acuña V, Ceriani R, Cavieres MF, Weinstein-Oppenheimer CR, Campos-Estrada C. Involvement of inflammation and its resolution in disease and therapeutics. *Int J Mol Sci*. (2022) 23(18):10719. doi: 10.3390/ijms231810719

177. Mapp PI, Walsh DA. Mechanisms and targets of angiogenesis and nerve growth in osteoarthritis. *Nat Rev Rheumatol*. (2012) 8(7):390–8. doi: 10.1038/nrrheum.2012.80

178. Liu X, Liu R, Croker BA, Lawlor KE, Smyth GK, Wicks IP. Distinctive pro-inflammatory gene signatures induced in articular chondrocytes by oncostatin M and il-6 are regulated by suppressor of cytokine signaling-3. *Osteoarthritis Cartilage*. (2015) 23(10):1743–54. doi: 10.1016/j.joca.2015.05.011

179. Kapoor M, Martel-Pelletier J, Lajeunesse D, Pelletier JP, Fahmi H. Role of proinflammatory cytokines in the pathophysiology of osteoarthritis. *Nat Rev Rheumatol*. (2011) 7(1):33–42. doi: 10.1038/nrrheum.2010.196

180. Marrelli A, Cipriani P, Liakouli V, Carubbi F, Perricone C, Perricone R, et al. Angiogenesis in rheumatoid arthritis: a disease specific process or a common response to chronic inflammation? *Autoimmun Rev*. (2011) 10(10):595–8. doi: 10.1016/j.autrev.2011.04.020

181. Yanagimachi M, Fukuda S, Tanaka F, Iwamoto M, Takao C, Oba K, et al. Leucine-rich alpha-2-glycoprotein 1 and angiotensinogen as diagnostic biomarkers for Kawasaki disease. *PLoS One*. (2021) 16(9):e0257138. doi: 10.1371/journal.pone.0257138

182. Kimura Y, Yanagimachi M, Ino Y, Aketagawa M, Matsuo M, Okayama A, et al. Identification of candidate diagnostic serum biomarkers for Kawasaki disease using proteomic analysis. *Sci Rep*. (2017) 7:43732. doi: 10.1038/srep43732

183. Xie XF, Chu HJ, Xu YF, Hua L, Wang ZP, Huang P, et al. Proteomics study of serum exosomes in Kawasaki disease patients with coronary artery aneurysms. *Cardiol J*. (2019) 26(5):584–93. doi: 10.5603/CJ.a2018.0032

184. Kessel C, Koné-Paut I, Tellier S, Belot A, Masjosthusmann K, Wittkowski H, et al. An immunological axis involving interleukin 1β and leucine-rich-α2-glycoprotein reflects therapeutic response of children with Kawasaki disease: implications from the Kawakinra trial. *J Clin Immunol*. (2022) 42(6):1330–41. doi: 10.1007/s10875-022-01301-w

185. Umezawa N, Mizoguchi F, Maejima Y, Kimura N, Hasegawa H, Hosoya T, et al. Leucine-rich alpha-2 glycoprotein as a potential biomarker for large vessel vasculitides. *Front Med (Lausanne)*. (2023) 10:1153883. doi: 10.3389/fmed.2023.1153883

186. Ishizaki J, Takemori A, Suemori K, Matsumoto T, Akita Y, Sada KE, et al. Targeted proteomics reveals promising biomarkers of disease activity and organ involvement in antineutrophil cytoplasmic antibody-associated vasculitis. *Arthritis Res Ther*. (2017) 19(1):218. doi: 10.1186/s13075-017-1429-3

187. Kronbichler A, Lee KH, Denicolò S, Choi D, Lee H, Ahn D, et al. Immunopathogenesis of ANCA-associated vasculitis. *Int J Mol Sci*. (2020) 21 (19):7319. doi: 10.3390/ijms21197319

188. Sorriento D, Iaccarino G. Inflammation and cardiovascular diseases: the most recent findings. *Int J Mol Sci*. (2019) 20(16):3879. doi: 10.3390/ijms20163879

189. Pang KT, Ghim M, Liu C, Tay HM, Fhu CW, Chia RN, et al. Leucine-rich α-2-glycoprotein 1 suppresses endothelial cell activation through Adam10-mediated shedding of TNF-α receptor. *Front Cell Dev Biol*. (2021) 9:706143. doi: 10.3389/fcell.2021.706143

190. Behzadifard M, Soleimani M. NETosis and SARS-COV-2 infection related thrombosis: a narrative review. *Thromb J*. (2022) 20(1):13. doi: 10.1186/s12959-022-00375-1

191. Vorobjeva NV, Chernyak BV. NETosis: molecular mechanisms, role in physiology and pathology. *Biochemistry (Mosc)*. (2020) 85(10):1178–90. doi: 10.1134/s0006297920100065

192. Mutua V, Gershwin LJ. A review of neutrophil extracellular traps (NETS) in disease: potential anti-nets therapeutics. *Clin Rev Allergy Immunol*. (2021) 61 (2):194–211. doi: 10.1007/s12016-020-08804-7

193. Lin M, Liu J, Zhang F, Qi G, Tao S, Fan W, et al. The role of leucine-rich alpha-2-glycoprotein-1 in proliferation, migration, and invasion of tumors. *J Cancer Res Clin Oncol*. (2022) 148(2):283–91. doi: 10.1007/s00432-021-03876-0

194. Göbel A, Rachner TD, Hoffmann O, Klotz DM, Kasimir-Bauer S, Kimmig R, et al. High serum levels of leucine-rich α-2 glycoprotein 1 (LRG-1) are associated with poor survival in patients with early breast cancer. *Arch Gynecol Obstet*. (2024). doi: 10.1007/s00404-024-07434-0

195. Andersen JD, Boylan KL, Jemmerson R, Geller MA, Misemer B, Harrington KM, et al. Leucine-rich alpha-2-glycoprotein-1 is upregulated in sera and tumors of ovarian cancer patients. *J Ovarian Res*. (2010) 3:21. doi: 10.1186/1757-2215-3-21

196. Choi YJ, Yoon W, Lee A, Han Y, Byun Y, Kang JS, et al. Diagnostic model for pancreatic cancer using a multi-biomarker panel. *Ann Surg Treat Res*. (2021) 100 (3):144–53. doi: 10.4174/astr.2021.100.3.144

197. Ladd JJ, Busald T, Johnson MM, Zhang Q, Pitteri SJ, Wang H, et al. Increased plasma levels of the APC-interacting protein MAPRE1, LRG1, and IGFBP2 preceding a diagnosis of colorectal cancer in women. *Cancer Prev Res (Phila)*. (2012) 5 (4):655–64. doi: 10.1158/1940-6207.Capr-11-0412

198. Lee DH, Yoon W, Lee A, Han Y, Byun Y, Kang JS, et al. Multi-biomarker panel prediction model for diagnosis of pancreatic cancer. *J Hepatobiliary Pancreat Sci*. (2023) 30(1):122–32. doi: 10.1002/jhbp.986

199. Walker MJ, Zhou C, Backen A, Pernemalm M, Williamson AJ, Priest LJ, et al. Discovery and validation of predictive biomarkers of survival for non-small cell lung cancer patients undergoing radical radiotherapy: two proteins with predictive value. *EBioMedicine*. (2015) 2(8):841–50. doi: 10.1016/j.ebiom.2015.06.013

200. Wu J, Yin H, Zhu J, Buckanovich RJ, Thorpe JD, Dai J, et al. Validation of LRG1 as a potential biomarker for detection of epithelial ovarian cancer by a blinded study. *PLoS One*. (2015) 10(3):e0121112. doi: 10.1371/journal.pone.0121112

201. Luan L, Hu Q, Wang Y, Lu L, Ling J. Knockdown of lncRNA NEAT1 expression inhibits cell migration, invasion and EMT by regulating the miR-24-3p/LRG1 axis in retinoblastoma cells. *Exp Ther Med*. (2021) 21(4):367. doi: 10.3892/etm.2021.9798

202. Rathore M, Wright M, Martin D, Huang W, Taylor D, Miyagi M, et al. LRG1 is a novel Her3 ligand to promote growth in colorectal cancer. *J bioRxiv*. (2023):2023.02.18.529070. doi: 10.1101/2023.02.18.529070

203. Zhang Y, Luo Q, Wang N, Hu F, Jin H, Ge T, et al. LRG1 suppresses the migration and invasion of hepatocellular carcinoma cells. *Med Oncol*. (2015) 32 (5):146. doi: 10.1007/s12032-015-0598-7

204. Jain RK. Normalizing tumor microenvironment to treat cancer: bench to bedside to biomarkers. *J Clin Oncol*. (2013) 31(17):2205–18. doi: 10.1200/jco.2012.46.3653

205. Wicks EE, Semenza GL. Hypoxia-inducible factors: cancer progression and clinical translation. *J Clin Invest*. (2022) 132(11):e159839. doi: 10.1172/jci159839

206. Magnussen AL, Mills IG. Vascular normalisation as the stepping stone into tumour microenvironment transformation. *Br J Cancer*. (2021) 125(3):324–36. doi: 10.1038/s41416-021-01330-z

207. Martin JD, Seano G, Jain RK. Normalizing function of tumor vessels: progress, opportunities, and challenges. *Annu Rev Physiol*. (2019) 81:505–34. doi: 10.1146/annurev-physiol-020518-114700

208. Teuwen LA, De Rooij L, Cuypers A, Rohlenova K, Dumas SJ, García-Caballero M, et al. Tumor vessel co-option probed by single-cell analysis. *Cell Rep*. (2021) 35 (11):109253. doi: 10.1016/j.celrep.2021.109253

209. Amer R, Tiosano L, Pe'er J. Leucine-rich α-2-glycoprotein-1 (LRG-1) expression in retinoblastoma. *Invest Ophthalmol Visual Sci*. (2018) 59(2):685–92. doi: 10.1167/iovs.17-22785

210. Murgai M, Ju W, Eason M, Kline J, Beury DW, Kaczanowska S, et al. KLF4-dependent perivascular cell plasticity mediates pre-metastatic niche formation and metastasis. *Nat Med*. (2017) 23(10):1176–90. doi: 10.1038/nm.4400

Frontiers in Cardiovascular Medicine

TYPE Original Research
PUBLISHED 20 June 2024
DOI 10.3389/fcvm.2024.1395036

OPEN ACCESS

EDITED BY
Yun Fang,
The University of Chicago, United States

REVIEWED BY
Sun-Joo Jang,
Yale University, United States
Mete Civelek,
University of Virginia, United States

*CORRESPONDENCE
Marie A. Guerraty
✉ marie.guerraty@pennmedicine.upenn.edu

RECEIVED 02 March 2024
ACCEPTED 07 June 2024
PUBLISHED 20 June 2024

CITATION
Wayne N, Wu Q, Moore SC, Ferrari VA, Metzler SD and Guerraty MA (2024) Multimodality assessment of the coronary microvasculature with TIMI frame count versus perfusion PET highlights coronary changes characteristic of coronary microvascular disease.
Front. Cardiovasc. Med. 11:1395036.
doi: 10.3389/fcvm.2024.1395036

# Multimodality assessment of the coronary microvasculature with TIMI frame count versus perfusion PET highlights coronary changes characteristic of coronary microvascular disease

Nicole Wayne[1], Qufei Wu[2], Stephen C. Moore[3], Victor A. Ferrari[1], Scott D. Metzler[3] and Marie A. Guerraty[1]*

[1]Department of Medicine, University of Pennsylvania Perelman School of Medicine, Philadelphia, PA, United States, [2]Center for Clinical Epidemiology and Biostatistics, University of Pennsylvania Perelman School of Medicine, Philadelphia, PA, United States, [3]Department of Radiology, University of Pennsylvania Perelman School of Medicine, Philadelphia, PA, United States

**Background:** The diagnosis of coronary microvascular disease (CMVD) remains challenging. Perfusion PET-derived myocardial blood flow (MBF) reserve (MBFR) can quantify CMVD but is not widely available. Thrombolysis in Myocardial Infarction (TIMI) frame count (TFC) is an angiography-based method that has been proposed as a measure of CMVD. Here, we compare TFC and PET-derived MBF measurements to establish the role of TFC in assessing for CMVD. We use coronary modeling to elucidate the relationship between MBFR and TFC and propose TFC thresholds for identifying CMVD.
**Methods:** In a cohort of 123 individuals (age 58 ± 12.1, 63% women, 41% Caucasian) without obstructive coronary artery disease who had undergone perfusion PET and coronary angiography for clinical indications, we compared TFC and perfusion PET parameters using Pearson correlation (PCC) and linear regression modeling. We used mathematical modeling of the coronary circulation to understand the relationship between these parameters and performed Receiver Operating Curve (ROC) analysis.
**Results:** We found a significant negative correlation between TFC and MBFR. Sex, race and ethnicity, and nitroglycerin administration impact this relationship. Coronary modeling showed an uncoupling between TFC and flow in epicardial vessels. In ROC analysis, TFC performed well in women (AUC 0.84–0.89) and a moderately in men (AUC 0.68–0.78).
**Conclusions:** We established an inverse relationship between TFC and PET-derived MBFR, which is affected by patient selection and procedural factors. TFC represents a measure of the volume of the epicardial coronary compartment, which is increased in patients with CMVD, and performs well in identifying women with CMVD.

KEYWORDS

TIMI frame count, cardiac perfusion PET, coronary microvascular disease, myocardial blood flow (MBF), imaging

---

Abbreviations
TFC, thrombolysis in myocardial infarction frame count; PET, positron emission tomography; MBF(R), myocardial blood flow (reserve); CMVD, coronary microvascular disease; PCC, pearson correlation coefficient; NTG, nitroglycerin; RCA, right coronary artery; LCX, left circumflex artery; LAD, left anterior descending artery.

# Introduction

Coronary microvascular disease (CMVD) leads to angina, myocardial infarction, and heart failure (1, 2). CMVD also worsens the prognosis in patients with coronary artery disease (CAD) and is an independent risk factor for major adverse cardiovascular events (3, 4). However, challenges in diagnosing CMVD have limited both research efforts and clinical care of individuals with suspected or confirmed CMVD. Furthermore, although the prevalence of CMVD is similar in men and in women (5), the under-diagnosis of CMVD in women contributes to the discrepant burdens of untreated heart disease between women and men (1, 2, 6, 7).

Recent advances in imaging technology have allowed researchers to study and diagnose CMVD. Positron emission tomography (PET) perfusion imaging allows for the quantification of myocardial blood flow (MBF) and MBF reserve (MBFR), the ratio of MBF during hyperemic or stress conditions and rest MBF. In the absence of obstructive epicardial coronary stenoses, MBFR reflects coronary microvascular function, or the ability of the coronary microvasculature to vasodilate appropriately. PET is the current gold standard for non-invasive diagnosis of CMVD, but its availability is limited to selected tertiary care centers (8). Studies have established PET imaging as a reliable tool for detecting coronary microvascular dysfunction, and MBFR $< 2$ is often used as a measure of CMVD (9–12), and predicts adverse cardiovascular outcomes in patients (13). Other imaging modalities to diagnose CMVD are actively being studied and developed, including magnetic resonance imaging, echo doppler, and computed tomography (CT)-based techniques (8, 14, 15).

Coronary-angiography-based techniques have also been developed to assess the coronary microvasculature. Thrombolysis in Myocardial Infarction (TIMI) frame count (TFC) estimates the amount of time that contrast material takes to fill the epicardial vessels during a coronary angiogram. High TFC is associated with worse prognosis in the context of myocardial infarction and has also been shown to be an independent prognostic indicator of adverse events in women with signs and symptoms of ischemia without obstructive CAD (3, 16, 17). TFC also correlates well with invasive measures of coronary flow, such as average peak velocity (15, 16, 18, 19) and is associated with clinical outcomes, such as hospitalizations for chest pain (20). Coronary Vasomotion Disorders International Study recommendations recognize Coronary Slow Flow Phenomenon (defined as corrected TFC $> 27$) as evidence of impaired microvascular dysfunction which can be equated to a diagnosis of CMVD (15, 19, 21). Furthermore, whereas access to perfusion PET is limited by cost and availability, TFC is available for all patients undergoing coronary angiography and provides gold-standard epicardial CAD assessment along with measures of the coronary microvasculature. However, a recent study found that in patients with angina and non-obstructed coronary arteries, corrected TFC was not diagnostic of CMVD (22). Another study evaluated the correlation between coronary flow velocity reserve and TFC in patients undergoing non-emergent percutaneous coronary intervention (PCI) and found no correlation (23). Thus, despite the potential of TFC to be used in the diagnosis of CMVD (3, 24), it has not been widely adopted.

In this study, we compare PET myocardial blood flow values to TFC to gain insight into TFC measurements. We also use coronary flow modeling to better understand the relationship between TFC and flow parameters and reconcile disparate data. We then assess the effect of sex, race and ethnicity, and nitroglycerin administration on the relationship between TFC and flow parameters. Finally, we propose TFC thresholds that may in time be useful for clinically identifying CMVD and provide important context for interpreting TFC.

# Methods

## Population

We identified 350 patients who underwent both Rubidium-82 (Rb-82) perfusion PET stress testing and coronary angiography from 2012 to 2015 at the University of Pennsylvania Health System for clinical indications as part of routine medical care. We excluded those with prior heart transplantation, obstructive CAD on angiography (defined as >50% stenosis according to performing physician), or poor image quality on perfusion PET or coronary angiogram. TFC and Perfusion PET data were collected for the remaining 123 patients (age $58 \pm 12.1$, 63% women).

## Consent

The study was approved by the University of Pennsylvania Institutional Review Board and no informed consent was required for this retrospective study using data from the Electronic Health Record.

## Rubidium-82 (Rb-82) cardiac PET perfusion imaging

Patients underwent $^{82}$Rb cardiac PET perfusion imaging under both rest and dipyridamole-induced stress conditions using a Siemens Biograph mCT PET/CT scanner. Briefly, low dose CT images were acquired for attenuation correction. Rest images were obtained with a 6 min list-mode dynamic PET acquisition imaging while 30 mCi of $^{82}$Rb was injected intravenously as a fast bolus. Dipyridamole (0.56 mg/kg) was then administered and dynamic PET imaging was repeated with an additional 30 mCi of $^{82}$Rb three minutes after the completion of the infusion. Iterative reconstruction was performed with 2 iterations and the matrix size of $128 \times 128$ (25, 26). Global and regional MBF and MBFR were calculated using Syngo® MBF software (27). MBF was quantified using Syngo MBF, which uses a 2-compartement model developed by Hutchins et al. (28).

## TIMI frame count (TFC)

Clinical coronary angiography images were used to measure TFC using anatomic landmarks outlined in Gibson et al. (3) Coronary angiograms were acquired during routine clinical care with a frame rate of 15 frames per second, and multiplied by 2 to calculate TFC. Since TFC is determined for each of the three coronary arteries, we included patients even when TFC was only available for two coronary arteries. A TFC was not measured in a coronary territory when image quality was poor or image availability was limited. Coronary angiograms were acquired within 12 months of PET scans. TFC was measured by an investigator blinded to PET parameters. TFC was measured using the coronary angiographic projection that best visualized proximal and distal landmarks.

## Computational coronary modeling

We implemented a modified version of the Zhou-Kassab-Molloi (ZKM) symmetric coronary-tree model, including 24 Strahler levels (or vessel sizes) with coronary branching based on anatomical observations (29) (more details of the implementation are in Supplementary Figure S1). Our implementation of this model included 24 Strahler levels (or vessel sizes), where the length and volume of each was estimated (Supplementary Figure S1A–C). The flow is computed as MBF = P/R, where P is the driving pressure (100 mmHg) and R is the tree resistance. R is calculated using Poiseuille's Law to determine the resistance of each Strahler level and combining segments of the same level in parallel and different levels in series. TFC is modeled as the time to fill the two largest Strahler levels. The model was modified from ZKM (29) by allowing the individual levels to contract and dilate from their nominal vessel diameters to determine the impact of MBF and TFC.

## Statistics

The relationship between TFC from different territories was analyzed using Pearson correlation coefficient (PCC). The relationship between TFC and MBF/MBFR was analyzed using linear regression analysis, and stratified by sex, race and ethnicity, and whether nitroglycerin was used during the procedure. Multivariant linear regression modeling was performed using SAS Version 9.4. Absolute numbers and percentages were used to describe the patient population. Continuous variables were expressed as mean ± standard deviation. *T*-test was used to compare groups, and $P < 0.05$ was considered significant. Adjusting MBF by heart rate-blood pressure product did not alter the results, and therefore the unadjusted MBF values are presented. Receiver operating curves (ROC) were generated and fitted using the maximum-likelihood approach (30) implemented in the program LABROC, which is available as part of the Metz ROC Software (University of Chicago). The ROC data were fitted using a semi-parametric method, "proper" binormal model (31), and the inverse information matrix was used to estimate parameter uncertainties. Area Under the Curve (AUC) is presented and $P < 0.05$ was considered significant.

## Results

We identified a cohort of 123 patients (age 58 ± 12.1, 63% women) who were eligible for this study (Table 1). This population was racially and ethnically diverse (54% black) with high prevalence of cardiovascular risk factors. There were a similar number of patients with and without CMVD. CMVD was defined as MBFR <2 on perfusion PET stress test.

Because patients with CAD were excluded, there was a strong positive correlation between the global MBFR and regional MBFR for each coronary territory, with PCC 0.91, 0.96, and 0.97 for the right coronary artery (RCA), left circumflex artery (LCX) and left anterior descending artery (LAD), respectively. There was a positive, although weaker, correlation in TFC between different regions (LAD vs. LCx: PCC = 0.76; LAD vs. RCA: PCC = 0.67; LCx vs. RCA: PCC = 0.65) ($p < 0.0001$ for all territories) (Figure 1).

We next compared the relationship between TFC for each coronary artery and corresponding regional MBFR. We found an inverse relationship with PCC −0.51, −0.54, and −0.51 for RCA, LCX, and LAD, respectively (Figure 2A, $p < 0.0001$ for all). We next examined the two components that comprise MBFR: rest MBF and stress MBF. There was no statistically significant correlation between TFC and rest MBF in all patients, but there was a trend towards increasing TFC with higher rest MBF in LAD and LCX. PCC between TFC and rest MBF were 0.127 ($p = 0.17$), −0.04 ($p = 0.67$), and 0.108 ($p = 0.24$) for LAD, RCA, and LCX, respectively (Figure 2B). There was a slight negative relationship between TFC and stress flows with correlations of −0.364, −0.512, −0.384 in LAD, RCA, and LCX, respectively (Figure 2C, $p < 0.0001$ for all).

TABLE 1 Population demographics.

| Characteristic | Total: $N = 124$ (%) | Men: $N = 46$ (%) | Women: $N = 78$ (%) |
|---|---|---|---|
| Age | 58 ± 12.1 | 58 ± 12.5 | 59 ± 12.0 |
| Race | | | |
| Asian | 3 (2.42%) | 1 (2.2%) | 2 (2.6%) |
| Hispanic | 3 (2.42%) | 0 (0%) | 3 (3.8%) |
| Black | 67 (54.03%) | 23 (50%) | 44 (56.4%) |
| White | 51 (41.13%) | 27 (58.7%) | 24 (30.8%) |
| BMI (mean ± SD) | 38.1 ± 9.7 | 36.3 ± 9.7 | 39.1 ± 9.8 |
| Hyperlipidemia | 97 (78.23%) | 36 (78.3%) | 60 (76.9%) |
| Hypertension | 115 (92.74%) | 39 (84.8%) | 76 (97.4%) |
| Diabetes Mellitus | 57 (45.97%) | 20 (43.5%) | 37 (47.4%) |
| Tobacco use (ever) | 36 (29.03%) | 14 (30.4%) | 22 (28.2%) |
| Abnormal global MBFR (defined as MBFR < 2) | 69 (55.6%) | 24 (52.2%) | 45 (57.7%) |
| LAD mean TFC (mean ± SD) | 36 ± 9.1 | 39.4 ± 11.6 | 33.9 ± 6.6 |
| LCX mean TFC (mean ± SD) | 34 ± 7.5 | 35.3 ± 9.0 | 32.9 ± 6.5 |
| RCA mean TFC (mean ± SD) | 36 ± 8.2 | 38.3 ± 10.2 | 34.4 ± 6.5 |

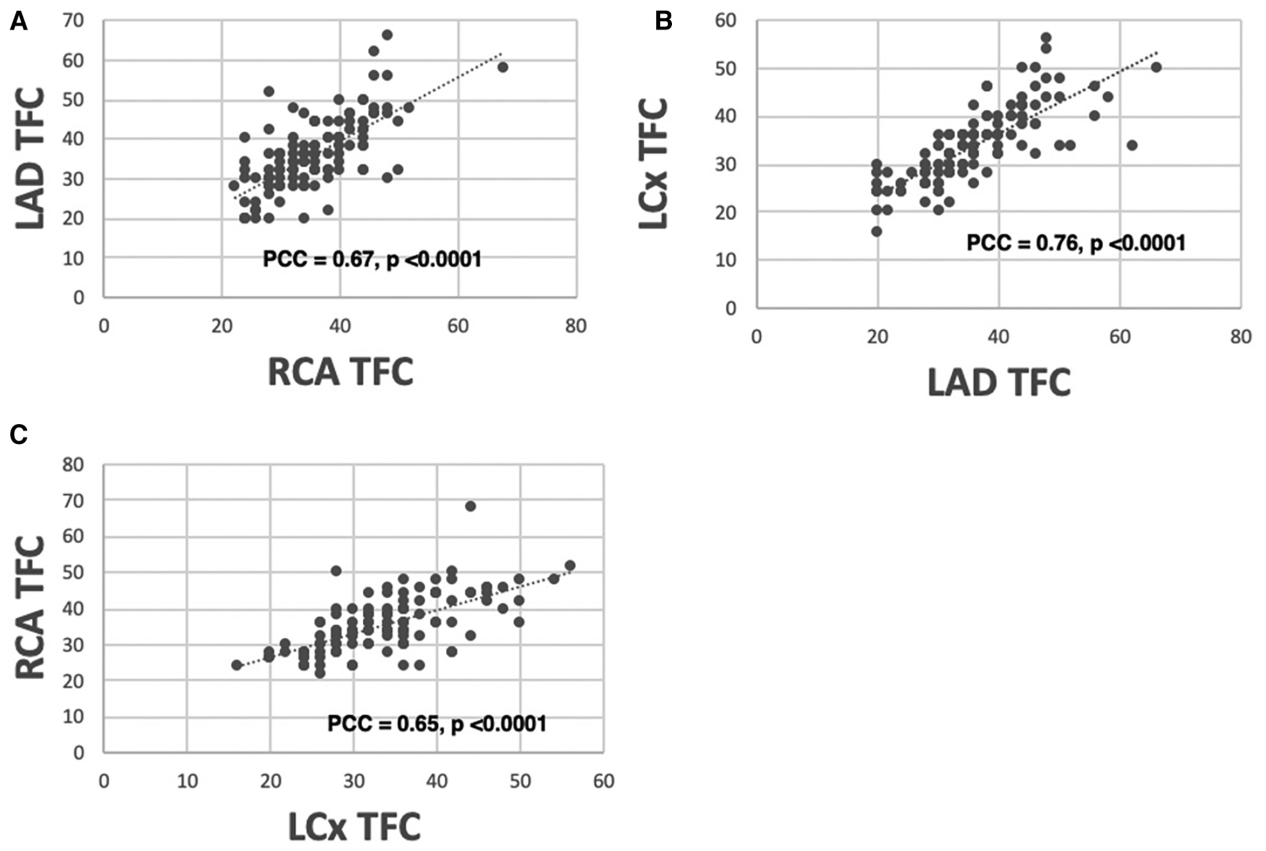

FIGURE 1
Correlation between TFC measured from different coronary territories. There is a high correlation between TFC obtained from LAD vs. RCA [(A) PCC = 0.67], LAD vs. LCX [(B) PCC = 0.76], and RCA vs. LCX [(C) PCC = 0.65].

The strong inverse relationship between MBFR and TFC was counterintuitive. TFC is a measure of how much time is required for epicardial coronary arteries to fill with contrast and has been linked to coronary flow measurements. Depending on the dose and type of moderate sedation used during the coronary angiogram, this may represent a rest or stress (hyperemic) state. However, we found a stronger association with MBFR, which is a unitless ratio and reflects the ability of the coronary microvasculature to vasodilate. To better understand the association between MBFR and TFC, and to reconcile disparate results with prior published work (22), we turned to coronary flow modeling.

We used a modified Zhou-Kassab-Molloi (ZKM) model (29) of the coronary circulation to investigate the association between MBFR and TFC. Figure 3 shows how TFC and flow varied as the diameters of the two largest and two smallest vessel levels are varied, with all other levels unchanged. In the largest vessels, there was minimal change in flow over a large range of diameters (Figures 3C,D), consistent with known coronary physiology where the large epicardial vessels are not the primary regulators of coronary flow. When looking at all 24 Strahler levels (or coronary vessel diameters), we found that TFC and blood flow were inversely correlated at all levels except the two largest diameter vessel compartments (Supplementary Figure S2). These are the epicardial coronaries visualized by coronary angiography and in which TFC is measured. Coronary modeling shows an uncoupling of blood flow and TFC in these largest vessels, suggesting TFC is predominantly affected by the volume of the epicardial coronary compartment rather than the flow rate. Thus, CMVD may result in larger proximal vessels due to remodeling, so that even though the flow rate is larger at rest (as measured by MBF), the clearance of contrast from the epicardial vessels (as measured by TFC) is decreased (Figure 3E).

Based on this model, we expect the relationship between TFC and MBFR to be stronger in patients with CMVD (MBFR <2). We therefore determined whether the degree of CMVD (defined as MBFR < 2) affected the correlation between MBFR and TFC. In all coronary territories, the correlation between MBFR and TFC was stronger in those with MBFR < 2 (LAD PCC −0.371 vs. −0.217, LCx PCC −0.454 vs. −0.293, RCA PCC −0.572 vs. −0.077; $p < 0.0001$ for MBFR < 2 vs. ≥2, respectively) (Figures 4A–C). This result gives insight into discrepant results between studies, since the relationship between TFC and MBFR depends on the prevalence of cardiovascular risk factors and CMVD (MBFR < 2) in the study population.

Since modeling showed that TFC is predominantly a measure of the volume of the epicardial compartment, medications that directly vasodilate the proximal coronaries, such as nitroglycerin (NTG), may affect TFC measurements. Therefore, we analyzed

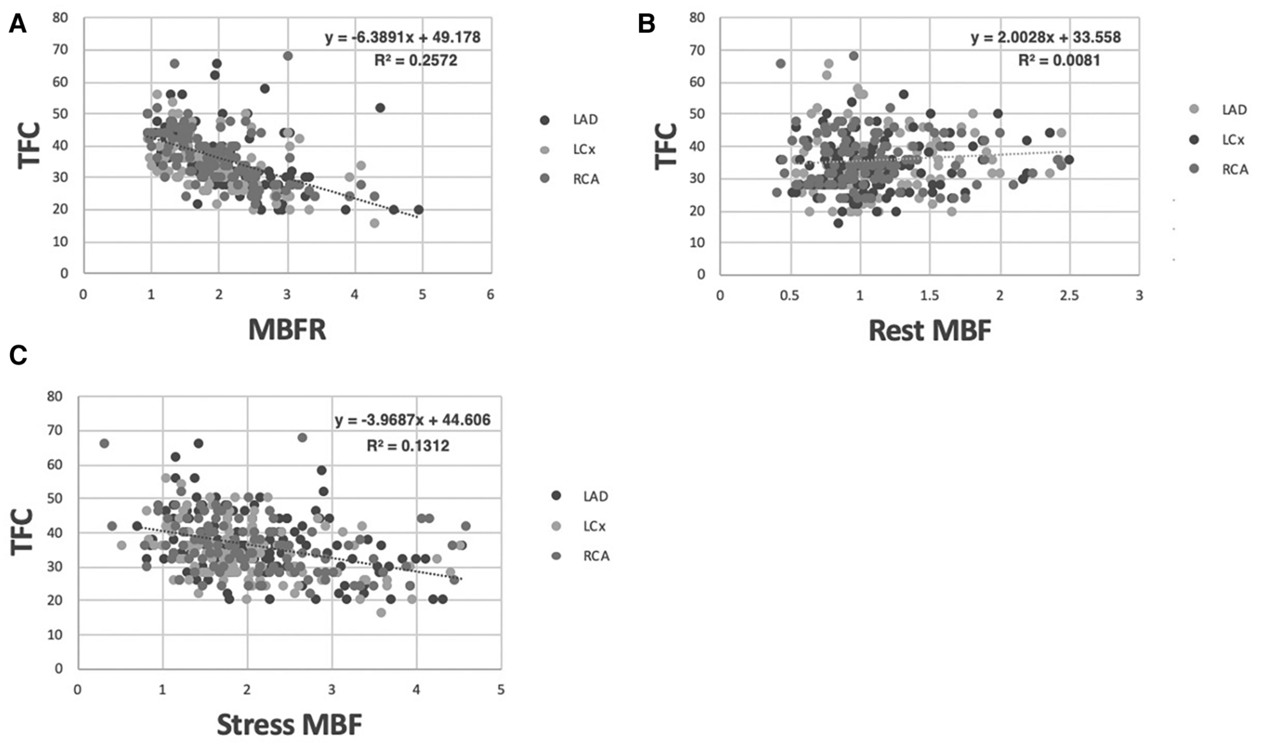

FIGURE 2
Correlation between TFC and MBFR, rest MBF, and stress MBF in all patients. (A) Correlation between MBFR and TFC in all patients ($p < 0.0001$ for all 3 coronary territories). (B) Resting myocardial blood flow vs. TFC across coronary territories in all patients lacks a significant relationship. (C) Stress myocardial blood flow vs. TFC across coronary territories in all patients shows a significant but only slight inverse relationship.

whether the relationship between MBFR and TFC was reduced for patients who had received NTG during coronary angiography. At our institution before 2010, patients underwent cardiac catheterization via femoral access and the vast majority of these patients did not receive NTG. Between 2010 and 2015, the institution transitioned from femoral to radial access and NTG was commonly used. Overall, 31 patients in this cohort (30% of men and 22% of women) received NTG. We re-evaluated the association between TFC and MBFR in each coronary territory, stratified by administration of NTG. In each coronary vessel, we found that the correlation between TFC and MBFR was stronger in patients who did not receive NTG than in those who did (NTG vs. no NTG, respectively: LAD PCC −0.211 vs. −0.513, LCx PCC −0.197 vs. −0.546, RCA PCC −0.234 vs. −0.605, $p < 0.0001$ for all). To ensure that these differences were not due to differences in sample sizes, we repeated the analysis with three randomly selected, down-sampled populations. The results were unchanged.

Race and ethnicity are known to affect response to NTG (32). We therefore assessed whether race and ethnicity impacted the effect of NTG on the relationship between MBFR and TFC. We found a moderate correlation between TFC and MBFR in white individuals who did and did not received NTG (PCC −0.439 and −0.753, respectively, $p < 0.0001$) (Figure 5A). However, in black individuals, there was no correlation between TFC and MBFR in those who received NTG (PCC 0.050, and only a mild correlation in those who did not PCC −0.378, $P < 0.0001$) (Figure 5B).

Prior studies have identified sex-based differences in remodeling (33). Thus, we looked at the effect of sex on the relationship between MBFR and TFC. Interestingly, there was a strong sex difference in the negative correlation between TFC and regional MBFR. In women, correlations between TFC and MBFR were −0.73, −0.74, and −0.78 for RCA, LCX, and LAD, respectively (Figure 5C, $p < 0.0001$ for all). The relationship between TFC and regional MBFR also existed in men but was weaker, with PCC −0.41, −0.38, and −0.35 for RCA, LCX, and LAD, respectively (Figure 5D, $p < 0.0001$ for all). As above, we repeated the analysis with three randomly down-sampled populations, and the results remained consistent. To formally establish whether these confounding factors interacted with TFC, we used multivariate linear regression analysis including sex, race and ethnicity, and nitroglycerin use. We found that all of these variables have a significant impact on the relationship between TFC and MBFR (Figures 5E–G).

Lastly, we sought to assess the ability of TFC to identify patients with CMVD, defined as MBFR < 2 (13). We performed receiver operating characteristic (ROC) analysis for each territory separately and all together, stratified by sex (Figures 6A–D). TFC showed excellent performance in identifying CMVD in women with some slight variability among territories (AUC = 0.86, 0.84, and 0.89 for LAD, RCA and LCX, respectively). TFC performed less well in men in all territories (AUC = 0.75, 0.78, and 0.68 for LAD, RCA and LCX, respectively). In women, TFC thresholds

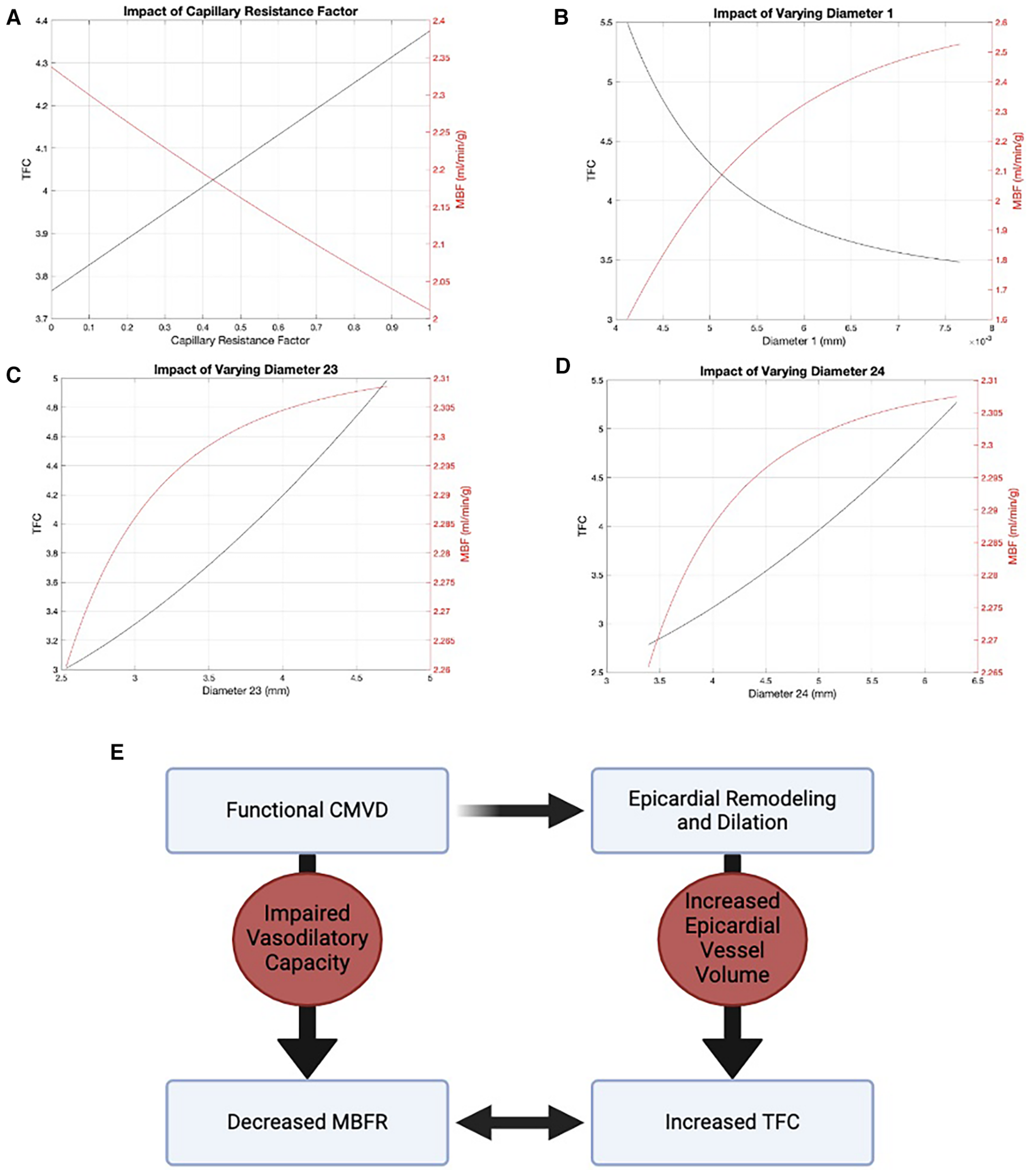

FIGURE 3
Modified ZKM model of the coronary circulation. There is an inverse relationship between flow (red) and TFC (black) in the two smallest vessel levels: (A) level 0 and (B) level 1. In the two largest vessels, there is an uncoupling of flow and TFC: (C) level 23 and (D) level 24. (E) Diagram demonstrating the relationship between MBFR and TFC via epicardial remodeling.

for identifying CMVD were 33 for the LAD (sensitivity 80.5%, specificity 83.9%), 33 for the RCA (sensitivity 82.5%, specificity 72.4%), and 31 for the LCx (sensitivity 82.9%, specificity 77.4%). In men, TFC thresholds for identifying CMVD were 31 for the LAD (sensitivity 61.9%, specificity 48%), 35 for the RCA (sensitivity 81.8%, specificity 60%), and 29 for the LCx (sensitivity 90.5%, specificity 52%) (Figures 6E–H). When all territories were considered, there was a statistically significant difference in TFC performance between women and men (AUC = 0.86 vs. 0.72, $p = 0.003$). Based on ROC curves, we

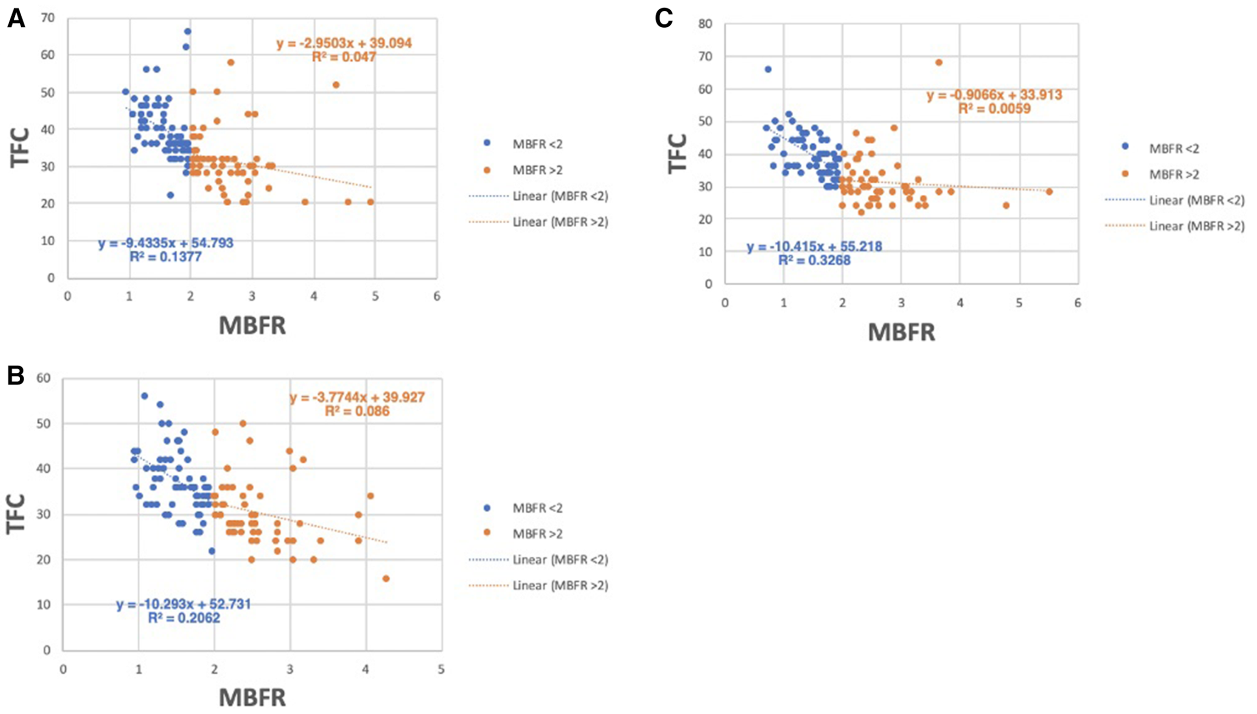

FIGURE 4
Relationship between TFC and MBFR in patients with and without CMVD (MBFR ≥ 2). (**A–C**) TFC vs. MBFR for participants with (MBFR < 2) and without CMVD in the (**A**) LAD, (**B**) LCx, and (**C**) RCA, respectively, highlights the strong relationship between TFC and MBFR present in those with CMVD (blue) and a more blunted slope in patients without CMVD (orange).

established TFC thresholds that identify CMVD with sensitivity > 80% in women for all three coronary arteries (Figures 6E,G). The high territory-specific variability limited the sensitivity in men (Figures 6F,H).

# Discussion

In a diverse cohort of patients, we demonstrated a relationship between TFC from clinical coronary angiograms and perfusion PET MBFR. Using computational modeling, we show how the relationship between coronary flow and TFC breaks down in the larger epicardial vessels that are used for TFC measurement. These data support a model where TFC is predominantly driven by epicardial coronary volume and reflects underlying disease rather than a physiologic parameter. We also identified several variables that confound the relationship between TFC and MBFR including sex, race and ethnicity, and nitroglycerin administration. Finally, we show that TFC has potential diagnostic utility in CMVD, especially in women.

We identified a strong relationship between TFC and MBFR, which was not driven by rest or stress MBF. TFC is thought to be primarily driven by coronary flow (18) and TFC correlated with coronary flow velocity under adenosine-induced hyperemic conditions in a cohort of 11 patients (34). In our study, there was a minimal relationship between rest MBF and TFC and a slight inverse relationship between TFC and stress MBF. Coronary modeling helps to explain these disparate data. We show that there is an uncoupling between flow and TFC in larger vessels, which allows for increased TFC in the presence of increased resting flow and/or decreased flow reserve. This indicates that TFC is predominantly reflective of the volume of the epicardial compartment, rather than the flow rate in the epicardial coronary artery.

CMVD is associated with distal endothelial dysfunction leading to impaired vasodilatory response to both pharmacological and physiological stimuli (2, 35). Some studies suggest CMVD is associated with vascular remodeling (33, 36). A recent study also showed that patients with functional CMVD have increased proximal epicardial vessel volume, suggestive of vascular remodeling in response to more distal microvascular dysfunction (37). These studies point to proximal remodeling in response to microvascular dysfunction with increased epicardial vessel volume, consistent with our findings. In summary, CMVD leads to epicardial remodeling and changes in epicardial vessel volume, which results in increased TFC (time to fill the vessel).

In support of this theory, we find that the relationship between TFC and MBFR is stronger in patients with CMVD (MBFR < 2), who are more likely to have remodeling. Additionally, the relationship between TFC and MBFR is diminished in patients who received nitroglycerin prior to catheterization. This would serve to artificially dilate the proximal coronary arteries in those without CMVD (MBFR > 2), artificially increase TFC, and obscure the difference between normal individuals and those with CMVD.

In summary, TFC serves as a measure of disease in individuals rather than a pure measure of coronary blood flow. At the patient

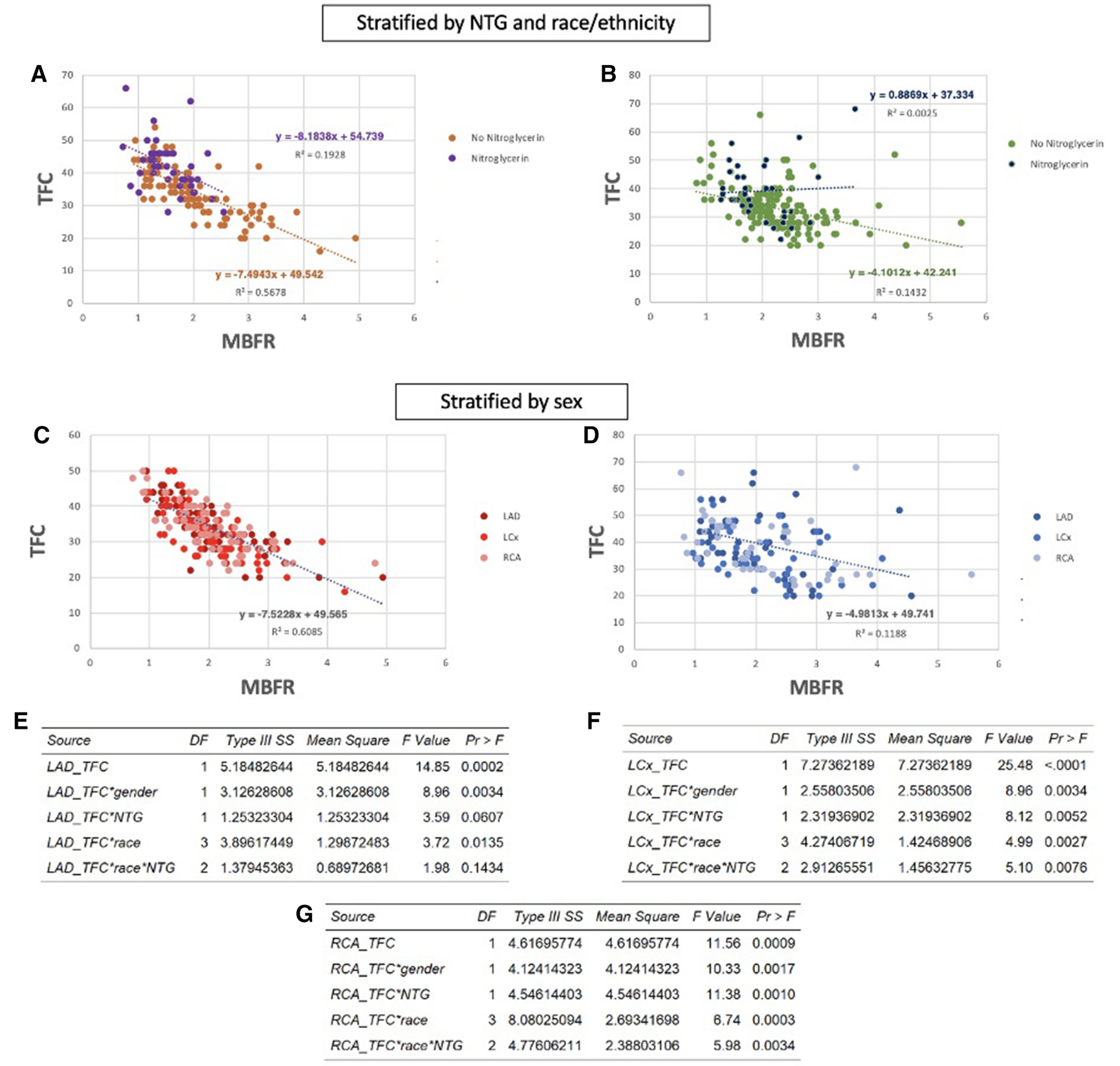

| Source | DF | Type III SS | Mean Square | F Value | Pr > F |
|---|---|---|---|---|---|
| LAD_TFC | 1 | 5.18482644 | 5.18482644 | 14.85 | 0.0002 |
| LAD_TFC*gender | 1 | 3.12628608 | 3.12628608 | 8.96 | 0.0034 |
| LAD_TFC*NTG | 1 | 1.25323304 | 1.25323304 | 3.59 | 0.0607 |
| LAD_TFC*race | 3 | 3.89617449 | 1.29872483 | 3.72 | 0.0135 |
| LAD_TFC*race*NTG | 2 | 1.37945363 | 0.68972681 | 1.98 | 0.1434 |

| Source | DF | Type III SS | Mean Square | F Value | Pr > F |
|---|---|---|---|---|---|
| LCx_TFC | 1 | 7.27362189 | 7.27362189 | 25.48 | <.0001 |
| LCx_TFC*gender | 1 | 2.55803506 | 2.55803506 | 8.96 | 0.0034 |
| LCx_TFC*NTG | 1 | 2.31936902 | 2.31936902 | 8.12 | 0.0052 |
| LCx_TFC*race | 3 | 4.27406719 | 1.42468906 | 4.99 | 0.0027 |
| LCx_TFC*race*NTG | 2 | 2.91265551 | 1.45632775 | 5.10 | 0.0076 |

| Source | DF | Type III SS | Mean Square | F Value | Pr > F |
|---|---|---|---|---|---|
| RCA_TFC | 1 | 4.61695774 | 4.61695774 | 11.56 | 0.0009 |
| RCA_TFC*gender | 1 | 4.12414323 | 4.12414323 | 10.33 | 0.0017 |
| RCA_TFC*NTG | 1 | 4.54614403 | 4.54614403 | 11.38 | 0.0010 |
| RCA_TFC*race | 3 | 8.08025094 | 2.69341698 | 6.74 | 0.0003 |
| RCA_TFC*race*NTG | 2 | 4.77606211 | 2.38803106 | 5.98 | 0.0034 |

FIGURE 5
Nitroglycerin (NTG) administration, race and ethnicity, and sex impact the relationship between TFC and MBFR. (A,B) Correlation between MBFR and TFC in all coronary territories in white patients (A) and black patients (B) who received nitroglycerin versus those who did not. The inverse relationship between TFC and MBFR is eliminated in Black patients who received NTG. (C,D) The association between TFC and MBFR was much stronger in women (C) compared to men (D) (E–G) Multivariant linear regression modeling highlights the significant effect of these confounding variables on the relationship between TFC and MBFR in the LAD (E), LCx (F), and RCA (G) territories.

level, this result is consistent. TFC and MBFR are both measures of CMVD, and patients with more severe CMVD have both lower MBFR and higher TFC. This is further supported by the fact that PET and coronary angiography were performed within days-months of each other but not at the same time, suggesting that this reflects underlying pathophysiology instead of a snapshot of hemodynamic parameters.

Prior work by Gibson et al. has advocated for the use of TFC for assessing the coronary microvasculature in patients undergoing coronary angiography (3, 24). Petersen et al. have shown that resting TFC independently predicts rates of hospitalization for angina in women with signs of ischemia without obstructive CAD (16). Our data support that these two groups of patients may have CMVD as the link between increased TFC and adverse outcomes. Our results further support the use of TFC as a measure of the coronary microvasculature by establishing the feasibility of quantifying TFC from clinical angiograms rather than angiograms performed as part of research protocols.

Recent studies have reported conflicting results. Dutta et al. measured CMVD using coronary pressure and flow velocity

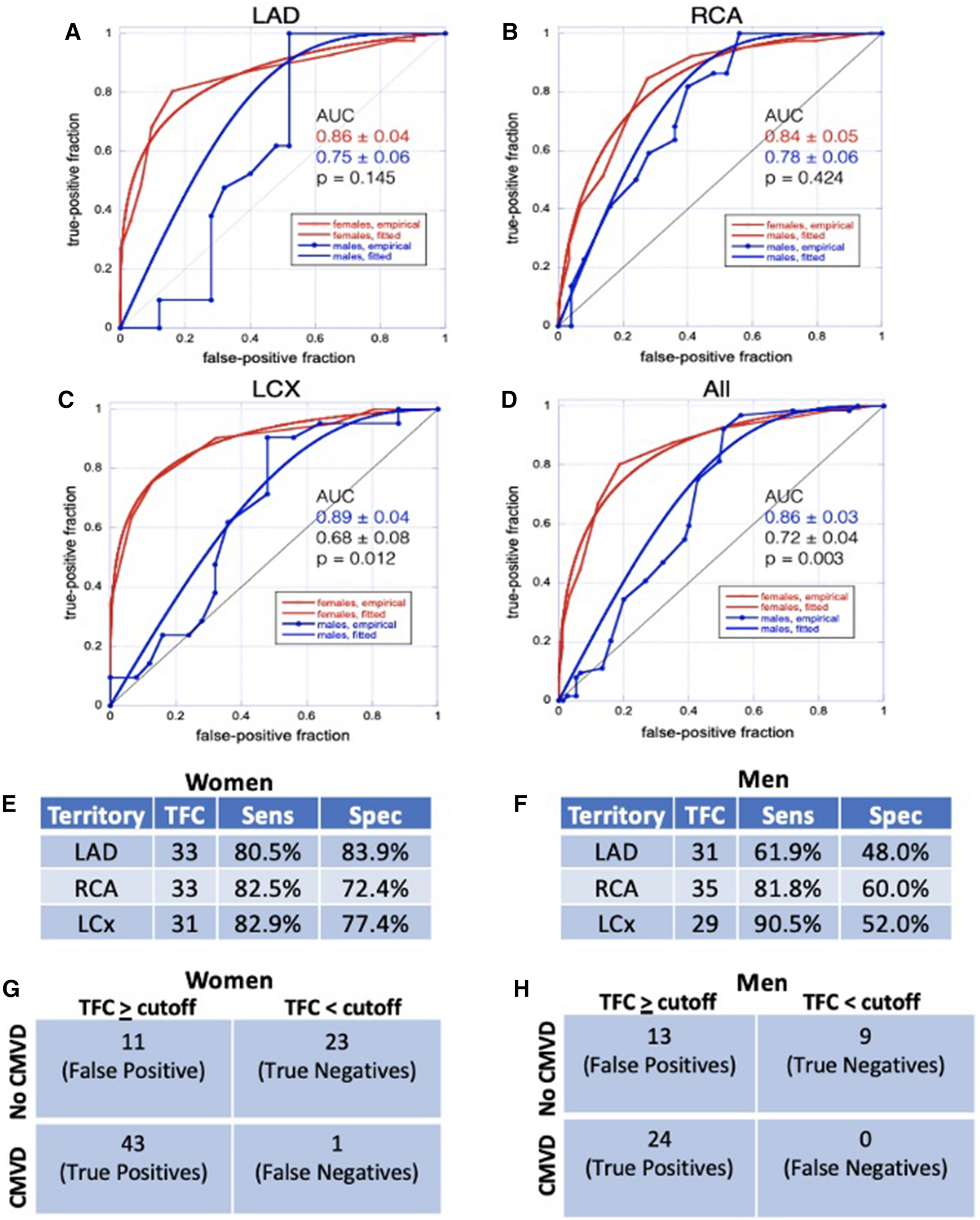

Women

| Territory | TFC | Sens | Spec |
|---|---|---|---|
| LAD | 33 | 80.5% | 83.9% |
| RCA | 33 | 82.5% | 72.4% |
| LCx | 31 | 82.9% | 77.4% |

Men

| Territory | TFC | Sens | Spec |
|---|---|---|---|
| LAD | 31 | 61.9% | 48.0% |
| RCA | 35 | 81.8% | 60.0% |
| LCx | 29 | 90.5% | 52.0% |

Women

| | TFC ≥ cutoff | TFC < cutoff |
|---|---|---|
| No CMVD | 11<br>(False Positive) | 23<br>(True Negatives) |
| CMVD | 43<br>(True Positives) | 1<br>(False Negatives) |

Men

| | TFC ≥ cutoff | TFC < cutoff |
|---|---|---|
| No CMVD | 13<br>(False Positives) | 9<br>(True Negatives) |
| CMVD | 24<br>(True Positives) | 0<br>(False Negatives) |

FIGURE 6
ROC analysis. (A–D) ROC analyses for TFC in LAD (A), RCA (B), LCX (C), and all territories combined (D) show that TFC performs better in women than in men. (E, F) Sensitivity and specificity for TFC values chosen from ROC analyses as diagnostic thresholds for CMVD in women (E) and in men (F) (G,H) Contingency table demonstrating true positives, true negatives, false positives, and false negatives for women (G) and men (H); CMVD is defined as MBFR < 2 and TFC ≥ cutoff is defined as TFC above defined threshold (E,F) in one or more coronary territory.

before and after adenosine administration and concluded that Coronary Slow Flow Phenomenon (defined as corrected TFC > 27) was a poor indicator of CMVD (22). However, individuals in this study represented a generally healthier population, with higher coronary flow reserve and lower rates of hypertension, diabetes, and hypercholesterolemia, and also received NTG. Both of these weaken the relationship between TFC and flow reserve measurements.

The underlying mechanism driving the sex-difference in the relationship between TFC and MBFR is unclear. Our study cohort is enriched for women, similar to prior studies that have found larger proportions of women with symptoms and non-obstructive coronaries (38). However the weaker relationship between TFC and MBFR in men appears to be at least partially due to greater variance in TFC rather than smaller sample size (Figures 5B). Additionally, in this cohort of patients, a greater percentage of men received nitroglycerin than women, which could contribute to the stronger correlation we see in women. We tested the hypothesis that having larger epicardial coronaries impacts the relationship between TFC and MBFR in coronary modeling by increasing the Strahler levels, but saw no change in the model's behavior to explain the finding. Prior studies have identified sex-based differences in plaque formation and deposition and vascular remodeling (33). Specifically, the Women's Ischemia Syndrome Evaluation (WISE) intravascular ultrasound (IVUS) study showed that in women with symptoms of ischemia but without luminal obstruction on catheterization, there was a high prevalence of positive remodeling which maintained the coronary lumen via compensatory enlargement secondary to external elastic membrane expansion (33). It is possible than men and women have differential outward remodeling, which may differentially change the epicardial volumes and thus the TFC. Lastly, non-obstructive atherosclerosis in men may also have subtle effects on flow and lead to greater variability in TFC and MBFR measurements.

This study has several limitations. First, it is a single-center, retrospective study, with a small population of men. Second, this study links two distinct imaging biomarkers, and additional work is needed to link the heterogenous pathophysiology of CMVD with these biomarkers. Third, we use clinically-acquired coronary angiograms. These prioritize clinical care and patient safety and thus use less radiation, fewer frames, and are of poorer image quality. Additionally, each institution has its own coronary catheterization protocols, including use of NTG and other vasodilators, which can affect TFC measurements.

Future studies are needed to understand differences due to sex and race and ethnicity, to establish TFC as a diagnostic test for CMVD, and to link TFC with adverse cardiovascular outcomes in a large population without obstructive CAD. TFC has great potential as an imaging biomarker to accelerate the research into CMVD pathogenesis and may be helpful for screening patients for CMVD trials. TFC may also be a useful imaging biomarker for phenotyping CMVD in large cohorts and biobanks, such as the PennMedicine Biobank, the UK Biobank, and the Veterans Administration Million Veterans Program. However, we propose that the greatest immediate impact of this work is to encourage additional studies into the use of TFC as a simple, cost-effective, and widely available tool that can be applied to clinical coronary angiograms to assess for CMVD, especially in women with cardiac symptoms who may otherwise be falsely reassured by non-obstructive coronary arteries.

## Data availability statement

The raw data supporting the conclusions of this article will be made available by the authors, without undue reservation.

## Ethics statement

The studies involving humans were approved by Hospital of the University of Pennsylvania Institutional Review Board. The studies were conducted in accordance with the local legislation and institutional requirements. Written informed consent for participation was not required from the participants or the participants' legal guardians/next of kin in accordance with the national legislation and institutional requirements.

## Author contributions

NW: Formal Analysis, Methodology, Visualization, Writing – original draft, Writing – review & editing. QW: Formal Analysis, Writing – review & editing. SCM: Formal Analysis, Methodology, Writing – review & editing. VF: Writing – review & editing. SDG: Formal Analysis, Methodology, Writing – review & editing. MG: Conceptualization, Supervision, Writing – original draft, Writing – review & editing.

## Funding

The author(s) declare financial support was received for the research, authorship, and/or publication of this article.

This work was supported by NIH K08HL136890, Burroughs Wellcome Fund, and Doris Duke Charitable Foundation (MAG) and NIH R01HL149801 (MAG, SDM).

## Conflict of interest

The authors declare that the research was conducted in the absence of any commercial or financial relationships that could be construed as a potential conflict of interest.

## Publisher's note

## Supplementary material

The Supplementary Material for this article can be found online at: https://www.frontiersin.org/articles/10.3389/fcvm.2024.1395036/full#supplementary-material

# References

1. Bairey Merz CN, Pepine CJ, Walsh MN, Fleg JL. Ischemia and no obstructive coronary artery disease (INOCA): developing evidence-based therapies and research agenda for the next decade. *Circulation*. (2017) 135:1075–92. doi: 10.1161/CIRCULATIONAHA.116.024534

2. Taqueti VR, Di Carli MF. Coronary microvascular disease pathogenic mechanisms and therapeutic options: JACC state-of-the-art review. *J Am Coll Cardiol*. (2018) 72:2625–41. doi: 10.1016/j.jacc.2018.09.042

3. Gibson CM, Cannon CP, Daley WL, Dodge JT, Alexander B, Marble SJ, et al. TIMI frame count: a quantitative method of assessing coronary artery flow. *Circulation*. (1996) 93:879–88. doi: 10.1161/01.CIR.93.5.879

4. Taqueti VR, Hachamovitch R, Murthy VL, Naya M, Foster CR, Hainer J, et al. Global coronary flow reserve is associated with adverse cardiovascular events independently of luminal angiographic severity and modifies the effect of early revascularization. *Circulation*. (2015) 131:19–27. doi: 10.1161/CIRCULATIONAHA.114.011939

5. Murthy VL, Naya M, Taqueti VR, Foster CR, Gaber M, Hainer J, et al. Effects of sex on coronary microvascular dysfunction and cardiac outcomes. *Circulation*. (2014) 129:2518–27. doi: 10.1161/CIRCULATIONAHA.113.008507

6. Shaw LJ, Merz CNB, Pepine CJ, Reis SE, Bittner V, Kelsey SF, et al. Insights from the NHLBI-sponsored women's ischemia syndrome evaluation (WISE) study part I: gender differences in traditional and novel risk factors, symptom evaluation, and gender-optimized diagnostic strategies. *J Am Coll Cardiol*. (2006) 47:4S–20S. doi: 10.1016/j.jacc.2005.01.072

7. Camici PG, Crea F. Medical progress—coronary microvascular dysfunction. *N Engl J Med*. (2007) 356:830–40. doi: 10.1056/NEJMra061889

8. Feher A, Sinusas AJ. Assessment of right ventricular metabolism: an emerging tool for monitoring pulmonary artery hypertension. *J Nucl Cardiol*. (2017) 24:1990–3. doi: 10.1007/s12350-016-0695-9

9. Guerraty M, Arany Z. A call for a unified view of coronary microvascular disease. *Trends Cardiovasc Med*. (2023) 34(3):145–7. doi: 10.1016/j.tcm.2022.12.007

10. Del Buono MG, Montone RA, Camilli M, Carbone S, Narula J, Lavie CJ, et al. Coronary microvascular dysfunction across the spectrum of cardiovascular diseases: JACC state-of-the-art review. *J Am Coll Cardiol*. (2021) 78:1352–71. doi: 10.1016/j.jacc.2021.07.042

11. Rahman H, Demir OM, Khan F, Ryan M, Ellis H, Mills MT, et al. Physiological stratification of patients with angina due to coronary microvascular dysfunction. *J Am Coll Cardiol*. (2020) 75:2538–49. doi: 10.1016/j.jacc.2020.03.051

12. Peri-Okonny PA, Patel KK, Garcia RA, Thomas M, McGhie AI, Bunte MC, et al. Coronary vascular dysfunction is associated with increased risk of death in patients with peripheral artery disease. *J Nucl Cardiol*. (2023) 30:2666–75. doi: 10.1007/s12350-023-03343-y

13. Ziadi MC, Dekemp RA, Williams KA, Guo A, Chow BJ, Renaud JM, et al. Impaired myocardial flow reserve on rubidium-82 positron emission tomography imaging predicts adverse outcomes in patients assessed for myocardial ischemia. *J Am Coll Cardiol*. (2011) 58:740–8. doi: 10.1016/j.jacc.2011.01.065

14. Mathew RC, Bourque JM, Salerno M, Kramer CM. Cardiovascular imaging techniques to assess microvascular dysfunction. *JACC Cardiovasc Imaging*. (2020) 13:1577–90. doi: 10.1016/j.jcmg.2019.09.006

15. Kunadian V, Chieffo A, Camici PG, Berry C, Escaned J, Maas A, et al. An EAPCI expert consensus document on ischaemia with non-obstructive coronary arteries in collaboration with European society of cardiology working group on coronary pathophysiology & microcirculation endorsed by coronary vasomotor disorders international study group. *Eur Heart J*. (2020) 41:3504–20. doi: 10.1093/eurheartj/ehaa503

16. Petersen JW, Johnson BD, Kip KE, Anderson RD, Handberg EM, Sharaf B, et al. TIMI frame count and adverse events in women with no obstructive coronary disease: a pilot study from the NHLBI-sponsored women's ischemia syndrome evaluation (WISE). *PLoS One*. (2014) 9:e96630. doi: 10.1371/annotation/41113674-7ca2-42a5-a364-f646ff85c2e7

17. Gibson CM, Murphy SA, Rizzo MJ, Ryan KA, Marble SJ, McCabe CH, et al. Relationship between TIMI frame count and clinical outcomes after thrombolytic administration. Thrombolysis in myocardial infarction (TIMI) study group. *Circulation*. (1999) 99:1945–50. doi: 10.1161/01.CIR.99.15.1945

18. Stankovic G, Manginas A, Voudris V, Pavlides G, Athanassopoulos G, Ostojic M, et al. Prediction of restenosis after coronary angioplasty by use of a new index: TIMI frame count/minimal luminal diameter ratio. *Circulation*. (2000) 101:962–8. doi: 10.1161/01.CIR.101.9.962

19. Ong P, Camici PG, Beltrame JF, Crea F, Shimokawa H, Sechtem U, et al. International standardization of diagnostic criteria for microvascular angina. *Int J Cardiol*. (2018) 250:16–20. doi: 10.1016/j.ijcard.2017.08.068

20. Barcin C, Denktas A, Garratt K, Higano S, Holmes D Jr, Lerman A. Relation of thrombolysis in myocardial infarction (TIMI) frame count to coronary flow parameters. *Am J Cardiol*. (2003) 91:466–9. doi: 10.1016/S0002-9149(02)03250-2

21. Aparicio A, Cuevas J, Moris C, Martin M. Slow coronary blood flow: pathogenesis and clinical implications. *Eur Cardiol*. (2022) 17:e08. doi: 10.15420/ecr.2021.46

22. Dutta U, Sinha A, Demir OM, Ellis H, Rahman H, Perera D. Coronary slow flow is not diagnostic of microvascular dysfunction in patients with angina and unobstructed coronary arteries. *J Am Heart Assoc*. (2023) 12:e027664. doi: 10.1161/JAHA.122.027664

23. Chugh SK, Koppel J, Scott M, Shewchuk L, Goodhart D, Bonan R, et al. Coronary flow velocity reserve does not correlate with TIMI frame count in patients undergoing non-emergency percutaneous coronary intervention. *J Am Coll Cardiol*. (2004) 44:778–82. doi: 10.1016/j.jacc.2004.05.048

24. Gibson CM, Murphy SA, Popma JJ. Insights into the pathophysiology of acute ischemic syndromes using the TIMI flow grade, TIMI frame count, and TIMI myocardial perfusion grade. In: Cannon CP, editor. *Management of Acute Coronary Syndromes Totowa*. NJ: Humana Press (2003). p. 95–118.

25. Lortie M, Beanlands RSB, Yoshinaga K, Klein R, DaSilva JN, Dekemp RA. Quantification of myocardial blood flow with Rb-82 dynamic PET imaging. *Eur J Nucl Med Mol Imaging*. (2007) 34:1765–74. doi: 10.1007/s00259-007-0478-2

26. Lautamaki R, George RT, Kitagawa K, Higuchi T, Merrill J, Voicu C, et al. Rubidium-82 PET-CT for quantitative assessment of myocardial blood flow: validation in a canine model of coronary artery stenosis. *Eur J Nucl Med Mol Imaging*. (2009) 36:576–86. doi: 10.1007/s00259-008-0972-1

27. Pan XBDJ. Validation syngo. *PET Myocardial Blood Flow*. Hoffman Estates, IL: Siemens Medical Solutions (2011). p. 1–17.

28. Hutchins GD, Schwaiger M, Rosenspire KC, Krivokapich J, Schelbert H, Kuhl DE. Noninvasive quantification of regional blood flow in the human heart using N-13 ammonia and dynamic positron emission tomographic imaging. *J Am Coll Cardiol*. (1990) 15:1032–42. doi: 10.1016/0735-1097(90)90237-J

29. Zhou Y, Kassab GS, Molloi S. On the design of the coronary arterial tree: a generalization of Murray's law. *Phys Med Biol*. (1999) 44:2929–45. doi: 10.1088/0031-9155/44/12/306

30. Metz CE, Herman BA, Shen JH. Maximum likelihood estimation of receiver operating characteristic (ROC) curves from continuously-distributed data. *Stat Med*. (1998) 17:1033–53. doi: 10.1002/(SICI)1097-0258(19980515)17:9<1033::AID-SIM784>3.0.CO;2-Z

31. Metz CE, Pan X. "Proper" binormal ROC curves: theory and maximum-likelihood estimation. *J Math Psychol*. (1999) 43:1–33. doi: 10.1006/jmps.1998.1218

32. Gokce N, Holbrook M, Duffy SJ, Demissie S, Cupples LA, Biegelsen E, et al. Effects of race and hypertension on flow-mediated and nitroglycerin-mediated dilation of the brachial artery. *Hypertension*. (2001) 38:1349–54. doi: 10.1161/hy1201.096575

33. Khuddus MA, Pepine CJ, Handberg EM, Bairey Merz CN, Sopko G, Bavry AA, et al. An intravascular ultrasound analysis in women experiencing chest pain in the absence of obstructive coronary artery disease: a substudy from the national heart, lung and blood institute-sponsored women's ischemia syndrome evaluation (WISE). *J Interv Cardiol*. (2010) 23:511–9. doi: 10.1111/j.1540-8183.2010.00598.x

34. Manginas A, Gatzov P, Chasikidis C, Voudris V, Pavlides G, Cokkinos DV. Estimation of coronary flow reserve using the thrombolysis in myocardial infarction (TIMI) frame count method. *Am J Cardiol*. (1999) 83:1562–5. A7. doi: 10.1016/S0002-9149(99)00149-6

35. Sinha A, Rahman H, Perera D. Coronary microvascular disease: current concepts of pathophysiology, diagnosis and management. *Cardiovasc Endocrinol Metab*. (2021) 10:22–30. doi: 10.1097/XCE.0000000000000223

36. Lanza GA, Camici PG, Galiuto L, Niccoli G, Pizzi C, Di Monaco A, et al. Methods to investigate coronary microvascular function in clinical practice. *J Cardiovasc Med (Hagerstown)*. (2013) 14:1–18. doi: 10.2459/JCM.0b013e328351680f

37. Sakai K, Collet CA, Mizukami T, Caglioni S, Bouisset F, Munhoz D, et al. Vascular remodeling in coronary microvascular dysfunction. *J Am Coll Cardiol*. (2023) 81:1255. doi: 10.1016/S0735-1097(23)01699-6

38. Jespersen L, Hvelplund A, Abildstrom SZ, Pedersen F, Galatius S, Madsen JK, et al. Stable angina pectoris with no obstructive coronary artery disease is associated with increased risks of major adverse cardiovascular events. *Eur Heart J*. (2012) 33:734–44. doi: 10.1093/eurheartj/ehr331

frontiers | Frontiers in Cardiovascular Medicine

TYPE Original Research
PUBLISHED 03 July 2024
DOI 10.3389/fcvm.2024.1412867

EDITED BY
Hiroshi Iwata,
Juntendo University, Japan

REVIEWED BY
Doran Mix,
University of Rochester, United States
Takeshi Okada,
Brigham and Women's Hospital and Harvard Medical School, United States
Yuichi Chikata,
Juntendo University, Japan

*CORRESPONDENCE
Mohammad Alfrad Nobel Bhuiyan
✉ Nobel.Bhuiyan@lsuhs.edu

†These authors have contributed equally to this work and share first authorship

RECEIVED 05 April 2024
ACCEPTED 31 May 2024
PUBLISHED 03 July 2024

CITATION
Ali S, Al-Yafeai Z, Hossain Md.I, Bhuiyan Md.S, Duhan S, Aishwarya R, Goeders NE, Bhuiyan Md.MR, Conrad SA, Vanchiere JA, Orr AW, Kevil CG and Bhuiyan MAN (2024) Trends in peripheral artery disease and critical limb ischemia hospitalizations among cocaine and methamphetamine users in the United States: a nationwide study.
Front. Cardiovasc. Med. 11:1412867.
doi: 10.3389/fcvm.2024.1412867

# Trends in peripheral artery disease and critical limb ischemia hospitalizations among cocaine and methamphetamine users in the United States: a nationwide study

Shafaqat Ali[1†], Zaki Al-Yafeai[1†], Md. Ismail Hossain[1], Md. Shenuarin Bhuiyan[2,3], Sanchit Duhan[4], Richa Aishwarya[2], Nicholas E. Goeders[5,6,7], Md. Mostafizur Rahman Bhuiyan[8], Steven A. Conrad[1,9], John A. Vanchiere[5,9], A. Wayne Orr[2,3], Christopher G. Kevil[2,3] and Mohammad Alfrad Nobel Bhuiyan[1,2,7*]

[1]Department of Medicine, Louisiana State University Health Sciences Center at Shreveport, Shreveport, LA, United States, [2]Department of Pathology and Translational Pathobiology, Louisiana State University Health Sciences Center at Shreveport, Shreveport, LA, United States, [3]Department of Molecular and Cellular Physiology, Louisiana State University Health Sciences Center at Shreveport, Shreveport, LA, United States, [4]Department of Medicine, Sinai Hospital of Baltimore, Baltimore, MD, United States, [5]Department of Pharmacology, Toxicology & Neuroscience, Louisiana State University Health Sciences Center at Shreveport, Shreveport, LA, United States, [6]Department of Psychiatry and Behavioral Medicine, Louisiana State University Health Sciences Center at Shreveport, Shreveport, LA, United States, [7]Louisiana Addiction Research Center, Louisiana State University Health Sciences Center at Shreveport, Shreveport, LA, United States, [8]Department of Pediatric Cardiology, Bangabandhu Sheikh Mujib Medical University, Dhaka, Bangladesh, [9]Department of Pediatrics, Louisiana State University Health Sciences Center at Shreveport, Shreveport, LA, United States

**Background:** Peripheral artery disease (PAD) is on the rise worldwide, ranking as the third leading cause of atherosclerosis-related morbidity; much less is known about its trends in hospitalizations among methamphetamine and cocaine users.
**Objectives:** We aim to evaluate the overall trend in the prevalence of hospital admission for PAD with or without the use of stimulant abuse (methamphetamine and cocaine) across the United States. Additionally, we evaluated the PAD-related hospitalizations trend stratified by age, race, sex, and geographic location.
**Methods:** We used the National Inpatient Sample (NIS) database from 2008 to 2020. The Cochran Armitage trend test was used to compare the trend between groups. Multivariate logistic regression was used to examine adjusted odds for PAD and CLI hospitalizations among methamphetamine and cocaine users.
**Results:** Between 2008 and 2020, PAD-related hospitalizations showed an increasing trend in Hispanics, African Americans, and western states, while a decreasing trend in southern and Midwestern states ($p$-trend <0.05). Among methamphetamine users, an overall increasing trend was observed in men, women, western, southern, and midwestern states ($p$-trend <0.05). However, among cocaine users, PAD-related hospitalization increased significantly for White, African American, age group >64 years, southern and western states ($p$-trend <0.05). Overall, CLI-related hospitalizations showed an encouraging decreasing trend in men and women, age group >64 years, and CLI-related amputations declined for women, White patient population, age group >40, and all regions ($p$-trend <0.05). However, among methamphetamine users, a

significantly increasing trend in CLI-related hospitalization was seen in men, women, White & Hispanic population, age group 26–45, western, southern, and midwestern regions.

**Conclusions:** There was an increasing trend in PAD-related hospitalizations among methamphetamine and cocaine users for both males and females. Although an overall decreasing trend in CLI-related hospitalization was observed for both genders, an up-trend in CLI was seen among methamphetamine users. The upward trends were more prominent for White, Hispanic & African Americans, and southern and western states, highlighting racial and geographic variations over the study period.

KEYWORDS

critical limb ischemia, peripheral arterial disease, cocaine, methamphetamine, trends

# Introduction

Peripheral arterial disease (PAD) is an obstructive atherosclerotic and microvascular disease mainly affecting vessels in the lower extremities (1–4). PAD is well recognized as an important cause of cardiovascular morbidity and mortality, affecting more than 230 million adults worldwide and 8–12 million adults in the US (4–6). Critical limb ischemia (CLI), a severe stage of PAD, is associated with a high amputation rate and manifested by resting pain and non-healing wounds (7). The global and national prevalence continues to rise, mainly affecting people above 65 (5). PAD is known to be a significant cause of non-traumatic amputation in the US, significantly impacting patients and healthcare systems (8). In addition, PAD is the third most common clinical manifestation of atherosclerosis after coronary artery disease (CAD) and stroke (1, 9). However, PAD has traditionally been understudied compared to other atherosclerotic diseases, leading to significant lags in overall awareness regarding PAD-related hospitalizations and essential geographical, ethnic, and sex-based disparities in the US and worldwide (1).

Substance use is among the modifiable risk factors associated with atherosclerotic cardiovascular disease (ASCVD) (10–13). Despite tremendous efforts to legalize some drugs and stem the availability of illegal drugs, substance use is rising. Methamphetamine and cocaine use are strongly associated with ASCVD development and progression (10, 14, 15). Yet the underlying mechanisms remain elusive (16). Surprisingly, the biological and clinical effects of methamphetamine and cocaine on PAD have received considerably little attention (10, 17).

In contrast to coronary and cerebrovascular diseases, the geographical, ethnic, and socioeconomic variations among PAD patients are less well-defined. While prior studies showed a marked prevalence of PAD among the non-Hispanic Black population compared to the non-Hispanic White and non-Hispanic population, recent research has contradicted this, demonstrating a difference of less than 10% (1, 3, 18, 19). However, the risk of non-traumatic amputation is 20% higher among non-Hispanic Black than non-Hispanic White patients (19). Prior studies have reported PAD to be a male-predominant disease, with one study reporting PAD incidence to be 50% lower in women than men among VA patients (19). The geographical and temporal association data for PAD-related hospitalizations in the US is minimal. While the overall rate of non-traumatic lower extremity amputations declined between 2000 and 2008, compared to the South Atlantic region, the rates of amputation were generally higher in East South Central and West South Central and lower in the Middle Atlantic region (20). However, temporal and geographical trends for PAD in the US are poorly characterized.

To address this knowledge deficit, we investigate the temporal, geographical, and sociodemographic trends in PAD-related hospitalizations in the general population as well as among cocaine and methamphetamine users in the US (2008–2020).

# Methods

## Study design and population

The Healthcare Cost and Utilization Project (HCUP) created the extensive deidentified National Inpatient Database (NIS) database. With more than 7 million hospital admissions annually, the NIS is one of the nation's most extensive and most used healthcare databases. Since more states have recently joined the HCUP, the NIS now covers −97% of all Americans. The information is gathered from hospitals throughout all 50 states. The HCUP website provides access to the NIS data, freely available to the public. The standard International Classification of Disease Clinical Modifications codes were used to identify all adults (>18 years of age) hospitalized for PAD, CLI, methamphetamine, or cocaine use. A complete list of the ICD 9 and 10 codes for PAD, CLI, amputation, methamphetamine, and cocaine use and the states in each region are presented in Supplementary Tables S1–S3, respectively. Hospitalizations related to PAD or CLI were defined as instances where patients were admitted to the hospital with PAD or CLI listed as primary or secondary diagnoses during their index hospitalization. Traumatic amputations and users of any other substances were omitted from the data we collected; only non-traumatic amputations, methamphetamine, and cocaine users were identified and retained for analysis. The NIS database was deidentified; hence, our study was exempt from requiring an institutional review board (IRB) approval. Helsinki guideline was followed for reporting the results.

## Study outcomes

The primary outcome of the study was demographic, racial, and regional trends of PAD-related hospitalizations in the general population of cocaine and methamphetamine users. The secondary outcomes included demographic, racial, and regional trends of CLI-related hospitalizations and amputations among the general population, cocaine and methamphetamine users in the US from 2008 to 2020.

## Statistical analysis

We examined the trends of hospital admissions due to PAD in general and PAD among methamphetamine and cocaine users separately. Similar trends of hospital admissions for CLI and amputations in the general population, methamphetamine and cocaine users among US adults categorized using sociodemographic characteristics based on 2008–2020 NIS data. Trend analysis was conducted to test the rates of hospital admissions, and the Cochran Armitage trend test was used to compare the trend between groups. We used hospital and patient-level weights to calculate the national estimates. Descriptive statistics were used to summarize continuous and categorical variables. The frequency of missing values was summarized, and *Little's MCAR (missing completely at random)* was used to screen for missing data patterns. A non-significant *p*-value ($P > 0.05$) represented randomly missing, while a significant *P*-value ($P < 0.05$) indicated missing not at random (MNAR). Variables with missing data were identified, and overall missing data was less than 5%; we marked it missing and excluded it from the analysis. Multivariate logistic regression was used to examine adjusted odds for PAD and CLI hospitalizations among methamphetamine and cocaine users between 2008 and 2020. Covariates were selected based on clinical correlation with PAD and CLI. We utilized univariate screening for building the regression model; *p*-value <0.2 was used as cut off for the covariates to be included in the final regression analysis ref. The multicollinearity among independent variables was assessed by measuring the variance inflation factor (VIF) and tolerance (1/VIF). VIF ≥5 and tolerance value ≤0.2 was taken as a marker of significant correlation among independent variables ref. We included more than 18 covariates for multivariate analysis, listed in Supplementary Table S4. All analyses used the open-source software R (version 4.3.1) to account for NIS complex sample design and sample weights. $P < 0.05$ (2-tailed) was considered statistically significant for each analysis.

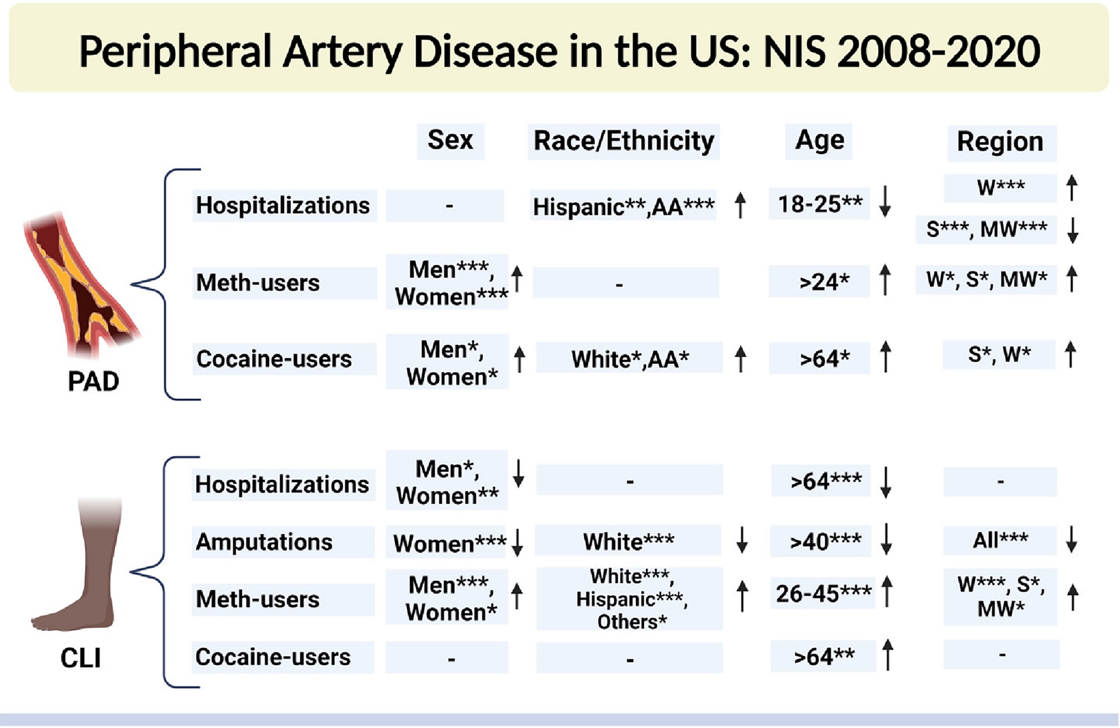

Peripheral Artery Disease in the US: NIS 2008-2020

| | | Sex | Race/Ethnicity | Age | Region |
|---|---|---|---|---|---|
| PAD | Hospitalizations | - | Hispanic**,AA*** ↑ | 18-25** ↓ | W*** ↑<br>S***, MW*** ↓ |
| | Meth-users | Men***, Women*** ↑ | - | >24* ↑ | W*, S*, MW* ↑ |
| | Cocaine-users | Men*, Women* ↑ | White*,AA* ↑ | >64* ↑ | S*, W* ↑ |
| CLI | Hospitalizations | Men*, Women** ↓ | - | >64*** ↓ | - |
| | Amputations | Women*** ↓ | White*** ↓ | >40*** ↓ | All*** ↓ |
| | Meth-users | Men***, Women* ↑ | White***, Hispanic***, Others* ↑ | 26-45*** ↑ | W***, S*, MW* ↑ |
| | Cocaine-users | - | - | >64** ↑ | - |

FIGURE 1
Sex-based, racial, ethical, Age-based, and region-based prevalence trends of PAD- and CLI-related hospitalizations and amputations between 2008 and 2020. NIS, national inpatient sample database; PAD, peripheral arterial disease; CLI, critical limb ischemia; AA, African American; W, west; S, south; MW, midwest. Che-square test was used to compare the categorical and t-test was used to compare the numerical values. *$P < 0.05$, **$P < 0.01$, and ***$P < 0.001$. ↑, increasing trend; ↓, decreasing trend; "–", no significant change. Created with Biorender.com.

TABLE 1 Demographic characteristics of PAD, CLI, who were also diagnosed as methamphetamine and cocaine users aged 18 or higher from 2008 to 2020 in the US.

| Characteristics | Group | PAD, *n* (%) (95% CI) | CLI *n* (%) (95% CI) | PAD among Meth users *n* (%) (95% CI) | PAD among Cocaine users *n* (%) (95% CI) |
|---|---|---|---|---|---|
| NIS data 2008–2020 | *N* | 6,436,612 | 1,591,291 | 8,011 | 13,753 |
| Sex | Men | 3,413,485 (53.04) (53–53.08) | 943,862 (59.32) (59.24–59.4) | 5,043 (62.99) (61.93–64.05) | 9,107 (66.22) (65.43–67.01) |
|  | Women | 3,022,487 (46.96) (46.92–47) | 647,295 (40.68) (40.6–40.76) | 2,963 (37.01) (35.95–38.07) | 4,646 (33.78) (32.99–34.57) |
| Age (years) | Mean, SD | 72, 12.02 | 69.61, 12.37 | 59.76, 11.85 | 56.25, 9.13 |
|  | 18–25 | 5,101 (0.08) (0.08–0.08) | 623 (0.04) (0.04–0.04) | 26 (0.32) (0.2–0.44) | 45 (0.33) (0.23–0.43) |
|  | 26–40 | 57,175 (0.89) (0.88–0.9) | 17,708 (1.11) (1.1–1.13) | 383 (4.78) (4.32–5.25) | 620 (4.51) (4.16–4.85) |
|  | 41–64 | 1,681,929 (26.13) (26.1–26.16) | 532,907 (33.49) (33.42–33.56) | 5,134 (64.09) (63.04–65.14) | 10,615 (77.19) (76.48–77.89) |
|  | ≥65 | 4,692,406 (72.9) (72.87–72.94) | 1,040,053 (65.36) (65.29–65.43) | 2,468 (30.81) (29.8–31.82) | 2,473 (17.98) (17.34–18.62) |
| Race/Ethnicity[a] | White | 4,291,992 (70.93) (70.89–70.97) | 952,244 (63.94) (63.86–64.01) | 5,607 (73.04) (72.04–74.03) | 3,322 (25.31) (24.57–26.05) |
|  | Black | 847,534 (14.01) (13.98–14.03) | 314,319 (21.1) (21.04–21.17) | 633 (8.25) (7.63–8.86) | 8,382 (63.87) (63.04–64.69) |
|  | Hispanic | 558,265 (9.23) (9.2–9.25) | 150,330 (10.09) (10.05–10.14) | 873 (11.38) (10.67–12.09) | 964 (7.35) (6.9–7.79) |
|  | Asian or Pacific Islander | 187,212 (3.09) (3.08–3.11) | 22,414 (1.5) (1.49–1.52) | 285 (3.71) (3.28–4.13) | 71 (0.54) (0.42–0.67) |
|  | Native American | 35,024 (0.58) (0.57–0.58) | 11,113 (0.75) (0.73–0.76) | 105 (1.37) (1.11–1.63) | 79 (0.6) (0.47–0.74) |
|  | Other | 131,060 (2.17) (2.15–2.18) | 38,964 (2.62) (2.59–2.64) | 174 (2.26) (1.93–2.6) | 306 (2.33) (2.07–2.59) |
| Primary payer | Medicare | 4,871,163 (75.76) (75.72–75.79) | 1,163,868 (73.24) (73.17–73.31) | 3,722 (46.49) (45.4–47.58) | 5,499 (39.98) (39.16–40.8) |
|  | Medicaid | 409,845 (6.37) (6.36–6.39) | 142,705 (8.98) (8.94–9.02) | 2,488 (31.07) (30.06–32.09) | 5,027 (36.55) (35.74–37.35) |
|  | Private Insurance | 927,617 (14.43) (14.4–14.45) | 217,274 (13.67) (13.62–13.73) | 1,088 (13.59) (12.84–14.34) | 1,514 (11.01) (10.48–11.53) |
|  | Self-pay | 110,535 (1.72) (1.71–1.73) | 33,877 (2.13) (2.11–2.15) | 489 (6.11) (5.59–6.64) | 1,189 (8.65) (8.18–9.12) |
|  | No charge | 12,560 (0.2) (0.19–0.2) | 3,541 (0.22) (0.22–0.23) | 34 (0.43) (0.29–0.57) | 147 (1.07) (0.9–1.24) |
|  | Other | 98,229 (1.53) (1.52–1.54) | 27,930 (1.76) (1.74–1.78) | 184 (2.3) (1.97–2.63) | 377 (2.74) (2.47–3.02) |
| Median household Income[b] ($) | <50,000 | 1,811,558 (28.64) (28.6–28.68) | 537,355 (34.42) (34.34–34.49) | 2,324 (30.89) (29.85–31.94) | 7,567 (56.68) (55.84–57.52) |
|  | 50,000–64,999 | 1,628,021 (25.74) (25.7–25.77) | 415,619 (26.62) (26.55–26.69) | 1,917 (25.49) (24.51–26.48) | 2,806 (21.02) (20.33–21.71) |
|  | 65,000–85,999 | 1,517,440 (23.99) (23.96–24.02) | 343,897 (22.03) (21.96–22.09) | 1,995 (26.52) (25.53–27.52) | 1,952 (14.62) (14.02–15.22) |
|  | >86,000 | 1,368,203 (21.63) (21.6–21.66) | 264,468 (16.94) (16.88–17) | 1,286 (17.09) (16.24–17.94) | 1,026 (7.69) (7.23–8.14) |
| US region | Northeast | 929,279 (14.44) (14.41–14.46) | 320,624 (20.15) (20.09–20.21) | 312 (3.9) (3.48–4.32) | 2,367 (17.21) (16.58–17.84) |
|  | Midwest | 1,387,164 (21.55) (21.52–21.58) | 358,497 (22.53) (22.46–22.59) | 1,128 (14.07) (13.31–14.84) | 2,847 (20.7) (20.03–21.38) |
|  | South | 2,245,973 (34.89) (34.86–34.93) | 660,944 (41.54) (41.46–41.61) | 1,703 (21.25) (20.36–22.15) | 6,199 (45.07) (44.24–45.9) |
|  | West | 1,874,196 (29.12) (29.08–29.15) | 251,225 (15.79) (15.73–15.84) | 4,869 (60.77) (59.7–61.84) | 2,340 (17.01) (16.38–17.64) |
| Length of hospital stay (days) | Mean, SD | 6, 7.26 | 9, 9.41 | 7.64, 8.23 | 7.61, 9.29 |
|  | 0–3 | 2,725,891 (42.35) (42.31–42.39) | 410,349 (25.79) (25.72–25.86) | 2,855 (35.63) (34.58–36.68) | 4,984 (36.24) (35.44–37.05) |
|  | 4–6 | 1,663,115 (25.84) (25.81–25.87) | 388,724 (24.43) (24.36–24.5) | 1,982 (24.74) (23.79–25.68) | 3,265 (23.74) (23.03–24.45) |
|  | 7–9 | 889,557 (13.82) (13.79–13.85) | 295,790 (18.59) (18.53–18.65) | 1,280 (15.97) (15.17–16.77) | 2,135 (15.53) (14.92–16.13) |
|  | 10–12 | 442,432 (6.87) (6.85–6.89) | 168,767 (10.61) (10.56–10.65) | 611 (7.63) (7.05–8.21) | 1,149 (8.36) (7.89–8.82) |
|  | >12 | 715,310 (11.11) (11.09–11.14) | 327,590 (20.59) (20.52–20.65) | 1,284 (16.03) (15.22–16.83) | 2,219 (16.13) (15.52–16.75) |
| Died during hospitalization | Died | 208,253 (3.24) (3.22–3.25) | 52,760 (3.32) (3.29–3.35) | 352 (4.39) (3.95–4.84) | 261 (1.9) (1.67–2.13) |
| Comorbidities |  |  |  |  |  |
| Anemia | Yes | 1,210,415 (21.99) (21.96–22.03) | 366,319 (26.5) (26.43–26.58) | 909 (15.36) (14.45–16.28) | 2,377 (20.59) (19.85–21.32) |
| Arthritis | Yes | 191,505 (3.48) (3.46–3.5) | 46,113 (3.34) (3.31–3.37) | 203 (3.43) (2.97–3.89) | 304 (2.63) (2.34–2.92) |
| Chronic pulmonary disease | Yes | 1,736,292 (28.86) (28.82–28.89) | 366,101 (24.47) (24.4–24.54) | 2,529 (33.54) (32.47–34.61) | 4,249 (33.1) (32.28–33.91) |
| Congestive heart failure | Yes | 872,257 (15.85) (15.82–15.88) | 238,668 (17.27) (17.2–17.33) | 1,535 (25.95) (24.84–27.07) | 2,074 (17.96) (17.26–18.66) |
| Coagulopathy | Yes | 310,373 (5.64) (5.62–5.66) | 59,516 (4.31) (4.27–4.34) | 403 (6.8) (6.16–7.45) | 560 (4.85) (4.46–5.24) |

(*Continued*)

TABLE 1 Continued

| Characteristics | Group | PAD, *n* (%) (95% CI) | CLI *n* (%) (95% CI) | PAD among Meth users *n* (%) (95% CI) | PAD among Cocaine users *n* (%) (95% CI) |
|---|---|---|---|---|---|
| Depression | Yes | 623,173 (10.36) (10.33–10.38) | 137,925 (9.22) (9.17–9.27) | 1,058 (14.03) (13.25–14.82) | 1,811 (14.1) (13.5–14.71) |
| Diabetes | Yes | 2,547,015 (42.33) (42.29–42.37) | 786,192 (52.55) (52.47–52.63) | 2,982 (39.54) (38.44–40.65) | 5,045 (39.3) (38.45–40.14) |
| Hypertension | Yes | 4,577,849 (76.09) (76.05–76.12) | 1,167,531 (78.04) (77.98–78.11) | 5,097 (67.59) (66.53–68.65) | 9,634 (75.04) (74.29–75.79) |
| Liver disease | Yes | 158,745 (2.88) (2.87–2.9) | 30,007 (2.17) (2.15–2.2) | 470 (7.94) (7.25–8.63) | 971 (8.41) (7.91–8.92) |
| Obesity | Yes | 761,724 (12.66) (12.63–12.69) | 159,865 (10.69) (10.64–10.74) | 1,246 (16.52) (15.68–17.36) | 1,462 (11.39) (10.84–11.94) |
| Peripheral vascular disorders | Yes | 5,047,331 (83.89) (83.86–83.92) | 1,027,273 (68.67) (68.59–68.74) | 6,878 (91.2) (90.56–91.84) | 10,990 (85.61) (85–86.22) |
| Pulmonary circulation disorders | Yes | 168,330 (3.06) (3.04–3.07) | 33,916 (2.45) (2.43–2.48) | 314 (5.3) (4.73–5.87) | 388 (3.36) (3.03–3.69) |
| Renal failure | Yes | 1,571,346 (28.55) (28.51–28.59) | 472,719 (34.2) (34.12–34.28) | 1,371 (23.17) (22.1–24.25) | 3,090 (26.75) (25.95–27.56) |

[a] Admitted patients were identified as non-Hispanic American Indian or Alaska Native, non-Hispanic Asian, non-Hispanic Black, Hispanic, and non-Hispanic White.

[b] Median household income of residents in the patient's ZIP Code based on 2020.

# Results

We identified 6,436,612 patients with peripheral arterial disease (PAD), 1,591,291 patients with critical limb ischemia (CLI), 8,011 patients with PAD among methamphetamine users, and 13,753 patients with PAD among cocaine users admitted to US hospitals between the years 2008 and 2020 using the National Inpatient Sample (NIS) database. Overall, Sex-based, Racial, Ethical, Age-based, and Region-based prevalence trends of PAD and CLI-related hospitalizations and amputations between 2008 and 2020 are shown in Figure 1.

## Baseline comorbidities and demographic characteristics of PAD patients

Our study population was predominantly male, particularly in groups with concomitant drug use: 53% vs. 46.9% among PAD patients, 59.32% vs. 40.68% among CLI patients, 63% vs. 37% in PAD patients with methamphetamine use, and 66.22% vs. 33.78% in PAD patients with cocaine use. Among these, 72.9% and 65.36% were over the age of 65 years in the PAD and CLI groups, respectively, while patients with PAD among methamphetamine and cocaine users were predominantly 41–64 years old (64.09% and 77.1%, respectively). The White patient population was predominant among PAD (70.9%), CLI (63.94%), and PAD in methamphetamine users (73.04%), while the Black patient population was predominant among PAD in cocaine users (63.87%). Baseline comorbidities and demographics are shown in Table 1.

## Demographic characteristics of methamphetamine and cocaine users

A total of 255,135 (unweighted) patients with methamphetamine use were identified using data from the NIS database 2008–2020. Our study population was predominantly male (58.43% vs. 41.57%), belonged mainly to the age groups 26–40 years (37.17%) and 41–64 years (44.89%), and was predominantly White population (68.8%). A total of 433,584 (unweighted) patients with cocaine use were identified. This cohort was mostly male (60.77% vs. 39.2%), belonged mainly to the age groups 26–40 years (27.2%) and 41–64 years (61.8%), and predominantly Black patients (53.2%), followed by White patients (32.9%). Demographic characteristics of patients diagnosed as methamphetamine and cocaine users are shown in Table 2.

## Demographic, race/ethnicity, sex-related, and regional disparities of trends in PAD-related hospitalizations from 2008 to 2020

In Figure 2, we observed an increasing trend among male, female, Non-Hispanic White population, Non-Hispanic Black

TABLE 2 Demographic characteristics of patients diagnosed as methamphetamine and cocaine users aged 18 or higher from 2008 to 2020 in the US.

| Characteristics | Group | Methamphetamine use | | Cocaine use | |
|---|---|---|---|---|---|
| | | Unweighted | Weighted | Unweighted | Weighted |
| | | *n* (%) (95% CI) | *n* (%) (95% CI) | *n* (%) (95% CI) | *n* (%) (95% CI) |
| 2008–2020 | | 255,135 | 1,268,584 | 433,584 | 2,133,887 |
| Sex | Men | 149,033 (58.43) | 741,669 (58.48) (58.39,58.56) | 263,420 (60.77) (60.62–60.91) | 1,297,598 (60.82) (60.75–60.89) |
| | Women | 106,038 (41.57) | 526,602 (41.52) (41.44,41.61) | 170,085 (39.23) (39.09–39.38) | 835,899 (39.18) (39.11–39.25) |
| Age (year) | Mean (SD) | 42.8, 14.32 | 42.8, 14.30 | 46, 12.27 | 46, 12.28 |
| | 18–25 | 27,767 (10.88) | 137,989 (10.88) (10.82,10.93) | 27,364 (6.31) (6.24–6.38) | 134,411 (6.3) (6.27–6.33) |
| | 26–40 | 94,823 (37.17) | 471,718 (37.18) (37.1,37.27) | 117,921 (27.2) (27.06–27.33) | 579,568 (27.16) (27.1–27.22) |
| | 41–64 | 114,533 (44.89) | 569,768 (44.91) (44.83,45) | 268,224 (61.86) (61.72–62.01) | 1,320,409 (61.88) (61.81–61.94) |
| | ≥65 | 18,012 (7.06) | 89,108 (7.02) (6.98,7.07) | 20,075 (4.63) (4.57–4.69) | 99,498 (4.66) (4.63–4.69) |
| Race/Ethnicity[a] | White | 166,259 (68.84) | 826,656 (68.81) (68.72,68.89) | 134,573 (32.98) (32.83–33.12) | 662,368 (32.93) (32.87–33) |
| | Black | 23,614 (9.78) | 117,498 (9.78) (9.73,9.83) | 217,268 (53.24) (53.09–53.39) | 1,070,674 (53.24) (53.17–53.3) |
| | Hispanic | 34,295 (14.2) | 170,858 (14.22) (14.16,14.28) | 39,574 (9.7) (9.61–9.79) | 195,749 (9.73) (9.69–9.77) |
| | Asian or Pacific Islander | 6,510 (2.7) | 32,405 (2.7) (2.67,2.73) | 2,286 (0.56) (0.54–0.58) | 11,384 (0.57) (0.56–0.58) |
| | Native American | 4,438 (1.84) | 22,142 (1.84) (1.82,1.87) | 2,004 (0.49) (0.47–0.51) | 10,046 (0.5) (0.49–0.51) |
| | Other | 6,403 (2.65) | 31,841 (2.65) (2.62,2.68) | 12,381 (3.03) (2.98–3.09) | 60,977 (3.03) (3.01–3.06) |
| Primary payer | Medicare | 48,658 (19.12) | 241,430 (19.08) (19.01–19.15) | 98,105 (22.69) (22.57–22.82) | 482,666 (22.68) (22.63–22.74) |
| | Medicaid | 123,436 (48.51) | 615,274 (48.63) (48.54–48.72) | 191,284 (44.25) (44.1–44.39) | 943,908 (44.36) (44.29–44.43) |
| | Private Insurance | 34,201 (13.44) | 169,454 (13.39) (13.33–13.45) | 52,708 (12.19) (12.09–12.29) | 259,237 (12.18) (12.14–12.23) |
| | Self-pay | 34,396 (13.52) | 170,857 (13.5) (13.44–13.56) | 64,038 (14.81) (14.71–14.92) | 313,405 (14.73) (14.68–14.78) |
| | No charge | 1,951 (0.77) | 9,707 (0.77) (0.75–0.78) | 7,582 (1.75) (1.71–1.79) | 37,301 (1.75) (1.74–1.77) |
| | Other | 11,806 (4.64) | 58,460 (4.62) (4.58–4.66) | 18,608 (4.3) (4.24–4.36) | 91,264 (4.29) (4.26–4.32) |
| Median household Income[b] ($) | <50,000 | 85,969 (36.8) | 428,086 (36.86) (36.78–36.95) | 219,198 (53.24) (53.09–53.39) | 1,078,432 (53.24) (53.17–53.31) |
| | 50,000–64,999 | 67,032 (28.69) | 333,142 (28.69) (28.61–28.77) | 91,219 (22.16) (22.03–22.28) | 448,670 (22.15) (22.09–22.21) |
| | 65,000–85,999 | 51,009 (21.83) | 253,126 (21.8) (21.72–21.87) | 62,384 (15.15) (15.04–15.26) | 306,542 (15.13) (15.08–15.18) |
| | >86,000 | 29,611 (12.67) | 146,894 (12.65) (12.59–12.71) | 38,915 (9.45) (9.36–9.54) | 191,851 (9.47) (9.43–9.51) |
| Length of stay (days) | 0–3 | 126,924 (49.75) | 631,001 (49.74) (49.66–49.83) | 219,445 (50.61) (50.47–50.76) | 1,079,710 (50.6) (50.53–50.67) |
| | 4–6 | 68,039 (26.67) | 338,489 (26.68) (26.61–26.76) | 116,204 (26.8) (26.67–26.93) | 572,278 (26.82) (26.76–26.88) |
| | 7–9 | 26,905 (10.55) | 133,822 (10.55) (10.5–10.6) | 45,500 (10.49) (10.4–10.59) | 223,883 (10.49) (10.45–10.53) |
| | 10–12 | 11,611 (4.55) | 57,688 (4.55) (4.51–4.58) | 19,501 (4.5) (4.44–4.56) | 96,075 (4.5) (4.47–4.53) |
| | >12 | 21,646 (8.48) | 107,535 (8.48) (8.43–8.53) | 32,911 (7.59) (7.51–7.67) | 161,827 (7.58) (7.55–7.62) |
| US region | Northeast | 11,872 (4.65) | 58,974 (4.65)(4.61,4.69) | 108,373 (24.99) (24.87–25.12) | 536,285 (25.13) (25.07–25.19) |
| | Midwest | 44,672 (17.51) | 221,886 (17.49)(17.42,17.56) | 89,885 (20.73) (20.61–20.85) | 442,534 (20.74) (20.68–20.79) |
| | South | 69,402 (27.2) | 345,324 (27.22)(27.14,27.3) | 190,155 (43.86) (43.71–44) | 932,452 (43.7) (43.63–43.76) |
| | West | 129,189 (50.64) | 642,501 (50.64)(50.55,50.73) | 45,171 (10.42) (10.33–10.51) | 222,615 (10.43) (10.39–10.47) |

[a] Admitted patients were identified as non-Hispanic American Indian or Alaska Native, non-Hispanic Asian, non-Hispanic Black, Hispanic, and non-Hispanic White.

[b] Median household income of residents in the patient's ZIP Code based on 2,020.

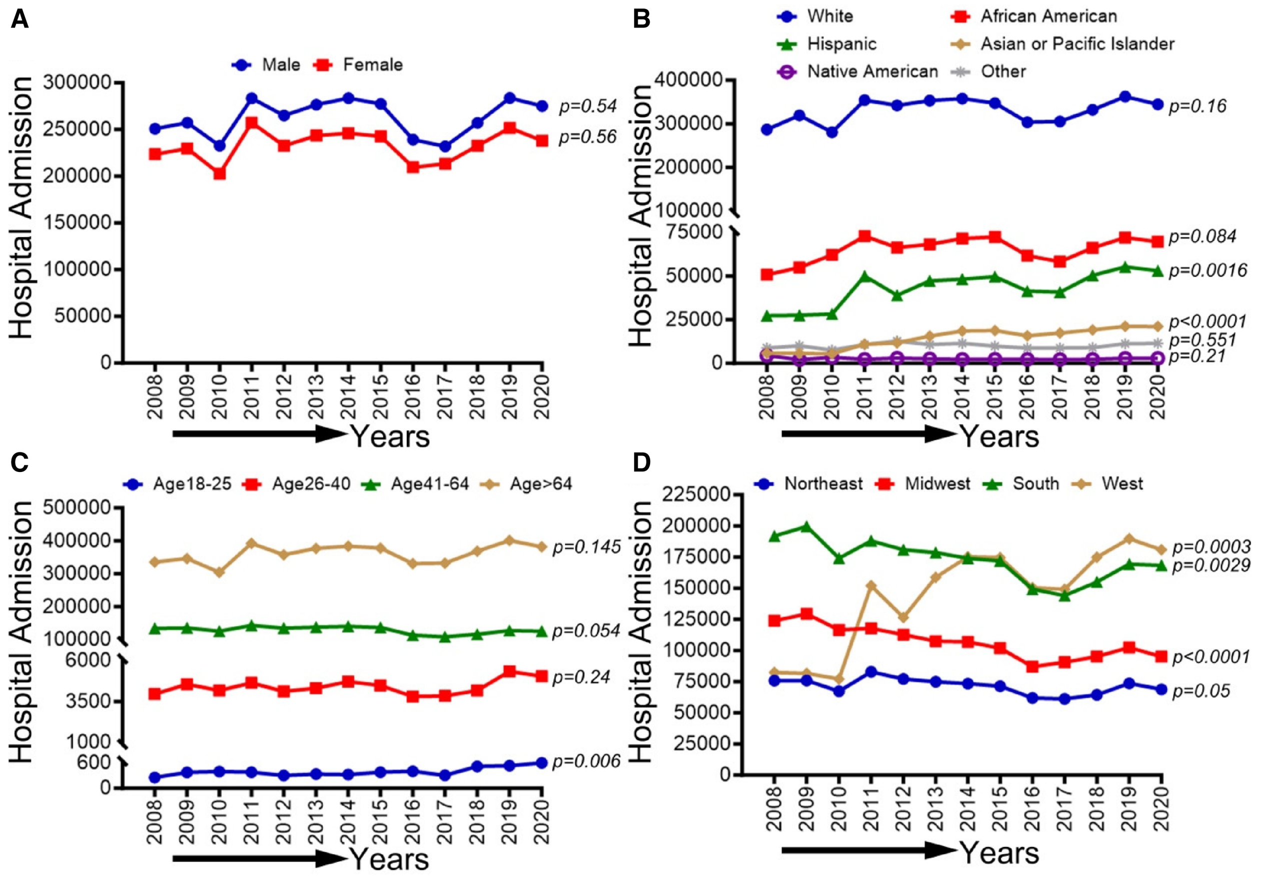

FIGURE 2
Trends in prevalence of PAD-related hospitalizations from 2008 to 2020 by sex (A), race/ethnicity (B), age groups (C), and region (D) in the US. Linear trend test was used to compare the trend from 2008 to 2020 and Cochran-Armitage test was used to compare the group trends. $*P < 0.05$, $**P < 0.01$, and $***P < 0.001$.

population, and age groups (26–40, 41–64, and ≥65 years old) that did not achieve statistical significance ($p$-trend >0.05). On the other hand, a statistically significant increasing trend in PAD-related hospitalization was observed in Hispanics ($p$-trend <0.001), Asian or Pacific Islanders ($p$-trend <0.001), patients 18–25 years old ($p$-trend <0.05), the western region ($p$-trend <0.001). At the same time, a decreasing trend in PAD-related hospitalization was observed in the midwestern region ($p$-trend <0.001) and the southern region ($p$-trend <0.01). Trends in the prevalence of PAD-related hospitalizations and in-hospital mortality from 2008 to 2020 by sex (A), race/ethnicity (B), age groups (C), region (D), and all-cause mortality in the US are shown in Figure 2.

## Demographic, race/ethnicity, sex-related, and regional disparities of trends in CLI-related hospitalizations from 2008 to 2020

In Figure 3, we observed an overall decreasing trend in CLI-related hospitalization among men ($p$-trend <0.001), women ($p$-trend: 0.036), and patients ≥65 years old ($p$-trend <0.001), and in the northeastern ($P$-trend <0.05), midwestern ($p$-trend <0.001), southern ($p$-trend <0.01), and western regions ($p$-trend <0.001). At the same time, an overall increasing trend was seen for the age group 26–40 years ($p < 0.05$). Trends in the prevalence of CLI-related hospitalizations from 2008 to 2020 by sex (A), race/ethnicity (B), age groups (C), region (D), and all-cause mortality in the US are shown in Figure 3.

## Demographic, race/ethnicity, sex-related, and regional disparities of trends in amputations among CLI-related hospitalizations in PAD patients from 2008 to 2020

In Figure 4, We observed an increasing trend in CLI-related amputations in hospitalized patients from 2008 to 2020 for men, women, White, African American, Asian or Pacific islanders, Hispanic, and Native Americans ($p$-trend <0.001). Similarly, CLI-related amputations significantly increased in all age groups except age 18–25 years ($p$-trend <0.05) and in the northeastern, midwestern, western, and southern regions ($p$-trend <0.001). Trends in the prevalence of CLI-related amputations among the

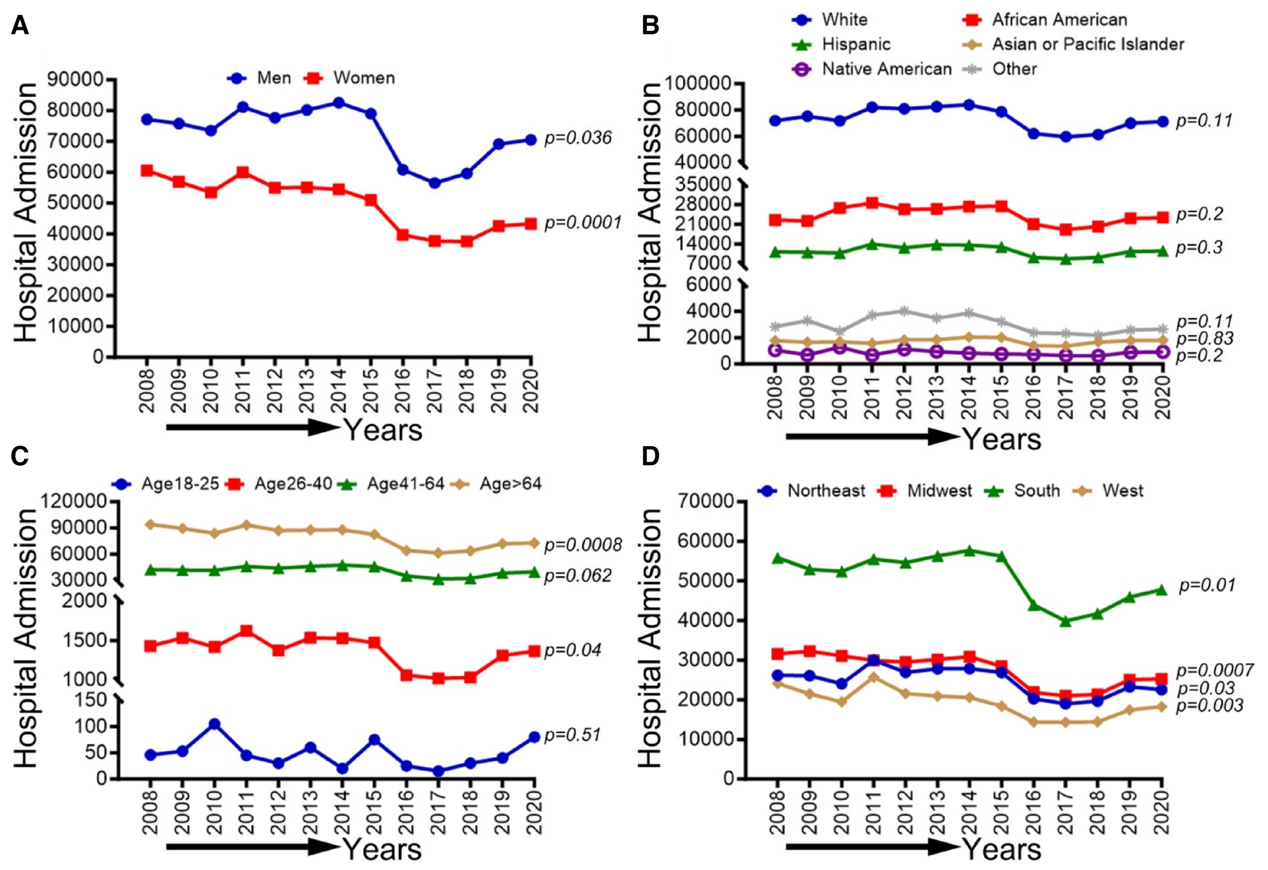

FIGURE 3
Trends in prevalence of CLI-related hospitalizations from 2008 to 2020 by sex (**A**), race/ethnicity (**B**), age groups (**C**), and region (**D**) in the US. Linear trend test was used to compare the trend from 2008 to 2020 and Cochran-Armitage test was used to compare the group trends. $*P < 0.05$, $**P < 0.01$, and $***P < 0.001$.

US population from 2008 to 2020 by sex (A), race/ethnicity (B), age groups (C), and region (D) are shown in Figure 4.

## Demographic, race/ethnicity, sex-related, and regional disparities of trends in PAD-related hospitalizations among methamphetamine users from 2008 to 2020

In Figure 5, an overall increasing trend was observed in PAD-related hospitalization among methamphetamine users in men and women ($p$-trend <0.05), although it was more remarkable for men than women. An overall increasing trend was observed in PAD-related hospitalization among methamphetamine users for all ethnic and racial groups ($p$-trend <0.05). However, the upward trend was more pronounced for the White patient population. Similarly, an upward trend in hospitalizations was seen for the age groups 26–40, 41–64, and >64 years ($p$-trend <0.05), and the midwestern, southern, and western regions ($p$-trend <0.05), with an upward spike noticed in the age group 41–64 years and the western region, particularly during the study period 2017–2020. Trends in PAD-related hospitalizations among methamphetamine users (2008–2020) by sex (A), race/ethnicity (B), age groups (C), and region (D) are shown in Figure 5.

## Demographic, race/ethnicity, sex-related, and regional disparities of trends in PAD-related hospitalizations among cocaine users from 2008 to 2020

In Figure 6, an overall increasing trend was observed in PAD-related hospitalization among cocaine users for men and women ($p$-trend <0.05). A similar uptrend was observed for both Black/African American and White patient populations ($p$-trend <0.05), but the upward trend was more pronounced in African Americans. No significant change in the overall trend was observed in other ethnic/racial groups ($p$-trend >0.05). Furthermore, an upward trend in hospitalizations was seen for the age group >64 years ($p$-trend <0.05) and in the southern and western regions ($p$-trend <0.05). However, these trends did not change significantly for other age groups and US regions ($p$-trend >0.05). Trends in PAD-related hospitalizations among cocaine users (2008–2020) by sex (A), race/ethnicity (B), age groups (C), and region (D) are shown in Figure 6.

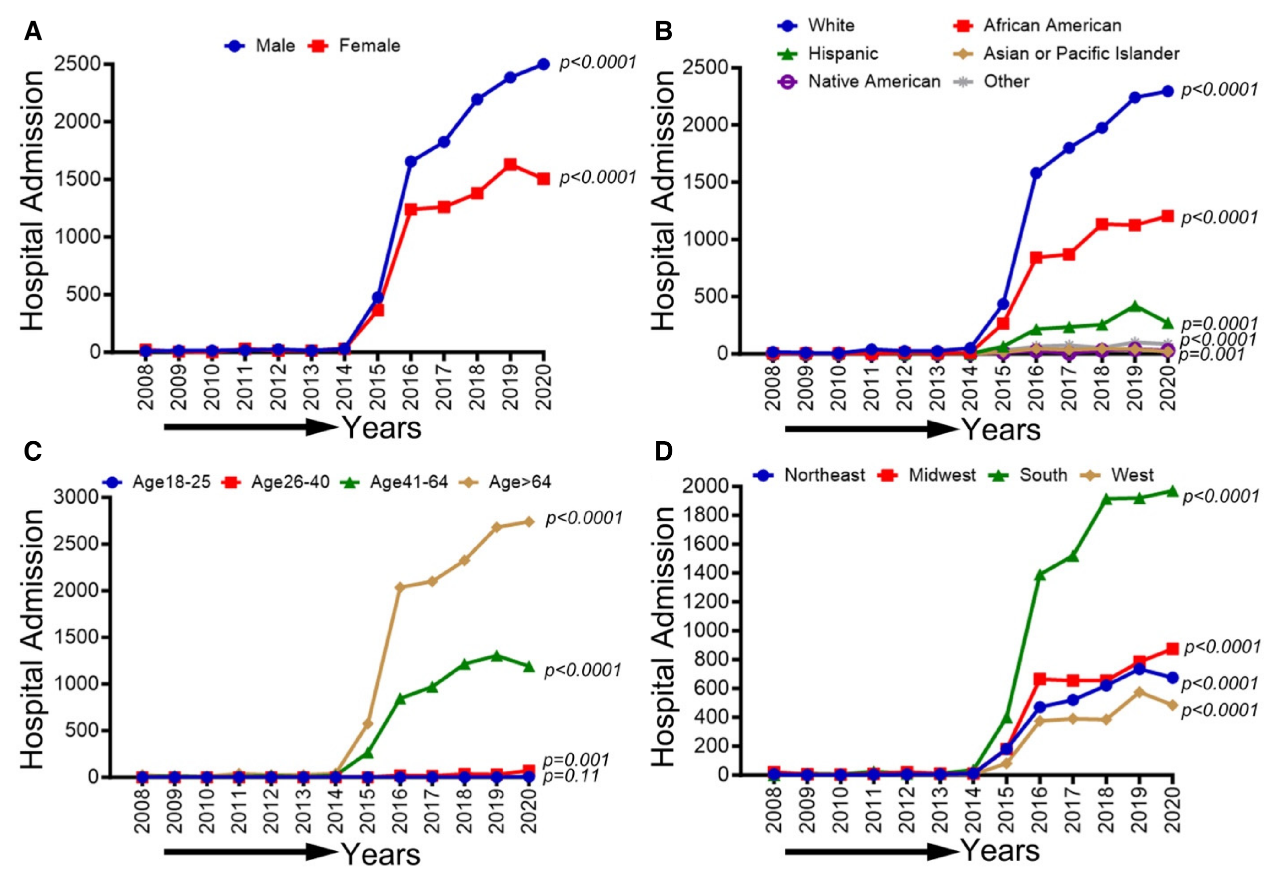

FIGURE 4
Trends in prevalence of amputations among CLI-related hospitalization patients from 2008 to 2020 by sex (**A**), race/ethnicity (**B**), age groups (**C**), and region in the US. Linear trend test was used to compare the trend from 2008 to 2020 and Cochran-Armitage test was used to compare the group trends. **P* < 0.05, ***P* < 0.01, and ****P* < 0.001.

## Demographic, race/ethnicity, sex-related, and regional disparities of trends in CLI-related hospitalizations among methamphetamine users from 2008 to 2020

In Figure 7, we observed an overall increasing trend in CLI-related hospitalization among methamphetamine users for both males and females from 2008 to 2017, which showed a concerning rapid upward spike from 2018 to 2020 ($p$-trend <0.01). A similar upward trend in CLI-related hospitalization in methamphetamine users was observed for the White population ($p$-trend <0.01), African Americans ($p$-trend <0.01), Hispanics ($p$-trend <0.01), Asian/PI ($p$-trend <0.01), Native Americans ($p$-trend <0.05) and population belong to age groups 26–40, 41–64 & >64 years ($p$-trend <0.01). Geographically, we observed an increasing trend in the midwestern ($p$-trend <0.01), the southern ($p$-trend <0.01), and the western regions ($p$-trend <0.01). An upward change, particularly after the study period 2017, was noticed in these trends. Trends in CLI-related hospitalizations among methamphetamine users (2008–2020) by sex (A), race/ethnicity (B), age groups (C), and region (D) are shown in Figure 7.

## Demographic, race/ethnicity, sex-related, and regional disparities of trends in CLI-related hospitalizations among cocaine users from 2008 to 2020

CLI-related hospitalization among cocaine users in patients ≥65 years old showed an overall increasing trend ($p$-trend <0.01). The other trends based on sex, ethnic/racial groups, and regions did not achieve statistical significance ($p$-trend >0.05). Trends in CLI-related hospitalizations among cocaine users (2008–2020) by sex (A), race/ethnicity (B), age groups (C), and region (D) are shown in Figure 8.

## The unadjusted and adjusted odds ratios for PAD and CLI among methamphetamine users from 2008 to 2020 in the adult population in the US

In Table 3, among methamphetamine users, there was no significant difference in the adjusted odds of PAD and CLI for women compared to men (aOR 0.79, 95% CI 0.6–1.04). Older

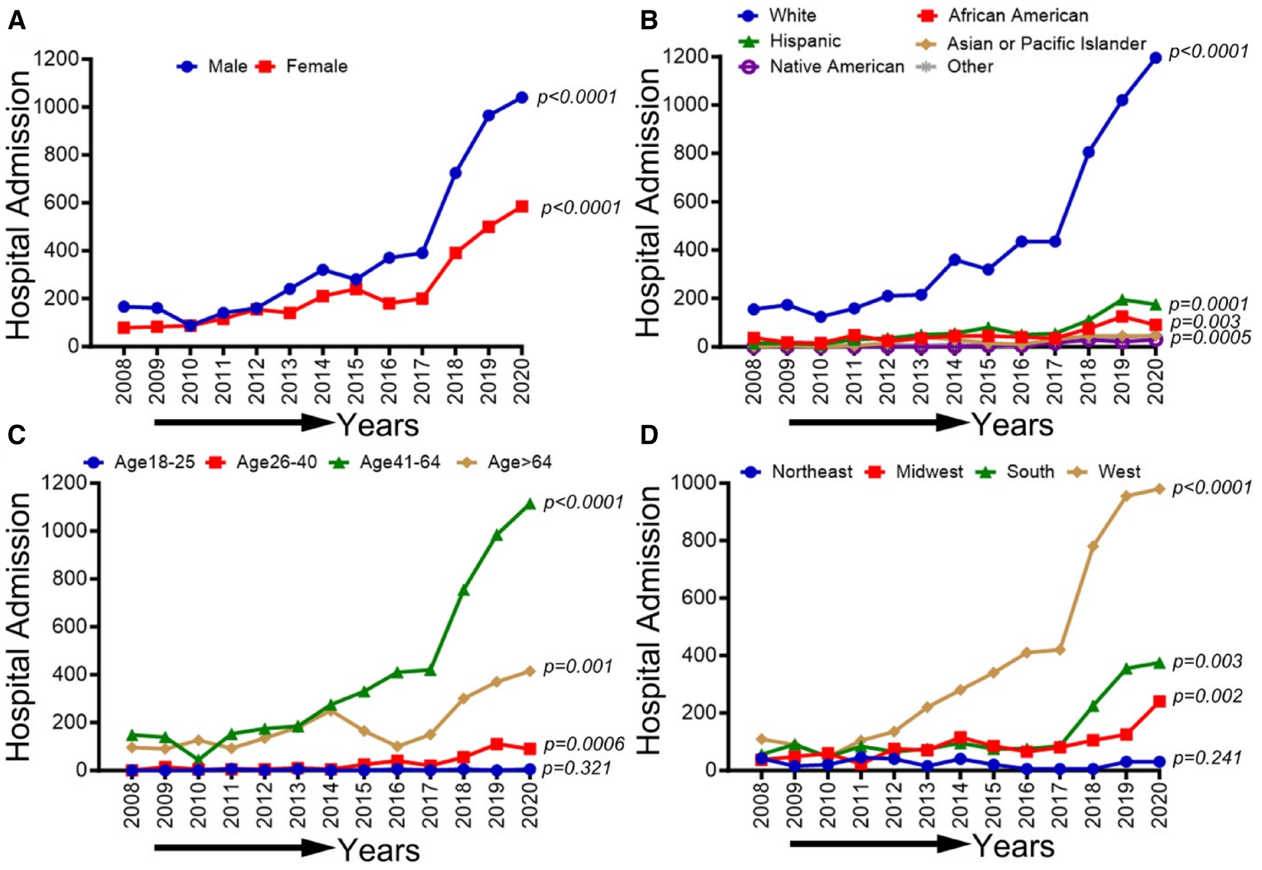

FIGURE 5
Trends in prevalence of PAD-related hospitalizations among methamphetamine users from 2008 to 2020 by sex (A), race/ethnicity (B), age groups (C), and region (D) in the US. Linear trend test was used to compare the trend from 2008 to 2020 and Cochran-Armitage test was used to compare the group trends. *$P < 0.05$, **$P < 0.01$, and ***$P < 0.001$.

age was significantly associated with higher adjusted odds of PAD and CLI among methamphetamine users; compared to the age group 18–25 years, patients in the age group 41–64 years had higher odds of PAD (aOR 5.57, 95% CI 3.1–11) and CLI (aOR 10.69, 95% CI 2.35–189). Similarly, patients in the age group ≥65 years had higher adjusted odds of PAD (aOR 8.18, 95% CI 4.46- 16.8) and CLI (aOR 10.2, 95% CI 2.12–183.5) compared to the patients in the age group 18–25 years. Methamphetamine-related hospitalizations from the western region had significantly higher adjusted odds of PAD (aOR 1.93, 95% CI 1.48–2.55) compared to those in the northeastern region, while there were no other significant regional differences for the adjusted odds of CLI in this cohort. Among various comorbidities identified in the methamphetamine-related hospitalizations, we observed higher adjusted odds of PAD in patients with arthritis (aOR 1.43, 95% CI 1.02–1.98), PAD (aOR 1.43, 95% CI 1.26–1.62), and CLI (aOR 2.69, 95% CI 2.07–3.5) in diabetics and PAD (aOR 1.16, 95% CI 1.02–1.31) in patients with hypertension. The unadjusted and adjusted odds ratios for PAD and CLI among methamphetamine users from 2008 to 2020 in the adult population in the US are presented in Table 3.

## Unadjusted and adjusted odds ratios for PAD and CLI among cocaine users from 2008 to 2020 in the adult population in the US

In Table 4, we observed women had significantly higher adjusted odds of CLI (aOR 1.2, 95% CI 1.1–1.3) compared to men, while there was no significant difference for PAD (aOR 0.94, 95% CI 0.8–1.09) among patients hospitalized with cocaine use. Older age was significantly associated with higher adjusted odds of PAD and CLI among cocaine users; compared to the age group 18–25 years, patients in the age group 26–40 years had higher adjusted odds of PAD (aOR 3.49, 95% CI 1.07–21.4) and CLI (aOR 2.4, 95% CI 1.36–4.73). Similarly, patients with cocaine use belonging to the age groups 41–64 and ≥65 years had higher adjusted odds of PAD (aOR 11.7, 95% CI 3.7–71 and aOR 14.3, 95% CI 4.4–87 respectively) and CLI (aOR 7, 95% CI 4–13.7 and aOR 9.7, 95% CI 5.5–18.97 respectively) when compared to patients in the age group 18–25 years. Non-Hispanic Blacks hospitalized with cocaine use had significantly higher adjusted odds of CLI compared to Non-Hispanic Whites

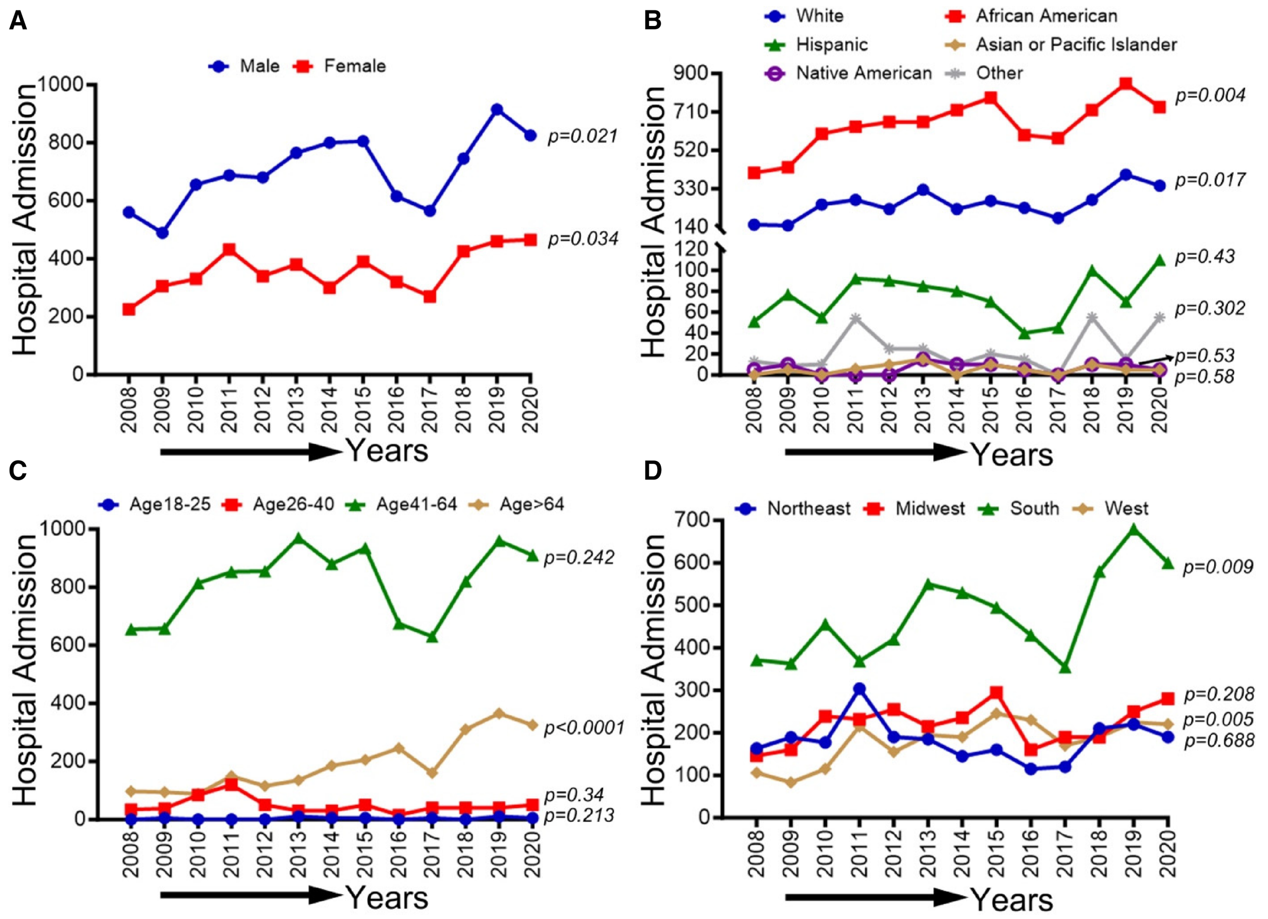

FIGURE 6
Trends in prevalence of PAD-related hospitalizations among cocaine users from 2008 to 2020 by sex (A), race/ethnicity (B), age groups (C), and region (D) in the US. Linear trend test was used to compare the trend from 2008 to 2020 and Cochran-Armitage test was used to compare the group trends. $*P < 0.05$, $**P < 0.01$, and $***P < 0.001$.

(aOR 1.1, 95% CI 1.01–1.21), while there was no significant difference when comparing the other ethnic/racial groups. Similarly, cocaine-related hospitalizations from the southern (aOR 1.22, 95% CI 1.11–1.36) and western regions (2.35, 95% CI 2.08–2.67) had significantly higher adjusted odds of CLI compared to the northeastern region. In all age groups, among various comorbidities identified in this cohort, diabetes had a higher adjusted odds of PAD (aOR 1.85, 95% CI 1.61–2.12) and CLI (aOR 1.36, 95% CI 1.25–1.47). Similarly, in all age groups, hypertension was associated with higher adjusted odds of PAD (aOR 1.4, 95% CI 1.2- 1.65) and CLI (aOR 1.31, 95% CI 1.2–1.43). The unadjusted and adjusted odds ratios for PAD and CLI among cocaine users from 2008 to 2020 in the US adult population are presented in Table 4.

## Discussion

PAD is a disease with an increasingly global reach that has risen in incidence every year since 1990. In the US, 8.5 million individuals (7.2% of the overall population) were affected by PAD in 2000 (5). In our study, we comprehensively investigated the prevalence and trends of PAD from 2008 to 2020. Our study showed a moderate increase in PAD prevalence with a consistently increased male-to-female ratio over the last decade. The geographical distribution of PAD in the US has dramatically changed. Specifically, the western region exhibited a more than twofold rise in PAD in 2020 compared to other areas of the country. Within this, Pacific Islanders and Hispanics showed a striking increase ranging from 2 to 3.6 times in PAD cases compared to other races and ethnicities. However, CLI remained relatively consistent overall. Notably, we observed a substantial surge in PAD cases among methamphetamine users during the study period, particularly in the western region.

Previous studies have shown that the prevalence of PAD increased by 13.1% in high-income countries and more than doubled (28.7%) in low/middle-income countries between 2000 and 2010 (5, 9). In the year 2000, US population-based estimates suggest that over 8 million people aged 40 years and older have been affected by PAD (3). However, some studies showed that

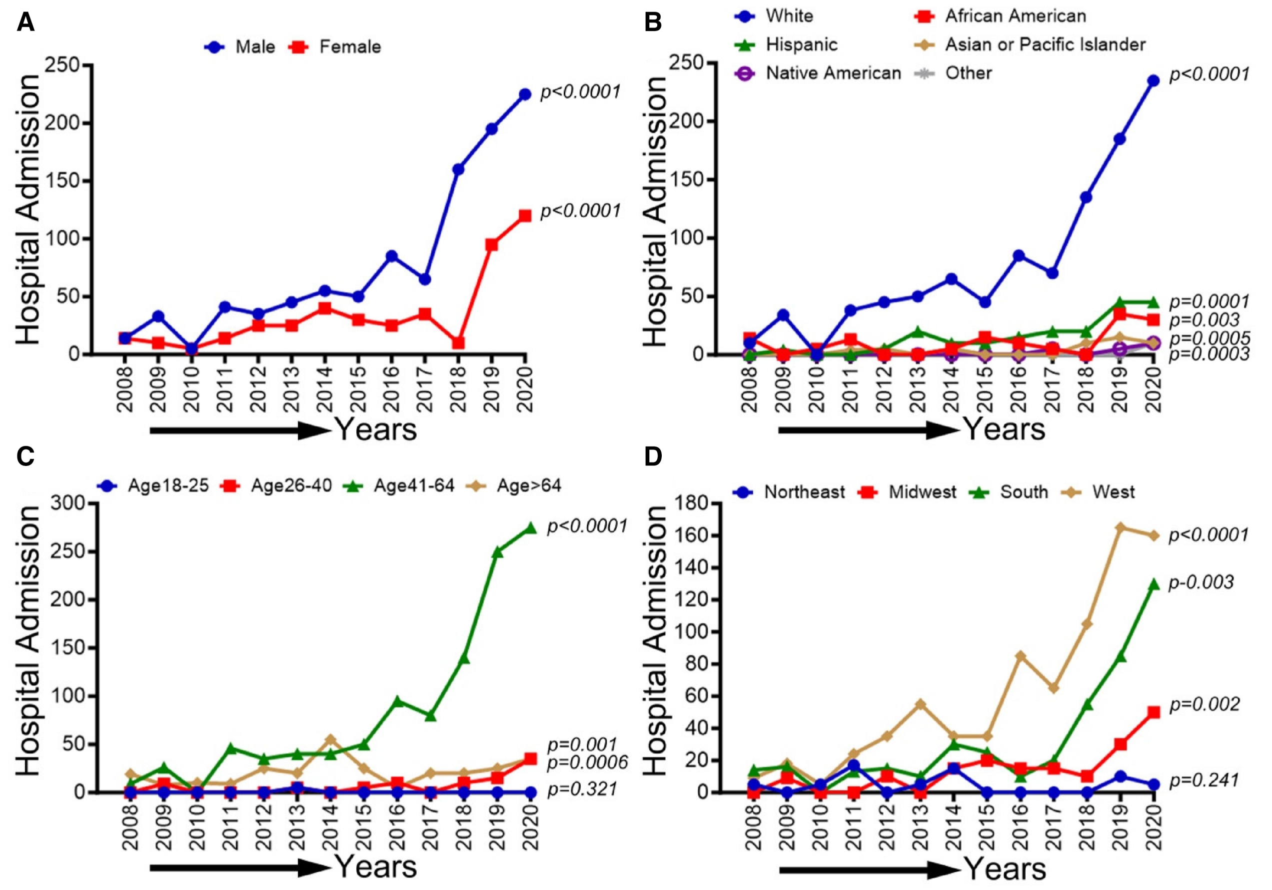

FIGURE 7
Trends in prevalence of CLI-related hospitalizations among methamphetamine users from 2008 to 2020 by sex (**A**), race/ethnicity (**B**), age groups (**C**), and region (**D**) in the US. Linear trend test was used to compare the trend from 2008 to 2020 and Cochran-Armitage test was used to compare the group trends. $*P < 0.05$, $**P < 0.01$, and $***P < 0.001$.

PAD as a primary discharge diagnosis declined between 2006 and 2016 (21), we provide data revealing temporal trends in PAD prevalence between 2008 and 2020. Conversely, while the incidence of CLI remained steady between 2003 and 2011 (22), our analysis of the NIS data showed a decrease in the first half of the last decade before it began to rise again in 2018, with a 1.21-fold increase between 2017 and 2020. Interestingly, previous reports indicated that lower extremity amputation decreased between 2000 and 2008, while diabetic patients showed an overall increase in non-traumatic amputations between 2009 and 2015 (20, 23). However, our results revealed a striking increase in the rate of amputation among PAD patients, up to 133-fold in 2020 compared to 2008 in the US.

The demographic profile of PAD is less clear compared to other ASCVD risk factors. Studies have shown that men have almost double the incidence of PAD compared to women based on intermittent claudication (24–26). However, when objective measures [e.g., ankle-brachial index (ABI)] were used, the sex discrepancy was much less drastic (25, 27). Our findings consistently show slight sex differences in PAD prevalence between men and women. However, our analysis showed that 60% of CLI reported between 2008 and 2020 were men. Furthermore, this gap increased across the last decade (the male-to-female ratio = 1.27 in 2008 compared to 1.62 in 2020). This may explain why symptomatic PAD tends to be more common among men. Additionally, the Multi-Ethnic Study of Atherosclerosis (MESA) found that borderline ABI (ABI 0.9–0.99) was more common in women while true PAD (ABI <0.9) tended to be equally represented in both sexes (28–30).

The prevalence of PAD varies heavily based on race and ethnicity. Prior studies showed that Non-Hispanic Blacks tend to have higher rates of PAD, with the highest prevalence after age 50 years in men and 60 years in women (3, 31–34). After the fifth decade, the incidence of PAD among Non-Hispanic Blacks is almost twice as high as that of other races and nearly three times higher in the eighth decade (3). However, a recent study among veterans reported that between 2008 and 2016, the incidence of PAD was less than 10% higher among Non-Hispanic Blacks compared to non-Hispanic whites at the mean age of 60.2 years (19). These inconsistent data are likely due to study design, ABI vs. symptomatic PAD, and different study lengths. Consistently, our study showed that while most PAD

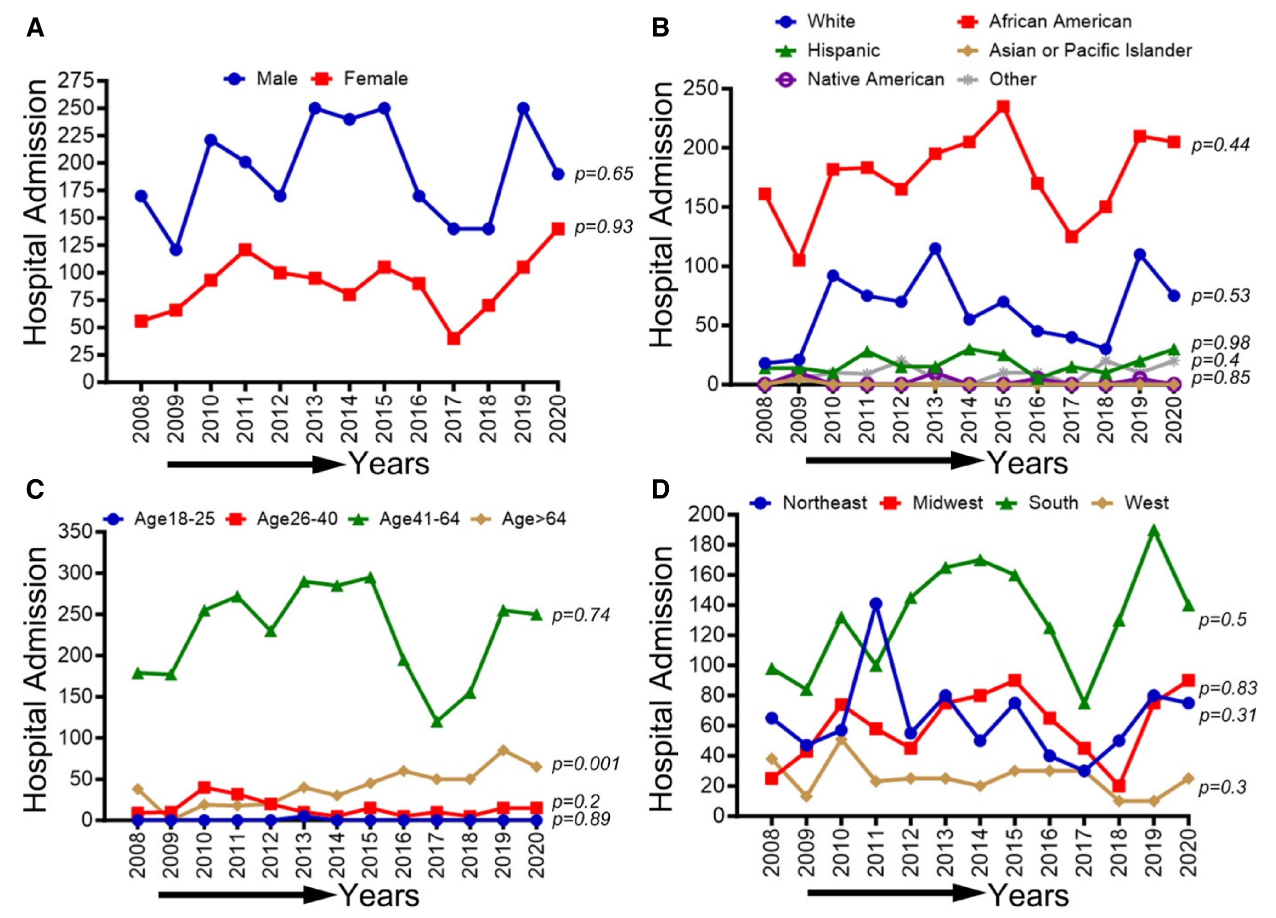

FIGURE 8
Trends in prevalence of CLI-related hospitalizations among cocaine users from 2008 to 2020 by sex (**A**), race/ethnicity (**B**), Age groups (**C**), and region (**D**) in the US. Linear trend test was used to compare the trend from 2008 to 2020 and Cochran-Armitage test was used to compare the group trends. *$P < 0.05$, **$P < 0.01$, and ***$P < 0.001$.

cases were reported among non-Hispanic whites, Asians or Pacific Islanders exhibited the most significant rise in PAD between 2008 and 2020. However, CLI was more than 1.5-fold higher among Non-Hispanic Blacks, followed by Native Americans (1.23-fold), compared to Non-Hispanic Whites.

The geographical distribution and trends associated with PAD have been poorly studied. Non-traumatic amputations showed significant regional variations, with higher rates tending to concentrate in the east south-central, west south-central, and south Atlantic regions (southeastern regions) compared to the mountain, New England, and west north-central regions of the US (20). Moreover, amputations were disproportionally higher among Non-Hispanic Blacks in the high amputation regions compared to other races (20). Our study provides the first data regarding the geographical disparity of PAD in the US. As we mentioned earlier, our findings show a significant increase in the incidence of PAD in the western region from 2008 to 2020. Interestingly, we observed that in 2008, the southern region had over twice the incidence of PAD compared to the western region. However, by 2020, the incidence of PAD in the western region had surpassed that of the southern region and the rest of the country.

Although the association between substance use, particularly methamphetamine and cocaine, and coronary artery disease and cerebrovascular diseases has been well studied (14, 17, 35–38), the epidemiological, clinical, and biological aspects of these drugs in relation to PAD are poorly characterized (39, 40). Our study showed that PAD among methamphetamine users is increasing annually, with an almost 6-fold change between 2008 and 2020. The incidence of PAD among methamphetamine users is predominantly concentrated in the western region of the US (60%), which increased significantly between 2008 and 2020. The observed increase in PAD among methamphetamine users in the western region could be a contributing factor to the geographical shift in PAD. In contrast, PAD among cocaine users is more prevalent in the southern region and has shown a modest increase over the last decade. It is noteworthy to state that methamphetamine has a much longer half-life compared to

TABLE 3 Unadjusted and adjusted odds ratio for PAD and CLI among methamphetamine users from 2,008–2,020 in the US.

| | | PAD patients with meth use | | CLI patients with meth use | |
|---|---|---|---|---|---|
| | | Unadjusted odds ratio (95% CI) | Adjusted odds ratio (95% CI) | Unadjusted odds ratio (95% CI) | Adjusted odds ratio (95% CI) |
| Gender | Men | [Reference] | [Reference] | [Reference] | [Reference] |
| | Women | 0.82 (0.75, 0.89) | 1.1 (0.97, 1.24) | 0.64 (0.52, 0.78) | 0.79 (0.6, 1.04) |
| Age (year) | 18–25 | [Reference] | [Reference] | [Reference] | [Reference] |
| | 26–40 | 3.21 (1.81, 6.31) | 1.45 (0.78, 3.02) | 8.39 (1.8, 149.43) | 2.66 (0.53, 48.15) |
| | 41–64 | 35.56 (20.71, 68.61) | 5.57 (3.1, 11.3) | 79.78 (18.04, 1,401.1) | 10.69 (2.35, 189.19) |
| | ≥65 | 127.96 (74.26, 247.47) | 8.18 (4.46, 16.83) | 164.92 (36.68, 2,909.27) | 10.2 (2.12, 183.51) |
| Race/Ethnicity[a] | White patients | [Reference] | [Reference] | [Reference] | [Reference] |
| | Black patients | 0.83 (0.72, 0.96) | 0.88 (0.72, 1.07) | 0.94 (0.67, 1.29) | 0.69 (0.44, 1.04) |
| | Hispanic patients | 0.81 (0.71, 0.93) | 0.9 (0.74, 1.08) | 0.86 (0.63, 1.15) | 0.68 (0.45, 1.02) |
| | Asian or Pacific Islander patients | 1.37 (1.07, 1.74) | 1.01 (0.72, 1.4) | 1.33 (0.7, 2.26) | 0.95 (0.45, 1.79) |
| | Native American patients | 0.7 (0.48, 0.97) | 1.03 (0.61, 1.64) | 0.7 (0.27, 1.43) | 0.93 (0.28, 2.28) |
| | Other patients | 0.76 (0.56, 1) | 0.81 (0.52, 1.22) | 0.54 (0.21, 1.11) | 0.44 (0.11, 1.2) |
| Primary payer | Medicare | [Reference] | [Reference] | [Reference] | [Reference] |
| | Medicaid | 0.26 (0.24, 0.29) | 0.76 (0.65, 0.9) | 0.41 ( 0.33, 0.51) | 1.26 (0.91, 1.76) |
| | Private insurance | 0.37 (0.32, 0.42) | 1.12 (0.92, 1.36) | 0.27 (0.18, 0.39) | 0.66 (0.37, 1.09) |
| | Self-pay | 0.17 (0.14, 0.2) | 1.02 (0.79, 1.32) | 0.23 (0.15, 0.33) | 1.18 (0.67, 2) |
| | No charge | 0.29 (0.17, 0.47) | 2.15 (1.08, 4.02) | 0.38 (0.09, 0.99) | 1.67 (0.26, 5.74) |
| | Other | 0.23 (0.17, 0.29) | 0.89 (0.63, 1.23) | 0.31 (0.17, 0.51) | 1.13 (0.54, 2.15) |
| Median household income[b] ($) | <50,000 | [Reference] | [Reference] | [Reference] | [Reference] |
| | 50,000–64,999 | 1.05 (0.93, 1.17) | 0.88 (0.76, 1.03) | 0.88 (0.69, 1.13) | 0.81 (0.59, 1.11) |
| | 65,000–85,999 | 1.38 (1.24, 1.55) | 1.07 (0.92, 1.26) | 0.87 (0.67, 1.14) | 0.8 (0.57, 1.13) |
| | >86,000 | 1.44 (1.26, 1.64) | 1.04 (0.86, 1.25) | 0.67 (0.46, 0.95) | 0.67 (0.43, 1.01) |
| US region | Northeast | [Reference] | [Reference] | [Reference] | [Reference] |
| | Midwest | 1.05 (0.83, 1.34) | 1.05 (0.78, 1.44) | 0.83 (0.49, 1.5) | 0.54 (0.28, 1.08) |
| | South | 1.1 (0.88, 1.4) | 1.26 (0.95, 1.69) | 1.42 (0.88, 2.45) | 0.92 (0.52, 1.73) |
| | West | 1.91 (1.55, 2.39) | 1.93 (1.48, 2.55) | 1.59 (1.01, 2.71) | 1.04 (0.61, 1.9) |
| Length of hospital stay (days) | 0–3 | [Reference] | [Reference] | [Reference] | [Reference] |
| | 4–6 | 1.28 (1.15, 1.43) | 1.06 (0.91, 1.22) | 2.86 (2.08, 3.97) | 2.03 (1.37, 3.04) |
| | 7–9 | 1.92 (1.69, 2.17) | 1.4 (1.17, 1.67) | 6.37 (4.58, 8.9) | 4.35 (2.91, 6.56) |
| | 10–12 | 2.35 (1.99, 2.75) | 1.49 (1.19, 1.87) | 8.89 (6.1, 12.91) | 4.63 (2.81, 7.5) |
| | >12 | 2.45 (2.16, 2.77) | 1.32 (1.1, 1.59) | 11.91 (8.81, 16.29) | 6.86 (4.71, 10.11) |
| Anemia | No | [Reference] | [Reference] | [Reference] | [Reference] |
| | Yes | 2.12 (1.86, 2.42) | 1.17 (0.99, 1.39) | 2.58 (1.9, 3.43) | 1.23 (0.87, 1.72) |
| Arthritis | No | [Reference] | [Reference] | [Reference] | [Reference] |
| | Yes | 2.48 (1.87, 3.22) | 1.43 (1.02, 1.98) | 1.78 (0.76, 3.49) | 1.45 (0.6, 2.97) |
| Chronic pulmonary disease | No | [Reference] | [Reference] | [Reference] | [Reference] |
| | Yes | 2.36 (2.16, 2.58) | 0.99 (0.88, 1.12) | 2.03 (1.64, 2.5) | 0.88 (0.66, 1.16) |
| Congestive heart failure | No | [Reference] | [Reference] | [Reference] | [Reference] |
| | Yes | 3.37 (3.01, 3.77) | 0.62 (0.54, 0.72) | 4.58 (3.56, 5.84) | 1.17 (0.87, 1.57) |
| Coagulopathy | No | [Reference] | [Reference] | [Reference] | [Reference] |
| | Yes | 2.02 (1.68, 2.41) | 0.92 (0.73, 1.15) | 1.87 (1.16, 2.84) | 0.6 (0.34, 0.99) |
| Depression | No | [Reference] | [Reference] | [Reference] | [Reference] |
| | Yes | 0.92 (0.82, 1.04) | 0.98 (0.83, 1.15) | 0.71 (0.52, 0.95) | 0.89 (0.61, 1.26) |
| Diabetes | No | [Reference] | [Reference] | [Reference] | [Reference] |
| | Yes | 3.49 (3.2, 3.81) | 1.43 (1.26, 1.62) | 6.48 (5.32, 7.9) | 2.69 (2.07, 3.5) |
| Hypertension | No | [Reference] | [Reference] | [Reference] | [Reference] |
| | Yes | 4.6 (4.2, 5.03) | 1.16 (1.02, 1.31) | 4.56 (3.71, 5.64) | 1.13 (0.86, 1.51) |
| Liver disease | No | [Reference] | [Reference] | [Reference] | [Reference] |
| | Yes | 1.36 (1.15, 1.6) | 0.98 (0.8, 1.2) | 1.37 (0.9, 2) | 0.94 (0.59, 1.42) |
| Obesity | No | [Reference] | [Reference] | [Reference] | [Reference] |
| | Yes | 1.69 (1.5, 1.9) | 1.04 (0.88, 1.23) | 1.3 (0.94, 1.74) | 0.77 (0.52, 1.11) |
| Peripheral vascular disorders | No | [Reference] | [Reference] | [Reference] | [Reference] |
| | Yes | 503.71 (436.06, 585.11) | 259.05 (219.12, 308.13) | 175 (137.15, 226.12) | 64.99 (48.39, 88.41) |
| Pulmonary circulation disorders | No | [Reference] | [Reference] | [Reference] | [Reference] |
| | Yes | 2.85 (2.27, 3.52) | 0.92 (0.7, 1.19) | 2.26 (1.2, 3.85) | 0.57 (0.29, 1.03) |

(*Continued*)

TABLE 3 Continued

| | | PAD patients with meth use | | CLI patients with meth use | |
|---|---|---|---|---|---|
| | | Unadjusted odds ratio (95% CI) | Adjusted odds ratio (95% CI) | Unadjusted odds ratio (95% CI) | Adjusted odds ratio (95% CI) |
| Renal failure | No | [Reference] | [Reference] | [Reference] | [Reference] |
| | Yes | 4.77 (4.24, 5.35) | 1.15 (0.98, 1.34) | 6.3 (4.85, 8.12) | 1.65 (1.2, 2.24) |

[a] Admitted patients were identified as non-Hispanic American Indian or Alaska Native people, non-Hispanic Asian people, non-Hispanic Black people, Hispanic people, and non-Hispanic White people.

[b] Median household income of residents in the patient's ZIP Code based on 2020.

TABLE 4 Unadjusted and adjusted odds ratio for PAD and CLI among cocaine users from 2008–2020 in the US.

| | | PAD patients with cocaine use | | CLI patients with cocaine use | |
|---|---|---|---|---|---|
| | | Unadjusted odds ratio (95% CI) | Adjusted odds ratio (95% CI) | Unadjusted odds ratio (95% CI) | Adjusted odds ratio (95% CI) |
| Gender | Male | [Reference] | [Reference] | [Reference] | [Reference] |
| | Female | 0.69 (0.61, 0.78) | 0.94 (0.8, 1.09) | 0.79 (0.74, 0.84) | 1.2 (1.1, 1.3) |
| Age (year) | 18–25 | [Reference] | [Reference] | [Reference] | [Reference] |
| | 26–40 | 6.77 (2.12, 41.33) | 3.49 (1.07, 21.42) | 3.33 (2.04, 5.87) | 2.4 (1.36, 4.73) |
| | 41–64 | 58.79 (19.01, 353.98) | 11.75 (3.76, 71.09) | 28.11 (17.61, 48.9) | 7.07 (4.08, 13.75) |
| | ≥65 | 175.64 (56.28, 1,061.18) | 14.29 (4.47, 87.23) | 105.97 (66.08, 184.88) | 9.68 (5.51, 18.97) |
| Race/Ethnicity[a] | White patients | [Reference] | [Reference] | [Reference] | [Reference] |
| | Black patients | 2.22 (1.94, 2.54) | 1.14 (0.97, 1.34) | 1.83 (1.72, 1.96) | 1.1 (1.01, 1.21) |
| | Hispanic patients | 1.23 (0.97, 1.54) | 0.92 (0.69, 1.2) | 1.09 (0.96, 1.22) | 0.99 (0.85, 1.15) |
| | Asian or Pacific Islander patients | 0.51 (0.08, 1.59) | 0 (0, 0) | 1.38 (0.89, 2.03) | 0.89 (0.49, 1.52) |
| | Native American patients | 2.15 (1.03, 3.93) | 1.73 (0.76, 3.43) | 1.34 (0.87, 1.97) | 1.02 (0.6, 1.67) |
| | Other patients | 1.46 (1.02, 2.02) | 1.29 (0.86, 1.89) | 1 (0.81, 1.21) | 1.12 (0.87, 1.43) |
| Primary payer | Medicare | [Reference] | [Reference] | [Reference] | [Reference] |
| | Medicaid | 0.48 (0.42, 0.54) | 1 (0.85, 1.18) | 0.43 (0.4, 0.46) | 0.91 (0.83, 1) |
| | Private insurance | 0.33 (0.26, 0.4) | 0.85 (0.66, 1.08) | 0.43 (0.39, 0.48) | 1.13 (1, 1.29) |
| | Self-pay | 0.25 (0.2, 0.31) | 0.77 (0.58, 1.01) | 0.29 (0.26, 0.32) | 1.03 (0.89, 1.19) |
| | No charge | 0.2 (0.1, 0.37) | 0.55 (0.23, 1.1) | 0.32 (0.24, 0.41) | 1.11 (0.79, 1.54) |
| | Other | 0.34 (0.24, 0.46) | 0.79 (0.53, 1.15) | 0.34 (0.28, 0.4) | 0.82 (0.66, 1.01) |
| Median household Income[b] ($) | <50,000 | [Reference] | [Reference] | [Reference] | [Reference] |
| | 50,000–64,999 | 0.82 (0.71, 0.95) | 1.03 (0.87, 1.22) | 0.88 (0.82, 0.95) | 0.99 (0.9, 1.08) |
| | 65,000–85,999 | 0.71 (0.6, 0.84) | 0.93 (0.76, 1.14) | 0.82 (0.75, 0.89) | 0.97 (0.87, 1.08) |
| | >86,000 | 0.51 (0.4, 0.63) | 0.78 (0.59, 1.02) | 0.65 (0.58, 0.72) | 0.93 (0.81, 1.08) |
| US region | Northeast | [Reference] | [Reference] | [Reference] | [Reference] |
| | Midwest | 1.24 (1.05, 1.46) | 0.83 (0.68, 1.01) | 1.75 (1.6, 1.92) | 1.09 (0.97, 1.22) |
| | South | 1.39 (1.21, 1.6) | 1.06 (0.9, 1.26) | 1.86 (1.71, 2.02) | 1.22 (1.11, 1.36) |
| | West | 1.25 (1.02, 1.53) | 0.96 (0.75, 1.22) | 2.96 (2.69, 3.26) | 2.35 (2.08, 2.67) |
| Length of hospital stay (days) | 0–3 | [Reference] | [Reference] | [Reference] | [Reference] |
| | 4–6 | 2.17 (1.82, 2.59) | 2 (1.63, 2.44) | 1.21 (1.12, 1.3) | 1.12 (1.01, 1.23) |
| | 7–9 | 4.66 (3.88, 5.6) | 3.6 (2.91, 4.45) | 2.01 (1.84, 2.19) | 1.57 (1.4, 1.76) |
| | 10–12 | 6.91 (5.61, 8.49) | 4.76 (3.72, 6.05) | 2.58 (2.31, 2.88) | 1.68 (1.45, 1.94) |
| | >12 | 9.08 (7.69, 10.73) | 6.55 (5.39, 7.98) | 2.72 (2.49, 2.96) | 1.87 (1.67, 2.09) |
| Anemia | No | [Reference] | [Reference] | [Reference] | [Reference] |
| | Yes | 2.78 (2.42, 3.19) | 1.37 (1.17, 1.61) | 2.17 (2.01, 2.35) | 1.12 (1.02, 1.23) |
| Arthritis | No | [Reference] | [Reference] | [Reference] | [Reference] |
| | Yes | 1.83 (1.19, 2.68) | 1.01 (0.62, 1.54) | 1.97 (1.6, 2.4) | 1.03 (0.81, 1.3) |
| Chronic pulmonary disease | No | [Reference] | [Reference] | [Reference] | [Reference] |
| | Yes | 1.35 (1.19, 1.53) | 0.79 (0.68, 0.91) | 1.78 (1.67, 1.9) | 0.97 (0.9, 1.06) |
| Congestive heart failure | No | [Reference] | [Reference] | [Reference] | [Reference] |
| | Yes | 3.07 (2.58, 3.62) | 0.81 (0.67, 0.98) | 3.38 (3.1, 3.68) | 0.75 (0.68, 0.84) |
| Coagulopathy | No | [Reference] | [Reference] | [Reference] | [Reference] |
| | Yes | 1.25 (0.92, 1.66) | 0.6 (0.43, 0.81) | 1.62 (1.41, 1.85) | 0.82 (0.69, 0.96) |

*(Continued)*

TABLE 4 Continued

| | | PAD patients with cocaine use | | CLI patients with cocaine use | |
|---|---|---|---|---|---|
| | | Unadjusted odds ratio (95% CI) | Adjusted odds ratio (95% CI) | Unadjusted odds ratio (95% CI) | Adjusted odds ratio (95% CI) |
| Depression | No | [Reference] | [Reference] | [Reference] | [Reference] |
| | Yes | 1.01 (0.86, 1.19) | 0.96 (0.8, 1.16) | 1.01 (0.92, 1.09) | 0.97 (0.87, 1.07) |
| Diabetes | No | [Reference] | [Reference] | [Reference] | [Reference] |
| | Yes | 4.4 (3.92, 4.94) | 1.85 (1.61, 2.12) | 3.27 (3.07, 3.48) | 1.36 (1.25, 1.47) |
| Hypertension | No | [Reference] | [Reference] | [Reference] | [Reference] |
| | Yes | 4.36 (3.83, 4.97) | 1.4 (1.2, 1.65) | 4.38 (4.1, 4.69) | 1.31 (1.2, 1.43) |
| Liver disease | No | [Reference] | [Reference] | [Reference] | [Reference] |
| | Yes | 1.57 (1.29, 1.89) | 1.13 (0.91, 1.39) | 1.56 (1.41, 1.73) | 1.12 (0.99, 1.26) |
| Obesity | No | [Reference] | [Reference] | [Reference] | [Reference] |
| | Yes | 1.15 (0.94, 1.39) | 0.78 (0.61, 0.97) | 1.29 (1.16, 1.42) | 0.84 (0.74, 0.95) |
| Peripheral vascular disorders | No | [Reference] | [Reference] | [Reference] | [Reference] |
| | Yes | 110.7 (97.63, 125.79) | 59.72 (51.5, 69.4) | 323.54 (297, 353.03) | 217.5 (197.1, 240.45) |
| Pulmonary circulation disorders | No | 0 (0, 0) | [Reference] | [Reference] | [Reference] |
| | Yes | 1.9 (1.21, 2.82) | 0.66 (0.41, 1) | 2.98 (2.48, 3.55) | 0.93 (0.75, 1.15) |
| Renal failure | No | [Reference] | [Reference] | [Reference] | [Reference] |
| | Yes | 4.27 (3.71, 4.9) | 1.02 (0.86, 1.21) | 3.96 (3.67, 4.27) | 0.95 (0.86, 1.04) |

[a] Admitted patients were identified as non-Hispanic American Indian or Alaska Native people, non-Hispanic Asian people, non-Hispanic Black people, Hispanic people, and non-Hispanic White people.

[b] Median household income of residents in the patient's ZIP Code based on 2020.

cocaine. Additionally, methamphetamine causes a distinct pattern of endothelial toxicity that affects multiple patterns of endothelial activation compared to cocaine (10, 41).

## Study strengths and limitations

The NIS data have both advantages and disadvantages. Among their strengths, (i) the NIS data on hospitalizations cover an extensive sample size, allowing for robust prevalence and trend analysis; (ii) NIS hospitalization data span numerous years and permit national and state-level estimates; (iii) they provide insightful information about hospital usage and outcomes at the national level in the US; and (iv) the NIS database makes use of standardized diagnosis coding and classification methods, making it possible to analyze trends in hospital usage caused by diseases over time in a consistent and repeatable manner.

Being a cross-sectional study, we could only report temporal association; no definitive conclusion regarding the casualty can be made based on our findings. The selection bias may occur given the retrospective design, ICD-based cohort creation, and inherent errors related to ICD coding. The treatments received by patients, the timing of the interventions, medications, and post-discharge information are unavailable. Moreover, the lack of screening methods to diagnose PAD or CLI among methamphetamine or cocaine users or non-users and the possibility of underestimating prevalence due to insufficient documentation poses further limitations. The analysis in this study focuses solely on PAD and CLI among methamphetamine or cocaine users or non-users and does not discriminate based on other biomarkers or routes of methamphetamine use. Other limitations of the NIS database have been detailed in previous studies (42–44). A larger-scale randomized study followed up on the prospective scale is needed to validate our findings further.

## Conclusion

In conclusion, our paper showed increased PAD in the US with significant geographical and demographic changes over the past decade. We also showed a strong trend of PAD among substance users, especially those who use methamphetamine. There was an increasing trend in PAD-related hospitalizations among methamphetamine and cocaine users for both males and females. Although an overall decreasing trend in CLI-related hospitalization was observed for both genders, an up-trend in CLI was seen among methamphetamine users. These up-trends were more prominent for White, Hispanic & African Americans, and southern and western states, highlighting racial and geographic variations over the study period. Moreover, substance use, especially methamphetamine, needs further investigation to identify risk factors and potential pathologies leading to enhanced PAD.

## Clinical perspective

### Competency in patient care

Certain demographic characteristics such as male sex, methamphetamine use, Pacific Islanders, and Hispanics have higher PAD rates than other populations. Educating at-risk populations and proactive measures might be needed to prevent the rising trends of CLI.

## Translational Outlook

Prospective trials to identify the underlying risk factors in at-risk demographic groups will help guide therapeutic interventions and guidelines.

## Data availability statement

The raw data supporting the conclusions of this article will be made available by the authors, without undue reservation.

## Author contributions

SA: Writing – original draft, Writing – review & editing. ZA-Y: Writing – original draft, Writing – review & editing. MH: Data curation, Formal Analysis, Methodology, Software, Validation, Visualization, Writing – review & editing. MSB: Writing – review & editing. SD: Writing – original draft, Writing – review & editing. RA: Validation, Visualization, Writing – review & editing. NG: Writing – review & editing. MMB: Writing – review & editing. SC: Writing – review & editing. JV: Writing – review & editing. AO: Writing – review & editing. CK: Writing – review & editing. MAB: Writing – original draft, Writing – review & editing.

## Funding

The author(s) declare financial support was received for the research, authorship, and/or publication of this article.

The National Institutes of Health grants supported this work: R01HL145753, R01HL145753-01S1, and R01HL145753-03S1; LSUHSC-S CCDS Finish Line Award, COVID-19 Research Award, and LARC Research Award to MSB; and Institutional Development Award (IDeA) from the National Institutes of General Medical Sciences of the NIH under grant number P20GM121307 and R01HL149264 to CK; NIH R01HL098435, R01HL133497, HL141155 to AO.

## Conflict of interest

The authors declare that the research was conducted in the absence of any commercial or financial relationships that could be construed as a potential conflict of interest.

The author(s) declared that they were an editorial board member of Frontiers, at the time of submission. This had no impact on the peer review process and the final decision.

## Publisher's note

## Supplementary material

The Supplementary Material for this article can be found online at: https://www.frontiersin.org/articles/10.3389/fcvm.2024.1412867/full#supplementary-material

## References

1. Criqui MH, Matsushita K, Aboyans V, Hess CN, Hicks CW, Kwan TW, et al. Lower extremity peripheral artery disease: contemporary epidemiology, management gaps, and future directions: a scientific statement from the American heart association. *Circulation*. (2021) 144(9):e171–91. doi: 10.1161/CIR.0000000000001005

2. Song P, Rudan D, Zhu Y, Fowkes FJI, Rahimi K, Fowkes FGR, et al. Global, regional, and national prevalence and risk factors for peripheral artery disease in 2015: an updated systematic review and analysis. *Lancet Glob Health*. (2019) 7(8): e1020–30. doi: 10.1016/S2214-109X(19)30255-4

3. Allison MA, Ho E, Denenberg JO, Langer RD, Newman AB, Fabsitz RR, et al. Ethnic-specific prevalence of peripheral arterial disease in the United States. *Am J Prev Med*. (2007) 32(4):328–33. doi: 10.1016/j.amepre.2006.12.010

4. Sonderman M, Aday AW, Farber-Eger E, Mai Q, Freiberg MS, Liebovitz DM, et al. Identifying patients with peripheral artery disease using the electronic health record: a pragmatic approach. *JACC Adv*. (2023) 2(7):100566. doi: 10.1016/j.jacadv.2023.100566

5. Lloyd-Jones D, Adams RJ, Brown TM, Carnethon M, Dai S, De Simone G, et al. Heart disease and stroke statistics–2010 update: a report from the American heart association. *Circulation*. (2010) 121(7):e46–215. doi: 10.1161/CIRCULATIONAHA.109.192667

6. Polonsky TS, McDermott MM. Lower extremity peripheral artery disease without chronic limb-threatening ischemia: a review. *JAMA*. (2021) 325(21):2188–98. doi: 10.1001/jama.2021.2126

7. Aday AW, Matsushita K. Epidemiology of peripheral artery disease and polyvascular disease. *Circ Res*. (2021) 128(12):1818–32. doi: 10.1161/CIRCRESAHA.121.318535

8. Creager MA, Matsushita K, Arya S, Beckman JA, Duval S, Goodney PP, et al. Reducing nontraumatic lower-extremity amputations by 20% by 2030: time to get to our feet: a policy statement from the American heart association. *Circulation*. (2021) 143(17):e875–91. doi: 10.1161/CIR.0000000000000967

9. Fowkes FG, Rudan D, Rudan I, Aboyans V, Denenberg JO, McDermott MM, et al. Comparison of global estimates of prevalence and risk factors for peripheral artery disease in 2000 and 2010: a systematic review and analysis. *Lancet*. (2013) 382 (9901):1329–40. doi: 10.1016/S0140-6736(13)61249-0

10. Kevil CG, Goeders NE, Woolard MD, Bhuiyan MS, Dominic P, Kolluru GK, et al. Methamphetamine use and cardiovascular disease. *Arterioscler Thromb Vasc Biol*. (2019) 39(9):1739–46. doi: 10.1161/ATVBAHA.119.312461

11. Xing DG, Horan T, Bhuiyan MdS, Faisal ASM, Densmore K, Murnane KS, et al. Social-geographic disparities in suicidal ideations among methamphetamine users in the USA. *Psychiatry Res*. (2023) 329:115524. doi: 10.1016/j.psychres.2023.115524

12. Bhuiyan MS, Faisal ASM, Venkataraj M, Goeders NE, Bailey SR, Conrad SA, et al. Disparities in Prevalence and Trend of Methamphetamine-Associated Cardiomyopathy in the United States. *J Am Coll Cardiol*. (2023) 81(18):1881–3. doi: 10.1016/j.jacc.2023.03.382

13. Batra V, Murnane KS, Knox B, Edinoff AN, Ghaffar Y, Nussdorf L, et al. Early onset cardiovascular disease related to methamphetamine use is most striking in individuals under 30: a retrospective chart review. *Addict Behav Rep*. (2022) 15:100435. doi: 10.1016/j.abrep.2022.100435

14. Camilleri N, Mizzi A, Gatt A, Papanas N, Formosa C. Peripheral vascular changes in the lower limbs following cocaine abuse. *J Addict Dis*. (2020) 38(3):326–33(3). doi: 10.1080/10550887.2020.1764160

15. Charoenpong P, Dhillon N, Murnane K, Goeders N, Hall N, Keller C, et al. Methamphetamine-associated pulmonary arterial hypertension: data from the national biological sample and data repository for pulmonary arterial hypertension (PAH Biobank). *BMJ Open Respir Res.* (2023) 10(1):e001917. doi: 10.1136/bmjresp-2023-001917

16. Abdullah CS, Remex NS, Aishwarya R, Nitu S, Kolluru GK, Traylor J, et al. Mitochondrial dysfunction and autophagy activation are associated with cardiomyopathy developed by extended methamphetamine self-administration in rats. *Redox Biol.* (2022) 58:102523. doi: 10.1016/j.redox.2022.102523

17. Havakuk O, Rezkalla SH, Kloner RA. The cardiovascular effects of cocaine. *J Am Coll Cardiol.* (2017) 70(1):101–13. doi: 10.1016/j.jacc.2017.05.014

18. Hackler EL, Hamburg NM, White Solaru KT. Racial and ethnic disparities in peripheral artery disease. *Circ Res.* (2021) 128(12):1913–26. doi: 10.1161/CIRCRESAHA.121.318243

19. Aday AW, Duncan MS, Patterson OV, DuVall SL, Alba PR, Alcorn CW, et al. Association of sex and race with incident peripheral artery disease among veterans with normal ankle-brachial indices. *JAMA Netw Open.* (2022) 5(11):e2240188. doi: 10.1001/jamanetworkopen.2022.40188

20. Jones WS, Patel MR, Dai D, Subherwal S, Stafford J, Calhoun S, et al. Temporal trends and geographic variation of lower-extremity amputation in patients with peripheral artery disease: results from U.S. medicare 2000–2008. *J Am Coll Cardiol.* (2012) 60(21):2230–6. doi: 10.1016/j.jacc.2012.08.983

21. Virani SS, Alonso A, Aparicio HJ, Benjamin EJ, Bittencourt MS, Callaway CW, et al. Heart disease and stroke statistics-2021 update: a report from the American heart association. *Circulation.* (2021) 143(8):e254–743. doi: 10.1161/CIR.0000000000000950

22. Agarwal S, Sud K, Shishehbor MH. Nationwide trends of hospital admission and outcomes among critical limb ischemia patients: from 2003–2011. *J Am Coll Cardiol.* (2016) 67(16):1901–13. doi: 10.1016/j.jacc.2016.02.040

23. Geiss LS, Li Y, Hora I, Albright A, Rolka D, Gregg EW. Resurgence of diabetes-related nontraumatic lower-extremity amputation in the young and middle-aged adult U.S. population. *Diabetes Care.* (2019) 42(1):50–4. doi: 10.2337/dc18-1380

24. Murabito JM, Evans JC, Nieto K, Larson MG, Levy D, Wilson PW. Prevalence and clinical correlates of peripheral arterial disease in the framingham offspring study. *Am Heart J.* (2002) 143(6):961–5. doi: 10.1067/mhj.2002.122871

25. Stoffers HE, Rinkens PE, Kester AD, Kaiser V, Knottnerus JA. The prevalence of asymptomatic and unrecognized peripheral arterial occlusive disease. *Int J Epidemiol.* (1996) 25(2):282–90. doi: 10.1093/ije/25.2.282

26. Kannel WB, McGee DL. Update on some epidemiologic features of intermittent claudication: the Framingham study. *J Am Geriatr Soc.* (1985) 33(1):13–8. doi: 10.1111/j.1532-5415.1985.tb02853.x

27. Meijer WT, Grobbee DE, Hunink MG, Hofman A, Hoes AW. Determinants of peripheral arterial disease in the elderly: the Rotterdam study. *Arch Intern Med.* (2000) 160(19):2934–8. doi: 10.1001/archinte.160.19.2934

28. McDermott MM, Liu K, Criqui MH, Ruth K, Goff D, Saad MF, et al. Ankle-brachial index and subclinical cardiac and carotid disease: the multi-ethnic study of atherosclerosis. *Am J Epidemiol.* (2005) 162(1):33–41. doi: 10.1093/aje/kwi167

29. Criqui MH, Aboyans V. Epidemiology of peripheral artery disease. *Circ Res.* (2015) 116(9):1509–26. doi: 10.1161/CIRCRESAHA.116.303849

30. Aboyans V, Criqui MH, McClelland RL, Allison MA, McDermott MM, Goff DC, et al. Intrinsic contribution of gender and ethnicity to normal ankle-brachial index values: the multi-ethnic study of atherosclerosis (MESA). *J Vasc Surg.* (2007) 45(2):319–27. doi: 10.1016/j.jvs.2006.10.032

31. Eraso LH, Fukaya E, Mohler ER, Xie D, Sha D, Berger JS. Peripheral arterial disease, prevalence, and cumulative risk factor profile analysis. *Eur J Prev Cardiol.* (2014) 21(6):704–11. doi: 10.1177/2047487312452968

32. Newman AB, Siscovick DS, Manolio TA, Polak J, Fried LP, Borhani NO, et al. Ankle-arm index as a marker of atherosclerosis in the cardiovascular health study. Cardiovascular heart study (CHS) collaborative research group. *Circulation.* (1993) 88(3):837–45. doi: 10.1161/01.CIR.88.3.837

33. Allison MA, Criqui MH, McClelland RL, Scott JM, McDermott MM, Liu K, et al. The effect of novel cardiovascular risk factors on the ethnic-specific odds for peripheral arterial disease in the multi-ethnic study of atherosclerosis (MESA). *J Am Coll Cardiol.* (2006) 48(6):1190–7. doi: 10.1016/j.jacc.2006.05.049

34. Collins TC, Petersen NJ, Suarez-Almazor M, Ashton CM. The prevalence of peripheral arterial disease in a racially diverse population. *Arch Intern Med.* (2003) 163(12):1469–74. doi: 10.1001/archinte.163.12.1469

35. Islam MN, Kuroki H, Hongcheng B, Ogura Y, Kawaguchi N, Onishi S, et al. Cardiac lesions and their reversibility after long-term administration of methamphetamine. *Forensic Sci Int.* (1995) 75(1):29–43. doi: 10.1016/0379-0738(95)01765-B

36. Yeo KK, Wijetunga M, Ito H, Efird JT, Tay K, Seto TB, et al. The association of methamphetamine use and cardiomyopathy in young patients. *Am J Med.* (2007) 120 (2):165–71. doi: 10.1016/j.amjmed.2006.01.024

37. Al-Yafeai Z, Ali S, Brown J, Venkataraj M, Bhuiyan MdS, Mosa Faisal AS, et al. Cardiomyopathy-associated hospital admissions among methamphetamine users: geographical and social disparities. *JACC: Advances.* (2024):100840. doi: 10.1016/j.jacadv.2024.100840

38. Abdullah CS, Aishwarya R, Alam S, Morshed M, Remex NS, Nitu S, et al. Methamphetamine induces cardiomyopathy by Sigmar1 inhibition-dependent impairment of mitochondrial dynamics and function. *Commun Biol.* (2020) 3 (1):1–20. doi: 10.1038/s42003-020-01408-z

39. Mazumder S, Khan MTF, Bhuiyan MAN, Kiser H. Historical trends of admitted patients by selected substances and their significant patient's level factors. *Addict Behav.* (2020) 109:106478. doi: 10.1016/j.addbeh.2020.106478

40. Ferdous Khan MT, Mazumder S, Rahman MH, Afroz MA, Kiser H, Nobel Bhuiyan MA. The transition of sociodemographic and substance abuse characteristics, pairwise co-occurrences and factors associated with polysubstance use among US adolescents and young adults. *Addict Health.* (2024) 16(1):42–50. doi: 10.34172/ahj.2024.1460

41. Abuse NI on D. How is Methamphetamine Different from Other Stimulants, such as Cocaine? National Institute on Drug Abuse. Available online at: https://nida.nih.gov/publications/research-reports/methamphetamine/how-methamphetamine-different-other-stimulants-such-cocaine (Accessed September 23, 2023).

42. Khera R, Krumholz HM. With great power comes great responsibility: big data research from the national inpatient sample. *Circ Cardiovasc Qual Outcomes.* (2017) 10(7):e003846. doi: 10.1161/CIRCOUTCOMES.117.003846

43. Khera R, Angraal S, Couch T, Welsh JW, Nallamothu BK, Girotra S, et al. Adherence to methodological standards in research using the national inpatient sample. *JAMA.* (2017) 318(20):2011–8. doi: 10.1001/jama.2017.17653

44. HCUP-US NIS Overview [Internet]. Available online at: https://hcup-us.ahrq.gov/nisoverview.jsp (Accessed August 26, 2023)

frontiers | Frontiers in Cardiovascular Medicine

TYPE Review
PUBLISHED 01 August 2024
DOI 10.3389/fcvm.2024.1431398

OPEN ACCESS

EDITED BY
Jennifer Fang,
Tulane University, United States

REVIEWED BY
Changjiang Yu,
Harbin Medical University Cancer Hospital, China
Ryan Temel,
University of Kentucky, United States

*CORRESPONDENCE
Masanori Aikawa
✉ maikawa@bwh.harvard.edu

RECEIVED 11 May 2024
ACCEPTED 15 July 2024
PUBLISHED 01 August 2024

CITATION
Katsuki S, Jha PK, Aikawa E and Aikawa M (2024) The role of proprotein convertase subtilisin/kexin 9 (PCSK9) in macrophage activation: a focus on its LDL receptor-independent mechanisms.
Front. Cardiovasc. Med. 11:1431398.
doi: 10.3389/fcvm.2024.1431398

# The role of proprotein convertase subtilisin/kexin 9 (PCSK9) in macrophage activation: a focus on its LDL receptor-independent mechanisms

Shunsuke Katsuki[1,2], Prabhash Kumar Jha[2], Elena Aikawa[2,3] and Masanori Aikawa[2,3,4]*

[1]Department of Cardiovascular Medicine, Kyushu University Hospital, Fukuoka, Japan, [2]Center for Excellence in Vascular Biology, Cardiovascular Division, Department of Medicine, Brigham and Women's Hospital, Harvard Medical School, Boston, MA, United States, [3]Center for Interdisciplinary Cardiovascular Sciences, Cardiovascular Division, Department of Medicine, Brigham and Women's Hospital, Harvard Medical School, Boston, MA, United States, [4]Channing Division of Network Medicine (MA), Brigham and Women's Hospital, Department of Medicine, Harvard Medical School, Boston, MA, United States

Recent clinical trials demonstrated that proprotein convertase subtilisin/kexin 9 (PCSK9) inhibitors reduce cardiovascular events without affecting systemic inflammation in the patients with coronary artery disease, as determined by high sensitivity C-reactive protein (CRP) levels. However, its pro-inflammatory effects in cardiovascular disease in humans and experimental animals beyond the traditional cholesterol receptor-dependent lipid metabolism have also called attention of the scientific community. PCSK9 may target receptors associated with inflammation other than the low-density lipoprotein receptor (LDLR) and members of the LDLR family. Accumulating evidence suggests that PCSK9 promotes macrophage activation not only via lipid-dependent mechanisms, but also lipid-independent and LDLR-dependent or -independent mechanisms. In addition to dyslipidemia, PCSK9 may thus be a potential therapeutic target for various pro-inflammatory diseases.

KEYWORDS
PCSK9 (proprotein convertase subtilisin/kexin type 9), macrophages, atherosclerosis, inflammation, vascular biology, coronary artery disease, LDL receptor (LDLR), dyslipidemia

## Introduction

PCSK9, the ninth member of the proprotein convertase family, belongs to a group of serine proteases that hydrolyze peptide bonds in their cognate substrates for activation. The discovery of gain- or loss-of-function mutations in PCSK9 in patients with dyslipidemia led to the development of PCSK9 inhibitors with unprecedented lipid-lowering properties (1). PCSK9 prevents LDLR recycling to the cell surface of hepatocytes, leading to an impaired LDL-C clearance from the plasma (2). Several molecules modulate the interaction between PCSK9 and LDLR. PCSK9 interacts with heparan sulfate proteoglycans on the hepatocyte surface through the interaction of surface-exposed basic residues with trisulfated heparan sulfate disaccharide repeats, which promotes LDLR degradation (3). Cytosolic adenylyl cyclase-associated protein 1 (CAP1), a surface receptor that binds the C-terminal domain of resistin (4), also binds the CHRD of PCSK9 and enhances the degradation of the PCSK9-LDLR complex (5). Both the

LDLR and PCSK9 are transcriptionally regulated by sterol regulatory element binding protein-2 (SREBP-2) (6). Mitochondrial reactive oxygen species increase PCSK9 secretion and associate with mitochondrial fission, of which dynamin-related protein 1 (DRP1) is a key driver (7). Rogers et al. of our group demonstrated that DRP1 inhibition promoted hepatic proteasomal degradation of PCSK9 to reduce hepatic PCSK9 secretion (8), by trafficking from ER to proteasomes via ER chaperone glucose-regulated protein 94 (GRP94) (9). DRP-1 inhibition also suppressed *PCSK9* mRNA levels in HepG2 cells via reduced SREBP-1c.

Pivotal studies such as the FOURIER trial (10) and ODYSSEY OUTCOMES trial (11) have demonstrated the efficacy of PCSK9 antibodies in reducing cardiovascular events in primary and secondary prevention, respectively, representing recent advancements in PCSK9-targeted intensive lipid lowering strategy. Building upon these findings, the GLAGOV (12) and HUYGENS trial (13) revealed that the LDL-C reduction by PCSK9 antibodies contributed to the stabilization of plaques as gauged by intracoronary imaging, offering a potential mechanism for their cardiovascular benefits. PACMAN-AMI trial (14) further provided evidence that an early and aggressive lipid lowering strategy with PCSK9 antibodies for high-risk patients may be beneficial. Insights from the ORION trials (15) have expanded the therapeutic landscape by indicating that a PCSK9 siRNA significantly lowers LDL-C levels. Lipoprotein (a) [Lp(a)] is a strong risk factor for atherosclerotic cardiovascular disease regardless of the reduction of LDL-C levels achieved by statins. Clinical trials such as FOURIER and ODYSSEY OUTCOMES trials demonstrated that PCSK9 inhibitors lower not only serum levels of LDL-C but also Lp(a) (16). Notably, The ODYSSEY OUTCOMES trial with alirocumab demonstrated for the first time that a reduction in Lp(a) associated with less major adverse cardiovascular events (17).

## Potential link between PCSK9 and inflammation

Genetic evidence suggests lipid-dependent effects of PCSK9 in gain-of-function and loss-of-function mutation carriers (18). Moreover, clinical trials investigating the clinical benefit of PCSK9 inhibitors using serial intracoronary imaging, such as HUYGENS (13) and PACMAN-AMI (14) trials, have revealed the relationship between achieved levels of LDL-C and change in percent atheroma volume with more intensive lipid-lowering therapies than statins or a statin plus ezetimibe (19). In addition, PCSK9 inhibitors did not change high sensitivity C-reactive protein (CRP) levels in the patients with coronary artery disease (20, 21). However, CRP may not solely capture changes in local inflammation produced by PCSK9 inhibition.

A recent clinical study showed that anti-inflammatory changes in monocyte phenotype with PCSK9 antibodies were not accompanied by a CRP reduction in patients with familial hypercholesterolemia (22). In addition, the ATHEROREMO-IVUS study (The European Collaborative Project on Inflammation and Vascular Wall Remodeling in Atherosclerosis—Intravascular Ultrasound) demonstrated a linear relationship between serum levels of PCSK9 and the fraction or amount of the necrotic core in the non-culprit lesions of patients with acute coronary syndrome, independently of serum levels of LDL-C. A recent observational study demonstrated that treatment with a PCSK9 inhibitor monotherapy is associated with a decreased major adverse cardiovascular events even after adjustment of multiple variables including LDL-C, associated with the decreased expression of inflammatory proteins within the atherosclerotic plaque (23). Collectively, these data suggested anti-inflammatory properties of PCSK9 inhibitors beyond lipid lowering (Figure 1).

PCSK9 of the hepatic origin binds to LDL particles and reaches the atherosclerotic plaque via the circulating blood (24). An *in vitro* experimental study suggested the possibility that PCSK9 released by vascular smooth muscle cells in the human atherosclerotic plaque could reduce LDLR expression in macrophages (25). Considering the accumulating evidence from over decades of research that macrophages play key roles in the initiation and the development of atherosclerosis and the onset of its acute thrombotic complications, these data indicate that circulating PCSK9 and/or local PCSK9 may induce plaque inflammation via macrophage activation. Our group reported that PCSK9 induces pro-inflammatory activation of macrophages and accelerates vein graft lesion development via LDLR-independent mechanisms (Figure 2) (26). This article will provide an overview on the current evidence that links PCSK9 and inflammation via (1) lipid-dependent, (2) lipid-independent and LDL receptor-dependent, or (3) lipid-independent and LDL receptor-independent mechanisms.

## Lipid-dependent pro-inflammatory effects of PCSK9

As described above, cholesterol-lowering with PCSK9 inhibitors attenuates the pro-inflammatory profile of monocytes in patients with hypercholesterolemia. LDL-C lowering with PCSK9 antibodies reduced monocyte CCR2 expression and migratory capacity of monocytes, which was correlated with intracellular lipid accumulation in monocytes (22). This data suggested that LDL-C lowering with PCSK9 inhibitors paralleled by reduced monocyte lipid accumulation itself contributes to the anti-inflammatory effects.

In a preclinical study, weekly subcutaneous injection of alirocumab dose-dependently decreased plasma lipids (27). In the same study, alirocumab added to a statin therapy increased smooth muscle and collagen content associated with decreased macrophage accumulation and necrotic core formation in APOE*3Leiden.CETP mice (27). A strong correlation between plasma total cholesterol levels and atherosclerotic lesion area in the aortic root was observed, suggesting cholesterol lowering with a PCSK9 inhibitor itself leads to inhibition of atherosclerosis development and improves plaque morphology.

## Lipid-independent and LDL receptor-dependent pro-inflammatory effects of PCSK9

Again, PCSK9 released by vascular smooth muscle cells reduces LDLR expression in macrophages *in vitro* (25). Evidence suggests

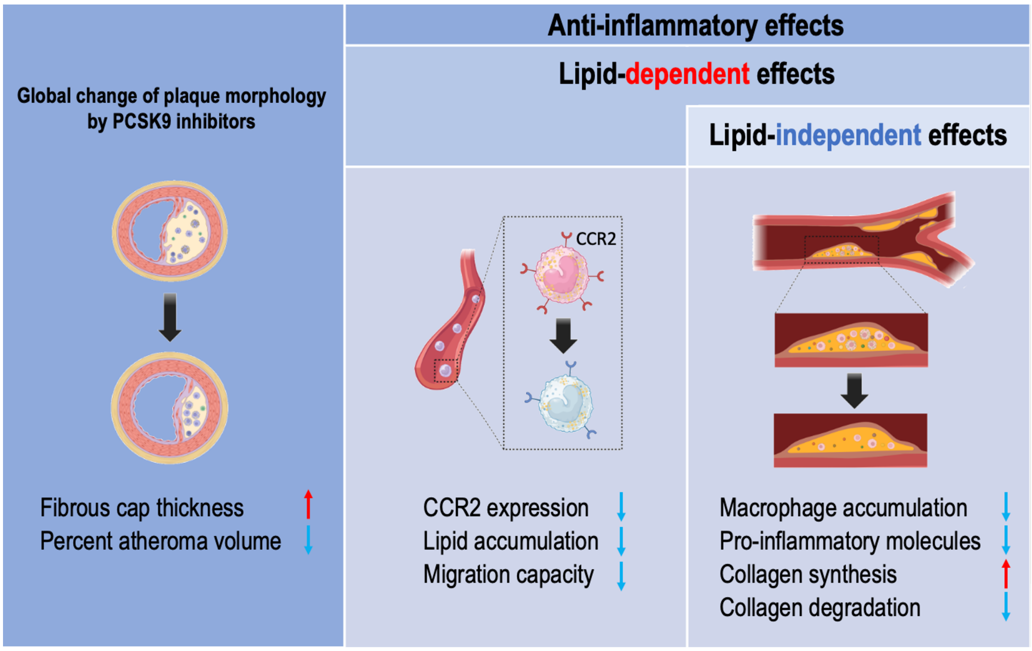

FIGURE 1
The vasculoprotective effects of PCSK9 inhibitors in humans. Lipid lowering effects of PCSK9 inhibitors include thickening of the fibrous cap thickness in coronary plaque and reduced percent atheroma volume. PCSK9 inhibitors have anti-inflammatory properties in a lipid-dependent effects and lipid-independent manner. Monocytes isolated from familial hypercholesterolemia show reduced intracellular lipid accumulation and lower CCR2 expression associated with reduced migration capacity by PCSK9 inhibitors. Patients treated with PCSK9 inhibitors have a reduced macrophage accumulation and pro-inflammatory molecules within the carotid plaque, leading to reduced collagen remodeling partially in a lipid-independent manner.

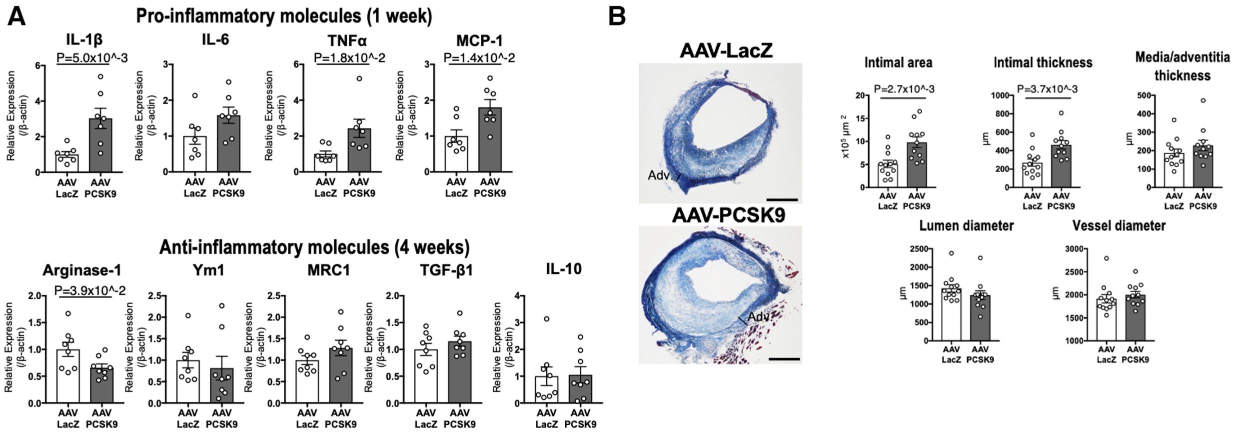

FIGURE 2
The role of circulating PCSK9 in proinflammatory macrophage activation and vein graft lesion development via LDLR-independent mechanisms. (A) mRNA levels of pro-inflammatory molecules and anti-inflammatory molecules were measured in murine peritoneal macrophages of *Ldlr*$^{-/-}$ mice 1 week (upper panels) or 4 weeks (lower panels) after intravenous injection with AAV-LacZ or AAV-PCSK9 ($n$ = 7–8 per group). (B) Left panel: Masson's trichrome staining of vein grafts from *Ldlr*$^{-/-}$ mice treated with AAV-LacZ or AAV-PCSK9 28 days after implantation. Right panel: The quantitative analysis of intimal area, intimal and media/adventitia thickness, and lumen and vessel diameter of vein grafts ($n$ = 12 and 11 for AAV-LacZ and AAV-PCSK9 group, respectively). Panels were reproduced from Katsuki et al. with permission of the publisher.

that pro-inflammatory responses to PCSK9 in macrophages and arterial atherosclerotic lesions may primarily depend on LDLR. Ricci et al. reported that recombinant PCSK9 induced a nuclear translocation of p65, a subunit of the proinflammatory transcription factor NF-κB, in macrophage-like THP-1 cells and pro-inflammatory cytokines and chemokines in THP-1 cells and human macrophages. They also showed that recombinant PCSK9 induced TNFα mRNA in murine bone marrow-derived macrophages mainly, but not exclusively, in an LDLR-dependent fashion (28).

The primary source of local PCSK9 production in atherosclerotic plaques was reported to be smooth muscle cells (25), but other vascular cells such as endothelial cells (29) and macrophages (30) also express PCSK9 under inflammatory stimuli. Giunzioni et al. detected PCSK9 expression in murine macrophages and further reported that overexpression of human PCSK9 in macrophages induced the accumulation of Ly-6C$^{high}$ monocytes in the atheroma and promoted atherosclerotic lesions in an LDLR-dependent mechanism, independently of blood lipid levels (31, 32). In contrast, deletion of the PCSK9 gene in the liver reduced atherosclerotic lesions without changing plasma cholesterol levels, primarily via LDLR-dependent mechanisms (33). These data suggest that PCSK9 exerts lipid-independent pro-inflammatory effects in an LDLR-dependent fashion.

## Lipid-independent and LDL receptor-independent pro-inflammatory effects of PCSK9

PCSK9 also targets other molecules than LDLR (e.g., very low-density lipoprotein receptor (VLDLR), apolipoprotein E receptor 2 (ApoER2), LDLR-related protein 1 (LRP1), CD36). Emerging evidence suggests that PCSK9 may have other targets associated with inflammation including the Toll-like receptor 4 (TLR4)/NF-κB signaling pathway and scavenger receptors.

The TLR4/NF-κB signaling pathway is one of the key signaling pathways mediating PCSK9-induced pro-inflammatory effects. PCSK9 silencing with lentivirus-mediated PCSK9 shRNA vector in *Apoe*$^{-/-}$ mice ameliorated the development of atherosclerotic plaques associated with reduced number of macrophages and decreased expression of vascular inflammation regulators such as TNFα, IL-1β, MCP-1, TLR4 and NF-κB. Silencing PCSK9 did not affect the plasma lipid profiles in these mice. PCSK9 overexpression increased TLR4 expression and increased p-IkBα degradation, and NF-κB nuclear translocation in macrophages, but PCSK9 silencing had the opposite effects in RAW264.7 cells treated by oxidized LDL (oxLDL) (34). An important step in atherogenesis includes formation of ox-LDL that is taken up by a host of scavenger receptors such as SR-A, CD36, and LOX-1 on monocytes and macrophages (35). In an inflammatory milieu, PCSK9 stimulates the expression of scavenger receptors, principally LOX-1, and ox-LDL uptake in macrophages and thus contribute to the process of atherogenesis (30).

No previous *in vivo* studies, however, have provided direct evidence that demonstrates LDLR-independent pro-inflammatory effects of PCSK9 in macrophage activation and vascular lesions. We, thus, investigated LDLR-independent mechanisms by which PCSK9 induces pro-inflammatory activation of macrophages and accelerates vein graft lesion development using *Ldlr*$^{-/-}$ mice. AAV vector encoding a gain-of-function mutant of PCSK9 (AAV-PCSK9) increased circulating PCSK9 without changing serum cholesterol and triglyceride levels (26). AAV-PCSK9 induced mRNA expression of the pro-inflammatory mediators IL-1β, TNFα, and MCP-1 in peritoneal macrophages, as underpinned by an *in vitro* analysis using *Ldlr*$^{-/-}$ mouse macrophages stimulated with endotoxin-free recombinant PCSK9 (Figure 2). AAV-PCSK9 also promoted vein graft lesion development in experimental vein grafts of *Ldlr*$^{-/-}$ mice. *In vivo* molecular imaging further demonstrated that AAV-PCSK9 increased macrophage accumulation and matrix metalloproteinase activity associated with decreased fibrillar collagen, a molecular determinant of atherosclerotic plaque stability. We then explored LDLR-independent pro-inflammatory signaling pathways in an unbiased manner, namely, a combination of unbiased global transcriptomics and network-based hyperedge entanglement prediction analysis. Potential targets of PCSK9 in macrophages include forementioned NF-κB signaling pathway and LOX-1, as well as a novel target, syndecan-4 (SDC4) (26). SDC4 is a heparan sulfate proteoglycan expressed on the surface of human macrophages (36). In addition, SDC4 mRNA is increased in bone marrow-derived macrophages stimulated with LPS, but not IL-4/IL-13 or IL-10 (37), suggesting a potential link between SDC4 and macrophage activation. Although Sdc4 was not a high-ranking differential expressed transcript when compared to NF-κB signaling molecules and Lox-1, its fold change after stimulation with recombinant PCSK9 in the transcriptomics was statistically significant. We performed *in vitro* experiments involving siRNA silencing in primary macrophages to substantiate our computational prediction platform and demonstrated that SDC4 indeed binds to PCSK9 *in vivo* and mediates PCSK9-induced pro-inflammatory responses. Understanding more detailed mechanisms by which SDC4 mediates the pro-inflammatory responses and their downstream signaling induced by PCSK9 requires future investigations (Figure 3). Collectively, we demonstrated LDLR-independent pro-inflammatory effects of PCSK9 in macrophage activation and vascular lesions, independently of serum lipid levels.

## Clinical application of PCSK9 inhibition in cardiovascular disease

Considering the role of PCSK9 in lipid metabolism, multiple therapeutic option including monoclonal antibodies (10, 11), small-molecule inhibitors (38), small interfering RNA (siRNA) molecules (15), antisense oligonucleotides (39), peptide vaccines (40, 41) and CRISPR/Cas9 editing (42) have been developed. While PCSK9 antibodies are administered biweekly, the frequency of PCSK9 siRNA administration is once every six months, substantially alleviating the burden on patients. As of today, the clinical impact caused by the distinction in the mechanisms of PCSK9 inhibition between PCSK9 antibodies and PCSK9 siRNA remains unknown. Elucidating this disparity requires further investigations. Nevertheless, patients with dyslipidemia eagerly await the development of orally administrable small molecular compounds since they are generally better tolerated than biotherapeutics, which require injection.

Over the past decade, we and other investigators have been exploring the potential for the development of a small molecule PCSK9 inhibitor. Miyosawa et al. from our group previously demonstrated that a new cholesteryl ester transfer protein (CETP) inhibitor, K-312, had dual inhibitory actions on CETP and PCSK9 (43). K-312 decreased the active forms of SREBP-1 and SREBP-2 by

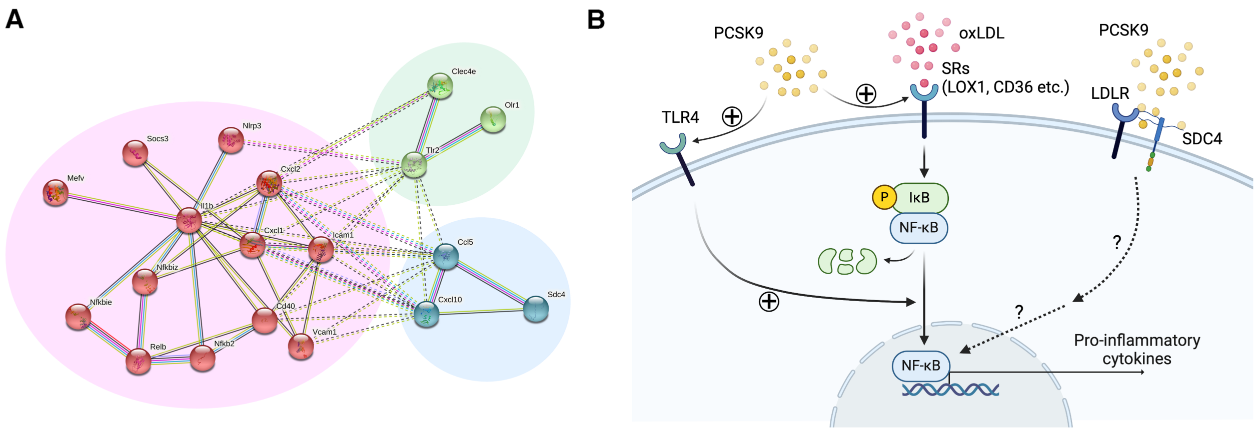

FIGURE 3
Lipid-independent and LDL receptor-independent pro-inflammatory effects of PCSK9 in macrophages. (A) Network analysis of the 24 overrepresented transcripts in *Ldlr*$^{-/-}$ mouse macrophages using STRING database. Nodes are colored according to k-means clustering (number of clusters = 3). Only connected nodes are shown here. Panels were reproduced from Katsuki et al. with permission of the publisher. (B) Potential signaling pathways involved in PCSK9-induced macrophage activation. oxLDL binds to scavenger receptors (LOX1, CD36 etc.), leading to the phosphorylation and degradation of IκB and subsequent activation of NF-κB. PCSK9 promotes this process by enhancing scavenger receptor expression and TLR4. SDC4 directly binds to PCSK9, thereby inducing the expression of pro-inflammatory cytokines possibly via the NF-κB signaling pathway.

regulating the occupancy of SREBP-1 and SREBP-2 on the sterol regulatory element of the PCSK9 promoter. K-312 treatment attenuates atherosclerotic lesions in hyperlipidemic rabbits. Moreover, these K-312-treated rabbits possess decreased plasma levels of PCSK9, providing the *in vivo* evidence for the impact of this compound on PCSK9. Collectively, K-312 may serve as a potent add-on therapy to existing LDL-C lowering drugs such as statins. Merck & Co. has developed MK-0616, an oral PCSK9 inhibitor. In their Phase 2b trial, oral administration of MK-0616 at daily doses ranging from 6 mg to 30 mg resulted in significant reductions of plasma levels of LDL-C, surpassing those achieved with a placebo, in individuals with hypercholesterolemia with a broad spectrum of risks associated with atherosclerotic cardiovascular disease and background statin therapies. In addition, all doses of MK-0616 were well tolerated, with a minimal occurrence of serious adverse events and discontinuations due to adverse events, comparable to the placebo group. They have recently started a phase III trial of its oral macrocyclic peptide inhibitor of PCSK9 for atherosclerotic cardiovascular disease (38). As Rogers et al. from our group previously noted, the inhibition of DRP1 results in a reduction of hepatic PCSK9 secretion through the induction of hepatic proteasomal degradation of PCSK9 and the suppression of SREBP-1c (9). Consequently, an alternative therapeutic approach for PCSK9 inhibition involves a DRP-1 inhibitor, such as mdivi-1.

## Application of PCSK9 overexpression in basic research

Investigating therapeutic targets requires *in vivo* pre-clinical studies to demonstrate proof-of-concept. PCSK9 is not only a promising therapeutic target for hypercholesterolemia, but also applied in the development of experimental animal models for atherosclerosis. A single injection of an adeno-associated virus vector (AAV) encoding a gain-of-function mutant form of PCSK9, along with an atherogenic diet, induces atherosclerosis in mice and hamsters without genetic modification (44, 45).

Vascular calcification is one of the major clinical concerns. We typically use *Ldlr*$^{-/-}$ or *Apoe*$^{-/-}$ mice fed with a high-fat and high-cholesterol diet for 15–20 weeks to induce intimal calcification, a costly and time-consuming process. Recent studies have reported that PCSK9 transgenic mice (46) and D374Y PCSK9 transgenic pigs (47, 48) develop atherosclerotic lesions with calcification. We further reported that a single injection of D377Y PCSK9 AAV vector can induce experimental vascular calcification in mice (49). After a single injection of PCSK9 AAV to C57BL/6J mice fed a high-fat and high-cholesterol diet, serum levels of PCSK9 remained elevated for 20 weeks and vascular calcification progressed to the same extent as that in *Ldlr*$^{-/-}$ mice. To validate the effectiveness of this experimental model of vascular calcification, our group demonstrated a reduction of aortic calcification in sortilin-deficient mice injected with PCSK9 AAV (50). Subsequently, we also demonstrated that DRP1 haplodeficiency did not alter aortic calcification using the same experimental approach (51). These data suggest that utilizing this experimental vascular calcification will enhance the efficiency of testing potential therapeutic agents for calcification *in vivo* without genetic manipulation to induce susceptibility to atherosclerosis.

## Summary and clinical perspective

Randomized clinical trials of PCSK9 inhibitors suggest that the lipid-lowering effect of PCSK9 monoclonal antibodies may be a major factor in the anti-inflammatory outcomes and reduction of cardiovascular events. However, the anti-inflammatory effects on vascular lesions of PCSK9 inhibitors, specifically in ameliorating macrophage activation beyond their lipid-lowering properties, remain largely unknown. In this review, we introduced a series of studies, including our own, that provide evidence supporting the hypothesis that PCSK9 may process pro-inflammatory properties independently of its lipid lowering effects. Part of the beneficial effects of PCSK9 inhibitors on cardiovascular morbidity and mortality in clinical trials might be attributed to a reduction in the low-grade inflammation. Potential future research directions include investigating whether PCSK9 inhibition can mitigate local inflammation in vascular lesions among patients, and elucidating the relative contributions of LDLR-dependent and independent mechanisms underlying the pro-inflammatory effects of PCSK9. In conclusion, the robust lipid-lowering effects of PCSK9 inhibitors with anti-inflammatory properties suggest their potential as a promising therapeutic option to treat cardiovascular diseases, including coronary artery disease, vein graft disease, ischemic stroke, peripheral artery disease, and other inflammatory disorders.

## Author contributions

SK: Conceptualization, Writing – original draft, Writing – review & editing. PJ: Conceptualization, Writing – original draft, Writing – review & editing. EA: Conceptualization, Writing – review & editing. MA: Conceptualization, Funding acquisition, Investigation, Project administration, Supervision, Writing – original draft, Writing – review & editing.

## Funding

The author(s) declare financial support was received for the research, authorship, and/or publication of this article.

This work was supported by the National Institute of Health grants R01HL126901 and R01HL149302, and Pfizer ASPIRE Award to MA; R01HL136431, R01HL147095, and R01HL141917 to EA; and the MSD Scholarships for Overseas Study, and Japan Society for the Promotion of Science Fellowships for Overseas Researchers to SK.

## Acknowledgments

The graphical figure was created with Biorender.com.

## Conflict of interest

Pfizer was not involved in the study other than funding. MA also received research grants from Kowa Company and Sanofi.

The remaining authors declare that the research was conducted in the absence of any commercial or financial relationships that could be construed as a potential conflict of interest.

The author(s) declared that they were an editorial board member of Frontiers, at the time of submission. This had no impact on the peer review process and the final decision.

## Publisher's note

## References

1. Katzmann JL, Laufs U. PCSK9-directed therapies: an update. *Curr Opin Lipidol.* (2024) 35:117–25. doi: 10.1097/MOL.0000000000000919

2. Seidah NG, Benjannet S, Wickham L, Marcinkiewicz J, Jasmin SB, Stifani S, et al. The secretory proprotein convertase neural apoptosis-regulated convertase 1 (NARC-1): liver regeneration and neuronal differentiation. *Proc Natl Acad Sci U S A.* (2003) 100:928–33. doi: 10.1073/pnas.0335507100

3. Gustafsen C, Olsen D, Vilstrup J, Lund S, Reinhardt A, Wellner N, et al. Heparan sulfate proteoglycans present PCSK9 to the LDL receptor. *Nat Commun.* (2017) 8:503. doi: 10.1038/s41467-017-00568-7

4. Lee S, Lee HC, Kwon YW, Lee SE, Cho Y, Kim J, et al. Adenylyl cyclase-associated protein 1 is a receptor for human resistin and mediates inflammatory actions of human monocytes. *Cell Metab.* (2014) 19:484–97. doi: 10.1016/j.cmet.2014.01.013

5. Jang HD, Lee SE, Yang J, Lee HC, Shin D, Lee H, et al. Cyclase-associated protein 1 is a binding partner of proprotein convertase subtilisin/kexin type-9 and is required for the degradation of low-density lipoprotein receptors by proprotein convertase subtilisin/kexin type-9. *Eur Heart J.* (2020) 41:239–52. doi: 10.1093/eurheartj/ehz566

6. Horton JD, Cohen JC, Hobbs HH. Molecular biology of PCSK9: its role in LDL metabolism. *Trends Biochem Sci.* (2007) 32:71–7. doi: 10.1016/j.tibs.2006.12.008

7. Ding ZF, Liu SJ, Wang XW, Mathur P, Dai Y, Theus S, et al. Cross-talk between PCSK9 and damaged mtDNA in vascular smooth muscle cells: role in apoptosis. *Antioxid Redox Sign.* (2016) 25:997–1008. doi: 10.1089/ars.2016.6631

8. Rogers MA, Hutcheson JD, Okui T, Goettsch C, Singh SA, Halu A, et al. Dynamin-related protein 1 inhibition reduces hepatic PCSK9 secretion. *Cardiovasc Res.* (2021) 117:2340–53. doi: 10.1093/cvr/cvab034

9. Poirier S, Mamarbachi M, Chen WT, Lee AS, Mayer G. GRP94 regulates circulating cholesterol levels through blockade of PCSK9-induced LDLR degradation. *Cell Rep.* (2015) 13:2064–71. doi: 10.1016/j.celrep.2015.11.006

10. Sabatine MS, Giugliano RP, Keech AC, Honarpour N, Wiviott SD, Murphy SA, et al. Evolocumab and clinical outcomes in patients with cardiovascular disease. *N Engl J Med.* (2017) 376:713–1722. doi: 10.1056/NEJMoa1615664

11. Schwartz GG, Steg PG, Szarek M, Bhatt DL, Bittner VA, Diaz R, et al. Alirocumab and cardiovascular outcomes after acute coronary syndrome. *N Engl J Med.* (2018) 379:2097–107. doi: 10.1056/NEJMoa1801174

12. Nicholls SJ, Puri R, Anderson T, Ballantyne CM, Cho L, Kastelein JJ, et al. Effect of evolocumab on progression of coronary disease in statin-treated patients: the GLAGOV randomized clinical trial. *JAMA.* (2016) 316:2373–84. doi: 10.1001/jama.2016.16951

13. Nicholls SJ, Kataoka Y, Nissen SE, Prati F, Windecker S, Puri R, et al. Effect of evolocumab on coronary plaque phenotype and burden in statin-treated patients following myocardial infarction. *JACC Cardiovasc Imaging.* (2022) 15:1308–21. doi: 10.1016/j.jcmg.2022.03.002

14. Raber L, Ueki Y, Otsuka T, Losdat S, Haner JD, Lonborg J, et al. Effect of alirocumab added to high-intensity statin therapy on coronary atherosclerosis in patients with acute myocardial infarction: the PACMAN-AMI randomized clinical trial. *JAMA.* (2022) 327:1771–81. doi: 10.1001/jama.2022.5218

15. Ray KK, Raal FJ, Kallend DG, Jaros MJ, Koenig W, Leiter LA, et al. Inclisiran and cardiovascular events: a patient-level analysis of phase III trials. *Eur Heart J*. (2023) 44:129–38. doi: 10.1093/eurheartj/ehac594

16. Stein EA, Mellis S, Yancopoulos GD, Stahl N, Logan D, Smith WB, et al. Effect of a monoclonal antibody to PCSK9 on LDL cholesterol. *N Engl J Med*. (2012) 366:1108–18. doi: 10.1056/NEJMoa1105803

17. Ruscica M, Greco MF, Ferri N, Corsini A. Lipoprotein(a) and PCSK9 inhibition: clinical evidence. *Eur Heart J Suppl*. (2020) 22:L53–6. doi: 10.1093/eurheartj/suaa135

18. Guo Q, Feng X, Zhou Y. PCSK9 variants in familial hypercholesterolemia: a comprehensive synopsis. *Front Genet*. (2020) 11:1020. doi: 10.3389/fgene.2020.01020

19. Di Giovanni G, Nicholls SJ. Intensive lipid lowering agents and coronary atherosclerosis: insights from intravascular imaging. *Am J Prev Cardiol*. (2022) 11:100366. doi: 10.1016/j.ajpc.2022.100366

20. Bohula EA, Giugliano RP, Leiter LA, Verma S, Park JG, Sever PS, et al. Inflammatory and cholesterol risk in the FOURIER trial. *Circulation*. (2018) 138:131–40. doi: 10.1161/CIRCULATIONAHA.118.034032

21. Pradhan AD, Aday AW, Rose LM, Ridker PM. Residual inflammatory risk on treatment with PCSK9 inhibition and statin therapy. *Circulation*. (2018) 138:141–9. doi: 10.1161/CIRCULATIONAHA.118.034645

22. Bernelot Moens SJ, Neele AE, Kroon J, van der Valk FM, Van den Bossche J, Hoeksema MA, et al. PCSK9 monoclonal antibodies reverse the pro-inflammatory profile of monocytes in familial hypercholesterolaemia. *Eur Heart J*. (2017) 38:1584–93. doi: 10.1093/eurheartj/ehx002

23. Marfella R, Prattichizzo F, Sardu C, Paolisso P, D'Onofrio N, Scisciola L, et al. Evidence of an anti-inflammatory effect of PCSK9 inhibitors within the human atherosclerotic plaque. *Atherosclerosis*. (2023) 378:117180. doi: 10.1016/j.atherosclerosis.2023.06.971

24. Kosenko T, Golder M, Leblond G, Weng W, Lagace TA. Low density lipoprotein binds to proprotein convertase subtilisin/kexin type-9 (PCSK9) in human plasma and inhibits PCSK9-mediated low density lipoprotein receptor degradation. *J Biol Chem*. (2013) 288:8279–88. doi: 10.1074/jbc.M112.421370

25. Ferri N, Tibolla G, Pirillo A, Cipollone F, Mezzetti A, Pacia S, et al. Proprotein convertase subtilisin kexin type 9 (PCSK9) secreted by cultured smooth muscle cells reduces macrophages LDLR levels. *Atherosclerosis*. (2012) 220:381–6. doi: 10.1016/j.atherosclerosis.2011.11.026

26. Katsuki S, Jha PK, Lupieri A, Nakano T, Passos LSA, Rogers MA, et al. Proprotein convertase subtilisin/kexin 9 (PCSK9) promotes macrophage activation via LDL receptor-independent mechanisms. *Circ Res*. (2022) 131:873–89. doi: 10.1161/CIRCRESAHA.121.320056

27. Kühnast S, van der Hoorn JWA, Pieterman EJ, van den Hoek AM, Sasiela WJ, Gusarova V, et al. Alirocumab inhibits atherosclerosis, improves the plaque morphology, and enhances the effects of a statin. *J Lipid Res*. (2014) 55:2103–12. doi: 10.1194/jlr.M051326

28. Ricci C, Ruscica M, Camera M, Rossetti L, Macchi C, Colciago A, et al. PCSK9 induces a pro-inflammatory response in macrophages. *Sci Rep*. (2018) 8:2267. doi: 10.1038/s41598-018-20425-x

29. Ding ZF, Liu SJ, Wang XW, Deng XY, Fan YB, Shahanawaz J, et al. Cross-talk between LOX-1 and PCSK9 in vascular tissues. *Cardiovasc Res*. (2015) 107:556–67. doi: 10.1093/cvr/cvv178

30. Ding Z, Liu S, Wang X, Theus S, Deng X, Fan Y, et al. PCSK9 regulates expression of scavenger receptors and ox-LDL uptake in macrophages. *Cardiovasc Res*. (2018) 114:1145–53. doi: 10.1093/cvr/cvy079

31. Giunzioni I, Tavori H, Covarrubias R, Major AS, Ding L, Zhang Y, et al. Local effects of human PCSK9 on the atherosclerotic lesion. *J Pathol*. (2016) 238:52–62. doi: 10.1002/path.4630

32. Tavori H, Giunzioni I, Predazzi IM, Plubell D, Shivinsky A, Miles J, et al. Human PCSK9 promotes hepatic lipogenesis and atherosclerosis development via apoE- and LDLR-mediated mechanisms. *Cardiovasc Res*. (2016) 110:268–78. doi: 10.1093/cvr/cvw053

33. Denis M, Marcinkiewicz J, Zaid A, Gauthier D, Poirier S, Lazure C, et al. Gene inactivation of proprotein convertase subtilisin/kexin type 9 reduces atherosclerosis in mice. *Circulation*. (2012) 125:894–901. doi: 10.1161/CIRCULATIONAHA.111.057406

34. Tang ZH, Peng J, Ren Z, Yang J, Li TT, Li TH, et al. New role of PCSK9 in atherosclerotic inflammation promotion involving the TLR4/NF-kappaB pathway. *Atherosclerosis*. (2017) 262:113–22. doi: 10.1016/j.atherosclerosis.2017.04.023

35. Steinberg D. Low density lipoprotein oxidation and its pathobiological significance. *J Biol Chem*. (1997) 272:20963–6. doi: 10.1074/jbc.272.34.20963

36. Hamon M, Mbemba E, Charnaux N, Slimani H, Brule S, Saffar L, et al. A syndecan-4/CXCR4 complex expressed on human primary lymphocytes and macrophages and HeLa cell line binds the CXC chemokine stromal cell-derived factor-1 (SDF-1). *Glycobiology*. (2004) 14:311–23. doi: 10.1093/glycob/cwh038

37. Tanino Y, Chang MY, Wang X, Gill SE, Skerrett S, McGuire JK, et al. Syndecan-4 regulates early neutrophil igration and pulmonary inflammation in response to lipopolysaccharide. *Am J Respir Cell Mol Biol*. (2012) 47:196–202. doi: 10.1165/rcmb.2011-0294OC

38. Ballantyne CM, Banka P, Mendez G, Garcia R, Rosenstock J, Rodgers A, et al. Phase 2b randomized trial of the oral PCSK9 inhibitor MK-0616. *J Am Coll Cardiol*. (2023) 81:1553–64. doi: 10.1016/j.jacc.2023.02.018

39. Lindholm MW, Elmen J, Fisker N, Hansen HF, Persson R, Moller MR, et al. PCSK9 LNA antisense oligonucleotides induce sustained reduction of LDL cholesterol in nonhuman primates. *Mol Ther*. (2012) 20:376–81. doi: 10.1038/mt.2011.260

40. Kawakami R, Nozato Y, Nakagami H, Ikeda Y, Shimamura M, Yoshida S, et al. Development of vaccine for dyslipidemia targeted to a proprotein convertase subtilisin/kexin type 9 (PCSK9) epitope in mice. *PLoS One*. (2018) 13:e0191895. doi: 10.1371/journal.pone.0191895

41. Ataei S, Momtazi-Borojeni AA, Ganjali S, Banach M, Sahebkar A. The immunogenic potential of PCSK9 peptide vaccine in mice. *Curr Med Chem*. (2023) 30:3024–31. doi: 10.2174/0929867329666220930114429

42. Musunuru K, Chadwick AC, Mizoguchi T, Garcia SP, DeNizio JE, Reiss CW, et al. In vivo CRISPR base editing of PCSK9 durably lowers cholesterol in primates. *Nature*. (2021) 593:429–34. doi: 10.1038/s41586-021-03534-y

43. Miyosawa K, Watanabe Y, Murakami K, Murakami T, Shibata H, Iwashita M, et al. New CETP inhibitor K-312 reduces PCSK9 expression: a potential effect on LDL cholesterol metabolism. *Am J Physiol Endocrinol Metab*. (2015) 309:E177–90. doi: 10.1152/ajpendo.00528.2014

44. Bjorklund MM, Hollensen AK, Hagensen MK, Dagnaes-Hansen F, Christoffersen C, Mikkelsen JG, et al. Induction of atherosclerosis in mice and hamsters without germline genetic engineering. *Circ Res*. (2014) 114:1684–9. doi: 10.1161/CIRCRESAHA.114.302937

45. Roche-Molina M, Sanz-Rosa D, Cruz FM, Garcia-Prieto J, Lopez S, Abia R, et al. Induction of sustained hypercholesterolemia by single adeno-associated virus-mediated gene transfer of mutant hPCSK9. *Arterioscler Thromb Vasc Biol*. (2015) 35:50–9. doi: 10.1161/ATVBAHA.114.303617

46. Awan Z, Denis M, Bailey D, Giaid A, Prat A, Goltzman D, et al. The LDLR deficient mouse as a model for aortic calcification and quantification by micro-computed tomography. *Atherosclerosis*. (2011) 219:455–62. doi: 10.1016/j.atherosclerosis.2011.08.035

47. Marfella R, D'Onofrio N, Sardu C, Scisciola L, Maggi P, Coppola N, et al. Does poor glycaemic control affect the immunogenicity of the COVID-19 vaccination in patients with type 2 diabetes: the CAVEAT study. *Diabetes Obes Metab*. (2022) 24:160–5. doi: 10.1111/dom.14547

48. Al-Mashhadi RH, Sorensen CB, Kragh PM, Christoffersen C, Mortensen MB, Tolbod LP, et al. Familial hypercholesterolemia and atherosclerosis in cloned minipigs created by DNA transposition of a human PCSK9 gain-of-function mutant. *Sci Transl Med*. (2013) 5:166ra1. doi: 10.1126/scitranslmed.3004853

49. Goettsch C, Hutcheson JD, Hagita S, Rogers MA, Creager MD, Pham T, et al. A single injection of gain-of-function mutant PCSK9 adeno-associated virus vector induces cardiovascular calcification in mice with no genetic modification. *Atherosclerosis*. (2016) 251:109–18. doi: 10.1016/j.atherosclerosis.2016.06.011

50. Goettsch C, Hutcheson JD, Aikawa M, Iwata H, Pham T, Nykjaer A, et al. Sortilin mediates vascular calcification via its recruitment into extracellular vesicles. *J Clin Invest*. (2016) 126:1323–36. doi: 10.1172/JCI80851

51. Rogers MA, Maldonado N, Hutcheson JD, Goettsch C, Goto S, Yamada I, et al. Dynamin-related protein 1 inhibition attenuates cardiovascular calcification in the presence of oxidative stress. *Circ Res*. (2017) 121:220–33. doi: 10.1161/CIRCRESAHA.116.310293

frontiers | Frontiers in Cardiovascular Medicine

TYPE Original Research
PUBLISHED 10 September 2024
DOI 10.3389/fcvm.2024.1435106

# The causal relationship between human blood metabolites and risk of peripheral artery disease: a Mendelian randomization study

Zhiyong Dong and Qingyun Wang*

Department of Cardiothoracic Surgery, Beijing Shunyi Hospital, Beijing, China

**Background:** Peripheral Artery Disease (PAD) is a common vascular disorder typically caused by atherosclerosis, leading to impaired blood supply to the lower extremities, resulting in pain, necrosis, and even amputation. Despite extensive research into the pathogenesis of PAD, many mysteries remain, particularly regarding its association with human blood metabolites.

**Methods:** To explore the causal relationship between 1,400 serum metabolites and PAD, a two-sample Mendelian randomization (MR) analysis was conducted. The Inverse Variance-Weighted (IVW) method was the primary technique used to estimate the causal impact of the metabolites on PAD. To enhance the analysis, several additional methods were employed: MR-Egger regression, weighted median, simple mode, and weighted mode. These methods provided a comprehensive evaluation beyond the primary IVW estimation. To ensure the validity of the MR findings, sensitivity analysis was performed. Furthermore, a bidirectional MR approach was applied to explore the possibility of a reverse causal effect between PAD and potential candidate metabolites.

**Results:** After rigorous selection, significant associations were found between 1-(1-enyl-stearoyl)-2-arachidonoyl-GPE (p-18:0/20:4) and X-17653 levels with PAD. 1-(1-enyl-stearoyl)-2-arachidonoyl-GPE (p-18:0/20:4) was positively associated with increased PAD risk (IVW OR = 1.13, 95% CI, 1.06–1.21; $P < 0.001$). X-17653 levels were associated with decreased PAD risk (IVW OR = 0.88, 95% CI, 0.83–0.94; $P < 0.001$). In the reverse direction, PAD was positively associated with increased 1-(1-enyl-stearoyl)-2-arachidonoyl-GPE (p-18:0/20:4) levels (IVW OR = 1.16, 95% CI, 1.01–1.34; $P = 0.036$). PAD was not associated with X-17653.

**Conclusion:** Among 1,400 blood metabolites, 1-(1-enyl-stearoyl)-2-arachidonoyl-GPE (p-18:0/20:4) and X-17653 are significantly associated with PAD risk. Importantly, in the reverse direction, PAD was found to be positively associated with increased levels of 1-(1-enyl-stearoyl)-2-arachidonoyl-GPE (p-18:0/20:4). This highlights the bidirectional nature of the association and suggests a potential feedback mechanism between PAD and this specific lipid species. 1-(1-enyl-stearoyl)-2-arachidonoyl-GPE (p-18:0/20:4) may serve as potential biomarkers for PAD, aiding early diagnosis and providing novel avenues for personalized treatment and management. However, further validation and research are warranted despite the promising results.

KEYWORDS

**peripheral artery disease, blood metabolites, Mendelian randomization, biomarkers, GWAS**

EDITED BY
Gabrielle Fredman,
Albany Medical College, United States

REVIEWED BY
Mohammad Alfrad Nobel Bhuiyan,
Louisiana State University Health Shreveport,
United States
Yigit Can Senol,
University of California, San Francisco,
United States

*CORRESPONDENCE
Qingyun Wang
✉ 15611428853@163.com

RECEIVED 19 May 2024
ACCEPTED 27 August 2024
PUBLISHED 10 September 2024

CITATION
Dong Z and Wang Q (2024) The causal relationship between human blood metabolites and risk of peripheral artery disease: a Mendelian randomization study.
Front. Cardiovasc. Med. 11:1435106.
doi: 10.3389/fcvm.2024.1435106

# 1 Introduction

Peripheral artery disease (PAD) represents a prevalent vascular ailment primarily instigated by atherosclerosis, precipitating compromised blood perfusion to the lower extremities (1), consequentially yielding symptoms of ischemic pain, necrosis, and, in severe cases, necessitating limb amputation. Beyond encumbering patients' daily routines, PAD escalates susceptibility to cardiovascular adversities such as myocardial infarction and stroke (2), profoundly impinging upon their overall well-being. Despite exhaustive inquiry into the pathophysiology of PAD, numerous enigmas persist, particularly concerning its nexus with human metabolic entities.

Human metabolites assume pivotal roles in sustaining vital activities and modulating physiological processes. In recent years, mounting empirical substantiation (3, 4) has underscored the intimate correlation between specific blood-borne metabolites and the etiology and progression of cardiovascular disorders. Some investigations have posited that metabolites influence the inception and advancement of diseases and emerge as plausible targets for therapeutic modalities (5, 6). Nevertheless, comprehension of the causative interplay between blood metabolites and PAD remains circumscribed.

To elucidate the intricate interplay between blood metabolites and PAD, this study employs the Mendelian randomization (MR) technique (7), a robust framework leveraging genetic variants to infer causality (8). Through amalgamating extensive genetic repositories with clinical datasets, our endeavor is geared towards unveiling latent causal connections between distinct blood metabolites and PAD, thereby furnishing novel theoretical underpinnings and clinical directives for the amelioration and management of PAD.

This exposition delineates the intricacies of our research blueprint, methodological approaches, and salient discoveries while underscoring the import of these revelations in deciphering the pathogenic mechanisms underpinning PAD and charting trajectories for clinical interventions.

# 2 Materials and methods

## 2.1 Research design

The research utilized a two-sample Mendelian randomization (MR) framework to methodically assess the causal link between 1,400 blood metabolites and the risk of PAD. Single nucleotide polymorphisms (SNPs) served as instrumental variables to mitigate the influence of confounders. The MR approach was grounded in three core principles: (1) relevance assumption, there must be a significant correlation between the SNPs and the exposure variable; (2) independence assumption: the SNPs should not be associated with any confounding variables; (3) exclusion restriction assumption, the SNPs are presumed to influence the outcome solely through the exposure variable. The study's adherence to these assumptions ensures the integrity of the causal inferences drawn from the MR analysis (Figure 1).

We employed a bidirectional Mendelian randomization (MR) approach, assessing both the effect of metabolites on PAD and the effect of PAD on potential candidate metabolites.

## 2.2 Data source

Previously, Shin and colleagues delved into the genetic determinants of human metabolism through a genome-wide association study (GWAS) focusing on untargeted metabolomics. The study encompassed 7,824 individuals from two distinct European cohorts. This extensive research led to the identification of 486 metabolites that exhibit genetic associations with human serum metabolite levels. Post rigorous quality control protocols, these 486 metabolites were further categorized into 309 known and 177 unknown entities (9). More recently (5), a comprehensive GWAS scrutinized 1,091 blood metabolites alongside the ratios pertaining to the aforementioned 309 metabolites. For those interested in exploring this data, it is readily available in the GWAS Catalog database. The entries for the extensive list of 1,400 blood metabolites are cataloged under the numbers GCST90199621 to GCS90201020.

The information on PAD was derived from a genome-wide association study (GWAS) spearheaded by Sakaue and colleagues in 2021. This extensive analysis included a cohort of 7,114 individuals diagnosed with PAD alongside 475,964 control subjects. The study meticulously analyzed over 24.18 million Single Nucleotide Polymorphisms (SNPs). A key ethical aspect of the original research was obtaining informed consent from every participant involved (10). The dataset is accessible online at the GWAS database (GWAS ID: ebi-a-GCST90018890).

## 2.3 Instrumental variable selection

We used standardized selection criteria to examine genetic variations among 1,400 metabolites. Understanding the possible constraints due to the limited number of SNPs achieving full genome-wide significance for metabolites, we adjusted the threshold by establishing a $p$-value of less than $1 \times 10^{-5}$ (11). Upon identifying significant SNPs corresponding to each metabolite, we conducted a linkage disequilibrium analysis, considering LD to be present if the LD parameter $r^2$ was <0.001 and the SNP distance was within 10,000 kb (12). Furthermore, to mitigate bias stemming from weak instrumental variables, we calculated the $F$-value for each SNP, designating SNPs with an $F$-value <10 as weak instruments (13).

## 2.4 MR analysis

In this study, the Inverse Variance-Weighted (IVW) method (14) served as the primary approach for estimating the causal relationship between metabolites and PAD (with a significance threshold of $p < 0.05$). The IVW method computes weighted estimates by leveraging the inverse of variances, assuming that all

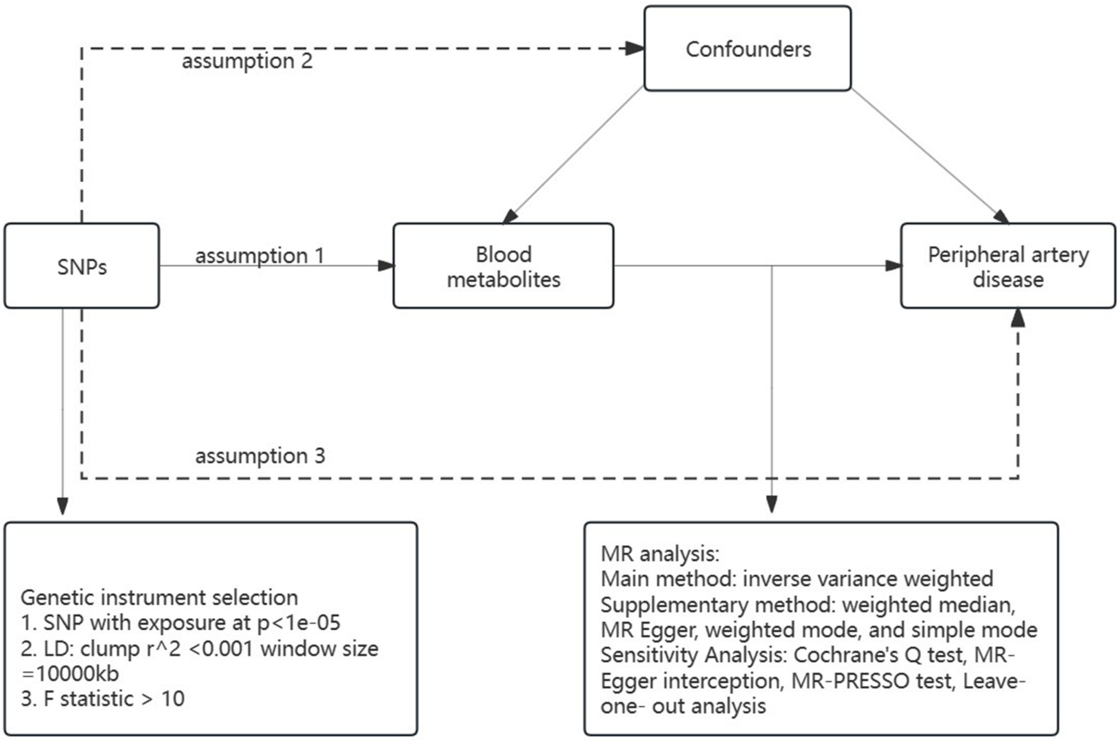

FIGURE 1
A summary of MR analysis and its three main hypotheses.

instrumental variables are valid. Specifically, it combines the Wald ratio associated with each Single Nucleotide Polymorphism (SNP) to derive a summary estimate (15). Despite its prominence in Mendelian randomization (MR) studies, it's essential to acknowledge that unknown confounding factors may still introduce genetic pleiotropy and bias when estimating effect sizes.

We employed several additional MR analysis methods, including weighted median (16), MR Egger (17), weighted mode (18), and simple mode (19), to complement our primary analysis. Heterogeneity was assessed using the Cochran *Q*-test (20), where a Cochran-Q derived $p$-value $< 0.05$ and $I^2 > 25\%$ indicated the presence of heterogeneity. To ascertain the stability of our findings, we conducted an analysis to see if the removal of any SNP would alter the results, thereby indicating the influence of a specific SNP (21, 22). This step is crucial to ensure that no individual SNP disproportionately affects the outcome. Additionally, we assessed the presence of horizontal pleiotropy by examining the Egger intercept (17). A $p$-value greater than 0.05 in this context was indicative of an absence of horizontal pleiotropy (23), suggesting that the instrumental variables used did not have pleiotropic effects that could bias the results. To investigate this phenomenon further, we utilized the MR-PRESSO global test to detect horizontal pleiotropy, where a genetic variant may influence multiple traits and complicate causal assessments. We also conducted heterogeneity tests on the instrumental variables we used. If these tests showed a $p$-value greater than 0.05, it meant that the heterogeneity wasn't significant and could be overlooked. All the Mendelian randomization (MR) analyses were carried out with the TwoSampleMR package in R (version 4.3.0).

Consequently, potential candidate metabolites implicated in the risk of PAD were selected based on the following criteria: (1) consistent associations across the five MR methods; (2) absence of detected pleiotropy; and (3) absence of high influence points identified by Leave-one-out analysis.

## 2.5 Reverse MR analyses

For our study, we extracted SNPs associated with PAD from GWAS summary statistics using a stringent significance threshold ($p$-value $< 5 \times 10^{-8}$). We then chose SNPs that were independent (with an r-squared value less than 0.001) within the European panel. These independent SNPs were utilized as instrumental variables (IVs) in Mendelian randomization (MR) analysis to investigate potential candidate metabolites.

# 3 Results

We conducted a comprehensive Mendelian randomization (MR) analysis for each of the 1,400 metabolites under investigation. Subsequently, adhering to stringent IV selection criteria, we incorporated an extensive set of 34,127 Single Nucleotide Polymorphisms (SNPs) associated with Peripheral Artery Disease (PAD) into our analysis. From the initial pool, 215 blood metabolites were singled out based on a significance threshold of $p < 0.05$ in at least five MR analyses. A circular map visually represented these metabolites (Figure 2). Our selection process focused on identifying metabolites that consistently exhibited significant associations across all five methods, with a significance threshold of $p < 0.05$ in IVW analysis and a significance threshold of pFDR < 0.2. Moreover, if the heterogeneity test result yielded a *p*-value greater than 0.05, the influence of heterogeneity was deemed negligible. Ultimately, we finally detected two metabolites associated with peripheral artery disease (PAD), one known (1-(1-enyl-stearoyl)-2-arachidonoyl-GPE (p-18:0/20:4)) and one unknown (X-17653) (Figure 3). Levels of 1-(1-enyl-stearoyl)-2-arachidonoyl-GPE (p-18:0/20:4) in blood showed a significant association with PAD. Specifically, we observed a marked elevation in 1-(1-enyl-stearoyl)-2-arachidonoyl-GPE (p-18:0/20:4) levels among PAD patients compared to non-PAD patients, indicating a significant difference (IVW OR = 1.13, 95% CI, 1.06–1.21; $P < 0.001$) (Figure 4). This suggests a potential correlation between this metabolite's levels and PAD's occurrence and progression. Similarly, X-17653 levels significantly decreased in PAD patients (IVW OR = 0.88, 95% CI, 0.83–0.94; $P < 0.001$). The correlation between elevated X-17653 levels and reduced risk of PAD further supports the potential role of blood metabolites in the pathogenesis of PAD (Figure 5).

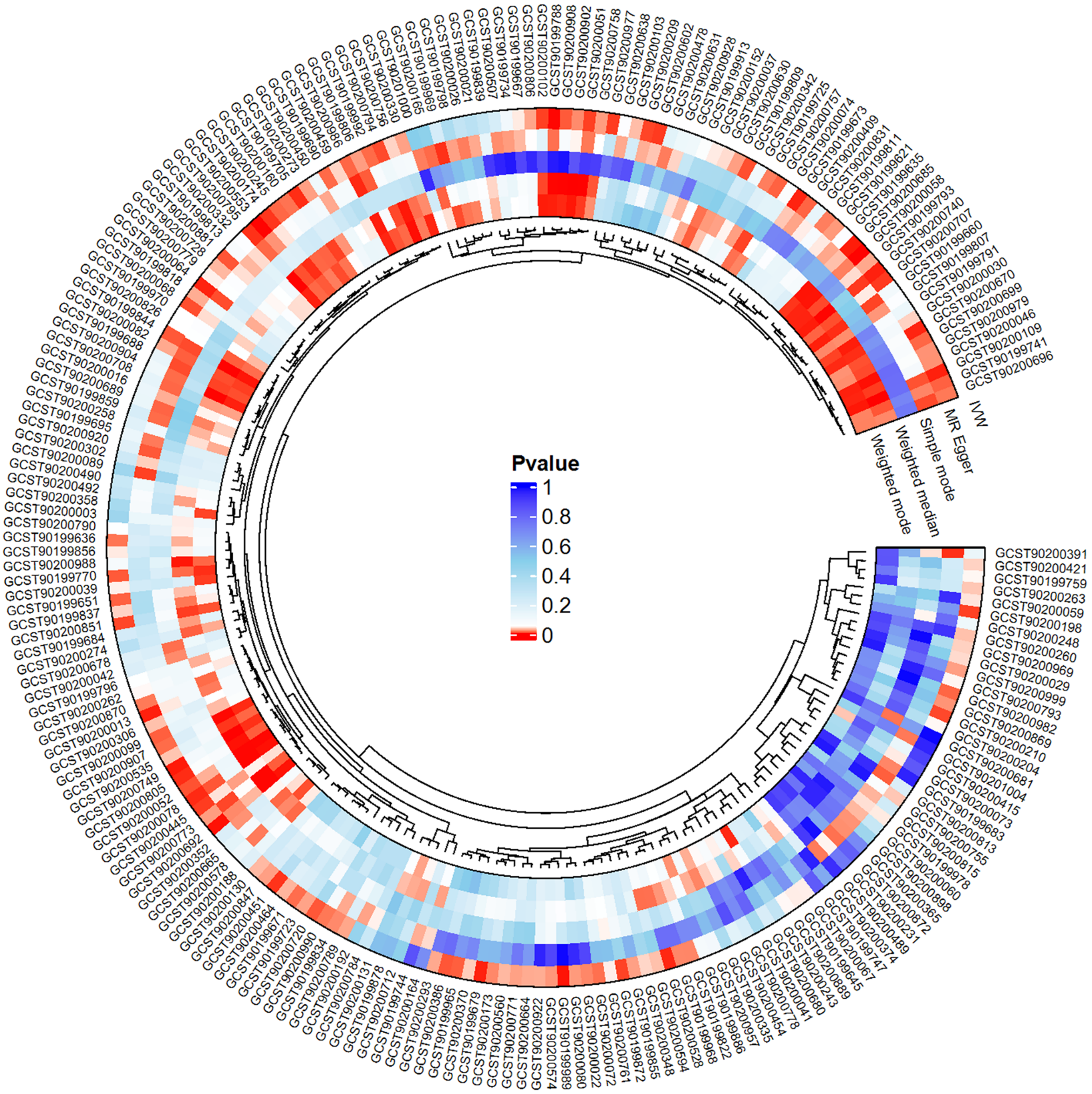

FIGURE 2
Circle map of the MR analysis results for metabolites and peripheral artery disease.

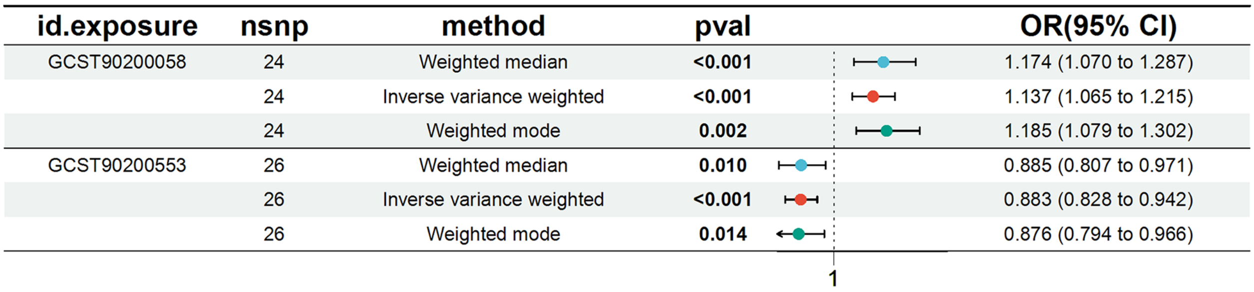

| id.exposure | nsnp | method | pval | OR(95% CI) |
|---|---|---|---|---|
| GCST90200058 | 24 | Weighted median | **<0.001** | 1.174 (1.070 to 1.287) |
| | 24 | Inverse variance weighted | **<0.001** | 1.137 (1.065 to 1.215) |
| | 24 | Weighted mode | **0.002** | 1.185 (1.079 to 1.302) |
| GCST90200553 | 26 | Weighted median | **0.010** | 0.885 (0.807 to 0.971) |
| | 26 | Inverse variance weighted | **<0.001** | 0.883 (0.828 to 0.942) |
| | 26 | Weighted mode | **0.014** | 0.876 (0.794 to 0.966) |

FIGURE 3
Forest plot for the causal effect of metabolites on the risk of peripheral artery disease derived from three methods (inverse variance weighted, weighted median, and weighted mode). OR, odds ratio; CI, confidence interval.

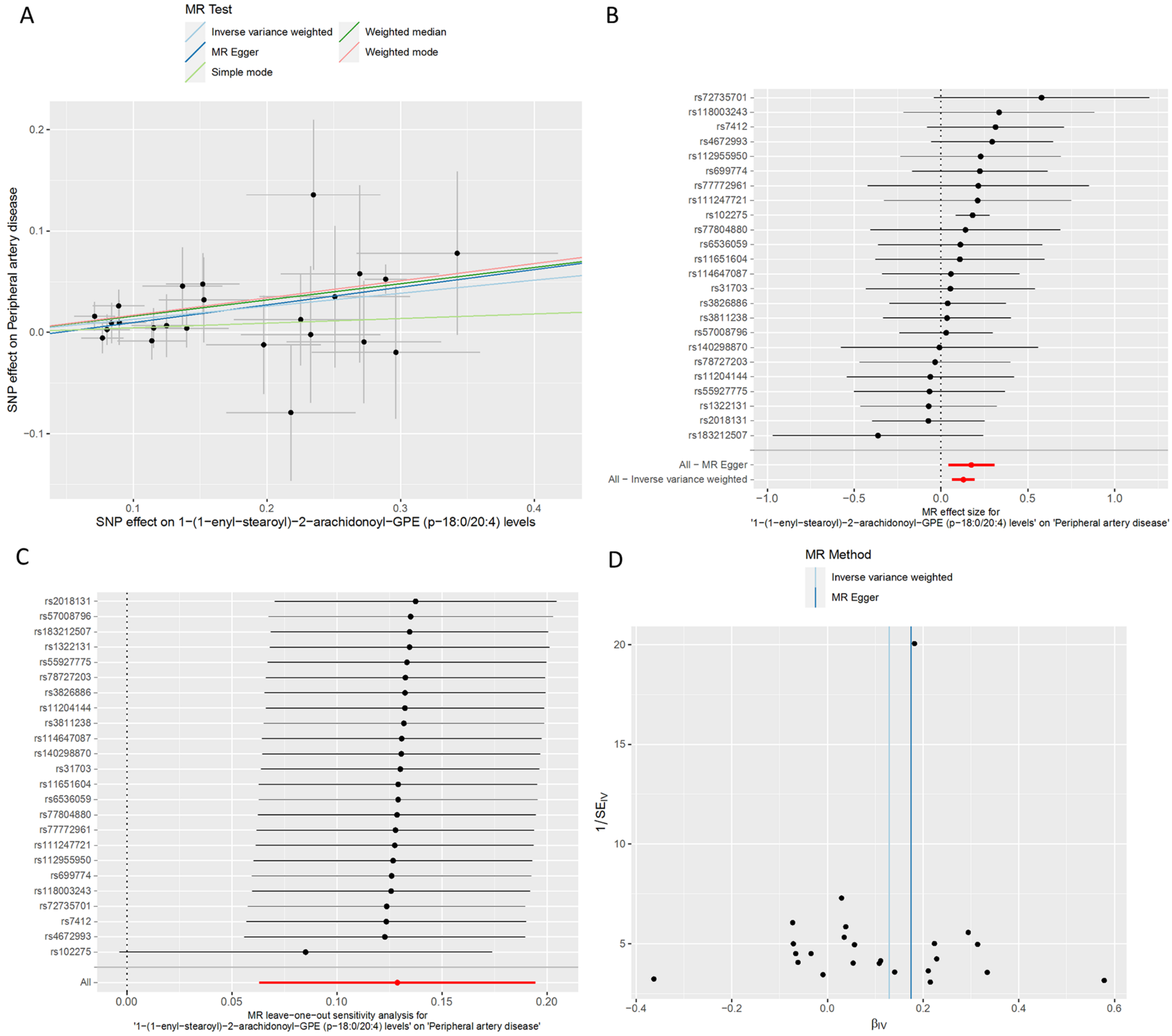

FIGURE 4
MR plots for the relationship of 1-(1-enyl-stearoyl)-2-arachidonoyl-GPE (p-18:0/20:4) with peripheral artery disease. **(A)** Scatter plot of SNP effects. **(B)** Forest plot presenting effect sizes estimated by individual and combined SNP MR analyses. **(C)** Leave-one-out plot. **(D)** Funnel plot.

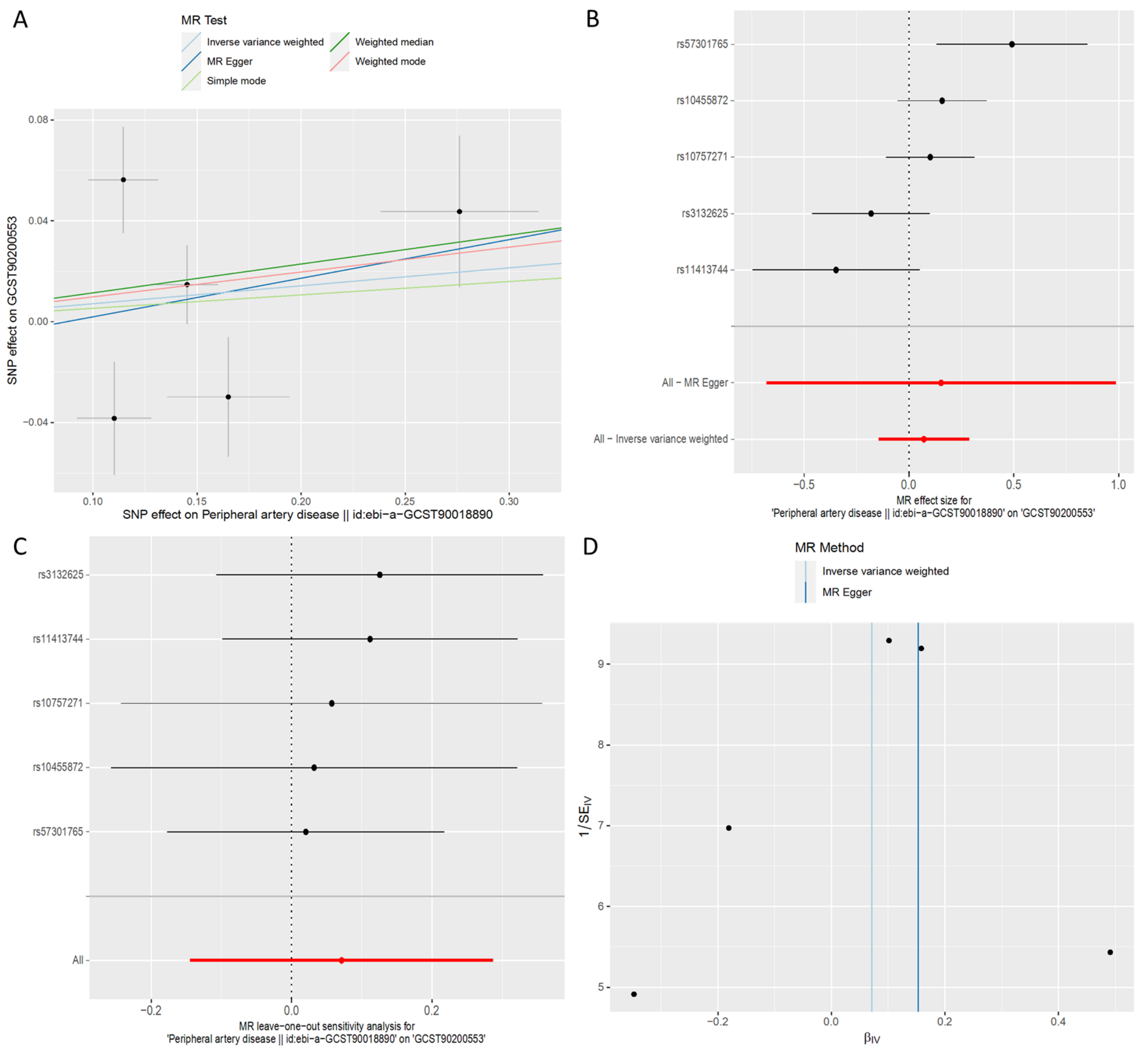

FIGURE 5
MR plots for the relationship of X-17653 with peripheral artery disease. **(A)** Scatter plot of SNP effects. **(B)** Forest plot presenting effect sizes estimated by individual and combined SNP MR analyses. **(C)** Leave-one-out plot. **(D)** Funnel plot.

To enhance the robustness of our findings and account for potential confounding factors, we employed a comprehensive set of statistical methods in our analysis. These methods included MR-Egger regression, Weighted median, Simple mode, and Weighted mode, in addition to the standard IVW analysis. We also conducted multiple-effect and heterogeneity tests to validate our results further (Tables 1, 2). By utilizing these rigorous approaches, we aimed to minimize potential biases and strengthen the reliability of our research outcomes. The F statistics of the genetic instruments indicated the absence of weak instrument bias. MR-PRESSO (24) did not identify any potential outliers.

In the context of reverse causation, where genetic predisposition to PAD is considered as an exposure, we

**TABLE 1** Heterogeneity results from the Cochran's *Q* test of significant causal links between blood metabolites and peripheral artery disease.

| Id. exposure | Outcome | Method | Q | Q_df | Q_pval |
|---|---|---|---|---|---|
| GCST90200058 | Peripheral artery disease | MR egger | 13.81 | 22 | 0.91 |
| GCST90200058 | | Inverse variance weighted | 14.39 | 23 | 0.92 |
| GCST90200553 | | MR egger | 17.46 | 24 | 0.83 |
| GCST90200553 | | Inverse variance weighted | 17.76 | 25 | 0.85 |

TABLE 2 Pleiotropy results from egger intercept analysis and MR presso.

| Id. exposure | outcome | MR egger_intercept | pval | MR-presso global |
|---|---|---|---|---|
| GCST90200058 | Peripheral artery disease | −0.007 | 0.452 | 0.871 |
| GCST90200553 | | 0.005 | 0.590 | 0.865 |

TABLE 3 Reverse MR analysis results for 2 specific blood metabolites.

| Id. exposure | OR (95%CI) | Pval | Q_pval_ IVW | Q_pval_MR. egger | Egger_intercept (pval) | MR-presso global |
|---|---|---|---|---|---|---|
| GCST90200058 | 1.16 (1.01–1.34) | 0.036 | 0.203 | 0.123 | 0.788 | 0.251 |
| GCST90200553 | 1.07 (0.87–1.33) | 0.52 | 0.010 | 0.004 | 0.853 | 0.036 |

conducted MR analyses to investigate the causal impact of PAD on 1-(1-enyl-stearoyl)-2-arachidonoyl-GPE (p-18:0/20:4) (GCST90200058) and X-17653 (GCST90200553).

Across all MR methodologies employed (Table 3), no indication of a causal association between PAD and X-17653 (GCST90200553) was observed (IVW OR = 1.07, 95% CI, 0.87–1.33; $P = 0.52$) (Figure 6). The F statistics of the genetic instruments suggested no presence of weak instrument bias. MR-PRESSO analysis did not uncover any potential outliers. Consistent effect patterns were observed with the weighted median, weighted mode, simple mode, and MR-Egger methods. Leave-one-SNP-out analysis did not show any high leverage points exerting substantial influence.

Utilizing inverse-variance weighted (IVW) methods, we observed a notable increase in the likelihood of PAD and 1-(1-enyl-stearoyl)-2-arachidonoyl-GPE (p-18:0/20:4) (GCST90200058) (IVW OR = 1.16, 95% CI, 1.01 to 1.34; $P = 0.036$) (Figure 7). However, other MR methodologies did not provide evidence of causal relationships ($P > 0.05$). The F statistics for the genetic instruments indicated the absence of weak instrument bias. MR-PRESSO analysis did not identify any potential outliers. Leave-one-SNP-out analysis did not reveal any high leverage points exerting significant influence.

## 4 Discussion

Our research findings confirm a causal relationship between two metabolites and PAD: 1-(1-enyl-stearoyl)-2-arachidonoyl-GPE (p-18:0/20:4) and X-17653. This research utilized available GWAS data and two-sample Mendelian randomization (MR) techniques to examine the causal link between PAD and blood metabolites. Rigorous sensitivity analyses were conducted to address confounding factors and enhance the robustness of our findings. Notably, this study represents an early endeavor to integrate metabolomic and genomic data, shedding light on the causal connections between serum metabolites and PAD.

Bidirectional Mendelian randomization analysis provides evidence supporting causal relationships between 1-(1-enyl-stearoyl)-2-arachidonoyl-GPE (p-18:0/20:4) and peripheral artery disease (PAD). Also known as PC[P-18:0/20:4(5Z,8Z,11Z,14Z)], 1-(1-enyl-stearoyl)-2-arachidonoyl-GPE (p-18:0/20:4) is a phosphatidylcholine (PC or GPCho) consisting of two distinct fatty acid chains: one comprising an 18-carbon atom acyl chain devoid of double bonds, and the other composed of a 20-carbon atom arachidonic acid chain with four double bonds. Arachidonic acid (25, 26), a polyunsaturated fatty acid, undergoes conversion into various inflammatory mediators, including prostaglandins (27), leukotrienes (28), and platelet-activating factors, capable of modulating vascular contraction and relaxation (29), thereby influencing blood pressure (4, 30). A recent study (31) found that 1-methylnicotinamide1-(1-enyl-stearoyl)-2-arachidonoyl-GPE was independently associated with the incidence of cardiovascular disease in fully adjusted models over a median period of 12.1 years (OR, 0.76; 95% CI, 0.65–0.89)). This suggests a potential mechanism whereby 1-(1-enyl-stearoyl)-2-arachidonoyl-GPE (p-18:0/20:4) may impact blood vessel tone and blood pressure by influencing arachidonic acid metabolism. Arul et al. (32) identified several key metabolites associated with acute ischemic stroke thrombi, including D-glucose, diacylglycerol, phytosphingosine, galabiosylceramide, glucosylceramide, and 4-hydroxynonenal. 1-(1-enyl-stearoyl)-2-arachidonoyl-GPE (p-18:0/20:4) is a plasmalogen involved in membrane composition and cell signaling. Compared to these metabolites, it may have a closer relationship with diacylglycerol and phytosphingosine because they all play important roles in lipid metabolism and cell membrane dynamics. Furthermore, the relationship between 1-(1-enyl-stearoyl)-2-arachidonoyl-GPE (p-18:0/20:4) and the glycolytic phenotype warrants further exploration. The glycolytic phenotype, characterized by increased glycolysis and reduced oxidative phosphorylation, is often associated with various pathological conditions, including cardiovascular diseases. Changes in plasmalogen levels may influence glycolytic activity, thereby contributing to the development of PAD. Further research is warranted to elucidate the precise molecular pathways linking 1-(1-enyl-stearoyl)-2-arachidonoyl-GPE (p-18:0/20:4) to PAD and to explore its therapeutic implications in the management of this condition.

X-17653 stands out among the metabolites associated with mitigated PAD risk, albeit its nature remains enigmatic, warranting further inquiry. Both 1-(1-enyl-stearoyl)-2-arachidonoyl-GPE (p-18:0/20:4) and X-17653 hold promise as prospective PAD biomarkers, potentially enhancing early diagnostic precision and offering innovative avenues for personalized therapeutic interventions and management strategies.

One of the principal strengths of our study lies in its comprehensive inclusion of a wide array of blood metabolites, totaling 1,400 in sum, for MR analysis. This renders our investigation the most extensive in probing the relationship

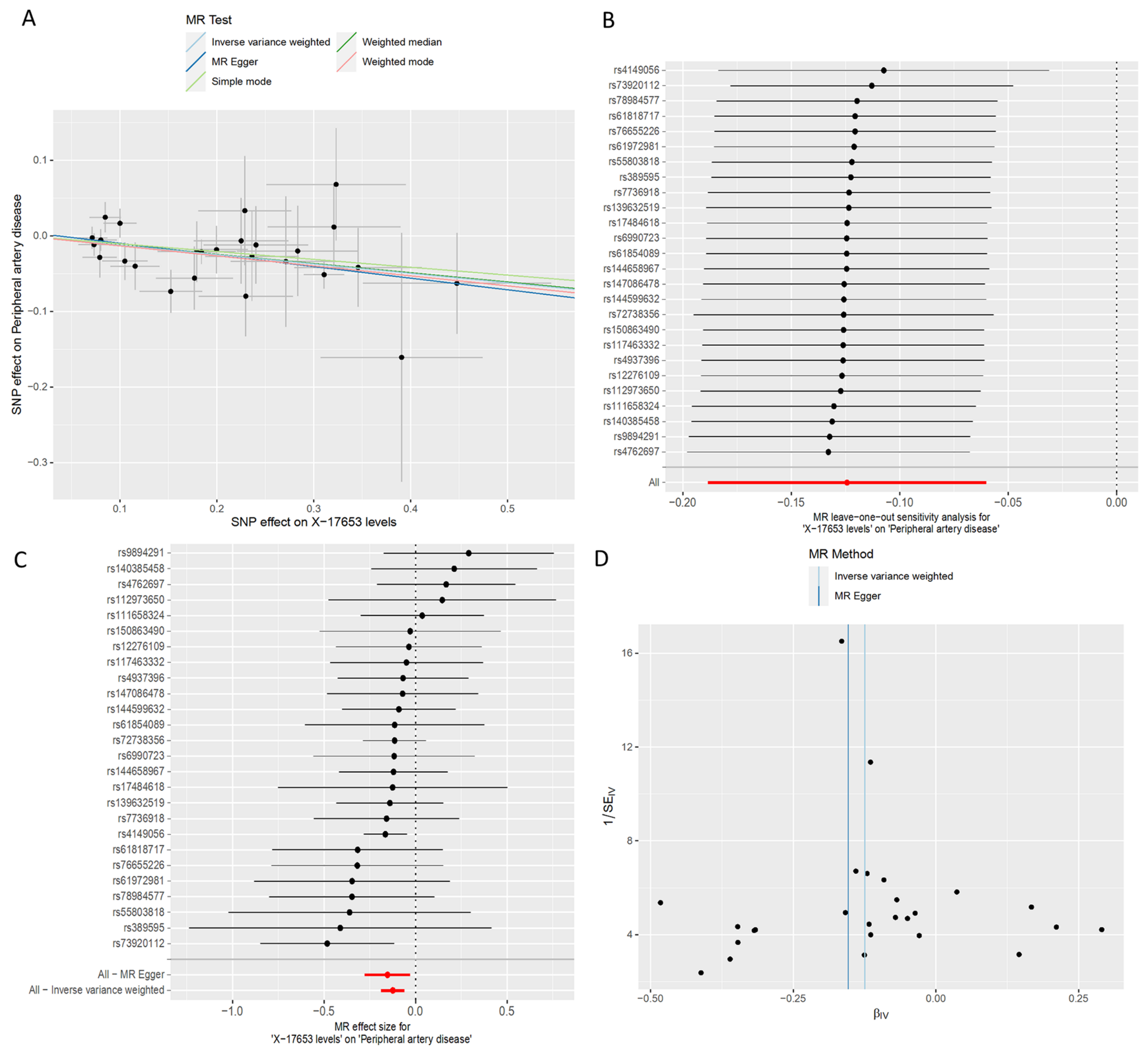

FIGURE 6
MR plots for the relationship of peripheral artery disease with X-17653. **(A)** Scatter plot of SNP effects. **(B)** Forest plot presenting effect sizes estimated by individual and combined SNP MR analyses. **(C)** Leave-one-out plot. **(D)** Funnel plot.

between blood metabolites and PAD. Moreover, utilizing the MR design helps reduce the impact of confounding variables and reverse causation. Nevertheless, our study is not without its limitations. Firstly, the GWAS datasets utilized in our analysis were sourced from European populations, prompting inquiry into the generalizability of our findings to other ethnic groups, which warrants further exploration in future studies. Additionally, delving into the specific metabolic pathways associated with the identified metabolites exhibiting causal relationships constitutes an essential avenue for future research. Secondly, while MR methods facilitate the exploration of causal relationships, it is imperative to acknowledge the intricate interplay between genetic and environmental factors when interpreting these results. Genetic predispositions and environmental factors influence the regulation of blood metabolite levels, potentially impacting our understanding of their causal association with PAD. Lastly, while our MR analysis offers valuable insights into metabolites linked to PAD, it is crucial to emphasize that validating our study results requires rigorous randomized controlled trials, fundamental research endeavors, and future replication studies employing larger GWAS datasets focusing on PAD and metabolites.

## 5 Conclusion

In summary, this MR study identifies that 1-(1-enyl-stearoyl)-2-arachidonoyl-GPE (p-18:0/20:4) and X-17653 are associated with the risk of PAD. PAD is associated with increased 1-(1-enyl-stearoyl)-2-arachidonoyl-GPE (p-18:0/20:4) levels. This offers

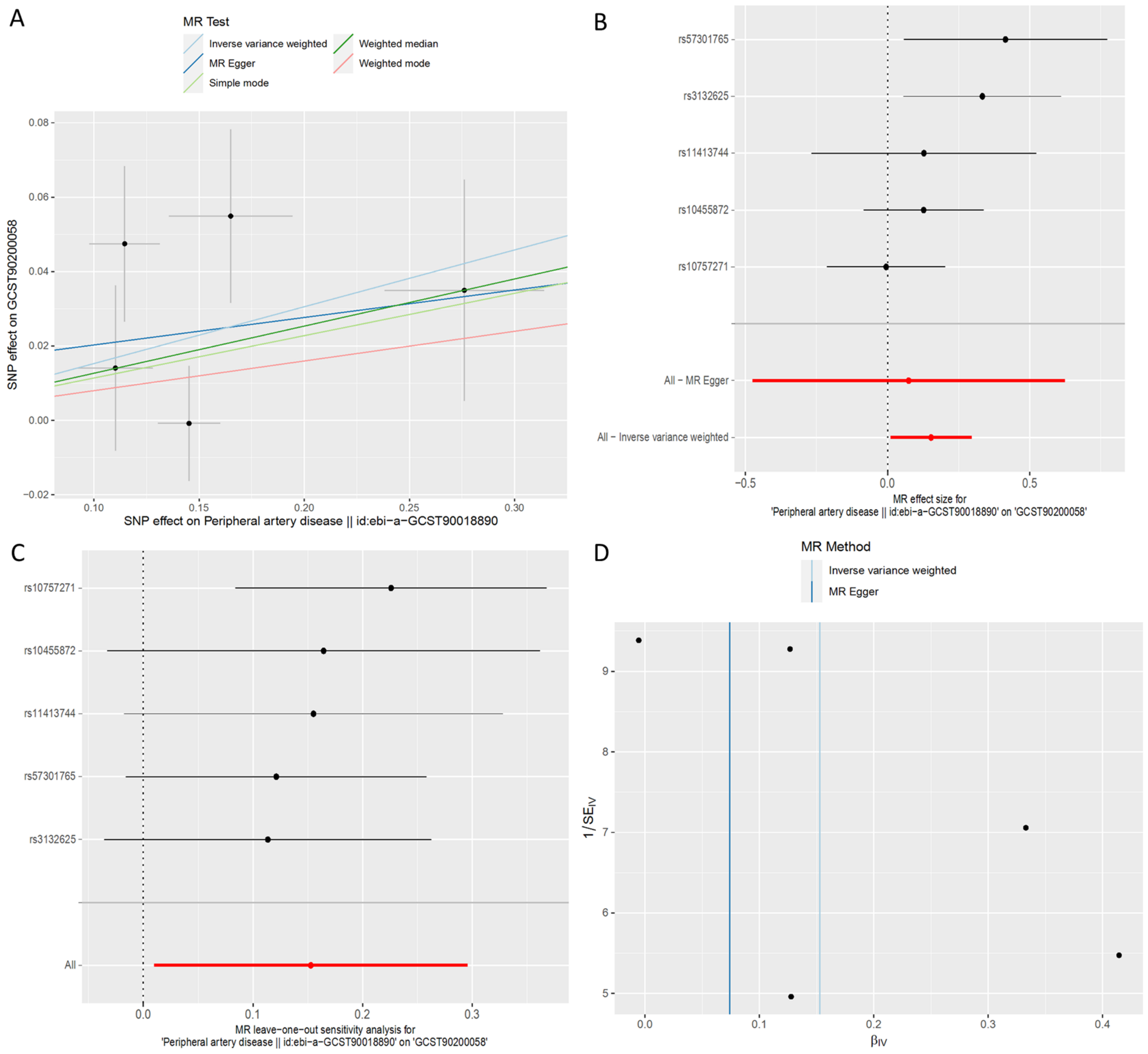

FIGURE 7
MR plots for the relationship of peripheral artery disease with 1-(1-enyl-stearoyl)-2-arachidonoyl-GPE (p-18:0/20:4). **(A)** Scatter plot of SNP effects. **(B)** Forest plot presenting effect sizes estimated by individual and combined SNP MR analyses. **(C)** Leave-one-out plot. **(D)** Funnel plot.

initial evidence regarding the influence of dysregulated blood metabolites on the risk of PAD.

## Data availability statement

The original contributions presented in the study are included in the article/Supplementary Material, further inquiries can be directed to the corresponding author.

## Ethics statement

The studies involving humans were approved by research ethics boards of the Jewish General Hospital, protocol number 2021-2762. The studies were conducted in accordance with the local legislation and institutional requirements. Written informed consent for participation was not required from the participants or the participants' legal guardians/next of kin because this study was analyzed using the publicly available GWAS pooled dataset. According to legal and institutional requirements, human participant studies do not require ethical review and approval or written informed consent.

## Author contributions

ZD: Conceptualization, Data curation, Formal Analysis, Funding acquisition, Investigation, Methodology, Project administration, Resources, Software, Supervision, Validation, Visualization, Writing – original draft, Writing – review & editing. QW: Conceptualization, Data curation, Formal Analysis, Funding acquisition, Investigation, Methodology, Project administration, Resources, Software, Supervision, Validation, Visualization, Writing – original draft, Writing – review & editing.

## Funding

The author(s) declare that no financial support was received for the research, authorship, and/or publication of this article.

## Conflict of interest

The authors declare that the research was conducted in the absence of any commercial or financial relationships that could be construed as a potential conflict of interest.

## Publisher's note

## Supplementary material

The Supplementary Material for this article can be found online at: https://www.frontiersin.org/articles/10.3389/fcvm.2024.1435106/full#supplementary-material

## References

1. Shishehbor MH, Jaff MR. Percutaneous therapies for peripheral artery disease. *Circulation*. (2016) 134(24):2008–27. doi: 10.1161/CIRCULATIONAHA.116.022546

2. Agnelli G, Belch JJF, Baumgartner I, Giovas P, Hoffmann U. Morbidity and mortality associated with atherosclerotic peripheral artery disease: a systematic review. *Atherosclerosis*. (2020) 293:94–100. doi: 10.1016/j.atherosclerosis.2019.09.012

3. Sun D, Tiedt S, Yu B, Jian X, Gottesman RF, Mosley TH, et al. A prospective study of serum metabolites and risk of ischemic stroke. *Neurology*. (2019) 92(16):e1890–8. doi: 10.1212/WNL.0000000000007279

4. Dai N, Deng Y, Wang B. Association between human blood metabolome and the risk of hypertension. *BMC Genom Data*. (2023) 24(1):1–8. doi: 10.1186/s12863-023-01180-z

5. Chen Y, Lu T, Pettersson-Kymmer U, Stewart ID, Butler-Laporte G, Nakanishi T, et al. Genomic atlas of the plasma metabolome prioritizes metabolites implicated in human diseases. *Nat Genet*. (2023) 55(1):44–53. doi: 10.1038/s41588-022-01270-1

6. Gieger C, Geistlinger L, Altmaier E, Hrabé De Angelis M, Kronenberg F, Meitinger T, et al. Genetics meets metabolomics: a genome-wide association study of metabolite profiles in human serum. *PLoS Genet*. (2008) 4(11):e1000282. doi: 10.1371/journal.pgen.1000282

7. Zuccolo L, Holmes MV. Commentary: Mendelian randomization-inspired causal inference in the absence of genetic data. *Int J Epidemiol*. (2017) 46(3):962–5. doi: 10.1093/ije/dyw327

8. Davey Smith G, Hemani G. Mendelian randomization: genetic anchors for causal inference in epidemiological studies. *Hum Mol Genet*. (2014) 23(R1):R89–98. doi: 10.1093/hmg/ddu328

9. The Multiple Tissue Human Expression Resource (MuTHER) Consortium, Shin SY, Fauman EB, Petersen AK, Krumsiek J, Santos R, et al. An atlas of genetic influences on human blood metabolites. *Nat Genet*. (2014) 46(6):543–50. doi: 10.1038/ng.2982

10. Sakaue S, Kanai M, Tanigawa Y, Karjalainen J, Kurki M, Koshiba S, et al. A cross-population atlas of genetic associations for 220 human phenotypes. *Nat Genet*. (2021) 53(10):1415–24. doi: 10.1038/s41588-021-00931-x

11. Yang J, Yan B, Zhao B, Fan Y, He X, Yang L, et al. Assessing the causal effects of human serum metabolites on 5 major psychiatric disorders. *Schizophr Bull*. (2020) 46(4):804–13. doi: 10.1093/schbul/sbz138

12. Gormley M, Dudding T, Thomas SJ, Tyrrell J, Ness AR, Pring M, et al. Evaluating the effect of metabolic traits on oral and oropharyngeal cancer risk using Mendelian randomization. *eLife*. (2023) 12:e82674. doi: 10.7554/eLife.82674

13. Zhu X, Huang S, Kang W, Chen P, Liu J. Associations between polyunsaturated fatty acid concentrations and Parkinson's disease: a two-sample Mendelian randomization study. *Front Aging Neurosci*. (2023) 15:1123239. doi: 10.3389/fnagi.2023.1123239

14. Burgess S, Scott RA, Timpson NJ, Davey Smith G, Thompson SG, EPIC-InterAct Consortium. Using published data in Mendelian randomization: a blueprint for efficient identification of causal risk factors. *Eur J Epidemiol*. (2015) 30(7):543–52. doi: 10.1007/s10654-015-0011-z

15. Pierce BL, Burgess S. Efficient design for Mendelian randomization studies: subsample and 2-sample instrumental variable estimators. *Am J Epidemiol*. (2013) 178(7):1177–84. doi: 10.1093/aje/kwt084

16. Bowden J, Davey Smith G, Haycock PC, Burgess S. Consistent estimation in Mendelian randomization with some invalid instruments using a weighted median estimator. *Genet Epidemiol*. (2016) 40(4):304–14. doi: 10.1002/gepi.21965

17. Bowden J, Davey Smith G, Burgess S. Mendelian randomization with invalid instruments: effect estimation and bias detection through egger regression. *Int J Epidemiol*. (2015) 44(2):512–25. doi: 10.1093/ije/dyv080

18. Hartwig FP, Davey Smith G, Bowden J. Robust inference in summary data Mendelian randomization via the zero modal pleiotropy assumption. *Int J Epidemiol*. (2017) 46(6):1985–98. doi: 10.1093/ije/dyx102

19. Wu Y, Zeng J, Zhang F, Zhu Z, Qi T, Zheng Z, et al. Integrative analysis of omics summary data reveals putative mechanisms underlying complex traits. *Nat Commun*. (2018) 9(1):918. doi: 10.1038/s41467-018-03371-0

20. Burgess S, Butterworth A, Thompson SG. Mendelian randomization analysis with multiple genetic variants using summarized data. *Genet Epidemiol*. (2013) 37(7):658–65. doi: 10.1002/gepi.21758

21. Feng Y, Liu X, Tan H. Causal association of peripheral immune cell counts and atrial fibrillation: a Mendelian randomization study. *Front Cardiovasc Med*. (2023) 9:1042938. doi: 10.3389/fcvm.2022.1042938

22. Zhang Z, Yin Y, Chen T, You J, Zhang W, Zhao Y, et al. Investigating the impact of human blood metabolites on the sepsis development and progression: a study utilizing two-sample Mendelian randomization. *Front Med*. (2023) 10:1310391. doi: 10.3389/fmed.2023.1310391

23. Cai J, Li X, Wu S, Tian Y, Zhang Y, Wei Z, et al. Assessing the causal association between human blood metabolites and the risk of epilepsy. *J Transl Med*. (2022) 20(1):437. doi: 10.1186/s12967-022-03648-5

24. Verbanck M, Chen CY, Neale B, Do R. Detection of widespread horizontal pleiotropy in causal relationships inferred from Mendelian randomization between complex traits and diseases. *Nat Genet*. (2018) 50(5):693–8. doi: 10.1038/s41588-018-0099-7

25. Badimon L, Vilahur G, Rocca B, Patrono C. The key contribution of platelet and vascular arachidonic acid metabolism to the pathophysiology of atherothrombosis. *Cardiovasc Res*. (2021) 117(9):2001–15. doi: 10.1093/cvr/cvab003

26. Wang B, Wu L, Chen J, Dong L, Chen C, Wen Z, et al. Metabolism pathways of arachidonic acids: mechanisms and potential therapeutic targets. *Signal Transduct Target Ther*. (2021) 6(1):1–30. doi: 10.1038/s41392-020-00451-w

27. Brash AR. Arachidonic acid as a bioactive molecule. *J Clin Invest*. (2001) 107 (11):1339–45. doi: 10.1172/JCI13210

28. Naraba H, Murakami M, Matsumoto H, Shimbara S, Ueno A, Kudo I, et al. Segregated coupling of phospholipases a2, cyclooxygenases, and terminal prostanoid synthases in different phases of prostanoid biosynthesis in rat peritoneal macrophages. *J Immunol Baltim Md 1950*. (1998) 160(6):2974–82.

29. Zhou Y, Khan H, Xiao J, Cheang WS. Effects of arachidonic acid metabolites on cardiovascular health and disease. *Int J Mol Sci*. (2021) 22(21):12029. doi: 10.3390/ijms222112029

30. Williams JM, Murphy S, Burke M, Roman RJ. 20-hydroxyeicosatetraeonic acid: a new target for the treatment of hypertension. *J Cardiovasc Pharmacol*. (2010) 56 (4):336. doi: 10.1097/FJC.0b013e3181f04b1c

31. Saeed A, McKennan C, Duan J, Kip KE, Finegold D, Vu M, et al. Mid-life plasmalogens and other metabolites with anti-inflammatory properties are inversely associated with long term cardiovascular disease events: heart SCORE study. *medRxiv* (2023). doi: 10.1101/2023.03.02.23286731v1

32. Arul S, Ghozy S, Mereuta OM, Senol YC, Orscelik A, Kobeissi H, et al. Metabolite signature in acute ischemic stroke thrombi: a systematic review. *J Thromb Thrombolysis*. (2023) 56(4):594–602. doi: 10.1007/s11239-023-02869-9

frontiers | Frontiers in Cardiovascular Medicine

TYPE Case Report
PUBLISHED 18 September 2024
DOI 10.3389/fcvm.2024.1460708

OPEN ACCESS

EDITED BY
Masanori Aikawa,
Brigham and Women's Hospital and Harvard Medical School, United States

REVIEWED BY
Margreet R. De Vries,
Leiden University Medical Center (LUMC), Netherlands
Pawel Latacz,
The Brothers of Saint John of God Hospital, Poland

*CORRESPONDENCE
Ruijing Zhang
✉ 15035180085@163.com
Honglin Dong
✉ honglindong@sxmu.edu.cn

RECEIVED 06 July 2024
ACCEPTED 27 August 2024
PUBLISHED 18 September 2024

CITATION
Ning Y, Hu J, Li H, Lu C, Zhang Z, Yan S, Shi P, Gao T, Wang H, Zhang R and Dong H (2024) Case Report: The application of novel imaging technologies in lower extremity peripheral artery disease: NIR-II imaging, OCTA, and LSFG.
Front. Cardiovasc. Med. 11:1460708.
doi: 10.3389/fcvm.2024.1460708

# Case Report: The application of novel imaging technologies in lower extremity peripheral artery disease: NIR-II imaging, OCTA, and LSFG

Yijie Ning[1], Jie Hu[1], Haifeng Li[1], Chuanlong Lu[1], Zeyu Zhang[2], Sheng Yan[1], Peilu Shi[1], Tingting Gao[1], Heng Wang[1,3], Ruijing Zhang[4]* and Honglin Dong[1]*

[1]Department of Vascular Surgery, The Second Hospital of Shanxi Medical University, Taiyuan, China, [2]Key Laboratory of Big Data-Based Precision Medicine of Ministry of Industry and Information Technology, School of Engineering Medicine, Beihang University, Beijing, China, [3]Centre for Transplant and Renal Research, Westmead Institute for Medical Research, The University of Sydney, Sydney, NSW, Australia, [4]Department of Nephrology, The Second Hospital of Shanxi Medical University, Taiyuan, China

Lower extremity peripheral artery disease (PAD) is a growing global health problem. New methods to diagnose PAD have been explored in recent years. At present, the majority of imaging methods for PAD focus on the macrovascular blood flow, and the exploration of microcirculation and tissue perfusion of PAD remains largely insufficient. In this report, we applied three new imaging technologies, i.e., second near-infrared region (NIR-II, 900–1,880 nm wavelengths) imaging, optical coherence tomography angiography (OCTA), and laser speckle flowgraphy (LSFG), in a PAD patient with a healthy human subject as control. Our results showed that the PAD patient had poorer tissue perfusion than the control without observed adverse effects. Moreover, compared with the first near-infrared region (NIR-I, 700–900 nm wavelengths) imaging results, NIR-II imaging had a higher signal-to-background ratio and resolution than NIR-I imaging and detected microvessels that were not detected by NIR-I imaging. These observations suggested that NIR-II imaging, OCTA, and LSFG are potentially safe and effective methods for diagnosing PAD.

KEYWORDS

**peripheral artery disease, NIR-II imaging, optical coherence tomography, laser speckle flowgraphy, imaging technology**

## Introduction

Peripheral artery disease (PAD) has been poorly defined at present (1). The American Heart Association (AHA) defines PAD as "atherosclerotic obstruction from the aortoiliac segments to the pedal arteries" (2), and we adopted the same definition in this report. PAD is the third leading cause of atherosclerotic morbidity, after coronary heart disease and stroke (3). The large number of patients and the poor prognosis of PAD have caused a heavy medical burden. PAD cases have risen each year since 1990 (4), and 238 million people were living with PAD in 2015 (1). Individuals with PAD have a higher risk of other cardiovascular diseases such as coronary heart disease, stroke, and abdominal aortic aneurysm (5, 6). Appropriate imaging technologies are key to preventing and treating PAD. The majority of imaging technologies for PAD detect vascular morphology on a macrovascular level. However, tissue oxygenation depends on the state of microcirculation (7). The AHA has noted PAD-related gaps, including new and non-invasive technologies to visualize peripheral perfusion (2), which emphasize the significance of evaluating microcirculation status in PAD patients.

We used three imaging technologies to evaluate microcirculation status in a PAD patient and a healthy human subject as control: second near-infrared region (NIR-II) imaging, optical coherence tomography angiography (OCTA), and laser speckle flowgraphy (LSFG) in this report. Previous studies of NIR imaging for diagnosing PAD have focused on the field of NIR-I (8). However, NIR-II imaging has shown lower scattering levels in tumor tissues and higher imaging resolution than NIR-I imaging (9). We applied NIR-II imaging to diagnose PAD for the first time and found that it had a higher signal-to-background ratio (SBR) and richer imaging details than NIR-I imaging. OCTA is a novel imaging method and has been widely used in ophthalmology and neuroscience research to observe retinal vessels and microvascular systems (10, 11). In this study, it was the first time that OCTA was applied to detect the microcirculatory system of the dorsal skin of the foot, to explore the potential of OCTA in diagnosing PAD. LSFG is a non-invasive detection technique for evaluating tissue perfusion, which is mainly used in retinal lesions (12). This study was also the first time that LSFG was used to detect the perfusion level of the dorsal skin of the foot .

This study is reported in accordance with the CARE guidelines (13).

# Case description

A 62-year-old male, with hypertension and type 2 diabetes mellitus, presented with intermittent claudication in both lower limbs for 2 years and worsening on the left side for 15 days. The patient was unable to walk more than 100 m at a time and was unable to complete the treadmill test. He did not experience rest pain or foot ulcers and did not receive any treatment for the above symptoms. Based on the findings from the medical history and examination, the patient was diagnosed with PAD, with Rutherford Category 3. Physical examination showed that the pulse of the popliteal artery, anterior tibial artery, and posterior tibial artery in the left lower limb was not palpated. The pulse of the posterior tibial artery in the right lower limb was not palpated. The ankle-brachial index (ABI) was 0.45 for the left and 0.81 for the right. Duplex ultrasound (DUS) showed severe stenosis of the left external iliac and superficial femoral arteries, multiple localized stenoses of the left popliteal artery, possible complete occlusion of the entire left posterior tibial artery, localized stenosis in the middle and lower segments of the right superficial femoral and popliteal arteries, and severe stenosis in the upper segment of the right posterior tibial artery. The results of computed tomography angiography (CTA) were consistent with DUS (Supplementary Figure S1).

A 52-year-old woman in good health was enrolled as a control. Physical examination showed that the pulsation of the femoral, popliteal, dorsalis pedis, and posterior tibial arteries in both lower limbs was palpated. DUS showed good blood flow filling in the arteries of both lower limbs. No significant abnormalities were observed in the spectral waveform or velocity of the blood flow. ABI was 1.08 for the left and 1.07 for the right limb.

# NIR imaging

NIR-II and NIR-I imaging were performed on both participants using a Full Spectrum Opening *in Vivo* Fluorescence Imaging System (DPM-IVFM-NIR-OF, Beijing Digital Precision Medicine Technology Co., Ltd., Beijing, China). An indent needle was placed in the basilic vein of the participants. The subject was in the supine position with both knee joints bent 90° and both feet put together. During NIR-II imaging, the selected filter was a 1,000 nm long pass. The power of the 808 nm wavelength laser emitter was adjusted to 10,000 mW with the aperture size adjusted to 2.0 and the exposure time set to 100 ms. The laser emitter was fixed at 20 cm vertical to the dorsal foot. Indocyanine green (ICG) solution (2.5 mg/ml, diluted with sterile water for injection) (Dandong Yichuang Pharmaceutical, Dandong, China) was administered intravenously via an indwelling needle. The dose of ICG injected was determined according to body weight: 0.1 mg/kg. The intensity of the fluorescence signal on both the dorsal feet was recorded within 5 min after the ICG solution was injected. The dorsal pedis region from the transverse tarsus joint to the distal metatarsal bone was selected as the region of interest (ROI). The ROI was analyzed to generate a time–intensity curve. The NIR-I imaging was performed 30 min after the NIR-II imaging. During NIR-I imaging, the xenon lamp was used as a laser emitter, with a xenon lamp filter of 750 nm band-pass and a NIR-I camera filter of 837 nm band-pass. The xenon lamp power was adjusted to 2,000 mW with the aperture size adjusted to 8.0 and the exposure time set to 200 ms. The laser emitter was fixed at 30 cm vertical to the dorsal foot. It is important to consider the impact of endogenous chromophores on NIR imaging based on ICG, as well as the influence of different skin tones on fluorescence intensity. Imaging parameters should be adjusted in response to changes in these factors (14).

During NIR-II imaging, fluorescence images of the PAD patient (Figures 1A,B) and the control (Figures 1C,D) were captured at 2 min 30 s and 5 min, respectively. Microvessel imaging and venous imaging were observed. Fluorescence initially appeared (T start) in the dorsal pedis of the feet and then gradually emerged in the microcirculation. Fluorescence signals in both venous and microcirculatory imaging reflected the perfusion levels. The arcus venosus dorsalis pedis was clearly visible in both participants (yellow arrow). The microvessel imaging in the left hallux of the PAD patient showed that the blood flow had almost disappeared (orange rectangle), indicating severe ischemia here. At 5 min 10 s, we observed the fluorescence image of the right calf of the PAD patient (Figure 1E) and found that the great saphenous vein (green arrow) continued with the dorsalis pedis vein. At 10 min, we observed that the fluorescence signal of the PAD patient had decreased significantly (Figure 1F). At 5 min 10 s, we captured fluorescence images of the left foot

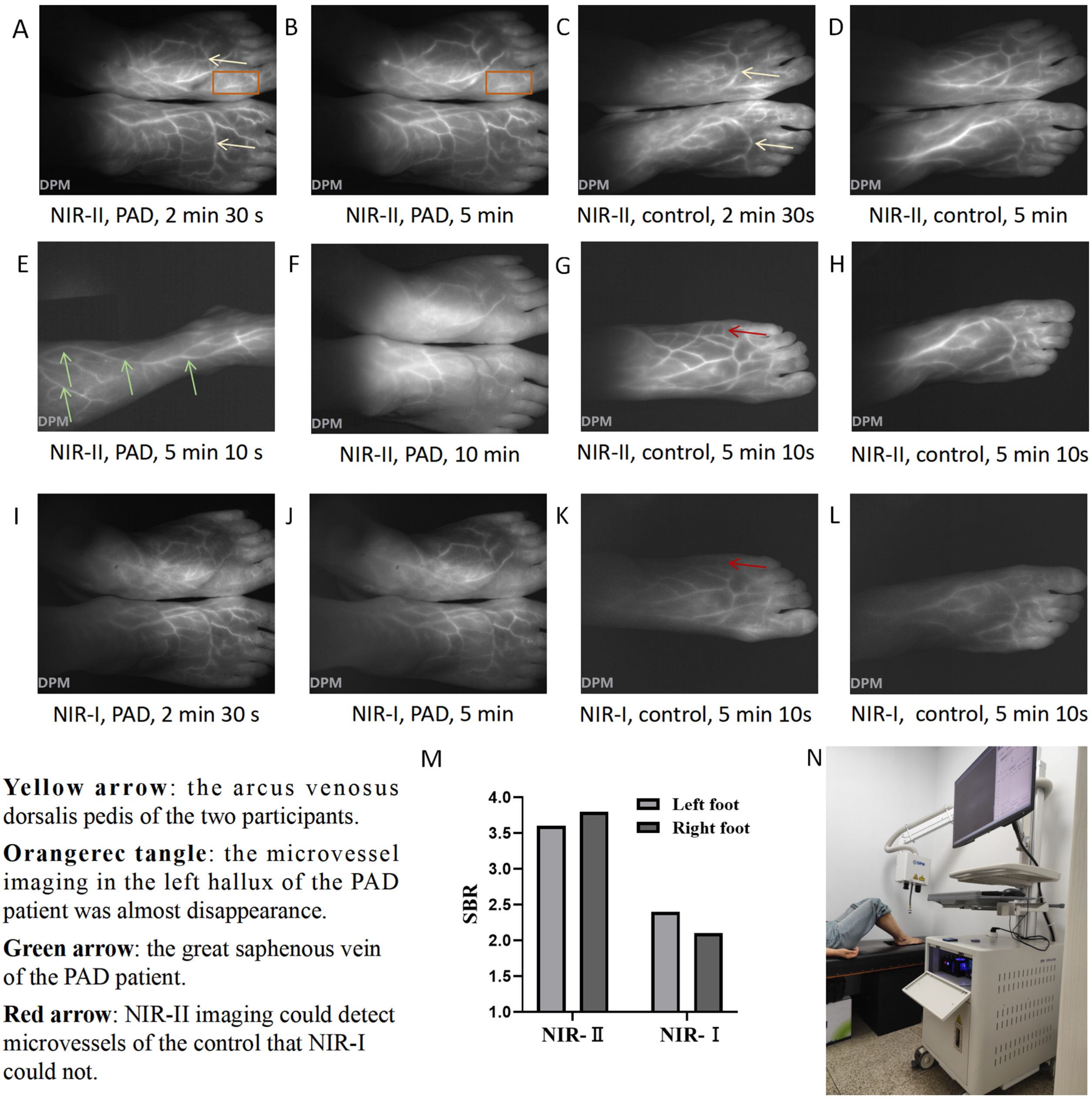

NIR-II, PAD, 2 min 30 s
NIR-II, PAD, 5 min
NIR-II, control, 2 min 30s
NIR-II, control, 5 min
NIR-II, PAD, 5 min 10 s
NIR-II, PAD, 10 min
NIR-II, control, 5 min 10s
NIR-II, control, 5 min 10s
NIR-I, PAD, 2 min 30 s
NIR-I, PAD, 5 min
NIR-I, control, 5 min 10s
NIR-I, control, 5 min 10s

**Yellow arrow**: the arcus venosus dorsalis pedis of the two participants.

**Orangerec tangle**: the microvessel imaging in the left hallux of the PAD patient was almost disappearance.

**Green arrow**: the great saphenous vein of the PAD patient.

**Red arrow**: NIR-II imaging could detect microvessels of the control that NIR-I could not.

FIGURE 1
NIR imaging of the PAD patient and control. NIR-II images of the feet of the PAD patient at **(A)** 2 min 30 s and **(B)** 5 min. NIR-II images of the feet of the control at **(C)** 2 min 30 s and **(D)** 5 min. **(E)** NIR-II image of the right calf of the PAD patient at 5 min 10 s. **(F)** NIR-II image of the feet of the PAD patient at 10 min. NIR-II images of the **(G)** left foot and **(H)** right foot of the control at 5 min 10 s. NIR-I images of the feet of the PAD patient at **(I)** 2 min 30 s and **(J)** 5 min. NIR-I images of the **(K)** left foot and **(L)** right foot of the control at 5 min 10 s. **(M)** SBR of the left foot and right foot of the control under NIR-I and NIR-II imaging at 5 min 10 s. **(N)** The diagram of NIR imaging. Yellow arrow: the arcus venosus dorsalis pedis of the two participants. Orange rectangle: microvessel imaging in the left hallux of the PAD patient showed that the blood flow had almost disappeared. Green arrow: the great saphenous vein of the PAD patient. Red arrow: NIR-II imaging could detect microvessels of the control that NIR-I could not.

(Figure 1G) and the right foot (Figure 1H) of the control, showing that a larger range of fluorescence signals in the dorsal foot could be observed by imaging with one foot. When imaging both feet, the laser toward the outermost part of the foot was frequently blocked by the slope of the dorsal foot, resulting in a lack of fluorescence signal. However, imaging with both feet was more consistent than imaging with one foot, by reducing the interference of operational errors. Furthermore, the injection of ICG solution was required only once, so imaging with both feet was chosen to record changes in fluorescence intensity. Imaging with one foot may be more suitable in certain circumstances, such as surgical operations. During NIR-I imaging, we observed that the resolution of imaging in the PAD patient at 2 min 30 s (Figure 1I) and 5 min (Figure 1J) was not as good as that of the resolution of NIR-II imaging at the corresponding times (Figures 1A,B). NIR-I fluorescence images of the left foot

(Figure 1K) and the right foot (Figure 1L) of the control were captured at 5 min 10 s, respectively. We found that NIR-II imaging displayed microvessels that NIR-I imaging did not (red arrow). Furthermore, the SBR of NIR-II imaging (left foot: 3.6, right foot: 3.8) was higher than that of NIR-I imaging (left foot: 2.4, right foot: 2.1) within the ROI (Figure 1M). NIR-II and NIR-I images of one foot of the PAD patient at 5 min 10 s are shown in Supplementary Figures S2A,B. The SBR of NIR-II imaging was higher than that of NIR-I imaging within the ROI (2.9 vs. 1.8) (Supplementary Figure S2C). Furthermore, the SBR of the PAD patient was lower than the corresponding SBR of the control. The diagram of NIR imaging is shown in Figure 1N.

The time–intensity curve of NIR-II imaging was selected to quantitatively analyze the imaging results. Eleven parameters were used, including Imax, I start, I end, T start, Tmax, T 1/2, TR, Ingress, Ingress rate, Egress, and Egress rate. The definitions of the 11 parameters are detailed in Supplementary Table S1, and the parameter values of the two participants are shown in Table 1. According to the time–intensity curve of the PAD patient (Supplementary Figure S3A), the T start of the left foot (36.9 s) was significantly longer than that of the right foot (26.1 s). The Imax of the left foot (107.9) was lower than that of the right foot (137.9). The above data indicated that the perfusion level of the right foot was higher than that of the left foot in the PAD patient. Compared to the PAD patient, the Tmax of both feet was shorter in the control (left foot: 30.7 s, right foot: 42.3 s) (Supplementary Figure S3B). The ingress rate of both feet (left: 2.52, right: 1.83) in the control was higher than that of the PAD patient (left: 0.73, right: 0.76). The above data indicated that the perfusion level of both feet in the control was higher than that of the PAD patient, demonstrating the potential of NIR-II imaging in diagnosing PAD.

## OCTA

OCTA imaging was performed in both participants using a Monitoring System of Vascular Microcirculation *in vivo* (Micro-VCC, Optoprobe Science Ltd, Pontypridd, UK). The imaging depth was 0–3 mm. The field of view scanned by OCTA was 9 mm × 9 mm. We selected the area between the first and second metatarsal heads of the dorsal foot as the ROI. The detection probe was adjusted to closely adhere to the skin of the ROI. The detection time of each foot was approximately 60 s without the injection of a developer. The diagram of OCTA imaging is shown in Supplementary Figure S4A. Using the analysis software Pyoct (version 8.0), we selected a depth of 300–1,000 um from the skin to analyze the results, set the analysis threshold of the image to 0.5, and then obtained a Gray Scale Image, Pseudocolor Image, Skeleton Image, and four kinds of heat maps: Area Heat Map, Complexity Heat Map, Diameter Heat Map, and Skeleton Heat Map. The images of each foot were quantitatively analyzed so that the average area, average complexity, average diameter, and average skeleton density could be obtained. In addition, to explore the influence of different imaging depths on the imaging effect of OCTA, we observed the right foot of the control at 0–200, 200–300, and 1,000–1,200 µm imaging depths, respectively.

TABLE 1 Time–intensity curve parameters of the two participants.

| Parameter | PAD patient | | Control | |
|---|---|---|---|---|
| | Left foot | Right foot | Left foot | Right foot |
| Imax | 107.9 | 137.9 | 162.1 | 160.9 |
| I start | 77.1 | 83.4 | 84.7 | 83.3 |
| I end | 89.5 | 98.5 | 113.1 | 113.3 |
| T start | 36.9 | 26.1 | 25.3 | 25.7 |
| Tmax | 42.3 | 74.7 | 30.7 | 42.3 |
| T 1/2 | 14.0 | 20.9 | 18.4 | 19.0 |
| TR | 0.33 | 0.28 | 0.60 | 0.45 |
| Ingress | 30.8 | 54.5 | 77.4 | 77.6 |
| Ingress rate | 0.73 | 0.76 | 2.52 | 1.83 |
| Egress | 14.1 | 54.5 | 49.0 | 47.6 |
| Egress rate | 0.06 | 0.27 | 0.20 | 0.21 |

At an imaging depth of 300–1,000 um, by comparing the images of the left foot (Figure 2A) and right foot (Figure 2B) of the PAD patient with those of the left foot (Figure 2C) and right foot (Figure 2D) of the control, we found that the microvessels in the OCTA images of the control were more densely distributed and larger in diameter. This was consistent with the OCTA quantification results (Supplementary Table S2). The average areas of the left and right feet of the PAD patient were 0.447 and 0.430, respectively, compared to 0.471 and 0.497 in the control. The average diameters of the left and right feet in the PAD patient were 34.157 and 32.790 µm, compared to 41.626 and 37.517 µm in the control. The average area and average diameter of microvessels in the feet of the control were higher than those of the PAD patient. We speculated that the average area and average diameter have the potential to be the key parameters in diagnosing PAD.

At an imaging depth of 0–200 µm, almost no microvessels could be observed in the OCTA image of the right foot of the control, while skin texture and hair could be observed (Supplementary Figure S4B). At an imaging depth of 200–300 µm, emerging microvessels in the papillary layer could be observed, but the microvascular profile could not be observed (Supplementary Figure S4C). At an imaging depth of 1,000–1,200 um, the connective tissue of the hypodermis could be observed, but it was difficult to observe the complete microvascular structure (Supplementary Figure S4D). Therefore, the appropriate depth for observing the microcirculatory system of the dorsal foot with OCTA was 300–1,000 µm.

## LSFG

LSFG was performed on both participants. The imaging device used was the Laser Speckle Imaging System (RFILSI ZW, RWD Life Science, Shenzhen, China) with an imaging depth of 0–1 mm. The perfusion image and the intensity image were captured at the same processing mode (Sliding mode), spatial filtering constant (3 s), temporal filtering constant (250 frames), and frame rate (40 fps). During the imaging, the participant sat on the examination chair,

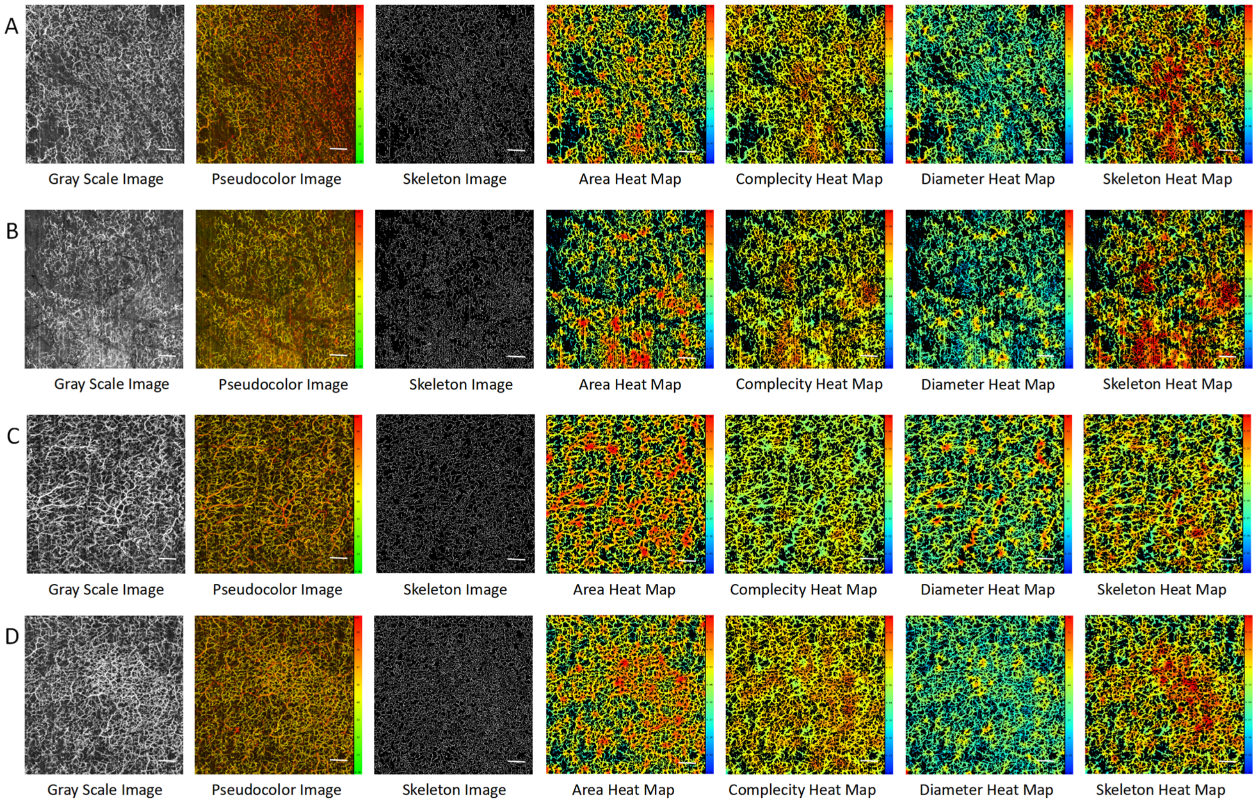

FIGURE 2
OCTA images in the PAD patient and the control at imaging depths of 300–1,000 μm. **(A)** The left foot of the PAD patient. **(B)** The right foot of the PAD patient. **(C)** The left foot of the control. **(D)** The right foot of the control. Scale bar = 100 um.

and the knee joint of the examination side was bent at 90° so that the foot could be flat on the black cardboard on the examination plane. The position of the speckle host was adjusted so that the dorsal foot was fully exposed in the center of the field of vision. The imaging diagram is shown in Supplementary Figure S5. The working distance was adjusted to 25 cm. The dorsal foot from the transverse tarsal joint to the distal metatarsal bone was selected as the ROI, and the change in perfusion volume in the ROI was observed. When the perfusion volume was relatively stable, the measurement was performed for 5 s. RFLSI Analysis software was used to obtain perfusion-related parameters (maximum perfusion, minimum perfusion, mean perfusion, and standard deviation) and intensity-related parameters (maximum intensity, minimum intensity, mean intensity, and standard deviation).

By comparing the gray images and pseudocolor images of the two participants, we found that the perfusion level and intensity of the left foot (Figure 3A) of the PAD patient were lower than those of the right foot (Figure 3B). The perfusion levels of the left foot (Figure 3C) and the right foot (Figure 3D) of the control were almost the same, and both were higher than those of the PAD patient. The perfusion volume results were consistent with the quantitative results (Supplementary Table S3). The mean perfusion of the left foot of the PAD patient was 156.44, which was lower than 178.66 in the right foot. The mean perfusion of the left foot and the right foot of the control was 198.68 and 191.80, respectively (Figure 3E), higher than that of the PAD patient, reflecting the consistency between the perfusion volume of the dorsal foot and the degree of PAD lesions. However, the mean intensity of the right foot of the control was 44.20, which was lower than 45.67 of the PAD patient (Figure 3F). This may be due to the different smoothness of the skin on the dorsal foot between the two participants and the intensity measurement being more easily affected by the smoothness of the skin.

## Discussion

When PAD occurs, in addition to the decrease in the patency of the large arteries, the microcirculatory system will also be affected accordingly. In the presence of atherosclerosis, the microcirculation function changes occur earlier than the macrovascular status (15). In intermittent claudication, decreased blood flow in the microcirculation is an important pathophysiological change (16). Tissue oxygenation depends on the state of microcirculation, and microcirculation-related diagnostic techniques can help us identify areas of poor perfusion, which has the potential to guide the surgery and predict the prognosis (7, 17). Therefore, diagnostic techniques for microcirculatory systems are as important as macrovascular

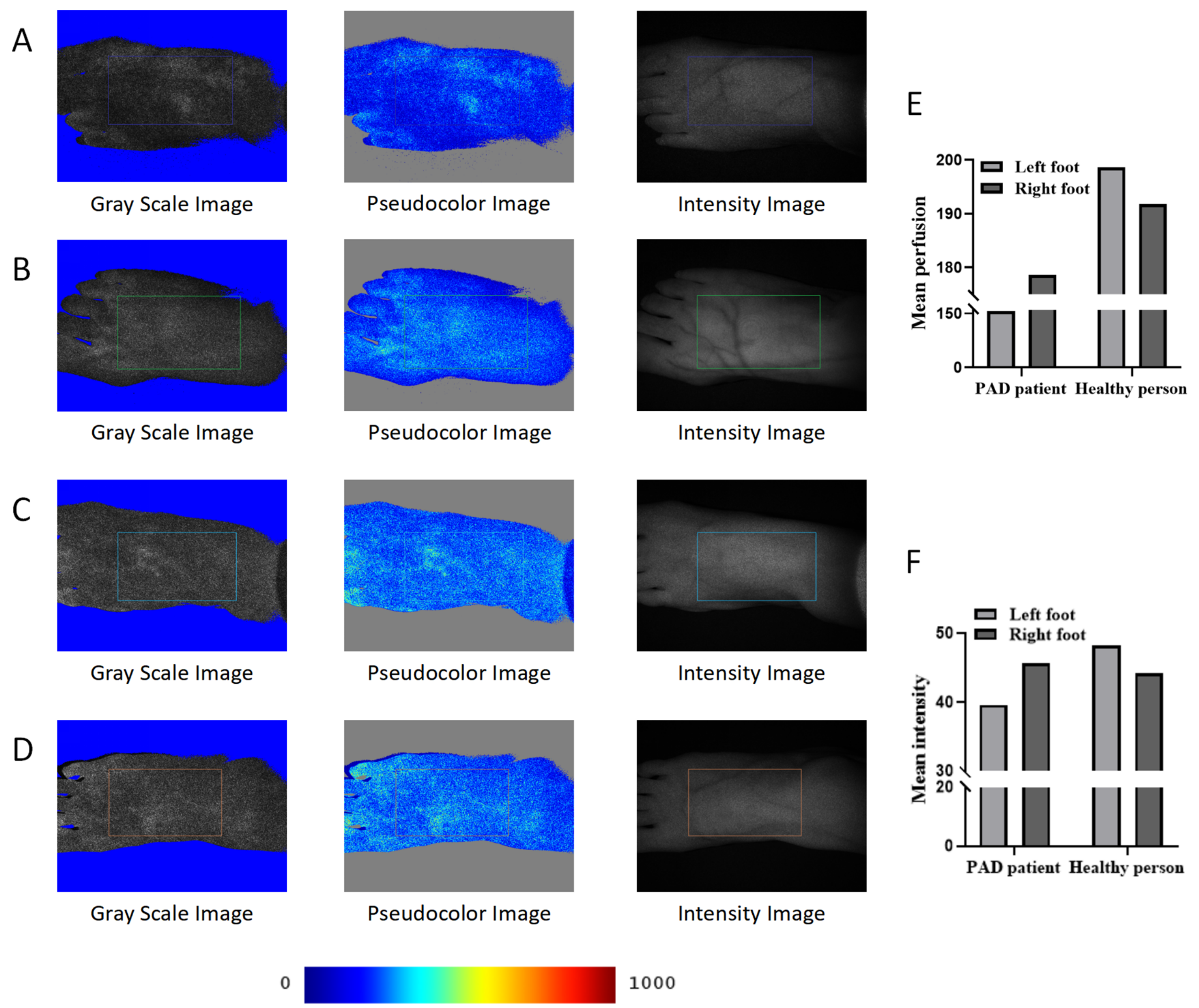

FIGURE 3
LSFG of the PAD patient and the control. **(A)** LSFG images of the left foot of the PAD patient. **(B)** LSFG images of the right foot of the PAD patient. **(C)** LSFG images of the left foot of the control. **(D)** LSFG images of the right foot of the control. **(E)** Mean perfusion of each foot of the two participants. **(F)** Mean intensity of each foot of the two participants. The color bar represents perfusion levels, from blue (low) to red (high). ROIs are framed with rectangles.

diagnostic techniques for PAD. However, the diagnostic technology for tissue perfusion still needs to be improved at present. Although transcutaneous oxygen pressure (TcPO$_2$) is the most commonly used diagnostic technology for tissue perfusion in clinical practice, it has shortcomings such as being time-consuming and having a small detection range (18). We report the clinical application of NIR-II imaging, OCTA, and LSFG, showing that these three novel technologies have the potential to detect microcirculatory structure and tissue perfusion levels in PAD.

Based on the imaging results of the two participants, NIR-II imaging had a higher resolution and SBR than NIR-I imaging in diagnosing PAD. NIR-II imaging could visualize the microvessels that were not visualized by NIR-I imaging. Furthermore, NIR-II imaging could visualize the poor perfusion area of the dorsal foot. Due to the differences in imaging conditions between NIR-II and NIR-I imaging (including imaging distance, imaging sequence, exposure time, and laser light source) and the limited sample size of this study, it is not rigorous to conclude that NIR-II imaging is better than NIR-I imaging. Future studies with larger sample sizes are needed to explore the effects of both types of imaging. The parameters of the time–intensity curve were significantly different between the control and the PAD patient, indicating that NIR-II imaging had a good ability to distinguish PAD. NIR-II imaging could visualize the microvessels of the dorsal foot in a non-contact manner in real-time, indicating its potential for intraoperative applications. NIR imaging has a wide range of applications (19). Previous studies have reported that NIR imaging could assess the perfusion status in patients with chronic limb ischemia vs. control patients (20). Meanwhile, NIR imaging could predict clinical outcomes after revascularization for lower extremity arterial disease (21). However, NIR-II imaging cannot determine the specific lesion site in lower extremity arteries, and each part of the time–intensity curve may contain information about the lesion site or the degree of the lesion, which needs to be explored with larger sample size studies. In addition, sex-related differences need to be considered in the evaluation of microcirculation, which may be due to differences in blood pressure or hormones (22). The prevalence of PAD also showed a sex difference, with men having a higher prevalence (23).

OCTA is widely used in ophthalmology and neuroscience research (9, 10), and has also been reported to have been applied to skin diseases (24). This study is the first to report the application of OCTA in diagnosing PAD. We found that the average area and average diameter were higher in the control than in the PAD patient, suggesting that the two parameters might be important for diagnosing PAD. The advantage of OCTA is that the microcirculation structures at different depths can be observed. Results showed that 300–1,000 nm was the appropriate depth to observe microcirculation in PAD patients. However, in OCTA imaging, the results can be interfered with by slight movement from the patient, leading to re-examination, so the skin in the ROI must be attached to the probe tightly.

LSFG has been used to observe the plantar skin for diagnosing PAD in previous reports (25). Since the imaging depth of the device is only 1 mm, the dorsal foot skin was selected as the ROI in this study. LSFG can assess the perfusion level easily and quickly, without touching the skin. The average perfusion of the two participants showed a significant difference in grayscale. The intensity-related parameters may be affected by the reflection of the skin, and their accuracy is not as good as that of the perfusion-related parameters. In the future, we will continue to pay close attention to this issue and further explore the diagnostic efficacy of intensity-related parameters.

## Conclusions

In summary, this study reported the clinical application of NIR-II imaging, OCTA, and LSFG for PAD. They showed differences in perfusion levels between the PAD patient and the control without adverse effects, suggesting promising potential for clinical application. Further larger-sample studies are warranted to determine the diagnostic thresholds for these three novel diagnostic technologies.

## Data availability statement

The original contributions presented in the study are included in the article/Supplementary Material, further inquiries can be directed to the corresponding authors.

## Ethics statement

The studies involving humans were approved by The Ethics Committee of the Second Hospital of Shanxi Medical University. The studies were conducted in accordance with the local legislation and institutional requirements. The participants provided their written informed consent to participate in this study. Written informed consent was obtained from the individual(s) for the publication of any potentially identifiable images or data included in this article.

## Author contributions

YN: Conceptualization, Data curation, Formal Analysis, Investigation, Methodology, Project administration, Resources, Software, Validation, Visualization, Writing – original draft. JH: Supervision, Writing – review & editing. HL: Validation, Writing – review & editing. CL: Validation, Writing – review & editing. ZZ: Conceptualization, Methodology, Writing – review & editing. SY: Supervision, Writing – review & editing. PS: Project administration, Writing – review & editing. TG: Visualization, Writing – review & editing. HW: Supervision, Writing – review & editing. RZ: Conceptualization, Data curation, Funding acquisition, Methodology, Project administration, Resources, Software, Supervision, Validation, Writing – review & editing. HD: Conceptualization, Data curation, Funding acquisition, Investigation, Methodology, Project administration, Resources, Supervision, Validation, Visualization, Writing – review & editing.

## Funding

The authors declare financial support was received for the research, authorship, and/or publication of this article. This work was supported by grants from the Regional Cooperation Program of Shanxi Province, China (Grant No. 202204041101038); the Leading Talent Team Building Program of Shanxi Province, China (Grant No. 202204051002010); Construction and Demonstration of Molecular Diagnosis and Treatment Platform for Vascular Diseases in Shanxi Province, China (Grant No. SCP-2023-17); Translational Medicine Engineering Research Center for Vascular Diseases of Shanxi Province, China (Grant No. 2022017); the Shanxi Provincial Science and Technology Department Centralized Guided Local Projects (Grant No. YDZJSX2021C026); and the National Natural Science Foundation of China (Grant No. 81770695, 81870354).

## Conflict of interest

The authors declare that the research was conducted in the absence of any commercial or financial relationships that could be construed as a potential conflict of interest.

The authors declared that they were an editorial board member of Frontiers, at the time of submission. This had no impact on the peer review process and the final decision.

## Publisher's note

All claims expressed in this article are solely those of the authors and do not necessarily represent those of

## Supplementary material

The Supplementary Material for this article can be found online at: https://www.frontiersin.org/articles/10.3389/fcvm.2024.1460708/full#supplementary-material

## References

1. Writing Committee to Develop Clinical Data Standards for Peripheral Atherosclerotic Vascular Disease, Creager MA, Belkin M, Bluth EI, Casey DE Jr, Chaturvedi S, et al. 2012 ACCF/AHA/ACR/SCAI/SIR/STS/SVM/SVN/SVS key data elements and definitions for peripheral atherosclerotic vascular disease: a report of the American College of Cardiology Foundation/American Heart Association Task Force on Clinical Data Standards (Writing Committee to Develop Clinical Data Standards for Peripheral Atherosclerotic Vascular Disease). *Circulation*. (2012) 125 (2):395–467. doi: 10.1161/CIR.0b013e31823299a1

2. Criqui MH, Matsushita K, Aboyans V, Hess CN, Hicks CW, Kwan TW, et al. Lower extremity peripheral artery disease: contemporary epidemiology, management gaps, and future directions: a scientific statement from the American Heart Association. *Circulation*. (2021) 144(9):e171–91. doi: 10.1161/CIR.0000000000001005

3. Fowkes FG, Rudan D, Rudan I, Aboyans V, Denenberg JO, McDermott MM, et al. Comparison of global estimates of prevalence and risk factors for peripheral artery disease in 2000 and 2010: a systematic review and analysis. *Lancet*. (2013) 382 (9901):1329–40. doi: 10.1016/S0140-6736(13)61249-0

4. Roth GA, Mensah GA, Johnson CO, Addolorato G, Ammirati E, Baddour LM, et al. Global burden of cardiovascular diseases and risk factors, 1990–2019: update from the GBD 2019 study. *J Am Coll Cardiol*. (2021) 76(25):2982–3021. doi: 10.1016/j.jacc.2020.11.010

5. Song P, Fang Z, Wang H, Cai Y, Rahimi K, Zhu Y, et al. Global and regional prevalence, burden, and risk factors for carotid atherosclerosis: a systematic review, meta-analysis, and modelling study. *Lancet Glob Health*. (2020) 8(5):e721–9. doi: 10.1016/S2214-109X(20)30117-0

6. Gerhard-Herman MD, Gornik HL, Barrett C, Barshes NR, Corriere MA, Drachman DE, et al. 2016 AHA/ACC guideline on the management of patients with lower extremity peripheral artery disease: executive summary: a report of the American College of Cardiology/American Heart Association Task Force on Clinical Practice Guidelines. *Circulation*. (2017) 135(12):e686–725. doi: 10.1161/CIR.0000000000000470

7. Poredos P. Involvement of microcirculation in critical ischemia: how to identify it? *Int Angiol*. (2020) 39(6):492–9. doi: 10.23736/S0392-9590.20.04428-4

8. Goncalves LN, van den Hoven P, van Schaik J, Leeuwenburgh L, Hendricks CHF, Verduijn PS, et al. Perfusion parameters in near-infrared fluorescence imaging with indocyanine green: a systematic review of the literature. *Life (Basel)*. (2021) 11 (5):433. doi: 10.3390/life11050433

9. Zhang Z, Du Y, Shi X, Wang K, Qu Q, Liang Q, et al. NIR-II light in clinical oncology: opportunities and challenges. *Nat Rev Clin Oncol*. (2024) 21(6):449–67. doi: 10.1038/s41571-024-00892-0

10. Li M, Huang K, Xu Q, Yang J, Zhang Y, Ji Z, et al. OCTA-500: a retinal dataset for optical coherence tomography angiography study. *Med Image Anal*. (2024) 93:103092. doi: 10.1016/j.media.2024.103092

11. Lauermann JL, Sochurek JAM, Plöttner P, Alten F, Kasten M, Prasuhn J, et al. Applicability of optical coherence tomography angiography (OCTA) imaging in Parkinson's disease. *Sci Rep*. (2021) 11(1):5520. doi: 10.1038/s41598-021-84862-x

12. Pai V, Bileck A, Hommer N, Janku P, Lindner T, Kauer V, et al. Impaired retinal oxygen metabolism and perfusion are accompanied by plasma protein and lipid alterations in recovered COVID-19 patients. *Sci Rep*. (2024) 14(1):8395. doi: 10.1038/s41598-024-56834-4

13. Gagnier JJ, Kienle G, Altman DG, Moher D, Sox H, Riley D, et al. The CARE guidelines: consensus-based clinical case reporting guideline development. *Headache*. (2013) 53(10):1541–7. doi: 10.1111/head.12246

14. Van Den Hoven P, Tange F, Van Der Valk J, Nerup N, Putter H, Van Rijswijk C, et al. Normalization of time-intensity curves for quantification of foot perfusion using near-infrared fluorescence imaging with indocyanine green. *J Endovasc Ther*. (2023) 30(3):364–71. doi: 10.1177/15266028221081085

15. Marcoccia A, Klein-Weigel PF, Gschwandtner ME, Wautrecht JC, Matuska J, Rother U, et al. Microcirculatory assessment of vascular diseases. *Vasa*. (2020) 49 (3):175–86. doi: 10.1024/0301-1526/a000851

16. Hamburg NM, Creager MA. Pathophysiology of intermittent claudication in peripheral artery disease. *Circ J*. (2017) 81(3):281–9. doi: 10.1253/circj.CJ-16-1286

17. Wermelink B, Ma KF, Haalboom M, El Moumni M, de Vries JPM, Geelkerken RH, et al. A systematic review and critical appraisal of peri-procedural tissue perfusion techniques and their clinical value in patients with peripheral arterial disease. *Eur J Vasc Endovasc Surg*. (2021) 62(6):896–908. doi: 10.1016/j.ejvs.2021.08.017

18. Fejfarová V, Matuška J, Jude E, Pithová P, Flekac M, Roztocil K, et al. Stimulation $TcPO_2$ testing improves diagnosis of peripheral arterial disease in patients with diabetic foot. *Front Endocrinol (Lausanne)*. (2021) 12:744195. doi: 10.3389/fendo.2021.744195

19. van den Hoven P, Ooms S, van Manen L, van der Bogt KEA, van Schaik J, Hamming JF, et al. A systematic review of the use of near-infrared fluorescence imaging in patients with peripheral artery disease. *J Vasc Surg*. (2019) 70 (1):286–97.e1. doi: 10.1016/j.jvs.2018.11.023

20. Van Den Hoven P, Goncalves LN, Quax PHA, Van Rijswijk CSP, Van Schaik J, Schepers A, et al. Perfusion patterns in patients with chronic limb-threatening ischemia versus control patients using near-infrared fluorescence imaging with indocyanine green. *Biomedicines*. (2021) 9(10):1417. doi: 10.3390/biomedicines9101417

21. Tange FP, van den Hoven P, van Schaik J, Schepers A, van der Bogt KEA, van Rijswijk CSP, et al. Near-infrared fluorescence imaging with indocyanine green to predict clinical outcome after revascularization in lower extremity arterial disease. *Angiology*. (2023) 75(9):884–92. doi: 10.1177/00033197231186096

22. Samils L, Henricson J, Strömberg T, Fredriksson I, Iredahl F. Workload and sex effects in comprehensive assessment of cutaneous microcirculation. *Microvasc Res*. (2023) 148:104547. doi: 10.1016/j.mvr.2023.104547

23. Aday AW, Duncan MS, Patterson OV, DuVall SL, Alba PR, Alcorn CW, et al. Association of sex and race with incident peripheral artery disease among veterans with normal ankle-brachial indices. *JAMA Netw Open*. (2022) 5(11):e2240188. doi: 10.1001/jamanetworkopen.2022.40188

24. Deegan AJ, Talebi-Liasi F, Song S, Li Y, Xu J, Men S, et al. Optical coherence tomography angiography of normal skin and inflammatory dermatologic conditions. *Lasers Surg Med*. (2018) 50(3):183–93. doi: 10.1002/lsm.22788

25. Kikuchi S, Miyake K, Tada Y, Uchida D, Koya A, Saito Y, et al. Laser speckle flowgraphy can also be used to show dynamic changes in the blood flow of the skin of the foot after surgical revascularization. *Vascular*. (2019) 27(3):242–51. doi: 10.1177/1708538118810664

Frontiers in Cardiovascular Medicine

TYPE Original Research
PUBLISHED 16 October 2024
DOI 10.3389/fcvm.2024.1491971

OPEN ACCESS

EDITED BY
Hong Chen,
Boston Children's Hospital and Harvard Medical School, United States

REVIEWED BY
Charles K. Thodeti,
University of Toledo, United States
Bisheng Zhou,
University of Illinois Chicago, United States

*CORRESPONDENCE
Tadanori Mammoto
✉ tmammoto@mcw.edu
Akiko Mammoto
✉ amammoto@mcw.edu

RECEIVED 05 September 2024
ACCEPTED 07 October 2024
PUBLISHED 16 October 2024

CITATION
Hunyenyiwa T, Kyi P, Scheer M, Joshi M, Gasparri M, Mammoto T and Mammoto A (2024) Inhibition of angiogenesis and regenerative lung growth in *Lep*$^{ob/ob}$ mice through adiponectin-VEGF/VEGFR2 signaling. Front. Cardiovasc. Med. 11:1491971. doi: 10.3389/fcvm.2024.1491971

# Inhibition of angiogenesis and regenerative lung growth in *Lep*$^{ob/ob}$ mice through adiponectin-VEGF/VEGFR2 signaling

Tendai Hunyenyiwa[1,2], Priscilla Kyi[1,2], Mikaela Scheer[1], Mrudula Joshi[1,2], Mario Gasparri[3], Tadanori Mammoto[1,4]* and Akiko Mammoto[1,2]*

[1]Department of Pediatrics, Medical College of Wisconsin, Milwaukee, WI, United States, [2]Department of Cell Biology, Neurobiology and Anatomy, Medical College of Wisconsin, Milwaukee, WI, United States, [3]Department of Thoracic Surgery, Medical College of Wisconsin, Milwaukee, WI, United States, [4]Department of Pharmacology and Toxicology, Medical College of Wisconsin, Milwaukee, WI, United States

**Introduction:** Obesity is associated with impairment of wound healing and tissue regeneration. Angiogenesis, the formation of new blood capillaries, plays a key role in regenerative lung growth after unilateral pneumonectomy (PNX). We have reported that obesity inhibits angiogenesis. The effects of obesity on post-PNX lung vascular and alveolar regeneration remain unclear.
**Methods:** Unilateral PNX is performed on *Lep*$^{ob/ob}$ obese mice to examine vascular and alveolar regeneration.
**Results:** Regenerative lung growth and expression of vascular endothelial growth factor (VEGF) and its receptor VEGFR2 induced after PNX are inhibited in *Lep*$^{ob/ob}$ obese mice. The levels of adiponectin that exhibits pro-angiogenic and vascular protective properties increase after unilateral PNX, while the effects are attenuated in *Lep*$^{ob/ob}$ obese mice. Post-PNX regenerative lung growth and increases in the levels of VEGF and VEGFR2 are inhibited in adiponectin knockout mice. Adiponectin stimulates angiogenic activities in human lung endothelial cells (ECs), which is inhibited by decreasing the levels of transcription factor Twist1. Adiponectin agonist, AdipoRon restores post-PNX lung growth and vascular and alveolar regeneration in *Lep*$^{ob/ob}$ obese mice.
**Discussion:** These findings suggest that obesity impairs lung vascular and alveolar regeneration and adiponectin is one of the key factors to improve lung regeneration in obese people.

KEYWORDS

**angiogenesis, lung regeneration, obesity, adiponectin, VEGF**

## Introduction

Obese population is increasing worldwide (1). In the United States, approximately 40% of the adult population is obese (2). Obesity is a risk factor for increased morbidity and mortality through its association with cardiovascular disease, type 2 diabetes (T2D) and certain types of cancer (2–4). Obesity is also a risk factor for respiratory diseases including acute lung injury (5), asthma (6), obstructive sleep apnea (7), and pulmonary hypertension (8). About 65% of the mild-moderate chronic obstructive pulmonary disease (COPD) population is overweight or obese (9).

Although lung transplantation is one of the strategies for end-stage lung diseases including COPD, it is not optimal due to the shortage of donor lungs, lower long-term survival rate, and serious complications (10). In addition, there is an association between obesity and poor outcomes in lung transplantation such as mortality and primary graft dysfunction after transplantation; obesity is currently a relative contraindication to adult lung transplantation (11). It has been reported that compensatory regenerative lung growth is induced after unilateral PNX in humans and other species (12–19); the remaining lung tissues grow to compensate for the initial loss. While it is known that obesity impairs wound healing (20) and attenuates tissue regeneration in other organs including muscle and liver (21, 22), the effects of obesity on post-PNX lung vascular and alveolar regeneration remain unknown. Understanding the mechanism by which obesity inhibits lung's regenerative ability will lead to the development of better therapeutic strategies to restore structures and functions in the end-stage lung diseases in obese patients.

We and other groups have demonstrated that endothelial cells (ECs) and angiogenic signaling are necessary for regenerative vascular and alveolar formation (13, 15, 17–19, 23, 24). In addition to their primary function to deliver oxygen, nutrients and cellular components, capillary ECs form the vascular niche and reciprocally crosstalk with resident lung cells (e.g., epithelial cells, mesenchymal cells, immune cells) to regulate lung homeostasis and regeneration (24). We have reported that angiogenesis is inhibited in obese adipose tissues (25). Insufficient blood vessels in obese animals result in decreases in oxygen tension, collagen synthesis, and immune responses, leading to suppression of wound healing and tissue repair processes (20). Stimulating angiogenesis may restore the regenerative program in the lungs in an obese condition.

One of the adipokines, adiponectin, exhibits pro-angiogenic and vascular protective properties (26, 27). Adiponectin induces angiogenesis through multiple signaling pathways [e.g., AMPK, eNOS, VEGF (3, 26)] and stimulates regeneration of muscle (28) and liver (29). The levels of adiponectin decrease in obese animals, which contributes to obesity-related diseases, such as type2 diabetes and cardiovascular diseases (26, 30). It has been reported that obesity-induced imbalance of adipokines leads to lung EC dysfunction and impairs injury repair (27). Although it is known that adiponectin stimulates proliferation and migration in human bronchial epithelial cells (31), the role of adiponectin in regenerative lung growth remains unclear.

Transcription factor Twist1 controls expression of angiogenic factors, including VEGFR2 and Tie2, and regulates angiogenesis (18, 32–34). We have demonstrated that Twist1 mediates age-dependent inhibition of angiogenesis and lung regeneration (18). Twist1 is also involved in pulmonary fibrosis (34) and endotoxin-induced decreases in vascular integrity (32). The levels of TWIST1 are lower in obese human subcutaneous adipose tissue ECs compared to that in lean adipose tissues, which results in impairment of angiogenesis in obese adipose tissues (25). The role of Twist1 in lung vascular regeneration in the obese lungs has not been studied before.

Here, we found that post-PNX regenerative lung growth is attenuated in *Lep*$^{ob/ob}$ obese mice. Knockdown of adiponectin decreases expression of Twist1, VEGF and VEGFR2, and inhibits post-PNX regenerative lung growth and vascular formation in the mouse lung, while adiponectin agonist, AdipoRon restores post-PNX lung growth in obese mice. Adiponectin could be one of the efficient targets for lung vascular and alveolar regeneration in obese patients.

# Materials and methods

## Materials

AdipoRon hydrochloride was from Tocris (Minneapolis, MN). Adiponectin was from R&D (Minneapolis, MN). Anti-CD31 antibody (553370) was from BD Pharmingen (San Jose, CA). Anti-SPB (ab40876), -AQP5 (ab78486), -TWIST1 (ab50887) and -ERG (ab92513) antibodies were from Abcam (Cambridge, MA). Anti-VEGF164 (AF-493-NA) and -RAGE (MAB1179) antibodies were from R&D. Anti-VEGFR2 antibody (2479) was from Cell Signaling (Danvers, MA). Anti-adiponectin antibody (MA1-054) was from Thermo Fisher Scientific (Waltham, MA). Anti-actin antibody (A5441) was from Sigma (St. Louis, MO).

## Molecular biological and biochemical methods

Quantitative reverse transcription (qRT)-PCR was performed with the iScript reverse transcription and iTaq SYBR Green qPCR kit (BioRad, Hercules, CA) using the BioRad real time PCR system. Cyclophilin and beta-2-microglobulin controlled for overall cDNA content. The primers for mouse Vegf, Vegfr2, Twist1 and cyclophilin and human TWIST1, VEGFR2, and beta-2-microglobulin were previously described (18, 35). The primers for mouse adiponectin forward; 5′-TGTTCCTCTTAATCCTGCCCA-3′ and reverse; 5′-CCAACCTGCACAAGTTCCCTT-3′, Adipor1 forward; 5'-AGACAACGACTACCTGCTACA-3' and reverse; 5'-GTGGATGCGGAAGATGCTCT-3'; Adipor2 forward; 5'-GCCAAACACCGATTGGGGT-3' and reverse; 5'-GGCTCCAAATCTCCTTGGTAGTT-3'. The protein levels of mouse VEGF and adiponectin were measured using ELISA (R&D systems). Immunoblotting was performed as we previously reported (19, 36). Gene knockdown was performed using the RNA interference technique as we previously reported (18, 35). In brief, we used siLentfect transfection reagent (BioRad) with siRNA (10 nM) following manufacturer instruction. The siRNA for human TWIST1 was previously described (18). As a control, siRNA duplex with an irrelevant sequence (QIAGEN, Hilden, Germany) was used.

## Mouse and human lung EC isolation

C57BL6 (stock# 664), adiponectin knockout (*B6;129-Adipoq*$^{tm1Chan}$*/J*; *Adipoq*$^{-/-}$, stock# 8195) and control B6129SF2/J (stock# 101045) mice were obtained from the Jackson Laboratory (Bar Harbor, ME). Adiponectin mRNA expression decreased by 82% in lungs isolated from *Adipoq*$^{-/-}$ mice compared with those from control B6129SF2/J mice (Figure 3A). Heterozygote

TABLE 1 Sample demographics.

| ID | Age | BMI | Sex | Race |
|---|---|---|---|---|
| Lean -1 | 60 | 26 | Male | N/A |
| Lean -2 | 75 | 23 | Female | White |
| Lean -3 | 68 | 21 | Male | White |
| Lean -4 | 34 | 26 | Female | White |
| Lean -5 | 65 | 27 | Female | Black |
| Obese -1 | 67 | 37 | Female | White |
| Obese -2 | 60 | 31 | Female | White |
| Obese -3 | 42 | 31 | Male | N/A |
| Obese -4 | 57 | 33 | Male | White |
| Obese -5 | 57 | 39 | Male | White |

*B6.V-Lepob/J* mice (stock# 632, $Lep^{ob/+}$) were obtained from the Jackson Laboratory and bred to obtain homozygote ($Lep^{ob/ob}$). $Lep^{ob/+}$ mice were maintained with standard diet (LabDiet 5LOD, 4.5% fat). For the PNX experiments, $Lep^{ob/+}$ and $Lep^{ob/ob}$ mice were fed with LabDiet 5K20 (10% fat) for 8 weeks, starting at 4 weeks of age. Human lung tissues were obtained as discarded surgical specimens from patients [Medical College of Wisconsin (MCW) tissue bank; Table 1]. De-identified patient demographic data were collected using the Generic Clinical Research Database at MCW. All protocols are approved by the Institutional Review Board (IRB) of MCW and Froedtert Hospital and ECs isolated from de-identified human lungs are determined as non-human subjects (PRO00047689).

ECs from mouse lungs and human lung ECs were isolated using anti-CD31 conjugated magnetic beads as previously described (17, 19, 25, 36). Briefly, lung tissue was cut into small pieces using small scissors and treated with collagenase A (1 mg/ml) for 30 min at 37°C. The tissue suspension was filtered through a 40 mm cell strainer (Falcon) to remove the undigested cell clumps and separate single cells. Cells were centrifuged (1,000 rpm, 5 min) at room temperature (RT) and the pellet was resuspended into 0.5 ml RBC Lysis Buffer (sigma, 1 min, RT). The lysis reaction was stopped by adding 10 ml 10% FBS/DMEM, and centrifuged (1,000 rpm, 5 min, RT). For mouse lung EC isolation, the pellet was resuspended into 0.5 ml 4% FBS/PBS with APC anti-mouse CD31 antibody (Biolegend, San Diego, CA, 1/100), incubated (20 min, on ice) and washed three times with 4% FBS/PBS. Cells were centrifuged (1,000 rpm, 5 min, RT) and resuspended into 0.1 ml 4% FBS/PBS with anti-APC conjugated microbeads (Miltenyl Biotec, Bergisch Gladbach, Germany), incubated (10 min, on ice) and washed three times with 4% FBS/PBS. The cells were then resuspended in 0.5 ml 4% FBS/PBS and CD31-positive mouse ECs were magnetically separated using MACS column (Miltenyl Biotec) according to the manufacturer's instruction. To increase the purity of the magnetically separated fraction, the eluted fraction was enriched over a second new MACS column. For human lung EC isolation, the cell pellet was resuspended into 1 ml 4% FBS/PBS with CD31-conjugated Dynabeads (Invitrogen/Thermo Fisher), incubated (30 min, 4°C), washed three times with 4% FBS/PBS, and magnetically separated using a magnetic stand. FACS analysis confirmed that more than 89% of isolated ECs cells are $CD31^+$ (Supplementary Figure S1A) (17, 19, 25, 36).

## Cell biological analysis

Human lung ECs were seeded ($1 \times 10^5$ cells/35 mm dish) and DNA synthesis was measured using the Click-iT EdU Cell Proliferation Kit (ThermoFisher). Cells were imaged using a Nikon A1R confocal laser scanning microscope and quantification was performed using ImageJ software (NIH) (18, 25, 36). EC migration was analyzed by seeding human lung ECs ($1 \times 10^5$ cells/100 µl) on a trans-well chamber (Corning Costar) coated with 0.5% gelatin. ECs migrating to 5% FBS for 16 h were stained with Wright Giemsa solution (Fisher Scientific) and counted (18, 25, 36).

## Unilateral PNX

The *in vivo* animal study was carried out in strict accordance with the recommendations in the Guide for the Care and Use of Laboratory Animals of the National Institutes of Health. The protocols were reviewed and approved by the Institutional Animal Care and Use Committee of MCW (AUA 5598). Unilateral PNX was performed as described (17–19). Briefly, mice (C57BL6, $Lep^{ob/+}$, $Lep^{ob/ob}$, $Adipoq^{-/-}$, or B6129SF2/J, 12–15 week old) were anesthetized with Ketamine (100 mg/kg)/Xylazine (10 mg/kg, intraperitoneal injection), intubated and mechanically ventilated using a rodent ventilator (MiniVent, Harvard Apparatus, Holliston, MA). After ensuring adequate anesthesia, thoracotomy was performed, and the left lung was lifted through the incision and a 5-0 silk suture was passed around the hilum and tied. The hilum was then transected distal to the tie. The remaining portions of the hilum and tie were returned to the thoracic cavity. Sham-operated mice underwent thoracotomy without PNX.

## Bulk RNA sequencing and analysis

RNA was collected from ECs isolated from C57BL6 mouse lungs 7 days after PNX and sham-operated mouse lungs using the RNeasy mini kit (Qiagen). The quantity and quality of RNA isolated from mouse lung ECs ($n = 3$ per group, each $n$ was pooled from 2 mice) were measured by Agilent 2200 TapeStation, and all samples have an RNA integrity number >9.3. Total RNA samples were submitted to the Institute for Systems Biology Molecular and Cell Core (Seattle, WA) for RNA sequencing. Library preparation was employed using the Illumina TruSeq Stranded mRNA kit. Sequencing was performed using the Illumina NextSeq500. Paired-end sequencing was performed on a high output 150 cycle kit v2.5. The RNA sequencing reads were aligned to the mouse genome (mm10 reference genome) and read counting and differential gene expression analysis were performed with Basepair Tech using the Deseq2 pipeline. 903 significantly differentially expressed genes defined as having a |log2 fold change| >1, and a $p$-adjusted value with the FDR cutoff of 0.01 calculated by the Benjamini-Hochberg adjustment and filtered to <0.01 were defined (Supplementary Table S1). Gene ontology (GO) analysis of significant targets was done via The Database for Annotation, Visualization and Integrated Discovery (DAVID) v 6.8 using the Functional Annotation Chart tool. Charts were filtered by Biological Processes Gene Ontology (BP GO) Terms and sorted by *p*-value (Supplementary Table S2). The 903 significantly differentially expressed genes generated 262 BP GO Term categories (Supplementary Table S2), which are further categorized into two different GO Term charts; 117 GO Term categories related to angiogenesis (Supplementary Table S3) and 141 GO Term related to metabolic process detected as appearing on a master list comprised of Gene Card (Supplementary Table S5). These GO Terms categories were color-coded into groups encompassing adhesion/migration, cell cycle/apoptosis, inflammatory/immune response, and cell signaling (Supplementary Tables S4, S6).

Network generation was performed on all genes from the top 50 GO Term categories by *p*-value related to angiogenic factors or metabolic process with Ingenuity Pathway Analysis (IPA) software (QIAGEN). The network of angiogenic genes was constructed by starting with the shortest connections between those connected to Twist1 and all others, and adding the shortest connections between all genes connected to Twist1 and the remaining unconnected genes. Genes were eliminated if they were connected to less than 3 other genes. The network of metabolic genes was constructed and interaction with adiponectin was analyzed as described for Twist1. The resulting IPA networks from the angiogenic factors and metabolic processes were combined to create a network illustrating the overlapping genes between the angiogenic factor and metabolic processes categories. RNAseq results are available in NCBI Geo (GSE179227).

## Statistics

All phenotypic analysis was performed by masked observers unaware of the identity of experimental groups. Error bars (SEM) and *p* values were determined from the results of three or more independent experiments. Student's *t*-test was used for statistical significance for two groups. For more than two groups, one-way ANOVA with a post-hoc analysis using the Bonferroni test was conducted.

# Results

## Post-PNX lung growth and vascular formation are inhibited in obese mice

Angiogenic signaling is necessary for lung vascular and alveolar regeneration after unilateral PNX (13, 15, 17–19, 23). Angiogenesis is inhibited in obese adipose tissues (25). The effects of obesity on regenerative ability of the lungs remain unknown. When we performed unilateral PNX on C57BL6 mice under normal chaw (4.5% fat, 5LOD) or on $Lep^{ob/+}$ or $Lep^{ob/ob}$ mice fed with 10% fat diet (5K20), there was a significant increase in the ratio of the weight of right lung lobe to mouse body length 7 days after left unilateral PNX in C57BL6 or $Lep^{ob/+}$ mice as consistent with previous reports (13, 15, 17–19); the ratio of lung weight to mouse body length was $14.2 \times 10^{-3}$ (g/cm) in the sham-operated control mice, while the ratio increased by 1.5-fold in the lungs 7 days after PNX (Figure 1A). Although the lung weight was not significantly different among C57BL6, $Lep^{ob/+}$ and $Lep^{ob/ob}$ sham-operated mice, the increases in the lung weight after PNX were significantly reduced in $Lep^{ob/ob}$ mice 7 days after PNX compared to those in C57BL6 or $Lep^{ob/+}$ mice (Figure 1A). We also analyzed the effects of obesity on blood vessel density in the lung using EC marker, ETS-related gene (ERG) staining; ERG-positive EC density was 2.2- or 2.1- times higher in the C57BL6 or $Lep^{ob/+}$ mouse lungs after PNX compared to those in the sham-operated control mouse lungs, while these effects were suppressed in $Lep^{ob/ob}$ mice after PNX (Figures 1B,C). These findings suggest that post-PNX lung growth and vascular regeneration are inhibited in obese mice.

A major angiogenic factor, VEGF is necessary for post-PNX lung growth and vascular regeneration (13). The protein levels of VEGF in the mouse lungs and the serum in C57BL6 mice and $Lep^{ob/+}$ mice increased 7 days after PNX, while these effects were attenuated in $Lep^{ob/ob}$ mice after PNX (Figure 1D). Immunohistochemical (IHC) analysis confirmed that VEGF expression in AQP5-positive alveolar type1 (AT1) cells (37) increased in the post-PNX C57BL6 and $Lep^{ob/+}$ mouse lungs. In contrast, the post-PNX increases in the VEGF expression were suppressed in $Lep^{ob/ob}$ mice after PNX (Figures 1B,C). Similarly, post-PNX increases in the VEGFR2 expression were inhibited in $Lep^{ob/ob}$ mice (Figures 1B,C; Supplementary Figure S1B). Among three VEGF isoforms (VEGF120, 164, and 188), the mRNA levels of Vegf164 increased after PNX in control $Lep^{ob/+}$ mouse lungs, but not in the $Lep^{ob/ob}$ mouse lungs (Supplementary Figure S1C). The levels of Vegf120 and 188 did not significantly change in the post-PNX mouse lungs (not shown). We have reported that angiopoietin (Ang)-Tie2 signaling is stimulated after PNX to control regenerative lung growth (17, 19, 38). Thus, we also examined the expression of Ang-Tie2 in the post-PNX mouse lungs. Ang2 and Tie2 expression significantly increased in the control $Lep^{ob/+}$ mouse lungs after PNX; in contrast, the effects were inhibited in $Lep^{ob/ob}$ mouse lungs (Supplementary Figure S1D).

## Suppression of adiponectin mediates obesity-dependent decline in angiogenesis and post-PNX lung growth

Adiponectin induces angiogenesis (26, 27) and stimulates tissue regeneration [muscle (28), liver (29)]. The levels of adiponectin decrease in obese animals (26). The protein levels of adiponectin in lungs and serum increased 7 days after PNX in $Lep^{ob/+}$ mice; in contrast, the effects were suppressed in post-PNX $Lep^{ob/ob}$ mice (Figure 2A). IHC analysis confirmed that increases in the levels of adiponectin in the post-PNX $Lep^{ob/+}$ mouse lungs were

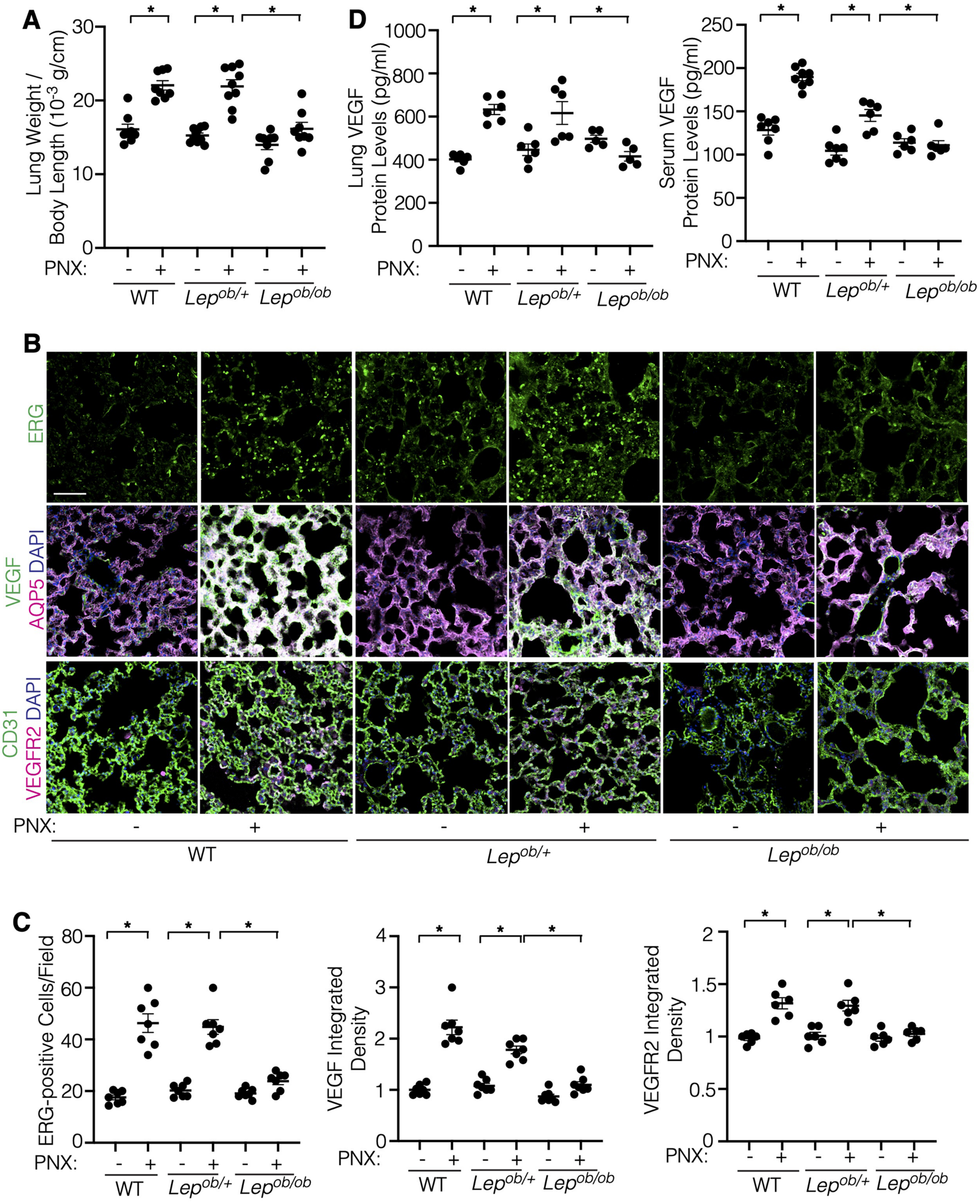

FIGURE 1

Post-PNX regenerative lung growth is inhibited in the $Lep^{ob/ob}$ mouse lungs. **(A)** Graph showing the ratio of the weight of right lung lobe to mouse body length in C57BL6 (WT), $Lep^{ob/+}$ or $Lep^{ob/ob}$ mice 7 days after PNX ($n = 8$–9, mean ± s.e.m., $*p < 0.05$). **(B)** Immunofluorescence (IF) micrographs showing ERG-positive ECs (*top*), VEGF expression, AQP5-positive alveolar epithelial cells and DAPI (*middle*) and CD31-positive blood vessels and VEGFR2 expression and DAPI (*bottom*) in the C57BL6 (WT), $Lep^{ob/+}$ or $Lep^{ob/ob}$ mouse lungs 7 days after PNX. Scale bar, 50 µm. **(C)** Graphs showing the quantification of ERG-positive ECs (*left*), VEGF (*middle*) and VEGFR2 (*right*) expression in the C57BL6 (WT), $Lep^{ob/+}$ or $Lep^{ob/ob}$ mouse lungs 7 days after PNX ($n = 6$–7, mean ± s.e.m., $*p < 0.05$). **(D)** Graphs showing the VEGF protein levels in the C57BL6 (WT), $Lep^{ob/+}$ or $Lep^{ob/ob}$ mouse lungs (*left*) and serum (*right*) 7 days after PNX ($n = 5$–8, mean ± s.e.m., $*p < 0.05$).

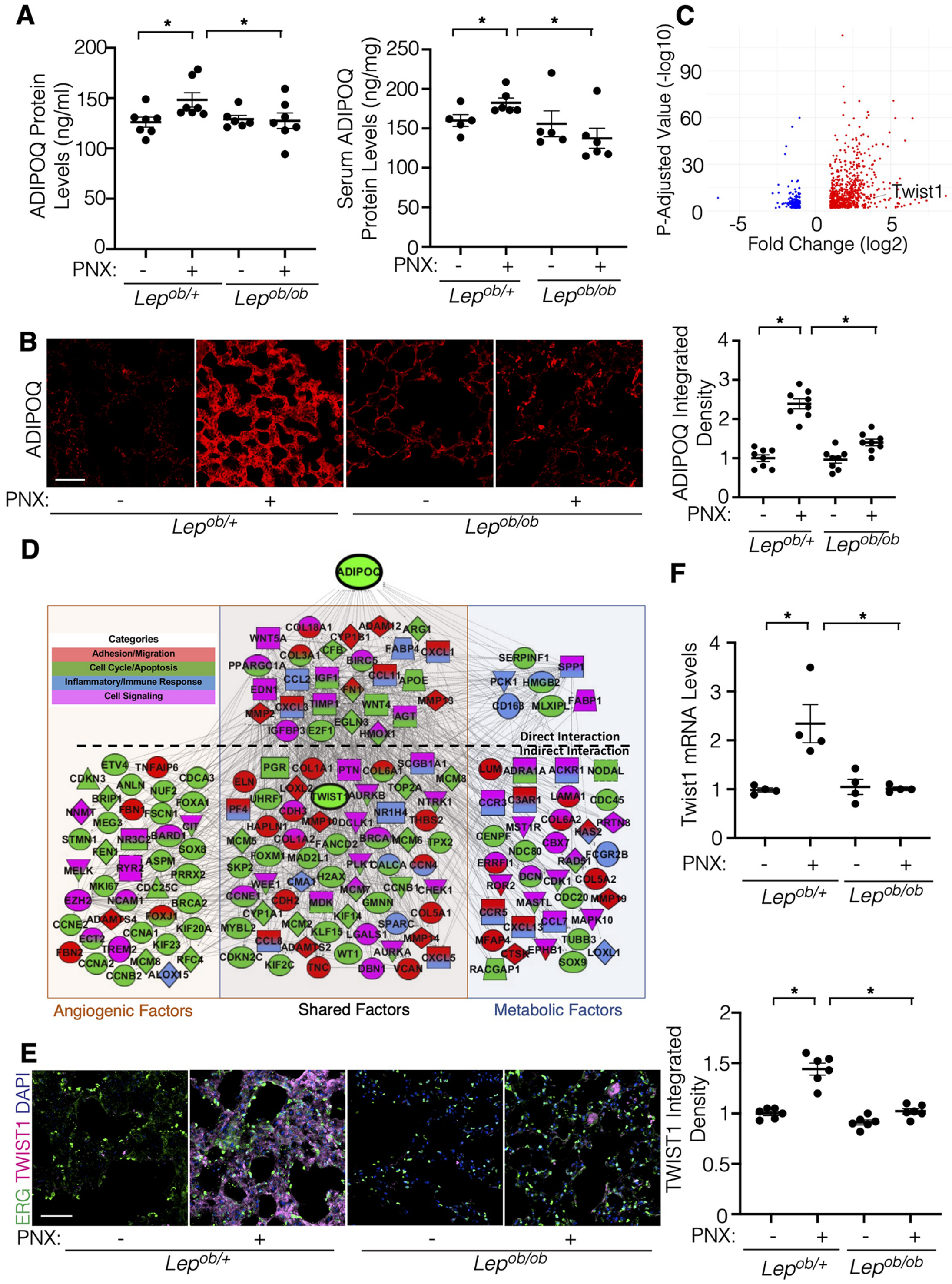

FIGURE 2

Post-PNX increases in the adiponectin (ADIPOQ) expression are suppressed in $Lep^{ob/ob}$ mice. **(A)** Graphs showing the quantification of ADIPOQ protein expression in the $Lep^{ob/+}$ or $Lep^{ob/ob}$ mouse lungs (*left*) and serum (*right*) 7 days after PNX ($n = 5–7$, mean ± s.e.m., $*p < 0.05$). **(B)** IF micrographs showing ADIPOQ expression in the $Lep^{ob/+}$or $Lep^{ob/ob}$ mouse lungs 7 days after PNX. Scale bar, 50 µm. Graph showing the ADIPOQ expression ($n = 8$, mean ± s.e.m., $*p < 0.05$). **(C)** Volcano plots of 903 significantly differentially expressed genes in ECs isolated from C57BL6 mouse lungs 7 days after PNX compared to those in sham-operated mouse lungs (GSE179227). Twist1 is a significantly differentially expressed gene. **(D)** Gene expression profiles and networks in ECs isolated from post-PNX (day 7) vs. sham-operated mouse lungs. **(E)** IF micrographs showing ERG-positive ECs, TWIST1 expression and DAPI in the $Lep^{ob/+}$ or $Lep^{ob/ob}$ mouse lungs 7 days after PNX. Scale bar, 50 µm. Graph showing the TWIST1 expression in the $Lep^{ob/+}$ or $Lep^{ob/ob}$ mouse lungs 7 days after PNX ($n = 6$, mean ± s.e.m., $*p < 0.05$). **(F)** Graph showing the Twist1 mRNA levels in the $Lep^{ob/+}$ or $Lep^{ob/ob}$ mouse lung ECs 7 days after PNX ($n = 4$, mean ± s.e.m., $*p < 0.05$).

attenuated in $Lep^{ob/ob}$ mouse lungs (Figure 2B). Expression of the adiponectin receptor, Adipor1 and Adipor2 did not change after PNX as well as $Lep^{ob/+}$ vs. $Lep^{ob/ob}$ mouse lungs (Supplementary Figure S1E). These results suggest that obesity suppresses the levels of adiponectin in the post-PNX mouse lungs.

Transcription factor Twist1 controls expression of angiogenic factors to regulate angiogenesis (18, 32–34). We have reported that the levels of TWIST1 are lower in obese human subcutaneous adipose tissue ECs compared to that in lean adipose tissues, which inhibits angiogenesis (25). Knockdown of endothelial Twist1 inhibited post-PNX lung growth (18). In the bulk RNAseq analysis (GSE179227, Supplementary Table S1), the levels of Twist1 significantly increased in ECs isolated from the post-PNX mouse lungs (7 days, Figure 2C). IPA network analysis demonstrated that genes listed in the top 50 BP GO terms of each category (129 genes in angiogenic and 131 genes in metabolic processes) interacted with Twist1, and 88 genes were present in both categories relating to angiogenic and metabolic processes; 27 genes interacted directly (e.g., ADAM12, CXCL1, MMP2, MMP13, COL3A, WNT5A) and 61 genes interacted indirectly (e.g., LOXL2, COL6A, FOXM1, WT1, THBS2, CXCL5) with adiponectin (Figure 2D).

Consistent with the RNAseq data, TWIST1 expression increased in the post-PNX $Lep^{ob/+}$ mouse lungs, but not in the $Lep^{ob/ob}$ mouse lungs (Figure 2E). Twist1 mRNA expression was also 2.2-times higher in ECs isolated from $Lep^{ob/+}$ mouse lungs 7 days after PNX, while the levels of Twist1 did not significantly change in post-PNX $Lep^{ob/ob}$ mouse lung ECs (Figure 2F), suggesting that obesity inhibits post-PNX induction of Twist1 expression.

## Adiponectin is required for vascular and alveolar regeneration in the mouse lungs

To analyze the effects of adiponectin on regenerative lung growth, we performed unilateral PNX on $Adipoq^{-/-}$ mice, in which the mRNA levels of adiponectin in the mouse lungs were lower by 82% compared to those in the background matched wild type (WT) B6129SF2/J mouse lungs (Figure 3A). While the weight of the remaining right lung lobe increased by 1.3-times in control WT B6129SF2/J mice 7 days after PNX, the increase in the post-PNX lung weight was suppressed in the $Adipoq^{-/-}$ mouse lungs (Figure 3B). Post-PNX increases in the number of surfactant protein B (SPB)-positive alveolar type-II (AT2) cells and ERG-positive ECs in the WT mouse lungs were suppressed in the $Adipoq^{-/-}$ mouse lungs (Figure 3C). Increases in the levels of VEGF, VEGFR2, and TWIST1 after PNX were also attenuated in the $Adipoq^{-/-}$ mouse lungs (Figures 3C,D; Supplementary Figure S1F).

To further examine the effects of adiponectin-TWIST1 signaling on EC behaviors, we isolated ECs from lean (BMI < 30) or obese (BMI > 30) human lungs as we reported (17, 19, 25, 36) (Table 1), treated ECs with adiponectin (300 ng/ml) or in combination with TWIST1 siRNA and investigated the effects. Adiponectin increased the mRNA and protein levels of VEGFR2, as well as stimulated DNA synthesis and migration in lean lung ECs; in contrast siRNA-based knockdown of TWIST1 attenuated the effects (Figures 4A–C). Adiponectin also stimulated DNA synthesis and migration in the obese lung ECs, which was inhibited by TWIST1 knockdown; however, adiponectin failed to increase VEGFR2 expression in the obese lung ECs (Figures 4A–C).

We then investigated whether stimulation of adiponectin signaling induces angiogenesis and regenerative lung growth in obese mice by treating mice with AdipoRon, an agonist of adiponectin receptors AdipoR1 and AdipoR2 (39). AdipoRon (oral gavage, 150 µg/mouse) stimulated post-PNX lung growth and increased $ERG^{+}$ EC density and expression of VEGF and VEGFR2 in $Lep^{ob/ob}$ obese mouse lungs after PNX when analyzed by IHC (Figures 5A,B). AdipoRon also increased the levels of VEGF and VEGFR2 in the post-PNX $Lep^{ob/ob}$ mouse lungs compared to that without treatment (Figure 5C). These results suggest that adiponectin signaling increases VEGF-VEGFR2 expression and restores lung vascular and alveolar regeneration in obese mice.

# Discussion

Here we have demonstrated that regenerative lung growth after unilateral PNX mediated by adiponectin-VEGF/VEGFR2 signaling is inhibited in $Lep^{ob/ob}$ obese mice (Figure 6). The levels of adiponectin, VEGF, and VEGFR2 increased after PNX were suppressed in $Lep^{ob/ob}$ obese mice, and post-PNX lung growth was inhibited in $Adipoq^{-/-}$ mice. Post-PNX increases in the levels of TWIST1 were also suppressed in $Lep^{ob/ob}$ and $Adipoq^{-/-}$ mouse lung ECs. Adiponectin stimulated angiogenic activities in lean and obese human lung ECs *in vitro*, while these effects were suppressed by TWIST1 knockdown. AdipoRon restored VEGF and VEGFR2 expression, vascular formation, and regenerative lung growth in post-PNX $Lep^{ob/ob}$ mice. These findings suggest that obesity impairs vascular and alveolar regeneration by suppressing adiponectin-VEGF/VEGFR2 signaling, and adiponectin may be one of the therapeutic targets to improve regenerative ability in obese lungs.

It has been reported that obesity correlates with poorer outcomes in respiratory diseases, including COVID-19 (40), acute respiratory distress syndrome (5), and idiopathic pulmonary fibrosis (IPF) (41), for which treatment options are limited. Reduced levels of circulating adiponectin and other adipokine are associated with COVID-19 severity (42). Adiponectin signaling suppresses profibrotic activation of fibroblast in IPF (43). Since impairment of angiogenesis and regenerative/repair ability contributes to lung disease pathology (24), modulating the adiponectin-VEGF/VEGFR2 signaling may also improve the outcomes of obesity-related lung diseases.

Interaction between epithelial cells and capillary ECs is necessary for organ regeneration and repair (24). Perturbation of the levels of angiogenic factors (3) and suppression of angiogenesis mediate impairment of wound healing and tissue repair in obese animals (20). VEGF signaling is necessary for regenerative lung growth after PNX (13). Since VEGF mainly expresses in AT1 cells (37), while VEGFR2 in ECs (35), crosstalk

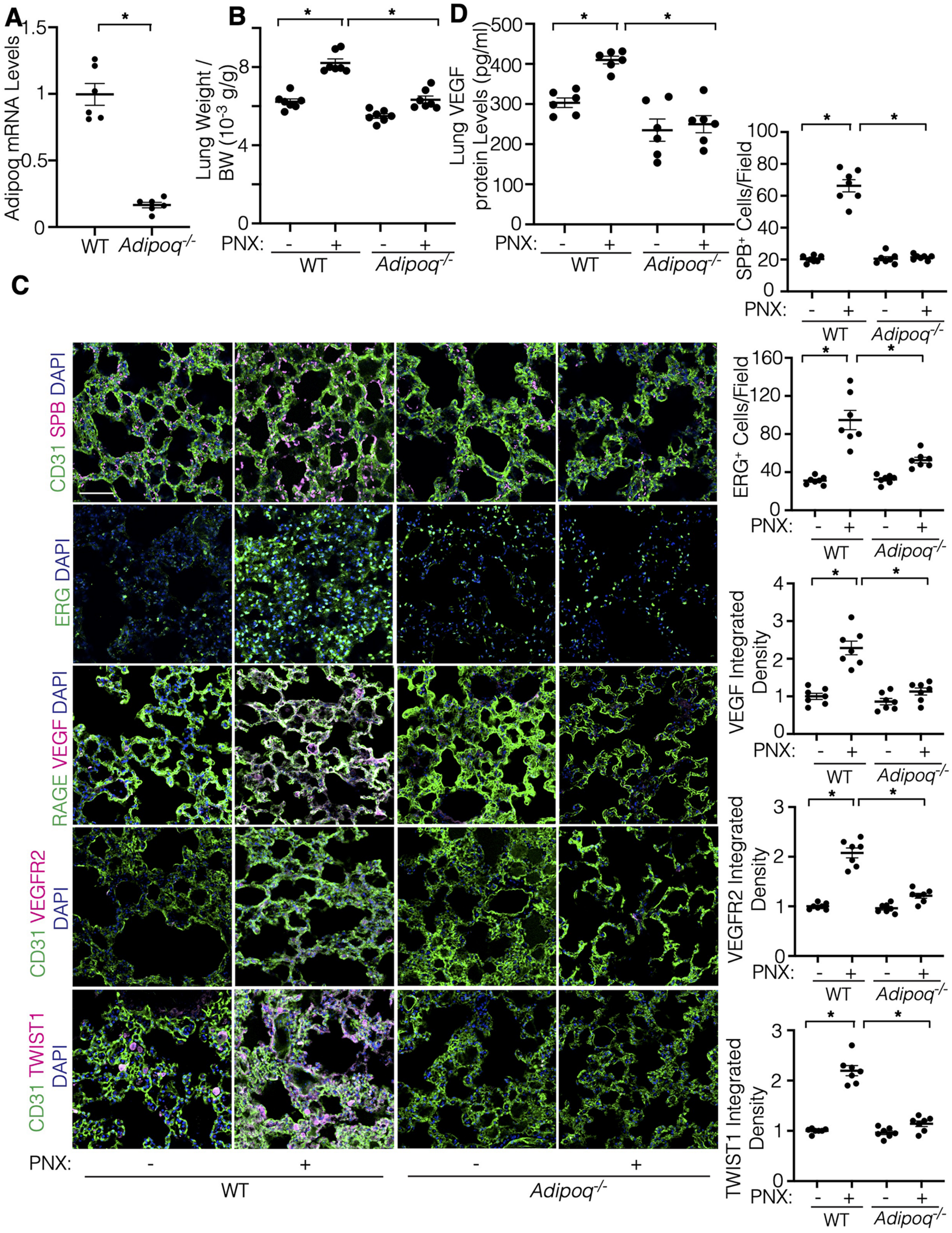

FIGURE 3
Post-PNX regenerative lung growth is inhibited in the *Adipoq*$^{-/-}$ mouse lungs. **(A)** Graph showing the adiponectin mRNA levels in the *Adipoq*$^{-/-}$ or control WT mouse lungs ($n = 6$, mean ± s.e.m., $*p < 0.05$). **(B)** Graph showing the ratio of the weight of right lung lobe to body weight (BW) in *Adipoq*$^{-/-}$ or control WT mice 7 days after PNX ($n = 7$, mean ± s.e.m., $*p < 0.05$). **(C)** IF micrographs showing CD31-positive blood vessels, SPB-positive AT2 cells and DAPI (*top*), ERG-positive ECs and DAPI (*2nd*), RAGE-positive alveolar epithelial cells, VEGF expression and DAPI (*3rd*), CD31-positive blood vessels, VEGFR2 expression and DAPI (*4th*), and CD31-positive blood vessels, TWIST1 expression and DAPI (*bottom*) in the *Adipoq*$^{-/-}$ or control WT mouse lungs 7 days after PNX. Scale bar, 50 μm. Graphs showing the quantification of SPB-positive AT2 cells (*top*), ERG-positive ECs (*2nd*), VEGF expression (*3rd*), VEGFR2 expression (*4th*), and TWIST1 expression (*bottom*) in the *Adipoq*$^{-/-}$ or WT mouse lungs 7 days after PNX ($n = 7$, mean ± s.e.m., $*p < 0.05$). **(D)** Graph showing the VEGF protein levels in the *Adipoq*$^{-/-}$ or control WT mouse lungs 7 days after PNX ($n = 6$, mean ± s.e.m., $*p < 0.05$).

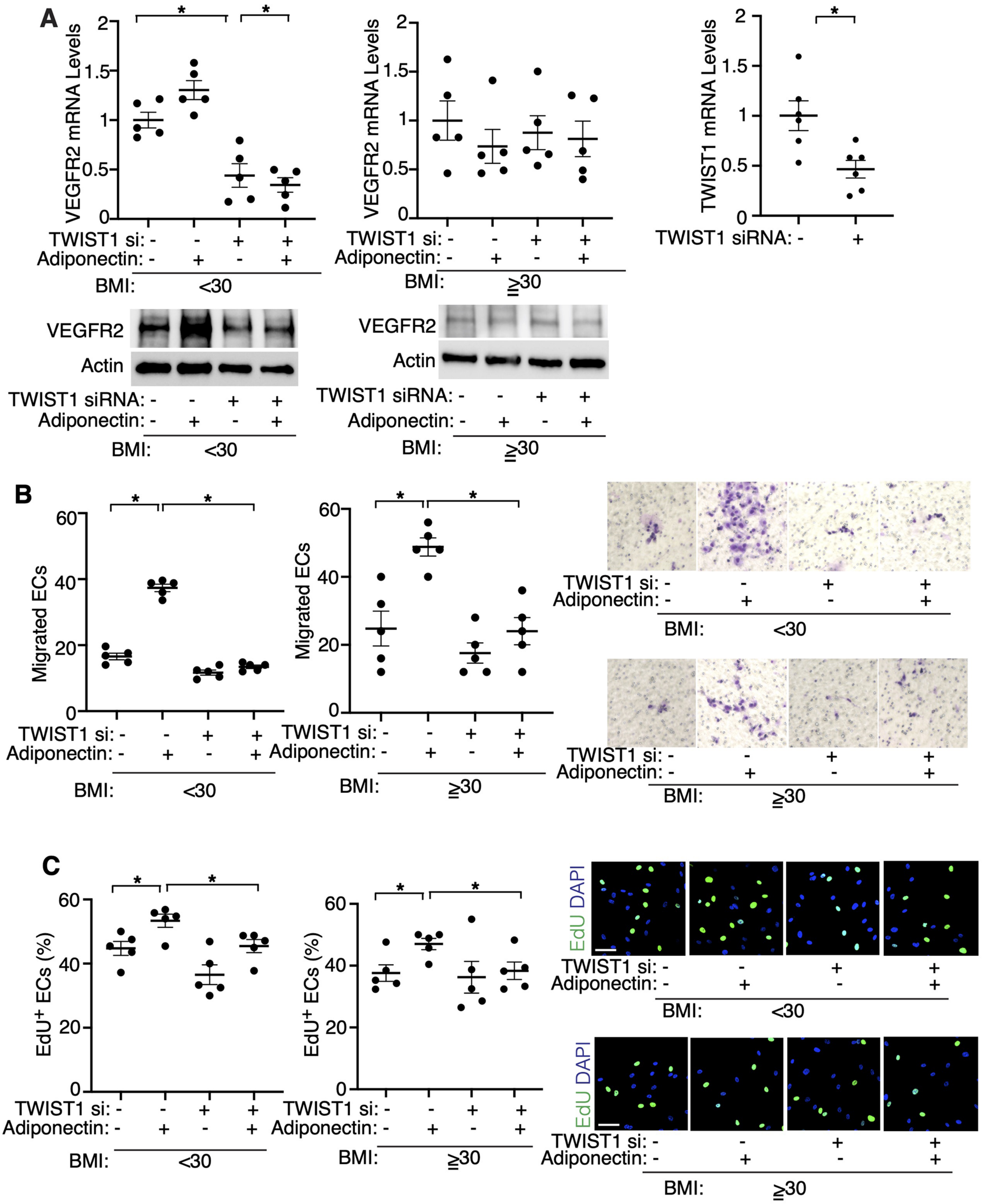

FIGURE 4

Adiponectin mediates angiogenic abilities in human lung ECs *in vitro*. **(A)** Graphs showing the mRNA levels of VEGFR2 in lean (BMI < 30, *left*) or obese (BMI ≥ 30, *middle*) human lung ECs treated with adiponectin or in combination with TWIST1 siRNA ($n = 5$, mean ± s.e.m., $^*p < 0.05$). Graph showing the mRNA levels of TWIST1 in human lung ECs treated with TWIST1 siRNA (*right*, $n = 6$, mean ± s.e.m., $^*p < 0.05$). IB showing the levels of VEGFR2 and Actin in lean (*left*) or obese (*right*) human lung ECs treated with adiponectin or in combination with TWIST1 siRNA. **(B)** Graphs showing migration of lean (*left*) or obese (*right*) human lung ECs treated with adiponectin or in combination with TWIST1 siRNA ($n = 5$, mean ± s.e.m., $^*p < 0.05$). Representative images of migrated ECs. **(C)** Graphs showing DNA synthesis of lean (*left*) or obese (*right*) human lung ECs treated with adiponectin or in combination with TWIST1 siRNA ($n = 5$, mean ± s.e.m., $^*p < 0.05$). Representative images of $\text{EdU}^+$ ECs and DAPI.

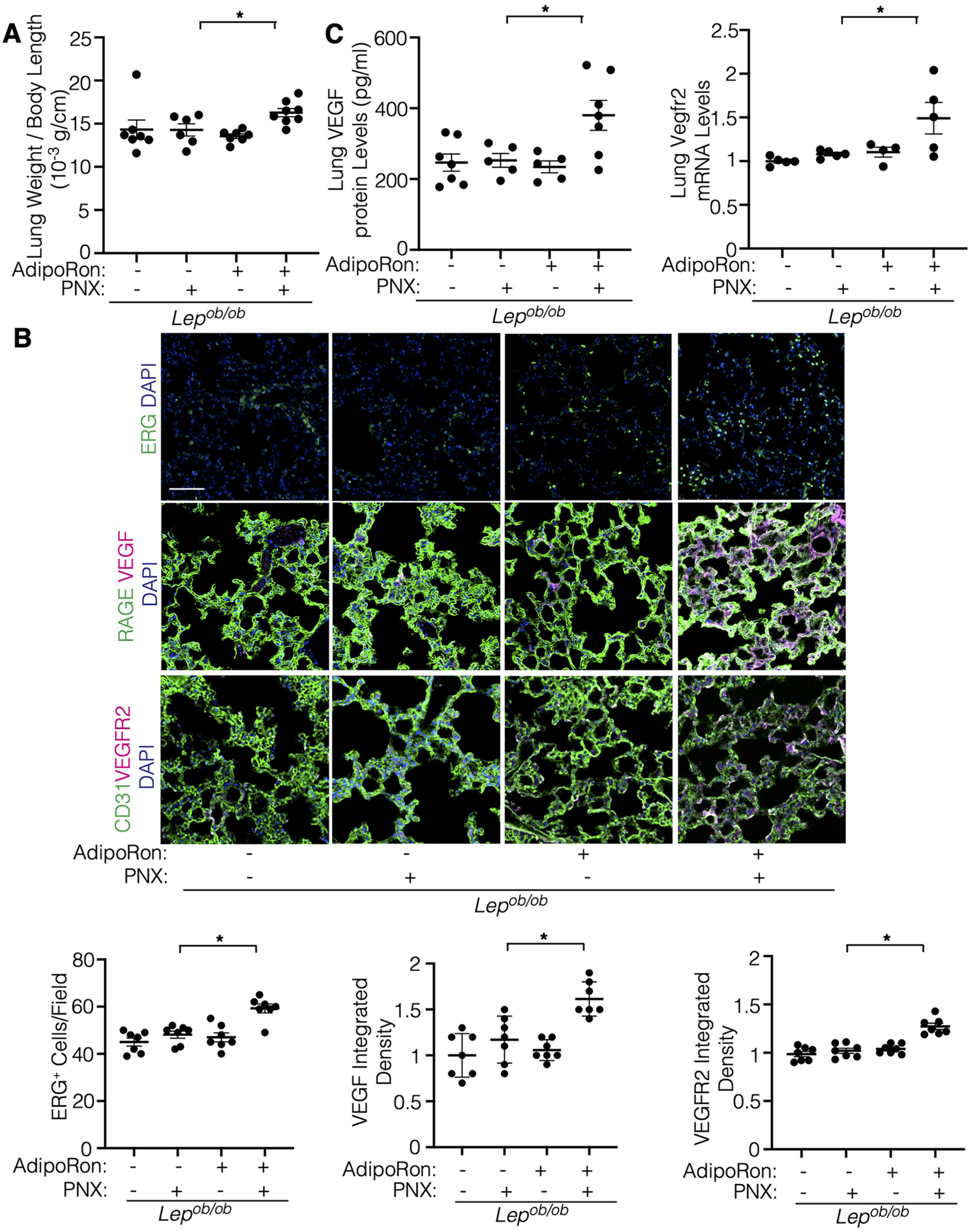

FIGURE 5

Adiporon restores post-PNX lung growth in the *Lep*$^{ob/ob}$ mouse lungs. **(A)** Graph showing the ratio of the weight of right lung lobe to mouse body length in *Lep*$^{ob/ob}$ mice 7 days after PNX or in combination with treatment with AdipoRon ($n = 6–8$, mean ± s.e.m., $*p < 0.05$). **(B)** IF micrographs showing ERG-positive ECs and DAPI (*top*), RAGE-positive alveolar epithelial cells, VEGF expression and DAPI (*2nd*), and CD31-positive blood vessels, VEGFR2 expression and DAPI (*bottom*) in the *Lep*$^{ob/ob}$ mice 7 days after PNX or in combination with treatment with AdipoRon. Scale bar, 50 µm. Graphs showing the quantification of ERG-positive ECs (*left*), VEGF expression (*middle*), and VEGFR2 expression (*right*) in the *Lep*$^{ob/ob}$ mouse lungs 7 days after PNX or in combination with treatment with AdipoRon ($n = 7$, mean ± s.e.m., $*p < 0.05$). **(C)** Graph showing the VEGF protein levels in the *Lep*$^{ob/ob}$ mouse lungs 7 days after PNX or in combination with treatment with AdipoRon (*left*, $n = 5\text{-}7$, mean ± s.e.m., $*p < 0.05$). Graph showing the Vegfr2 mRNA levels in the *Lep*$^{ob/ob}$ mouse lungs 7 days after PNX or in combination with treatment with AdipoRon (*right*, $n = 4–5$, mean ± s.e.m., $*p < 0.05$).

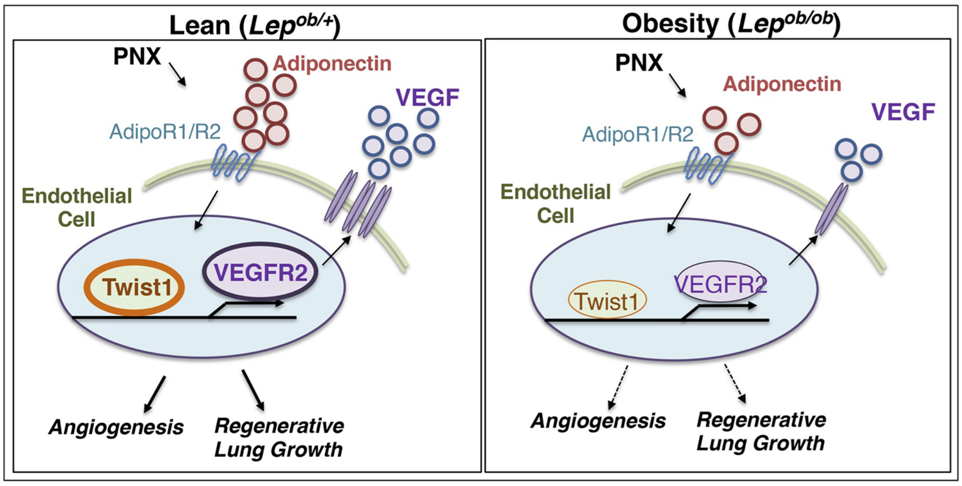

FIGURE 6
Schematic illustration of the angiogenic signaling pathway in lean vs. obese lungs. Schematic illustration showing that angiogenesis and regenerative lung growth after unilateral PNX mediated by adiponectin-TWIST1-VEGF/VEGFR2 signaling are inhibited in $Lep^{ob/ob}$ obese mice; post-PNX increases in the levels of adiponectin, TWIST1, VEGF, and VEGFR2 are suppressed in $Lep^{ob/ob}$ obese mice.

of AT1 cells and ECs controls vascular regeneration after PNX. Other angiogenic signaling may also be involved in the mechanism. We have reported that angiopoietin (Ang)-Tie2 signaling mediates post-PNX lung growth (17). Ang2 and Tie2 expression increased after PNX in $Lep^{ob/+}$ mice, which was inhibited in $Lep^{ob/ob}$ obese mouse lungs (Supplementary Figure S1D). Ang2 and Tie2 are involved in subcutaneous adipose tissue remodeling and subsequently contribute to systemic glucose tolerance and metabolic homeostasis (44). The plasma levels of Ang2 and soluble Tie2 are increased in pediatric obstructive sleep apnea and obesity (45). In addition, it is reported that angiopoietin-like proteins (ANGPTL-2, -3, -4, -6, -8), which potently control angiogenesis, regulate lipid, glucose and energy metabolism independent of angiogenic effects (46). For example, ANGPTL-2 mediates obesity and related metabolic diseases (47). Thus, in addition to VEGF signaling, other angiogenic and metabolic signaling may directly or indirectly contribute to the inhibition of lung regeneration in obese people. During lung development, VEGF is distributed uniformly throughout the airway epithelium in the early embryonic stages, while in the later stage the expression is restricted to the growing tips of airway branches in the distal lung where new blood vessels are recruited (48). Spatiotemporal changes in the distribution of angiogenic factors may also mediate inhibition of regenerative lung growth in the obese lungs.

Alternate splicing of the murine Vegf mRNA results in three isoforms (120, 164, and 188). Vegf120 isoform is diffusible, while Vegf164 and 188 isoforms bind to heparan sulfate on the cell surface or in the extracellular matrix (49). It is reported that lung vascular and alveolar structures are disrupted in mice only expressing Vegf120 compared with wild-type littermates expressing all three isoforms, suggesting the involvement of Vegf164 and 188 isoforms in lung microvascular and alveolar development (49, 50). In fact, the levels of Vegf164 significantly increased in the $Lep^{ob/+}$ lung after PNX; in contrast, it was inhibited in $Lep^{ob/ob}$ obese mice (Supplementary Figure S1C). In the adult, Vegf188 expression is the highest in lung and heart (49) and Vegf188 may also play active roles in lung regeneration; however, the levels of Vegf120 or 188 did not significantly change during lung growth after PNX (not shown). Although isoform-specific antibodies/probes are not available due to only 24 amino acids difference, further time course analysis of mRNA levels will elucidate the isoform-specific effects on obesity-dependent inhibition of lung regeneration.

Our results suggest that adiponectin is necessary for the expression of VEGF in AT1 cells and VEGFR2 in ECs, mediating vascular and alveolar regeneration after PNX (Figure 3). Adiponectin may induce angiogenesis through other signaling pathways as well (e.g., AMPK, eNOS) (3, 26). Suppression of adiponectin signaling also decreases PGC1α expression, which inhibits angiogenesis and mitochondrial biogenesis that suppresses tissue metabolism (18, 51). The levels of adiponectin increased in the post-PNX mouse lungs and interacted with angiogenesis- and metabolism-related genes (Figure 2). It remains unknown the mechanism by which adiponectin expression increases after PNX. Adiponectin is produced mainly by adipocytes (30). Post-PNX signaling in the lungs may control adiponectin expression in adipose tissue, which controls angiogenic signaling in the lung. Adiponectin is also produced by other cell types, such as skeletal- and cardio-myocytes and ECs (30), and exhibits energy metabolism, anti-diabetic, and anti-inflammatory effects (26, 27). It is reported that lipids are stored in lipid-laden adipocyte-like cells known as lipofibroblasts in the lung. Lipofibroblasts in the lung may also secrete adiponectin and regulate alveolar lipid homeostasis as well as pulmonary surfactant production (52) to stimulate lung development and regeneration, which may be impaired in obese animals.

Obesity contributes to various diseases such as hypertension, atherosclerosis and COPD, in which mechanical environment and EC signaling are involved in the disease progression (9, 53). TWIST1 is involved in the obesity- and angiogenesis-associated diseases such as pulmonary fibrosis (34), pulmonary hypertension (36), and atherosclerosis (53). TWIST1 regulates vascular development and regeneration (18, 25, 33, 34) by changing various angiogenic signaling (e.g., VEGF-VEGFR2, Ang-Tie2). We have reported that angiogenesis is impaired in obese human subcutaneous adipose tissue ECs through TWIST1-SLIT2 signaling (25). Increased TWIST1 expression in aged ECs decreases the expression of PGC1α to suppress mitochondrial biogenesis, leading to inhibition of regenerative lung growth and vascular formation in aged mouse lungs (18). TWIST1 is also involved in cellular senescence (36) as well as epithelial/endothelial to mesenchymal transition (EMT/EndMT), which is involved in atherosclerosis (53, 54). It has been reported that EMT/EndMT mediates lung development and regeneration (55). Thus, TWIST1 may mediate inhibition of post-PNX lung growth in obese mice by changing multiple signaling pathways.

In addition to chemical growth factors, the micromechanical environment controls vascular formation and function (24, 35). It has been demonstrated that mechanical forces change during post-PNX lung growth (15, 16, 19). We have reported that hydrostatic pressure increases after PNX, which stimulates post-PNX angiogenesis in the lung (19). In fact, TWIST1 and another mechanosensitive transcription co-activator YAP1 sense mechanical stimuli (*e.g.,* cell density, ECM stiffness, mechanical tension, flow) (56) and control vascular and alveolar regeneration after PNX (16–19, 53). In addition, a low serum adiponectin level is associated with arterial stiffness in hypertensive patients (57). Mechanical stretching also controls adiponectin protein expression in mesenchymal stem cells (58). Here we have demonstrated that **(1)** TWIST1 expression induced after PNX is inhibited in $Lep^{ob/ob}$ obese mouse or $Adipoq^{-/-}$ mouse lungs (Figures 2, 3) and **(2)** adiponectin increases VEGFR2 expression and migration/proliferation of human lung ECs, while the effects are inhibited by TWIST1 knockdown (Figure 4). Thus, post-PNX changes in the mechanical forces may stimulate adiponectin signaling and control vascular and alveolar regeneration in the lung through TWIST1-VEGFR2 signaling. Although AdipoRon restored VEGF and VEGFR2 expression and lung vascular and alveolar regeneration after PNX in obese mice (Figure 5), adiponectin did not induce VEGFR2 expression in obese human lung ECs in culture even it restores EC migration and proliferation (Figure 4). This may be because of the differences in the experimental condition (human and mouse lungs, *in vitro* and *in vivo*), in which mechanical and chemical environment are altered. Alternatively, different angiogenic signaling may be involved in the mechanism.

In this study, we used $Lep^{ob/ob}$ obese mice, in which leptin gene is mutated. Leptin is a neuroendocrine hormone that is secreted mainly from adipose tissue and acts primarily on brain, regulating metabolism and fat accumulation (52). Further investigation using a more physiological high fat diet-induced obese mouse model will uncover the direct metabolic effects on regenerative lung growth.

In summary, we have demonstrated that lung vascular and alveolar regeneration after unilateral PNX is inhibited in $Lep^{ob/ob}$ obese mice through suppression of adiponectin-VEGF/VEGFR2 signaling. Post-PNX regenerative lung growth is inhibited in $Lep^{ob/ob}$ obese mice or $Adipoq^{-/-}$ mice, while AdipoRon restores the effects. Modulation of adiponectin-VEGF/VEGFR2 signaling may improve the way for lung regeneration and potentially lead to the development of new therapeutic strategies for chronic lung diseases in obese patients.

## Data availability statement

The datasets presented in this study can be found in online repositories. The names of the repository/repositories and accession number(s) can be found in the article/Supplementary Material.

## Ethics statement

The studies involving humans were approved by the Institutional Review Board (IRB) of MCW and Froedtert Hospital and ECs isolated from de-identified human lungs are determined as non-human subjects (PRO00047689). The studies were conducted in accordance with the local legislation and institutional requirements. The human samples used in this study were acquired from primarily isolated as part of the previous study for which ethical approval was obtained. Written informed consent for participation was not required from the participants or the participants' legal guardians/next of kin in accordance with the national legislation and institutional requirements. The animal study was approved by Institutional Animal Care and Use Committee of MCW (AUA 5598). The study was conducted in accordance with the local legislation and institutional requirements.

## Author contributions

TH: Data curation, Investigation, Writing – review & editing. PK: Data curation, Formal Analysis, Investigation, Writing – review & editing. MS: Data curation, Investigation, Writing – review & editing. MJ: Data curation, Investigation, Writing – review & editing. MG: Methodology, Resources, Writing – review & editing. TM: Conceptualization, Data curation, Funding acquisition, Investigation, Writing – original draft, Writing – review & editing. AM: Conceptualization, Data curation, Funding acquisition, Investigation, Writing – original draft, Writing – review & editing.

## Funding

The author(s) declare financial support was received for the research, authorship, and/or publication of this article. This work was supported by funds from NIH R01HL139638 (to AM, to TM), NIH R01HL142578 (to AM, to TM), and American Heart Association (AHA) 18TPA34170129 (to AM), 967800 (to AM), 23DIVSUP1068738 (to TH) and Advancing a Healthier Wisconsin Endowment 9520737 (to AM).

## Conflict of interest

The authors declare that the research was conducted in the absence of any commercial or financial relationships that could be construed as a potential conflict of interest.

The author(s) declared that they were an editorial board member of Frontiers, at the time of submission. This had no impact on the peer review process and the final decision.

## Publisher's note

## Supplementary material

The Supplementary Material for this article can be found online at: https://www.frontiersin.org/articles/10.3389/fcvm.2024.1491971/full#supplementary-material

**SUPPLEMENTARY FIGURE S1**

Vegf/Vegfr2 and Adipor expression in post-PNX mouse lungs. **(A)** Representative FACS plots showing CD31$^+$ cells (fraction P2) in the mouse lungs. **(B)** Graph showing the Vegfr2 mRNA levels in the *Lep*$^{ob/+}$ or *Lep*$^{ob/ob}$ mouse lungs 7 days after PNX ($n = 5–6$, mean ± s.e.m., $*p < 0.05$). **(C)** Graph showing the Vegf164 mRNA levels in the *Lep*$^{ob/+}$ or *Lep*$^{ob/ob}$ mouse lungs 7 days after PNX ($n = 5$, mean ± s.e.m., $*p < 0.05$). **(D)** Graph showing the Ang2 and Tie2 mRNA levels in the *Lep*$^{ob/+}$ or *Lep*$^{ob/ob}$ mouse lungs 7 days after PNX ($n = 5–6$, mean ± s.e.m.). **(E)** Graph showing the Adipor1 and 2 mRNA levels in the *Lep*$^{ob/+}$ or *Lep*$^{ob/ob}$ mouse lungs 7 days after PNX ($n = 5–7$, mean ± s.e.m.). **(F)** Graph showing the Vegfr2 mRNA levels in the *Adipoq*$^{-/-}$ mouse lung ECs 7 days after PNX ($n = 5–6$, mean ± s.e.m.).

**SUPPLEMENTARY FIGURE S2**

Original gel images of Figure 4A.

## References

1. Mortality GBD and Causes of Death, C. Global, regional, and national life expectancy, all-cause mortality, and cause-specific mortality for 249 causes of death, 1980–2015: a systematic analysis for the global burden of disease study 2015. *Lancet.* (2016) 388(10053):1459–544. doi: 10.1016/S0140-6736(16)31012-1

2. Cao Y. Adipose tissue angiogenesis as a therapeutic target for obesity and metabolic diseases. *Nat Rev Drug Discov.* (2010) 9(2):107–15. doi: 10.1038/nrd3055

3. Shibata R, Ouchi N, Kihara S, Sato K, Funahashi T, Walsh K. Adiponectin stimulates angiogenesis in response to tissue ischemia through stimulation of amp-activated protein kinase signaling. *J Biol Chem.* (2004) 279(27):28670–4. doi: 10.1074/jbc.M402558200

4. O'Sullivan J, Lysaght J, Donohoe CL, Reynolds JV. Obesity and gastrointestinal cancer: the interrelationship of adipose and tumour microenvironments. *Nat Rev Gastroenterol Hepatol.* (2018) 15(11):699–714. doi: 10.1038/s41575-018-0069-7

5. O'Brien KB, Vogel P, Duan S, Govorkova EA, Webby RJ, McCullers JA, et al. Impaired wound healing predisposes obese mice to severe influenza virus infection. *J Infect Dis.* (2012) 205(2):252–61. doi: 10.1093/infdis/jir729

6. Shore SA. Obesity and asthma: possible mechanisms. *J Allergy Clin Immunol.* (2008) 121(5):1087–93. quiz 1094–1085. doi: 10.1016/j.jaci.2008.03.004

7. Zammit C, Liddicoat H, Moonsie I, Makker H. Obesity and respiratory diseases. *Int J Gen Med.* (2010) 3:335–43. doi: 10.2147/IJGM.S11926

8. Dixon AE, Peters U. The effect of obesity on lung function. *Expert Rev Respir Med.* (2018) 12(9):755–67. doi: 10.1080/17476348.2018.1506331

9. Verberne LDM, Leemrijse CJ, Swinkels ICS, van Dijk CE, de Bakker DH, Nielen MMJ. Overweight in patients with chronic obstructive pulmonary disease needs more attention: a cross-sectional study in general practice. *NPJ Prim Care Respir Med.* (2017) 27(1):63. doi: 10.1038/s41533-017-0065-3

10. Orens JB, Garrity ER Jr. General overview of lung transplantation and review of organ allocation. *Proc Am Thorac Soc.* (2009) 6(1):13–9. doi: 10.1513/pats.200807-072GO

11. Bozso SJ, Nagendran J, Gill RS, Freed DH, Nagendran J. Impact of obesity on heart and lung transplantation: does pre-transplant obesity affect outcomes? *Transplant Proc.* (2017) 49(2):344–7. doi: 10.1016/j.transproceed.2016.12.002

12. Hsia CC, Herazo LF, Fryder-Doffey F, Weibel ER. Compensatory lung growth occurs in adult dogs after right pneumonectomy. *J Clin Invest.* (1994) 94(1):405–12. doi: 10.1172/JCI117337

13. Sakurai MK, Lee S, Arsenault DA, Nose V, Wilson JM, Heymach JV, et al. Vascular endothelial growth factor accelerates compensatory lung growth after unilateral pneumonectomy. *Am J Physiol Lung Cell Mol Physiol.* (2007) 292(3):L742–747. doi: 10.1152/ajplung.00064.2006

14. Butler JP, Loring SH, Patz S, Tsuda A, Yablonskiy DA, Mentzer SJ. Evidence for adult lung growth in humans. *N Engl J Med.* (2012) 367(3):244–7. doi: 10.1056/NEJMoa1203983

15. Konerding MA, Gibney BC, Houdek JP, Chamoto K, Ackermann M, Lee GS, et al. Spatial dependence of alveolar angiogenesis in post-pneumonectomy lung growth. *Angiogenesis.* (2012) 15(1):23–32. doi: 10.1007/s10456-011-9236-y

16. Liu Z, Wu H, Jiang K, Wang Y, Zhang W, Chu Q, et al. MAPK-mediated YAP activation controls mechanical-tension-induced pulmonary alveolar regeneration. *Cell Rep.* (2016) 16(7):1810–9. doi: 10.1016/j.celrep.2016.07.020

17. Mammoto T, Muyleart M, Mammoto A. Endothelial YAP1 in regenerative lung growth through the angiopoietin-Tie2 pathway. *Am J Respir Cell Mol Biol.* (2019) 60:117–27. doi: 10.1165/rcmb.2018-0105OC

18. Hendee K, Hunyenyiwa T, Matus K, Toledo M, Mammoto A, Mammoto T. Twist1 signaling in age-dependent decline in angiogenesis and lung regeneration. *Aging (Albany NY).* (2021) 13(6):7781–99. doi: 10.18632/aging.202875

19. Mammoto T, Hunyenyiwa T, Kyi P, Hendee K, Matus K, Rao S, et al. Hydrostatic pressure controls angiogenesis through endothelial YAP1 during lung regeneration. *Front Bioeng Biotechnol.* (2022) 10:823642. doi: 10.3389/fbioe.2022.823642

20. Pierpont YN, Dinh TP, Salas RE, Johnson EL, Wright TG, Robson MC, et al. Obesity and surgical wound healing: a current review. *ISRN Obes.* (2014) 2014:1. doi: 10.1155/2014/638936

21. Selzner M, Clavien PA. Failure of regeneration of the steatotic rat liver: disruption at two different levels in the regeneration pathway. *Hepatology.* (2000) 31(1):35–42. doi: 10.1002/hep.510310108

22. Xu P, Werner JU, Milerski S, Hamp CM, Kuzenko T, Jahnert M, et al. Diet-induced obesity affects muscle regeneration after murine blunt muscle trauma—a broad spectrum analysis. *Front Physiol.* (2018) 9:674. doi: 10.3389/fphys.2018.00674

23. Ding BS, Nolan DJ, Guo P, Babazadeh AO, Cao Z, Rosenwaks Z, et al. Endothelial-derived angiocrine signals induce and sustain regenerative lung alveolarization. *Cell.* (2011) 147(3):539–53. doi: 10.1016/j.cell.2011.10.003

24. Mammoto A, Mammoto T. Vascular niche in lung alveolar development, homeostasis, and regeneration. *Front Bioeng Biotechnol.* (2019) 7:318. doi: 10.3389/fbioe.2019.00318

25. Hunyenyiwa T, Hendee K, Matus K, Kyi P, Mammoto T, Mammoto A. Obesity inhibits angiogenesis through TWIST1-SLIT2 signaling. *Front Cell Dev Biol.* (2021) 9:693410. doi: 10.3389/fcell.2021.693410

26. Ouchi N, Parker JL, Lugus JJ, Walsh K. Adipokines in inflammation and metabolic disease. *Nat Rev Immunol.* (2011) 11(2):85–97. doi: 10.1038/nri2921

27. Shah D, Romero F, Duong M, Wang N, Paudyal B, Suratt BT, et al. Retracted article: obesity-induced adipokine imbalance impairs mouse pulmonary vascular endothelial function and primes the lung for injury. *Sci Rep*. (2015) 5:11362. doi: 10.1038/srep11362

28. Fiaschi T, Magherini F, Gamberi T, Modesti PA, Modesti A. Adiponectin as a tissue regenerating hormone: more than a metabolic function. *Cell Mol Life Sci*. (2014) 71(10):1917–25. doi: 10.1007/s00018-013-1537-4

29. Correnti JM, Cook D, Aksamitiene E, Swarup A, Ogunnaike B, Vadigepalli R, et al. Adiponectin fine-tuning of liver regeneration dynamics revealed through cellular network modelling. *J Physiol*. (2015) 593(2):365–83. doi: 10.1113/jphysiol.2014.284109

30. Achari AE, Jain SK. Adiponectin, a therapeutic target for obesity, diabetes, and endothelial dysfunction. *Int J Mol Sci*. (2017) 18(6):1321. doi: 10.3390/ijms18061321

31. Zhu XL, Qin XQ, Xiang Y, Tan YR, Qu XP, Liu HJ. Adipokine adiponectin is a potential protector to human bronchial epithelial cell for regulating proliferation, wound repair and apoptosis: comparison with leptin and resistin. *Peptides*. (2013) 40:34–41. doi: 10.1016/j.peptides.2012.11.017

32. Mammoto T, Jiang E, Jiang A, Lu Y, Juan AM, Chen J, et al. Twist1 controls lung vascular permeability and endotoxin-induced pulmonary edema by altering Tie2 expression. *PLoS One*. (2013) 8:e73407. doi: 10.1371/journal.pone.0073407

33. Li J, Liu CH, Sun Y, Gong Y, Fu Z, Evans LP, et al. Endothelial TWIST1 promotes pathological ocular angiogenesis. *Invest Ophthalmol Vis Sci*. (2014) 55 (12):8267–77. doi: 10.1167/iovs.14-15623

34. Mammoto T, Jiang A, Jiang E, Mammoto A. Role of Twist1 phosphorylation in angiogenesis and pulmonary fibrosis. *Am J Respir Cell Mol Biol*. (2016) 55:633–44. doi: 10.1165/rcmb.2016-0012OC

35. Mammoto A, Connor KM, Mammoto T, Yung CW, Huh D, Aderman CM, et al. A mechanosensitive transcriptional mechanism that controls angiogenesis. *Nature*. (2009) 457(7233):1103–8. doi: 10.1038/nature07765

36. Kyi P, Hendee K, Hunyenyiwa T, Matus K, Mammoto T, Mammoto A. Endothelial senescence mediates hypoxia-induced vascular remodeling by modulating PDGFB expression. *Front Med (Lausanne)*. (2022) 9:908639. doi: 10.3389/fmed.2022.908639

37. Vila Ellis L, Cain MP, Hutchison V, Flodby P, Crandall ED, Borok Z, et al. Epithelial vegfa specifies a distinct endothelial population in the mouse lung. *Dev Cell*. (2020) 52(5):617–30.e6. doi: 10.1016/j.devcel.2020.01.009

38. Mammoto T, Chen Z, Jiang A, Jiang E, Ingber DE, Mammoto A. Acceleration of lung regeneration by platelet-rich plasma extract through the low-density lipoprotein receptor–related protein 5–Tie2 pathway. *Am J Respir Cell Mol Biol*. (2016) 54:103–13. doi: 10.1165/rcmb.2015-0045OC

39. Okada-Iwabu M, Iwabu M, Yamauchi T, Kadowaki T. Drug development research for novel adiponectin receptor-targeted antidiabetic drugs contributing to healthy longevity. *Diabetol Int*. (2019) 10(4):237–44. doi: 10.1007/s13340-019-00409-6

40. Gao M, Piernas C, Astbury NM, Hippisley-Cox J, O'Rahilly S, Aveyard P, et al. Associations between body-mass index and COVID-19 severity in 6.9 million people in England: a prospective, community-based, cohort study. *Lancet Diabetes Endocrinol*. (2021) 9(6):350–9. doi: 10.1016/S2213-8587(21)00089-9

41. Guo X, Sunil C, Qian G. Obesity and the development of lung fibrosis. *Front Pharmacol*. (2022) 12:812166. doi: 10.3389/fphar.2021.812166

42. Flikweert AW, Kobold ACM, van der Sar-van der Brugge S, Heeringa P, Rodenhuis-Zybert IA, Bijzet J, et al. Circulating adipokine levels and COVID-19 severity in hospitalized patients. *Int J Obes (Lond)*. (2023) 47(2):126–37. doi: 10.1038/s41366-022-01246-5

43. Nemeth J, Skronska-Wasek W, Keppler S, Schundner A, Gross A, Schoenberger T, et al. Adiponectin suppresses stiffness-dependent, profibrotic activation of lung fibroblasts. *Am J Physiol Lung Cell Mol Physiol*. (2024) 327(4):L487–502. doi: 10.1152/ajplung.00037.2024

44. An YA, Sun K, Joffin N, Zhang F, Deng Y, Donze O, et al. Angiopoietin-2 in white adipose tissue improves metabolic homeostasis through enhanced angiogenesis. *Elife*. (2017) 6:e24071. doi: 10.7554/eLife.24071

45. Gozal D, Khalyfa A, Qiao Z, Smith DL, Philby MF, Koren D, et al. Angiopoietin-2 and soluble Tie-2 receptor plasma levels in children with obstructive sleep apnea and obesity. *Obesity (Silver Spring)*. (2017) 25(6):1083–90. doi: 10.1002/oby.21859

46. Kadomatsu T, Tabata M, Oike Y. Angiopoietin-like proteins: emerging targets for treatment of obesity and related metabolic diseases. *FEBS J*. (2011) 278 (4):559–64. doi: 10.1111/j.1742-4658.2010.07979.x

47. Tabata M, Kadomatsu T, Fukuhara S, Miyata K, Ito Y, Endo M, et al. Angiopoietin-like protein 2 promotes chronic adipose tissue inflammation and obesity-related systemic insulin resistance. *Cell Metab*. (2009) 10(3):178–88. doi: 10.1016/j.cmet.2009.08.003

48. Healy AM, Morgenthau L, Zhu X, Farber HW, Cardoso WV. VEGF is deposited in the subepithelial matrix at the leading edge of branching airways and stimulates neovascularization in the murine embryonic lung. *Dev Dyn*. (2000) 219(3):341–52. doi: 10.1002/1097-0177(2000)9999:9999<::AID-DVDY1061>3.0.CO;2-M

49. Ng YS, Rohan R, Sunday ME, Demello DE, D'Amore PA. Differential expression of VEGF isoforms in mouse during development and in the adult. *Dev Dyn*. (2001) 220(2):112–21. doi: 10.1002/1097-0177(2000)9999:9999<::AID-DVDY1093>3.0.CO;2-D

50. Galambos C, Ng YS, Ali A, Noguchi A, Lovejoy S, D'Amore PA, et al. Defective pulmonary development in the absence of heparin-binding vascular endothelial growth factor isoforms. *Am J Respir Cell Mol Biol*. (2002) 27(2):194–203. doi: 10.1165/ajrcmb.27.2.4703

51. Iwabu M, Yamauchi T, Okada-Iwabu M, Sato K, Nakagawa T, Funata M, et al. Adiponectin and AdipoR1 regulate PGC-1α and mitochondria by Ca2+ and AMPK/SIRT1. *Nature*. (2010) 464(7293):1313–9. doi: 10.1038/nature08991

52. Palma G, Sorice GP, Genchi VA, Giordano F, Caccioppoli C, D'Oria R, et al. Adipose tissue inflammation and pulmonary dysfunction in obesity. *Int J Mol Sci*. (2022) 23:13. doi: 10.3390/ijms23137349

53. Mahmoud MM, Kim HR, Xing R, Hsiao S, Mammoto A, Chen J, et al. TWIST1 integrates endothelial responses to flow in vascular dysfunction and atherosclerosis. *Circ Res*. (2016) 119(3):450–62. doi: 10.1161/CIRCRESAHA.116.308870

54. Honda S, Ikeda K, Urata R, Yamazaki E, Emoto N, Matoba S. Cellular senescence promotes endothelial activation through epigenetic alteration, and consequently accelerates atherosclerosis. *Sci Rep*. (2021) 11(1):14608. doi: 10.1038/s41598-021-94097-5

55. Rout-Pitt N, Farrow N, Parsons D, Donnelley M. Epithelial mesenchymal transition (EMT): a universal process in lung diseases with implications for cystic fibrosis pathophysiology. *Respir Res*. (2018) 19(1):136. doi: 10.1186/s12931-018-0834-8

56. Mammoto T, Mammoto A, Ingber DE. Mechanobiology and developmental control. *Annu Rev Cell Dev Biol*. (2013) 29:27–61. doi: 10.1146/annurev-cellbio-101512-122340

57. Tsioufis C, Dimitriadis K, Selima M, Thomopoulos C, Mihas C, Skiadas I, et al. Low-grade inflammation and hypoadiponectinaemia have an additive detrimental effect on aortic stiffness in essential hypertensive patients. *Eur Heart J*. (2007) 28 (9):1162–9. doi: 10.1093/eurheartj/ehm089

58. Hemphill J, Liu Q, Uprety R, Samanta S, Tsang M, Juliano RL, et al. Conditional control of alternative splicing through light-triggered splice-switching oligonucleotides. *J Am Chem Soc*. (2015) 137(10):3656–62. doi: 10.1021/jacs.5b00580

frontiers | Frontiers in Cardiovascular Medicine

TYPE Original Research
PUBLISHED 24 October 2024
DOI 10.3389/fcvm.2024.1438396

OPEN ACCESS

EDITED BY
Ryuichi Morishita,
Osaka University, Japan

REVIEWED BY
Masayuki Yoshida,
Tokyo Medical and Dental University, Japan
Martina B. Lorey,
Wihuri Research Institute, Finland

*CORRESPONDENCE
Masanori Aikawa
✉ maikawa@bwh.harvard.edu

†These authors have contributed equally to this work

RECEIVED 25 May 2024
ACCEPTED 23 September 2024
PUBLISHED 24 October 2024

CITATION
Iwata A, Chelvanambi S, Asano T, Whelan M, Nakamura Y, Aikawa E, Sasaki Y and Aikawa M (2024) Gene expression profiles of precursor cells identify compounds that reduce NRP1 surface expression in macrophages: Implication for drug repositioning for COVID-19.
Front. Cardiovasc. Med. 11:1438396.
doi: 10.3389/fcvm.2024.1438396

# Gene expression profiles of precursor cells identify compounds that reduce NRP1 surface expression in macrophages: Implication for drug repositioning for COVID-19

Akira Iwata[1†], Sarvesh Chelvanambi[1†], Takaharu Asano[1], Mary Whelan[1], Yuto Nakamura[1], Elena Aikawa[1,2], Yusuke Sasaki[1] and Masanori Aikawa[1,2,3*]

[1]Center for Interdisciplinary Cardiovascular Sciences, Cardiovascular Division, Department of Medicine, Brigham and Women's Hospital, Harvard Medical School, Boston, MA, United States, [2]Center for Excellence in Vascular Biology, Cardiovascular Division, Department of Medicine, Brigham and Women's Hospital, Harvard Medical School, Boston, MA, United States, [3]Channing Division of Network Medicine, Department of Medicine, Brigham and Women's Hospital, Harvard Medical School, Boston, MA, United States

Coronavirus disease 2019 (COVID-19) is transitioning from a pandemic to an endemic phase through recurring mutations. Initial efforts focused on developing strategies to mitigate infection of lung epithelial cells which are the primary targets of the SARS-CoV-2 virus using the affinity of the spike protein to human ACE2 receptor. SARS-CoV-2, however, infects additional cell types present in the lung such as macrophages through the alternate entry receptor Neuropilin 1 (NRP1). Developing novel therapeutic strategies to prevent SARS-CoV-2 infection of cells crucial for immunosurveillance could thus be integral to treat post-acute sequelae of COVID-19 (PASC). Since traditional drug development process takes a long time, it is imperative to establish new strategies that can be rapidly deployed to combat the dynamic nature of COVID-19 evolution and to contribute to prevention of future pandemics. We obtained the gene expression profiles of THP-1 monocytes from L1000-based Connectivity Map using CLUE, cloud- based software platform for the analysis of perturbational datasets to identify compounds that could reduce the expression level of NRP1. Out of 33,590 compounds, we analyzed the profiles of 45 compounds for their ability to reduce NRP1 expression. We selected the top five small molecule inhibitors predicted to decrease the expression of NRP1 for validation studies. All five selected compounds showed low cytotoxicity at tested doses and their ability to reduce NRP1 surface expression was evaluated in THP-1 monocytes, THP-1-derived macrophage like cells and human peripheral blood mononuclear cell (PBMC)-derived primary macrophages. Five compounds with the largest predicted reduction of NRP1 expression decreased macrophage NRP1 surface expression measured using flow cytometry and fluorescent microscopy assays in both cell line and primary macrophages. Using our computational approach, we identified 45 compounds that could potentially decrease NRP1 surface expression in macrophages based on their effect on THP-1 monocytes. Validation studies showed that such an approach can help to identify compounds for drug repositioning in target cells that are absent in the L1000 database. Our proposed approach can be applicable for the rapid compound exploration to combat novel cell types that SARS-CoV-2 targets for infection and could provide molecular bases for the development of new drugs.

KEYWORDS

**COVID-19, L1000-based Connectivity Map, SARS-CoV-2, Neuropilin 1, drug screening, drug development, gene expression profiling, macrophage**

## Introduction

A pandemic outbreak of severe acute respiratory syndrome coronavirus 2 (SARS-CoV-2) has caused coronavirus disease 2019 (COVID-19), which spread throughout the world. Rapid mutation of the virus gave rise to multiple variants that were circulating within the global human population and made it challenging to develop the COVID-19 treatment, despite the rapid development and approval of various mRNA vaccines and antiviral drugs, such as Nirmatrelvir and Ensitrelvir. In 2024, COVID-19 has turned into an endemic phase. To develop the therapeutics remedy, the initial research efforts were focused on identifying the host cell receptors, such as angiotensin-converting enzyme 2 (ACE2) from lung cells, to develop inhibitors (1). As COVID-19 becomes an endemic disease, it has become increasingly important to redirect efforts to prevent overactive immune inflammatory response, caused by inflammatory macrophages. SARS-CoV2 induced macrophage activation, reduced immune surveillance, and an impaired ability to clear the SARS-CoV2 infection. Recent studies showed that SARS-CoV2 uses an alternate entry receptor, Neuropilin 1 (NRP1) to infect cells not expressing ACE2 (2–4). NRP1 was found to be highly expressed in macrophages within atherosclerotic lesions, particularly in plaque-associated foamy macrophages (5). Experimental silencing of NRP1 gene reduced SARS-CoV2 infectivity of human primary macrophages (5). Overall, NRP1 is involved in mediating SARS-CoV-2 infection of the atherosclerotic plaque, indicating its importance in viral pathogenesis. Our previous reports also suggest that expression of NRP1 could be associated with increased acute inflammatory responses in coronavirus infection (6). Similarly, NRP1 has been implicated in the infection of macrophage reservoirs in the nasal epithelium (3) as well as astrocytes in the brain (7). This creates the need for adaptable drug discovery pipelines to target specific reservoirs of SARS-CoV2 infection to treat the diverse range of outcomes seen in COVID-19 patients such as neurocognitive disorders and cardiovascular complications.

The process of drug development involves several steps, including compound discovery, screening, and clinical trials. Developing hit compounds from screening into the lead candidate compounds and conducting clinical trials may take more than 10 years, often due to unexpected off-target effects resulting in adverse events. To address this issue, drug repositioning approach has been gaining increased attention. This approach contributes to discovering new indications for existing drugs, by saving time and cost compared to traditional drug screening (8, 9). The main reason is that existing candidate compounds have already proven their safety in preclinical and clinical trials. Moreover, they are cost-effective due to their established synthesis methods. In addition, computational drug repositioning has been evolved in recent years (10). This approach requires the publicly available large-scale biological data for existing drugs. Broad Institute constructed a database of gene expression profiles induced by exposing a variety of cell types to various perturbations including small molecules, called the Connectivity MAP (CMap). The expansion of this database has resulted in more than a million gene expression profiles using more than 30,000 small molecules and 200 cell types through the introduction of L1000 assay technology (11, 12). L1000-based Connectivity Map is one of the largest libraries of integrated network-based cellular signatures available and many studies have been conducted using this database. Candidate molecules could be predicted by comparing L1000 perturbation profiles and the disease-specific profiles obtained by the gene expression omnibus (GEO). An important application of L1000-based CMap is rapid drug repositioning, which is based on finding small molecules that cancel or mimic differences in gene expression caused by diseases (13, 14). In addition, these drug repositioning approaches using L1000-based CMap can save time and cost during the drug development process.

Recently, we reported the *in-silico* drug screening approach using L1000-Based Connectivity Map and its application to the entry receptor for the SARS-CoV-2 virus, ACE2 (15) and another disease context, including atherosclerosis (16). Using this method, we could rapidly identify small molecule inhibitors of target gene in specific cell lines. While the L1000 database contains 248 types of cells, only 12 of those are primary or non-tumor cells. Of note, there are no non-tumorous immune cell types in this database currently. We used THP-1 monocytes, a tumor-derived monocytic cell line, which is a precursor to our cell type of interest, macrophages.

In this study, aiming at further utilizing our rapid compound exploration method, we computationally identified small molecule compounds that were predicted to decrease NRP1 expression using the gene expression profiles for THP-1 monocytes as an alternative to expression profiles for macrophages. Furthermore, we conducted validation experiments in both THP-1 derived macrophage-like cells and peripheral blood mononuclear cell (PBMC)-derived macrophages to verify the effect of the compounds predicted to decrease NRP1 surface expression using flow cytometry and fluorescence microscopy. Overall, this study suggests the potential to rapidly identify compounds that decrease NRP1 expression in macrophages, which is not covered by L1000, using gene expression levels of precursor THP-1 monocytes.

# Materials and methods

## Gene expression profiles in L1000-based CMap dataset

The level 5 gene expression profiles of L1000-based CMap were downloaded from clue.io. This Level 5 dataset contains over 10,000 genes with differential expression values, and 1,201,944 profiles were induced by several conditions. This dataset consists of 46934 perturbagens on 248 types of cells, 162 doses, and 23-time points. The profile values represent the level of mRNA expression in comparison to a control (the background of the plate). In each gene expression profile, 12,328 genes are measured directly (called landmark genes). 9,196 genes are well inferred, and their expression level did correlate with the actual measured levels with p values ≤0.05, and the remaining 2,154 genes are less-well inferred genes. The well-inferred Genes include both NRP1 and ACE2.

## Cell culture and reagents

THP-1 monocytes (TIB-202, ATCC) were cultured in RPMI1640 (MT10040CV, Gibco) supplemented with 10% fetal bovine serum (Gibco) and 1% penicillin-streptomycin (15140163, Gibco). THP-1 cells were differentiated into macrophage-like cells using 10 ng/ml phorbol 12-myristate 13-acetate (PMA) (Catalog #P8139, Sigma) for 48 h followed by 24 h rest before experiments. Human primary peripheral blood mononuclear cells were isolated from buffy coat using the Ficoll-based density gradient centrifugation method. Monocytes were allowed to adhere to the plate for 1 h and non-adhered leucocytes were removed. Monocytes were differentiated into macrophages by culturing cells with RPMI + 5% human serum for 7–10 days (17–27). In total, cells obtained from 8 different de-identified healthy donors were used in this study. ONO-4059 (Catalog # 32957), gefitinib (Catalog # 13166), bosutinib (Catalog # 12030), doxorubicin (Catalog #15007), and docetaxel (Catalog #11637) were purchased from Cayman Chemicals and resuspended in DMSO according to manufacturer instructions and used at indicated doses in the study. Cells were treated for 12 h using all compounds prior to evaluation of viability using Propidium Iodide (Catalog#R37108, Thermofisher) and surface expression of NRP1.

## Flow cytometry

Cells were stained for flow cytometry using viability dye (Propidium iodide) and either isotype (Catalog #407107, Biolegend) or anti-NRP1 antibody (Clone 12C2, Catalog #354503, Biolegend) for 30 min on ice. Cells were washed 3× using PBS followed by fixation with 4% paraformaldehyde fixation. Surface expression of NRP1 was measured using Cytek Aurora flow cytometer (Cytek Bioscience). FCS files were analyzed in FlowJo version 10.10.0.

## Immuno-fluorescent staining with high content imaging (HCI) for quantifying NRP1 expression

Cells were fixed using 4% paraformaldehyde for 15 min at room temperature and washed 3 times with PBS. Cells were then stained overnight with either isotype (Catalog #407107, Biolegend) or anti-NRP1 antibody (Clone 12C2 Catalog #354503, Biolegend) with gentle agitation. Cells were washed 3 times using PBS followed by counterstain for nucleus (DAPI) and actin cytoskeleton (Phalloidin) expression of NRP1 was measured using Molecular Devices ImageXpress Pico (Molecular Devices). Cell counting was performed using DAPI staining and cellular NRP1 expression was quantified using 3-cell scoring program in CellReporter Xpress (Molecular Devices). Mean fluorescence per cell, total NRP1 fluorescence and percent of NRP1+ cells were calculated using this program.

## Statistical methods

All data was analyzed using Graphpad Prism v10 (GraphPad Software). For multiple group comparisons in THP1 monocytes and THP1 derived macrophages, One-way ANOVA followed by post-hoc multi-group comparisons were performed with $p < 0.05$ used to determine statistical significance. For comparison across donors in primary cells, values for NRP1 expression were averaged across technical replicates and fold change to vehicle treated macrophages (control) was calculated for each treatment. One-sample $t$-test was used to compare the value across multiple donors to value of 1.0 (normalized to control) with $p$-value < 0.05 used to determine compounds that reduced NRP1 surface expression with statistical significance.

# Results

The goal of this study was to identify small molecules that decrease NRP1 expression in macrophages. As the L1000-based CMap dataset contains many profiles under multiple conditions, including perturbagens, cell types, doses, and time points, appropriate filters are necessary to narrow it down (Figure 1A). To find the desired molecules, we applied the following filters to this dataset according to the indicated filters (Figure 1B).

## Selection of small molecules from L1000-based CMap dataset with drug repurposing hub

Perturbagens include reagents such as small molecules, CRISPR/Cas9 and short hairpin RNA. Drug Repurposing Hub is an open-access repository of 6,232 molecules, which is curated and annotated of FDA-approved drugs, drugs in clinical trials, and pre-clinical tool compounds with resource information. In addition, it describes the mechanisms of action of these compounds (drug information version: 3/24/2020) (28). Among the 33,590 molecules

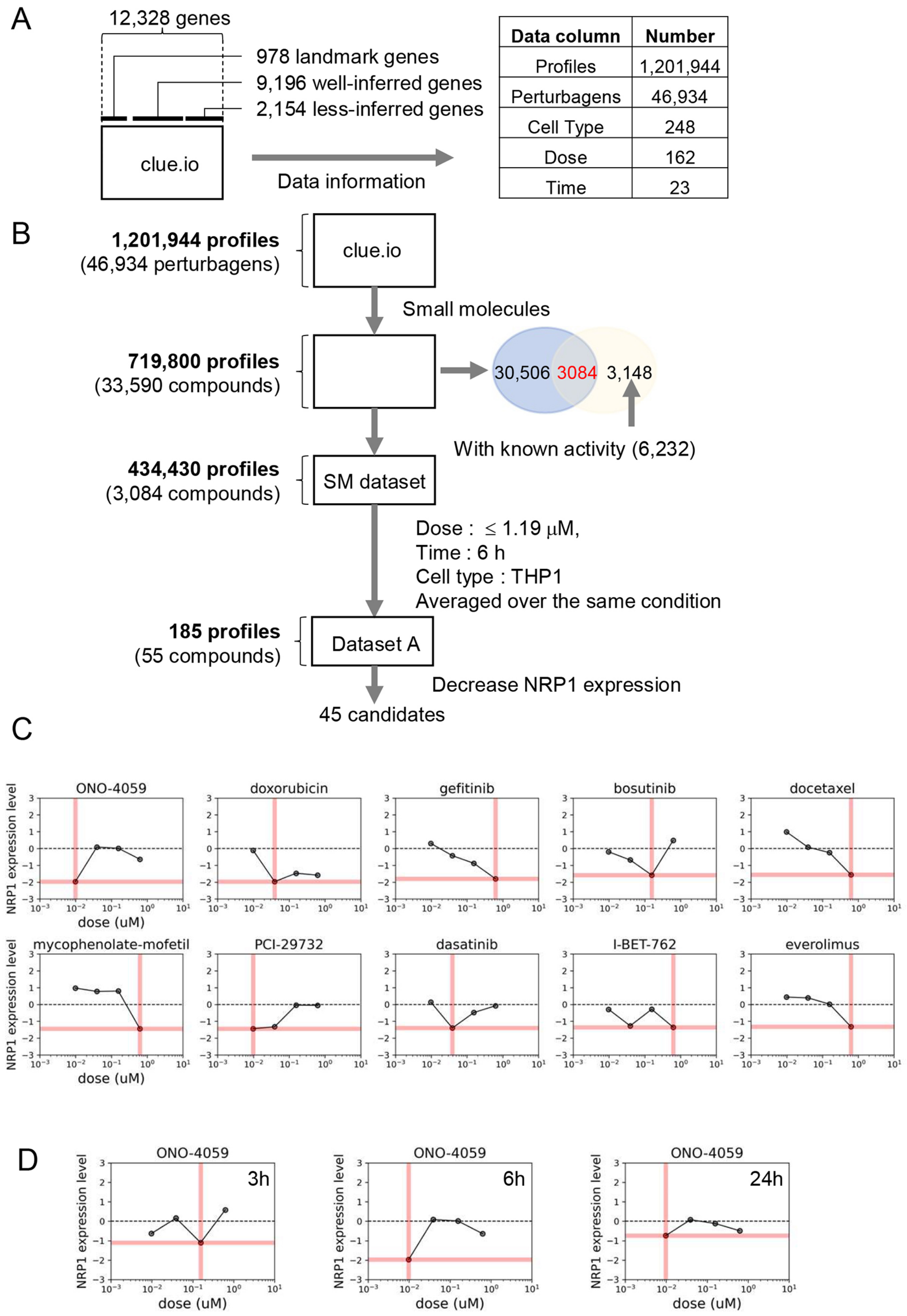

FIGURE 1
Drug screening process of reducing NRP1 expression in THP-1 monocytes. (A) The Structure of L1000-based connectivity MAP (CMap) dataset. (B)) Drug Identification process (workflow). (C) Dose-response relationships of NRP1 expression in top 10 small molecules in THP-1 monocytes at 6 h time point. Pink bars indicate the dosages in each small molecule summarized in Table 1. (D) Dose-response relationships of NRP1 expression in ONO-4059 in THP-1 at 3, 6 and 24 h time points.

contained in L1000-based CMap dataset, 3,084 small molecules overlap with 6,232 drugs in this repository. We then extracted the 434,430 gene expression profiles with conditions treated with these 3,084 small molecules.

## Dosage, time, and cell type selection

Each profile was measured at various dosages, time points, and cell types in the L1000-based CMap dataset. To facilitate comparison and easy handling of data, several doses from a similar range were converted to single values in Supplementary Table S1. Among dosages, we eliminated high dosages both from concerns about toxicity and drug discovery and we applied the filter of 1.19 µM (Figure 1B). Next, in the narrowed-down profiles by dose selection, the profiles with the most data continue in the order of 24 h, 6 h, and 3 h. In terms of drug discovery, the profiles measured over 24 h were excluded to identify fast-acting drugs. For the subsequent analysis, we focused on a larger amount of data from 6 h timepoint to compare between compounds. Despite applying the same small molecules to each type of cell, the gene expression profiles differ, so that gene expression profiles should be used in a specific type of cell. Ideally, we would obtain profiles measured in macrophage-derived cells from the L1000-based CMap dataset. However, in the absence of data for macrophages, we chose the profiles measured in THP-1 monocytes since these are routinely used to evaluate inflammatory responses in cardiovascular disease and contained the most number of compounds and timepoints tested in the L1000-based CMap. Finally, after filtering, 190 profiles were obtained and we averaged profiles collected multiple times, resulting in the final set of 185 profiles treated by 55 small molecules in THP-1 for 6 h.

## Identification of small molecules that decrease NRP1 expression in THP-1

We focused on the expression level of NRP1 in the preprocessed dataset, including both compounds that could increase and decrease NRP1 expression. Among 55 compounds, we selected 45 small molecule inhibitors that were predicted to decrease NRP1 expression. We then sought to extract the combinations of 45 small molecules and their doses that most significantly decrease the expression of NRP1 in the preprocessed dataset. Among these combinations, the top 10 small molecules that most significantly decrease the expression level of NRP1 are shown in Table 1. Furthermore, the preprocessed dataset contained NRP1 expression levels at 4 dose points, and Figure 1C depicts the dose-response relationship of NRP1 expression in each small molecule. A dose-dependent decrease in NRP1 expression tended to be observed in several small molecules in the ranges up to their optimal doses. In the result, we expected these small molecules to decrease NRP1 expression at the appropriate dose in THP-1. We then observed the dose-response relationship of ONO-4059 at each time point (i.e., 3 h, 6 h, and 24 h) (Figure 1D). Among three time points, this molecule was predicted to reduce NRP1 expression at 6 h. As a result of these findings, we selected the top combinations of 5 small molecules and their doses that could decrease the expression of NRP1 at 6 h for subsequent validation studies.

## Regulation of surface expression of NRP1 in THP-1 monocytes

Our analysis of L1000 CMap identified multiple compounds predicted to decrease NRP1 expression in THP-1 monocytes. We selected the top 5 compounds based on their predicted ability to decrease NRP1 expression. Since NRP1 is a surface receptor that acts as an entry receptor for SARS-CoV2, we chose to measure the surface protein expression of NRP1 as the ideal parameter to quantify the ability of these predicted compounds to decrease NRP1 expression and thereby potentially prevent SARS-CoV2 infection. We first screened whether these compounds would impact cell viability through flow cytometry (Figure 2A) using propidium iodide staining. We observed that all compounds had minimal effect on THP-1 monocyte viability (Figure 2B) at the dosage predicted by our L1000 CMap analysis. We next investigated the capacity of these compounds to reduce surface expression of NRP1 (Figure 2C) and observed that these compounds only had marginal effects on reducing NRP1 expression in THP-1 monocytes (Figure 2D). However, baseline expression of NRP1 at the surface of THP-1 monocytes itself was

**TABLE 1** The top 10 small molecules identified, NRP1 expression levels, dose and known activity.

| Rank | Compound name | Expression level | Dose | Known activity |
|---|---|---|---|---|
| 1 | ONO-4059 | −1.972 | 0.01 µM | Bruton's tyrosine kinase (BTK) inhibitor |
| 2 | Doxorubicin | −1.968 | 0.04 µM | Topoisomerase inhibitor |
| 3 | Gefitinib | −1.797 | 0.66 µM | EGFR inhibitor |
| 4 | Bosutinib | −1.576 | 0.125 µM | Abl kinase inhibitor\|Bcr-Abl kinase inhibitor\|SRC inhibitor |
| 5 | Docetaxel | −1.563 | 0.66 µM | Tubulin polymerization inhibitor |
| 6 | Mycophenolate-mofetil | −1.443 | 0.66 µM | Dehydrogenase inhibitor\|inositol monophosphatase inhibitor |
| 7 | PCI-29732 | −1.438 | 0.01 µM | Bruton's tyrosine kinase (BTK) inhibitor |
| 8 | Dasatinib | −1.396 | 0.04 µM | Bcr-Abl kinase inhibitor\|ephrin inhibitor\|KIT inhibitor\|<br>PDGFR tyrosine kinase receptor inhibitor\|SRC inhibitor\|<br>Tyrosine kinase inhibitor |
| 9 | I-BET-762 | −1.351 | 0.66 µM | Bromodomain inhibitor |
| 10 | Everolimus | −1.324 | 0.66 µM | mTOR inhibitor |

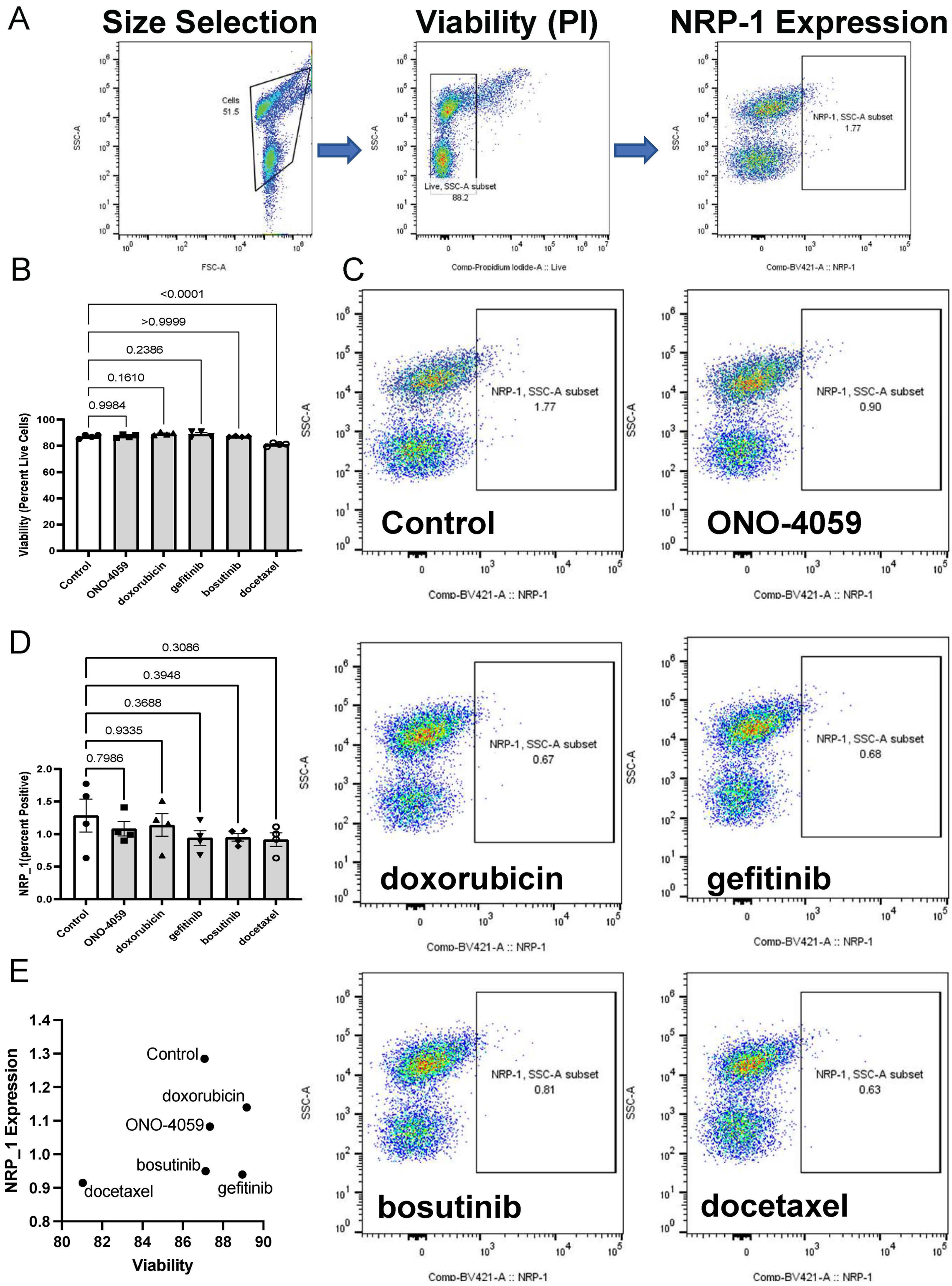

FIGURE 2

Cell surface NRP1 expression analysis in THP-1 monocytes. **(A)** Gating strategy for the fluorescent activated cell sorter (FACS). **(B)** Cell viability after treating the top 5 candidate small molecules (ONO-4059, doxorubicin, gefitinib, bosutinib, and docetaxel). **(C)** Cell surface NRP1 expression analysis after treating the top 5 candidate small molecules. **(D)** Summary of cell surface NRP1 expression. **(E)** The correlation between NRP1 expression and cell viability. Data were shown as mean (bar) plus individual value (dots), *n* = 4 per group. One-way ANOVA followed by post-hoc multi-group comparison test was used to assess statistical differences.

considerably low. Finally, we compared the ability of these compounds to reduce NRP1 surface expression with minimal effect on cellular viability (Figure 2E).

## Regulation of NRP1 surface expression in THP-1 derived macrophage-like cells

To investigate the appropriate cell type in which NRP1 surface expression is linked to SARS-CoV2 infection, we evaluated whether THP-1 cell differentiated into macrophage-like cells using PMA would induce NRP1 surface expression. Indeed, we observed surface expression of NRP1 in THP-1-derived macrophage-like cells using confocal microscopy (Figure 3A). We also validated these findings using flow cytometry in cells which were not permeabilized to show that macrophages would be an optimal candidate to validate the ability of these compounds to reduce surface expression of NRP1. We observed that none of the compounds had a significant impact on cell viability (Figures 3B,C) suggesting these compounds have minimal cytotoxicity in THP-1 derived macrophage-like cells. Flow cytometry analysis was performed to describe the ability of these compounds to reduce surface expression of NRP1 in THP-1 derived macrophage-like cells (Figure 3D). We observed that all five compounds tested caused a statistically significant reduction in the percentage of NRP1-positive cells (Figure 3E). We compared the ability of these compounds to reduce NRP1 surface expression with its effect on cellular viability (Figure 3F) to identify compounds with the best safety profile for macrophage cytotoxicity and maximal NRP1 downregulation.

## Regulation of NRP1 surface expression in human primary PBMC-derived macrophages

SARS-CoV2 infection of innate immune cells such as macrophages has been shown to be related using the NRP1 receptor *in vivo*. Therefore, we isolated human primary PBMCs from de-identified healthy donors and differentiated them into macrophages. NRP1 surface expression was found to be heterogeneous and present within a subset of macrophages through confocal microscopy (Figure 4A). Using high content imaging, we created masks for NRP1 positive (green) and NRP1 negative (red) cells (Figure 4B). We added all five compounds at the doses predicted by our L1000 CMap analysis and measured surface expression of NRP1 using high-content imaging (Figure 4C). Across five independent donors, we observed that our top 2 predicted compounds, ONO-4059 and doxorubicin were successfully able to reduce the percentage of NRP1-positive cells with statistical significance using high content imaging (Figure 4D). To sample a larger number of cells per condition and more accurately measure mean NRP1 surface expression at single cell resolution, we supplemented our high content imaging approach with flow cytometry (Figure 4E). Here we observed that in three different, de-identified healthy donors, all five predicted compounds were able to reduce the mean fluorescence intensity of NRP1 surface expression compared to vehicle treated control primary PBMC-derived macrophages (Figure 4F). Our findings using high-content imaging (Figure 4D) and flow cytometry (Figure 4F) suggest that our predicted compounds using L1000-based CMap dataset were validated in their capacity to regulate NRP1 surface expression in human primary PBMC-derived macrophages across multiple donors.

# Discussion

Based on the drug repositioning approaches for the L1000-based CMap dataset, we identified 45 candidate small molecules that could potentially decrease NRP1 surface expression in macrophages. The gene expression profiles induced by exposing macrophages were not included in this dataset. We, therefore, employed alternative approaches to identify candidate small molecules using THP-1 monocytes, which are routinely used as a macrophage-like cell after differentiation using PMA. We expected these candidates with the ability to decrease NRP1 mRNA to reduce NRP1 surface expression in macrophages. We verified the effect of the candidate compounds through validation experiments in both THP-1-derived macrophages and PBMC-derived macrophages using flow cytometry and fluorescence microscopy. Our study successfully translates predictions made in tumor cell lines such as THP1 monocytes to primary non-cancer cells (PBMC-derived macrophages from 8 different de-identified healthy donors) showing the generalizability of the predictions made using L1000.

We previously identified small molecules that could potentially decrease ACE2 mRNA levels in the lung epithelial cell lines by processing the L1000-based CMap dataset (15). Most candidates were shown to decrease ACE2 surface expression in the target cells BEAS-2B derived from the same organ. This current study revealed the potential to identify compounds that decrease gene expression in macrophages using the gene expression level of precursor THP-1 monocytes. These results indicate that our proposed approach could be adapted to identify compounds for drug repositioning in several cells using the precursor cells. Since primary cell data are limited in the L1000-based CMap dataset, this approach would make it possible to identify the compounds that modulate target gene expression using precursor cells, which is often used in primary cell studies. We have also employed such approaches to validate candidate small molecules using *in vivo* studies reversing disease phenotype (16, 26). Future studies can extend our findings into *in vivo* studies to accelerate translation to preclinical testing.

However, there are a few restrictions on using the L1000-based CMap dataset. First, as mentioned in the method, many genes are not covered in the L1000 dataset, resulting in the limitation of drug discovery for half of the human protein-coding genes. To address this limitation, a deep-learning model that transforms L1000 profiles to RNA-seq-like profiles has already been developed (29). Second, most data were obtained by performing anticancer drugs in cancer cell lines. The goal of drug repositioning is to obtain

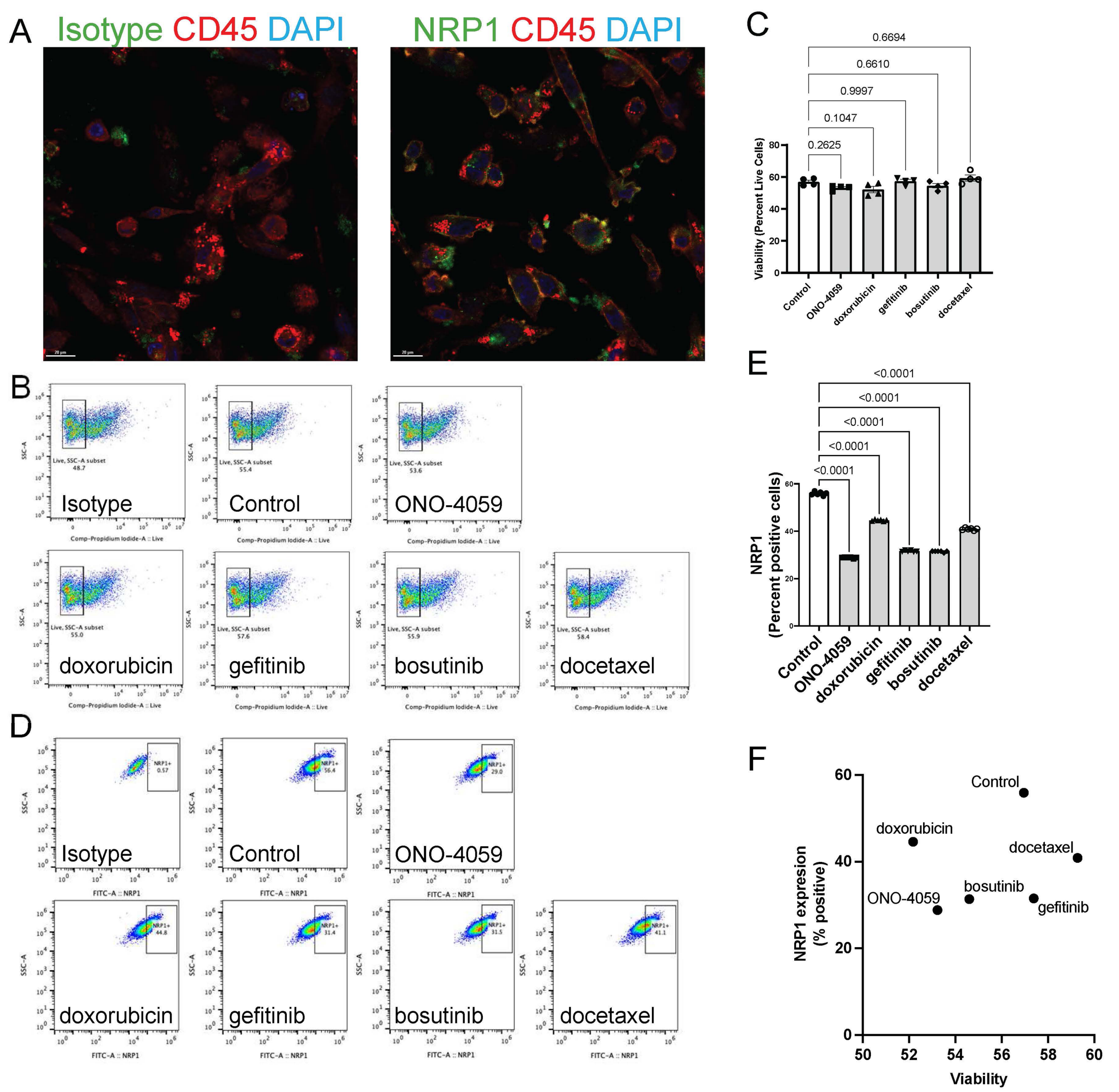

FIGURE 3
Cell surface NRP1 expression analysis in THP-1 derived macrophages. **(A)** The immunocytochemistry staining on cell surface NRP1 expression in THP-1-derived macrophage-like cells (Green: NRP1 or isotype, Red: CD45, and Blue: DAPI). **(B,C)** Live cell quantification analysis after treating the top 5 candidate small molecules. Representative of cell viability after treating the top 5 candidate small molecules. Scale bar, 20 µm. **(B)** (ONO-4059, doxorubicin, gefitinib, bosutinib, and docetaxel) and summary of cell viability **(C–E)** Cell surface NRP1 expression analysis after treating the top 5 candidate small molecules. Representative images **(D)** and summary of cell surface NRP1 expression **(E,F)** The correlation between NRP1 expression and cell viability. Data were shown as mean (bar) plus individual value (dots), *n* = 4 **(C)** and 6 **(E)** per group. One-way ANOVA followed by post-hoc multi-group comparison test was used to assess statistical differences.

the candidate drugs without inducing high toxicity. It is noteworthy that in this study we extracted the small molecules that decrease NRP1 surface expression using a dose filter and identified the candidate compounds without significant cytotoxicity or cell viability reduction in each assay. One advantage of our approach is that the L1000-based CMap dataset contains data from multiple cell types. While we focused on monocytes and monocyte-derived macrophages in this study, the effect of drug treatment on regulation of NRP1 expression in other cell types can also be obtained. For example, the L1000 contains 12 different cell types treated with ONO-4059. Future studies investigating the potential reduction of NRP1 in other cell types and tissues can also be guided using these approaches. On the other hand, since the L1000 is built on data measured primarily from cell lines, it is difficult to make inferences about the sex-dependent and age-dependent effects of drug compounds. In our study, we used the same cell line (THP-1) as the L1000 and supplemented these findings in macrophages

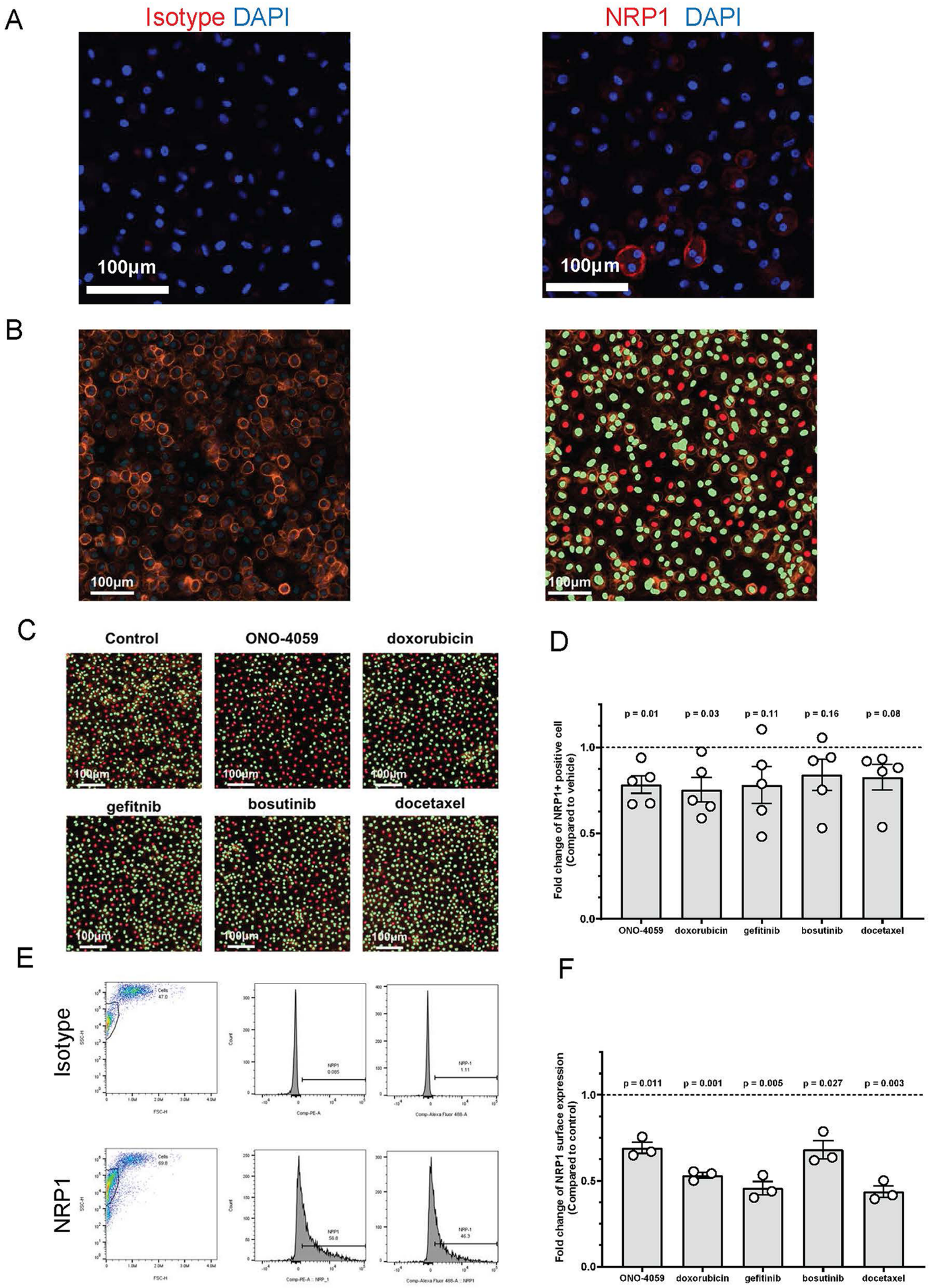

FIGURE 4
Cell surface NRP1 expression analysis in human primary peripheral blood mononuclear cell (PBMC)-derived macrophages. **(A)** The immunocytochemistry staining on cell surface NRP1 expression in PBMC-derived macrophages (Red: NRP1 or isotype, and Blue: DAPI). Scale bar, 100 µm. **(B)** Cell surface NRP1 surface expression (Orange) analysis in high-content imaging using ImageXpress Pico. Cell masks created by cell scoring program in CellReporter Xpress for cells with positive NRP1 expression (green) and cells with negative NRP1 expression (red). **(C)** Cell masks for NRP1 positive (green) and negative (red) cells after treating the top 5 candidate small molecules (ONO-4059, doxorubicin, gefitinib, bosutinib, and docetaxel). **(D)** Summarized results for five independent de-identified healthy donors with each dot representing each donor. **(E)** Gating strategy for the fluorescent activated cell sorter (FACS). **(F)** Cell surface NRP1 expression analysis after treating the top 5 candidate small molecules in FACS. Summarized with NRP1 MFI ratio corrected by donor. Summarized results for three independent de-identified healthy donors with each dot representing each donor. For figures **(D,F)**, the average NRP1 expression was normalized to control (vehicle treated) sample in each donor. One-sample *t*-test was used to compare mean NRP1 expression across donors. *P*-value < 0.05 was used to determine statistically significant changes.

differentiated from PBMC of de-identified healthy donors. Future studies interested in investigating sex-dependent and age-dependent effects of such compounds in regulating NRP1 expression can use appropriately powered validation models (e.g., male and female mice) to answer these questions.

In recent years, drug development has become more challenging due to the depletion of drug targets. However, there is still significant demand for treatments that slow, stop or reverse disease progression. L1000-based CMap database has been used for drug repositioning to identify small molecules that induce gene expression profiles similar to or opposite to those caused by diseases (26, 30). Increasing publicly available large-scale biological data would facilitate computational drug repositioning. If the profiles induced by exposing various cells using drugs already proven safe are expanded, we expect that drug discovery using L1000-based drug repositioning would aid in the expansion of new indications for existing drugs.

During the evolution of viral epidemics, viruses such as SARS-CoV-2 rapidly acquire mutations on their surface receptors, which impacts the tropism of these viruses. As a result, SARS-CoV2 could continue to infect multiple cell types using diverse range of entry receptors and co-receptors. While traditional vaccination and antiviral drug strategies that prevent viral replication are key tools in curbing the spread of viral infection, our approach provides a strong complementary strategy. Electronic medical record-based approaches have been used to identify at-risk populations, such as obese individuals who are at increased risk for productive infection upon exposure to SARS-CoV2 virus. Our approach to finding drugs that could be repurposed to prevent the spread of infection could be a powerful tool to mitigating spread of viral infection (31). Rapidly screening compounds to identify specific candidates to prevent infectivity of cells such as macrophages, endothelial cells or neurons could serve as a supportive strategy to prevent the diverse range of post-acute sequelae of COVID-19. Specifically, therapies targeting cell types which play a key role in inflammation and resolution of inflammation could be a potent strategy to reduce the risk for post-acute sequelae of COVID-19 (32). While this approach facilitates rapid identification of compounds that could reduce surface expression of NRP1, the mechanisms through which these compounds are able to induce these effects are unknown. This is a limitation which requires orthogonal studies to investigate how these compounds are able to regulate NRP1 expression. For certain patients with pre-existing atherosclerosis, inhibition of NRP suppresses infection but cause an aberrant pro-inflammatory response. NRP1-null macropjages are known to increase the release of inflammatory cytokines, such as IL-6. However, the inclusion of parameters to test cell viability as utilized in this study can help further filter compounds with best safety profile and maximal efficacy. Furthermore, the use of compounds which have already obtained FDA approval and have well documented safety profile could be an additional layer in the selection of compounds to combat the infection of SARS-CoV2 into diverse cell types. In our proposed model, drugs with prior FDA approval will be repurposed for transient reduction of NRP1 expression in macrophages to reduce the risk of infection with SARS-CoV2. While some studies have shown that myeloid specific knockout of NRP1 could increase pro-inflammatory responses (33, 34), our approach is aimed at short-term, transient downregulation of NRP1.

Many small molecules with potential anti-COVID-19 effects have been developed as our understanding of SARS-CoV2 structure and function has evolved (35). The development of new compounds and antibodies targeting NRP1 can be effective (36, 37), but a significant amount of time is required to evaluate safety of these new compounds in preclinical testing and clinical trials. In addition, rapid and large-scale supplies are essential in the event of a pandemic. The drug repositioning approach used in this study applies compounds with established synthetic methods and safety profiles. Such an approach could serve to support therapies directly targeting NRP1 as a cheaper and faster complementary therapeutic option. Future studies can compare the safety and efficacy of agents directly targeting NRP1 with our proposed drugs indirectly lowering NRP1 to help select appropriate therapeutic strategy for patients with COVID-19.

The ability of innate immune cells such as macrophages to sense and respond to viruses is regulated through a wide range of mechanisms. Poly (ADP-ribose) polymerase form a key role in sensing viruses using their macrodomain (38–40). PARPs have been shown to play a key role in the regulation of macrophage heterogeneity in response to virus infection-related factors such as interferon γ (21). Similarly, infection-associated signaling factors such as extracellular vesicles (41) and TLR signaling (42) play a role in severity of inflammatory responses. Specifically, the role of extracellular vesicle-associated viral proteins in determining chronic inflammatory responses has also been shown in HIV (43, 44), influenza (45) and SARS-CoV-2 (46). Use of L1000-based CMap approaches could be employed to find novel receptors and regulators of inflammation. While the L1000-based CMap contains interferon $\gamma$ as a ligand in 84 conditions, it has not been evaluated in THP-1 monocytes. Therefore, we focused on unstimulated monocytes and macrophages to validate the ability of the predicted compounds to reduce NRP1 surface expression. Future studies can focus on evaluating NRP1 expression under pathophysiological stimulation such as interferon $\gamma$ in appropriate cell types. L1000-based CMap could also be used to guide studies to reverse gene expression profiles based on disease specific stimulation. We have previously used such an approach to identify compounds to reduce the pro-inflammatory phenotype induced by interferon $\gamma$ in human primary macrophages (26). Similar studies can be performed to repurpose drug compounds to target specific phenotypes of polarized macrophages. These could be targeted using our drug repurposing approach to reduce virus-induced chronic inflammation.

## Data availability statement

The authors confirm that the data supporting the findings of this study are available within the article and its supplementary materials.

## Ethics statement

All studies were conducted in accordance with Mass General Brigham Institutional Biosafety Committee approval. Human primary peripheral blood mononuclear cells from de-identified healthy donors were purchased from Stem Cell Technology. Written informed consent for participation was not required from the participants or the participants' legal guardians/next of kin in accordance with the national legislation and institutional requirements.

## Author contributions

AI: Conceptualization, Data curation, Formal Analysis, Investigation, Methodology, Resources, Software, Validation, Visualization, Writing – original draft, Writing – review & editing. SC: Conceptualization, Data curation, Formal Analysis, Investigation, Methodology, Resources, Software, Validation, Visualization, Writing – original draft, Writing – review & editing. TA: Conceptualization, Data curation, Formal Analysis, Investigation, Methodology, Resources, Software, Validation, Visualization, Writing – review & editing. MW: Investigation, Validation, Writing – review & editing. YN: Investigation, Writing – review & editing. EA: Investigation, Project administration, Writing – review & editing. YS: Investigation, Project administration, Supervision, Writing – review & editing. MA: Conceptualization, Funding acquisition, Project administration, Supervision, Writing – review & editing.

## Funding

The author(s) declare financial support was received for the research, authorship, and/or publication of this article. This study was supported by research grants from Kowa Company, Ltd, Nagoya, Japan (A11014) and the National Institutes of Health (R01HL126901, R01HL149302, R01HL174066) to MA.

## Conflict of interest

AI, TA, YN and YS are employees of Kowa Company, Ltd and were visiting scientists at Brigham and Women's Hospital when experiments demonstrated in this study were performed. Kowa had no role in the study design, data collection, analysis, decision to publish, or preparation of the article.

The remaining authors declare that the research was conducted in the absence of any commercial or financial relationships that could be construed as a potential conflict of interest.

The author(s) declared that they were an editorial board member of Frontiers, at the time of submission. This had no impact on the peer review process and the final decision.

## Publisher's note

## Supplementary material

The Supplementary Material for this article can be found online at: https://www.frontiersin.org/articles/10.3389/fcvm.2024.1438396/full#supplementary-material

## References

1. Rabi FA, Al Zoubi MS, Kasasbeh GA, Salameh DM, Al-Nasser AD. SARS-CoV-2 and coronavirus disease 2019: what we know so far. *Pathogens*. (2020) 9(3):231. doi: 10.3390/pathogens9030231

2. Gao J, Mei H, Sun J, Li H, Huang Y, Tang Y, et al. Neuropilin-1-Mediated SARS-CoV-2 infection in bone marrow-derived macrophages inhibits osteoclast differentiation. *Adv Biol (Weinh)*. (2022) 6(5):e2200007. doi: 10.1002/adbi.202200007

3. Cantuti-Castelvetri L, Ojha R, Pedro LD, Djannatian M, Franz J, Kuivanen S, et al. Neuropilin-1 facilitates SARS-CoV-2 cell entry and infectivity. *Science*. (2020) 370 (6518):856–60. doi: 10.1126/science.abd2985

4. Daly JL, Simonetti B, Klein K, Chen KE, Williamson MK, Anton-Plagaro C, et al. Neuropilin-1 is a host factor for SARS-CoV-2 infection. *Science*. (2020) 370 (6518):861–5. doi: 10.1126/science.abd3072

5. Eberhardt N, Noval MG, Kaur R, Amadori L, Gildea M, Sajja S, et al. SARS-CoV-2 infection triggers pro-atherogenic inflammatory responses in human coronary vessels. *Nat Cardiovasc Res*. (2023) 2(10):899–916. doi: 10.1038/s44161-023-00336-5

6. Jha PK, Vijay A, Halu A, Uchida S, Aikawa M. Gene expression profiling reveals the shared and distinct transcriptional signatures in human lung epithelial cells infected with SARS-CoV-2, MERS-CoV, or SARS-CoV: potential implications in cardiovascular complications of COVID-19. *Front Cardiovasc Med*. (2020) 7:623012. doi: 10.3389/fcvm.2020.623012

7. Crunfli F, Carregari VC, Veras FP, Silva LS, Nogueira MH, Antunes A, et al. Morphological, cellular, and molecular basis of brain infection in COVID-19 patients. *Proc Natl Acad Sci*. (2022) 119(35):e2200960119. doi: 10.1073/pnas.2200960119

8. Ashburn TT, Thor KB. Drug repositioning: identifying and developing new uses for existing drugs. *Nat Rev Drug Discov*. (2004) 3(8):673–83. doi: 10.1038/nrd1468

9. Krishnamurthy N, Grimshaw AA, Axson SA, Choe SH, Miller JE. Drug repurposing: a systematic review on root causes, barriers and facilitators. *BMC Health Serv Res*. (2022) 22(1):970. doi: 10.1186/s12913-022-08272-z

10. Jarada TN, Rokne JG, Alhajj R. A review of computational drug repositioning: strategies, approaches, opportunities, challenges, and directions. *J Cheminform*. (2020) 12(1):46. doi: 10.1186/s13321-020-00450-7

11. Lamb J, Crawford ED, Peck D, Modell JW, Blat IC, Wrobel MJ, et al. The connectivity map: using gene-expression signatures to connect small molecules, genes, and disease. *Science*. (2006) 313(5795):1929–35. doi: 10.1126/science.1132939

12. Subramanian A, Narayan R, Corsello SM, Peck DD, Natoli TE, Lu X, et al. A next generation connectivity map: L1000 platform and the first 1,000,000 profiles. *Cell*. (2017) 171(6):1437–52 e17. doi: 10.1016/j.cell.2017.10.049

13. Duan Q, Reid SP, Clark NR, Wang Z, Fernandez NF, Rouillard AD, et al. L1000CDS(2): LINCS L1000 characteristic direction signatures search engine. *NPJ Syst Biol Appl*. (2016) 2:16015. doi: 10.1038/npjsba.2016.15

14. Musa A, Ghoraie LS, Zhang SD, Glazko G, Yli-Harja O, Dehmer M, et al. A review of connectivity map and computational approaches in pharmacogenomics. *Brief Bioinform*. (2017) 18(5):903. doi: 10.1093/bib/bbx023

15. Asano T, Chelvanambi S, Decano JL, Whelan MC, Aikawa E, Aikawa M. In silico drug screening approach using L1000-based connectivity map and its application to COVID-19. *Front Cardiovasc Med*. (2022) 9:842641. doi: 10.3389/fcvm.2022.842641

16. Tanaka T, Asano T, Okui T, Kuraoka S, Singh SA, Aikawa M, et al. Computational screening strategy for drug repurposing identified niclosamide as inhibitor of vascular calcification. *Front Cardiovasc Med*. (2021) 8:826529. doi: 10.3389/fcvm.2021.826529

17. Fung E, Tang SM, Canner JP, Morishige K, Arboleda-Velasquez JF, Cardoso AA, et al. Delta-like 4 induces notch signaling in macrophages: implications for inflammation. *Circulation*. (2007) 115(23):2948–56. doi: 10.1161/CIRCULATIONAHA.106.675462

18. Deguchi JO, Yamazaki H, Aikawa E, Aikawa M. Chronic hypoxia activates the Akt and beta-catenin pathways in human macrophages. *Arterioscler Thromb Vasc Biol*. (2009) 29(10):1664–70. doi: 10.1161/ATVBAHA.109.194043

19. Nakano T, Katsuki S, Chen M, Decano JL, Halu A, Lee LH, et al. Uremic toxin indoxyl sulfate promotes proinflammatory macrophage activation via the interplay of OATP2B1 and Dll4-notch signaling. *Circulation*. (2019) 139(1):78–96. doi: 10.1161/CIRCULATIONAHA.118.034588

20. Fukuda D, Aikawa E, Swirski FK, Novobrantseva TI, Kotelianski V, Gorgun CZ, et al. Notch ligand delta-like 4 blockade attenuates atherosclerosis and metabolic disorders. *Proc Natl Acad Sci*. (2012) 109(27):E1868–77. doi: 10.1073/pnas.1116889109

21. Iwata H, Goettsch C, Sharma A, Ricchiuto P, Goh WW, Halu A, et al. PARP9 And PARP14 cross-regulate macrophage activation via STAT1 ADP-ribosylation. *Nat Commun*. (2016) 7:12849. doi: 10.1038/ncomms12849

22. Aikawa M, Rabkin E, Sugiyama S, Voglic S, Fukumoto Y, Furukawa Y, et al. An HMG-CoA reductase inhibitor, cerivastatin, suppresses growth of macrophages expressing matrix metalloproteinases and tissue factor *in vivo* and *in vitro*. *Circulation*. (2001) 103:276–83. doi: 10.1161/01.CIR.103.2.276

23. Koga J, Nakano T, Dahlman JE, Figueiredo JL, Zhang H, Decano J, et al. Macrophage notch ligand delta-like 4 promotes vein graft lesion development: implications for the treatment of vein graft failure. *Arterioscler Thromb Vasc Biol*. (2015) 35(11):2343–53. doi: 10.1161/ATVBAHA.115.305516

24. Itou T, Maldonado N, Yamada I, Goettsch C, Matsumoto J, Aikawa M, et al. Cystathionine gamma-lyase accelerates osteoclast differentiation: identification of a novel regulator of osteoclastogenesis by proteomic analysis. *Arterioscler Thromb Vasc Biol*. (2014) 34(3):626–34. doi: 10.1161/ATVBAHA.113.302576

25. Decano JL, Singh SA, Gasparotto Bueno C, Ho Lee L, Halu A, Chelvanambi S, et al. Systems approach to discovery of therapeutic targets for vein graft disease: pPARalpha pivotally regulates metabolism, activation, and heterogeneity of macrophages and lesion development. *Circulation*. (2021) 143(25):2454–70. doi: 10.1161/CIRCULATIONAHA.119.043724

26. Decano JL, Maiorino E, Matamalas JT, Chelvanambi S, Tiemeijer BT, Yanagihara Y, et al. Cellular heterogeneity of activated primary human macrophages and associated drug-gene networks: from biology to precision therapeutics. *Circulation*. (2023) 148(19):1459–78. doi: 10.1161/CIRCULATIONAHA.123.064794

27. Katsuki S, Jha PK, Lupieri A, Nakano T, Passos LS, Rogers MA, et al. Proprotein convertase subtilisin/kexin 9 (PCSK9) promotes macrophage activation via LDL receptor-independent mechanisms. *Circ Res*. (2022) 131(11):873–89. doi: 10.1161/CIRCRESAHA.121.320056

28. Corsello SM, Bittker JA, Liu Z, Gould J, McCarren P, Hirschman JE, et al. The drug repurposing hub: a next-generation drug library and information resource. *Nat Med*. (2017) 23(4):405–8. doi: 10.1038/nm.4306

29. Jeon M, Xie Z, Evangelista JE, Wojciechowicz ML, Clarke DJB, Ma'ayan A. Transforming L1000 profiles to RNA-Seq-like profiles with deep learning. *BMC Bioinformatics*. (2022) 23(1):374. doi: 10.1186/s12859-022-04895-5

30. Amadori L, Calcagno C, Fernandez DM, Koplev S, Fernandez N, Kaur R, et al. Systems immunology-based drug repurposing framework to target inflammation in atherosclerosis. *Nat Cardiovasc Res*. (2023) 2(6):550–71. doi: 10.1038/s44161-023-00278-y

31. Matamalas JT, Chelvanambi S, Decano JL, França RF, Halu A, Santinelli-Pestana DV, et al. Obesity and age are transmission risk factors for SARS-CoV-2 infection among exposed individuals. *PNAS Nexus*. (2024) 3(8):294. doi: 10.1093/pnasnexus/pgae294

32. Cagnina RE, Duvall MG, Nijmeh J, Levy BD. Specialized pro-resolving mediators in respiratory diseases. *Curr Opin Clin Nutr Metab Care*. (2022) 25(2):67–74. doi: 10.1097/MCO.0000000000000805

33. Dai X, Okon I, Liu Z, Bedarida T, Wang Q, Ramprasath T, et al. Ablation of neuropilin 1 in myeloid cells exacerbates high-fat diet-induced insulin resistance through Nlrp3 inflammasome *in vivo*. *Diabetes*. (2017) 66(9):2424–35. doi: 10.2337/db17-0132

34. Dai X, Okon I, Liu Z, Wu Y, Zhu H, Song P, et al. A novel role for myeloid cell-specific neuropilin 1 in mitigating sepsis. *FASEB J*. (2017) 31(7):2881–92. doi: 10.1096/fj.201601238R

35. Lei S, Chen X, Wu J, Duan X, Men K. Small molecules in the treatment of COVID-19. *Signal Transduct Target Ther*. (2022) 7(1):387. doi: 10.1038/s41392-022-01249-8

36. Perez-Miller S, Patek M, Moutal A, Duran P, Cabel CR, Thorne CA, et al. Novel compounds targeting neuropilin receptor 1 with potential to interfere with SARS-CoV-2 virus entry. *ACS Chem Neurosci*. (2021) 12(8):1299–312. doi: 10.1021/acschemneuro.0c00619

37. Kolaric A, Jukic M, Bren U. Novel small-molecule inhibitors of the SARS-CoV-2 spike protein binding to neuropilin 1. *Pharmaceuticals (Basel)*. (2022) 15(2):165. doi: 10.3390/ph15020165

38. Comar CE, Otter CJ, Pfannenstiel J, Doerger E, Renner DM, Tan LH, et al. MERS-CoV endoribonuclease and accessory proteins jointly evade host innate immunity during infection of lung and nasal epithelial cells. *Proc Natl Acad Sci*. (2022) 119(21):e2123208119. doi: 10.1073/pnas.2123208119

39. Grunewald ME, Chen Y, Kuny C, Maejima T, Lease R, Ferraris D, et al. The coronavirus macrodomain is required to prevent PARP-mediated inhibition of virus replication and enhancement of IFN expression. *PLoS Pathog*. (2019) 15(5):e1007756. doi: 10.1371/journal.ppat.1007756

40. Santinelli-Pestana DV, Aikawa E, Singh SA, Aikawa M. PARPs and ADP-ribosylation in chronic inflammation: a focus on macrophages. *Pathogens*. (2023) 12(7):964. doi: 10.3390/pathogens12070964

41. Clauss M, Chelvanambi S, Cook C, ElMergawy R, Dhillon N. Viral bad news sent by EVAIL. *Viruses*. (2021) 13(6):1168. doi: 10.3390/v13061168

42. Brandao SCS, Ramos JOX, Dompieri LT, Godoi E, Figueiredo JL, Sarinho ESC, et al. Is toll-like receptor 4 involved in the severity of COVID-19 pathology in patients with cardiometabolic comorbidities? *Cytokine Growth Factor Rev*. (2021) 58:102–10. doi: 10.1016/j.cytogfr.2020.09.002

43. Chelvanambi S, Bogatcheva NV, Bednorz M, Agarwal S, Maier B, Alves NJ, et al. HIV-Nef protein persists in the lungs of aviremic patients with HIV and induces endothelial cell death. *Am J Respir Cell Mol Biol*. (2019) 60(3):357–66. doi: 10.1165/rcmb.2018-0089OC

44. Chelvanambi S, Gupta SK, Chen X, Ellis BW, Maier BF, Colbert TM, et al. HIV-Nef protein transfer to endothelial cells requires Rac1 activation and leads to endothelial dysfunction implications for statin treatment in HIV patients. *Circ Res*. (2019) 125(9):805–20. doi: 10.1161/CIRCRESAHA.119.315082

45. Lu H, Chelvanambi S, Poirier C, Saliba J, March KL, Clauss M, et al. EMAPII monoclonal antibody ameliorates influenza a virus-induced lung injury. *Mol Ther*. (2018) 26(8):2060–9. doi: 10.1016/j.ymthe.2018.05.017

46. Krishnamachary B, Cook C, Kumar A, Spikes L, Chalise P, Dhillon NK. Extracellular vesicle-mediated endothelial apoptosis and EV-associated proteins correlate with COVID-19 disease severity. *J Extracell Vesicles*. (2021) 10(9):e12117. doi: 10.1002/jev2.12117

frontiers | Frontiers in Cardiovascular Medicine

TYPE Original Research
PUBLISHED 28 October 2024
DOI 10.3389/fcvm.2024.1445193

# Trends and patterns in pulmonary arterial hypertension-associated hospital admissions among methamphetamine users: a decade-long study

Amanda Husein[1], Jolie Boullion[1], Md Ismail Hossain[1], Diensn Xing[1], Md Tareq Ferdous Khan[2], Md. Shenuarin Bhuiyan[3,4], Gopi K. Kolluru[4], Md Mostafizur Rahman Bhuiyan[5], Nicholas E. Goeders[6,7,8], Steven A. Conrad[1,9], John A. Vanchiere[1,9], A. Wayne Orr[3,4], Christopher G. Kevil[3,4] and Mohammad Alfrad Nobel Bhuiyan[1,4,8]*

[1]Department of Medicine, Louisiana State University Health Sciences Center at Shreveport, Shreveport, LA, United States, [2]Department of Mathematics and Statistics, Cleveland State University, Cleveland, OH, United States, [3]Department of Molecular and Cellular Physiology, Louisiana State University Health Sciences Center at Shreveport, Shreveport, LA, United States, [4]Department of Pathology and Translational Pathobiology, Louisiana State University Health Sciences Center at Shreveport, Shreveport, LA, United States, [5]Department of Pediatric Cardiology, Bangabandhu Sheikh Mujib Medical University, Dhaka, Bangladesh, [6]Department of Pharmacology, Toxicology & Neuroscience, Louisiana State University Health Sciences Center at Shreveport, Shreveport, LA, United States, [7]Department of Psychiatry and Behavioral Medicine, Louisiana State University Health Sciences Center at Shreveport, Shreveport, LA, United States, [8]Louisiana Addiction Research Center, Louisiana State University Health Sciences Center at Shreveport, Shreveport, LA, United States, [9]Department of Pediatrics, LSU Health Sciences Center Shreveport, Shreveport, LA, United States

**Background:** Pulmonary arterial hypertension (PAH) is a rare, chronic, progressive form of pulmonary hypertension in which increased arterial pressure causes remodeling of the arterial system and is associated with heart failure. Methamphetamine is a stimulant that has recently become a focus in PAH research, but the recent trends and demographics of this cohort of patients are not known. The study aimed to analyze the overall trends and demographics of PAH patients with and without concurrent methamphetamine usage.

**Methods:** The study used the National Inpatient Sample (NIS), Healthcare Cost and Utilization Project (HCUP), and Agency for Healthcare Research and Quality (AHRQ) from 2008 to 2020 to calculate nationally weighted estimates for both conditions by ICD-9 and ICD-10 diagnosis codes. We used several statistical measures, including descriptive statistics with design-based chi-square and *t*-tests, trend analysis with Cochran-Armitage test, generalized linear models, and other data preprocessing measures.

Check for updates

OPEN ACCESS

EDITED BY
Hiroshi Iwata,
Juntendo University, Japan

REVIEWED BY
Yuichi Chikata,
Juntendo University, Japan
Lisa Smith,
Arizona State University, United States

*CORRESPONDENCE
Mohammad Alfrad Nobel Bhuiyan
✉ Nobel.Bhuiyan@lsuhs.edu

RECEIVED 06 June 2024
ACCEPTED 09 October 2024
PUBLISHED 28 October 2024

CITATION
Husein A, Boullion J, Hossain MI, Xing D, Khan MTF, Bhuiyan MS, Kolluru GK, Bhuiyan MMR, Goeders NE, Conrad SA, Vanchiere JA, Orr AW, Kevil CG and Bhuiyan MAN (2024) Trends and patterns in pulmonary arterial hypertension-associated hospital admissions among methamphetamine users: a decade-long study.
Front. Cardiovasc. Med. 11:1445193.
doi: 10.3389/fcvm.2024.1445193

**Results:** A significant increase was evident in patients with pulmonary arterial hypertension (PAH) and concurrent methamphetamine use (9.2-fold). Most of the hospitalized patients were males (59.16%), aged 41–64 (45.77%), White (68.64%), from the West (53.09%), with Medicaid (50.48%), and with median income <$25,000. The rate of increase over the period was higher for males (11.8-fold), race (not sure which race; please check and modify), aged 41–64 (11.3-fold), and in the South (15.1-fold). An overall adjusted prevalence ratio (PR) for PAH hospitalizations among concurrent methamphetamine users was 32.19 (CI = 31.19–33.22) compared to non-users. With respective reference categories, the significantly higher PR was evident for males, patients aged 41–64, White, with Medicare, median income <$25,000, all regions compared to Northeast, length of hospital stays, and conditions, including chronic pulmonary disease, diabetes, hypertension, obesity, and peripheral vascular disorders.

**Conclusion:** This study reveals a national overall and demographic-specific trend of increasing PAH with concurrent methamphetamine usage and associated factors. The findings may help to understand the current patterns and identify the vulnerable sociodemographic cohorts for further research and to take appropriate policy measures.

KEYWORDS

**pulmonary arterial hypertension, methamphetamine, substance use disorder, methamphetamine use disorder, disparity**

## 1 Introduction

Pulmonary hypertension is defined as an increase in the mean arterial pressure (MAP) of the lungs by greater than 20 mmHg (1, 2). Cardiopulmonary pathologies that cause an increase of pressure in the lungs are categorized into 5 groups: pulmonary arterial hypertension, pulmonary hypertension due to center heart disease, pulmonary hypertension due to lung disease, pulmonary hypertension due to blood clots in the lungs, and pulmonary hypertension due to unknown causes (3). Pulmonary arterial hypertension (PAH) is one of the most damaging forms of pulmonary hypertension, with an estimated 10.6 per 1 million adults in the US affected (4). PAH is defined as increased MAP in the pulmonary arteries, measured by right heart catheterization, in the absence of cardiac disease, abnormal lung pathology, and thromboembolic causes (5). Increased arterial pressure in PAH causes remodeling of the arterial system, increasing vascular resistance and right ventricular afterload, which may eventually develop into heart failure (6).

PAH is characterized as arterial remodeling in pulmonary vasculature that leads to vasculature resistance, right heart failure, and potential death. The vasculature displays medial hypertrophy and both intimal and adventitial proliferation. These changes may lead to concentric sclerosis from the endothelial cells and pulmonary arterial smooth muscle cells migrating and proliferating, causing endothelial dysfunction and vasoconstriction (7). Endothelial cells can create growth factors that stimulate matrix deposition and smooth muscle hypertrophy, leading to vascular formations called plexiform lesions, the hallmark sign of PAH remodeling (7). Pharmacologic treatments of PAH thus target these specific pathways to resist the vasoconstrictive causes and promote vasodilation (8). The most recent pharmacotherapies focus on targeting pathways such as TGF-B and tyrosine kinases to primarily inhibit the inflammatory cell proliferation in the vasculature (9, 10).

The pathology of drug-induced PAH is similar to idiopathic PAH, with both having plexiform lesions as signs of remodeling (11). Many drug compounds have been associated with PAH, including anorexigens, SSRIs, oral contraceptives, and stimulants. Methamphetamine is a stimulant that has become a focus in PAH research and is now labeled in the "definite" category as a causative agent of PAH. Although the pathology is similar to idiopathic PAH, methamphetamine-induced PAH has been shown to cause severe consequences in long-term damage and functional status (12). Methamphetamine has been shown to have harmful overall effects, such as CNS toxicity, cardiomyopathy, cellular remodeling, and its general addictive quality due to interfering with the long-term production of the brain's dopamine (13–15). Among patients with cardiovascular disease (CVD), patients with prior methamphetamine usage have been shown to develop the disease eight years earlier than patients without prior methamphetamine usage (16). PAH among meth users have also been shown to have significantly higher right atrial pressure and lower stroke volume (17). The national level of methamphetamine-associated cardiac failure has risen since 2002 (18). On the cellular level, a prior study using rat models revealed that methamphetamine can also affect the function of the mitochondria and stimulate autophagy (15). Methamphetamine is now also classified as a substance with numerous physical and psychotic side effects (19) and its usage has increased in mentally vulnerable populations with higher rates of suicidal ideation (20).

A previous study found that 28.9% of patients with "idiopathic PAH" had a history of stimulant use, compared to 3.8% of patients who had PAH due to well-known risk factors, such as genetics, hypertension, arterial disease, or connective tissue disease (11). Pathologic lung samples taken from PAH among meth users showed vascular changes similar to those in other PAH patients, including the plexiform lesions and slit-like vascular channel with occlusive disease. Serotonin has been suspected to be a cause of PAH among meth users due to its ability to stimulate pulmonary smooth muscle cells, causing arterial narrowing and increased pressures (21). With the concerning increases in methamphetamine-related overdose deaths and methamphetamine-related hospitalizations that have led the US to declare methamphetamine an emerging drug threat, it is important to re-examine the trends in PAH with and without methamphetamine use (22–25). Thus, the focus of this study is to analyze the overall trends and demographics of PAH alone in comparison to PAH with concurrent methamphetamine usage.

## 2 Methods

To analyze the yearly trends of PAH and methamphetamine use, this study utilized the National Inpatient Sample, Healthcare Cost and Utilization Project, and Agency for Healthcare Research and Quality (AHRQ) collected between 2008 and 2020. The NIS is the US's largest all-payer inpatient care database, representing about 7 million hospital stays annually. Recent modifications to the NIS improved the sample's representativeness and the accuracy and stability of weighted national estimates. This new approach was also applied to existing data, allowing trend analysis across long periods. The new NIS data is formatted so that every datum corresponds to a unique hospitalization and includes details on more than 100 clinical characteristics, including patient demographics and primary and secondary (up to 24) diagnoses. Using the ICD-9 and ICD-10 codes listed in Supplementary Tables S3, S4 in the supplemental information document, we identified all adults (>18 years of age) hospitalized with a primary or secondary diagnosis of PAH and methamphetamine use and their associated sociodemographic characteristics. All tests have been performed at 5% level of significance and reported Cis are with 95% confidence level. The NIS database was deidentified; hence, our study was exempt from requiring an institutional review board (IRB) approval.

### 2.1 Statistical analysis

For the statistical analysis, we followed the guidelines for the AHRQ. All statistical tests were conducted using the software R (version 4.2.1). Survey-specific statements with hospital and patient-level weights were utilized for national estimates, and trend weight was used to produce national estimates for trend analysis. The NIS year's hospital discharges all used equal discharge weights each year. Thus, the trend weight files were combined with the original NIS files by year and hospital ID. The frequencies and percentages of categorical variables were summarized for unweighted (raw hospital admission data) and weighted (nationally representative data) hospital admissions. We used design-based chi-squared tests for categorical variables, and design-based *t*-tests for continuous variables to account for NIS sample design and sample weight (26). To observe any patterns in the missing data, we employed Little's MCAR (missing completely at random). A nonsignificant *p*-value ($p > 0.05$) was used to detect random missing, and the missing value was less than 5%. Thus, no imputation was performed. We utilized propensity score matching with the nearest neighbor method to match the case and control for methamphetamine users (27). The prevalence ratio and 95% confidence interval were calculated using a generalized linear model with a binomial link function (26). The model was adjusted for gender, age, race, primary payer, median household income, length of hospital stays, region, anemia, arthritis, chronic pulmonary disease, congestive heart failure, coagulopathy, depression, diabetes, liver disease, hypertension, obesity, peripheral vascular disorders, pulmonary circulation disorders, and renal failure. Multicollinearity among the variables was investigated using the variance inflation factor (VIF). We used eta-squared to measure the proportion of the total variability in a dependent variable that is explained by the variability in an independent variable. Eta-squared is calculated by dividing the sum of squares associated with an effect (e.g., treatment) by the total sum of squares (28). The *p*-value was determined by linear trend analysis, and the trend, stratified by age, sex, race, and region, was compared using the Cochran-Armitage trend test. There are existing descriptions of the design and analytical guidelines for NIS data (29, 30). The Healthcare Cost and Utilization Project criteria were followed for performing the analysis (30).

## 3 Results

Between 2008 and 2020, there were 114,177,810 reported hospitalizations for PAH in the US without concurrent usage of methamphetamine and 1,104,142 hospitalizations for PAH with concurrent methamphetamine usage.

### 3.1 Demographic characteristics among idiopathic PAH vs. PAH among meth users hospitalizations

Table 1 summarizes the PAH hospitalizations with and without concurrent methamphetamine use in the US between 2008 and 2020. Significantly ($p < 0.05$) more hospitalizations due to idiopathic PAH alone were seen among female patients (51.97%, CI = 51.96–51.98) than among male patients (48.03%, CI = 48.02–48.04). For hospitalizations due to PAH with concurrent methamphetamine, 59.16% (CI = 59.07–59.25) were male, and 40.84% (CI = 40.75–40.93) were female.

Hospitalizations due to PAH without concurrent methamphetamine use were most prevalent among patients older than age 64 (60.60%, CI = 60.69–60.60), followed by ages 41–64 (33.38%, CI = 33.37–33.39), ages 26–40 (4.87%, CI = 4.87–4.87), and ages 18–24 (1.16%, CI = 1.16–1.16). In contrast,

**TABLE 1** Sociodemographic characteristics (weighted) of hospitalized patients with PAH and status of concurrent methamphetamine use from 2008 to 2020 in the US[a].

| Characteristics | Group | PAH with methamphetamine use | | PAH without methamphetamine use | | *p*-value |
|---|---|---|---|---|---|---|
| | | Weighted *n* (%) | (95% confidence interval) | Weighted *n* (%) | (95% confidence interval) | |
| | | *N* = 1,104,142 | | *N* = 114,177,810 | | |
| Sex | Male | 653,076 (59.16) | (59.07–59.25) | 54,835,651 (48.03) | (48.02–48.04) | <0.05 |
| | Female | 450,802 (40.84) | (40.75–40.93) | 59,328,378 (51.97) | (51.96–51.98) | |
| Age | 18–25 years | 117,780 (10.67) | (10.61–10.72) | 1,321,806 (1.16) | (1.16–1.16) | <0.05 |
| | 26–40 years | 414,303 (37.43) | (37.43–37.61) | 5,559,560 (4.87) | (4.87–4.87) | |
| | 41–64 years | 505,367 (45.77) | (45.68–45.86) | 38,109,382 (33.38) | (33.37–33.39) | |
| | ≥65 years | 66,689 (6.04) | (6.00–6.08) | 69,187,059 (60.60) | (60.59–60.60) | |
| Race/ethnicity | White | 7,19,223 (68.64) | (68.56–68.73) | 80,476,632 (75.60) | (75.59–75.61) | <0.05 |
| | Black | 100,189 (9.56) | (9.51–9.62) | 15,043,765 (14.13) | (14.13–14.14) | |
| | Hispanic (ethnicity) | 152,850 (14.59) | (14.52–14.66) | 6,567,027 (6.17) | (6.16–6.17) | |
| | Asian or Pacific Islander | 28,177 (2.69) | (2.66–2.72) | 1,542,218 (1.45) | (1.45–1.45) | |
| | Native American | 19,859 (1.90) | (1.87–1.92) | 577,557 (0.54) | (0.54–0.54) | |
| | Other | 27,452 (2.62) | (2.59–2.65) | 2,241,879 (2.11) | (2.10–2.11) | |
| US Region | Northeast | 41,877 (3.79) | (3.76–3.83) | 21,261,991 (18.62) | (18.61–18.63) | <0.05 |
| | Midwest | 185,691 (16.82) | (16.75–16.89) | 28,820,342 (25.24) | (25.23–25.25) | |
| | South | 290,336 (26.30) | (26.21–26.38) | 44,646,423 (39.10) | (39.09–39.11) | |
| | West | 586,237 (53.09) | (53.0–53.19) | 19,449,051 (17.03) | (17.03–17.04) | |
| Primary payer | Medicare | 202,831 (18.42) | (18.35–18.49) | 75,691,243 (66.40) | (66.39–66.40) | <0.05 |
| | Medicaid | 555,906 (50.48) | (50.39–50.57) | 11,760,803 (10.31) | (10.31–10.32) | |
| | Private Insurance | 133,985 (12.17) | (12.11–12.23) | 20,622,134 (18.09) | (18.08–18.10) | |
| | Self-pay | 148,388 (13.47) | (13.41–13.54) | 2,942,186 (2.58) | (2.58–2.58) | |
| | No charge | 8,259 (0.75) | (0.73–0.77) | 291,847 (0.26) | (0.26–0.26) | |
| | Other | 51,891 (4.71) | (4.67–4.75) | 2,692,341 (2.36) | (2.36–2.36) | |
| Median household income ($) | <25,000 | 376,473 (37.47) | (37.38–37.57) | 34,526,400 (30.84) | (30.83–30.85) | <0.05 |
| | 26,000–50,000 | 289,714 (28.84) | (28.75–28.93) | 30,279,683 (27.05) | (27.04–27.06) | |
| | 51,000–75,000 | 217,979 (21.70) | (21.62–21.78) | 26,260,495 (23.46) | (23.45–23.47) | |
| | 76,000–100,000 | 120,440 (11.99) | (11.93–12.05) | 20,875,638 (18.65) | (18.64–18.66) | |

[a] The designed-based chi-square for categorical variables and *t*-tests for continuous variables were applied to obtain the *p*-values.

hospitalizations due to PAH among meth users were increased among middle-aged patients. The majority occurred at ages 41–64 (45.77%, CI = 45.68–45.86), followed by ages 26–40 (37.52%, CI = 37.43–37.61), ages 18–25 (10.67%, CI = 10.61–10.72), and older than 64 years of age (6.04%, CI = 6.00–6.08).

By race/ethnic group, non-Hispanic White (henceforth White) patients comprised the majority of hospitalizations (75.60%, CI = 75.59–75.61) for PAH alone, followed by non-Hispanic Black (henceforth Black) patients (14.13%, CI = 14.13–14.14). For hospitalizations of PAH with concurrent methamphetamine usage, although White patients retained its majority (68.64%, CI = 68.56–68.73), Hispanic patients were in the next majority group (14.59%, CI = 14.52–14.66), followed by Black patients (9.56%, CI = 9.51–9.62). A similar race was noted between both groups, except PAH hospitalizations among meth users were more commonly attributed to Hispanic patients than Black patients.

Regarding primary payer, the highest amount of hospitalizations (66.40%, CI = 66.39–66.40) due to PAH alone were Medicare patients, followed by private insurance patients (18.09%, CI = 18.08–18.10), Medicaid patients (10.32%, CI = 10.31–10.320, self-pay patients (2.58%, CI = 2.58–2.58), patients with no charge (0.26%, CI = 0.26–0.26), and those who did not report (2.36%, CI = 2.36–2.36). The highest number of hospitalizations due to PAH with concurrent methamphetamine were Medicaid patients (50.48%, CI = 50.39–50.57), followed by Medicare patients (18.42%, CI = 18.35–18.49), self-pay patients (13.47%, CI = 13.41–13.54), private insurance patients (12.17%, CI = 12.11–12.23), patients with no charge (0.75%, CI = 0.73–0.77), and patients who reported "Other" (4.71%, CI = 4.67–4.75).

The hospitalized patients' distribution by primary insurance showed most patients with PAH and without concurrent methamphetamine use had Medicare (66.4%, CI = 66.39–66.40) as their primary insurance compared to Medicaid for PAH with concurrent methamphetamine use (50.48%, CI = 50.39–50.57). Private insurance (18.09%, CI = 18.08–18.10), followed by Medicaid (10.32%, CI = 10.31–10.32), was the second primary insurance source for Patients with PAH alone; for patients with PAH and concurrent methamphetamine, Medicare (18.42%, CI = 18.35–18.49) followed by self-pay patients (13.47%, CI = 13.41–13.54) were the next primary sources.

Regarding US geographic region, the highest number of hospitalizations due to PAH alone were located in the South

United States (39.10%, CI = 39.09–39.11), followed by the Midwest region (25.24%, CI = 25.23–25.25. For hospitalizations of PAH with concurrent methamphetamine usage, patients in the West made up the majority (53.09%, CI = 53.00–53.19), followed by the South (26.30%, CI = 26.21–26.38).

Regarding household income, the number of hospitalizations due to PAH alone was inversely correlated to household income. Among patients with PAH alone, the most significant number of hospitalizations occurred in patients with an income of <$25,000 (30.84%, CI = 30.83–30.85), followed by <$50,000 (27.05%, CI = 27.04–27.06). The highest number of hospitalizations due to PAH with concurrent methamphetamine also followed an inverse correlation, 37.47% (CI = 37.38–37.57) for <$25,000 income, followed by 28.84% (CI = 28.75–28.93) for <$50,000 income.

## 3.2 Temporal trend of pulmonary arterial hypertension hospitalizations without methamphetamine use

Figure 1 exhibits the trends of hospitalizations of patients with PAH without concurrent methamphetamine use. From 2008 to 2020, hospitalizations associated with PAH without concomitant methamphetamine use increased from 7,706,820 to 8,278,579 (1.1-fold, $p = 0.07$). Throughout this period, PAH-related hospitalizations without concomitant methamphetamine use of both male and female patients initially increased from 2008 to 2015 and later fluctuated and down-trended from 2015 to 2020. Female patients showed a higher prevalence every year than male patients; however, male patients had an overall statistically significant ($p < 0.05$) upward trend (1.16-fold increase) compared to the female patient fluctuation ($p = 0.45$, 1-fold increase). Hospitalizations by race significantly increased for all races ($p < 0.05$). White patients had a substantially higher yearly prevalence compared to other races. However, the rate of change was not the highest (1.2-fold), compared to the overall rate of change in Hispanic patients (1.7-fold increase), Black patients (1.6-fold increase), Asian/Pacific Islander (1.4-fold increase), and Native Americans (1.2-fold increase). Patients aged 26–40 and 41–64 had a statistically significant upward trend throughout the years ($p < 0.05$) with overall increases of 1.2-fold and 1.1-fold, respectively). Patients aged 18–25 and greater than 64 years had insignificant trends ($p = 0.05$ and $p = 0.15$, respectively) with an overall decrease (0.8-fold increase). Patients located in the West

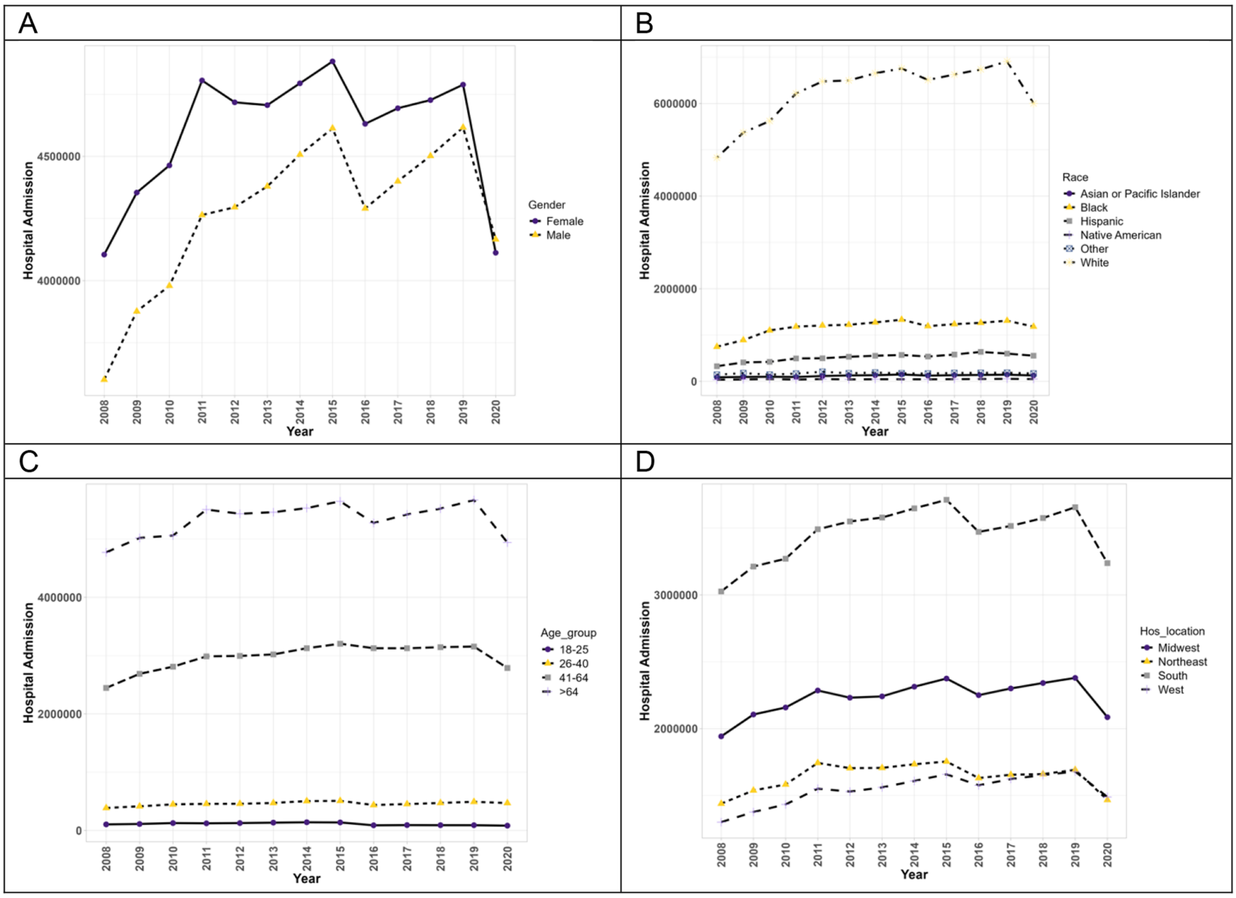

FIGURE 1
The hospitalization trends of PAH patients without concurrent methamphetamine usage by sex (A), race (B), age (C), and geographic region (D) from 2008 to 2020 in the US.

showed the only significant ($p < 0.05$) upward trend of PAH (1.2-fold increase), while the other regions (South, Midwest, and Northeast) showed insignificant trend ($p > 0.05$) with some fluctuations throughout the years (1.1-fold increase, 1.1-fold increase, and 1.1-fold increase, respectively).

## 3.3 Temporal trend of pulmonary arterial hypertension hospitalizations with concurrent methamphetamine use

Figure 2 exhibits the trends of hospitalizations of patients with PAH with concurrent methamphetamine use. From 2008 to 2020, hospitalizations of PAH among meth users increased (9.2-fold) from 21,738 in 2008 to 199,715 in 2020. Throughout this period, hospitalizations of both male and female patients increased significantly ($p < 0.05$). Moreover, male patients of PAH among meth users showed a higher prevalence each year and a higher overall increase throughout the years (11.8-fold increase vs. 6.7-fold increase). Hospitalizations statistically increased for all races ($p < 0.05$). Native American patients had the highest overall increase throughout the years (20.4-fold increase), followed by Black patients (16.4-fold), Hispanic patients (13.9-fold), White patients (10.1-fold), and Asian/Pacific Islander patients (8.5-fold). The trend in race for PAH patients with concurrent methamphetamine use differed slightly from the trend for PAH patients without concurrent methamphetamine use, where Hispanic patients' overall trend was higher than Black patients' overall trend. With respect to hospitalizations by age, the trend differed slightly from PAH patients without methamphetamine use, with all patients showing a statistically significant upward trend throughout the years ($p < 0.05$). Patients aged 41–64 had the highest overall increase (11.3-fold), followed by patients aged 26–40 (9.7-fold), aged 18–25 (5.3-fold), and aged more significant than 64 years (4.7-fold). In terms of geographic regions, PAH patients with concurrent methamphetamine use in all regions of the US showed a statistically significant upward trend ($p < 0.05$), with patients in the South having the highest overall increase throughout the years (15.1-fold increase), followed by Midwest patients (8.4-fold), West patients (8.0-fold increase), and Northeast patients (5.4-fold).

Overall, hospitalizations of PAH among meth users from 2008 to 2020 demonstrated a 1.53 adjusted prevalence ratio (PR) in methamphetamine users compared to non-methamphetamine users (Table 2). When examining mental health disorder-related hospitalizations from 2008 to 2020 with concurrent

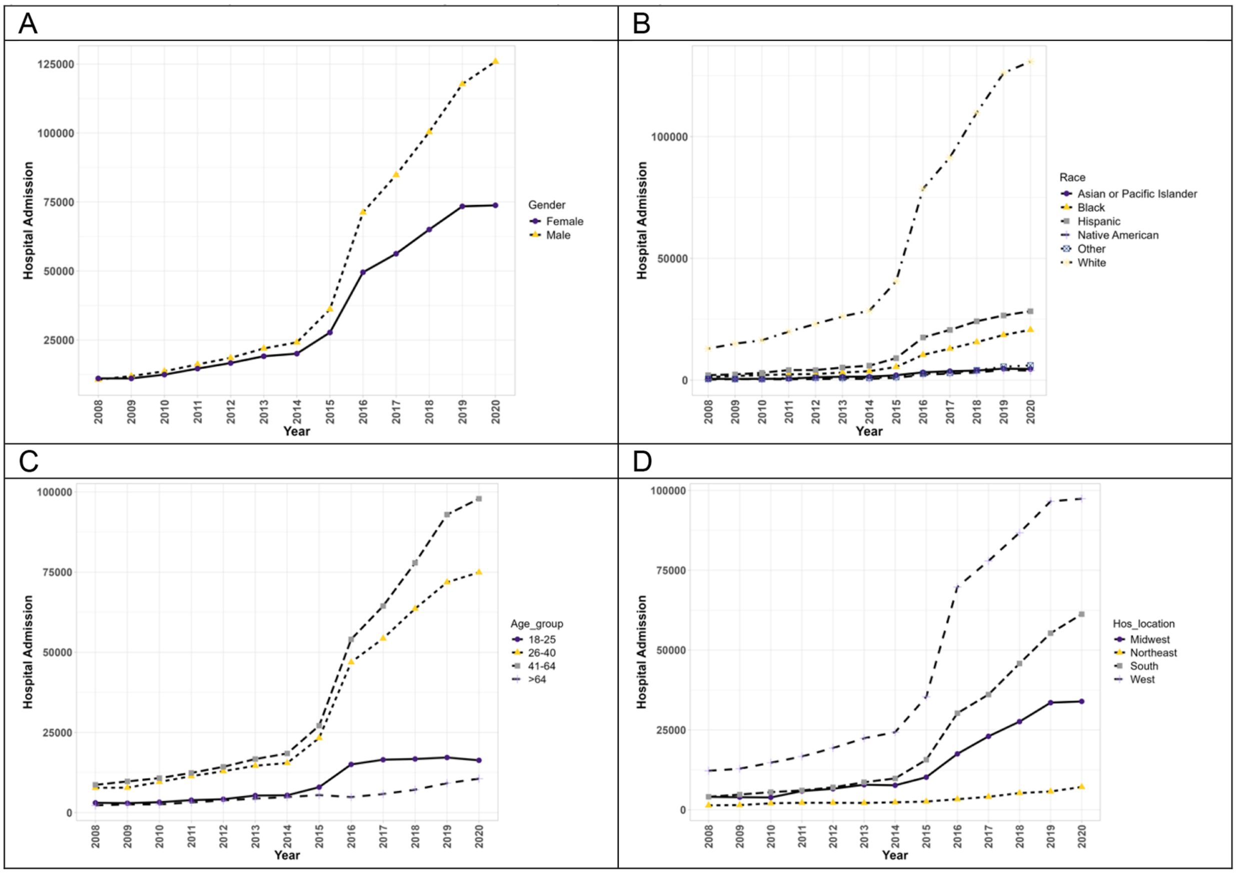

FIGURE 2
The hospitalization trends of PAH patients with concurrent methamphetamine usage by sex (A), race (B), age (C), and geographic region (D) from 2008 to 2020 in the US.

TABLE 2 Adjusted PR of PAH hospitalizations with concurrent methamphetamine use with 95% CI.

| Characteristics | Group | PAH hospitalizations with concurrent methamphetamine use | |
|---|---|---|---|
| | | Adjusted prevalence ratio | 95% confidence interval |
| Methamphetamine user | Yes | 32.19 | (31.19, 33.22) |
| Sex | Male | 1 [Reference] | |
| | Female | 0.77 | (0.72, 0.79) |
| Age | 18–25 years | 0.76 | (0.72–0.80) |
| | 26–40 years | 0.90 | (0.86, 0.95) |
| | 41–64 years | 1.33 | (1.27, 1.40) |
| | ≥65 years | 1 [Reference] | |
| Race/ethnicity | White | 1 [Reference] | |
| | Black | 0.82 | (0.79, 0.84) |
| | Hispanic (ethnicity) | 0.75 | (0.73, 77) |
| | Asian or Pacific Islander | 0.73 | (0.68, 0.77) |
| | Native American | 0.91 | (0.85, 0.97) |
| | Other | 0.81 | (0.77, 0.86) |
| Primary payer | Medicare | 1 [Reference] | |
| | Medicaid | 0.92 | (0.90, 0.95) |
| | Private insurance | 0.63 | (0.61, 0.65) |
| | Self-pay | 0.87 | (0.84, 0.90) |
| | No charge | 0.74 | (0.67, 0.83) |
| | Other | 0.86 | (0.82, 0.91) |
| Median household income($) | <25,000 | 1 [Reference] | |
| | 25,000–50,000 | 0.95 | (0.93, 0.97) |
| | 51,000–75,000 | 0.90 | (0.88, 0.92) |
| | 76,000–100,000 | 0.80 | (0.78, 0.83) |
| US Region | Northeast | 1 [Reference] | |
| | Midwest | 1.51 | (1.42, 1.60) |
| | South | 1.48 | (1.40, 1.57) |
| | West | 1.91 | (1.81, 2.02) |
| Length of hospital stay | 0–3 days | 1 [Reference] | |
| | 4–6 days | 1.32 | (1.29, 1.34) |
| | 7–9 days | 1.41 | (1.37, 1.46) |
| | 10–12 days | 1.34 | (1.28, 1.40) |
| | >12 days | 1.26 | (1.21, 1.31) |
| Chronic pulmonary disease | Yes | 6.00 | (5.84, 6.19) |
| Diabetes | Yes | 1.17 | (1.14, 1.20) |
| Hypertension | Yes | 1.23 | (1.21, 1.26) |
| Obesity | Yes | 1.80 | (1.75, 1.85) |
| Peripheral vascular disorders | Yes | 1.61 | (1.51, 1.70) |

methamphetamine use, female patients showed a higher adjusted PR (1.53, CI = 1.51–1.56) compared to males. Patients aged 18–25 showed the highest adjusted PR, with those aged 26–40 and 41–64 showing a comparable but lower adjusted PR of 0.89 (CI = 0.87–0.92) and 0.71 (CI = 0.69–0.73) compared to patients aged 18–25. White patients showed the highest adjusted PR, with Native American patients showing the next highest adjusted PR (0.73, CI = 0.69–0.78) compared to White patients. When examining household income, those with income of $50,000–64,999, $65,000–85,999, or >$86,000 showed a similar adjusted PR of 1.02 (CI = 1–1.04), 1.06 (CI = 1.03–1.08) and 1.09 (CI = 1.06–1.12), respectively compared to those with household income <$50,000. When examining regions, the Midwest showed the highest adjusted PR (1.24, CI = 1.18–1.30) compared to the Northeast, with the South showing a similar adjusted PR (0.90, CI = 0.86–0.95) compared to the Northeast.

An overall adjusted prevalence ratio (PR) for PAH hospitalizations among concurrent methamphetamine users was 32.19 (CI = 31.19–33.22) compared to non-users (Table 2). Female patients showed a lower adjusted PR (0.77, CI = 0.72–0.79) than males. Patients aged 41–64 showed the highest adjusted PR (1.33, CI = 1.27–1.40) compared to the reference cohort 65 years or older, and those aged 26–40 and 41–64 showed lower adjusted PRs of 0.90 (CI = 0.86–0.95) and 0.71 (CI = 0.69–0.73), respectively. Compared to White patients, other races showed lower PRs ranging from 0.73 to 0.91. With the increase in patients' income, the PR decreases. Compared to patients' median income of less than $25,000, the PR for the highest median income of $76,000–100,000 was 0.80 (CI = 0.78–0.83). By regions, the West showed the highest adjusted PR of 1.91 (CI = 1.81–2.02), followed by the Midwest of 1.51 (CI = 1.42–1.60) and the South of 1.48 (CI = 1.40–1.57) compared to the Northeast. Patients with other insurances showed significantly lower PRs, ranging from 0.63 to 0.92, compared to Medicare as the primary source of insurance. With the increase in hospital stays, the PRs were also increased significantly.

Chronic pulmonary disease is associated with increasing prevalence 6 times (CI = 5.84–6.19). Similarly, the history of diabetes (PR = 1.17, CI = 1.14–1.20), hypertension (PR = 1.23, CI = 1.21–1.26), obesity (PR = 1.80, CI = 1.75–1.85) and peripheral vascular disorders (PR = 1.61, CI = 1.51–1.70) were also associated with increasing prevalence.

## 4 Discussion

According to NIS data from 2008 to 2020, a total of 0.9% of PAH hospitalizations were concurrent methamphetamine users. During this period, there has been a significant overall increase in hospitalizations of PAH among meth users (9.2-fold). For PAH hospitalizations alone, the overall increase was only 1.1-fold and not statistically significant, likely due to the large decline in hospitalizations for PAH alone in 2015 and 2019. The disparity seen between the increases in PAH-related hospitalizations with concurrent methamphetamine use compared to those without concurrent methamphetamine use are paralleled by the increasing widespread use of methamphetamine in the US (31) and overall increase in drug use-related hospital admissions in the nation (32), suggesting that, in this patient population, the increase in methamphetamine use is contributory to the increase in PAH-related hospitalizations. The demographic groups that had the highest overall prevalence in PAH hospitalizations without concurrent methamphetamine use from 2008 to 2020 were patients who are White, female, those older than age 64, those in the Southern US, Medicare patients, and those with a salary of less than $25,000.

The results showed a significant disparity in the prevalence of hospitalizations within each demographic. These disparities are consistent in a previous methamphetamine study that solely focused on the differing demographics of methamphetamine users in the US in the same ten-year time frame (33). Previous studies analyzing the demographics of idiopathic PAH patients show the predominant sex was consistently female and the mean age was 53, but have not analyzed race, geographic region, or financial/insurance statuses (34, 35). The demographic groups that have the highest overall trend but not the highest overall prevalence reveal the change in the epidemiology of methamphetamine use and associated PAH.

Males had a higher overall prevalence of PAH with concurrent methamphetamine use compared to females and a higher overall increase in trend. Previous studies have shown that methamphetamine use occurs more commonly among males than females (36, 37). Studies have also shown that idiopathic PAH has a higher incidence in females due to the effects of estrogen on the cardiovascular system (38). These results of previous studies help to suggest that for this study, methamphetamine use itself is suspected to be responsible for the higher PAH in males. Given the effects of methamphetamine shown to decrease systolic function, the combination of the cardiotoxic effects of PAH and methamphetamine can lead to a significant risk for cardiac failure. With this in mind, it is important for physicians to mainly evaluate male methamphetamine user patients for cardiac function and screen for any risk factors, such as hypertension, diabetes, or hyperlipidemia, that may lead to higher chances of cardiac failure.

Both hospitalizations due to PAH alone and PAH among meth users showed significant differences among age groups. While hospitalizations due to PAH without methamphetamine use were most common in those ages ≥65 years and 41–64 years, hospitalizations due to PAH with methamphetamine use were most common in those 41–64 and 26–40 and least common with those ages ≥65 years. This suggests that when PAH is combined with comorbid methamphetamine use, disease severity is likely greater, as younger patients are being affected. The low prevalence in those aged ≥65 could also suggest that the disease is so severe that survival with both conditions is lower. However, this could be due to decreased prevalence of methamphetamine use in that population. Furthermore, the age group with the highest increase in trend was 41–64, followed by the younger age groups of 26–40 and 18–25, respectively. These increases further our point that comorbid PAH and methamphetamine use are a growing issue and support our idea that these patients are affected at younger ages. This is also likely related to age differences seen in methamphetamine use, as studies have shown that those ages 26–64 make up the majority of methamphetamine users (31, 37). Physicians are more likely to assess for PAH in older patients due to the disease normally occurring with chronic conditions of CAD or dyspneic effects (39). Since methamphetamine use prevalence is highest in the middle-aged population, younger patients with methamphetamine use should be counseled on their higher PAH risk compared to the general population.

White patients had the highest prevalence of PAH with concurrent methamphetamine use. For PAH alone, there are different pathogenic causes for PAH development among each race. White patients are more likely to develop PAH from genetics or drug/toxin use. Hispanic patients are more likely to develop PAH from congenital heart disease, and Black patients from connective tissue disease (40). Thus, White patients are expected to have the highest prevalence of drug-induced PAH in the US. However, regarding overall trend rather than prevalence, Native American patients had the highest overall increase from 2008 to 2020 in the US. These results highlight the epidemiological shift in methamphetamine usage. Although historically, methamphetamine has been primarily used by White persons, the drug is becoming increasingly more popular in other racial groups, such as those who are Native American. Previous studies have shown that methamphetamine use is higher among those who are Native American than any other racial group in the United States, with an earlier onset age as well, which may explain the reason for Native American patients having the highest increase in PAH with concurrent methamphetamine use (41). Cardiovascular disease is one of the highest causes of mortality among the Native American population (42). With this already high risk, it is important to be aware of the potential cardiovascular danger in Native American methamphetamine users.

The South had an overall higher prevalence of PAH without concurrent methamphetamine usage, while the West had the highest overall prevalence of PAH with concurrent methamphetamine usage. This aligns with previous studies that have shown overall higher PAH among meth users in the general southwestern region of the US (43). However, in terms of the trends in PAH hospitalizations with concurrent methamphetamine use from 2008 to 2020 in the US, the South had the highest overall trend increase, which may correlate with the rise of illicit drug use in formerly low prevalence areas (44). The South United States has been shown to have a higher prevalence of a multitude of chronic diseases that increase morbidity, including obesity, diabetes, hypertension, and cardiovascular disease. With methamphetamine's damaging cardiovascular effects, the increase in the overall methamphetamine trend in the South can worsen a population already vulnerable to cardiovascular disease (45).

Physicians can incorporate this knowledge as they counsel patients about drug use, including patients with no current risk factors who may simply have demographic or social risk factors. Physicians should be educated both on the signs and symptoms of methamphetamine use and PAH to know when a drug screening may be necessary. Acute symptoms of methamphetamine include increased energy, euphoria, decreased need for sleep, excessive talking, weight loss, sweating, tightened jaw muscles, grinding teeth, and loss of appetite. Methamphetamine may also cause psychotic symptoms (such as hallucinations, unusual behavior, and suspiciousness), psychomotor symptoms (such as tension, excitability, and motor hyperactivity), and affective symptoms (such as depression or suicidality) (46). On a larger scale, the results of this study can be utilized to understand better the target audience that would most benefit from a drug intervention or education program. Outside of the one-on-one patient interaction, this study reveals the need for an overall national public health movement aimed toward stopping the continuous rise in both PAH and methamphetamine use (44). This public health movement can aim towards educating physicians as well as psychiatric and substance use treatment centers and continuing to track and release records of drug use data. A previous study suggests options for an effective public health solution is data documentation in programs such as the CDC's Overdose Data to Action (OD2A), the State Unintentional Drug Overdose Reporting System (SUDORS), the Drug Overdose Surveillance and Epidemiology (DOSE), or National Drug Early Warning System (NDEWS) (25). These programs support state, territorial, county, or city health department's use of methamphetamine overdose data collection for prevention and response efforts. Overall, our results further support the movement for the documentation, research, and education on PAH among meth users to decrease the national disease trend.

The findings of this study have several important implications for public health policies and interventions. First, the significant increase in PAH hospitalizations among specific sociodemographic groups—particularly Hispanics, males, individuals aged 41–64, and those living in the South—highlights the need for targeted public health campaigns aimed at these vulnerable populations. Proper education and outreach programs can raise awareness about the risks of methamphetamine use and its link to PAH, encouraging preventive behaviors and early intervention. Additionally, these trends suggest the need for more comprehensive healthcare policies that address both substance use and disease management, particularly in regions and demographics most affected. Expanding access to addiction treatment services and ensuring adequate healthcare resources in high-risk communities could help mitigate the growing burden of PAH among methamphetamine users. Moreover, these findings should prompt policymakers to consider revising current strategies and policies related to drug use, healthcare access, and disease prevention. By integrating these insights into national and local health initiatives, public health authorities can better address the dual challenges of substance abuse and its long-term health consequences, ultimately reducing the incidence of PAH and improving health outcomes in at-risk populations.

## 5 Strength and limitations

One of the primary advantages is its large sample size, which enhances the statistical power of studies and allows for more robust and generalizable findings across diverse populations. Additionally, the NIS provides comprehensive coverage of hospitalizations across the United States, capturing data from a wide range of healthcare facilities. This broad representation enables the investigation of national trends and patterns in hospital admissions. Furthermore, the NIS allows for the analysis of a wide variety of health conditions and procedures, facilitating large-scale studies on healthcare utilization, outcomes, and disparities. However, the study also had limitations. One key limitation is that the NIS data primarily focuses on hospitalizations, making it challenging to capture outpatient interactions or post-discharge outcomes, potentially leading to an underrepresentation of overall healthcare utilization and outcomes. Additionally, the inability to identify patients with multiple admissions introduces the possibility of counting the same patient more than once, which could skew the results. Other limitations include potential biases and confounding factors inherent in observational data. For instance, the NIS lacks detailed clinical data, such as specific biological or behavioral factors, that could influence both methamphetamines use and the development of pulmonary arterial hypertension. This introduces the possibility of confounding variables that are not accounted for in the analysis. Future research is necessary to address these gaps by incorporating more detailed clinical data and tracking patients across various care settings.

## Data availability statement

Publicly available datasets were analyzed in this study. This data can be found here: https://hcup-us.ahrq.gov/db/nation/nis/nisdbdocumentation.jsp.

## Author contributions

AH: Writing – original draft, Writing – review & editing. JB: Writing – original draft, Writing – review & editing. MH: Writing – original draft, Writing – review & editing. DX: Writing – original draft, Writing – review & editing. MK: Writing – original draft, Writing – review & editing. MSB: Writing – review & editing. GK: Writing – original draft, Writing – review & editing. MMRB: Writing – original draft, Writing – review & editing. NG: Writing – original draft, Writing – review & editing. SC: Writing – original draft, Writing – review & editing. JV: Writing – original draft, Writing – review & editing. AO: Writing – original draft, Writing – review & editing. CK: Writing – original draft, Writing – review & editing. MANB: Conceptualization, Writing – original draft, Writing – review & editing.

## Funding

The author(s) declare financial support was received for the research, authorship, and/or publication of this article. This work was supported by Institutional Development Award (IDeA) from the National Institutes of General Medical Sciences of the NIH under grant number P20GM121307 to MANB, National Institutes of Health grants R01HL172970, R01HL145753, R01HL145753-01S1, and R01HL145753-03S1 to MSB; and R01HL149264 to CK; NIH R01HL173972, R01HL098435, R01HL133497, R01HL141155 to AO; and Institutional Development Award (IDeA) from the National Institutes of General Medical Sciences of the NIH under grant number P20GM121307 to CK. The project was partially supported by the Ike Muslow, MD Endowed Chair in Healthcare Informatics of LSU Health Sciences Center Shreveport.

## Conflict of interest

The authors declare that the research was conducted in the absence of any commercial or financial relationships that could be construed as a potential conflict of interest.

## Publisher's note

## Supplementary material

The Supplementary Material for this article can be found online at: https://www.frontiersin.org/articles/10.3389/fcvm.2024.1445193/full#supplementary-material

## References

1. Naeije R, Richter MJ, Rubin LJ. The physiological basis of pulmonary arterial hypertension. *Eur Respir J.* (2022) 59:2102334. doi: 10.1183/13993003.02334-2021

2. Santos-Gomes J, Gandra I, Adao R, Perros F, Bras-Silva C. An overview of circulating pulmonary arterial hypertension biomarkers. *Front Cardiovasc Med.* (2022) 9:924873. doi: 10.3389/fcvm.2022.924873

3. Bousseau S, Sobrano Fais R, Gu S, Frump A, Lahm T. Pathophysiology and new advances in pulmonary hypertension. *BMJ Med.* (2023) 2:e000137. doi: 10.1136/bmjmed-2022-000137

4. Ruopp NF, Cockrill BA. Diagnosis and treatment of pulmonary arterial hypertension. *JAMA.* (2022) 327:1379–91. doi: 10.1001/jama.2022.4402

5. Montani D, Seferian A, Savale L, Simonneau G, Humbert M. Drug-induced pulmonary arterial hypertension: a recent outbreak. *Eur Respir Rev.* (2013) 22:244–50. doi: 10.1183/09059180.00003313

6. Luna-Lopez R, Ruiz Martin A, Escribano Subias P. Hipertensión arterial pulmonar. *Med Clin (Barc).* (2022) 158:622–9. doi: 10.1016/j.medcli.2022.01.003

7. Kolaitis NA, Zamanian RT, de Jesus Perez VA, Badesch DB, Benza RL, Burger CD, et al. Clinical differences and outcomes between methamphetamine-associated and idiopathic pulmonary arterial hypertension in the Pulmonary Hypertension Association Registry. *Ann Am Thorac Soc.* (2021) 18:613–22. doi: 10.1513/AnnalsATS.202007-774OC

8. Alamri AK, Ma CL, Ryan JJ. Novel drugs for the treatment of pulmonary arterial hypertension: where are we going? *Drugs.* (2023) 83:577–85. doi: 10.1007/s40265-023-01862-z

9. Hoeper MM, Badesch DB, Ghofrani HA, Gibbs JSR, Gomberg-Maitland M, McLaughlin VV, et al. Phase 3 trial of sotatercept for treatment of pulmonary arterial hypertension. *N Engl J Med.* (2023) 388:1478–90. doi: 10.1056/NEJMoa2213558

10. Montani D, Chaumais MC, Guignabert C, Gunther S, Girerd B, Jais X, et al. Targeted therapies in pulmonary arterial hypertension. *Pharmacol Ther.* (2014) 141:172–91. doi: 10.1016/j.pharmthera.2013.10.002

11. Orcholski ME, Yuan K, Rajasingh C, Tsai H, Shamskhou EA, Dhillon NK, et al. Drug-induced pulmonary arterial hypertension: a primer for clinicians and scientists. *Am J Physiol Lung Cell Mol Physiol.* (2018) 314:L967–83. doi: 10.1152/ajplung.00553.2017

12. Charoenpong P, Dhillon N, Murnane K, Goeders N, Hall N, Keller C, et al. Methamphetamine-associated pulmonary arterial hypertension: data from the national biological sample and data repository for pulmonary arterial hypertension (PAH biobank). *BMJ Open Respir Res.* (2023) 10. doi: 10.1136/bmjresp-2023-001917

13. Ali S, Al-Yafeai M, Hossain I, Bhuiyan MS, Duhan S, Aishwarya R, et al. Trends in peripheral artery disease and critical limb ischemia hospitalizations among cocaine and methamphetamine users in the United States: a nationwide study. *Front Cardiovasc Med.* (2024) 11:1412867. doi: 10.3389/fcvm.2024.1412867

14. Al-Yafeai Z, Ali S, Brown J, Venkataraj M, Bhuiyan MS, Faisal ASM, et al. Cardiomyopathy-associated hospital admissions among methamphetamine users: geographical and social disparities. *JACC Adv.* (2024) 3(7):100840. doi: 10.1016/j.jacadv.2024.100840

15. Abdullah CS, Remex NS, Aishwarya R, Nitu S, Kolluru GK, Traylor J, et al. Mitochondrial dysfunction and autophagy activation are associated with cardiomyopathy developed by extended methamphetamine self-administration in rats. *Redox Biol.* (2022) 58:102523. doi: 10.1016/j.redox.2022.102523

16. Batra V, Murnane KS, Knox B, Edinoff AN, Ghaffar Y, Nussdorf L, et al. Early onset cardiovascular disease related to methamphetamine use is most striking in individuals under 30: a retrospective chart review. *Addict Behav Rep.* (2022) 15:100435. doi: 10.1016/j.abrep.2022.100435

17. Zamanian RT, Hedlin H, Greuenwald P, Wilson DM, Segal JI, Jorden M, et al. Features and outcomes of methamphetamine-associated pulmonary arterial hypertension. *Am J Respir Crit Care Med.* (2018) 197:788–800. doi: 10.1164/rccm.201705-0943OC

18. Dickson SD, Thomas IC, Bhatia HS, Nishimura M, Mahmud E, Tu XM, et al. Methamphetamine-associated heart failure hospitalizations across the United States: geographic and social disparities. *J Am Heart Assoc.* (2021) 10:e018370. doi: 10.1161/JAHA.120.018370

19. Prakash MD, Tangalakis K, Antonipillai J, Stojanovska L, Nurgali K, Apostolopoulos V. Methamphetamine: effects on the brain, gut and immune system. *Pharmacol Res.* (2017) 120:60–7. doi: 10.1016/j.phrs.2017.03.009

20. Xing DG, Horan T, Bhuiyan MS, Faisal ASM, Densmore K, Murnane KS, et al. Social-geographic disparities in suicidal ideations among methamphetamine users in the USA. *Psychiatry Res*. (2023) 329:115524. doi: 10.1016/j.psychres.2023

21. Ramirez RL 3rd, Perez VJ, Zamanian RT. Methamphetamine and the risk of pulmonary arterial hypertension. *Curr Opin Pulm Med*. (2018) 24:416–24. doi: 10.1097/MCP.0000000000000513

22. US Congress. *Methamphetamine Response Act of 2021*. (2022).

23. Office of National Drug Control Policy. *Plan to address methamphetamine supply, use, and consequences*. (2022). Available online at: https://www.congress.gov/bill/117th-congress/senate-bill/854#:~:text=Shown%20Here%3A-,Public%20Law%20No%3A%20117%2D99,(03%2F14%2F2022)&text=This%20bill%20designates%20methamphetamine%20as,implement%20a%20methamphetamine%20response%20plan (accessed January 01, 2023).

24. Han B, Compton WM, Jones CM, Einstein EB, Volkow ND. Methamphetamine use, methamphetamine use disorder, and associated overdose deaths among US adults. *JAMA Psychiatry*. (2021) 78:1329–42. doi: 10.1001/jamapsychiatry.2021.2588

25. Jones CM, Houry D, Han B, Baldwin G, Vivolo-Kantor A, Compton WM. Methamphetamine use in the United States: epidemiological update and implications for prevention, treatment, and harm reduction. *Ann N Y Acad Sci*. (2022) 1508:3–22. doi: 10.1111/nyas.14688

26. Bitsko RH, Claussen AH, Lichstein J, Black LI, Jones SE, Danielson ML, et al. Mental health surveillance among children—United States, 2013–2019. *MMWR Suppl*. (2022) 71:1–42. doi: 10.15585/mmwr.su7102a1

27. Chomchai C, Chomchai S. Global patterns of methamphetamine use. *Curr Opin Psychiatry*. (2015) 28:269–74. doi: 10.1097/YCO.0000000000000168

28. Maher JM, Markey JC, Ebert-May D. The other half of the story: effect size analysis in quantitative research. *CBE Life Sci Educ*. (2013) 12:345–51. doi: 10.1187/cbe.13-04-0082

29. Khera R, Krumholz HM. With great power comes great responsibility: big data research from the National Inpatient Sample. *Circ Cardiovasc Qual Outcomes*. (2017) 10:e003846. doi: 10.1161/CIRCOUTCOMES.117.003846

30. Khera R, Pandey A, Kumar N, Singh R, Bano S, Golwala H, et al. Variation in hospital use and outcomes associated with pulmonary artery catheterization in heart failure in the United States. *Circ Heart Fail*. (2016) 9:e003226. doi: 10.1161/CIRCHEARTFAILURE.116.003226

31. Jones CM, Olsen EO, O'Donnell J, Mustaquim D. Resurgent methamphetamine use at treatment admission in the United States, 2008–2017. *Am J Public Health*. (2020) 110:509–16. doi: 10.2105/AJPH.2019.305527

32. Mazumder S, Khan MTF, Bhuiyan MAN, Kiser H. Historical trends of admitted patients by selected substances and their significant patient's level factors. *Addict Behav*. (2020) 109:106478. doi: 10.1016/j.addbeh.2020.106478

33. Bhuiyan MS, Faisal ASM, Venkataraj M, Goeders NE, Bailey SR, Conrad SA, et al. Disparities in prevalence and trend of methamphetamine-associated cardiomyopathy in the United States. *J Am Coll Cardiol*. (2023) 81:1881–3. doi: 10.1016/j.jacc.2023.03.382

34. Maron BA, Abman SH, Elliott CG, Frantz RP, Hopper RK, Horn EM, et al. Pulmonary arterial hypertension: diagnosis, treatment, and novel advances. *Am J Respir Crit Care Med*. (2021) 203:1472–87. doi: 10.1164/rccm.202012-4317SO

35. Levine DJ. Pulmonary arterial hypertension: updates in epidemiology and evaluation of patients. *Am J Manag Care*. (2021) 27:S35–41. doi: 10.37765/ajmc.2021.88609

36. Han BH, Palamar JJ. Multimorbidity among US adults who use methamphetamine, 2015–2019. *J Gen Intern Med*. (2022) 37:1805–7. doi: 10.1007/s11606-021-06910-6

37. Palamar JJ, Han BH, Keyes KM. Trends in characteristics of individuals who use methamphetamine in the United States, 2015–2018. *Drug Alcohol Depend*. (2020) 213:108089. doi: 10.1016/j.drugalcdep.2020.108089

38. Mair KM, Johansen AK, Wright AF, Wallace E, MacLean MR. Pulmonary arterial hypertension: basis of sex differences in incidence and treatment response. *Br J Pharmacol*. (2014) 171:567–79. doi: 10.1111/bph.12281

39. Rothbard N, Agrawal A, Fischer C, Talwar A, Sahni S. Pulmonary arterial hypertension in the elderly: clinical perspectives. *Cardiol J*. (2020) 27:184–93. doi: 10.5603/CJ.a2018.0096

40. Cansu DU, Korkmaz C. Pulmonary hypertension in connective tissue diseases: epidemiology, pathogenesis, and treatment. *Clin Rheumatol*. (2023) 42:2601–10. doi: 10.1007/s10067-022-06446-y

41. Coughlin LN, Lin LA, Jannausch M, Ilgen MA, Bonar EE. Methamphetamine use among American Indians and Alaska natives in the United States. *Drug Alcohol Depend*. (2021) 227:108921. doi: 10.1016/j.drugalcdep.2021.108921

42. Eberly LA, Shultz K, Merino M, Brueckner MY, Benally E, Tennison A, et al. Cardiovascular disease burden and outcomes among American Indian and Alaska native medicare beneficiaries. *JAMA Netw Open*. (2023) 6:e2334923. doi: 10.1001/jamanetworkopen.2023.34923

43. Dubroff J, Melendres L, Lin Y, Beene DR, Ketai L. High geographic prevalence of pulmonary artery hypertension: associations with ethnicity, drug use, and altitude. *Pulm Circ*. (2020) 10:2045894019894534. doi: 10.1177/2045894019894534

44. Gonzales R, Mooney L, Rawson RA. The methamphetamine problem in the United States. *Annu Rev Public Health*. (2010) 31:385–98. doi: 10.1146/annurev.publhealth.012809.103600

45. Hall WD, Ferrario CM, Moore MA, Hall JE, Flack JM, Cooper W, et al. Hypertension-related morbidity and mortality in the southeastern United States. *Am J Med Sci*. (1997) 313:195–209. doi: 10.1097/00000441-199704000-00002

46. Paulus MP, Neurobiology SJ, Presentation C. Neurobiology, clinical presentation, and treatment of methamphetamine use disorder. *JAMA Psychiatry*. (2020) 77:959–66. doi: 10.1001/jamapsychiatry.2020.0246

# Frontiers in
# Cardiovascular Medicine

**Innovations and improvements in cardiovascular treatment and practice**

Focuses on research that challenges the status quo of cardiovascular care, or facilitates the translation of advances into new therapies and diagnostic tools.

---

## Discover the latest Research Topics

See more →

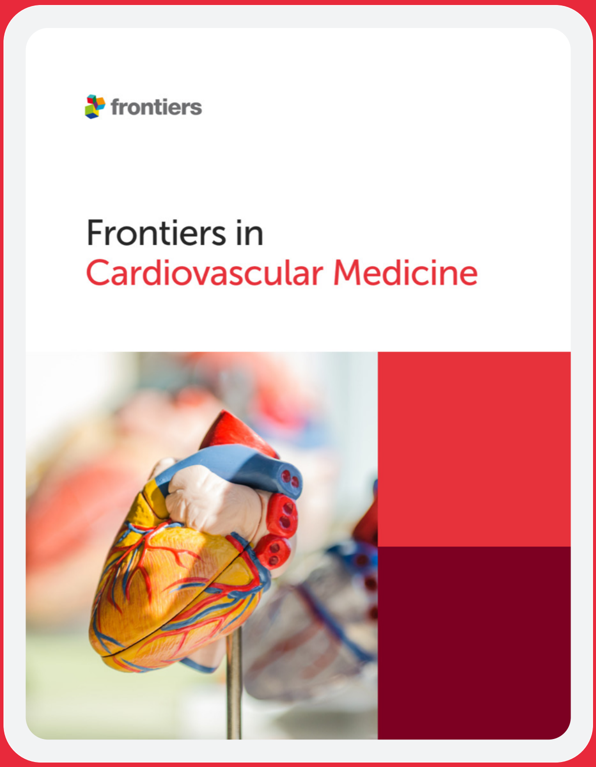

**Frontiers**

Avenue du Tribunal-Fédéral 34
1005 Lausanne, Switzerland
frontiersin.org

**Contact us**

+41 (0)21 510 17 00
frontiersin.org/about/contact